

SCHOLARLY PUBLICATIONS

*A CURRENT AWARENESS BULLETIN
OF RESEARCH OUTPUT*

@DTU

(36th Edition)

DECEMBER 2015

BY: CENTRAL LIBRARY

DELHI TECHNOLOGICAL UNIVERSITY

(FORMERLY *DELHI COLLEGE OF ENGINEERING*)

GOVT. OF N.C.T. OF DELHI

SHAHBAD DAULATPUR, MAIN BAWANA ROAD

DELHI 110042

PREFACE

This is the **Thirty Sixth** Issue of Current Awareness Bulletin started by Delhi Technological University, Central Library. The aim of the bulletin is to compile, preserve and disseminate information published by the faculty, students and alumni for mutual benefits. The bulletin also aims to propagate the intellectual contribution of Delhi Technological University (DTU) as a whole to the academia.

The bulletin contains information resources available in the internet in the form of articles, reports, presentations published in international journals, websites, etc. by the faculty and students of DTU. The publications of faculty and student which are not covered in this bulletin may be because of the reason that the full text either was not accessible or could not be searched by the search engine used by the library for this purpose.

The learned faculty and students are requested to provide their uncovered publications to the library either through email or in CD, etc to make the bulletin more comprehensive.

This issue contains the information published during **December 2015**. The arrangement of the contents is alphabetical. The full text of the article which is either subscribed by the university or available in the web is provided in this bulletin.

Central Library

CONTENTS

1. A Dc/Dc Modular Current-Source Differential-Mode Inverter, Priyadharshini T. Sivasubramanian, Sudip K. Mazumder, Harshit Soni, **8.1.Ankit Gupta & 8.1.Nikhil Kumar**, Electrical Engineering, DTU
2. A Low Power High Gain Low Noise Amplifier for Wireless Applications, **3.P. K. Verma & 3.Priyanka Jain**, Electronics and Communication Engineering, DTU
3. A Review of Spectral Unmixing Techniques in Target Detection, **6.Amrita Bhandari & 3.Dr. K.C. Tiwari**, Civil Engineering, DTU
4. An Investigation into the Factors Affecting the Consumer's Behavioral Intention towards Mobile Coupon Redemption, **3.Harsh Agarwal** and **3.Syed Fazal Karim**, DSM, DTU
5. ANCHORING EFFECT IN INVESTMENT DECISION MAKING- A SYSTEMATIC LITERATURE REVIEW, **6.Priya Kansal & 3.Dr. Seema Singh**, Humanities, DTU
6. Assessment of Fixed Bed Column Reactor using Low Cost Adsorbent (Rice Husk) for Removal of Total Dissolved Solids, **3.S.K.Singh & 8.Neha Narwal**, Environmental Engineering, DTU
7. Catalytic Hydrothermal Liquefaction of Solid Food Waste for Light Bio-oil Production: Process Optimisation, **3.Yahaya Alhassan & 3.Naveen Kumar**, Advanced Studies and Research in Automotive Engineering, DTU
8. CBR VALUE OF SANDY SUBGRADE BLENDED WITH COARSE AGGREGATE, Kesharwani R.S., **3.Sahu A. K.**, Khan N.U, Civil Engineering, DTU

9. Citizen Engagement on Government Facebook Pages: A Study on Select Government Departments, *7.Mohit Solanki, 7.Nishant Guvvada, 7.Nancy Yadav, 7.Narender Dhakerwal & 7.Ripusudan Adhikari*, DSM, DTU
10. Control of Switched-Mode Boost Converter by Using Classical and Optimized Type Controllers, *6.Arnab Ghosh & 8.Subrata Banerjee*, Electrical Engineering, DTU
11. Denovo Designing, Virtual Screening and Lead Optimization of Potential Drug Candidate for Herpes Disease, *3.Monica Sharma, 3.Puneet Rawat and 3.Ankita Mehta*, Biotechnology, DTU
12. Design and Analysis of a High Speed Carry Select Adder, *3.Simarpreet Singh Chawla, 3.Swapnil Aggarwal, 3.Anshika & 3.Nidhi Goel*, Electronics and Communication Engineering, DTU
13. Electron irradiation induced buckling, morphological transformation, and inverse Ostwald ripening in nanorod filled inside carbon nanotube, *6.Anshika Singha, 6.Reetu Kumari, 6.Vinay Kumar, 6.Lucky Krishnia, 6.Zainab Naqvi, 3.Amrish K. Panwar, Umananda M. Bhatta, Arnab Ghosh, P.V. Satyam & 6.Pawan K. Tyagi*, Applied Physics, DTU
14. Hybrid Dynamic MCML style (H-DyCML): A high speed Dynamic MCML style, *3.Neeta Pandey, 3.Damini Garg, Kirti Gupta & 3.Bharat Choudhary*, Electronics and Communication Engineering, DTU
15. Measurement Uncertainty in Airborne Sound Insulation and Single- Number Quantities: Strategy and Implementation in Indian Scenario, *3.N. Garg, A. Kumar and 3.S. Maji*, DTU
16. Modification in Weighted Clustering Algorithm for Faster Clustering Formation by Considering Absolute Attributes of Mobile Nodes and Greedy Method for Role Selection of Mobile Nodes in MANET, *3.Vijayanand Kumar & 3.Rajesh Kumar Yadav* Computer Science and Engineering, DTU

17. Molecular logic operations based on optical detection of sulfur mustard simulant using pyridine appended Mg-porphyrazine complex, **7.1.Neelam**, Vikram Singh, Bhaskaran Shankar, Ramasamy Shanmugam, Satish K. Awasthi & Rinkoo D. Gupta, Polymer Technology, DTU
18. Nanostructured zirconia decorated reduced graphene oxide based efficient biosensing platform for non-invasive oral cancer detection, **3.Suveen kumar**, **3.Jai Gopal Sharma**, **3.Sagar Maji** & **3.Bansi Dhar Malhotra**, Biotechnology, DTU
19. New Generation Antibiotics/Antibacterials: Deadly Arsenal for Disposal of Antibiotic Resistant Bacteria, **3.Monica Sharma**, **3.Shashank Singh** and **3.Sidharth Sharma**, Biotechnology, DTU
20. Non-invasive topical delivery of plasmid DNA to the skin using a peptide carrier Manika Vij, Poornemaa Natarajan, Bijay Ranjan Pattnaik, Shamshad Alam, **3.Nidhi Gupta**, **3.Deenan Santhiya**, Rajpal Sharma, Archana Singh, Kausar M. Ansari, Rajesh S. Gokhale, Vivek T. Natarajan, Munia Ganguli, DTU
21. OTRA BASED R-2R LADDER AND WEIGHTED RESISTOR DAC REALIZATIONS, **3.Rohan Chandra**, **3.Ravi Teja**, **3.Neeta Pandey** & Rajeshwari Pandey, Electronics and Communication Engineering, DTU
22. Oxygen stress: impact on innate immune system, antioxidant defence system and expression of HIF-1 α and ATPase 6 genes in *Catla catla*, Samar Pal Singh **3.JaiGopal Sharma**, Tauqueer Ahmad & Rina Chakrabarti, Biotechnology, DTU
23. Performance Evaluation Of Bandwidth Scheduling Techniques In Passive Optical Networks, **7.1.Dr. Vibhakar Shrimali**, Dr. Manoj Kumar Taneja & Mr. Abhishek Gaur, Electronics and Communication Engineerin, DTU
24. Single CDDBA Based Voltage Mode Bistable Multivibrator and Its Applications, Rishi Pal, **3.Rajeshwari Pandey**, **3.Neeta Pandey** & Ramesh Chandra Tiwari, Electronics and Communication Engineering, DTU

25. Social CRM: An Emerging Medium, *3.Anurag Tiruwa* and *3.Rajan Yadav*, DSM, DTU
26. Sustainable bis-benzoxazines from cardanol and PET derived terephthalamides, 3.Pratibha Sharma,, Bimlesh Lochab, *3.Devendra Kumar* & Prasun Kumar Roy, Applied Chemistry and Polymer Technology, DTU
27. Theoretical modeling of the plasma-assisted catalytic growth and field emission properties of graphene sheet, *3.Suresh C. Sharma* and *3.Neha Gupta*, Applied Physics, DTU
28. Ultrasensitive THz - plasmonics gaseous sensor using doped grapheme, Amrita Purkayastha, *3.1.Triranjita Srivastava* and Rajan Jha, Applied Physics, DTU

1. Vice Chancellor

2. Pro Vice Chancellor

3. Faculty

4. Teaching-cum-Research Fellow

5. Alumni

6. Research Scholar

7. PG Scholar

8. Undergraduate Student

1.1. Ex Vice Chancellor

2.1. Ex Pro Vice Chancellor

3.1. Ex Faculty

6.1. Ex Research Scholar

7.1. Ex PG Scholar

8.1. Ex Undergraduate Student

A Dc/Dc Modular Current-Source Differential-Mode Inverter

Priyadharshini T. Sivasubramanian, Sudip K. Mazumder, *Fellow, IEEE*, Harshit Soni, *IEEE*, Ankit Gupta, *Student Member, IEEE* and Nikhil Kumar, *Student Member, IEEE*

Abstract— A single-stage differential-mode current-fed zero-current-switching inverter has been designed. This inverter has two modules of dc/dc converters that are connected differentially to the input source. This inverter does not require 60-Hz transformer, front-end dc/dc converter, and can boost a low-voltage input to ac output using a compact low-turns-ratio transformer because of the added voltage gain of the topology. Main switches of the inverter are soft-switched. The inverter requires a smaller high-frequency transformer because of high-frequency switching, bipolar transformer current and voltage in every switching cycle, and because the transformer sees only half of the input current. The modularity of the inverter extends the scope of the topology to be used as a dc/dc converter, single-phase inverter, and also the possibility of extending the topology to both split-phase and three-phase. A harmonic compensation control is designed and implemented to reduce the total harmonic distortion of the output waveform using a proportional-resonant controller. The design and analysis of the inverter has been validated using simulation results in saber simulator.

Keywords—*differential-mode; high-frequency link; current source inverter; modulation; renewable/alternative energy; switch-mode power supply (SMPS)*

I. INTRODUCTION

Several single-stage inverters, both isolated and non-isolated inverters have been proposed in the past for applications including solar energy. One of the single-stage topologies outlined in [1] achieves dc/ac conversion by connecting the inputs of two identical dc/dc boost converters in parallel with a dc source and the load is connected across the outputs of the two dc/dc converters. As opposed to a conventional buck voltage source inverter (VSI), this topology can generate an output voltage higher than the input voltage. However, the topology has a non-isolated architecture, the switches operate at a low switching frequency, and the size of the magnetics is large leading to a larger footprint for a non-isolated topology. A differential buck-boost inverter, proposed in [2], operates similar to the differential boost inverter in [1]. This inverter can produce an output voltage either higher or lower than the input dc voltage. Another single-stage buck – boost topology was outlined in [3] and overcomes the disadvantage of small input voltage range of the buck-boost topology proposed in [2]. However, this inverter requires a split input dc voltage source. Two sets of input voltage sources and buck-boost chopper type circuits are connected in anti-parallel to the output capacitor, which generates the output. Both the chopper circuits are operated at fixed-frequency in discontinuous conduction mode (DCM). Both the buck-boost topologies do not provide a high-frequency galvanic isolation and operate at a low switching frequency; however, they have

lower component count. Overall, one of the common challenges with the buck-boost derived topologies is the high peak inductor current stress due to the sudden transfer of energy through the inductors from source to load during each switching cycle. A single-stage flyback inverter topology was described in [4]. It comprised bidirectional flyback converters that are connected in parallel to the input voltage source and the load is connected across the two converters. The major advantage of this topology over the above mentioned topologies is the galvanic isolation provided by the high-frequency transformers in both the flyback converters. However, the galvanic isolation in this topology requires increased foot print. The switches also incur switching losses and hence are limited to low switching frequency operation. In [5], a single-stage full-bridge buck-boost inverter is outlined. Even though the inverter topology has four power switches and two diodes, only two switches are soft switched. Also, the generated sinusoidal waveform consists of quasi-sinusoidal pulses. This topology also does not isolate the source and the load or grid. A single stage buck-boost PWM power inverter is provided in [6]. It has two buck-boost choppers forming a four switch bridge and an additional two more power switches for synchronous commutation in each half cycle of the output. The major advantage of this topology is the galvanic isolation provided by the high-frequency transformer. However, this topology is only suitable for low-power applications with a reported maximum power of 140 W. Finally, another single-stage topology, employing differential Ćuk topology [7] achieves direct dc/ac conversion by connecting the load differentially across two bidirectional dc/dc Ćuk converters and by modulating them sinusoidally with 180 degrees phase difference. This topology utilizes only four main switches, making the inverter topology simple and reducing the cost. The differential Ćuk inverter also has room for magnetics integration, thereby reducing the foot print of the inverter. However, this topology while employing continuous modulation scheme does not employ any loss-mitigating techniques for the main switches and need special care for alleviating voltage spikes.

Several single-stage direct-power-conversion (DPC) architectures proposed in the past [8]-[19] have increased foot print, no galvanic isolation, lower boost capability, stresses in the power switches due to hard switching, stress in the components due to spikes that arise because of difference in the energies between source and the load and are not suitable for medium-power applications. The proposed inverter (shown in Fig. 1b) is based on such a topological approach. It is a differential-mode (Fig. 1b) current-fed zero-current-switching (ZCS) based voltage-doubling PV inverter. This inverter has the following features:

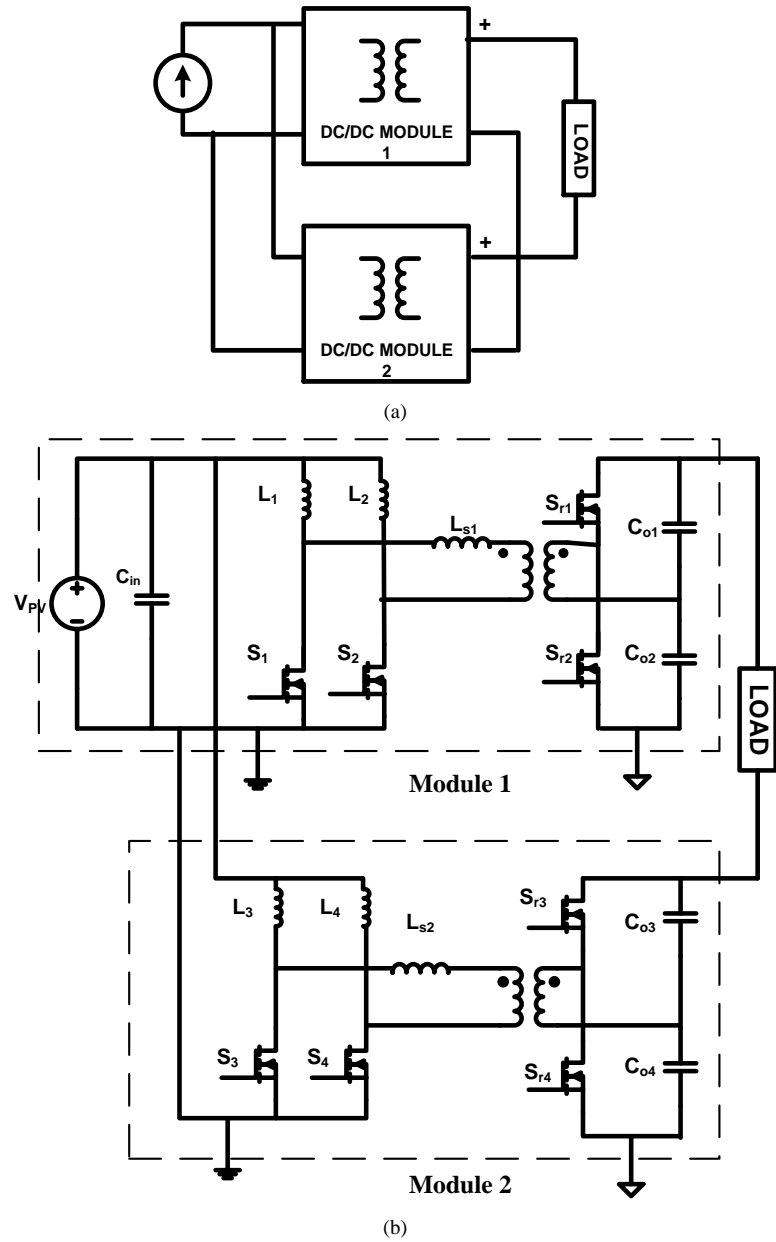


Fig. 1: (a) and (b) Architecture and topology of the proposed differential-mode zero-current-switched (ZCS) inverter.

- Boosts low-voltage (30-60 V) input to a 120-V (RMS)/60-Hz output;
- Does not require a bulky line transformer;
- Does not require a front-end dc/dc converter;
- Has inherent voltage boost/gain property thereby reducing the reliance on the transformer turns ratio;
- Voltage-doubling half-bridge reduces the need to two secondary switches and the transformer turns ratio to half;
- A smaller isolation transformer is needed because the inverter switches at 100 kHz, the transformer voltage and current are bipolar in every switching cycle, and

only half the input current flows through the transformer at any given instant of time;

- Since the operation of the inverter is in differential mode, the ZCS scheme for individual dc/dc converters [20] retains in effectiveness for the inverter.

II. PRINCIPLE OF OPERATION

The basic inverter has two individual dc/dc converter modules as shown in Fig. 1a. The primaries of the two individual dc/dc converters, sourced by the photovoltaic energy source, are connected in differential mode and the output of the proposed current-sourced inverter is the difference of the outputs of the two individual dc/dc converter

modules. Each module has two primary-side switches, namely S_1 and S_2 and S_3 and S_4 and corresponding secondary-side switches S_{r1} and S_{r2} and S_{r3} and S_{r4} respectively. The switching frequency of the inverter is 100 kHz. The switches in each module are modulated so that the individual converters produce a dc-biased sine wave output so that each converter only produces a unipolar voltage. The modulation of each converter is 180° out of phase with the other, so that the voltage excursion at the load is maximized. That is, switch pairs S_1 and S_2 and S_3 and S_4 are operated in the same way but with a phase difference of 180° . Since the load is connected differentially across the converters, the dc-bias appearing at either end of the load with respect to ground gets cancelled and the differential dc voltage across the load is zero. Switch pairs S_1 - S_{r1} , S_2 - S_{r2} , S_3 - S_{r3} , and S_4 - S_{r4} are triggered with complementary pulses. Under hard-switching condition, the output voltages of the individual converters are given by the following equations:

$$V_{o1} = \frac{2nV_{PV}}{1-d_1}, \quad V_{o2} = \frac{2nV_{PV}}{1-d_2}$$

where d_1 and d_2 are the duty ratios of the primary-side switches of the first and second modules, respectively, described in Section III.B. The symbol n represents the turns ratio of the transformers in both the modules. The output voltage of the inverter is the difference in the output voltages of the individual dc/dc converter modules and is given by the following equations:

$$V_o = V_{o1} - V_{o2}, \quad V_o = \frac{2nV_{PV}}{1-d_1} - \frac{2nV_{PV}}{1-d_2},$$

$$V_o = 2nV_{PV} \left[\frac{d_1-d_2}{(1-d_1)(1-d_2)} \right]$$

Let $d_1 = D + D' \sin(\omega t)$ and $d_2 = D - D' \sin(\omega t)$, then the voltage gain of the inverter is given by the following equation:

$$\frac{V_o}{V_{PV}} = 4n \sin(\omega t) \left[\frac{D'}{(1-D)^2 - D'^2 \sin^2(\omega t)} \right]$$

The voltage gain of the inverter depends on the transformer turns ratio and the duty ratio. Thus, an optimum balance between the turns ratio (n) and duty ratio is the key. The primary-side switches have a duty ratio range of 50% to 100%. The inverter cannot be operated below a duty ratio of 50% to avoid a condition of inconsistency in the input inductor currents. Finally, the overall timing sequence of the inverter (shown in Fig. 1a) is illustrated in Fig. 2. Using that as a reference, the hard- and soft-switching modes of the inverter are illustrated.

A) Hard-Switched Inverter Modes

The hard-switched modes of the topology in Fig. 1b are presented in Figs. 3a-3f. When S_1 and S_2 or S_3 and S_4 of each of the modules are turned on simultaneously, the boost mode

of the individual converters is initiated. During this mode, the output capacitors of one module feed energy to the output capacitors of the other module through the load. For all other switching configurations, there is an exchange of power between the primary and secondary of the individual dc/dc converter module as well as from one dc/dc converter module to another. In addition, in these modes, there is a localized charging of output capacitor of one of the dc/dc converter modules. The direction of power flow between the individual modules depends on the time-domain voltage and current waveforms. For instance, for a unity-power-factor passive load, during a positive line cycle of the output voltage (across the load), power flows from the PV source via the upper module to the bottom module while during the negative half cycle, power flows via bottom module to the upper module.

The operation of the inverter in the positive half cycle of the output is analyzed by the following modes:

Mode 1: Fig. 3a represents this hard-switched mode of the inverter. During this interval, the primary-side switches of both the modules, S_1 , S_2 , S_3 and S_4 are turned on. Hence, current in both the transformers is zero. Power to the load is supplied by the output capacitors of the upper module C_{o1} and C_{o2} . The output capacitors of the lower module, C_{o3} and C_{o4} are charged in this mode. The lower dc/dc converter acts as the receiving module in this mode. The input current in the upper and the lower modules from the PV source is given by i_{in1} and i_{in2} , respectively. The currents through the primary-side switches are given by the following equations:

$$i_{s1} = i_{s2} = \frac{i_{in1}}{2}, \quad i_{s3} = i_{s4} = \frac{i_{in2}}{2}$$

Mode 2: Fig. 3b represents this hard-switched mode of the inverter. In this interval, primary-side switches of the upper and the lower module, S_1 and S_3 respectively, and secondary-side switches of the upper and the lower module, S_{r2} and S_{r4} respectively are turned on. The negative current raises through the leakage of the upper module's transformer, L_{s1} and the current through switch S_1 raises with the same slope as the current through L_{s1} . Output capacitor C_{o2} of the upper module is charged and capacitor C_{o1} discharges through the load, C_{o3} and the secondary of the transformer of the lower module. Output capacitor C_{o4} of the lower module is also charged in this mode. The current through the leakage inductance L_{s2} of the transformer in the lower module is positive and begins to increase with the same slope as the current through the leakage inductance L_{s1} . The currents through the primary-side switches and the leakage inductors are given by the following equations:

$$i_{Ls1} = -\frac{V_{o1}}{2nL_{s1}}(\Delta t), \quad i_{Ls2} = \frac{V_{o2}}{2nL_{s2}}(\Delta t),$$

$$i_{s1} = \frac{i_{in1}}{2} + i_{Ls1}, \quad i_{s3} = \frac{i_{in2}}{2} + i_{Ls2}$$

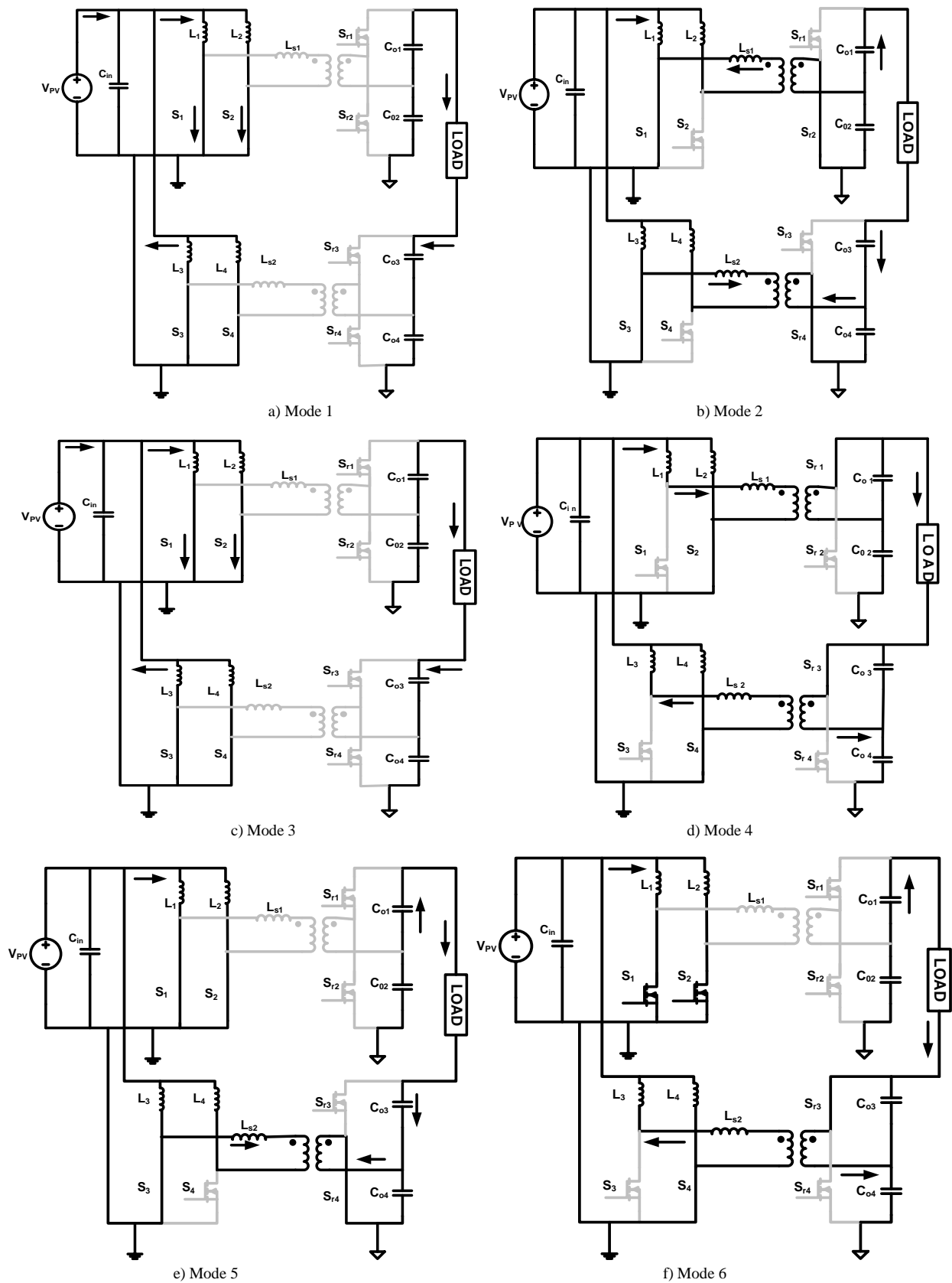


Fig. 3: Hard-switching modes of the inverter shown in Fig. 1b.

where Δt is the time interval for Mode 2.

Mode 3: Fig. 3c represents this hard-switched mode of the inverter. This mode is similar to the mode1 where all of the primary-side switches in both the modules are turned on and all of the secondary-side switches of both the modules are turned off. The current through the transformers in both the modules is zero. The output capacitors of the upper module feed the load and the lower module.

Mode 4: Fig. 3d represents this hard-switched mode of the inverter. In this mode, the primary-side switches of the upper and lower modules, S_2 and S_4 respectively and secondary-side switches of the upper and lower module, S_{r1} and S_{r3} respectively, are turned on. The current through the primary-side switch in the upper module, S_1 in Mode 3 is diverted to L_{s1} due to the voltage across the primary of the upper transformer, which in turn, is due to the voltage across output capacitor of the upper module, C_{o2} . Output capacitors C_{o1} and C_{o3} are charged by the PV source. Output capacitor C_{o2} discharges through the load, the transformers' secondary, and C_{o4} . Current through S_2 and the negative current through L_{s2} rise with the same slope as the current through L_{s1} . The currents through the primary-side switches and the leakage inductors are given by

$$i_{Ls1} = \frac{V_{o1}}{2nL_{s1}}(\Delta t), \quad i_{Ls2} = -\frac{V_{o2}}{2nL_{s2}}(\Delta t),$$

$$i_{s2} = \frac{i_{in1}}{2} + i_{Ls1}, \quad i_{s4} = \frac{i_{in2}}{2} + i_{Ls2}$$

Mode 5: Fig. 3e represents this hard-switched mode of the inverter. In this mode, primary-side switches of the upper module, S_1 and S_2 and primary-side switch of the lower module, S_3 and secondary-side switch of the lower module, S_{r4} are turned on. The current through the transformer in the upper module is zero. Output capacitors of the upper module, C_{o1} and C_{o2} , discharge through the load, output capacitor of the lower module, C_{o3} , and the secondary of the transformer of the lower module. Output capacitor C_{o4} of the lower module is also charged in this mode. The current through the leakage inductance of the lower module, L_{s2} is positive. The currents through switch S_3 and L_{s2} are given by

$$i_{s3} = \frac{i_{in2}}{2} + i_{Ls2}, \quad i_{Ls2} = \frac{V_{o2}}{2nL_{s2}}(\Delta t)$$

Mode 6: Fig. 3f represents this hard-switched mode of the inverter. In this mode, primary-side switches of the upper module, S_1 and S_2 , primary-side switch of the lower module, S_4 , and secondary -side switch of the lower module, S_{r3} are turned on. The current in the transformer of the upper module is zero. Output capacitors of the upper module, C_{o1} and C_{o2} , discharge through the load, secondary of the transformer of the lower module, and capacitor C_{o4} . Output capacitor of the

lower module, C_{o3} is also charged in this mode. The currents through L_{s2} and switch S_4 are given by

$$i_{Ls2} = -\frac{V_{o2}}{2nL_{s2}}(\Delta t), \quad i_{s4} = \frac{i_{in2}}{2} + i_{Ls2}$$

Modes 5 and 6 determine the maximum point and the zero crossing of the output. The zero crossing occurs when difference in the output of the two modules is zero; while the maximum point occurs when the difference of the individual outputs is maximum. The feasible switching states of the inverter are provided in Table. I. The first set of three switching states (i.e. a-c) form major part of a switching cycle. The last set of four switching states (i.e., d-g) exists for a shorter duration and may exist either in the positive half cycle or in the negative half cycle. Switching states, d-g, occur in the vicinity of the maximum, the minimum, or the zero-crossing point of the output voltage.

Table. I: Possible switching states of the inverter under hard-switched operation.

Switching states of the inverter	S_1	S_2	S_3	S_4
a.	1	1	1	1
b.	1	0	1	0
c.	0	1	0	1
d.	1	1	1	0
e.	1	1	0	1
f.	0	1	1	1
g.	1	0	1	1

B) Zero-Current-Switching (ZCS) Inverter Modes

For the ZCS based soft-switched operation, in between the Modes 1-6, every time a primary switch has to be turned off, one secondary switch is also turned on for a very short duration, leading to additional modes, as illustrated in Fig. 4. For instance, secondary-side switch S_{r2} is turned on before the turn off of primary-side switch S_1 in the upper module. The duration for which S_{r2} has to be turned on depends on the current through switch S_1 . The following modes are the additional ZCS modes of the inverter. The ZCS inverter modes build on [24], which addresses dc-dc converter; for the differential-mode inverter outlined in this paper, there are some operational difference since each dc-dc module is subjected to time-varying operation.

Mode 1→2: (Fig. 4a) This mode is introduced to turn off primary-side switches S_2 and S_4 in the top and bottom modules respectively before Mode 2. Secondary -side switches S_{r1} and S_{r3} are turned on to aid ZCS of S_2 and S_4 in Mode 2. When S_{r1} is turned on, voltage across output capacitor C_{o1} is applied across the secondary of the transformer. This causes a voltage at the primary of the transformer and hence the current through switch S_2 is diverted to leakage inductor L_{s1} , allowing the switch to turn off in ZCS condition. The capacitor C_{o2} discharges through the load, C_{o3} , and the secondary of the transformer.

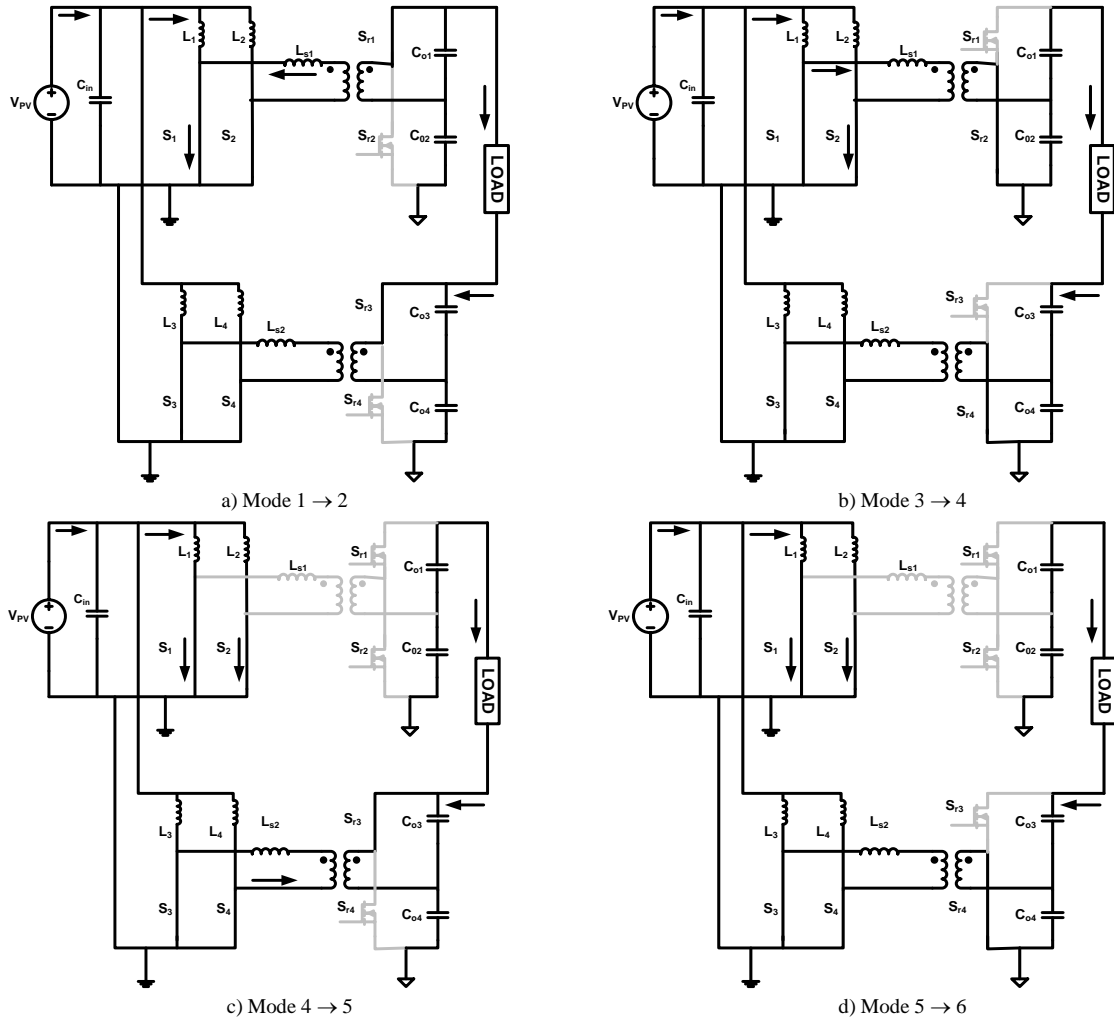


Fig. 4: Soft-switching modes of the inverter shown in Fig. 1b.

Mode 3→4: (Fig. 4b) This mode is introduced to turn off primary-side switches S_1 and S_3 in the top and bottom modules respectively before Mode 4. Secondary-side switches S_{r2} and S_{r4} are turned on to aid ZCS of S_1 and S_3 . When S_{r2} is turned on, the voltage across output capacitor C_{o2} is applied across the secondary of the transformer. This causes a voltage at the primary of the transformer and hence the current through switch S_1 is diverted to leakage inductance L_{s1} , allowing the switch to turn off in ZCS condition. In this mode the capacitor C_{o1} discharges through the load, capacitor C_{o3} and the secondary of the transformer.

Mode 4→5: (Fig. 4c) This mode is introduced to turn off primary-side switch S_4 in the bottom module by turning on secondary-switch S_{r3} before Mode 5. When switch S_{r3} is turned on, the voltage across output capacitor C_{o3} is applied across the secondary of the lower transformer. This causes voltage across the primary of the transformer and hence the current through primary switch S_4 is diverted to leakage inductance L_{s2} . Thus, S_4 turns off in ZCS condition.

Mode 5→6: (Fig. 4d) This mode is introduced to turn off primary-side switch of bottom module S_3 by turning on S_{r4} before Mode 6. When switch S_{r4} is turned on, the voltage across output capacitor C_{o4} is applied across the secondary of the lower transformer. This causes voltage across the primary of the transformer and hence the current through switch S_3 is diverted to leakage inductor L_{s2} , thereby enabling ZCS turn off of the switch S_3 . This additional duty ratio of the secondary side switches is represented as d_r .

III. INVERTER POWER-STAGE DESIGN

The power stage specifications of the differential inverter are as follows:

- Input voltage (V_{pv}): 36 V
- Root-mean-square (RMS) output voltage (V_{rms}): 120 V
- Output power (P_o): 500 W
- Switching frequency (f_s): 100 kHz

The lower limit of the duty ratios of the two modules, d_1 and d_2 is 0.5 to avoid a condition of inconsistency in the currents through the input inductors. For further analysis, the constant offset D is fixed at 0.64 and the upper and lower limits of d_1 and d_2 vary between 0.5 and 0.78. The key factors that influence the design of the inverter are outlined below.

A) Input Inductors

The design of the input inductors for the current-source inverters has important trade-off with regard to the size. The larger the input inductors, the lower the current ripple and hence the photovoltaic average power loss. The input inductors in both the modules are identical. The average energy stored in the inductors is given by the following equation:

$$E_L = \frac{1}{2} L i_L^2$$

where i_L is the current through the input inductor. Larger energy storage (lower current ripple) ensures lower average PV power loss. But, larger the input inductor, the size and losses associated with the inductor also increases. Fig. 5 shows various values of input inductors as a function of input current ripple and size (number of windings for a given wire dimension). The optimum value of input inductor is chosen as 500 μ H.

B) Primary-Side Switches

The primary-side switches S_1, S_2, S_3 and S_4 of both the modules are operated in a sinusoidal manner with a duty ratio range of 50-100% having a constant dc offset. The duty ratios of the primary-side switches are given by the following equations:

$$d_1 = D + D' \sin(\omega t), \quad d_2 = D - D' \sin(\omega t)$$

where D is the constant dc offset in the duty ratios. For the analysis, the dc offset D is fixed and the upper and lower-

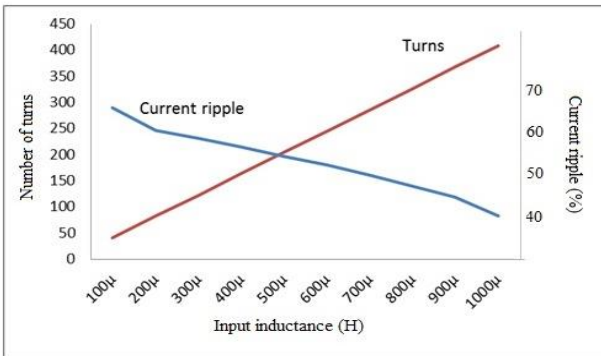


Fig. 5: Input inductor versus input current ripple versus number of turns in the input inductors.

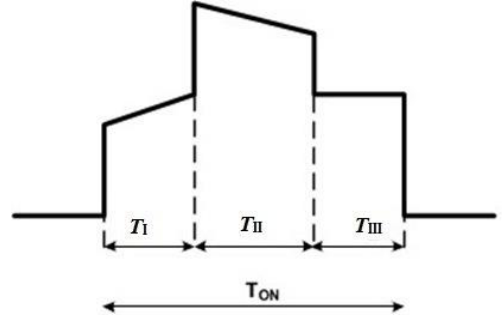


Fig. 6: Current through a primary-side switch.

limits of d_1 and d_2 vary between 0.5 and 0.78. The maximum voltage across the primary-side switches in both the modules is given by the following equations:

$$V_{sw1} = \frac{V_{o1}}{2n}, \quad V_{sw2} = \frac{V_{o2}}{2n}$$

where V_{o1} and V_{o2} are the output voltages at Module 1 and Module 2, respectively. The current through the primary-side switches in both the modules is given by the following the equations:

$$i_{s1} = \frac{i_{in}}{2} + i_{Ls1}, \quad i_{s2} = \frac{i_{in}}{2} + i_{Ls1},$$

$$i_{s3} = \frac{i_{in}}{2} + i_{Ls2}, \quad i_{s4} = \frac{i_{in}}{2} + i_{Ls2}$$

where i_{Ls1} , i_{Ls2} are the currents through the leakage inductances and i_{in} is the current input to the inverter. Fig. 6 shows the current through the primary-side switch during one switching cycle under hard-switching condition. The turn-on time of the switches during one switching cycle can be divided into three intervals for the ease of the analysis, namely T_I , T_{II} and T_{III} . Thus, the duty ratio, d_1 (or d_2) of the primary-side switches can be represented as the following equation:

$$T_{ON} = T_I + T_{II} + T_{III}$$

The switches are modulated such that

$$(1 - T_{ON}) = T_{II}$$

Some important factors that govern the selection of a semiconductor device are the maximum voltage across the switch, the conduction and switching losses, and the switch capacitance. The conduction loss is the energy lost in the switch during the on-state and it depends on the voltage across the switch and the current through it. The power loss associated with a semiconductor device during conduction is given by the following equation:

Table II: Theoretical [21] and Saber simulated values of the conduction losses in the primary-side switches calculated for a 500 W inverter with a 0.64 constant dc off set in duty ratio.

R _{DS(on)} in Ohms	Theoretical projection of conduction loss per primary switch in Watts	Simulated conduction loss per primary switch in Watts
Single 0.02Ω switch	11.493	12.67
Four 0.02 Ω switches in parallel	2.88	3.17

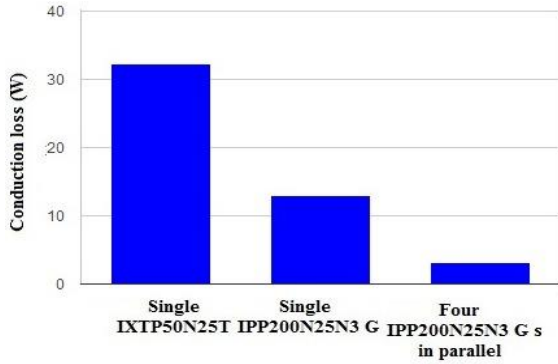


Fig. 7: Conduction loss in the primary-side switches for a 500 W load.

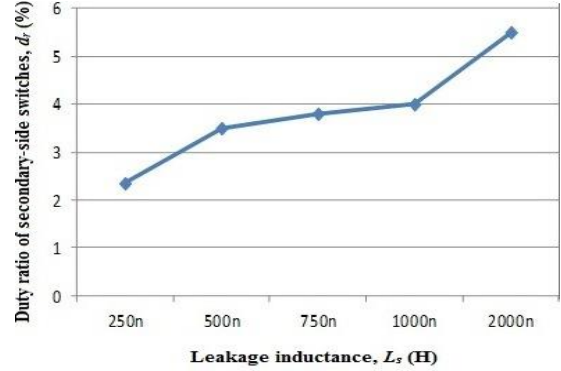


Fig. 8: Duty ratio of secondary-side switches, d_r in percentage as a function of leakage inductance, L_s (for a 500 W load).

$$P_{cond,loss} = \frac{1}{T_{SW}} \int_0^{T_{SW}} r_{on} i_{sw}(t)^2 dt$$

where r_{on} is the on-state resistance of the switch, T_{SW} is the switching period, $i_{sw}(t)$ is the instantaneous value of the current through the switch and $i_{sw,rms}$ is the rms value of the current through the switch.

The RMS current of any one of the primary-side switches in Module 1 and Module 2 are derived as follows:

$$I_{sw,rms,Primary} = \sqrt{\frac{1}{T_{SW}} \left[\int_0^{T_{ON}} (I_{sw})^2 dt + \int_{T_{ON}}^{T_{OFF}} (I_{sw})^2 dt \right]}$$

Between the time interval T_{ON} to T_{OFF} , the switch current is 0. The time interval between 0 to T_{ON} is divided into three intervals. Between the time interval 0 and T_I , the current through the switch is half the input current to the particular module. The switch current between time interval T_I and T_{II} is $(\frac{i_{in1}}{2} + i_{Ls1})$. The switch current between intervals T_{II} and T_{III} is half the input current to the particular module. Further,

$$d_I = \frac{T_I}{T_{SW}}, \quad d_{II} = \frac{T_{II}}{T_{SW}}, \quad d_{III} = \frac{T_{III}}{T_{SW}},$$

Substituting these, the RMS switch current through each primary switch in each module is obtained as follows:

$$i_{sw,rms,Primary1} = \sqrt{\left(\frac{i_{in1}}{2}\right)^2 d_{III} + i_{Ls1}(i_{Ls1} + i_{in1})[d_{II} - d_I]}$$

$$i_{sw,rms,Primary2} = \sqrt{\left(\frac{i_{in2}}{2}\right)^2 d_{III} + i_{Ls2}(i_{Ls2} + i_{in2})[d_{II} - d_I]}$$

where, $i_{sw,rms,Primary1}$ is the rms switch current through each primary-side switch in Module 1, i_{Ls1} is the current through the leakage inductance of the transformer in Module 1, $i_{sw,rms,Primary2}$ is the rms switch current through each primary-side switch in Module 2 and i_{Ls2} is the current through the leakage inductance of the transformer in Module 2.

The chosen switch is IPP200N25N3 G, with an on-state resistance of 20 mΩ, maximum continuous drain current (I_D) of 64 A and drain-source breakdown voltage (V_{DS}) of 250 V. Table II shows the theoretical and simulated conduction loss for the primary switches. Fig. 7 shows the conduction loss in all the primary-side switches for both modules for a single IXP50N25T switch, single IPP200N25N3-G and four IPP200N25N3-G switches in parallel. The switch number IXP50N25T has a 50 mΩ on-state resistance while the chosen switch IPP200N25N3 G has a 20 mΩ on-state resistance.

C) Leakage Inductance

When both the primary-side switches in a module are on, the current through the transformer (or leakage inductance) is

zero. For all other cases, the current through the leakage inductance is given by the following equations:

$$i_{LS1} = \frac{V_o}{2nL_{s1}}(\Delta t), \quad i_{LS2} = \frac{V_o}{2nL_{s2}}(\Delta t)$$

where L_{s1} and L_{s2} are the leakage inductance of Module 1 and Module 2 respectively and n is the transformers' turns ratio. The leakage inductance of the transformer must be designed to divert the current through one of the primary-side switches within the additional ZCS duty ratio (d_r) of the secondary-side switches. The lower limit of the leakage inductance is primarily influenced by the ZCS duty ratio and the load. The difference in the energies between the input inductors and the leakage inductance restricts the use of a higher value of leakage inductance. The leakage inductance of individual modules is given by the following equation:

$$L_s = \frac{V_o d_r}{ni_{in1}f_s}$$

where n is the transformer turns ratio, i_{in1} (i_{in2}) is the input current through Module 1 (Module 2), f_s is the switching frequency of the inverter, V_o is the output voltage and d_r is the soft-switching duty ratio. From the above equation, it can be seen that the leakage inductance affects the soft-switching duty ratio (d_r) and Fig. 8 shows the leakage inductance as a function of the soft-switching range. A leakage inductance of 1 μ H is chosen for the analysis of the inverter.

D) Transformer

Apart from providing a galvanic isolation to the source from the load, the transformer also affects two aspects of the inverter. The transformer's turns ratio influences the conduction losses in the switches and the THD of the output. A higher turns ratio in the transformer reduces the voltage across the switches on the primary side, thereby eliminating the need for higher voltage switches. This reduces the on-state resistance of the primary-side switches, thereby bringing down the conduction losses on the primary-side, where the switches are turned on for a longer duration when compared to those at the secondary-side. On the contrary higher turns ratio results in higher switch current and also increased THD at the load, apart from increasing the size of the magnetics and the transformer losses. One of the major advantages of this topology is that the transformer sees a bipolar voltage and current whose average is zero, thereby reducing the size of the transformer. As the turns ratio increases the loss in the device also increase. From Figs. 9 and 10, an optimum value of n is found to be 2. Fig. 10 shows the conduction losses in primary-side switches as a function of transformer turns ratio.

E) Secondary-Side Switches

The secondary-side switches are operated complementarily to the primary-side switches. When the modules are operated as dc/dc converters, the secondary switches are only turned on

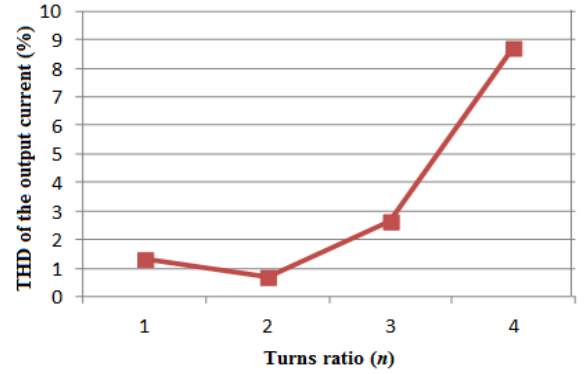


Fig. 9: THD of the output current in percentage versus transformer turns ratio, n (for a 500 W load).

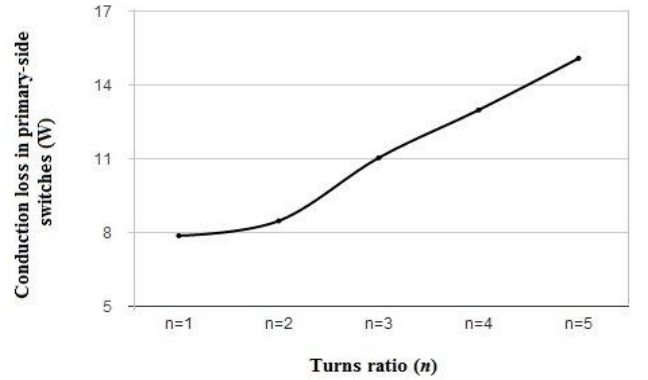


Fig. 10: Conduction losses in a single primary-side switch as a function of the transformer turns-ratio for a 500-W load under soft-switching conditions. Each switch is a single chosen switch having an on-state resistance of 0.02 Ohms.

during the turn off of the primary-side switches (to aid the ZCS of the primary-side switches), whereas in the inverter operation there is considerable conduction loss in the secondary-side switches, since they are turned on for a longer duration. Maximum voltage across the secondary-side switches is V_o . Fig. 11 shows the current through a secondary-side switch during one switching cycle under hard-switched condition. The RMS current of any one of the secondary-side switches in Module 1 and Module 2 are derived as follows:

$$I_{sw,rms,Secondary} = \sqrt{\frac{1}{T_{SW}} \left[\int_0^{T_{ON}} (I_{SW})^2 dt + \int_{T_{ON}}^{T_{OFF}} (I_{SW})^2 dt \right]}$$

Between the time interval T_{ON} to T_{OFF} , the switch current is 0. Between the time interval 0 and T_{ON} , the current through the switch is $\frac{i_{LS}}{n}$. Further, $T_{ON,sec} = 1 - T_{ON,pri}$, where, $T_{ON,pri}$ is the time for which any primary-side switch is turned on and $T_{ON,sec}$ is the time for which its complimentary switch is turned on. Solving further, the RMS current through any secondary-side switch is obtained:

$$i_{rms,Secondary} = \sqrt{\left(\frac{i_{LS}}{n}\right)^2 [1 - d_1]}$$

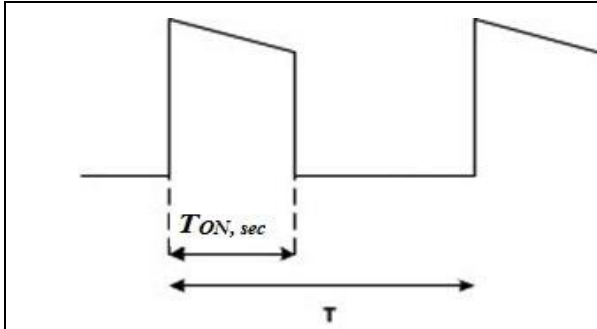


Fig. 11: Current through a secondary-side switch during a switching cycle.

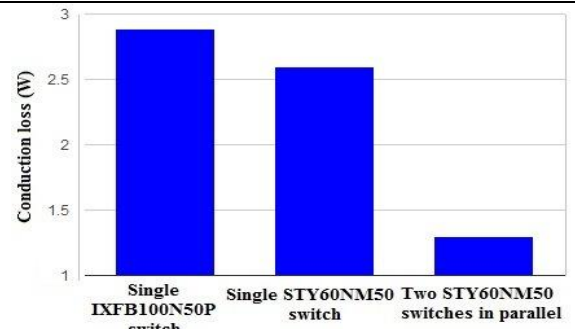


Fig. 12: Conduction loss in the secondary-side switches (for a 500-W load).

Table III: Projected conduction losses in the secondary-side switches are calculated for a 500-W inverter.

$R_{DS(on)}$ in Ohms	Theoretical projection of conduction loss per secondary-side switch in Watts	Simulated conduction loss per secondary-side switch in Watts
Single 0.045Ω switch	2.12	2.6
Two switches in parallel	1.06	1.3

Table IV: Impedances offered by different values of capacitors, for various orders of harmonics of the inverter for a 500-W load.

C_o in μF	X_c at n (Ω)	X_c at $3n$ (Ω)	X_c at $5n$ (Ω)	X_c at $7n$ (Ω)
10	265.2	88.4	53.1	37.9
25	106.1	35.6	21	15.2
50	53	17.7	10.6	7.6
100	26.5	8.8	5.3	3.7

where, i_{Ls} is the current through the leakage inductance of the transformer in any module and d_1 (or d_2) is the duty ratio of the Module 1 (or Module 2). The chosen switch is STY60NM50, with an on-state resistance of 45 mΩ and drain-source breakdown voltage (V_{DS}) of 500 V. Table III shows the theoretical and simulated conduction loss for the secondary-side switches. Fig. 12 shows the conduction loss in all the secondary-side switches for both modules for a switch (IXFB100N50P) with on-state resistance 50 mΩ, single STY60NM50 switch and two STY60NM50 switches in parallel.

F) Output Capacitors

The voltage across the output capacitances is given by the following equations:

$$V_{Co1} = V_{Co2} = \frac{V_{o1}}{2}, \quad V_{Co3} = V_{Co4} = \frac{V_{o2}}{2}$$

where V_{o1} and V_{o2} are the output voltages of the individual modules. Output capacitors are chosen to balance the total harmonic distortion (THD) of the load current as well as aid the control strategy by not forming a low impedance path for the high-frequency components. A larger capacitor mitigates higher-order harmonics at the output. But, a very large output capacitor provides a low impedance path for the fundamental frequency component. For a 500-W load,

Table IV shows the impedances offered by different values of capacitors in open loop for various orders of harmonics. Symbol X_c represents the impedance offered by the output capacitor and n represents the fundamental-frequency, 60 Hz. Fig. 13 shows the rms output voltage of the inverter as a function of the output capacitor.

G) Switching Losses

Switching losses refer to the energy losses that occur during the switching transient as the conducting semiconductor device is changed from on to off state or vice versa. These losses depend on the voltage across the switch during the switching transient, the current through the switch during the transient and the time taken to move from one state to another (or the switching time). The energy associated with the turning on of a switch is given by the following equation:

$$E_{on} = \int_0^{T_{ri}+T_{fv}} V_{DS}(t) i_D(t) dt$$

where $V_{DS}(t)$ is the instantaneous value of the drain-source voltage of the switch, $i_D(t)$ is the drain current of the switch, T_{ri} is the time taken for the current to rise from zero to i_D and T_{fv} is the time taken for the voltage to drop from V_{DS} to zero. The energy associated with the turning off of a switch is given by the following equation:

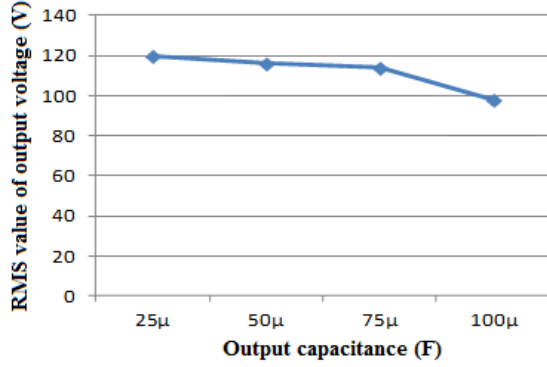


Fig. 13: Output voltage versus output capacitance of the inverter for a 500-W load.

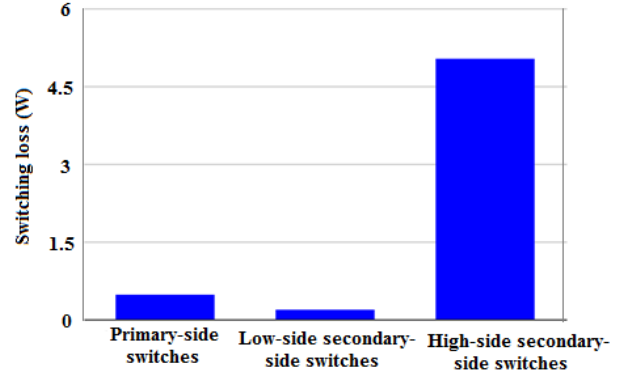


Fig. 14: Estimated switching losses for a switching frequency of 100 kHz (for a 500 W load). The chosen primary-side switch is IPP200N25N3 G and the chosen secondary-side switch is STY60NM50.

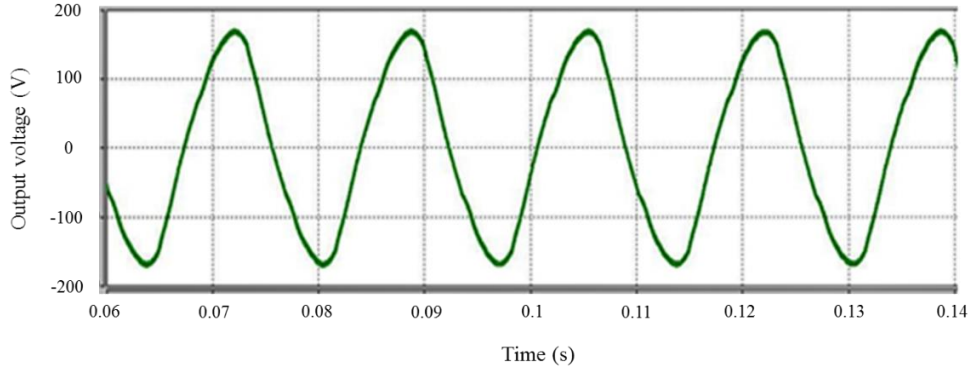


Fig. 15: Output voltage in volts (vertical axis) as a function of time in seconds (horizontal axis) for the inverter operating in open-loop condition. It shows distortion in the output voltage due to nonlinear gain of the open-loop inverter.

$$E_{off} = \int_0^{T_{rv}+T_{fi}} V_{DS}(t) i_D(t) dt$$

where T_{rv} is the time taken for the voltage to rise from zero to V_{DS} and T_{fi} is the time taken for the current to drop from I_D to zero. The power loss during the switching of the devices is given by the following equation:

$$P_{sw} = (E_{on} + E_{off}) f_s$$

where f_s is the switching frequency of the inverter. Fig. 14 shows the estimated switching losses in all the primary-side switches and the secondary-side devices in both the modules.

IV. INVERTER CONTROL SCHEME

Fig. 15 shows the output voltage of the inverter under open-loop control condition. The clear distortion evident in the output voltage is reflective of the nonlinear gain of the inverter. Therefore, to reduce the total harmonic distortion (THD) of the load current of the inverter which has a nonlinear dc gain, a harmonic compensation control is implemented using a proportional-resonant (PR) controller.

Further, the control scheme accounts for the dynamics of the primary-side inductors and the secondary-side capacitors. Essentially, and as implied in Fig. 16, a sinusoidal voltage reference yields additional harmonic components in the actual feedback. Therefore, while the fundamental current reference is extracted from the voltage loop, a zero reference is set for the higher-order harmonics that have tangible impact on the output voltage. The PR controller with harmonic compensators achieves high gain at the fundamental and harmonic frequencies thereby yielding low steady-state error and non-sinusoidal perturbation in the duty ratio thereby yielding a low THD output. The PR controller is represented as follows:

$$G(s) = k_p + \frac{k_o s}{[s^2 + (n^2 \omega^2)]}$$

where $\omega (= 2\pi n * 60)$ represents the line or fundamental ($n = 1$) frequency and $n (= 3, 5, \dots)$ represents the higher-order harmonics. For $n = 1$, the feedback voltage is compared with a reference 60-Hz sinusoidal voltage and the error is passed through a PR controller, which is tuned at the line frequency. The current command of this voltage loop is compared with a differential-current feedback and passed through a PR

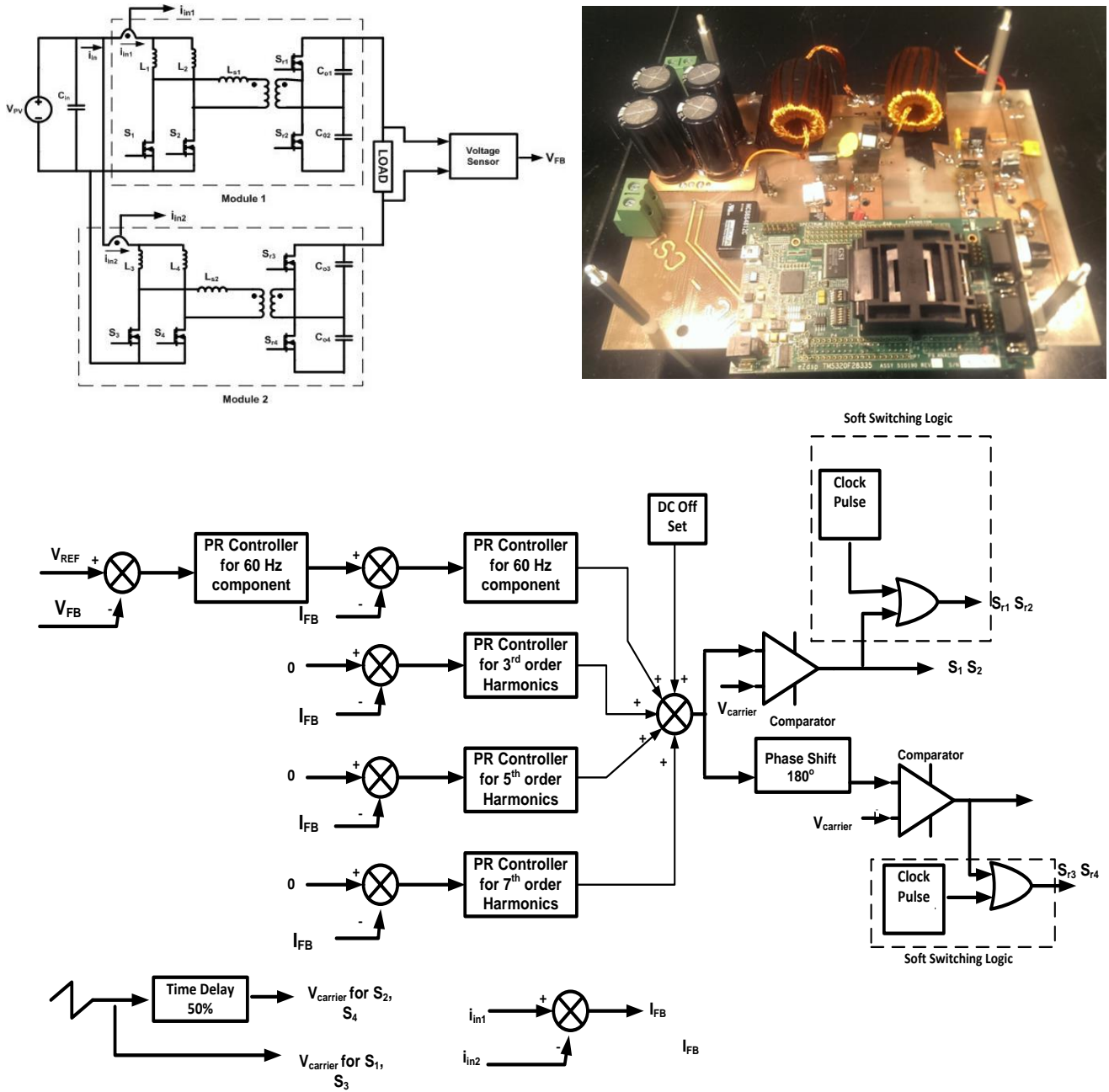


Fig. 16: Closed-loop control scheme of the differential-mode inverter. One module of an experimental inverter operated using a DSP controller, which is currently underway, is shown on the top right.

controller with harmonic compensators achieves high gain at the fundamental and harmonic frequencies thereby yielding low steady-state error and non-sinusoidal perturbation in the duty ratio thereby yielding a low THD output. The PR controller is represented as follows:

$$G(s) = k_p + \frac{k_o s}{[s^2 + (n^2 \omega^2)]}$$

where $\omega (= 2\pi n * 60)$ represents the line or fundamental

($n = 1$) frequency and $n (= 3, 5, \dots)$ represents the higher-order harmonics. For $n = 1$, the feedback voltage is compared with a reference 60-Hz sinusoidal voltage and the error is passed through a PR controller, which is tuned at the line frequency. The current command of this voltage loop is compared with a differential-current feedback and passed through a PR controller which is tuned at the fundamental frequency. The differential current is synthesized by taking the difference of the input currents (i_{in1} and i_{in2}) of Modules 1 and 2. To mitigate the higher-order (odd) harmonics (i.e., $n = 3, 5, \dots$), separate control loops are implemented that emulate the structure of the

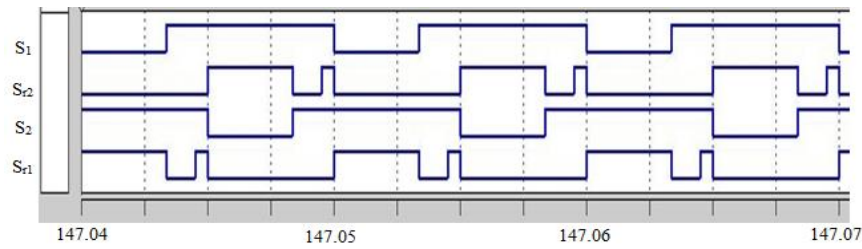


Fig. 17: Gate signals of switches S_1 , S_2 , S_2 , S_1 (starting from the top) as a function of time (in milliseconds) of Module 1 under soft-switched condition.

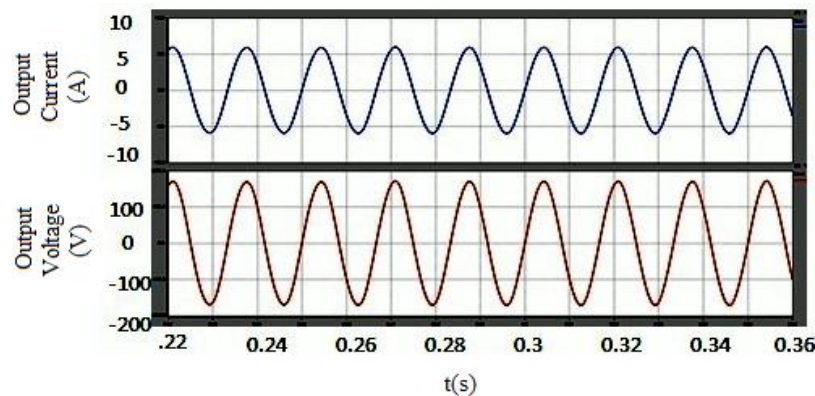


Fig. 18: Load current (top) and output voltage (below) of the inverter operating under closed-loop control condition.

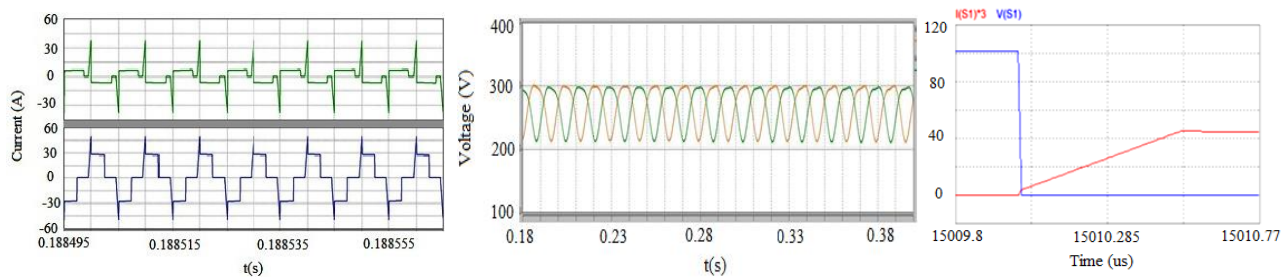


Fig. 19: (left) Leakage-inductance currents of Module 1 (top trace) and Module 2 during negative half cycle of the load voltage. (middle) Output-capacitor voltages of the two inverter modules. (right) ZCS of S_1 for (waveforms are scaled for clarity).

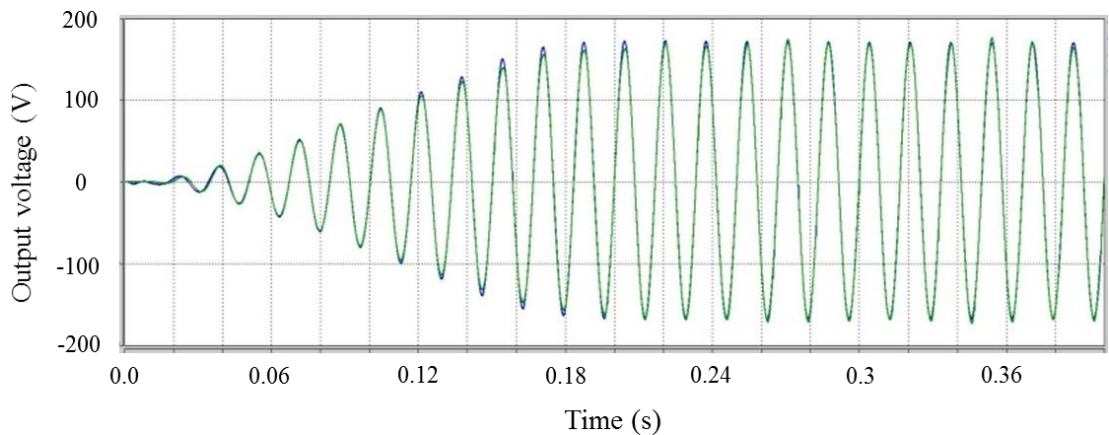


Fig. 20. Comparison of the inverter output voltage during start-up with and without proportional gain for the PR compensator. (Blue trace: with proportional gain, and green trace: without proportional gain). The difference in the time to reach the steady state for the controlled inverter with and without proportional gain for the PR compensator is about 2 60-Hz line cycles. It is noted that, the voltage reference is ramped up in 150 ms to the desired steady-state magnitude.

fundamental frequency control loop. However, for the harmonics compensation, the current reference is set to 0 and the PR controller is tuned at a frequency that matches the harmonic frequency. The perturbation outputs of the fundamental and high-order harmonic controllers are added to a dc offset such that the duty ratio of the (primary-side) inverter switches do not fall below 0.5. This duty-cycle signal and a 180° phase-shifted signal of the same are then used to generate the pulse trains for the switches S_1 and S_2 and S_3 and S_4 , respectively. The signals for the secondary-side switches S_{r1} and S_{r2} are generated by complementing the binary switching signals of primary-side switches S_1 and S_2 respectively, and then adding to the pulse train information (d_r) for achieving soft-switching. The signals for the secondary-side switches S_{r3} and S_{r4} are generated by complementing the binary switching signals of primary-side switches S_3 and S_4 respectively, and then adding to the pulse train information (d_r) for achieving soft-switching. Fig. 17 shows the switching signals of Module 1.

Fig. 18 shows the inverter output voltage and output current using the closed-loop control scheme described above. Comparing the results of Figs. 15 and 18, it is evident that the harmonic-compensation based closed-loop control shown in Fig. 16 addresses the harmonic distortion of the open-loop inverter effectively. For this condition, Fig. 19 shows the leakage-inductance current and output-capacitor voltages of the two modules, and ZVS turn-on of S_1 . Finally, Fig. 20 shows the acceptable dynamic response of the inverter during start-up. The presence of the proportional gain of the PR compensator yields better transient response at the cost of slightly higher distortion.

V. CONCLUSIONS

This paper describes a current-source high-frequency-link inverter. It comprises two dc/dc isolated converters that are connected in a differential-mode configuration thereby yielding an inverter output. The inverter has several key features including the following: single-stage topology, high-frequency instead of bulky line transformer, inherent voltage boost/gain capability, voltage-doubling secondary reduces transformer turns ratio to half, reduced transformer core size due to bipolar flux at the origin, and soft switching of most of the inverter switches. However, the inherent nonlinearity of the inverter yields harmonic distortion under open-loop condition. To mitigate that problem a harmonic-compensation based control scheme is outlined. The resultant closed-loop-controlled inverter significantly reduces the harmonic distortion of the inverter output voltage and current and yields acceptable dynamic response. Finally, work in underway currently to synthesize an experimental inverter. A preliminary prototype module is shown in Fig. 16. Following are projected performance parameters for such an inverter at 500-W output: efficiency of 94% (device conduction and switching losses of 2%, transformer losses: 2%, filter losses: 1.5%, additional losses: 0.5%), output voltage THD of about 2%, and dynamic time lag between reference and feedback

voltage using proportional-gain based PR compensator of up to 1 60-Hz line cycle. An adaptive tracking controller as outlined in [22] for a differential-mode inverter will also be pursued to reduce the time lag.

REFERENCES

- [1] R. Caceres and I. Barbi, "A boost dc-ac converter: operation, analysis, control and experimentation", IEEE Industrial Electronics Conference, 1995, pp. 546-551.
- [2] N. Vazquez, J. Almazan, J. Alvarez, C. Aguilar, and J. Arau, "Analysis and experimental study of the buck, boost and buck-boost inverters", in Proc. IEEE Power Electronics Specialists Conference, 1999, pp. 801-806.
- [3] N. Kasa, T. Iida, H. Iwamoto, "An inverter using buck-boost type chopper circuits for popular small-scale photovoltaic power system", in Proc. IEEE IECON '99, San Jose, CA, Nov/Dec 1999, pp. 185-190.
- [4] S.B. Kaer and F. Blaabjerg, "A novel single-stage inverter for the ac-module with low frequency ripple penetration", in Proc. 10th EPE European Conf. Power Electronics and Applications, Toulouse, France, Sept. 2-4, 2003.
- [5] C-M. Wang, "A novel single-stage full-bridge buck-boost inverter", in Proc IEEE APEC'03, Florida, Feb 9-13, 2003, pp. 51-57.
- [6] M. Nagao and K. Harada, "Power flow of photovoltaic system using buck-boost PWM power inverter", in Proc. IEEE PEDS'97, Singapore, May 26-29, 1997, pp. 144-149.
- [7] M. Kusakawa, H. Nagayoshi, K. Kamisako, and K. Kurokawa, "Further improvement of a transformerless, voltage boosting inverter for ac-modules", Solar Energy Mater. Solar Cells, vol. 67, pp. 379-387, Mar.2001.
- [8] T.J. Liang, Y.C. Kuo, and J.F. Chen, "Single-stage photovoltaic energy conversion system", in Proc. IEE Electric Power Applications, Vol. 148, no. 4, pp. 339-344, 2001.
- [9] S.K. Mazumder, R.K. Burra, R. Huang, and V. Arguelles, "A low-cost single-stage isolated differential Cuk inverter for fuel-cell application", in Proc. IEEE Power Electronics Specialist Conference, pp. 4426-4431, June 2008.
- [10] Q. Li and P. Wolfs, "Recent development in the topologies for photovoltaic module integrated converters", IEEE Power Electronics Specialists Conference, pp. 1-8, 2006.
- [11] B.S. Prasad, S. Jain, and V. Agarwal, "Universal single-stage grid-connected inverter", IEEE transaction on Energy Conversion, Vol. 23, Issue 1, pp. 128-137.
- [12] S. Jain, "Single-stage, single-phase grid connected PV systems with fast MPPT techniques", Annual Ph.D. progress report, Department of EE, IIT Bombay, India, Aug 2004.
- [13] Y. Chen, K.M. Smedley, "A cost effective single-stage inverter with maximum power point tracking", IEEE transactions on Power Electronics, Vol. 19, Issue 5, Sep 2004, pp. 1289-1294.
- [14] S. Harb, H. Haibing, N. Kutkut, I. Batarseh, and Z.J. Shen, "A three-port photovoltaic micro-inverter with power decoupling capability" in Proc. IEEE Applied Power Electronics Conference and Exposition, Mar 2011, pp. 203-208.
- [15] S.K. Mazumder, "A novel hybrid modulation scheme for an isolated high-frequency-link fuel cell inverter", IEEE Power and Energy Society General Meeting, DOI: 10.1109/PES.2008.4596911, pp. 1-7, 2008.
- [16] S.K. Mazumder and R. Huang, "Multiphase converter apparatus and method", USPTO Patent# 7,768,800 B2, awarded on Aug 3, 2010.
- [17] S.K. Mazumder, "Differential mode inverters for renewable and alternative energy systems", filed by the University of Illinois at Chicago with the USPTO on 06/23/11 with patent application number 61/500,344.
- [18] P. Sivasubramanian and S.K. Mazumder, "A modular approach for current-source multi-phase inverter", IEEE Industrial Electronics Conference, pp. 5698-5701, 2012.

[19] S. Mehrmami and S.K. Mazumder, "Discontinuous modulation scheme for a differential-mode Cuk inverter", IEEE Transactions on Power Electronics, vol. 30, no. 3, pp. 1242-1254, 2014.

[20] A.K. Rathore and S.K. Mazumder, "Novel zero-current switching current-fed half-bridge isolated dc/dc converter for fuel-cell based applications", IEEE Energy Conversion Conference and Exposition, pp. 3523-3529, 2010.

[21] P. Sivasubramanian, A differential-mode current-sourced high-frequency-link photovoltaic inverter, MS Thesis, Department of Electrical and Computer Engineering, University of Illinois, Chicago.

[22] S.K. Mazumder and H. Soni, "Modular control of a differential-mode inverter", IEEE Energy Conversion Conference and Exposition, 2015.



Priyadharshini T Sivasubramanian received her Bachelor of Engineering degree in Electrical and Electronics Engineering from Anna University, Chennai, India. She received her M.S. degree in Electrical and Computer Engineering from the University of Illinois at Chicago in 2013. Her M.S. Thesis project at UIC was A Differential-Mode Current-Sourced High-Frequency-Link Photovoltaic Inverter. Currently, she is working as a Business Intelligence Consultant.



Sudip K. Mazumder (S'97-M'01-SM'03-F'15) received his Ph.D. degree from Virginia Tech in 2001. He is a Professor at the University of Illinois, Chicago (UIC) and is the President of NextWatt LLC. He has over 24 years of professional experience and has held R&D and design positions in leading industrial organizations and has served as a Technical Consultant for several industries.

He has published about 200 refereed papers and delivered over 70 invited presentations. He is the recipient of UIC's Inventor of the Year Award (2014), University of Illinois' University Scholar Award (2013), ONR Young Investigator Award (2005), NSF CAREER Award (2003), and IEEE PELS Transaction Paper Award (2002).

In 2015, he was elevated to the rank of an IEEE Fellow and he was invited to serve as a Distinguished Lecturer for IEEE PELS beginning in 2016. He served/serving as the Guest Editor-in-Chief/Editor for IEEE PELS/IES Transactions between 2013-2014, as the first Editor-in-Chief for Advances in Power Electronics (2006-2009), and as an Associate Editor for IEEE IES/PELS/TAES Transactions (2003-/2009-/2008-). Currently, he serves as the Chair for IEEE PELS TC on Sustainable Energy Systems.



Harshit Soni (S'14) received the B.E. degree in Electronics and Communication Engineering from PES School of Engineering, Bengaluru, India in 2012. He received his M.S. degree in Electrical and Computer Engineering from University of Illinois at Chicago in 2015. His MS Thesis project at UIC was on modular control of differential mode Cuk inverter. Currently, he is working at Tagore Technology Inc.

His research area includes but are not limited to high frequency link inverter, dc/dc converters, control engineering, GaN based switching power converters.



Ankit Gupta (S'07) received his B.E. degree in Electrical Engineering from Delhi College of Engineering (DCE), Delhi, India in 2011. From 2011-2013, he worked as an engineer at the super critical Turbo-Generator manufacturing facility of Bharat Heavy Electrical Ltd (BHEL), HEPP, Haridwar unit.

In 2013, Ankit joined the Laboratory of Energy and Switching Electronics System (LESES) at the

University of Illinois, Chicago, USA, and is currently working on his Ph.D. degree. In 2015 he was selected as the IEEE Region 4 student representative. His research interests include but not limited to power converters, high frequency power transmission, microgrids and grid integration of renewable energy. He also serves as a reviewer for the IEEE Transaction on Power Electronics and IEEE transaction on Industrial Electronics.



Nikhil Kumar (S'15) received the B.E. degree in Electrical Engineering from Delhi College of Engineering, Delhi, India in 2011. He also worked as executive engineer at Larsen & Toubro, Mumbai, India from 2011-13. He received his M.S. degree in Electrical and Computer Engineering from University of Illinois at Chicago in 2015. His MS Thesis project at UIC was on developing frequency-dependent criterion to mitigate effects of transmission line terminated with linear loads. He is currently working towards his PhD degree from University of Illinois at Chicago. His research area includes but are not limited to high frequency link inverter, signal integrity issues in high frequency power transfer, dc/dc converters and GaN based switching power converters.

See discussions, stats, and author profiles for this publication at: <http://www.researchgate.net/publication/285494149>

A Low Power High Gain Low Noise Amplifier for Wireless Applications

CONFERENCE PAPER · NOVEMBER 2015

READS

15

2 AUTHORS, INCLUDING:



[P. K. Verma](#)

Delhi Technological University

3 PUBLICATIONS 0 CITATIONS

SEE PROFILE

A Low Power High Gain Low Noise Amplifier for Wireless Applications

P. K. Verma

Department of Electronics and Communication Engineering,
Delhi Technological University,
(Formerly Delhi College of Engineering), New Delhi, India
E-mail Id: vermapk87@gmail.com

Priyanka Jain

Department of Electronics and Communication Engineering,
Delhi Technological University,
(Formerly Delhi College of Engineering), New Delhi, India
E-mail Id: priyajain2000@rediffmail.com

Abstract—This paper presents the design and simulation of low noise amplifier (LNA) for wireless applications operating in the 2.4-2.5 GHz band. In this paper inductive source degeneration topology has been used to provide low noise figure, high forward gain and low power consumption. The simulation was made using Advance Design System (ADS) software. Proposed work emphasis on reduction in noise figure with increase in power gain at low power consumption as compared to previous results at 1.2V power supply.

Keywords: Power Consumption; Noise Figure; S Parameters; Advance Design System; Wireless Applications

I. INTRODUCTION

With the advance development of the communication industry, different types of wireless communication devices are needed. Low noise amplifier (LNA) is the very crucial element of RF receiver, which is the RF front end circuit [1-3]. LNA increases the gain level or amplify the signal and suppress the noise figure of the signal. While designing an LNA, there are different parameters which are taken into consideration such as low noise figure, low input/output return losses, a high IIP3, high gain and lower power consumption. In order to achieve the required gain it is essential to make sure that reflection coefficients S_{11} (input reflection coefficient) and S_{22} (output reflection coefficient) minimized. In the literature, LNA design with reduction in power consumption and noise figure as well as increase in gain has been reported [6-13]. In [13] low power low noise LNA has been proposed, So in proposed paper aimed to improving the parameters by using another C-S stage could be added to the cascode output of LNA. For this design, Agilent CMOS 14 0.5- μm RF CMOS process is used that allows a minimum gate length of 0.6 μm .

There some topologies for LNA design such as resistive matching, common gate amplifier, shunt series feedback common source, inductive source degeneration and cascode inductive source degeneration [6]. This paper presents an inductive source degeneration topology for providing low noise figure, high forward gain and low power consumption.

The proposed design has been simulated through ADS software.

The ADS software is microwave circuit and communication system software developed by Agilent Technologies. It has very powerful ability in RF circuit design and simulation analysis. In this simulation, S parameter gives the information about the gain, stability, noise figure and linearity.

The organization of the rest of the paper is as follows. In section II, describe the input/output matching of LNA. In section III, different types of topologies of LNA are presented and in section IV & V presents the circuit design and simulated results. Section VI, gives the conclusion of proposed LNA.

II. INPUT/ OUTPUT MATCHING

First stage of the LNA will be the input matching stage which will insure that maximum signal is going into LNA for processing and in order to get maximum power, signal received by the LNA show minimum reflection. According to maximum power theorem, the input impedance of the LNA must be complex conjugate of the source impedance. Here for simplicity it is assumed the source impedance is real and its value is 50 Ω . The topology is matched to a 50 Ω source using the inductive source degeneration L_s . Maximum power transfer from previous stage to the LNA is achieved by minimizing the input return loss [13]. The expression of the input impedance for the LNA is defined as

$$Z_{in} = \frac{V_g}{I_g} \quad (1)$$

$$Z_{in} = \frac{I_g R_g + V_c + I_s \cdot j\omega L_s}{I_g} \quad (2)$$

$$V_c = \frac{I_g}{sC_{gs}} = \frac{I_g}{j\omega C_{gs}} \quad (2a)$$

Where

And $I_s = I_g + g_m V_c$ (2b)

From equation (2), we have

$$Z_{in} = \frac{I_g R_g + \frac{I_g}{s C_{gs}} + s L_s \left(I_g + g_m \cdot \frac{I_g}{s C_{gs}} \right)}{I_g} \quad (3)$$

$$Z_{in} = R_g + \frac{1}{s C_{gs}} + s L_s \left(1 + \frac{g_m}{s C_{gs}} \right) \quad (3a)$$

$$Z_{in} = R_g + \frac{L_s g_m}{C_{gs}} + s \left(L_s + \frac{1}{s^2 C_{gs}} \right), s = j\omega \quad (4)$$

$$Z_{in} = R_g + \frac{L_s g_m}{C_{gs}} + j\omega \left(L_s + \frac{1}{(j\omega)^2 C_{gs}} \right) \quad (5)$$

$$Z_{in} = R_g + \frac{L_s g_m}{C_{gs}} + j \left(\omega L_s - \frac{1}{\omega C_{gs}} \right) \quad (6)$$

Above equation can be re-written as,

$$Z_{in} = R_g + R_a + j \left(X_{L_s} - X_{C_{gs}} \right) \quad (7)$$

$$R_a = \frac{L_s g_m}{C_{gs}}$$

Where,

In this work, MOSFETs, R_g is taken as zero. Therefore the impedance of the MOSFET without feedback is

$$Z_{in} = -jX_{C_{gs}} \quad (8)$$

Adding series feedback adds the following term to the original input impedance: $R_a + jX_{L_s}$

To achieve input matching, the Z_{in} should be 50Ω . So,

$$Z_{in} = \frac{L_s g_m}{C_{gs}} \quad (9)$$

So to give required Z_{in} , the value of L_s is taken randomly and the values of g_m and C_{gs} are calculated.

III. DIFFERENT TYPES OF TOPOLOGIES

There are different types of topologies for LNA design such as resistive matching, common gate, shunt series common feedback, inductive source degeneration, and cascode inductor source degeneration. These topologies have their own merits/demerits which are tabulated in table 1.

TABLE 1: ADVANTAGES AND DISADVANTAGES OF LNA TOPOLOGIES

Type of Topology	Advantages	Disadvantages
Resistive Matching [17, 22]	Broad band amplifier	Adding the noise from resistor
Common Gate [16, 18, 20, 22]	The input impedance is equal to $1/g_m$. It is practical to get 50Ω	The impedance varies with bias current
Shunt Series Common Feedback [17-19]	Broad band amplifier	Adding noise from resistor
Inductive Source Degeneration [14, 19, 22, 24, 25]	The source and gate inductors make the input impedance 50Ω and not adding noise from input	The inductor is off chip at low frequency and low isolation
Cascode Inductor Source Degeneration [15, 21, 23, 25]	Isolation of input/output is good, higher gain, low noise figure	The inductor is off chip at low frequency

As all the above topologies, inductive source degeneration configuration is best from other topologies. So we have chosen inductive source degeneration, with inductive load it provides sufficient gain without adding significant noise and also provide better matching in comparison to other topologies.

IV. CIRCUIT DESIGN

Designing of LNA circuit include three steps. In the first step, basic LNA with a bias resistor including a current mirror and current source has been designed. In the simulation, ideal inductor i.e. no Q value has been entered and therefore have no loss.

Second step is the simulation of LNA with additional cascode stage. In this schematic inductive source degeneration feedback amplifier with the gate inductor for input matching is shown in fig. 1. The source inductor is used provide the desired input impedance 50Ω and to achieve simultaneous input and noise matching. The cascode structure is combination of common source devices (i.e. LNA) with a common gate load. The additional cascode device has been used as a diode. To optimize the gain response of the LNA, an inductor between cascode source and supply has been provided. Its value may be varied and it also blocks any RF leaking to the supply rail.

Finally in the third stage i.e. our proposed LNA (fig. 1), to increase the gain of the LNA another C-S stage could be added to the cascode output. This output stage is DC coupled to the output of the first cascode stage so that it receives the correct bias. The increased gain is greatly improving the noise figure of the receiver as the noise figure of the second stage reduces to $\sim 1/\text{gain_LNA}$.

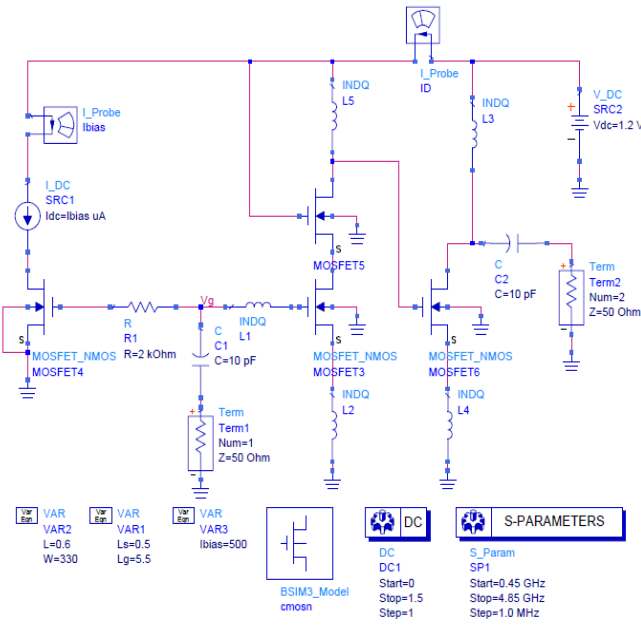


Fig. 1: Schematic of the C-S LNA with a Simple C-S Stage Added to the Cascode

V. SIMULATION RESULTS

Proposed LNA is simulated using Advance Design System (ADS) software. The low noise amplifier provides a maximum gain of 26.486 dB as shown in Fig. 2. C_{gs} and g_m are selected according to (9) to make the input matching Z_{in} as possible to 50 Ω . This circuit operated with 1.2 V supply voltage. The reverse isolation S_{12} (Fig. 2) is good with more than -52.533 dB at the operating frequency. A minimum noise figure of 1.044 dB is achieved around the desired frequency 2.4-2.5 GHz for the proposed LNA's as shown in fig. 6.

A. S Parameters

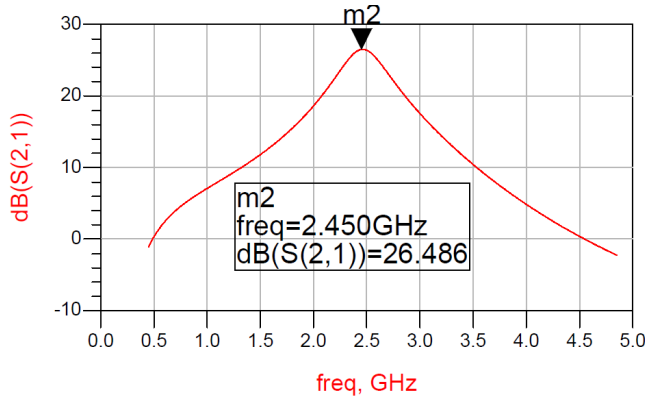


Fig. 2: Forward Gain (S_{21})

S_{21} is forward transmission coefficient and it represents, measure how well the signal goes from input to output. It is also known as forward gain and the value of S_{21} at 2.45 GHz frequency is 26.486 dB as shown in fig. 2.

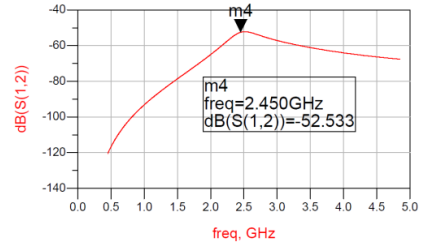


Fig. 3: Scattering Parameter (S_{12})

S_{12} is reverse transmission coefficient, and measure how much the input signal is reflected back and it is also known as reverse isolation and the value of S_{12} at 2.45 GHz frequency is -52.533 dB as shown in fig. 3.

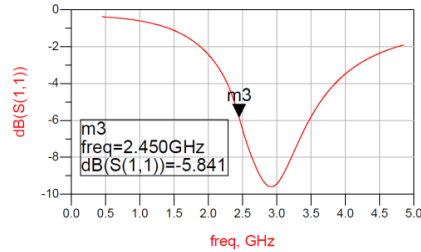


Fig. 4: Scattering Parameter (S_{11})

S_{11} is input reflection coefficient, represents measure of how well the input impedance is match to the reference impedance. It is also known as input return loss and the input reflection coefficient S_{11} for 2.45 GHz frequency is -5.841 dB as shown in Fig. 4.

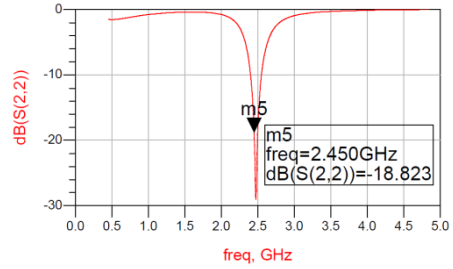


Fig. 5: Scattering Parameter (S_{22})

S_{22} is output reflection coefficient and it represents measure of how well the output impedance is matched to load impedance. It is also known as output return loss, and the value of S_{22} at the 2.45 GHz frequency is -18.823 dB as shown in fig. 5.

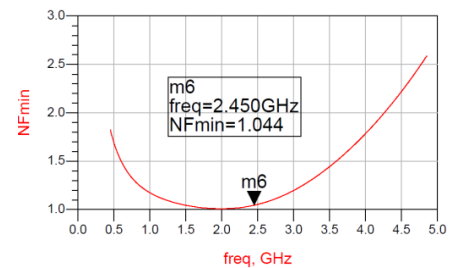


Fig. 6: Minimum Noise Figure (NF_{min})

B. Noise Figure

Noise Figure indicates the noise performances of device at high frequency at 2.45 GHz, the minimum Noise Figure 1.044 dB has been obtained as shown in Fig. 6.

C. Power Consumption

Power consumption of proposed LNA design is calculated by the following current and voltage values given in table 2. The values of drain current and gate voltage can be obtained using the ADS simulation by pin up the I_D and V_g in the schematic window of ADS simulator. After running the simulation, got the values of I_D and V_g .

TABLE 2: VALUES OF CURRENT AND VOLTAGE

Frequency	ID, i	Vg
0.0000 GHz	4.865 mA	924.8 mV

Power consumed by LNA design using above design is 4.49 mW only.

D. Linearity

The linearity of the LNA is another concern that must be taken into account. Linear operation is crucial, particularly when the input signal is weak with a strong interfering signal in close proximity. This is because in such a scenario there is a possibility for undesired inter-modulation distortion such as blocking and cross modulation. The odd order distortion produced by an LNA can give rise to distortion products which can interfere with the desired signal. This point is represented as third order intercepts point as it specifies distortion signal amplitudes equal the input signals. The 1dB compression point is also specified in power amplifier designs as it gives information where the amplifier goes into compression and becomes non-linear. Operation should occur below this point in the linear region. These points are specified in fig. 7 for the proposed design.

We can get rough estimated values of compression of the LNA, a non-linear expression of the input and output parameters can be expanded using Taylor's theorem. These results are as follows [26]

$$I_{D_{SAT}} = W_{V_{sat}} C_{ox} \frac{V_{od}^2}{V_{od} + E_{sat} L} \quad (10)$$

With

$$V_{od} = V_{gs} - V_t = \text{Voltage Overdrive}$$

$$E_{sat} = \frac{2V_{sat}}{\mu_{eff}} \text{ where } \mu_{eff} = \frac{\mu_0}{1 + \theta V_{od}} = \text{Velocity saturation}$$

field strength

$$P_{1dB} \sim 0.29 \frac{V_{sat} \cdot L}{\mu_1 \cdot R_s} V_{od} \left(1 + \frac{\mu_1 \cdot V_{od}}{4V_{sat} \cdot L} \right) \left(1 + \frac{\mu_1 \cdot V_{od}}{2V_{sat} \cdot L} \right)^2 \quad (11)$$

$$P_{IIP3} \sim \frac{8 V_{sat} \cdot L}{3 \mu_1 \cdot R_s} V_{od} \left(1 + \frac{\mu_1 \cdot V_{od}}{4V_{sat} \cdot L} \right) \left(1 + \frac{\mu_1 \cdot V_{od}}{2V_{sat} \cdot L} \right)^2 \quad (12)$$

$$\text{Where, } \mu_1 \cong \mu_0 + 2\theta V_{sat} \cdot L$$

Mathematically calculated the values of P_{1dB} , P_{IIP3} by eq. 11 and 12 and simulated results using ADS are approximately same, shown in fig. 7

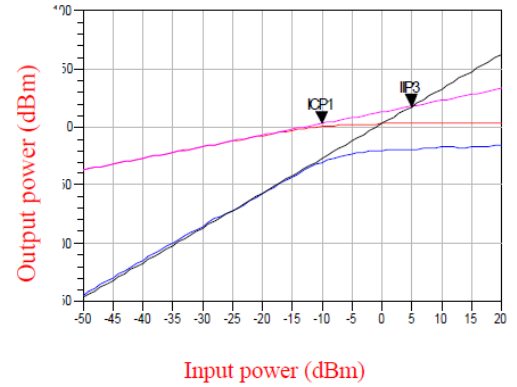


Fig. 7: Simulated Compression Point (ICP1) and Third-Order Intercept (IIP3)

At $K1 > 1$, the design circuit is stable unconditionally and the stability factor is defined as

$$K1 = \frac{1 - |S_{11}|^2 - |S_{22}|^2 + |\Delta|^2}{2|S_{21}S_{12}|} \quad (13)$$

$$\text{Where, } \Delta = |S_{11}S_{22} - S_{12}S_{21}| \quad (14)$$

When input and output matching are good that shows the decrease in the absolute value of S_{12} , increase in the stability factor $K1$ as shown in the fig. 8, LNA is stable unconditionally.

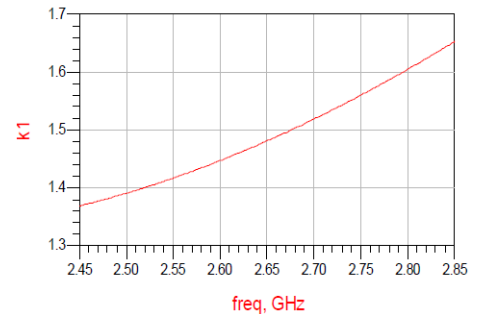


Fig. 8: Simulated Stability Factor (K_1)

Comparison of different parameters of LNA: Based on the simulation results of LNA Table 3 shows the various performance parameters result of the design and it gives the conclusion that proposed LNA for wireless application is for better than the previous results.

TABLE 3: COMPERISION OF DIFFERENT PARAMETERS OF LNA

[Ref]	Power (mW)	Gain (dB)	N.F (dB)	IIP3 (dBm)	F0 (GHz)
[6]	30	22	3.5	-9.5	1.5
[7]	12	22	2.5	-10	2.5
[8]	22.4	19.8	3	4.5	2.4
[9]	7.2	15	2.2	1.3	2.4
[10]	4.5	13.4	3	0	2.5
[11]	-	15.9	2.88	-2.6/-11.2	2.45
[12]	13.2	11	2.2	3	2.4
[13]	7.33	20.34	1.98	5	2.4-2.5
Proposed LNA	4.49	26.48	1.044	5	2.45

VI. CONCLUSION

This paper describes the approach of designing an LNA operating 2.4-2.5 GHz with low power consumption, low noise figure and high gain. At very low power consumption i.e. 4.49 mW, low noise figure of 1.044 and high forward gain 26.486 dB is obtained. Along with these great characteristic, a high IIP3 of 10 dBm which shows the good linearity has been observed. This compares favourably to the earlier available designs in the literature [6-13].

REFERENCES

- [1] I Comer, D.J. and Comer, D.T. (2004), "Using the Weak Inversion Region to Optimize Input Stage Design of CMOS op Amps [J]", *IEEE Transactions on Circuits and System*, Vol. 51, No. 1, pp. 8-14, Jan.
- [2] Mou, S.X., Ma, J.G. and Seng, Y.K., et al. (2005), "A Modified Architecture Used for Input Matching in CMOS Low-noise Amplifiers [J]", *IEEE Transactions on Circuits and System*, Vol. 52, No. 11, pp. 784-788,
- [3] Liao, C.H., and Chuang, H.R. (2003), "A 5.7 GHz 0.18- μ m CMOS Gain-Controlled Differential LNA with Current Reuse for WLAN Receiver [J]", *IEEE Microwave and Wireless Components Letters*, Vol. 13, No. 12, pp. 526-528.
- [4] Floyd, B.A., Mehta, J., Gamero, C. and Kenneth, K.O. (1999), "A 900-MHz, 0.8 μ m CMOS Low Noise Amplifier with 1.2-dB Noise Figure," *IEEE Custom Integrated Circuit Conference*, pp. 661-664.
- [5] Konishi, Y. and Honjo, K. (1993), *Microwave Semiconductor Circuits*, Tokyo, Japan: Nikan, p. 114.
- [6] Shaeffer, D.K. and Lee, T.H. (1997), "A 1.5 V, 1.5 GHz CMOS Low Noise Amplifier," *IEEE J. Solid-State Circuits*, Vol. 32, No. 5, pp. 745-759, May.
- [7] Rafla, R.A. and El-Gamal, M.N. (1999), "Design of a 1.5 V CMOS Integrated 3 GHz LNA," *In Proceedings of the 1999 IEEE Int'l Symposium on Circuits and Systems*, Vol. 2, pp. 440-443.
- [8] Huang, C., Weng, R.M., Lung, H. Chih. and Lin, K.Y. (2001), "A 2 V 2.4 GHz Fully Integrated CMOS LNA with Qenhancement Circuit," *In Asia-Pacific Microwave Conference*, Vol. 3, pp. 1028-1031.
- [9] Yang, X., Wu, T. and McMacken, J. (2001), "Design of LNA at 2.4 GHz using 0.25 μ m Technology," *In Topical Meeting on Silicon Monolithic Integrated Circuits in RF Systems*, pp. 12-17,.
- [10] Fournier, T. J.M. and Haidar, J. (2001), "Noise Contribution in a Fully Integrated 1-V, 2.5-GHz LNA in CMOS-SOI Technology," *18th IEEE International Conference on Electronic Circuits and Systems*, pp. 1611-1614.
- [11] Li, X., Brogan, T., Esposito, M., Myers, B. and O, K.K. (2001), "A Comparison of CMOS and SiGe LNA's and Mixers for Wireless LAN Application," *IEEE Conference on Custom Integrated Circuits*, pp. 531-534.
- [12] Lagnado, I., de la Houssaye, P.R., Dubbelday, W.B., Koester, S.J., Hammond, R., Chu, J.O., Ott, J.A., Mooney, P.M., Perraud, L. and Jenkins, K.A. (2000), "Silicon-onsapphire for RF Si Systems," *2000 Topical Meetings On Silicon Monolithic Integrated Circuits in RF Systems*, pp. 79-82.
- [13] Nadia, Ayari, Belgacem, Hamdi and Aymen, Fradi (2013), "A Low Power Low Noise CMOS Amplifier for Bluetooth Applications", *International Conference on Applied Electronics (AE)*.
- [14] Andreani, Pietro and Sjoland, Henrik (2001), "Noise Optimization of an Inductively Degenerated CMOS Low Noise Amplifier", *IEEE Transaction on Circuits and Systems-II: Analog and Digital Signal Processing*, Vol. 48, No. 9, Sept.
- [15] Lerdworatawee, Jongrit and Namgoong, Won (2005), "Wide-Band CMOS Cascode Low-Noise Amplifier Design Based on Source Degeneration Topology", *IEEE Transaction on Circuits and Systems-I: Regular Papers*, Vol. 52, No. 11, Nov.
- [16] Liscidini, A., Martini, G., Mastantuono, D. and Castello, R. (2008), "Analysis and Design of Configurable LNAs in Feedback Common", *IEEE Transaction on Circuits and Systems-I: Express Briefs*, Vol. 55, No. 8, August.
- [17] Chi, Baoyong, Zhang, Chun and Wang, Zhihua (2008), "Bandwidth Extension for Ultra-Wideband CMOS Low-Noise Amplifiers", *IEEE International Symposium on Circuits and Systems (ISCAS)*, 18-21 May.
- [18] Balashov, Evgeniy V. and Korotkov, Alexander S. (2008), "Ultra Wideband Low Noise Amplifier with Source Degeneration and Shunt series Feedback", *4th European Conference on Circuits and Systems for Communications (ECCSC)*, 10-11 July.
- [19] Balashov, Evgeniy V. and Korotkov, Alexander S. (2009), "Dual Feedback Low Noise Amplifier for Ultra Wideband Application", *IEEE EUROCON*, pp. 18-23, May.
- [20] Wang, Hongrui, Zhang, Li, and Yu, Zhiping (2010), "A Wideband Inductorless LNA with Local Feedback and Noise Cancelling for Low-Power Low-Voltage Applications", *IEEE Transactions on Circuits and Systems-I: Regular Papers*, Vol., 57, No., 8, August.
- [21] Lian, Low Li, Noh, Norlaili Mohd, Mustaffa, Mohd Tafir, Manaf, Asrulnizam Bin Abd and Sidek, Othman Bin (2011), "A dual-band LNA with 0.18- μ m CMOS Switches", *IEEE Regional Symposium on Micro and Nanoelectronics (RSM)*, 28-30 Sept.
- [22] Chien, Kaun-Hsiu and Chiou, Hwann-Kaeo (2013), "A 0.6-6.2 GHz Wideband LNA Using Resistive Feedback and Gate Inductive Peaking Techniques for Multiple Standards Application", *Asia-Pacific Microwave Conference Proceedings*, 5-8 Nov.
- [23] Murad, S.A.Z., Ismail, R.C., Isa, M.N.M., Ahamd, M.F. and Han, W.B. (2013), "High Gain 2.4 GHz CMOS Low Noise Amplifier for Wireless Sensor Network Applications", *IEEE International RF and Microwave Conference (RFM)*, 09-11 Dec.
- [24] Kurniawan, Taufiq Alif and Wibisono, Gunawan (2013), "Noise Modeling of Source Inductive Degeneration Low Noise Amplifier in 0.18- μ m CMOS Technology", *IEEE International Conference on Communication, Networks and Satellite (COMNETSAT)*, 3-4 Dec.
- [25] Motamarri, Naveen, Islam, Munshi Nurul and Apurbaranjana, P., Deepu, S P. and Prasantakumar, S. (2014), "A High-gain Source Degenerative Cascode LNA for Wi-Max and W-CDMA Applications at 3.5 GHz", *IEEE International Conferences on Control, Instrumentation, Communication and Computational Technologies (ICCICCT)*.
- [26] Soorapanth, T. and Lee, T.H. (1997), "RF Linearity of Short Channel MOSFETs", *IEEE Journal of Solid State Circuits*, Vol. 32, No. 5, May.

A Review of Spectral Unmixing Techniques in Target Detection

Amrita Bhandari*, Dr. K.C. Tiwari**

* Research scholar, Department of Civil Engineering,
Delhi technological university, 110088 – Delhi, India

** Professor, Department of Civil Engineering,
Delhi technological university, 110088 – Delhi, India

Abstract: Hyperspectral data has enhanced the scope of applications of remote sensing in various domains. However, exploitation of hyperspectral data is still subject to development and research of newer algorithms/techniques for extraction of application specific significant/relevant data. Hyperspectral data is extremely suitable in target detection; however, its full potential is still to be exploited. Spectral unmixing for the purpose of target detection and enhancement, when target either occupies a mixed pixel or a sub pixel, is one area which continues to be researched. Aim of this paper is to review various existing spectral unmixing techniques with an objective of analysing the algorithms and procedures followed by them and their utility in target detection.

Keywords- Spectral unmixing, target detection, end members, hyperspectral imaging

I. Introduction

With the advancements in technologies, remote sensing today is being increasingly used in diversified areas such as terrain classification, target detection and classification, environmental mapping, weather prediction, atmospheric pollution monitoring *etc.* Study of these application areas gets facilitated as the classes and objects that may appear in any scene (such as vegetation, water body, vehicles, aircrafts *etc.*) can be effectively characterized. This is possible due to the fact that objects reflect, emit, scatter, and absorb electromagnetic (EM) radiation differently. The sensors measure radiation which comes after propagation from the atmosphere. Since it is practically not possible to record information at each individual wavelength of the EM spectrum, the sensors are often designed to record data in certain discrete bands only. These sensors are known as single band panchromatic, multiband or multispectral imaging systems (3-12 bands) which sense visible, shortwave, thermal and infrared regions of the EM spectrum. These sensor systems provide improved spatial resolution but since the data is acquired only in a few discrete wavelength bands, it lacks accurate detection and identification of small objects as their reflectance gets mixed with the background scene. To obtain data of a higher spectral resolution compared to multispectral data, hyperspectral sensors are used [1]. Sensors acquire data in many, very narrow, contiguous spectral bands throughout visible, NIR, MIR (from 0.4 to 2.5 μm), and thermal IR (from 8 μm – 14 μm) portions of EM spectrum [2].

Contiguous narrow bandwidths which is characteristic of hyperspectral data allows for in-depth examination of earth surface features which may otherwise be ‘lost’ within the relatively coarse bandwidths acquired with multispectral scanners [3].

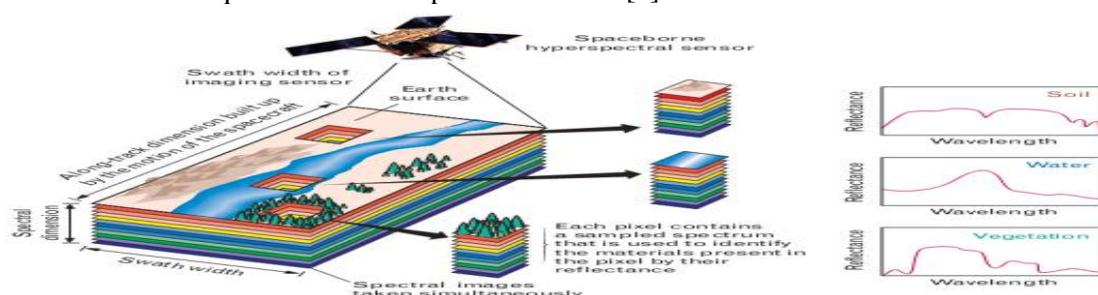


Figure 1.1: Overview of collection capabilities of a hyperspectral sensor system. Shown are materials with distinctive spectroscopic characteristics obtained through many bands or channels collected by instrument [2].

The above given image provides an overview of collection capabilities of a hyperspectral sensor system. It shows materials with distinctive spectroscopic characteristics obtained through many bands or channels collected by instrument. The reflected intensities with respect to any material/object on ground across different contiguous wavelength bands are known as its spectra/spectral signature. It has been reported that all materials in nature have unique spectral signatures [2]. This makes hyperspectral data particularly suitable for detection of objects that may reside in only a few pixels.

A large number of hyperspectral bands result in an increase in the volume of data and hence adds to the problems in data transmission, storage and analysis. Besides, based upon the spatial resolution, the targets may be defined as full pixel (target occupies one full pixel) and sub-pixel target (target occupies more than one pixel) (Figure. 1.2). Most target detection algorithms can at best detect full pixel targets, leaving out several partially occupied/mixed pixels. This reduces the number of pixels of the target (all pixels not being full pixels) and it is a challenge to recover all the pixels (both full and partially occupied).

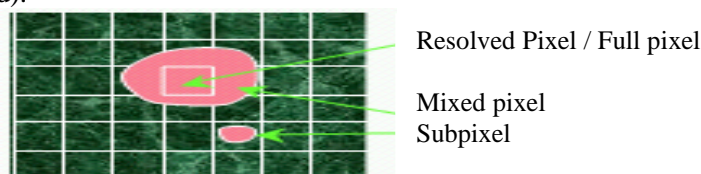


Figure 1.2: Types of Resolutions [4]

Due to low spatial resolution of Hyperspectral sensors the adjacent end members jointly occupy a single pixel thereby leading to a mixed pixel. Also if distinct materials are combined into a homogenous mixture, mixed pixels generate. Thus the obtained spectrum of any image pixel is a mixture of spectral signatures of different end members that may be present in that pixel. Spectral unmixing thus needs to be performed in order to determine the fraction of pixel area covered by each material present in the image.

Also, in order to accomplish target detection, spectral unmixing is required. The target detection process involves performing detection, classification, discrimination, identification/recognition and quantification as shown in Figure 1.3.

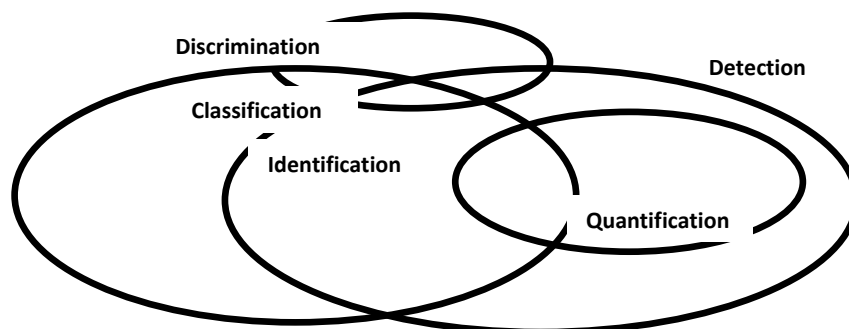


Figure 1.3: Target detection process

For identification *i.e.* to find out what the target actually is (a tank, a person, an aircraft *etc.*), it needs to be separated from the background components. This process is accomplished by using spectral unmixing. First step is to reduce the dimension of acquired hyperspectral data, followed by determining the number of end members present in scene and then estimating the abundance fraction of end members as shown in fig. 1.4.

The paper is constructed with a view to provide an overview of the unmixing techniques, as a follow-up to comparative efforts done by many researchers in this domain [10, 13, 17, 18, 19, 20, 21] and with more focus on applying unmixing in target detection for hyperspectral data.

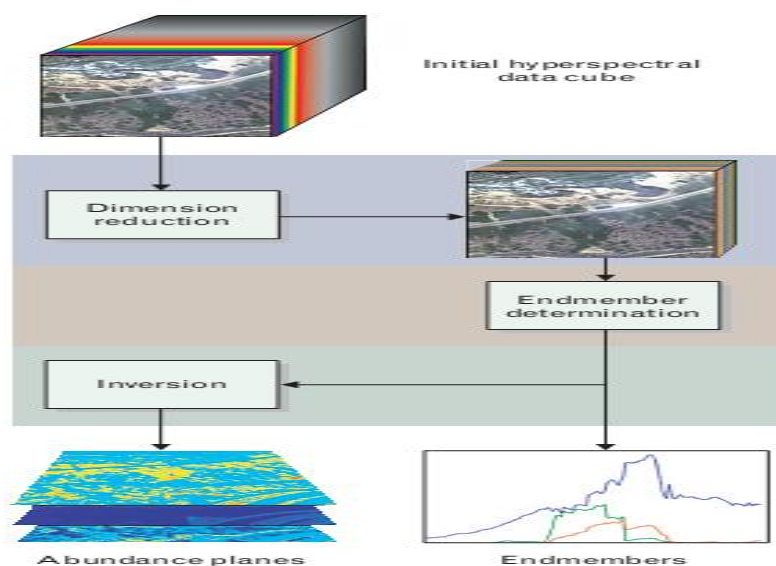


Figure 1.4: End to end spectral unmixing process [4]

This review paper is organized into five sections. Section 2 presents a literature review which provides an overview of work that has been done so far in order to obtain endmembers and their abundance fractions. The existing spectral unmixing algorithms found after detailed literature review have been listed in Section 3. Section 4 of the document outlines the comparative analysis of these algorithms and discussions on them. Conclusions drawn from the review and analysis have been discussed in Section 5. Towards the end of the paper is the references section that includes the details of reviewed and the referred research papers.

II. Literature review

Keshava et al. in his paper [4] performed a survey on unmixing algorithms with a view to find out commonalities and differences between these and to map them into some taxonomy [4, 5]. The work explained how mixed pixels are generated and what leads to the need of unmixing. The organization of unmixing algorithms was done on the basis of three criteria: Interpretation of captured data by the algorithms, description of randomness and optimization criterion.

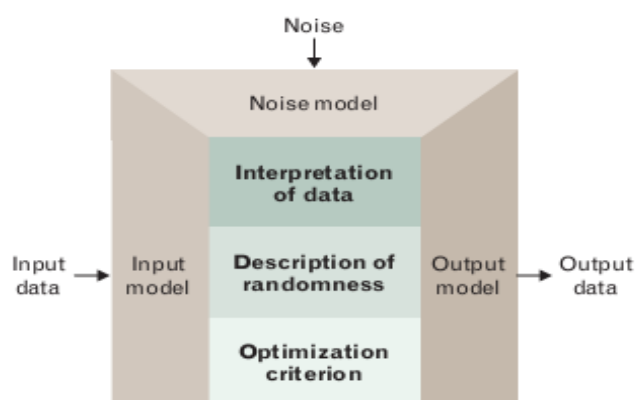


Figure 2.1: Model for algorithm features.

The taxonomies were built by studying and estimating important physical parameters from an electromagnetic signal that has interacted with the material of interest. He explained that in order to effectively un-mix the hyperspectral data, it must be clear that how constituent material substances in a pixel combine which lead to generation of a composite spectrum by the sensor. Thus mixing models were categorized to be linear mixing model and non linear mixing model as shown in figure 2.2. The created taxonomies reflect the wide amount of disparity that exists in the approaches undertaken to solve the same problem.

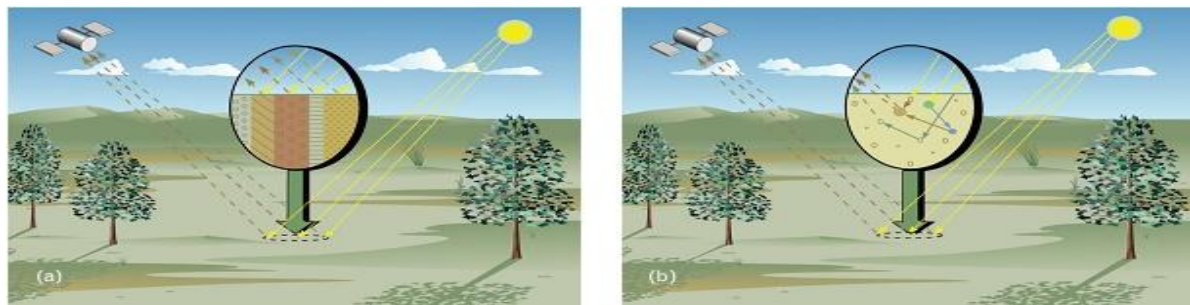


Figure 2.2: (a) The linear mixing model assumes a well-defined proportional mixture of materials, with a single reflection of the illuminating solar radiation. (b) Nonlinear mixing models assumes a homogeneous mixture of materials

Antonio Plaza and Mario Parente in [6] provided a quantitative assessment of unmixing techniques with main focus on differentiating between statistical and geometrical approaches for spectral unmixing. They compared the performance of some statistical versus geometrical end member extraction algorithms using Cuprite data set obtained by NASA's airborne visible infrared imaging spectrometer (AVIRIS) [7]. Spectral angles obtained after comparing the USGS library spectra of five highly representative minerals in the Cuprite mining district with the corresponding endmembers extracted by different algorithms from the AVIRIS Cuprite scene were tabulated. It was shown that geometrical methods such as N-FINDR, VCA or OSP provide endmembers which are similar to the USGS reference signatures. They outlined that statistical methods based on the incorporation of spatial information have the potential to improve the quality of the endmembers.

Chang and others [8] in their paper on Spectral Unmixing, Classification, and Concentration Estimation of Chemical and Biological Agents, investigated OSP and NCLS for chemical biological agent detection and concentration estimation. The experimental datasets used included chemical and biological agent signatures collected by the infrared spectrum technique. The experiments conducted showed that NCLS method provided more accurate abundance fraction.

Manolakis, Siracusa, and Shaw in their paper [9] explored the linear mixing model (LMM) to characterize the targets and the interfering background. They focussed on algorithms for the detection of low probability, whole-pixel or subpixel targets with known spectral signature.

Antonio Plaza and others in [10] presented a comparative study of standard end member extraction algorithms using a custom-designed quantitative and comparative framework that involves both the spectral and spatial information. The results showed that end member selection and mixed-pixel interpretation by a linear mixture model are more successful while using methods that combine spatial and spectral information. It was assumed that reliable ground-truth spectral signatures are available. The estimated abundance planes were compared to ground-truth reference maps representing the spatial distribution of end member constituents in simulated imagery. The experiments showed that combination of spatial and spectral information produces results that are superior to those found by using the spectral information alone.

III. Unmixing Algorithms

LMM (Linear mixing model)

Manolakis *et al.* [9] explained that the spectrum of a mixed pixel is represented as a linear combination of component spectra (endmembers). The abundance of each end member is proportional to the fraction of the pixel area covered by it. In case of L spectral bands, the spectrum of any pixel and the spectra of the endmembers can be represented by L -dimensional vectors. Therefore, the general equation for LMM is

$$x = \sum_{k=1}^M a_k s_k + w \triangleq Sa + w$$

$$S \triangleq [s_1 \ s_2 \ \cdots \ s_M]$$

$$a \triangleq [a_1 \ a_2 \ \cdots \ a_M]^T$$

x spectrum of the mixed pixel;

$$\begin{aligned}
 & s_k \text{ spectra of endmembers;} \\
 & a_k \text{ their abundances;} \\
 & M \text{ number of the endmembers;} \\
 & w \text{ } L \text{ dimensional error vector accounting for lack of fit and noise effects} \\
 & a_k \geq 0 \text{ (non negativity constraint)} \\
 & \sum_{k=1}^M = 1 \text{ (additivity constraint)}
 \end{aligned}$$

PPI (Pixel Purity Index)

This algorithm requires close human supervision during the process of determining the endmembers and works by projecting each pixel onto one vector from a set of random generated vectors. A pixel purity score is calculated for each point in the image cube by randomly generating L lines in the N -D space comprising the MNF-transformed data. All the points in that space are projected onto these lines, and the ones falling at the extremes of each line are counted. After many repeated projections to different random lines, those pixels that count above a certain cut off threshold are declared “pure” pixels [10].

N-FINDR

The N-FINDR method [11] is a fully automated geometric method that finds the set of pure pixels that define the space with the maximum volume within the dataset. This method requires a dimension reduction step, originally an orthogonal subspace projection (OSP). It works on random selection as pixels as endmembers and then calculates a trial volume. Let EM be defined as: $EM = \begin{bmatrix} 1 & 1 & \dots & 1 \\ e_1 & e_2 & \dots & e_E \end{bmatrix}$, where e_i are end member column vectors, and EM is the number of endmembers used to calculate the simplex volume. The volume of the simplex formed by the endmembers is proportional to the determinant of EM . In order to refine the initial volume estimate, a trial volume is calculated for every pixel in each end member position by replacing that end member and recalculating the volume. If the re-placement results in a volume increase, the pixel replaces the end member. This procedure, which does not require any input parameters, is repeated until there are no replacements of end-members possible as shown in [11].

ORASIS (Optical Real-time Adaptive Spectral Identification System)

Once pre-processing is performed on given data, a selection process is run with the purpose of pre-screening the data for unique spectra, thus creating a representative set of exemplar vectors that can be used as endmembers for spectral unmixing [12]. Spectral angle distance is calculated so as to remove the redundant spectra that may appear in the data by discarding all vectors that are not separated by a certain threshold. Next step is to project the spectra onto a lower dimension subspace created using Gram – Schmidt process and finding a simplex using minimum volume transform.

IEA (Iterative error analysis)

IEA [13] works on the existence of relatively pure pixels. In this method, a series of linear, constrained unmixing is performed. While performing unmixing, the pixels that minimize the remaining error are chosen iteratively as endmembers.

CCA (Convex cone analysis)

CCA [14] is also a geometric algorithm that works on creating a convex cone around the data. It begins from an orthogonal basis set obtained from a subset of the eigenvectors of the data correlation matrix. The number of basis vectors is used as an input to the algorithm.

ICE (Iterated Constrained Endmembers)

ICE [15] minimizes the regularized residual sum of squares (RSS) by finding the volume of the simplex. It does not need a dimension reduction step. Given that the free parameters are the endmembers and their abundances, for each pixel the algorithm iterates the solution of the low interleaved and interdependent minimization problems. First the proportions are computed by quadratic programming assuming that the endmembers are known, and then the endmembers are computed as the direct minimization of the RSS functional.

VCA (Vertex Component Analysis)

It is an unsupervised algorithm that utilizes orthogonal subspace projections [22]. Endmembers are assumed as the vertices of a simplex, and the affine transformation of a simplex is

considered as a simplex too [16]. A hyper plane is chosen by using projections and another simplex is created whose vertices are the final endmembers. After successfully projecting the data on this selected hyper plane, algorithm proceeds by projecting all image pixels in a random direction. The pixel with the largest projection is selected as the first end member. The remaining dataset is then iteratively projected in a direction orthogonal to the subspace created by the successfully determined endmembers. This process is repeated until a complete set of end members is determined [16].

ICA (Independent Component Analysis)

It is a statistical approach for end member extraction. This algorithms with its basis in signal analysis, does not require any *a priori* information about the target data [23]. It works by finding statistically independent components by representing non Gaussian data in a linear format. The artificial targets in a natural environment are generally statistically independent. Thus ICA can be applied on different bands of hyperspectral data. The targets most likely appear in either one or a few number of transformed components [23].

IV. Comparative analysis

A summary of reviewed spectral unmixing algorithms for hyperspectral images is given in the following table:

Table 1: A summary of spectral unmixing algorithms for hyperspectral images

Algorithms	Characteristics
Pixel purity index (PPI)	Non-statistical, supervised end member extraction method Limitations: <ul style="list-style-type: none"> It requires a human interference to work on. It requires a way out to produce an appropriate initial set of endmembers as the number of iterations will otherwise be very high. It requires a proper learning on how to procure accurate values of threshold for the pixel purity index counts Only considers the spectral information in endmembers detection with no attention to spatial information.
N – FINDR	Geometric end member extraction method, non-parameterized and a simplex-growing, selection algorithm Limitations: <ul style="list-style-type: none"> It works for finding all the present endmembers thereby increasing the computational complexities. Requires prior knowledge of the number of endmembers that are required to be extracted. Does not include spatial information for end member detection
Optical Real-time Adaptive Spectral Identification System (ORASIS)	It is a fully automated, parameterized method for end member extraction. It provides low computational complexity and converges once all the exemplar spectra are found in data. It mostly applies in oceanography and target detection. Limitations: <ul style="list-style-type: none"> It is a simplex-shrinking algorithm that finds endmembers from a scene autonomously.
Iterative error analysis (IEA)	It is a fully automated, non – parameterized algorithm that shows minimum error in unmixing. It is mostly applicable to land cover and mineral mapping. Limitations:

	<ul style="list-style-type: none"> Does not include spatial information for end member detection
Convex cone analysis (CCA)	<p>It is a fully automated, geometric, parameterized algorithm. It is mostly applicable to anomaly detection and target detection.</p> <p>Limitations:</p> <ul style="list-style-type: none"> Complexity is very high if there are large numbers of corners in the convex cone. Does not include spatial information for end member detection
Iterated Constrained Endmembers	This algorithm does need a dimension reduction step.
Vertex Component Analysis (VCA)	<p>Geometric end member extraction method, unsupervised algorithm</p> <ul style="list-style-type: none"> Limitations: Computational complexity is high as the algorithm iterates until all endmembers are exhausted Only considers the spectral information in endmembers detection with no attention to spatial information
Independent component analysis (ICA)	Nonparametric statistical unmixing approach. It considers spatial information and thus has the potential to improve the quality of the endmembers. It does not require a priori information about target.

V. Conclusions

The review presented indicates that most of the spectral unmixing algorithms adopt one of the following assumptions, viz, linear mixing, Gaussian distribution, and the minimization of squared error. Many researchers have worked on non-linear unmixing but it is still under evaluation and testing and its application in target detection needs to be explored further. In case of sub-pixel target detection, where target size is too small to detect leading to loss of its important features, statistical methods have proved to provide better results. Many spectral unmixing algorithms have been introduced and implemented in literature; however there is still a scope for evaluating them for finding accuracy of these algorithms in terms of estimating the endmembers and their abundance fractions.

VI. References

- P. Shippert, "Why Use Hyperspectral Imagery," *Photogrammetric engineering & remote sensing*, April 2004, pp. 377 – 380
- G. Shaw and H.K. Burke, "Spectral Imaging for Remote Sensing," *lincoln laboratory journal*, vol. 14, no. 1, 2003, pp. 3-28
- M. Govender, K. Chetty and H. Bulcock, "A review of hyperspectral remote sensing and its application in vegetation and water resource studies," ISSN 0378-4738, *Water SA*, vol. 33, no. 2, April 2007, pp. 145 – 152
- N. Keshava, "A Survey of Spectral Unmixing Algorithms," *Lincoln laboratory journal*, vol. 14, no. 1, 2003, pp. 55-78
- N. Keshava, J. Kerekes, D. Manolakis, G. Shaw, "An Algorithm Taxonomy for Hyperspectral Unmixing", Algorithms for Multispectral, Hyperspectral, and Ultraspectral Imagery VI, *Proceedings of SPIE*, vol. 4049, 2000, pp. 42-63
- A. Plaza, M. Parente, "Survey of geometric and statistical unmixing algorithms for hyperspectral images", *IEEE*, 978-1-4244-8907-7/10/2010
- R. O. Green, M. L. Eastwood, C. M. Sarture, T. G. Chrien, M. Aronsson, B. J. Chippendale, J. A. Faust, B. E. Pavri, C. J. Chovit, M. Solis, et al., "Imaging spectroscopy and the airborne visible/infrared imaging spectrometer (AVIRIS)," *Remote Sensing of Environment*, vol. 65, no. 3, pp. 227–248, 1998.

8. C. Kwan , B. Ayhan, G. Chen, J. Wang and Chang “A novel approach for Spectral Unmixing, Classification, and Estimation of Chemical and Biological Agents”, *IEEE transactions on geo-science and remote sensing*, vol. 44, no. 2, 2006, pp. 409- 419.
9. D. Manolakis, C. Siracusa, and G. Shaw, “Hyperspectral Subpixel Target Detection Using the Linear Mixing Model,” *IEEE transactions on geo-science and remote sensing*, vol. 39, no. 7, July 2001, pp. 1392-1409
10. A. Plaza, P. Martínez, R. Pérez, and J. Plaza, “A Quantitative and Comparative Analysis of Endmember Extraction Algorithms From Hyperspectral Data,” *IEEE transactions on geo-science and remote sensing*, vol. 42, no. 3, 2004, pp. 650 – 663
11. M. E. Winter, “N-FINDR: An algorithm for fast autonomous spectral end-member determination in hyperspectral data,” *Proc. SPIE*, vol. 3753, pp. 266 –275, 1999.
12. J. Bowles, J. Antoniadis, M. Baumbach, J. Grossman, D. Haas, P. Palmadesso, and J. Stracka, “Real Time Analysis of Hyperspectral Data Sets Using NRL’s ORASIS Algorithm,” *SPIE* 3118, 1997 , pp. 38–45
13. M.A. Veganzones and M. Grana, “End member extraction methods: A short review,” 12th international conference on knowledge-based intelligent information and engineering systems, vol. 5179, pp. 400–407, Jan 2008.
14. A. Ifarraguerri and C. Chang, “Multispectral and Hyperspectral Image Analysis with Convex Cones”, *IEEE*, 1999, pp. 756 – 770
15. M. Berman, H. Kiiveri, R. Lagerstrom, A. Ernst, R. Dunne, and J.F. Huntington, “ICE: a statistical approach to identifying endmembers in hyperspectral images. *Geo-science and Remote Sensing, IEEE Transactions*, 2004.
16. D. Craig, “Minimum-volume transforms for remotely sensed data”, *Geo-science and Remote Sensing, IEEE Transactions*, 1994.
17. R. P. Karchi, B.K Nagesh, “A Review of Spectral Unmixing Algorithms in the context of Mars Dataset”, *International Journal of Latest Trends in Engineering and Technology (IJLTET)*, 2013, ISSN: 2278-621X, pp. 55-60
18. Q. Du, N. Raksuntorn, N.H. Younan, and R.L. King, “End-member extraction for hyperspectral image analysis,” *Applied Optics*, vol. 47, no. 28, pp. 77–84, 2008.
19. A. Garcia, M. Reyes, S. Torres, and J.D. Chinea, “A comparison of unmixing algorithms for hyperspectral imagery,” *Proceedings of SPIE*, vol. 7334, Jan 2009.
20. N. Dobigeon and V. Achard, “Performance comparison of geometric and statistical methods for endmembers extraction in hyperspectral imagery,” *Proceedings of SPIE*, vol. 5982, pp. 598213–1, 2005.
21. José M. Bioucas-Dias , A. Plaza, N. Dobigeon, M. Parente, Q. Du, P. Gader and J. Chanussot, “Hyperspectral Unmixing Overview: Geometrical, Statistical, and Sparse Regression-Based Approaches,” *IEEE journal of topics in applied earth observations and remote sensing*, vol. 5, no. 2, April 2012, pp. 354-379
22. M. Ahmad and Dr. Ihsan Ul Haq, “Linear Unmixing and Target Detection of Hyperspectral Imagery Using OSP,” *International Conference on Modeling, Simulation and Control IPCSIT*, vol.10, 2011, pp. 179-183
23. K.C. Tiwari, M.K. Arora, D. Singh and D. Yadav, “Military target detection using spectrally modeled algorithms and independent component analysis,” *Proceedings of SPIE*, vol. 5, 2013, 026402: 1 -11



**ANCHORING EFFECT IN INVESTMENT DECISION MAKING-
A SYSTEMATIC LITERATURE REVIEW**

Priya Kansal

*Research Scholar, Department of Humanities,
Delhi Technological University.*

Dr. Seema Sing

*Head and Associate Professor, Department of Humanities,
Delhi Technological University*

ABSTRACT

While studying investment behavior, the most common bias which impact the decision making is anchoring. Anchoring is defined as the tendency of investors to rely on some piece of information to take decision. The present study made an effort to systematically review the literature available on the existence and effect of anchoring bias in stock market investments. For the purpose of the analysis, the research work published in last 15 years has been taken. Total 16 articles were selected on the basis of defined criteria and analyzed in terms of their publication year, journal, methodology used, data used, country of data collection, citation and content.

Keyword: Anchoring, systematic Literature review, Statistical Techniques, Citation Analysis, Content Analysis

1. Introduction:

In behavioral economics research, the pioneer work to study anchoring effect is done by Tversky and Kahneman (1974). According to Tversky and Kahneman, decision makers are generally influenced by an initially presented value called anchor. And this influence is known as anchoring effect.

Following the work of Tversky and Kahneman (1974), many studies discussed the anchoring effect in several domains and lead to the existence of robust and substantial anchoring effects. For example, Sudgen et al. (2013), Adaval and Wyer (2011), Bateman et al. (2008), Cricther and Gilovich (2008), Nunes and Boatwright (2004), Simonson and Drolet (2004), Ariely et al. (2003) and Mussweiler et al. (2000) studied the anchoring effect in price estimation and willingness to pay in different experimental settings for individuals of different countries. Also in credit market, anchoring appears to be important as the firm anchor the past credit spread to pay current credit spread.

Moreover, Liao et al (2013) studied the anchoring effect in Foreign Institutional Investment and concluded that prior foreign ownership influences the momentum of foreign investments. Anchoring effect is also studied in different type of financial markets such as horse race betting (Johnson and Schnytzer (2009) real estate investment [(Einio, Kaustia & Putton, 2008), Saieler et al. (2010), (Bucchianeri & Minson, 2013)]. The anchoring effect has also been found important in analyst's forecasting of firm's earning (Cen, Hillary & Wei (2013) and in macroeconomic releases (Campbell and Sharpe, 2009 and Hess & Orbe, 2013). A robust and rigorous review of all major studies of anchoring effect is done by Furham & Boo (2011). This study tries to take the study of Furnham and Boo a step ahead by narrowing the type of market and anchor. This study systematically reviews the literature on anchoring effect in investment decision making of individuals particularly in stock market.

2. Purpose:

The purpose of this paper is to systematically review the literature published in past 15 years (2001-2015) on anchoring effect in investment decision making. The paper highlights the major gaps in the existing studies on anchoring effect. It also aims to raise specific question for future research.

3. Data and Methodology:

3.1 Strategy for literature search: We establish search criteria and conducted a search by identifying relevant keywords, time frame, various databases. We used keywords like "anchoring", reference point", and "anchoring heuristics". etc. We used Taylor and Francis, Elsevier, Online Wiley Library and other databases such as Google Scholar and Research Gate for the literature search. We have selected a time span of 16 years (2001-2015). We have considered those articles which are published in peer reviewed journals and published only in English. Articles are of different types such as research paper, case study, review paper, conceptual papers are not considered as they are not published work. We have focused only those articles which are having discussion on anchoring in stock markets. All other articles like anchoring in real estate, anchoring in policy formulation and specially, anchoring in consumer buying behavior, which are abundant in number, were not satisfying the purpose of literature review.

We conducted our database search in July '2015 and it included all the articles which satisfy the above mentioned criteria. In our search, we found several articles. After reviewing the title and abstract 16 articles found suitable to review.

4. Classification and analysis of Literature: In this section we have classified all the research papers on the basis of publication, time, location, journal, data, technique etc.

4.1 Year of Publication: Table 2 shows the year wise distribution of the articles published from 2001 to 2015. There are very few studies available on anchoring bias which shows the less interest of researchers in studying anchoring bias. The reason of this may be that ample research has been conducted on anchoring bias in past decades.

4.2

Year	No. of Articles
2001	1
2002	1
2003	1
2004	2
2005	1
2006	0
2007	0
2008	1
2009	1
2010	1
2011	1
2012	2
2013	3
2014	0
2015	1

Table 1: Year-wise frequency of articles

Database	Date of Search	Time Frame	No. of Selected Articles
Elesvier	July'2015	2000-2015	5
Online Wiley Library	July'2015	2000-2015	4
Others	July'2015	2000-2015	3
Taylor And Francis	July'2015	2000-2015	2
Cambridge	July'2015	2000-2015	2

Table:2 Database protocol: Database wise distribution of Articles

4.3 Journal of Publication: The literature was analyzed with respect to the journal of publication to identify important journals in this area. Results revealed that the dataset of 16 articles is spread over 9 journals. Four journals had two or more published articles, and these are shown in Figure:1. The remaining journals had only one published article each. The 4 journals comprise around 75 percent of the journals covered in this study. Figure1 shows that the top three journals in terms of the number of research articles published are Journal of Financial Economics, The Journal of Finance and The Journal of Behavioral Finance, with 4, 3 and 3 articles, respectively.

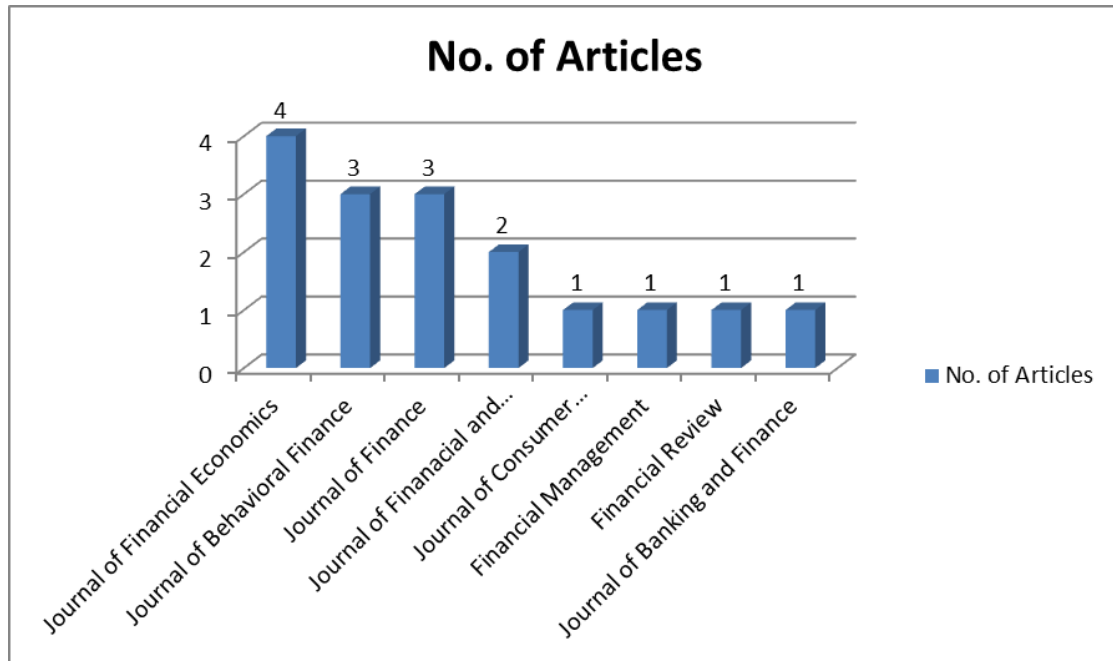


Figure:1 Distribution of Articles based on journal

4.4 Country of Sample data collection:

Figure 2 gives the frequency of countries from where the data has been collected either in primary or in secondary form in the articles selected for review. The classification shows that majority of studies are conducted in U. S. stock exchange. There are 11 studies out of total 16 studies which are conducted in United States. There are only two studies which are conducted in Finland, whereas only one paper is found where the sample data has been collected from each other country like Germany, Stockholm and China.

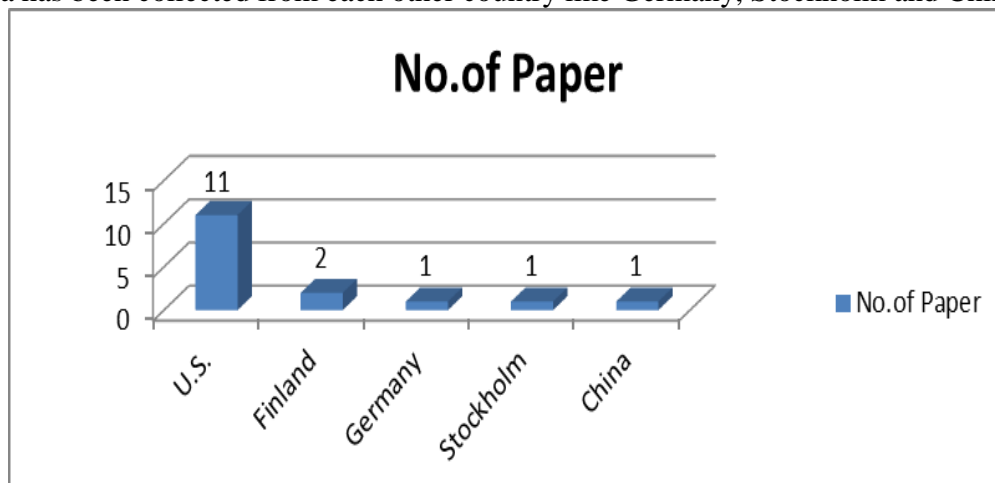


Figure:2 Distribution of Articles based on country of sample data

4.4. Type of Study and Data:

A review of literature on the basis of type of study and data helps to identify the focus area of past research studies. Figure: 3 shows the distribution of type of studies along with type of data used for the study. We have classified the research studies into four categories: descriptive, empirical, analytical, and conceptual. In descriptive research, we have included studies that are related to surveys or fact findings. In empirical research, we have included studies based on observations or experiments, while in conceptual research; we have included articles related to the development of some model or theory. Figure:3 shows that the majority of studies, that is 8, are analytical in nature, and that most of them are based on secondary data. Our analysis shows that secondary data have been generally collected through the brokerage houses and are longitudinal in nature. There are very few research studies that are based on primary data and that are empirical in nature.

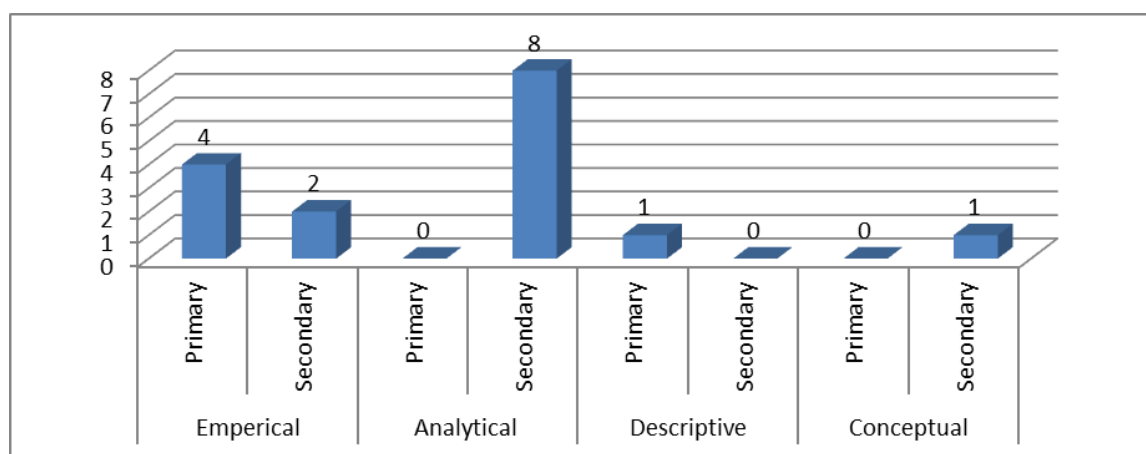


Figure:3 Distribution of Articles based on the type of data used in research

Year	Primary	Secondary	Total
2001	0	1	1
2002	0	1	1
2003	1	0	1
2004	1	1	2
2005	0	1	1
2006	0	0	0
2007	0	0	0
2008	1	0	1
2009	0	1	1
2010	0	1	1
2011	0	1	1
2012	0	2	2
2013	0	3	3
2014	0	0	0
2015	1	0	1
Total	4	12	16

Table:3 Year- wise Frequency of Article in terms of type of data collected

Further Table:3 shows that primary data is used in very less no. of studies in this research area. Only 4 out of total 16 studies are conducted on primary data, whereas the others are based on secondary data. However, in the most recent studies, the primary data has been used for the research.

4.5 Statistical Techniques/ Methods:

In this section of the study, we analyzed the selected previous researches on the basis of the statistical technique used in the studies. This analysis provides the information about the most widely and popular statistical technique used for confirming anchoring bias. The figure_ shows that the most widely used technique is regression analysis.

Table:4 Distribution of Articles based on Research Design

Technique	No. of papers	%age
Multiple Techniques	2	12.5
Regression Analysis	8	50
Correlation	1	6.25
Paired t- test	1	6.25
Simulation	1	6.25
Decomposition Analysis	1	6.25
Time Series Analysis	1	6.25
Other	1	6.25
Total	16	100

Table 4 shows that 8 out of 16 studies used regression analysis as a statistical tool. Various type of regression such as panel regression, cross sectional was used. Only two studies applied multiple techniques including the combination of regression analysis, decomposition analysis, t-test etc.

4.6 Citation Analysis:

In this section, we have analyzed the selected articles on the basis of their citation in other publications to identify the most relevant and important paper available on anchoring bias. We used Google Scholar to find the citations. We found that 15 out of 16 articles were cited outside which shows that all the articles are important in our research area. Although the citation for some papers is is very low. The treason may be that these articles are very recent. We don't find citation for one article published in 2015. Table:5 represent the citation of all the 16 articles which shows that there are only four articles whose citation is more than 100.

S. no.	Article	Citation
1	Grinblatt and Keloharju (2001)	981
2	Grinblatt & Han (2005)	482
3	Chapman and Johanson(2002)	354
4	George and Hwang (2004)	345
5	Baker, Pan & Wugler (2012)	83
6	Torngern & Montgomery (2004)	81
7	Campbell & Sharpe (2009)	70
8	Kaustia, Alho and Puttonen(2008)	70
9	Li and Yu (2012)	53
10	Cen, Hillary and Wei (2013)	27
11	Mussweiler and Schneller (2003)	14
12	Park(2010)	11
13	Chang, Luo and Ren (2013)	8
14	George, Hwang and Li (2013)	4
15	Chang et. al(2011)	2
16	Ducles (2015)	0

Table:5 Distribution of Articles based on Citation

4.7 Content Analysis:

Content analysis provides all the information about the objectives, techniques and result of the study. In this section we have discussed all the empirical findings of research studies selected for the purpose of systematic review of papers on anchoring bias.

Table:6 shows the empirical findings of anchoring effect in investment decision – making. The empirical evidence is divided into following categories on the basis of the anchor or reference point fixed by the investors:

- i) Chart pattern
- ii) Moving Averages
- iii) 52 week high and low prices
- iv) Initial Values/ Prices
- v) Recent Prices/ Last Day Prices

Anchor	Empirical Findings
Chart pattern	Ducles (2015) found that if last day closing price is higher than the opening price i.e. the last day was a upward moving day, then the prediction for the next day is for upward movements and result in higher investments that day. Mussweiler and Schneller (2004) suggested that investor buy more and sell less when the chart is characterized by salient high than low.
Moving Averages	Park (2010) documented that the ratio of 50 days moving averages to 200 days moving averages are used to predict moving averages are used to predict the future returns. And when this ratio is combined with 52-week high, these values works as an anchor for momentum profits not only in short term but in long term also.
52 weeks high & low stock price	George and Hang (2004) revealed that 52weeks high and lows are set as the anchor for forecasting future returns but it works only in short term not in long term. Grinblatt and Keloharaju (2001) also shown that investor more likely to sell a stock whose price is near a historical high and more likely to buy a stock that is near a historical. Further Li and Yu (2012) suggested that nearness to the DOW historical high, positively predict future market return. But if the prices are anchored near or far 52- week high, market underreact to extreme earnings news for individual stock [George, Hwang & Li (2013)] that indicates that these prices do not act as an anchor.
Initial Values/ Prices	Kaustia, Alho and Puttonen (2008) studied the management graduates and suggested that initial prices act as an anchor irrespective of the investment experience.
Recent Prices	Baker, Pan and Wurgler (2012) documented that recent prices act as an anchor at the time of valuation. Chang et al (2011) suggested that there is a strong positive correlation between ex-day (last day) price and cum day (present day) price. Previous month data is also considered as an anchor and consensus forecasts are biases towards the value of previous month's data (Campbell and Sharpe,2009, Torngern and Montgomery (2004) found that previous price movements are used as anchor by only by lay investors.

Table:5 Empirical Findings on Anchoring bias in investment decision making

5. Findings:

In this section, we discuss the findings and identify the research gaps on anchoring bias in investment decision making. As discussed above, anchoring bias has flourished in every field, we have made the efforts to review all the studies related to stock market investments only and identify the following:

- i) Irrelevant anchors affect the judgment and lead to higher losses and additional regret of not selling/ buying at time (Chapman and Johanson, 2002)
- ii) Kaustia, Alho and Puttonen (2008) and George and Hwang (2004) suggested that professional investors are less prone to anchoring bias than naïve investors. However, if the anchor is purchase price or initial value, effect is same.
- iii) Anchors works in short term only. However, Grinblatt and Han (2005), Park (2010) suggested that, if these anchors are supported by some other determinants of stock prices, profit can be earned in long term also.
- iv) Chart patterns are also used as anchors and next day returns and price movements are predicted by the professional investors. [Chang, Luo and Ren (2013)], [Baker, Pan & Wugler (2012)]

6. Research Gaps:

6.1 Limited number of studies:

We have found only 16 studies in last 15 years of time period on anchoring bias in stock market investment which is very less in number. In the emerging fields like behavioral finance, the studies should be more and more models should be created to identify the anchoring bias in stock market.

6.2 Dearth of studies in emerging markets:

As the above analysis shows most of the studies are conducted in US stock market set up which is a developed market. Limited research has been done in emerging countries.

6.3 Most studies are based on secondary research:

Most of the studies are based on secondary data which demonstrate the past behavior. A very few studies used primary data through experiment to analyse the anchoring bias. There is a scope of study conducted on the basis of primary data so that the present and future behaviors of the investor could be predicted.

6.4 Limited studies on individual investors:

There are very few studies available on individual behavior. Most of the studies generalize the market as a whole.

7. Scope for Future Research:

The main purpose of this paper was to review the available literature on past 15 year on anchoring effect in stock market to identify the type of researches conducted and to analyse their findings. The analysis of these studies has come up with the new issues in the area of research which are discussed above. So, as discussed, there is a very few researches have conducted to analyse the anchoring bias. Hence there should be more studies. Moreover, these studies should also focus the emerging markets as it has been observed that after the era of globalization, emerging economies have higher growth potential and institutional and individual investors are more interesting in investing in these markets. Also, the research should be done equally on all types of investors like individuals, institutional; market etc and a comparison should be made to get a clear picture of the effect of anchoring in investment on different categories of investors. There is a scope of study conducted on the basis of primary data so that the present and future behaviors of the investor could be predicted.

References:

- Adaval, R. and Wyer, R.S. (2011). Conscious and Nonconscious Influences of a Price Anchor: Effects on Willingness to Pay for Related and Unrelated Products. *Journal of Marketing Research*, 48, 355-365.
- Ariely, D., Loewenstein, G., Prelec, D. (2003). "Coherent arbitrariness": Stable demand curves without stable preferences. *Quarterly Journal of Economics*, 118, 73-105.
- Baker, M., X. Pan, and J. Wurgler. (2012). The effect of reference point prices on mergers and acquisitions. *Journal of Financial Economics*, 106, 49-71.
- Bateman, I.J., Burgess, D., Hutchinson, W.G. and Matthews, D.I. (2008). Learning Design Contingent Valuation (LDCV): NOAA Guidelines, Preference Learning, and Coherent Arbitrariness. *Journal of Environmental Economics and Management*, 55, 127-41.
- Bucchianeri, G.W., Minson, J. (2013). A homeowner's dilemma: Anchoring in residential real estate transactions. *Journal of Economic behavior and Organisation*, 89, 76-92.
- Campbell, S. D., and S. A. Sharpe. (2009). Anchoring bias in consensus forecasts and its effect on market prices. *Journal of Financial and Quantitative Analysis*, 44,369-90.
- Chang, E. C., Luo, Y. and Ren, J. (2013). Cross-listing and pricing efficiency: The informational and anchoring role played by the reference price. *Journal of Banking & Finance*, 37,4449-64.
- Chang, E.C., Luo,Y. and Ren, J., (2011).Ex-day Returns for Stock Distributions: An Anchoring Explanation. Working paper, University of HongKong.
- Chapman, G.B. and Johnson, E.J., (2002). Incorporating the Irrelevant: Anchors in Judgments of Belief and Value. *The Psychology of Judgment: Heuristics and Biases*. Cambridge University Press, NewYork.
- Cen, L., G. Hilary, and K. C. J. Wei. (2013). The role of anchoring bias in the equity market: Evidence from analysts' earnings forecasts and stock returns. *Journal of Financial and Quantitative Analysis*, 48,47-76.
- Critcher, C.R. and Gilovich, T. (2008). Incidental environmental anchors. *Journal of Behavioral Decision Making*, 21, 241-251.
- Duclos, R, (2015), The psychology of investment behavior: (De)biasing financial decision-making one graph at a time. *Journal of Consumer Psychology*, 25(2), 317-25
- Furnham, A. and Boo, H.C. (2011). A literature review of the anchoring effect. *The Journal of Socio-Economics*, 40, 35-42.
- George, T. J., and C.Y. Hwang. (2004). The 52-week high and momentum investing. *The Journal of Finance*, 59,2145-76.
- George, T., Hwang, C. and Li, Y., (2013). Anchoring, the 52-week high and post earnings announcement drift. *Working Paper*.
- Grinblatt, M., and B. Han. (2005). Prospect theory, mental accounting, and momentum. *Journal of Financial Economics*, 78, 311-39.
- Grinblatt,M.,and Matti Keloharju. (2001), What makes investors trade? *Journal of Finance*, 51,589–616.
- Hess, D. and Orbe, S. (2013). Irrationality or efficiency of macroeconomic survey forecasts? Implications from the anchoring bias test. *Review of Finance* 17 (6), 2097-2131.
- Kaustia, M., Alho, E. and Puttonen, V. (2008), How Much Does Expertise Reduce Behavioral Biases? The Case of Anchoring Effects in Stock Return Estimates. *Financial Management*, 37 (3), 391-411.

- Johnson, J.E.V., Schnytzer, A. and Liu, S. (2009). To what extent do investors in a financial market anchor their judgements excessively? Evidence from the Hong Kong horserace betting market. *Journal of Behavioral Decision Making* 22, 410-434.
- Liao, Li- Chuan , Yeutien Chou, Ray and Chiu, Banghan. (2013). Anchoring Effect on Foreign Institutional Investors' Momentum Trading Behavior: Evidence from Taiwan Stock Market. *North American Journal of Economics and Finance* , 26, 72-91.
- Li, J., and J. Yu. (2012). Investor attention, psychological anchors, and stock return predictability. *Journal of Financial Economics*, 104, 401-19.
- Mussweiler, T. and Schneller, K. (2003). What Goes Up Must Come Down-How Charts Influence Decisions to Buy and Sell Stocks. *The Journal of Behavioral Finance* , 4(3), 121-130
- Mussweiler, T., Strack, F. and Pfeiffer, T. (2000). Overcoming the inevitable anchoring effect: considering the opposite compensates for selective accessibility. *Personality and Social Psychology Bulletin*, 26, 1142-1150.
- Nunes, J.C. and Boatwright, P. (2004). Incidental prices and their effect on willingness to pay. *Journal of Marketing Research*, 41 (4), 457-466.
- Park, S.C. (2010). The moving average ratio and momentum. *Financial Review*, 45, 415-447.
- Seiler, Michael J., Vicky L. Seiler, and Mark A. Lane (2012). Mental accounting and false reference points in real estate investment decision making. *Journal of Behavioral finance* 13.1, 17-26
- Simonson, I. and Drolet, A. (2004). Anchoring Effects on Consumers' Willingness-to-Pay and Willingness-to-Accept. *Journal of consumer research* 31 (3), 681-90
- Sugden, R. and Zheng, J., Zizzo, D.J. (2013). Not all anchors are created equal. *Journal of Economic Psychology*, 39, 21-31.
- Törngren, G. and Montgomery, H. (2004). Worse than chance? Performance and confidence among professionals and laypeople in the stock market. *Journal of Behavioral Finance*, 5, 148-153.
- Tversky, A. and Kahneman. (1974). Judgment under uncertainty: heuristics and biases. *Science*, 185, 1124-1131



ISSN NO. 2320-5407

Journal homepage: <http://www.journalijar.com>

INTERNATIONAL JOURNAL
OF ADVANCED RESEARCH

RESEARCH ARTICLE

Assessment of Fixed Bed Column Reactor using Low Cost Adsorbent (Rice Husk) for Removal of Total Dissolved Solids

S.K. Singh¹, Neha Narwal²

1. Professor, Department of Environmental Engineering, Delhi Technological University, New Delhi-42, India

2. B Tech, Environmental Engineering (2010-14), Delhi Technological University, New Delhi-42, India

Manuscript Info

Manuscript History:

Received: 15 September 2015

Final Accepted: 29 October 2015

Published Online: November 2015

Key words:

*Corresponding Author

S.K. Singh

Abstract

A continuous fixed bed column reactor was designed using low cost media and was assessed for its efficiency of treatment of ground water. The sorption capability of Rice Husk (media) for removing Total Dissolved Solids and Calcium, Magnesium and Chloride ions was evaluated in a fixed bed column reactor. The column experiment was conducted by varying the bed height and solution flow rate. It was observed that by increasing the flow rate of influent synthetic sample, the TDS removal efficiency decreased from 21% to 10.56% as the flow rate was increased from 40 to 102 mL/min. Due to increase in the influent flow rate, the contact period of ground water with the rice husk (media) decreased which resulted in less amount of adsorption of TDS by the media and therefore less removal. At a flow rate (40 mL/min), it was observed that removal efficiency of TDS is 20.79% at a height of 10 cm from the base of column; 13.81% and 10.10% for the heights 20 cm and 30 cm respectively. It was inferred that removal efficiency increases as the depth of the adsorption media increases due to greater surface area available for the sample for adsorption. It was also observed that rice husk has a tendency to adsorb a greater amount of calcium ions in comparison to chloride and magnesium ions. This was verified from our observations when at flow rate of 40 mL/min and at a height of 10 cm from the base of the column, removal efficiency for calcium ions is 37.5% and for chloride and magnesium ions is 22.33% and 19.9% respectively.

Copy Right, IJAR, 2015., All rights reserved

Introduction

Rapid industrialization and massive urbanization in the past decades has led to increase in the concentration of total dissolved solids in the ground water. The industrial effluent is discharged into river bodies without being adequately treated leading to increase in TDS content. Also, the rise in the application of fertilizers and pesticides in agricultural activities has raised the concentration of arsenic and fluoride in the ground water. TDS concentration has been observed to be considerably more in areas with agricultural activities. The use of modern technologies like reverse osmosis to reduce the TDS content to make water potable involves discharging the reject back in to the water table thereby further increasing the concentration of dissolved solids in the ground water. The above scenario necessitates the adoption of new cost effective, easily adaptable, efficient techniques for removal of TDS from ground water.

In the past studies have been carried out to evaluate Rice husk, as an adsorbent for the removal of various pollutants from water and wastewaters. Activated carbons, prepared from low-cost mahogany sawdust and rice husk have been utilized as the adsorbents for the removal of acid dyes[1] from aqueous solution in the past[2-4]. Mechanisms in the biosorption process such as chemisorption, complexation, adsorption-complexation on surface and pores, ion exchange, micro precipitation, and surface adsorption have been studied to assess the process of treatment of water

and wastewater [5][6]. Rice husk, which is a relatively abundant and inexpensive material, has been investigated as an adsorbent for the removal of various pollutants from water, wastewaters.[7-9]and agricultural wastes[10][11].

Fixed bed adsorption studies of Rhoda mine B dye, for As(III),As(V), Cu²⁺ removal from solution using expanding rice husk [12-14]have assessed the potential of Rise husk for removal of these ions through isotherm and kinetics studies[15-17].Low cost Adsorbents can potentially be an effective solution in future for treatment of water in rural areas[18-29].

Through this study, we further evaluate the efficiency of Rice Husk in removal of TDS and ions such as Calcium, Magnesium and Chloride from ground water.

2. Materials and Methods

2.1. Media used

Rice husk was used as the adsorption media for removal of TDS .It was obtained from a rice mill in Bawana village (located in North West Region of Delhi). It was crushed to form finer aggregates to be used as media in the column reactor.

2.2. Synthetic Sample Preparation

The water sample used for testing purposes of the adsorption column was a synthetic salt solution of T.D.S 1890 mg/L prepared by dissolving sodium chloride (common salt), salt of calcium and salt of magnesium in distilled water.

2.3. Column set up

A PVC column with an inner diameter of 10.15 cm and a length 70 cm was used. The bottom of the column was sealed off with a plastic cap to prevent the loss of adsorbent during the process.

4 different outlets are provided at different heights with 10 cm in the column (as shown in the figure). Water reservoir (bucket) is kept at a certain height above the column to allow water to flow under the action on gravity into the column. A clinical drip was attached from the water reservoir to the column to maintain a constant flow rate of water.

Rice husk (media) is compacted tightly inside the column through which the sample water flows downward. Head loss maintained for the proper functioning of the apparatus and continuously maintained. Finally the water passing through the packed media is collected from one of the outlets into a collecting device (beaker).

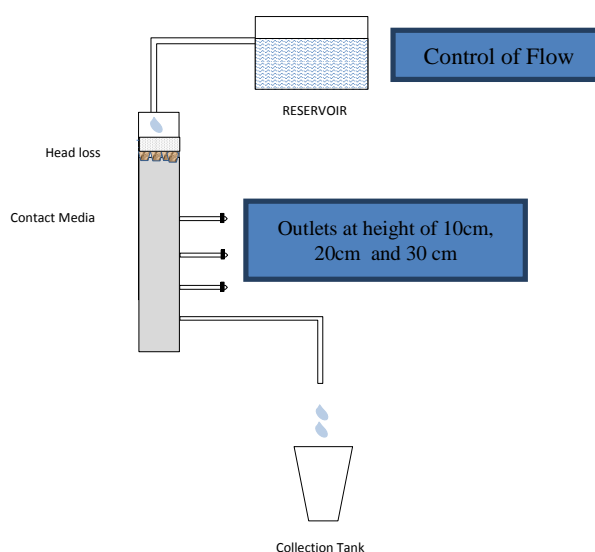


Figure 1. Experimental Setup of the reactor for treating ions

3. Results and Discussion

3.1 Sieve analysis

Sieve analysis was performed to determine the particle size of the risk husk that we used in our study . This test is necessary because it provides us with treatment efficiency of risk husk with respect to a particular size of particles

Physical characteristics of the absorption media (rice husk) used:

- Weight of rice husk used in column: 636 gm.
- Height of husk in column: 70 cm
- Diameter of column: 10.15 cm or 4 inch
- Volume of husk column: 5675.12 cm³
- Density of rice husk: 112 kg/m³

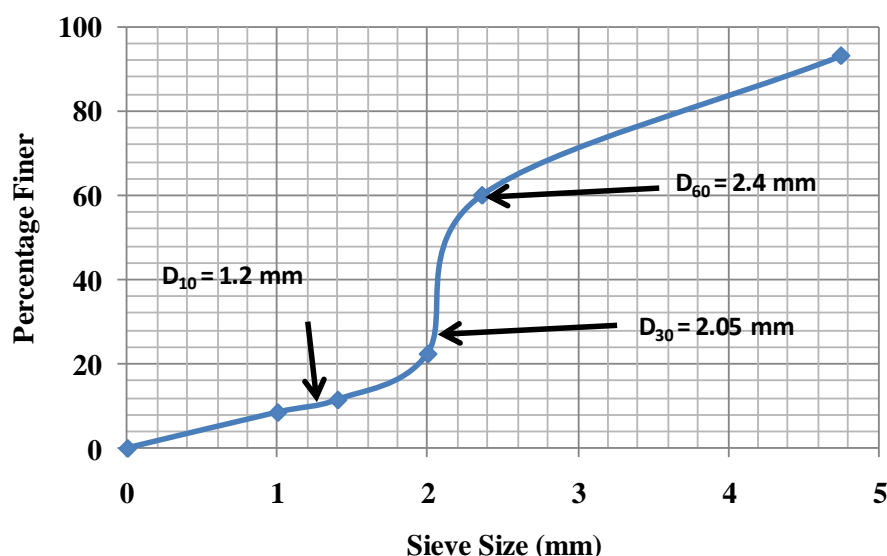


Figure 2. Sieve analysis of rice husk

The following points can be inferred from the sieve analysis of rice husk:

- Effective Size of rice husk, $D_{10} = 1.2\text{mm}$
- Coefficient of uniformity, $C_u = D_{60}/D_{10} = 2.4/1.2 = 2$
- Coefficient of curvature, $C_c = D_{30}^2/(D_{60} \times D_{10}) = 2.05^2/(1.2 \times 2.4) = 1.45$

3.2 Assessment of efficiency at different flow rates

The adsorption column was set-up in the Environmental Engineering Laboratory in a PVC pipe of 4-inch diameter .The flow rate in the reactor was controlled using an Intravenous set which was purchased from a medical store. The flow rate was kept in the range of 40 mL/min to 120 mL/min using the IV set and tests were carried out on the samples within this range of flow rate.

The outlets were kept at gaps of 10 cm of depth. At one point of time effluent was collected a single outlet only while the others were closed using clips. A synthetic solution similar in characteristics to ground water in North West region of Delhi was used for testing of the adsorption column.

Table 1: Experiment at Flow rate of 40 mL/min

Characteristic	Influent (mg/L)	Effluent (mg/L) at 30 cm from base	Removal at 30 cm	Effluent (mg/L) at 20 cm from base	Removal at 20 cm	Effluent (mg/L) at 10 cm from base	Removal at 10 cm
Calcium	370	260	29.75%	241	34.75%	231	37.5%
Magnesium	350	316	9.7%	290	16.9%	280	19.9%
Chloride	1140	912	20.1%	903	20.8%	885	22.33%
TDS	1890	1618	14.39%	1535	18.7%	1497	20.79%

Table 2: Experiment at Flow rate of 80 mL/min

Characteristic	Influent (mg/L)	Effluent (mg/L) at 30 cm from base	Removal at 30 cm	Effluent (mg/L) at 20 cm from base	Removal at 20 cm	Effluent (mg/L) at 10 cm from base	Removal at 10 cm
Calcium	370	323	12.75%	291	21.25%	268	27.5%
Magnesium	350	322	7.69%	305	12.8%	300	14.1%
Chloride	1140	977	14.25%	975	14.5%	951	16.5%
TDS	1890	1744	7.7%	1687	10.74%	1629	13.81%

From the following readings we observed that the removal efficiency decreases as the flow rate of the influent is increased, this was because the contact period for the adsorption of dissolved solids is decreased if the flow rate is increased. Hence we observe maximum removal efficiency which is around 21% of TDS removal for flow rate of 40 mL/min and minimum for flow rate of 120 mL/min which is around 10% of TDS removal.

Also, it can be observed that removal efficiency is maximum when the depth of outlet is the maximum, thus providing maximum contact area for the sample before the effluent is taken out. Considering a particular flow rate (40 mL/min), we note that removal efficiency of TDS is 20.79% at a height of 10cm from the base of column and 13.81% and 10.10% for the heights 20cm and 30cm respectively. Therefore, we infer that removal efficiency increases as the depth of the adsorption media increases due to greater surface area available for the sample for adsorption.

Rice husk has a tendency to adsorb a greater amount of calcium ions in comparison to chloride and magnesium ions. This can be verified from our observations where at flow rate of 40mL/min and at a height of 10cm from the base of the column in table 5.6 where, removal efficiency for calcium ions is 37.5% and for chloride and magnesium ions is 22.33% and 19.9% respectively.

Table 3: Experiment at Flow rate of 120 mL/min

Characteristic	Influent (mg/L)	Effluent (mg/L) at 30 cm from base	Removal at 30 cm	Effluent (mg/L) at 20 cm from base	Removal at 20 cm	Effluent (mg/L) at 10 cm from base	Removal at 10 cm
Calcium	370	334	9.75%	301	18.75%	281	24.75%
Magnesium	350	331	5.3%	317	9.4%	309	11.53%
Chloride	1140	1017	10.75%	1008	11.5%	991	13.1%
TDS	1890	1819	3.7%	1744	7.74%	1699	10.1%

Figures 3-5 indicate removal efficiency of rice husk for various ions at different flow rates and depths.

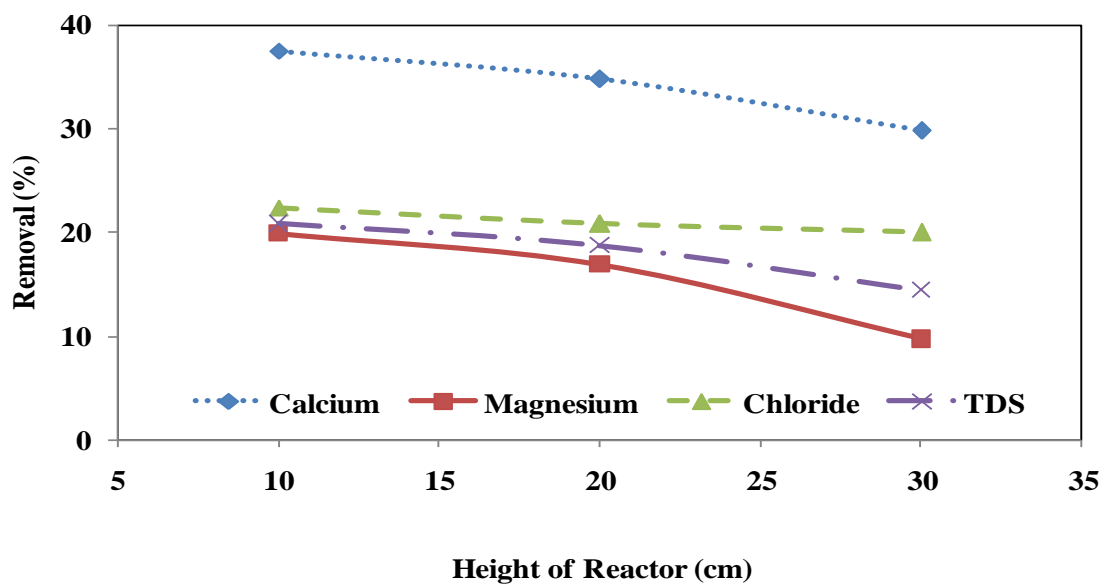


Figure 3: Removal efficiency for various ions at flow rate of 40 mL/min

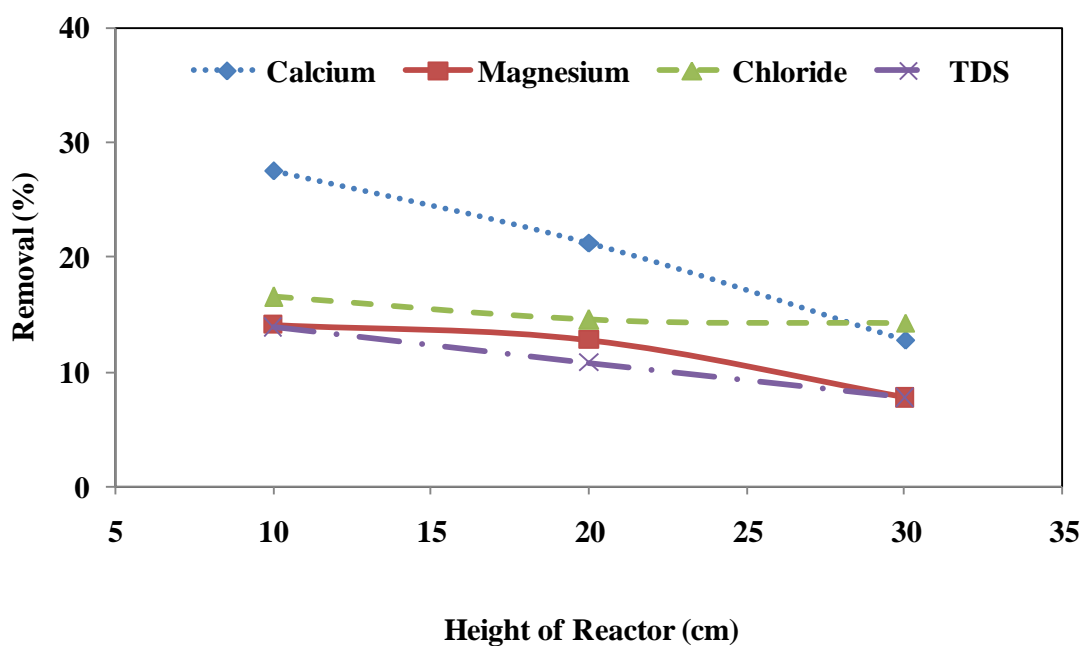


Figure 4: Removal efficiency for various ions at flow rate of 80 mL/min

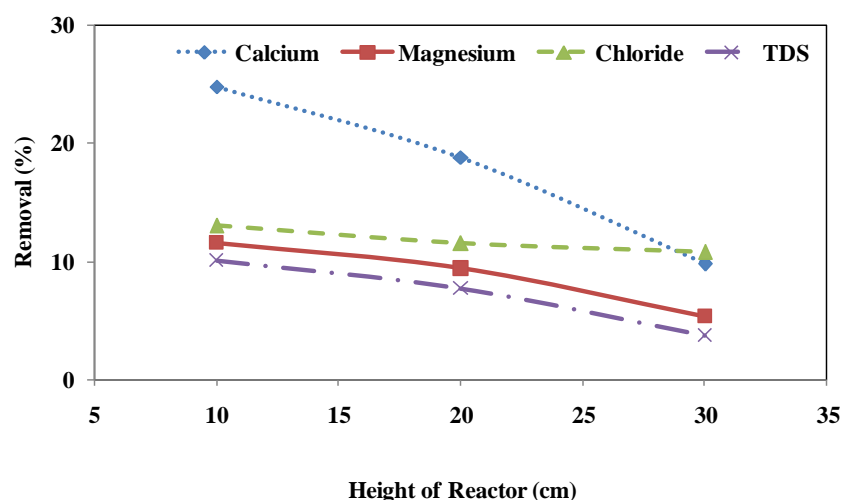


Figure 5: Removal efficiency for various ions at flow rate of 120 mL/min

4. Conclusion

Low cost material rice husk was employed for removal of TDS. Synthetic samples suggested that 20.79% removal can be achieved using rice husk as the adsorption media. It was observed that the percentage removal decreased with increase in the flow rate. When the flow rate was increased from 40mL/min to 120mL/min, the percentage removal of TDS decreased from 20.79% to 10.56%. It was observed that rice husk has a tendency to adsorb a greater amount of calcium ions in comparison to chloride and magnesium ions. This was verified from our observations when at flow rate of 40mL/min and at a height of 10cm from the base of the column, removal efficiency for calcium ions is 37.5% and for chloride and magnesium ions is 22.33% and 19.9% respectively.

References

- [1]P.K. Malik (2003). "Use of activated carbons prepared from sawdust and rice-husk for adsorption of acid dyes: a case study of Acid Yellow 36". *Dyes and Pigments*, 56(3):239-249
- [2]V.K. Gupta, Suhas (2009), "Application of low-cost adsorbents for dye removal– A review", *Journal of Environmental Management*, 90 (8)
- [3]Aenab AM, SK Singh (2014), "Critical Assessment of River water Quality and Wastewater Treatment Plant (WWTP)", *IOSR Journal of Environmental Science, Toxicology And Food Technology (IOSR-JESTFT)*, 8(2): 44-48
- [4]JN Sharma, Raj Shailesh Kanakiya, SK Singh, (2015), "Characterisation Study and Correlation Analysis For Water Quality of Dal Lake, India", *International Journal of Lakes and Rivers*, 8(1), 25-33.
- [5]Shashank Shekhar Singh, S.K.Singh (2015). "Identification and Comparison of Flaws in Conventional Treatment Techniques of Fluoride", *International journal of Engineering and Management Research* 5(3):215-217
- [6]Deepika and S. K. Singh (2015). "Water Quality Index Assessment of Bhalswa Lake ,New Delhi" , *International Journal of Advanced Research* 3(5): 1052-1059
- [7]Gupta, V. K., Mittal, A., Gajbe, V. (2004). "Adsorption kinetics and column operations for the removal and recovery of malachite green from wastewater using bottom ash". *Separation and Purification Technology*, Vol 40: 87-96.
- [8]T.G. Chuah, A. Jumariah, I. Azni, S. Katayon, S.Y. Thomas Choong, (2005). "Rice Husk as a Potentially Low-Cost Biosorbent for Heavy Metal and Dye Removal: An Overview", *Desalination*, 175(3):305-316

- [9]Ayhan Demirbas (2008).”Heavy metal adsorption onto agro-based waste materials: A review”. Journal of Hazardous Material , 2008 Sep 15;157(2-3):220-229
- [10]S.K. Singh, Dhruv Katoria, Dhruv Mehta , Dhruv Sehgal(2015) . “Fixed Bed Column Study and Adsorption Modelling on the Adsorption of Malachite Green dye from wastewater using Acid Activated Sawdust”. International Journal of Advanced Research, 3(7):521-529
- [11]SK Singh, Anshika Bisht, (2015). “Environmental Management in Mass Gatherings”, International Journal of Engineering Science & Management. (IJESM), 5(1): 130-138.
- [12]Manase Auta (2012).”Fixed bed adsorption studies of Rhoda mine B dye using oil palm empty fruits bunch activated carbon”. Journal of Engineering Research and Studies, Vol. 3.
- [13]Khattari, S.D Singh, M.K. (1999). “Color removal from dye wastewater using sugar cane dust as an adsorbent”. Adsorption Science & Technology, 269-282
- [14]Dhruv Mehta, Siddharth Mazumdar , S.K. Singh(2015). “Magnetic adsorbents for the treatment of water/wastewater— A review”, Journal of Water Process Engineering 7(9), 244-265
- [15]K.Y. Foo, B.H. Hameed(2009). “Utilization of rice husk ash as novel adsorbent: A judicious recycling of the colloidal agricultural waste”. Advances in Colloid and Interface Science,152(1), 39-47
- [16]Biswajit Singha, Sudip Kumar Das (2013). “Fixed-bed column study for As(III) and As(V) removal and recovery by bacterial cells immobilized on Sawdust/MnFe₂O₄ composite”. Colloids and Surfaces B: Biointerfaces, 107, 97-106
- [17]Imran Ali, Mohd. Asim, Tabrez A. Khan (2012).”Low cost adsorbents for the removal of organic pollutants from wastewater”. Journal of Environmental Management, 113,170-183
- [18]Md. Ahmaruzzaman (2008).”Adsorption of phenolic compounds on low cost Adsorbents: A review”. Advances in Colloid and Interface Science, 143,(1–2, 4), 48-67
- [19]Xuegang Luo, Zaifang Deng, Xiaoyan Lin, Chi Zhang. “Fixed-bed column study for Cu²⁺ removal from solution using expanding ricehusk.Journal of Hazardous Materials”, Volume 187, Issues 1–3, 15 March 2011, Pages 182-189
- [20]Lokesh Kumar, S.K.Singh (2015). “Removal of Chloride from Groundwater by Bio adsorption, International Journal of Advance Research”, 3(5), 140-154
- [21]Neetu Sharma, D.P. Tiwari, S.K. Singh, (2014), “The Efficiency Appraisal for Removal of Malachite Green by Potato Peel and Neem Bark: Isotherm and Kinetic Studies”, *International Journal of Chemical and Environmental Engineering*, 5(2): 83-88
- [22]D.P.Tiwari, S.K.Singh, Neetu Sharma (2014), “Sorption of Methylene Blue on Treated Agricultural Adsorbents: Equilibrium and Kinetic Studies”, Journal of Applied water Science, 4(1)
- [23]Abhas Jain, S.K. Singh (2014), “Defluoridation of Water Using Alum Impregnated Brick Powder And Its Comparison with Brick Powder”, International Journal of Engineering Science and Innovative Technology , 3(2)
- [24]Neetu Sharma, D.P.Tiwari, S.K.Singh, (2014), “Efficiency of chemically treated potato peel and neem bark for Sorption of direct Red Dye-81 from aqueous solution”, Rasayan, 7(4): 399-407
- [25]Allaa M. Aenab and S.K. Singh (2012), “Evaluation of Drinking Water Pollution and Health Effects in Baghdad”, Iraq . Journal of Environment Protection, 2012 (3): 533-537.

[26]Neetu Sharma, DP Tiwari and S.K. Singh (2012), “Decolorisation of synthetic dyes by Agricultural Waste: a Review”, International Journal at Scientific & Engineering Research, 3(2): 1-10.

[27]SK Singh, Lokesh Kumar (2014), “Characterization of rural drinking water sources in Bhiwani District, Haryana: A Case Study”. International Journal of Interdisciplinary Research and Innovations 2(4) : 27-37

[28]Tarundeep Gill ,S.K.Singh, P. Albino Kumar (2015). “Treatment of Heavy Metals Contaminated industrial waste water by Functionalized Polymers”, International Journal of Advanced Research, 3(9), 178-181

[29]C.M.VivekVardhan and J.Karthikeya (2011).”Removal of Floride from water using low cost materials”, Fifteenth International Water Technology Conference, IWTC-15 2011, Alexandria, Egypt,2011

Catalytic Hydrothermal Liquefaction of Solid Food Waste for Light Bio-oil Production: Process Optimisation

Yahaya Alhassan^{1,2*}, Naveen Kumar¹

¹Centre for Advanced Studies and Research in Automotive Engineering, Delhi Technological University,
New Delhi-110042, India

²Petrochemicals and Allied Department, National Research Institute for Chemical Technology, P.M.B. 1052,
Basawa-Zaria, Nigeria

*Corresponding author email id: lahassan897@yahoo.com

ABSTRACT

Feedstocks availability has posed a big question on sustainability of biodiesel, bioethanol and biogas production. FWs (food wastes) are emerging sustainable renewable energy feedstocks, especially with the bio-refinery concept and other emerging technologies like pyrolysis and HTL (hydrothermal liquefaction). In this research work, process optimisation for the production of light bio-oil from solid restaurant waste is been reported. Solid restaurant waste was thermally liquefied using hot water under highpressure condition. Effects of heating temperature (150°C, 200°C and 250°C), biomass to solvent ratios (1:5, 1:10 and 1:15) as well as catalyst loading (5 wt%, 7.5 wt% and 10 wt%) are investigated. From the results as expected, increasing reaction temperature improved the production of light bio-oil and its fuel quality as well, with an optimum reaction temperature of 225°C. In contrast, increasing biomass to solvent ratio from 1:10 to 1:15 did not increase the oil yield. As such, the optimum biomass to solvent ratio was 1:10. Similarly, catalyst concentration of 5 wt% (weight of slurry) gives the best oil production. It could be concluded that HTL of solid restaurant waste into light bio-oil is a sustainable renewable energy source.

Keywords: Food wastes, Fuel properties, Lightbio-oil, Liquefaction

1. INTRODUCTION

Recently, there are vigorous developments in different countries and regions leading to industrialisation and consequently, issues of waste generation and management emanated. In the light of this, renewable fuels from different sources are been investigated by researchers. However, feedstocks availability has posed a big question on sustainability of biodiesel, bioethanol and biogas production especially, during largescale production of these fuels[1,2].

Interestingly, one emerging feedstocks source is FW (food waste) has superior advantages over other lignocellulosic materials. For example, they are widely available worldwide; they are non-seasonal unlike other feedstocks and most importantly, do not compete with the food chain. FW includes specific energy rich chemical components other than cellulose, hemicelluloses and lignin[3]. These include ketones and aldehydes, which have great tendencies to undergo thermal degradation during high temperatures reactions like pyrolysis and HTL (hydrothermal liquefaction).

HTL is one of the most widely used and efficient thermally processes to obtain liquid fuel from FW and other lignocellulosic containing materials at moderate temperature range from 150°C to 350°C. HTL is a thermal conversion process of heating organic matter in the absence of oxygen and supported by catalyst, forming bio-char, bio-crude or heavy oil and gaseous products including CO, CH₄ and H₂ are produced[4], in the ratio depending on the extent of heating. The factors that affect HTL conversion of FW materials into bio-oil include reaction temperature, heating rate, material residence time, moisture content and catalyst concentration/loading[5]. It is imperative to note that, not all biomass and FW materials are suitable for HTL.

The liquefaction of pinewood waste[4], microalgae[5] and wheat straw showed varying yields. For example,

maximum reducing sugar yield (60.80%) was obtained during hydrolysis of wheat straw as reported by Ji *et al.* [6].

The use of ILs (ionic liquids), as non-aqueous solvents with unique properties and advantages such as low vapor pressure, high dissolution ability to wide range of compounds, ionic conductivity and most interestingly high thermal and chemical stability has been reported [7,8]. However, in order to effectively replace them (conventional ILs) with more promising ones, DES (deep eutectic solvents) otherwise called RTILs (room temperature ionic liquids) have emerged. They showed additional advantages with regards to their simple preparations, low toxicity, low cost, and low-temperature stability than conventional ILs [9,10].

According to literature surveyed, HTL of several wastes materials has been investigated. For examples, Tungal and Shende [4], investigated the HTL of pinewood (*Pinus ponderosa*) reported maximum bio-crude yield of 55 wt % obtained at heating temperature of 250°C and 200 psi Nitrogen gas pressure. They noted that increasing reaction temperature from 225°C to 250°C results in increasing bio-crude yield from 24.02 wt % to 30.5 wt %, while higher temperatures favoured H₂ production and low residue formation. Similarly, marine microalgae liquefaction was reported with an optimum sulphonic acid functionalised ion exchange resin (Amberlyst-15) of 15 wt% within 150 min and biomass to solvent ratio of 1:7.5, reporting highest reducing sugar yield of 61 g/L [11]. The authors reported increasing active sites of catalysts and its expanded surface area as the major reasons behind the increasing reducing sugar production obtained with 20 wt % catalyst loading.

In this research work, catalytic HTL of solid food waste from college restaurant using alternative ILs as catalysts is presented. Reaction parameters suitable for the maximum production of light bio-oil are also reported. In addition, fuel properties of the produced oil are evaluated with the view for ensuring fuel quality.

2. MATERIALS AND METHODS

2.1. Materials and Methods

Solid restaurant FW were obtained from the Delhi technological university canteen, New Delhi, India. Chemical reagents used were Central Drug House chemicals purchased from a chemical store in Delhi, India. All chemicals and reagents were analytical grade chemicals except otherwise stated. In addition, glasswares, containers and other laboratory instruments were initially washed and rinsed with diluted nitric acid and distilled water. Thereafter, allowed to dry in an oven overnight.

2.2. Preparation of DES (Deep Eutectic Solvents)

For each DES, one mole of ChCl (139.63 g) was mixed with different molar ratio of HBD. DES 1 is formed by mixing ChCl and Urea 1:2; DES 2 is formulated by mixing ChCl and TsOH in the ratio 1:4 and DES 3 by mixing ChCl and Glycerol in the ratio 1:3, respectively. Other reaction conditions are: temperature 120°C, reaction time 180 min, stirring speed of 750 rpm and initial pressure of 5.0 MPa.

2.3. Production of light Bio-Oil

A 100 mL capacity laboratory scale reactor unit (Figure 1) was used. Nitrogen gas was initially supplied into the reactor through a control valve. HTL was conducted at 150°C for 30 min reaction time. Other conditions included the catalyst concentration of 5 wt% and biomass to water ratio was 1:10, while the initial pressure was 6.0 MPa. After reaction completion, the supernatants were filtered, while the residue was used for the light bio-oil extraction. The acetone extraction was conducted. Other reaction conditions are reaction temperature of 150°C or 250°C, and reaction time was 60 min while stirring speed was 750 rpm.

2.4. Analyses

Light bio-oil yield was by measured using the formula reported by Alhassan *et al.* [12].

$$\text{Yield} = \frac{\text{Mass of oil (g)}}{\text{Mass of feedstock used (g)}} \times 100\%$$

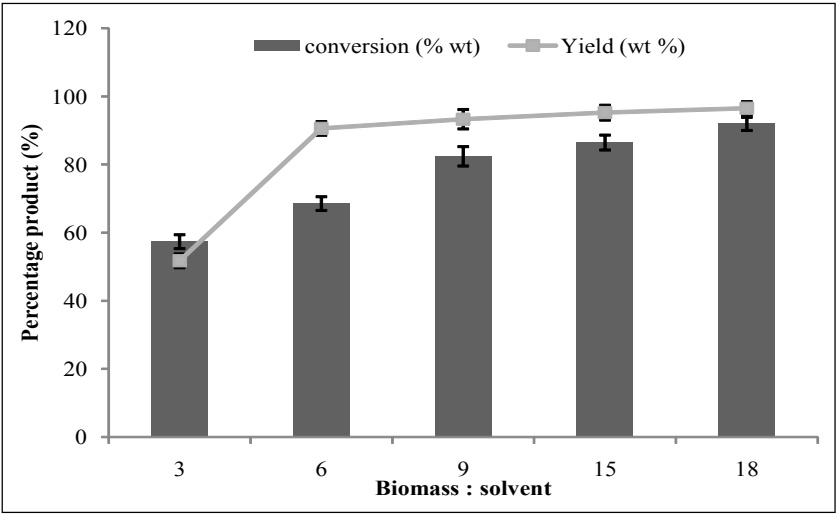


Figure 2: Effect of biomass to solvent ratio on the product yield

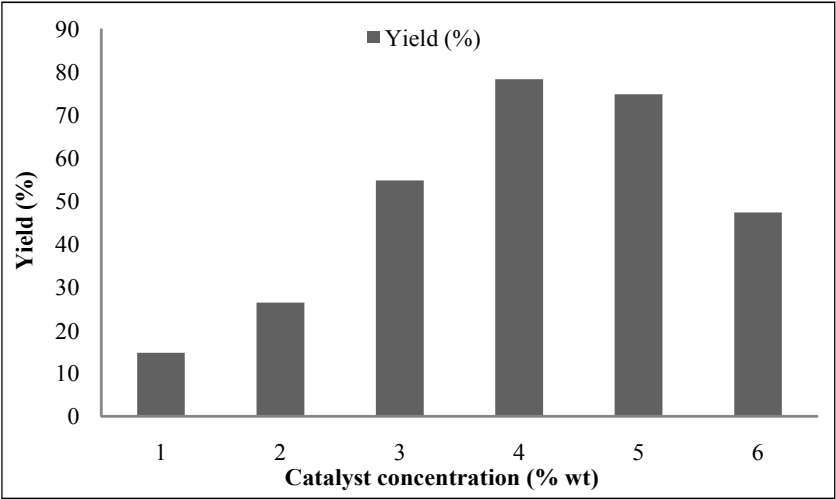


Figure 3: Effect of catalyst loading on the product yield

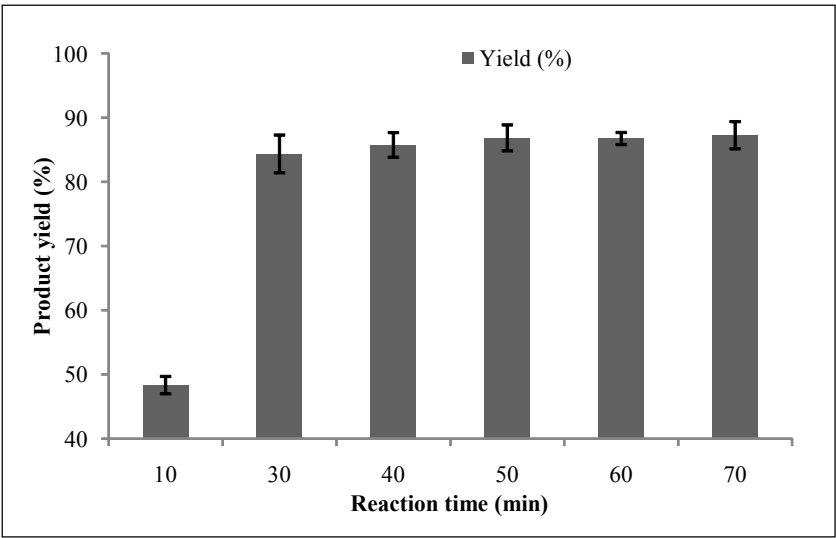


Figure 4: Effect of reaction time on the product yield

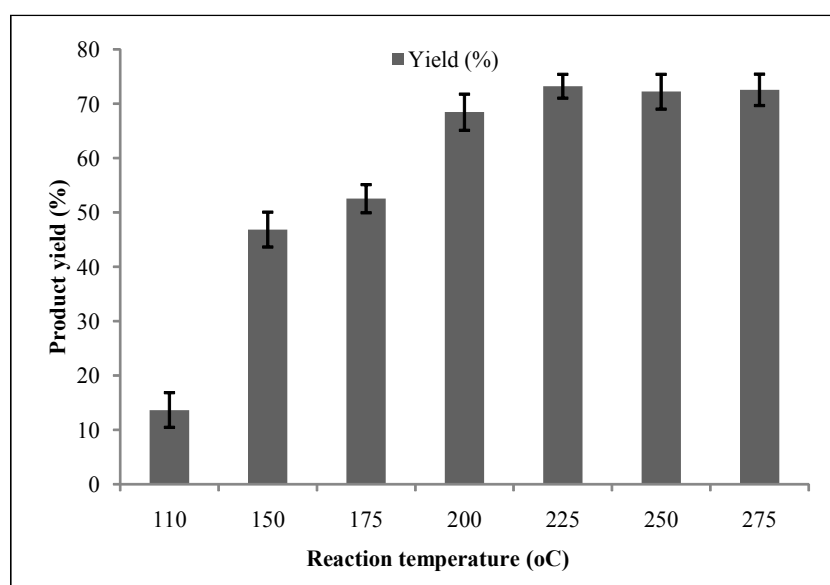


Figure 5: Effect of reaction temperature on the product yield

Increasing reaction temperature significantly increases the light bio-oil production. Although, thermal decomposition has been reported, it could be suggested that the thermal degradation temperature has not been attained yet. The decomposition temperature was reported to be around 350–550°C[16].

4. CONCLUSION

The paper herein reports the hydrothermal liquefaction of solid restaurant waste into light bio-oil as a potential burning fuel. The reaction conditions suitable for the production of the oil are herein reported. Optimal reaction conditions include reaction temperature of 225°C and reaction time of 30 min. The optimum catalysts concentration was 4 wt% and the biomass to solvent ratio of 1:10, as the best conditions for the production of light bio-oil. It is suggested that the most influential factors are temperature and catalysts concentration.

ACKNOWLEDGEMENT

The principal author is grateful to the support of the management of the National Research Institute for Chemical Technology, Zaria-Nigeria.

REFERENCES

- [1] Atabani AE, Silitonga AS, Ong HC, Mahlia TMI, Masjuki HH, Badruddin IA *et al.* Non-edible oils: A critical evaluation of oil extraction, fatty acid compositions, biodiesel production, characteristics, engine performance and emissions production. *Renew Sustain Energy Rev* **2013**;18:211–45.
- [2] Blanco-Marigorta. Exergetic analysis of a biodiesel production process from *Jatropha curcas*. *Appl Energy* **2012**;101:218–25. <http://dx.doi.org/10.1016/j.apenergy.2012.05.037>.
- [3] Zhou L, Wang Y, Huang Q, Cai J. Thermogravimetric characteristics and kinetic of plastic and biomass blends co-pyrolysis. *Fuel Process* **2006**:1–9. doi:10.1016/j.fuproc.2006.07.002.
- [4] Tungal R, Shende RV. Hydrothermal liquefaction of pinewood (*Pinus ponderosa*) for H₂, biocrude and bio-oil generation. *Appl Energy* **2014**;134:401–12. <http://dx.doi.org/10.1016/j.apenergy.2014.07.060>.
- [5] Ji W, Shen Z, Wen Y. Hydrolysis of wheat straw by dilute sulfuric acid in a continuous mode. *Chem Eng J* **2015**;260:20–27. <http://dx.doi.org/10.1016/j.cej.2014.08.089>.
- [6] Jin B, Zhang C, Xu Y, Zhang L, Wang F. Non-catalytic liquefaction of microalgae in sub- and supercritical acetone. *Chem Eng J* **2014**;254: 384–92. <http://dx.doi.org/10.1016/j.cej.2014.05.137>.

- [7] Yang S, Yuan T, Li MF, Sun RC. Hydrothermal degradation of lignin: products analysis for phenol formaldehyde adhesive synthesis. *Int J Biol Macromol* **2015**;72:54–62. <http://dx.doi.org/10.1016/j.ijbiomac.2014.07.048>.
- [8] Dickerson T, Soria J. Catalytic fast pyrolysis: a review. *Energies* **2013**;6(1):514–38. doi:10.3390/en6010514.
- [9] Jutika B, Thakur AJ, Deka D. Solid oxide derived from waste shells of *Turbonilla striatula* as a renewable catalyst for biodiesel production. *Fuel Process Technol* **2011**;92:2061–67. doi:10.1016/j.fuproc.2011.06.008.
- [10] Hayyan A, Hashim MA, Hayyan M, Mjalli FS, AlNashef IM. A new processing route for cleaner production of biodiesel fuel using a choline chloride based deep eutectic solvent. *J Clean Prod* **2014**;65:246–51. <http://dx.doi.org/10.1016/j.jclepro.2013.08.031>.
- [11] Taubert J, Raghavan S. Effect of composition of Post-etch residues (PER) on their removal in choline chloride-malonic acid deep eutectic solvent (DES) system. *Microelectron Eng* **2014**;114:141–47. <http://dx.doi.org/10.1016/j.mee.2012.12.009>.
- [12] Alhassan Y, Kumar N, Bugaje IM, Pali HS, Katchkar P. Co-solvent transesterification of cotton seed oil into biodiesel: Effects of reaction conditions on the quality of fatty acids methyl esters. *Energy Convers Manag* **2014**;84:640–48. <http://dx.doi.org/10.1016/j.econman.2014.080>.
- [13] Pali HS, Kumar N, Alhassan Y. Performance and emission characteristics of an agricultural engine with Sal methyl ester and diesel. *Energy Convers Manag* **2015**;90:146–53.
- [14] Wang S, Li YW, Feng X, Li Y, Wang E. New synthetic route of polyoxometalate-based hybrids in choline chloride/urea eutectic media. *Inorg Chem Acta* **2010**;363:1556–60. doi:10.1016/j.ica.2009.12.012.
- [15] Abbott AP, Boothby D, Capper G, Davies DL, Rasheed RK. Deep eutectic solvents formed between choline chloride and carboxylic acids: versatile alternatives to ionic liquids. *J Am Chem Soc* **2004**;126 (29):9142–47. doi:10.1021/ja048266j. PMID15264850.
- [16] Hassan SZ, Vinjamur M. Parametric effects on kinetics of esterification for biodiesel production: A Taguchi approach. *Chem Eng Sci* **2014**;110:94–104. <http://dx.doi.org/10.1016/j.ces.2013.11.049>.

CBR VALUE OF SANDY SUBGRADE BLENDED WITH COARSE AGGREGATE

Kesharwani R.S.¹ Sahu A. K.² Khan N.U.³

^{1,3}Department of Civil Engineering, Jamia Milia Islamia, New Delhi, India

²Department of Civil Engineering, Delhi Technological University, Delhi, India.

ABSTRACT:-In several parts of India, soil deposits consist of a matrix like soil with inclusions of coarser aggregates of various sizes. The CBR test is used for the design of sub grade for highways & pavement. Therefore in the present investigation, the CBR tests were carried out on the sand blended with coarse aggregates of various sizes and proportions. To strengthen the sub grade strata, coarse aggregates of 10mm and 20mm sizes were mixed in the sand, in various proportions. The soil samples were prepared and tested first without coarse aggregates, then by mixing coarse aggregates in varying percentages by weight, starting from 5% to 30%. The results of CBR tests shows that with the increase in the percentage of coarse aggregates, the CBR value of the soil increases. It is observed that the percentage improvements in the CBR values ranges from 20.99 % to 115.83% and 31.30% to 151.94% for 10mm and 20mm coarse aggregates respectively at OMC. In soaked condition, this improvement ranges from 23.20% to 202.48% and 31.35% to 233.17% for 10mm and 20mm coarse aggregates respectively.

Keywords: *Soil, Coarse aggregates, CBR, Subgrade*

1. INTRODUCTION

In engineering practice, the earth construction requires compactions of existing sub grade by improving the density & strength of the strata. All types of earth structures i.e. highways, pavements etc. rest directly on the soil beneath them. The safety of these entities depend upon the strength/bearing capacity of the soil over which these are constructed. Therefore, a proper analysis of the soil properties and the design of their compression parameter become necessary to ensure that these structures remain stable and are safe against unequal settlements. To determine the suitability of any soil type for use as sub grade, sub base or base material, one of the parameter generally used is the California bearing ratio (CBR).

CBR is frequently used as test value for civil engineers particularly to those who are in pavement construction to access the stiffness modulus and shear strength of the sub grade. It is actually an indirect measure which represents the strength of a crushed rock as a percentage value. Usually the CBR values are used by the pavement engineers to design the thickness of the pavement to be laid on the sub grade.

The thickness of the pavement will be more for the sub grades having lesser value of CBR and vice versa. In other words the designed thickness of the pavement is very much depending upon the CBR value of the sub grade soil. Different types of soils

give different values of CBR even though these were compacted to same amount of energy and rate of penetration. To enhance the strength of sub grade soil, several techniques like compaction, mechanical/electrical/thermal stabilization, addition of geotextile, geosynthetic, fly ash or randomly distributed discrete fibers are used. In the present study, the variation in CBR value or sub grade strength of soil is carried out due to the addition of coarse aggregates. The coarse aggregates are the rock fragments usually restricted to round or sub rounded particles. The review of literature is carried out for the improvement to the CBR value by various technique.

Srivastava et al [1] reported that the CBR of the soil increases when the geotextile layer intercepts the pressure bulb generated due to the application of the applied load and further by using geotextile in layers the thickness of road pavement can be reduced by virtue of increased failure stresses. Jain et al [2] observed that with the addition of 4% discrete natural fiber in sand at a density of 16.60 KN/m³ there is 114% and 80% increase in the CBR value of soil both in unsoaked and soaked conditions. While the direct shear test indicates that there is increase in the cohesion of the soil. Pandian et al [3] while working on soil, fly ash mixes reported that with the addition of 20% fly ash in black cotton soil the CBR value of black cotton can be improved while the CBR of fly ash can be improved with the addition of 30% black cotton soil. The study also indicate that the low value of CBR of black cotton soil or fly ash is due to poor gradation,

thus, the gradation and the compacted strength can be significantly improved by mixing the two materials in proper proportions.

Singh & Kumar [4] studied the effects of surcharge and the compaction on the CBR value of alluvial soil and concluded that the surcharge load and the compacting effort both influences the CBR value of the soil i.e. the CBR value of soil increases with the increase in surcharge load as well as the compacting effort. Amu et al [5] observed that up to 60% stabilization the CBR value increases and beyond which it starts decreasing. At 60% stabilization, the CBR value obtained was highest at 110.73% for lime and 92.26% for wood ash. The CBR values of soil samples were found better when stabilized with lime and when stabilized with wood ash the maximum dry density of the soil sample was found better.

Duncan-Williams & Attoh-Okine [6] show that the soil having low CBR values benefited more as compared to soil having higher CBR values both in un-soaked and soaked conditions when reinforced with geosynthetic though the improvement in strength and the CBR value depends upon the characteristics of the geosynthetic used. Naeini & Mirzakhani [7] used geotextile as a reinforcing material and reported that though it improves the CBR value, its inclusion in soils leads to decreased penetration and deformation thus improving the stress distribution of the soil sample. Duncan-Williams and Attoh-Okine [6] also concluded similar results. The strength and the CBR value increases when its layer is placed in the middle of the granular soils but the same decreases when used in the fine grained soils.

Modak et al [8] studied the combined effect of lime and fly ash in black cotton soil and concluded that with increasing the percentage of lime and fly ash in black cotton soil, (CBR) and maximum dry density (MDD) values are also increases. Mehta et al [9] stabilized black cotton soil using lime. The CBR value of the lime stabilized clayey soil was improved due to decrease in the plastic behaviour of the soil. Mudgal et al [10] studied the effects of lime & stone dust on CBR value of black cotton soil with the addition of 9% lime and 20% stone dust by weight with black cotton soil, the CBR value increased.

A review of the literature reveals that most of the work has been carried out using either fly ash/geotextile/lime or rice husk ash as a reinforcing material to enhance the CBR value of the soil and very few or none studies have been carried out using coarse aggregates as a reinforcing material in

the soil to enhance its properties. Hence study is needed to evaluate this aspect too since in areas where coarse aggregates are available in abundance and procuring of other reinforcing materials proves to be uneconomical, adding coarse aggregate will be a suitable option.

Table 1. Geotechnical properties of soil.

Particulars	Values
Natural Moisture Content	4.26%
Bulk Density (KN/m ³)	17.2
Specific Gravity	2.65
Uniformity Coefficient (Cu)	2
Coefficient of Curvature (Cc)	1.14
Maximum Dry Density (MDD) (KN/m ³)	17.7
Optimum Moisture Content (OMC)	11.41%
Cohesion	0
Angle of internal friction	32°
Classification of soil	SP

2. MATERIALS & METHODOLOGY USED

2.1 Sandy Soil:

The sandy soil used in the study is procured from river basin transported by stream etc. The different geotechnical properties of soil are summarized in Table-1 and the particle size distribution curve is shown in Fig-1.

2.2 Coarse Aggregates:

The coarse aggregates obtained in this study are the same as used for making plain cement concrete. The different physical properties of the coarse aggregates used are given in Table-2.

2.3 Water

The CBR tests in the study have been carried out in the laboratory. Therefore, water used for mixing during the preparation of the samples is taken as available in the laboratory which is an ordinary tap water. The various physical properties of water used are given in Table-3.

3. EXPERIMENTAL INVESTIGATION

3.1 Introduction

The bulk quantity of sand and aggregates of 20 mm & 10 mm nominal sizes are procured in the laboratory and stored properly. The collected sample

of sand and coarse aggregate were characterized in the laboratory. The tests were carried out to determine the physical and chemical properties of the material. The Proctor's compaction test were performed on the sand to determine the optimum moisture content and maximum dry density of the sand. The coarse aggregate of 20 mm & 10 mm sizes in various proportions (5% to 30% by weight) are mixed with the sand and the CBR values of each mixes were determined under soaked and un-soaked condition.

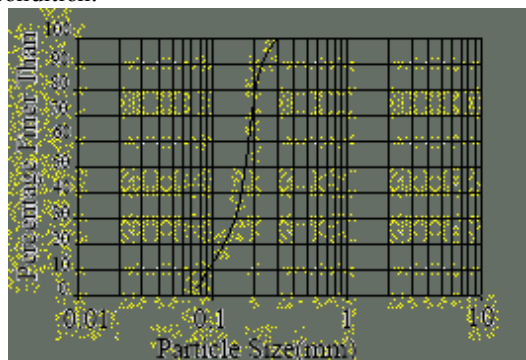


Fig. 1. Particle size distribution curve.

Table 2. Physical properties of coarse aggregates.

Particulars	Values
Aggregate Crushing Value (ACV)	11.21%
Aggregate Impact Value (AIV)	9.86%
Specific Gravity (G)	2.64
Water Absorption	2.36%
Fineness Modulus	7.36

3.2 Details of Test Conducted

The details of experimental programs are summarized in Table-4. The tests were performed conforming to Indian standard specifications listed in the reference. A known quantity of coarse aggregates was mixed in the soil with the water contents corresponding to the maximum dry density of the soil. The prepared soil coarse aggregate mix was then kept in a sealed polythene bag for maturing for 24 hours. The re-moulded samples were then prepared by compacting matured soil coarse aggregate mix in the CBR mould in three equal layers giving each layer 56 blows of rammer weighing 26 N, using dynamic compaction method at maximum dry density. For each test, two samples

were prepared first for immediate penetration test at OMC and the second one was soaked in water before the penetration test for 96 hours for free accesses of water from the top and bottom of the mould with a surcharge weights 50 N. The test on soaked sample serves as a precaution to allow for the increase in moisture content due to either rise in water table or floods in the region and the surcharge weight simulates the effect for the thickness of the road pavement overlaying the base course.

3.3 CBR Tests

California bearing ratio tests on soil coarse aggregate mixes were conducted at OMC and soaked conditions using the standard method as described in IS: 2720 (Part 16) – 1979.

Table 3. Physical and chemical properties of water.

Particulars	Values
pH value	6.87
Dissolved Solids	32.00 mg/l
Suspended Solids	144.00 mg/l
Sulphates	86.00 mg/l
Chlorides	128.00 mg/l
Turbidity	3.50 NTU
Alkalinity	25.00 mg/l
Hardness	74.00 mg/l

The experimental setup for penetration test consists of a loading machine of 50 KN capacity equipped with a movable base enabling the plunger of 50 mm dia. to penetrate into the test specimen at a rate of 1.25 mm per minute, proving ring of 50 KN capacity for measuring the load, a metal mould of 150 mm internal diameter and 175 mm in height fitted with 60mm high collar and a perforated base plate, Two annular weights each of 25 N, spacer disc, a metal rammer weighing 26 N and dial gauge for recording penetration of plunger up to 25 mm.

4. RESULTS AND DISCUSSION

4.1 Geotechnical Properties of Soil

The particle size distribution curve obtained by plotting the result of sieve analysis indicates that the soil contains nearly 96.40% particles passing through 4.75 mm IS sieve and larger than 75 micron IS sieve. This shows that the soil falls in the category of sand. Since the uniformity coefficient is

2.1 and the coefficient of curvature is 1.18, therefore the soil is designated as SP, i.e. the poorly graded sand.

Table 4. Experimental program me

Material	Details of The Experiments
Sandy Soil	Natural Moisture Contents, Bulk Density, Specific Gravity, Grain size distribution, Compaction Characteristics, CBR Tests (As per IS: 2720, various parts)
Aggregates	Aggregate Crushing Value, Aggregate Impact Values, Specific Gravity, Water Absorption, Fineness Modulus(as Per IS:383 & IS:2386, Various Parts)
Water	pH, Dissolved Solids, Suspended Solids, Sulphates, Chloride, Turbidity, Alkalinity, Hardness(Standard Methods)
Sand mix with aggregates	CBR Tests

The moisture content-dry density relation revealed that due to addition of water the dry density increases uniformly to a maximum value of 17.70 KN/m³ at 11.41% moisture content thereafter shows a declining behavior. On the basis of the results obtained from direct shear test, the angle of internal friction is 32° which shows that there is better mobilization of shear strength through interlocking of soil particles and the soil will fail by local shear failure. Since the value of cohesion is zero, the shear strength in the soil will result from intergranular friction alone. The geotechnical properties of the soil under investigation are presented in Table 1.

4.2 Physical Properties of Coarse aggregates

The 20 mm & 10 mm nominal sizes of coarse aggregates were taken as per IS:383-1970. The aggregates having impact value 9.86% and crushing value as 11.21 % shows that the coarse aggregates collected can withstand relatively larger heavy loads. The physical properties of coarse aggregates are shown in Table – 2.

4.3 Physical& Chemical Properties of Water

The pH value of the water obtained is 7.24 which is greater than 7, therefore, it is alkaline. The presence of sulphate in water affects the durability and strength of mix and chlorides produces efflorescence. The tests on water indicate that the

sulphate content in water is 86 mg per liter and chlorides 128.00 mg per liter, which is within acceptable limits. Table – 3 shows the properties of water being used in the study. These properties of water shows that the water is potable and is fit for drinking purposes and hence can be used for the present experimentation.



Fig. 2. Experimental setup for CBR test.

Source: IS: 2720 (Part 16) “Methods of Test for Soils: Part-16, Laboratory Determination of California Bearing Ratio”

4.4 CBR Values of Sand Mixed With Coarse Aggregates

CBR tests have been carried out on the soil samples, at OMC as well as in soaked condition, first without mixing coarse aggregates and then by mixing coarse aggregates in varying percentages ranging from 0% to 30% by Weight of the dry soil at a constant optimum moisture content of 11.41%. The results obtained are presented in graphical form:

- CBR value of soil without mixing coarse aggregates:
 - At OMC: 26.78%
 - In Soaked Condition: 18.15%
- CBR value of soil mixed with coarse aggregates(by Weight) in varying percentages:

The load penetration curves for the soil mixed with various percentages of coarse aggregates are shown in Fig.-3 to Fig.-9 for various conditions of the soil such as at OMC and at soaked condition. The load increases with the various penetration values in both at OMC and at soaked conditions of the soil. After a certain value of the load, penetration

increases at a constant load condition in each case. The CBR values of the soil samples containing different percentages of coarse aggregates are shown in Table – 5. CBR value of soil without coarse aggregates is found to be 26.78% and 18.15% at OMC and in soaked condition respectively. The CBR value of soil is contributed due to the apparent cohesion and friction. The soil used in this present study is cohesion less; therefore due to the coarser particles of sand, friction alone contributes to the mobilization of the strength. From Table –5, it is revealed that the CBR value of soil increases with the addition of the coarse aggregates. The CBR values increases to 35.19% & 32.40% at OMC and 23.84% & 22.36% in soaked condition for 20mm & 10mm size coarse aggregates respectively by adding 5% coarse aggregates and enhanced to 67.47% & 57.80% for 20mm and 60.47% & 54.90% for 10mm size at OMC and in soaked condition when mixed with 30% coarse aggregates.

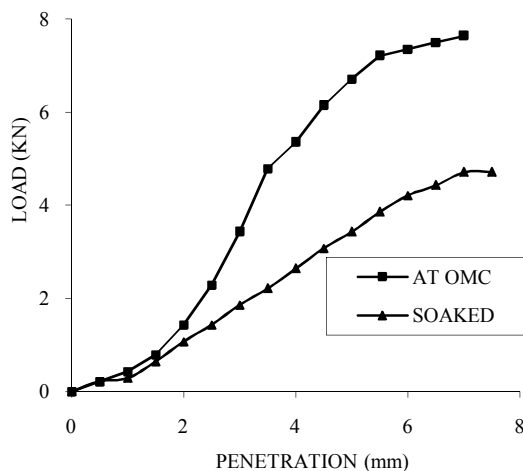


Fig.3. Load penetration curve for soil mixed with 0% coarse aggregates.

The load carrying capacity of soil mix is more at OMC than at soaked condition. With the increase in the percentage of coarse aggregates in the soil mix, the load carrying capacity increases at any level of penetration. This increase in strength of the soil coarse aggregates mixes is attributed to the increased weight per cubic meter due to the inclusion of more dense coarse aggregates in to the soil. The 20mm coarse aggregates has the ability to take greater loads as compared to the 10mm coarse aggregates. This increase in CBR values is attributed to the density of the coarse aggregates added and the

interlocking of soil particles with them. With the increase in the coarse aggregate percentage, the CBR of the soil further increase. Fig. 10 shows the relationship between percentages of coarse aggregates added and corresponding CBR values at OMC and in soaked condition. From this, it seen that the relation is linear up to 15% inclusion of 20 mm coarse aggregates.

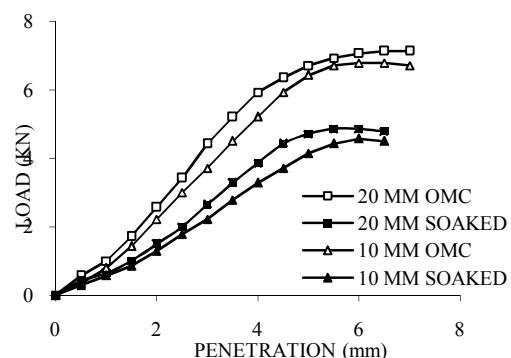


Fig.4. Load penetration curve for soil mixed with 5% coarse aggregates.

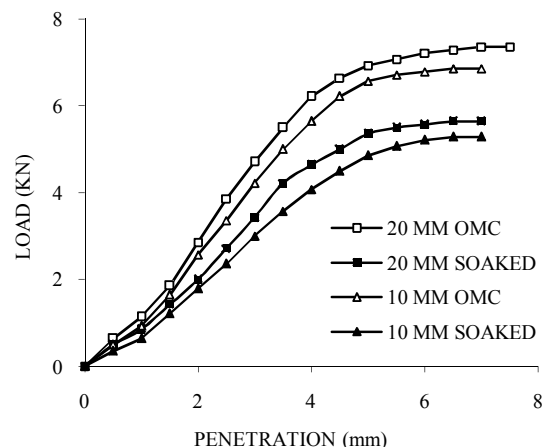


Fig.5. Load penetration curve for soil mixed with 10.0 % coarse aggregates.

At 15% to 20% inclusion of coarse aggregates, there is sudden increase in the CBR value and there after it again becomes linear. In the case of 10mm coarse aggregates also, the relation remains linear up to 15% inclusion of coarse aggregates and at 15 % to 20% there is sudden increase in the CBR value thereafter the relation again become linear. This accumulation of the strength is attributed to the

improvement in the frictional resistance of the soil coarse aggregate mix. From this table it is observed that the percentage variation in the CBR values improved from 20.99% to 115.83% and 31.30% to 151.94% for 10mm and 20mm coarse aggregates respectively at OMC. In soaked condition this improvement ranges from 23.20% to 202.48% and 31.35% to 233.17% for 10mm and 20mm coarse aggregates respectively.

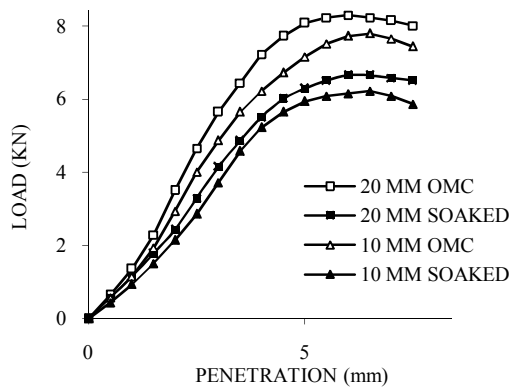


Fig.6. Load penetration curve for soil mixed with 15.0 % coarse aggregates.

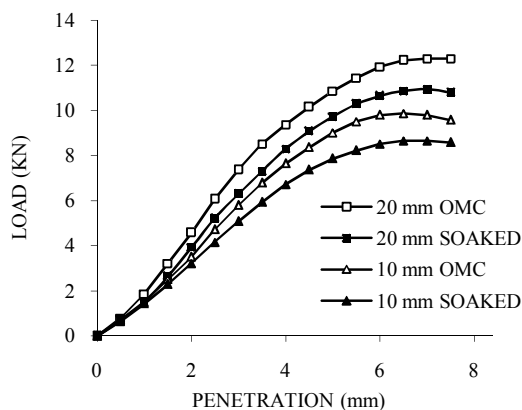


Fig.7. Load penetration curve for soil mixed with 20.0 % coarse aggregates.

The percentage increase in the CBR values with the addition of coarse aggregates is given in Table 5.

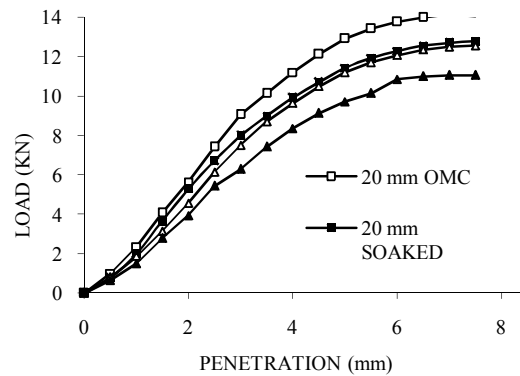


Fig.8. load penetration curve for soil mixed with 25.0 % coarse aggregates.

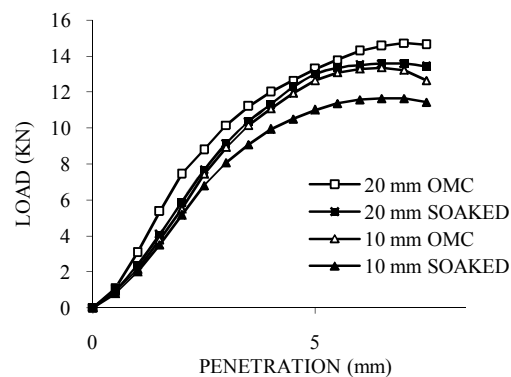


Fig.9. Load penetration curve for soil mixed with 30% coarse aggregates.

Table 5. Percentage increase in the CBR values with the addition of coarse aggregates.

% of coarse aggregate	CBR Values (%)			
	At OMC		In Soaked Condition	
	10 mm	20 mm	10 mm	20 mm
0	26.78	26.78	18.15	18.15
5	32.4	35.19	22.36	23.84
10	34.46	38.44	26.48	28.3
15	37.01	40.86	30.83	34.1
20	46.44	59.98	43.54	49.48
25	51.88	64.33	49.09	56.11
30	57.8	67.47	54.9	60.47

As expected, the CBR values of the soil mixes obtained with the inclusion of 10mm coarse aggregates remains lower than that obtained with the 20mm. This is attributed to the strength of the coarse aggregates since the strength of small coarse aggregates is less as compared to the larger particles, therefore the CBR of the soil remains low with 10mm coarse aggregates as compared to the 20mm.

Table 5. CBR values of soil Mixed with Different % of Coarse Aggregate (By Weight).

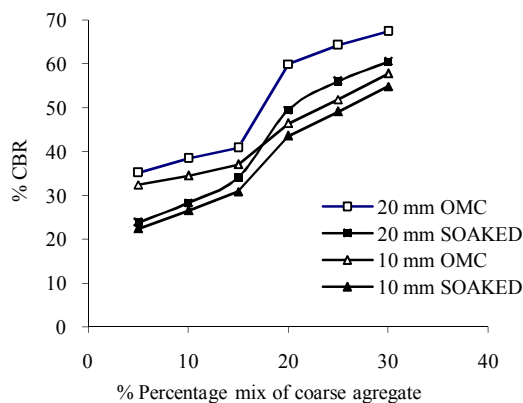


Fig.10.Variation of CBR Value with Percentage of Coarse aggregates.

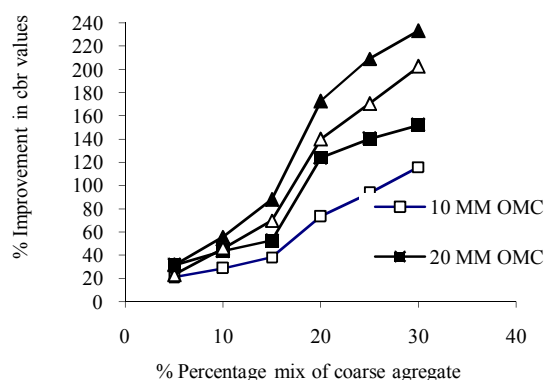


Fig.11.Percent improvement in CBR values for various mix of coarse aggregates.

It is evident from the Fig 3 to Fig 11and the Table 5 to Table 6, that soaking of the sample causes a decrease in the CBR value of the soil both with and without mixing of coarse aggregates but the behavior of increase in CBR is same in soaked condition as well as at OMC for the increase in the

percentage of the added coarse aggregates. This decrease in CBR value is due to increase in the moisture content of the mixes above OMC during their soaking period thus making the soil soft and a decrease in the effective stresses. More over the particles are also mobilized therefore the load carrying capacity decreases due to soaking. The coarse aggregates used in the study have good interlocking and frictional properties which provides resistance to the lateral movements and improves the strength of the soil sample.

Table 6.Percentimprovement in CBR values of soil mixed with different % of coarse aggregate (by weight)

Percentage Improvement of CBR Values for addition of Aggregate				
% of Aggregate (By Weight)	At OMC		In Soaked Condition	
	10 mm	20 mm	10 mm	20 mm
5	20.99	31.3	23.2	31.35
10	28.68	43.54	45.9	55.92
15	38.2	52.58	69.86	87.88
20	73.41	123.97	139.89	172.62
25	93.73	140.22	170.47	209.15
30	115.8	151.94	202.48	233.17

5. CONCLUSIONS

The experimentation conducted shows favorable results as the CBR of soil enhanced by the inclusion of coarse aggregates. However with the increase of coarse aggregate percentage, the problem of workability was experienced during the experimentation because the coarse aggregate replaces the soil mass with their increased density. However following specific conclusions are made from this study:

1. The CBR value of soil increases with the increase in coarse aggregate percentage.
2. The CBR value of soil when mixed with 20mm size coarse aggregates is more than that with 10 mm sized coarse aggregates.
3. With the increase in the percentage of coarse aggregates in the soil, the workability is affected and will be uneconomical.

6. REFERENCES

- [1] Srivastava, R. K., Jalota, A. V., Sahu, A. K., Singh, R. (1995), "Model studies on geo-textile

- reinforced Pavements". Journal of Indian Highways, September 1995, pp.31-39
- [2] Jain, R.K., Mathur, B.L., Mathur, R.C. (1997) "Sand subgrade reinforcement using discrete natural fibers" proceedings of the Indian Geotechnical Conference, Vadodara, Theme. 5-21, Dec. 1997, pp 325-328.
- [3] Pandian, N. S., Krishna, K. C., Sridharan, A. (2001), "California Bearing Ratio Behavior of Soil/ Fly Ash Mixtures". Journal of Testing and Evaluation, JTEVA, ASTM, Vol. 29, No. 2. March 2001, pp 220-226.
- [4] Singh, Virender, Kumar, Parkash. (2002) "Effects of Surcharge Load and Compaction on CBR of Alluvial Soil" Proceedings of the Indian Geotechnical Conference, Allahabad, Dec. 2002, pp 62-65.
- [5] Amu, O. O., Adewumi, I. K., Ayodele, A. L., Mustapha, R. A., Ola, O. O. (2005), "Analysis of California Bearing Ratio Values of Lime and Wood Ash Stabilized Lateritic Soil". Journal of Applied Sciences, Asian Network for Scientific Information, pp.1479-14483
- [6] Eric Duncan-William, Nii O. Attah-Okine (2007), "Effect of geogrid in granular base strength – An experimental investigation" a Journal of Construction and Building Materials, ScienceDirect, Vol. 22(2008), pp 2180 – 2184.
- [7] Naeini, S.A., Mirzakhani, M. (2008), "The Effect of Geotextile and Grading on the Bearing Capacity of Granular Soils". Journal of EJGE, Vol. 13, Bund. J, pp.1-10
- [8] Modak, R., Nangare, P.B., Nagrale, S.D., Nalwade, R.D. and Chavhan, V.S. (2012) Stabilization of Black Cotton Soil using admixture, International Journal of Engineering and Innovative Technology, Vol.1 No.5, pp.11-13
- [9] Kavish S. Mehta, Rutvij J. Sonecha, Parth D. Daxini, Parth B. Ratanpara, Miss Kapilani S. Gaikwad, Journal of Engineering Research and Applications, Vol.4, Issue5 (Version3), May 2014, pp.25-32.
- [10] Mudgal Ankur, Raju Sarkar and A.K. Sahu "Effect of Lime & stone dust in the geotechnical Properties of Black cotton soil. Int. Journal of GEOMATE Dec, 2014, Vol.7, No.2 (Sl.14), pp.1033-1039
- [11] IS: 2386 (Part I) – 1963, Reaffirmed 1997, "Methods of Testing for Aggregates for Concrete: Particle Size & Shape", Bureau of Indian Standards.
- [12] IS: 2386 (Part III) – 1963, Reaffirmed 1997, "Methods of Testing for Aggregates for Concrete: Specific Gravity, Density, Voids, Absorption & Bulking", Bureau of Indian Standards.
- [13] IS: 2386 (Part IV) – 1963, Reaffirmed 1997, "Methods of Testing for Aggregates for Concrete: Mechanical Properties", Bureau of Indian Standards.
- [14] IS: 2720 (Part III/ Sec 1) – 1980. (1980), Reaffirmed 2002, "Methods of Test for Soils: Part-3, Determination of Specific Gravity, Fine Grained Soils", Bureau of Indian Standards.
- [15] IS: 2720 (Part 4) – 1985. (1986), Reaffirmed 2006, "Methods of Test for Soils: Part-2, Determination of Grain Size Analysis", Bureau of Indian Standards.
- [16] IS: 2720 (Part VII) – 1980. (2003), Reaffirmed 2003, "Methods of Test for Soils: Part-7, Determination of Water Content Dry Density Relation using Light Compaction", Bureau of Indian Standards.
- [17] IS: 2720 (Part 16) – 1987. 1988), Reaffirmed 2002, "Methods of Test for Soils: Part-16, Laboratory Determination of California Bearing Ratio", Bureau of Indian Standards.
- [18] IS: 3025 – 1984, Reaffirmed 2002, "Methods of Sampling and Test (Physical and Chemical) for water and waste water". Bureau of Indian Standards.
- [19] IS: 383-1970, Reaffirmed 1997, "Specification For Coarse and Fine Aggregates From Natural Sources For Concrete."

Int. J. of GEOMATE, April, 2016, Vol. 10, No. 2 (Sl. No. 20), pp. 1743-1750.

MS No. 48585 received on Sept. 11, 2015 and reviewed under GEOMATE publication policies. Copyright © 2015, International Journal of GEOMATE. All rights reserved, including the making of copies unless permission is obtained from the copyright proprietors. Pertinent discussion including authors' closure, if any, will be published in Dec. 2016 if the discussion is received by June 2016.

Corresponding Author: Kesharwani R.S.

Control of Switched-Mode Boost Converter by Using Classical and Optimized Type Controllers

Arnab Ghosh*, Subrata Banerjee**

* Research Scholar, Department of Electrical Engineering, National Institute of Technology, Durgapur-713209, India.
(e-mail: aghosh.ee@gmail.com)

** Professor, Department of Electrical Engineering, National Institute of Technology, Durgapur-713209, India.
(e-mail: bansub2004@yahoo.com)

Abstract: In this paper design and implementation of Type controllers have been performed by using *k-factor* approach and two different optimization techniques Gravitational Search Algorithm (GSA) and Particle Swarm Optimization (PSO) for obtaining better stability and performance for a closed loop DC-DC Switched Mode Boost Converter. Boost converter have a *right-half-plane zero* (*non minimum phase system*), so it is difficult for the PID controller to exhibit good performance with *load, line variations and parametric uncertainty*. The comparative closed-loop performances of a boost converter with classical and optimized Type II/Type III controllers have been produced. Simulations and experimental results are provided to demonstrate the effectiveness of optimized controllers for the proposed converter.

Keywords: Switched-Mode Boost Converter, Non-Minimum Phase System, Type-II & Type-III Controller, Particle Swarm Optimization (PSO), Gravitational Search Algorithm (GSA).

1. INTRODUCTION

The DC-DC power supplies have played important role in every sphere of engineering with wide range of applications from a few tens of watts to several hundreds of megawatts. The most common and essential applications are in personal/laptop computers, cellular phones, Microcontroller/DSP kit, battery chargers, office equipments, spacecraft, power systems devices, telecommunication equipments, high voltage DC transmission, adjustable motor drives and many others (Mohan et al., 2003; Rashid, 2014).

In the early days, the potential dividers (PD's) were used to control and transfer the DC power from one level to another level. Though the operation of PD's is much easier to realize but the conversion is less energy efficient. For improving the energy efficiency, the linear regulators were introduced. The operations of linear regulators are almost similar to the PD's, embedded with load regulation features and the series resistance is replaced by solid state device. In linear regulators the solid state device operates in active zone that causes a significant amount of power losses across it. Due to the presence of larger heat sinks, and line-frequency transformer, the size and the weight of the power supply is bulky in nature and it is not suitable and economical for large power applications where energy efficiency is a major issue. But in Switch-Mode Power Supplies (SMPS) (Mohan et al., 2003; Rashid, 2014) the solid state device works *like* a switch *i.e.* either completely *on* or *off*. When the device is *on i.e.* conducting, large current flows through it with taking almost zero voltage across it. Similarly when the device is *off*, the voltage across the device is high with almost zero current through it. In both the cases the total power losses across the device is almost zero, so there are less conduction losses in

switching regulators. So, energy efficiency is very high (extended up to 95%) in switching regulator and those are found wide applications in many fields engineering *like as* electronic goods and gadgets, DC servo drives, electric transportation system, process control plant and robot automated factories, high-voltage DC transmission (HVDC) system, interconnection of photovoltaic and wind-electric systems to the utility grid, critical medical equipments/instruments, defence equipments *etc.*

Over the last decades the technical developments of DC-DC switching regulators are taken place by the introduction of different kinds of controller (Erickson et al., 2001) for achieving fast dynamic responses as well as better reliability and power density. The performance of DC-DC switching converter can broadly be classified into two categories: (a) transient performance, and (b) steady-state performance. The steady-state performance is mainly guided by the converter-topology, structural configuration of energy storage elements and operating frequency of the power supplies. On the other hand, the transient performance of converter is maintained by the control scheme *i.e.* nature of the controllers (Veerachary, 2012). There are several classical controllers *like* PI, PID controllers; have been developed over the years to ensure desired performance of the converter under specific conditions. Some converters *like* boost, buck-boost, and fly-back have a *right-half-plane zero* (*non minimum phase system*) (Ogata, 2010), so it is difficult for the PID controller to exhibit good performance with load, line variations and parametric uncertainty. For this reason *Type-controllers* (Venable, 1983; Reatti et al., 2003; Escobar et al., 2005; Bryant et al., 2006; Lee, 2014; Ghosh et al., 2014; Ghosh et al., 2015) are best suited. In the proposed work, the design of Type controllers have been aimed by using '*k-factor*' approach and then

controller parameters have to be optimized further by using different optimization techniques for obtaining better stability and performance for a DC-DC Switched Mode Boost Converter.

In recent years, the attention of the researchers have been devoted to implement different optimization techniques over the classical (traditional) control approaches for achieving best and optimised performance of the controllers. The optimal controllers are based on certain methods *such as* characteristics and behaviour of biological, molecular, swarm of insects, neurobiological systems *etc.* There is no specific algorithm to achieve the best solution for all optimization problems. Some algorithms give a better solution for some particular problems than others (Rashedi et al., 2009). Here, *Particle Swarm Optimization* (PSO) and *Gravitational search algorithm* (GSA) are used for design the optimal controllers. The *Particle Swarm Optimization* (PSO) (Eberhart et al., 1995; Al Rashidi et al., 2009; Kennedy, 2010; Clerc, 2010) is based on the behavior of a colony of living things, *like* as swarm of insects, flock of birds, or school of fish. The insects, fishes, animals, especially birds *etc.* always travel in a group without crashing each other from their group members by adjusting their positions and velocities from using their group information. Because this method reduces individual effort for searching the food, shelter *etc.* PSO is an evolutionary algorithm (technique) that optimizes the continuous or discrete, linear or nonlinear, constrained or unconstrained, non differentiable functions by iteratively trying to improve the solutions for different parameter values. *Gravitational search algorithm* (GSA) was introduced by (Rashedi et al., 2009). GSA is based on Newtonian law of gravity (Rashedi et al., 2009; Sabri et al., 2013). This algorithm is simple to understand, easy to implement and gives the optimum controller performance. The DC-DC power supplies are required to deliver regulated output voltage with fast dynamical response, low overshoot, minimal steady-state output error, and low sensitivity to the noise. Recent literatures have been reported, based on the applications of different optimized controllers (Beccuti et al., 2005; Poodeh et al., 2007), PSO and GSA based optimized PI, PID controllers for improving the performance of the DC-DC converter (Yousefi et al., 2008; Emami et al., 2008; David et al., 2009; Abdul-Malek et al., 2009; Liu et al., 2010; Tehrani et al., 2010; Altinoz et al., 2010; Jalilvand et al., 2011; Chung et al., 2011; Khare et al., 2013; Dorf et al., 2011; Siano et al., 2014; Duman et al., 2011; Sarkar et al., 2013). The prior researchers worked on the optimized PI, PID controllers, the optimized Type-II/III has not been reported anywhere. All these requirements have to be satisfied both through the correct design of the circuit parameters and components and mostly by the implementation of appropriate control methodologies. So the optimized controllers are the best suited for any application of DC-DC power supplies in terms of several advantages.

The converter is designed and fabricated in laboratory scale and the specifications are given in Table I. The thumb rule of the design is strictly followed to obtain the required voltage & power output of the converter. The implementation of the overall closed loop system is performed by utilizing dSPACE real time controller. The schematic diagram of the overall control system which is being implemented is shown in Fig.1.

It is seen (Fig.1) that the converter uses voltage mode controller where the output voltage of the converter is sensed by LEM make Hall effect voltage sensor. The voltage signal from sensor is appropriately conditioned (filtered & scaled) before feeding to the ADC port of dSPACE controller. The overall control system has been implemented in real time platform by using Simulink module. The conditioned digital voltage output from ADC is compared with a reference input; an error signal is generated and is passed through the optimized Type Controllers which in turn generates the modulating signal. This control signal is then compared with the high frequency triangular waveform to produce PWM signal. This PWM output from dSPACE is passed through DAC, Optoisolator and Astable multivibrator circuit before inputting to the gate of MOSFET switch of Boost converter.

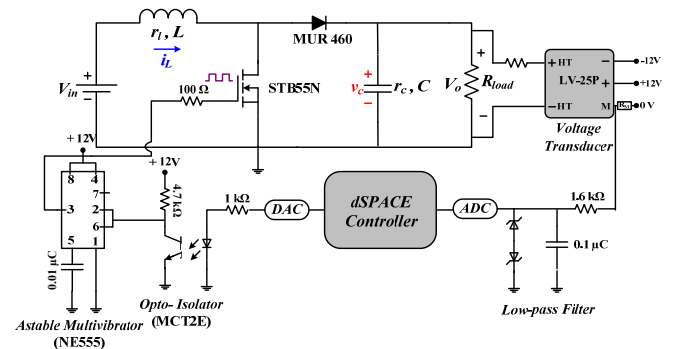


Fig. 1. Schematic diagram of closed-loop operation for boost converter.

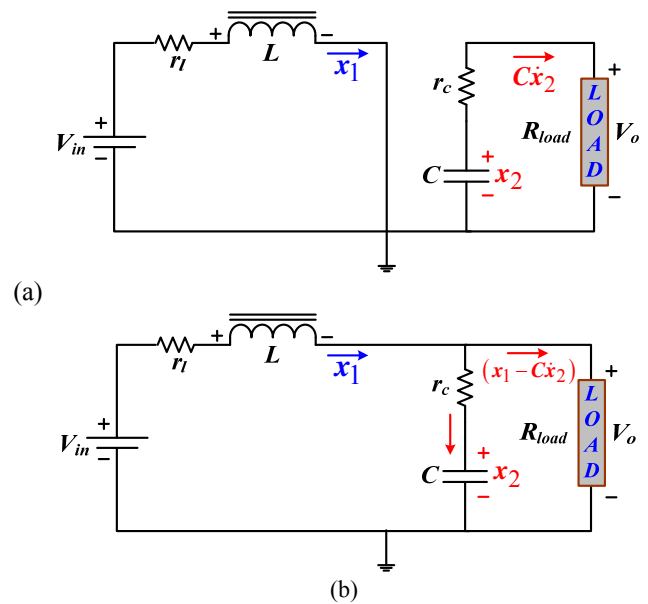


Fig. 2. Equivalent circuit of a boost converter (a) switch on and (b) switch off instant.

2. MODELING OF BOOST CONVERTER

The switching converters are non-linear time varying system. State-Space Averaging (SSA) is an approximation technique that approximates the switching converter as a continuous linear system. In State-Space Averaging method, the corner frequency (f_{corner}) of the output filter to be much smaller than the converter's switching frequency (f_{sw}) (*i.e.* $f_{corner}/f_{sw} \ll 1$). That implies low output-switching ripple. From the SSA technique, the mathematical modelling can be found from

equivalent circuit model of the converter. The small-signal transfer functions can be derived from the mathematical model of the switching converter. The major advantages of this method are the establishment of a complete converter model with both steady-state and dynamic quantities. (Ang et al., 2005)

Boost converter during switch on condition:

Let, $x_1 = i_L(t)$ = Inductor Current and $x_2 = v_c(t)$ = Capacitor Voltage are two state variables.

Applying kirchoffs law

$$V_{in} - \eta x_1 - L\dot{x}_1 = 0$$

$$\text{or, } L\dot{x}_1 = -\eta x_1 + V_{in} \quad (1)$$

$$\text{Again, } x_2 + r_c C\dot{x}_2 - R_{load}(-C\dot{x}_2) = 0$$

$$\text{or, } C\dot{x}_2 = -\frac{1}{R_{load} + r_c} x_2 \quad (2)$$

Therefore, in state space form, one can write

$$\begin{bmatrix} L & 0 \\ 0 & C \end{bmatrix} \begin{bmatrix} \dot{x}_1 \\ \dot{x}_2 \end{bmatrix} = \begin{bmatrix} -\eta & 0 \\ 0 & -\frac{1}{r_c + R_{load}} \end{bmatrix} \begin{bmatrix} x_1 \\ x_2 \end{bmatrix} + \begin{bmatrix} 1 \\ 0 \end{bmatrix} V_{in} \quad (3)$$

$$\text{Therefore, } A_1 = \begin{bmatrix} -\frac{\eta}{L} & 0 \\ 0 & -\frac{1}{C(r_c + R_{load})} \end{bmatrix}, B_1 = \begin{bmatrix} \frac{1}{L} \\ 0 \end{bmatrix}$$

Applying KVL, the output equation becomes

$$v_o = R_{load} i_o = -R_{load} i_c; (\text{as } i_o = -i_c)$$

$$\text{or, } v_o = -R_{load}(C\dot{x}_2) = -\left(-\frac{R_{load}}{R_{load} + r_c}\right) x_2 \quad (5)$$

$$\text{Therefore, } v_o = \begin{bmatrix} 0 & \frac{R_{load}}{R_{load} + r_c} \end{bmatrix} \begin{bmatrix} x_1 \\ x_2 \end{bmatrix} + [0] V_{in} \quad (6)$$

$$\text{where, } C_{m1} = \begin{bmatrix} 0 & \frac{R_{load}}{R_{load} + r_c} \end{bmatrix}, E_1 = [0] \quad (7)$$

Boost converter during switch off:

A boost converter during switch off condition can be shown in the Fig 2 (b).

Therefore, state-space equations are

$$\begin{bmatrix} L & 0 \\ 0 & C \end{bmatrix} \begin{bmatrix} \dot{x}_1 \\ \dot{x}_2 \end{bmatrix} = \begin{bmatrix} -\left(r_L + \frac{R_{load} \times r_c}{R_{load} + r_c}\right) & -\frac{R_{load}}{R_{load} + r_c} \\ \frac{R_{load}}{R_{load} + r_c} & -\frac{1}{R_{load} + r_c} \end{bmatrix} \begin{bmatrix} x_1 \\ x_2 \end{bmatrix} + \begin{bmatrix} 1 \\ 0 \end{bmatrix} V_{in} \quad (8)$$

and output equation is as follows

$$v_o = \begin{bmatrix} \frac{R_{load} \times r_c}{R_{load} + r_c} & \frac{R_{load}}{R_{load} + r_c} \end{bmatrix} \begin{bmatrix} x_1 \\ x_2 \end{bmatrix} + [0] V_{in} \quad (9)$$

$$\text{cSo, } A_2 = \begin{bmatrix} -\frac{1}{L} \left(\eta + \frac{R_{load} \times r_c}{R_{load} + r_c} \right) & -\frac{R_{load}}{L(R_{load} + r_c)} \\ \frac{R_{load}}{C(R_{load} + r_c)} & -\frac{1}{C(R_{load} + r_c)} \end{bmatrix}, B_2 = \begin{bmatrix} \frac{1}{L} \\ 0 \end{bmatrix},$$

$$C_{m2} = \begin{bmatrix} \frac{R_{load} \times r_c}{R_{load} + r_c} & \frac{R_{load}}{R_{load} + r_c} \end{bmatrix}, E_2 = [0] \quad (10)$$

$$\text{Also, } \frac{V_o}{V_{in}} = -C_m A^{-1} B \quad (11)$$

$$\text{where, } A = DA_1 + (1-D)A_2, B = DB_1 + (1-D)B_2,$$

$$C_m = DC_{m1} + (1-D)C_{m2}$$

The desired transfer function of the power state, $T_p(s)$

$$T_p(s) = \frac{\tilde{v}_0(s)}{\tilde{d}(s)} = C_m [sI - A]^{-1} [(A_1 - A_2)X + (B_1 - B_2)V_{in}] + [(C_{m1} - C_{m2})X] \quad (12)$$

where, I = Identity matrix, D = Duty ratio (Steady-state) and X = State variables (Steady-state).

Finally, output to control transfer function of the Boost plant is

$$T_p(s) = \frac{\tilde{v}_0(s)}{\tilde{d}(s)} \approx G_{do} \frac{\{1 + (s/\omega_{z-ESR})\} \{1 - (s/\omega_{z-RHP})\}}{[1 + (s/\omega_o Q) + (s/\omega_o)^2]} \quad (13)$$

$$\text{where, DC Gain}(G_{do}) = V_{in}/(1-D)^2;$$

$$\text{Zero due to ESR}(\omega_{z-ESR}) = 1/(r_c C) \text{ rad/sec};$$

$$\text{RHP-Zero}(\omega_{z-RHP}) = (1-D)^2 (R_{load} - \eta)/L \text{ rad/sec};$$

$$\text{Natural Frequency}(\omega_o) = \frac{1}{\sqrt{LC}} \sqrt{\frac{\eta + (1-D)^2 R_{load}}{R_{load}}} \text{ rad/sec};$$

$$\text{Quality Factor}(Q) = \omega_o / \left(\frac{\eta}{L} + \frac{1}{C(R_{load} + r_c)} \right)$$

Transfer function of boost converter after putting the parameter values (ref Table 1).

$$T_{P_Boost} = \frac{-0.005696s^2 - 0.02559s + 4.983 \times 10^6}{s^2 + 825.3s + 542410} \quad (14)$$

A *right-half plane zero* (RHP) is present in the plant transfer function of the boost-converter (Eqn. (13) & Eqn. (14)) and there is an effect of non-minimum phase due to this RHP.

Table 1. Parameters of Boost Converter.

Circuit Components	Values
Input Voltage V_{in}	5 Volt
Output Voltage V_o	12 Volt
Inductance L	250 μ H
Output Capacitance C	1056 μ F
Inductor Resistance r_l	10 m Ω
ESR of Capacitor r_c	30 m Ω
Load Resistance R_{load}	25 Ω
Switching Period T	50 μ s

3. DESCRIPTION AND DESIGN OF TYPE CONTROLLERS

The design of controllers will play an important factor for maintaining good dynamic performances and regulation of a power supply. In this paper ‘Classical Type-II/III’ controllers have been used for keeping overall closed loop stability and good dynamic response of the boost converter.

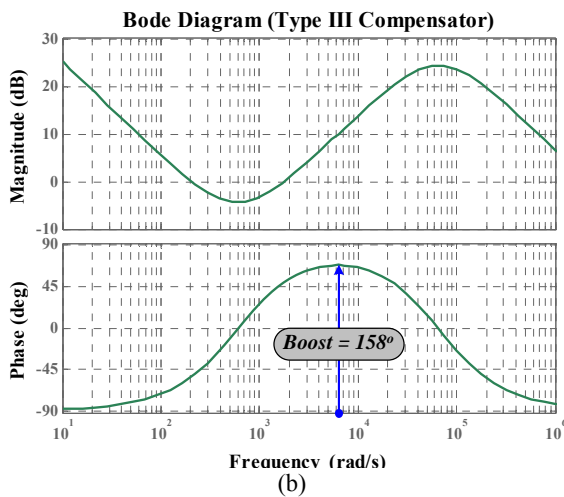
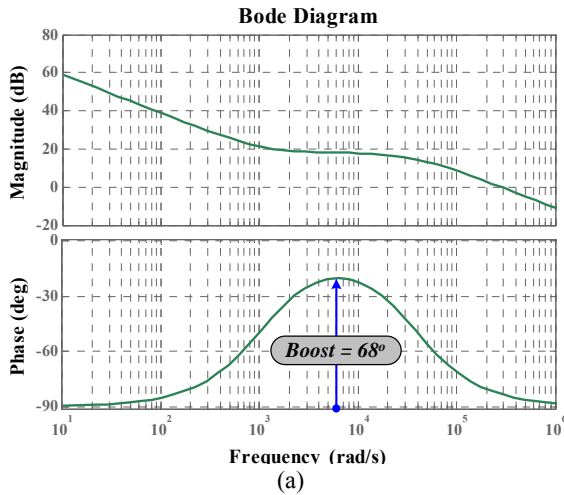


Fig. 3. The Bode diagram of (a) Type-II and (b) Type-III controller.

3.1. Type-II Controller Design

The ‘Type-II’ controller is one kind of lead controller with a pole at origin. So, this controller provides maximum 90° phase boost with zero steady state error. Even though boost converter having *non-minimum phase* problem, it exhibits a better closed loop performance with a cascaded Type-II controller. With proper tuning of this controller the converter may perform faster response, with minimal overshoots and zero steady-state error (Ghosh *et al.*, 2015).

3.1.1. Mathematical Approach

The transfer function of Type-II controller is:

$$T_{c_II}(s) = \frac{\left(1 + \frac{s}{\omega_{z_II}}\right)}{\left(\frac{s}{\omega_{po_II}}\right) \left(1 + \frac{s}{\omega_{p_II}}\right)} \quad (15)$$

where, ω_{p_II} and ω_{z_II} are respective pole and zero frequency of Type-II controller.

The magnitude of such transfer function is

$$|T_{c_II}(j\omega)| = \frac{\left|1 + j\frac{\omega}{\omega_{z_II}}\right|}{\left|j\frac{\omega}{\omega_{po_II}}\right| \left|1 + j\frac{\omega}{\omega_{p_II}}\right|} \quad (16)$$

The argument is written as

$$\arg T_{c_II}(j\omega) = \tan^{-1}\left(\frac{\omega}{\omega_{z_II}}\right) - \tan^{-1}\left(\frac{\omega}{\omega_{p_II}}\right) - \frac{\pi}{2} \quad (17)$$

The bode diagram of Type-II controller is shown in Fig. 3 (a) where the pole-zero combination has created a localized *phase boost* of 68° at a certain frequency. The *frequency* where the *maximum phase boost* will be occurred can be obtained by taking derivate of Eqn. (17).

$$\begin{aligned} \frac{d}{df}(\arg T_{c_II}(j\omega)) &= \frac{d}{df} \left(\tan^{-1}\left(\frac{f}{f_{z_II}}\right) - \tan^{-1}\left(\frac{f}{f_{p_II}}\right) - \frac{\pi}{2} \right) \\ &= \frac{1}{f_{z_II} \left(\frac{f^2}{f_{z_II}^2} + 1 \right)} - \frac{1}{f_{p_II} \left(\frac{f^2}{f_{p_II}^2} + 1 \right)} = 0 \end{aligned} \quad (18)$$

To solve the Eqn. (18), the maximum phase *boost* is obtained at the *geometric mean* of the pole and zero frequencies, $f_{\max_II} = \sqrt{f_{p_II} f_{z_II}}$. Generally this geometric mean frequency is considered as crossover frequency (f_{c_II}) of the controller.

3.1.2. Derivation of ‘k’ in Type-II Controller

The ‘k’ is defined as the ratio of the pole frequency to the zero frequency in Type-II controller (Venable, 1983). These pole/zero combinations provide an adjustable phase *boost* from 0° to 90° at the crossover frequency. The relation between ‘k’ and the phase *boost* provided by the controller is given by Eqn.(19) (Ghosh *et al.*, 2015):

$$k = \tan\left(\frac{\text{boost}}{2} + \frac{\pi}{4}\right) \quad (19)$$

As $k = f_{p_II}/f_{z_II}$, the location of pole frequency will be

$$f_{p_II} = k \cdot f_{c_II} = \tan\left(\frac{\text{boost}}{2} + \frac{\pi}{4}\right) f_{c_II} \quad (20)$$

and the zero frequency will be derived from

$$f_{z_II} = \frac{f_{c_II}}{k} = f_{c_II} / \tan\left(\frac{\text{boost}}{2} + \frac{\pi}{4}\right) \quad (21)$$

Assuming crossover frequency (supposed to be less than the switching frequency) and phase boost, the exact locations of pole/zero can easily be found from Eqn. (20) and Eqn. (21).

3.1.3. Mid-Band Gain Adjustment for the Controller

A Type-II controller is simply combination of *single pole/zero pair* with an *origin pole*. Controller has been described in Eqn. (3) and may be described as follows:

$$T_{c_II}(s) = \frac{(s/\omega_{z_II})(1+\omega_{z_II}/s)}{(s/\omega_{po_II})(1+s/\omega_{p_II})} = \frac{\omega_{po_II}}{\omega_{z_II}} \frac{1+\omega_{z_II}/s}{1+s/\omega_{p_II}} \\ = G_{o_II} \frac{1+\omega_{z_II}/s}{1+s/\omega_{p_II}} \quad (22)$$

In the above expression, the term G_{o_II} is called the mid-band gain and G_{o_II} is equal to $\omega_{po_II}/\omega_{z_II}$ where the value of ω_{po_II} depends on the desired gain/attenuation at crossover frequency.

3.1.4. Design Example of Type-II Controller

Let's assume a boost converter with having a gain deficit of -18 dB at selected crossover frequency (f_{c_II}) of 1 kHz. The necessary phase *boost* is 68° . So, the pole can be placed at (from Eqn. (20))

$$f_{p_II} = \tan\left(\frac{\text{boost}}{2} + \frac{\pi}{4}\right) f_{c_II} = \tan\left(\frac{68^\circ}{2} + 45^\circ\right) \times 1000 \\ = 5.14 \text{ kHz} \quad (23)$$

From Eqn. (21) the zero location will be at

$$f_{z_II} = f_{c_II} / \tan\left(\frac{\text{boost}}{2} + \frac{\pi}{4}\right) = 1000 / \tan\left(\frac{68^\circ}{2} + 45^\circ\right) \\ = 194.38 \text{ Hz} \quad (24)$$

So the transfer function of the designed Type-II controller is given by $\frac{1000(s+1221.3)}{s(s+32324)}$.

3.2. Type-III Controller Design

The "Type-III" controller is lead-lead controller with a pole at origin. So, this controller can provide maximum phase *boost* of 180° with *zero steady state error*. Even though the presence of non-minimum phase problem in boost converter, the converter may exhibit the best closed loop performance with a Type-III controller. By the proper tuning of this controller the converter may provide the *fastest response* (better than "Type-II" controller) with minimal overshoots and zero steady-state error (Ghosh et al., 2014).

3.2.1. Mathematical Approach

The transfer function of the Type-III controller is as follows:

$$T_{c_III}(s) = \frac{(1+s/\omega_{z1_III})(1+s/\omega_{z2_III})}{(s/\omega_{po_III})(1+s/\omega_{p1_III})(1+s/\omega_{p2_III})} \quad (25)$$

Now the two zeros have been assumed at same point and similarly the two poles are also presumed same point so the

location of *double pole* and *double zero* have been considered at $\omega_{z1_III} = \omega_{z2_III} = \omega_{z1,2_III}$ and $\omega_{p1_III} = \omega_{p2_III} = \omega_{p1,2_III}$.

$$T_{c_III}(s) = \frac{(1+s/\omega_{z1,2_III})^2}{(s/\omega_{po_III})(1+s/\omega_{p1,2_III})^2} \quad (26)$$

The magnitude of the Type-III controller can be written as

$$|T_{c_III}(j\omega)| = \frac{\left|1+j\frac{\omega}{\omega_{z1,2_III}}\right| \left|1+j\frac{\omega}{\omega_{z1,2_III}}\right|}{\left|j\frac{\omega}{\omega_{po_III}}\right| \left|1+j\frac{\omega}{\omega_{p1,2_III}}\right| \left|1+j\frac{\omega}{\omega_{p1,2_III}}\right|} \quad (27)$$

The argument of the controller is

$$\arg T_{c_III}(j\omega) = 2 \tan^{-1}(\omega/\omega_{z1,2_III}) - 2 \tan^{-1}(\omega/\omega_{p1,2_III}) - \frac{\pi}{2} \quad (28)$$

The Bode diagram of Type-III controller is shown in Fig. 3 (b) where the pole-zero combinations create a phase *boost* of 158° at a certain frequency. In this controller the maximum phase *boost* of 180° may be found by changing the poles/zeros locations. The *maximum phase boost* may be obtained by taking the derivate of Eqn. (28) with respect to frequency f . Finally the *maximum phase boost* can be obtained at the *geometric mean* of the double zero-double pole frequencies in Type-III controller.

$$f_{\max_III} = \sqrt{f_{z1,2_III} f_{p1,2_III}} \quad (29)$$

This geometric mean frequency is considered as crossover frequency (f_{c_III}) in the Type-III controller.

3.2.2. Derivation of 'k' in Type-III Controller

The 'k' is defined as the ratio of the double pole frequency to the double zero frequency in Type-III controller (Venables, 1983). These poles-zeros combination provide maximum phase *boost* 180° at the crossover frequency. The relation between 'k' and the phase *boost* of this controller can be written as follows (Ghosh et al., 2014):

$$k = \left\{ \tan\left(\frac{\text{boost}}{4} + \frac{\pi}{4}\right) \right\}^2 \quad (30)$$

So the pole location will be in Type-III controller

$$f_{p1,2_III} = \sqrt{k} \cdot f_{c_III} = \tan\left(\frac{\text{boost}}{4} + \frac{\pi}{4}\right) f_{c_III} \quad (31)$$

and the zero location can be derived from Eqn. (32)

$$f_{z1,2_III} = \frac{f_{c_III}}{\sqrt{k}} = f_{c_III} / \tan\left(\frac{\text{boost}}{4} + \frac{\pi}{4}\right) \quad (32)$$

If the crossover frequency (f_{c_III}) is known with the values of necessary phase *boost*, the exact locations of the double-pole/double-zero may be found from Eqn. (31) and Eqn. (32).

3.2.3. Mid-Band Gain Adjustment for the Controller

The controller of Eqn. (25) may be described as follows:

$$T_{c_III}(s) = \frac{s}{\omega_{z1_III}} \frac{(1 + \omega_{z1_III}/s)(1 + s/\omega_{z2_III})}{(s/\omega_{po_III})(1 + s/\omega_{p1_III})(1 + s/\omega_{p2_III})}$$

$$= G_{o_III} \frac{(1 + \omega_{z1_III}/s)(1 + s/\omega_{z2_III})}{(1 + s/\omega_{p1_III})(1 + s/\omega_{p2_III})} \quad (33)$$

Here G_{o_III} is known as *mid-band gain* and $G_{o_III} = \omega_{po_III}/\omega_{z1_III}$. The value of ω_{po_III} depends upon the required gain/attenuation at crossover frequency.

$$\text{Now, } G_{o_III} = G_{III} \frac{\sqrt{1 + \left(\frac{\omega_{c_III}}{\omega_{p1_III}}\right)^2} \sqrt{1 + \left(\frac{\omega_{c_III}}{\omega_{p2_III}}\right)^2}}{\sqrt{1 + \left(\frac{\omega_{z1_III}}{\omega_{c_III}}\right)^2} \sqrt{1 + \left(\frac{\omega_{c_III}}{\omega_{z2_III}}\right)^2}} \quad (34)$$

G_{III} is an *assumed gain* at crossover frequency f_{c_III} .

$$\omega_{po_III} = G_{III} \cdot \omega_{z1_III} \frac{\sqrt{1 + \left(\frac{\omega_{c_III}}{\omega_{p1_III}}\right)^2} \sqrt{1 + \left(\frac{\omega_{c_III}}{\omega_{p2_III}}\right)^2}}{\sqrt{1 + \left(\frac{\omega_{z1_III}}{\omega_{c_III}}\right)^2} \sqrt{1 + \left(\frac{\omega_{c_III}}{\omega_{z2_III}}\right)^2}} \quad (35)$$

If double coincident poles/zeros pair has been considered, the formula becomes

$$\omega_{po_III} =$$

$$= G_{III} \frac{\omega_{z1,2_III} [\omega_{p1,2_III}^2 + \omega_{c_III}^2]}{\omega_{p1,2_III}^2 \sqrt{\left(\frac{\omega_{z1,2_III}}{\omega_{c_III}}\right)^2 + 1} \sqrt{\left(\frac{\omega_{c_III}}{\omega_{z1,2_III}}\right)^2 + 1}} \quad (36)$$

3.2.4. Design Example with a Type III

Let's assume a power supply that has a gain deficit of -10 dB at a 1 kHz selected crossover frequency. The necessary phase boost is 158° . From Eqn. (31) and Eqn. (32), the position of the double pole will be as follows:

$$f_{p1,2_III} = \tan\left(\frac{\text{boost}}{4} + \frac{\pi}{4}\right) f_{c_III} = \tan\left(\frac{158^\circ}{4} + 45^\circ\right) \times 1000$$

$$= 10.38 \text{ kHz} \quad (37)$$

The double zero is placed at

$$f_{z1,2_III} = f_{c_III} / \tan\left(\frac{\text{boost}}{4} + \frac{\pi}{4}\right) = 1000 / \tan\left(\frac{158^\circ}{4} + 45^\circ\right)$$

$$= 96.28 \text{ Hz} \quad (38)$$

The gain G at 1 kHz has chosen -10 dB. So the position of the 0-dB crossover pole at

$$f_{po_III} = G \frac{f_{z1_III} (f_{p1,2_III}^2 + f_{c_III}^2)}{f_{p1,2_III}^2 \sqrt{\left(\frac{f_{z1,2_III}}{f_{c_III}}\right)^2 + 1} \sqrt{\left(\frac{f_{c_III}}{f_{z1,2_III}}\right)^2 + 1}}$$

$$= 29.30 \text{ Hz} \quad (39)$$

So the transfer function of the designed Type-III controller is given by $\frac{3.003 \times 10^6 (s + 605)^2}{s(s^2 + 1.31 \times 10^5 s + 4.26 \times 10^9)}$.

4. PARTICLE SWARM OPTIMIZATION (PSO)

4.1 Overview

Particle Swarm Optimization (PSO) is an evolutionary algorithm (technique) that optimizes the continuous or discrete, linear or nonlinear, constrained or unconstrained, non differentiable functions by iteratively trying to improve the solutions for different parameter values (Dorf et al., 2011; Khare et al., 2013). The PSO is based on the behaviour of a colony of living things, *like* as swarm of insects, flock of birds, or school of fish. The insects, fishes, animals, especially birds *etc.* always travel in a group without crashing each other from their group members by adjusting their positions and velocities from using their group information. Because this method reduces individual effort for searching the food, shelter *etc.* Though particle swarm optimization (PSO) and genetic algorithm (GA) both are population based evolutionary techniques, PSO has better computational efficiency because it has been required less memory space, lesser speed of CPU and less number of parameters to adjust (Khare et al., 2013). But GA and other similar techniques (*like* simulated annealing *etc.*) only work with discrete variables, whereas PSO works with flexibly for discrete as well as continuous systems because it is inherently continuous, so D/A or A/D conversion has not been required (Khare et al., 2013).

4.2 Computational Implementation of PSO

Definition of Objective Function: The definition of *objective function* with typical *performance criteria* is the first step for designing the PSO based *Optimized Type-II/III Controllers* with desired specifications and constraints under input step signal. Some important output specifications in the time domain are *overshoot*, *rise time*, *settling time*, and *steady-state error*. Generally, there are four kinds of *performance criteria* (Dorf et al., 2011), such as the Integral Absolute Error (IAE), the Integral of Squared Error (ISE), the Integral of Time weighted Squared Error (ITSE), and the Integral of Time weighted Absolute Error (ITAE). Since ITAE performance criterion provides fastest response with small overshoot for a class of optimization techniques, so $\text{fit}_{ITAE}(t)$ is used in this simulation study and is represented by:

$$\text{fit}_{ITAE}(t) = \int_0^\tau t |e(t)| dt \quad (40)$$

where, the upper limit τ is chosen as steady-state value.

A concise idea about the PSO algorithm has been described here for a \bar{E} -dimensional search space with n_u particles. Consider the i^{th} particle and the particle can be expressed by a position vector : $S_i = (s_{i1}, s_{i2}, \dots, s_{i\bar{E}})$ and a velocity vector : $V_i = (v_{i1}, v_{i2}, \dots, v_{i\bar{E}})$.

The historical best value of position vector for the i^{th} particle can be described as $pbest_i = (p_{i1}, p_{i2}, \dots, p_{iE})$, and group best can be expressed as $gbest = (p_{g1}, p_{g2}, \dots, p_{gE})$.

The positive constants c_1 and c_2 are the individual (cognitive) and group (social) learning rates, respectively, and r_1 and r_2 are uniformly distributed random numbers in the range $[0, 1]$. The parameters c_1 and c_2 denote the relative importance of the memory (position) of the particle itself to the memory (position) of the swarm. The values of c_1 and c_2 are usually assumed to be 2 so that $c_1 r_1$ and $c_2 r_2$ ensure that the particles would overfly the target about half the time. The inertia weight constant w has to be chosen carefully for obtaining the optimum result with fast convergence and l denotes the iteration number.

The basic steps of the PSO algorithm are as follows:

Step 1: Initialize the particles of n_u population.

Step 2: Compute the error fitness value for the current position S_i of each particle.

Step 3: Each particle can remember its best position ($pbest$) which is known as cognitive information and that would be updated with each iteration.

Step 4: Each particle can also remember the best position the swarm has ever attained ($gbest$) and is called social information and the value would be updated in each iteration.

Step 5: Velocity and position vector of each particle are modified according to (41) and (42), respectively.

$$V_i^{(l+1)} = wV_i^{(l)} + c_1 r_1 [pbest_i^{(l)} - S_i^{(l)}] + c_2 r_2 [gbest^{(l)} - S_i^{(l)}] \quad (41)$$

$$S_i^{(l+1)} = S_i^{(l)} + V_i^{(l+1)} \quad (42)$$

Step 6: The iteration stops when maximum number of cycles is reached and the desired solution can be found for the corresponding particle. Otherwise the iterative process repeats.

4.3 Optimization Specifications

The parameters of the Type-II and Type-III controllers are to be optimized using PSO based optimization technique. There are actually four parameters for Type-II controllers, but for optimization three parameters are considered, namely DC gain, one zero and one pole. Similarly for Type-III controller for optimization one DC gain, one pair of zeros and one pair of poles have been considered. In both the cases the pole at origin has not been considered because of fixed location. The flowchart of the optimization process is given in Fig. 5. The routine for Particle Swarm Optimization (PSO) has been written in MATLAB (version R2011a). A swarm of 50 particles characterized by three parameters has been initialized. The controller parameters have been initialized and the values are constrained within a range. Optimized result has been obtained after 100 iterations beyond which significant improvement has not been observed. The values for the PSO parameters are given in Table 2.

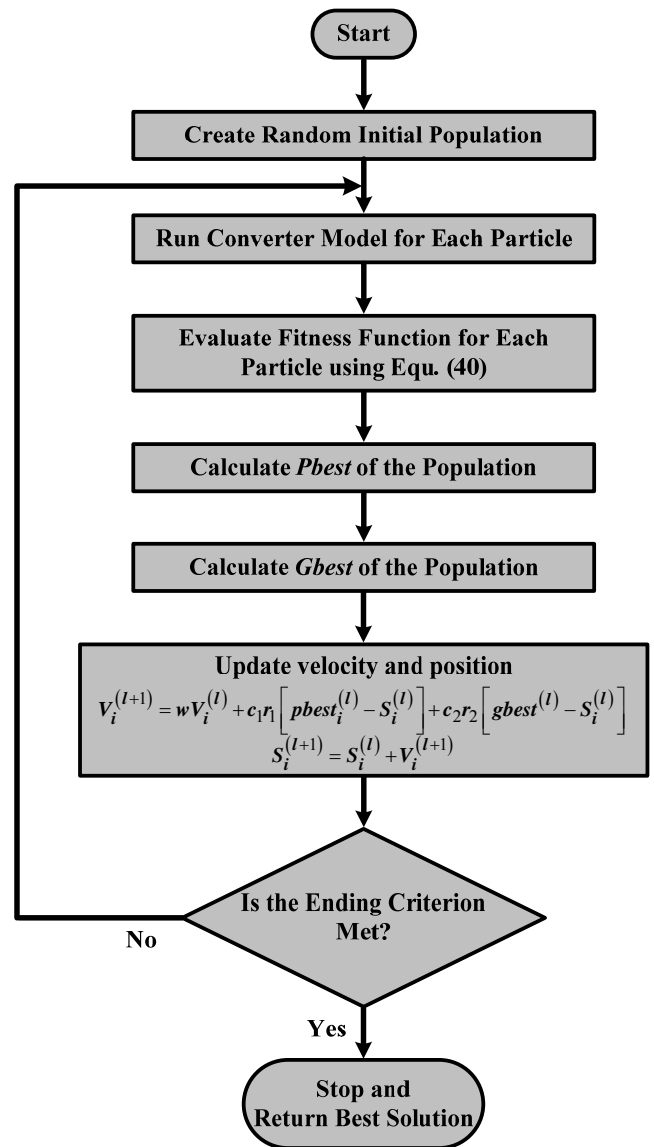


Fig. 4. Flowchart of the Particle Swarm Optimization process.

Table 2. Parameters of PSO Method.

Sl. No.	Parameter	Value
1.	Inertia Weight Constant (w)	0.73
2.	Cognitive Constant (c_1)	1.44495
3.	Group Constant (c_2)	1.44495
4.	Number of Particles (n_u)	50
5.	Number of Iteration (l)	100

5. GRAVITATIONAL SEARCH ALGORITHM (GSA)

5.1 Overview

Gravitational Search Algorithm (GSA), a new optimization algorithm, is based on the law of gravity (Rashedi et al., 2009; Sabri et al., 2013). In this computing technique, the particles are considered as objects and their performance is measured by

their masses. All these objects attract each other by the gravity force, and this force causes a global movement of all objects. Hence, masses cooperate using a direct form of communication, through gravitational force. The heavy masses (which correspond to good solutions) move more slowly than lighter ones. This guarantees the exploitation step of the algorithm. Three kinds of masses are defined in theoretical physics: (a) Active gravitational mass (M_a) is a measure of the strength of the gravitational field due to a particular object, (b) Passive gravitational mass (M_p) is a measure of the strength of an object's interaction with the gravitational field, and (c) Inertial mass (M_i) is a measure of an object's resistance to changing its state of motion when a force is applied (Rashedi et al., 2009; Sarkar et al., 2013). An object with small inertial mass changes it rapidly.

In GSA, each mass (particle) has four specifications: position, internal mass, active gravitational mass, and passive gravitational mass. The position of mass corresponds to a solution of problem, and its gravitational and inertial masses are determined using a fitness function. In other words, each mass presents a solution, and the algorithm is navigated by properly adjusting the gravitational and inertia masses.

The GSA could be considered as an isolated system of masses. It is like a small artificial world of masses obeying the Newtonian laws of gravitation and motion. More precisely, masses obey the following laws:

a). *Law of gravity*: Every particle in the universe attracts every other particle and the gravitational force between two particles is directly to the product of their masses and inversely proportional to the square of the distance (R) between them. Rashedi *et al.* used R instead of R^2 because R offered better results than R^2 in all their experimental cases with benchmark functions. Using single exponent instead of double exponent for R causes the departure of the present GSA from exact Newtonian Law of gravitation.

b). *Law of motion*: The current velocity of any mass is equal to the sum of the fraction of its previous velocity and the variation in the velocity. Variation in velocity or acceleration of any mass is equal to the force acted on the system divided by the mass of inertia.

5.2 Computational Implementation of GSA

Let, the position of the q^{th} particle (masses) among the n_p total number of particle vectors (population) can be explained by:

$$Z_q = (Z_q^1, Z_q^2, Z_q^3, \dots, Z_q^d, \dots, Z_q^n) \text{ for } q = 1, 2, \dots, n_p \quad (43)$$

where Z_q^d represents the position of q^{th} particle vector in the d^{th} dimension.

In our study each particle vector of the population n_p denotes three parameters or dimension for Type-II controller (Z_q^1 = controller gain, Z_q^2 = zero location, and Z_q^3 = pole location) and five parameters or dimension for Type-III controller (Z_q^1 = controller gain, Z_q^2 = 1st zero location, Z_q^3 = 2nd zero location, Z_q^4 = 1st pole location, and Z_q^5 = 2nd pole location).

At time ' t ' a gravitational force is acting on particle ' q ' from particle ' j ' can be written as Eqn. (44)

$$F_{qj}^d(t) = G(t) \frac{M_{pq}(t) \times M_{qj}(t)}{R_{qj}(t) + \varepsilon} (Z_j^d(t) - Z_q^d(t)) \quad (44)$$

where, $G(t)$ is gravitational constant at time t , M_{qj} is the active mass and M_{pq} is the passive mass related to the particles q and j . ε is a small constant, and $R_{qj}(t)$ is the Euclidian distance between two particles q and j .

$$R_{qj}(t) = \|Z_q(t) - Z_j(t)\|_2 \quad (45)$$

In other words, the gravitational constant $G(t)$ is a function of the initial value (G_0) and iteration time t :

$$G(t) = G_0 e^{-\alpha \left(\frac{t}{t_{\max}} \right)} \quad (46)$$

where t_{\max} is the maximum iteration. α is positive constant.

In this algorithm, it is assumed that the total force on particle q , F_q^d is the sum of randomly weighted the force components F_{qj}^d from other particles at time t in a dimension d :

$$F_q^d(t) = \sum_{j=1, j \neq q}^{n_p} rand_j F_{qj}^d(t) \quad (47)$$

where $rand_j$ is a random number in the interval $[0, 1]$.

The technique is used to perform a good compromise between exploration and exploitation is to decrease the number of agents with lapse of iteration number in Eqn. (47). Therefore, only a set of agents with higher masses apply their forces to others but it may be because the exploration power and increase the exploration capability. To control exploration and exploitation, only $Kbest$ agents will attract each other. $Kbest$ is the function of iteration cycle number. $Kbest$ is computed in such a manner that it decreases linearly with time and at last iteration the value of $Kbest$ becomes 2 % of the initial number of agents. Now, the modified force equation becomes

$$F_q^d(t) = \sum_{j=Kbest, j \neq q}^{n_p} rand_j F_{qj}^d(t) \quad (48)$$

According to the law of motion, the acceleration of q^{th} particle at d^{th} dimension,

$$a_q^d(t) = \frac{F_q^d(t)}{M_{qq}(t)} \quad (49)$$

where M_{qq} is the inertial mass of q^{th} particle.

The velocity (\hat{h}) and position updating formulae are given below:

$$\hat{h}_q^d(t+1) = rand_q \times \hat{h}_q^d(t) + a_q^d(t) \quad (50)$$

$$Z_q^d(t+1) = Z_q^d(t) + \hat{h}_q^d(t+1) \quad (51)$$

where $rand_q$ is a uniform random variable in the interval $[0, 1]$.

The Gravitational and inertia masses are simply calculated by using Eqn. (53) and (54).

$$M_{aq} = M_{pq} = M_{qq} = M_q, \quad \text{where } q = 1, 2, \dots, n_p. \quad (52)$$

$$\hat{m}_q(t) = \frac{fit_q(t) - worst(t)}{best(t) - worst(t)} \quad (53)$$

$$M_q(t) = \frac{\hat{m}_q(t)}{\sum_{j=1}^{n_p} \hat{m}_j(t)} \quad (54)$$

where $fit_q(t)$ represent the fitness value of the particle q at time t , and, $worst(t)$ and $best(t)$ are defined as follows :

$$best(t) = \min_{j \in \{1, 2, \dots, n_p\}} fit_j(t) \quad (55)$$

$$worst(t) = \max_{j \in \{1, 2, \dots, n_p\}} fit_j(t) \quad (56)$$

The flow chart of GSA has been given in Fig. 5.

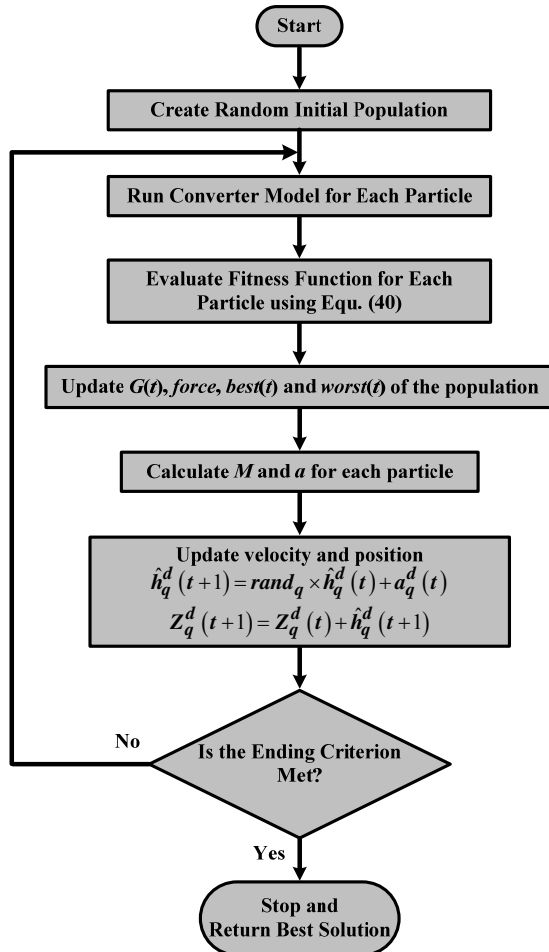


Fig. 5. Flowchart of the GSA optimization process.

5.3 Optimization Specifications

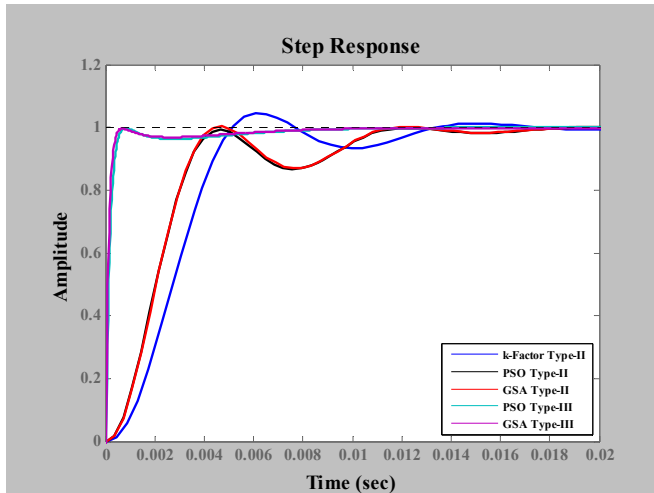
The parameters of the Type-II and Type-III controllers are to be optimized using GSA based optimization technique. There are actually four parameters for Type-II controllers, but for optimization three parameters are considered, namely DC gain, one zero and one pole. Similarly for Type-III controller for optimization one DC gain, one pair of zeros and one pair of poles have been considered. In both the cases the pole at origin has not been considered because of fixed location. The flowchart of the optimization process is given in Fig. 5. The routine for Gravitational Search Algorithm (GSA) has been written in MATLAB (version R2011a). The values for the GSA parameters are given in Table 3:

Table 3. Parameters of GSA method.

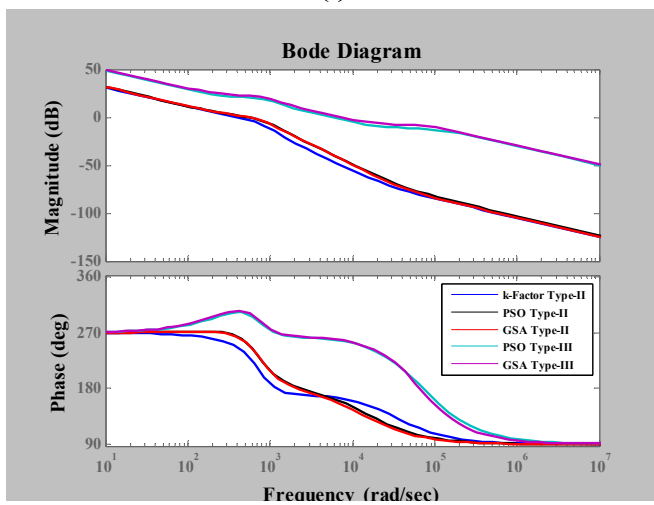
Sl. No.	Parameter	Value
1.	Constant (G_0)	3
2.	Constant (α)	2
3.	Number of Particles (n_p)	50
4.	Number of Iteration (t_{max})	100

6. SIMULATION RESULTS AND DISCUSSION

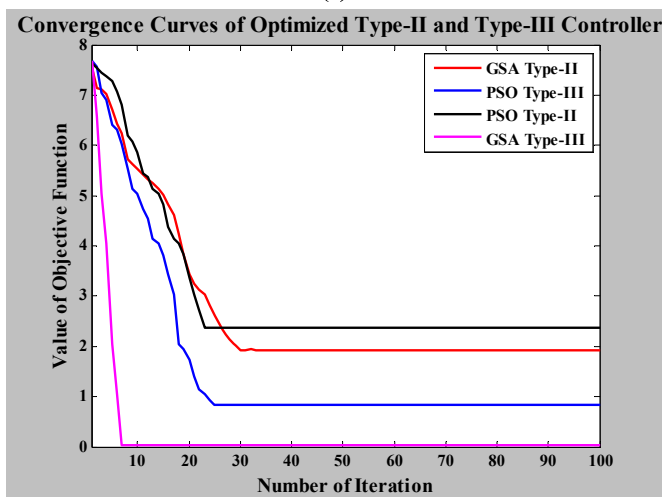
Extensive simulation has been carried out to determine the parameters of Type-II/Type-III controllers using classical and two different optimization techniques (PSO & GSA) so that the closed loop performance of the converter becomes satisfactory. The dynamic performances in terms of step & frequency response of the DC-DC boost converter with Type-II & Type-III controllers have been reported in Fig. 6(a) & (b) and corresponding specifications are given in Table IV (ref in Appendix). It is clear that optimized Type-III controllers provide best dynamic response than other controllers. The time response with optimized Type-III controllers shows very fast response with no overshoot and zero steady-state error. It is to be mentioned here that the ' k -factor' approach is a standard method for design of Type controllers and in the present case it worked well for the closed loop Boost converter. But keeping in view the demand for very fast response of power supply, the controller parameters are further optimized using PSO and GSA method. In the frequency domain analysis it is observed that GSA based Type-III controller generates maximum phase margin (79.3°) and highest gain crossover frequency (7260 rad/sec). Due to have an edge in performance, GSA based technique is considered for practical application. Fig. 6 (c) shows the plot of minimum values of the objective function ($fit_{ITAE}(t)$) versus number of iterations for Type-II and Type-III controller. It is seen that the GSA based Type-III controller produces the least objective function ($fit_{ITAE}(t)$) value than other optimized Type-II and Type-III controllers.



(a)



(b)



(c)

Fig. 6. (a) Step responses (b) Bode Diagram of closed-loop performances of a boost converter for different Type-II controllers and (c) Convergence curves of objective function ($fit_{ITAE}(t)$) for optimized Type-II and Type-III controller.

7. EXPERIMENTAL RESULTS

The closed loop Boost converter has been implemented practically with the designed controllers utilizing dSPACE based real time system. The overall experimental setup of the system is shown in Fig.7. From the simulation results (Fig. 6), it is clear that for the given converter GSA based optimized Type-III controller exhibits best performance & '*k-factor*' based classical Type-II controller produces relatively worst result while comparing the closed loop performances with different control algorithms. Hence in the implementation part, the above two controllers have been adopted for the closed-loop control of the proposed Boost converter. Fig. 8 (a) & (b) show the dynamic responses of output voltage, coil-current & coil-voltage for the case of optimized GSA controller with positive and negative step change in load voltage respectively. It is clear that in both the cases the output voltage response exhibits faster response without producing any overshoot. The coil-current & coil-voltage dynamics also been observed. The coil current is measured by a current probe with a scale of 100 mV= 1A. The coil voltage appears equal to positive supply voltage during ON time of the switch and the difference between output voltage & input supply voltage comes across the coil during the OFF condition of the switch. As expected, there is overshooting in the output voltage response due to step change in load in case of '*k-factor*' approach (Fig. 8(c)).

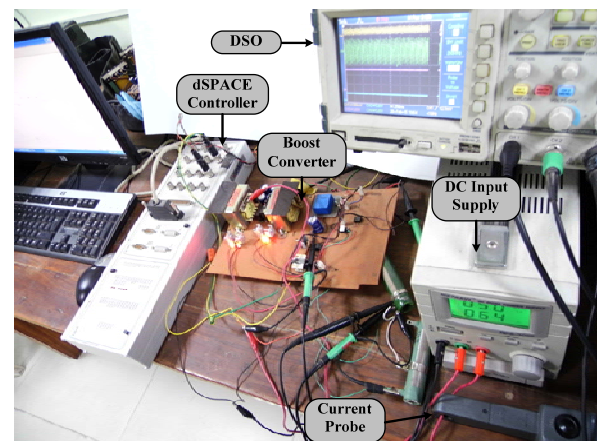
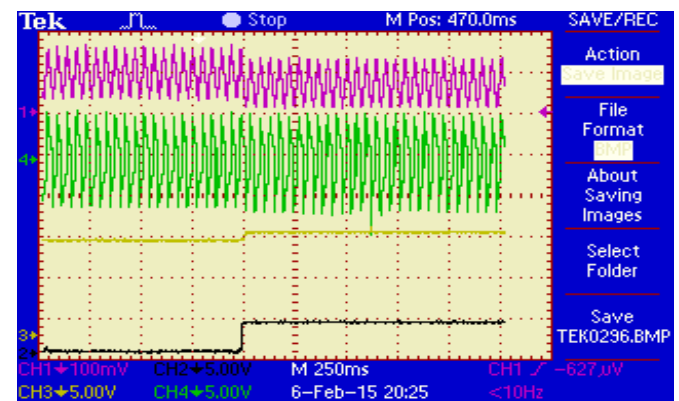


Fig. 7. Overall experimental setup.



(a)

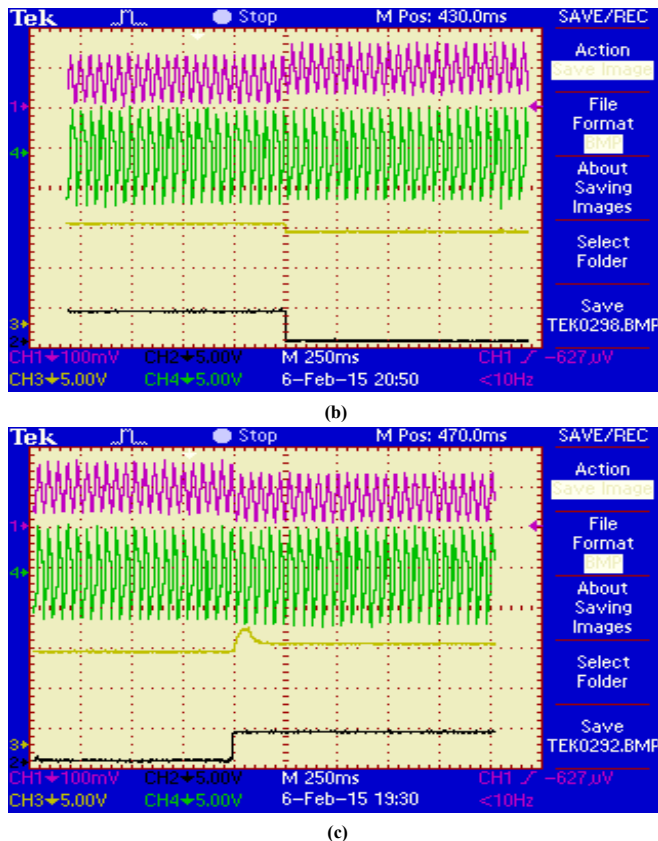


Fig. 8. Transient response with (a) positive step (b) negative step load disturbance with GSA Type-III controller and (c) Transient response with step load disturbance with 'k-factor' Type-II controller. [where Ch1: Inductor Current, Ch2: Load Disturbance, Ch3: Load Voltage and Ch4: Inductor Voltage]

8. CONCLUSIONS

In this work the closed loop performances and the comparative analysis for classical and optimized Type-II/III controllers for the Boost Converter have been studied both in simulation and experimentation. It may be concluded that the GSA based optimized Type-III controller exhibits the best closed-loop performance, highest system bandwidth and largest margin of stability. So GSA based optimized Type-III controllers may be used for the design and implementation of Switch Mode Power Boost converter to improve the overall closed loop stability and performance. The proposed control algorithm though applied for lower rated converter, but it may be applicable for higher rating also.

REFERENCES

- Abdul-Malek, M. A. and Abido, M. A. (2009). STATCOM based controller design using Particle Swarm Optimization for power system stability enhancement. *IEEE International Symposium on Industrial Electronics (ISIE 2009)*, 1218-1223.
- Al Rashidi, M.R. and El-Hawary, Mohamed E. (2009). A survey of particle swarm optimization applications in electric power systems. *IEEE Transactions on Evolutionary Computation*, 13 (4) 913-918.
- Altinoz, O. T. and Erdem, H. (2010). Evaluation function comparison of particle swarm optimization for buck converter. *IEEE International Symposium on Power Electronics Electrical Drives Automation and Motion (SPEEDAM)*, 798-802.
- Ang, S., and Oliva, A. (2005). *Power-switching converters*, CRC press.
- Beccuti, A. G., Papafotiou, G. and Morari, M. (2005). Optimal control of the boost DC-DC converter. *44th IEEE Conference on Decision and Control and European Control Conference (CDC-ECC'05)*, 4457-4462.
- Bryant, B. and Kazimierczuk, M. K. (2006). Voltage loop of boost PWM DC-DC converters with peak current-mode control. *Transactions on Circuits and Systems I: Fundamental Theory and Applications*, 53 (1) 99-105.
- Chung, I. Y., Liu, W., Schoder, K. and Cartes, D. A. (2011). Integration of a bi-directional dc-dc converter model into a real-time system simulation of a shipboard medium voltage dc system. *Electric Power Systems Research*, 81 (4), 1051-1059.
- Clerc, M. (2010). *Particle swarm optimization*, Vol. 93, John Wiley & Sons.
- David, R. C., Radac, M. B., Preitl, S., and Tar, J. K. (2009). Particle swarm optimization-based design of control systems with reduced sensitivity. *IEEE 5th International Symposium on Applied Computational Intelligence and Informatics (SACI'09)*, 491-496.
- Dean Venable, H. (1983). The k-factor: A New Mathematical Tool for Stability Analysis and Synthesis. *Proceedings of Powercon 10*, CA.
- Dorf, R. C., and Bishop, R. H. (2011). *Modern control systems*, Pearson.
- Duman, S., Maden, D., and Guvenc, U. (2011). Determination of the PID controller parameters for speed and position control of DC motor using gravitational search algorithm. *IEEE 7th International Conference on Electrical and Electronics Engineering (ELECO)*, 1-225.
- Eberhart, R. C. and Kennedy, J. (1995). A new optimizer using particle swarm theory. *Proceedings of the sixth international symposium on micro machine and human science*, vol.1, 39-43.
- Emami, S. A., Poudeh, M. B. and Eshtehardiha, S. (2008). Particle Swarm Optimization for improved performance of PID controller on Buck converter, *IEEE International Conference on Mechatronics and Automation (ICMA 2008)*, 520-524.
- Erickson, R. W., and Maksimovic, D. (2001). *Fundamentals of power electronics*, Springer.
- Escobar, G., Leyva-Ramos, J., Martinez, P. R., and Valdez, A.A. (2005). A repetitive-based controller for the boost converter to compensate the harmonic distortion of the output voltage. *IEEE Transactions on Control Systems Technology*, 13 (3) 500-508.
- Ghosh, A. and Banerjee, S. (2014). Design of Type-III Controller for DC-DC Switch-Mode Boost Converter. *6th IEEE Power India International Conference (PIICON-2014)*, pp. 1-6, 5th-7th December 2014, Delhi Technological University, New Delhi, India. (IEEE Xplore D.O.I. 10.1109/34084POWERI.2014.7117679)
- Ghosh, A. and Banerjee, S. (2015). Design and Implementation of Type-II Compensator in DC-DC Switch-Mode Step-up Power Supply. *3rd International*

- Conference on Computer, Communication, Control and Information Technology (C3IT-2015)*, pp. 1-5, 7th-8th February 2015 Academy of Technology, Hooghly, India. (IEEE Xplore D.O.I. 10.1109/C3IT.2015.7060164)
- Jalilvand, A., Kimiyaghalam, A., Ashouri, A. and Kord, H. (2011). Optimal tuning of PID controller parameters on a DC motor based on advanced particle swarm optimization algorithm. *International Journal on Technical and Physical Problems of Engineering, optimization*, 3 (4) 10-12.
- Kennedy, J. (2010). Particle swarm optimization. *Encyclopedia of Machine Learning* (Springer), 760-766.
- Khare, A., and Rangnekar, S. (2013). A review of particle swarm optimization and its applications in Solar Photovoltaic system. *Applied Soft Computing*, 13 (5), 2997-3006.
- Lee, S.W. (2014). Practical Feedback Loop Analysis for Voltage-Mode Boost Converter. *Application Report* (SLVA633), Texas Instruments.
- Liu, C. H. and Hsu, Y. Y. (2010). Design of a self-tuning PI controller for a STATCOM using particle swarm optimization. *IEEE Transactions on Industrial Electronics*, 57 (2), 702-715.
- Mohan, N., Undeland, T. M., and Robbins, W. P. (2003). *Power Electronics*, 3rd ed. Wiley, New York.
- Namnabat, M., Bayati Poodeh, M. and Eshtehardiha, S. (2007). Comparison the control methods in improvement the performance of the DC-DC converter, *IEEE 7th International Conference on Power Electronics (ICPE'07)*, 246-251.
- Ogata, K. (2010). *Modern Control Engineering*, Pearson Education, India.
- Poodeh, M. B., Eshtehardiha, S. and Namnabat, M. (2007). Optimized state controller on DC-DC converter. *IEEE 7th International Conference on Power Electronics (ICPE'07)*, 153-158.
- Rashedi, E., Nezamabadi-Pour, H. and Saryazdi, S. (2009). GSA: a gravitational search algorithm. *Information sciences*, 179 (13), 2232-2248.
- Rashid, M. H. (2014). *Power Electronics – Devices, Circuits and Applications*, Pearson.
- Reatti, A. and Kazimierczuk, M. K. (2003). Small-signal model of PWM converters for discontinuous conduction mode and its application for boost converter. *IEEE Transactions on Circuits and Systems I: Fundamental Theory and Applications*, 50 (1) 65-73.
- Sabri, N. M., Puteh, M., and Mahmood, M. R. (2013). A review of gravitational search algorithm. *International Journal of Advance. Soft Comput*, 5 (3).
- Sarkar, M.K., Banerjee, S., Saha, T. K., and Ghoshal, S. P. (2013). Implementation of GSA based optimal lead-lead controller for stabilization and performance enhancement of a DC electromagnetic levitation system. *Journal of Control Engineering and Applied Informatics*, 15 (3), 11-20.
- Siano, P., and Citro, C. (2014). Designing fuzzy logic controllers for DC-DC converters using multi-objective particle swarm optimization. *Electric Power Systems Research*, 112, 74-83.
- Tehrani, K. A., Amirahmadi, A., Rafiei, S. M. R., Griva, G. Barrandon, L., Hamzaoui, M., Rasoanarivo, I., and Sargos, F. M. (2010). Design of fractional order PID controller for boost converter based on multi-objective optimization. *14th International Power Electronics and Motion Control Conference (EPE/PEMC)*, T3-179.
- Veerachary, M. (2012). *Control of Power Electronic Systems – Digital Solutions*, India.
- Yousefi, M. R., Emami, S. A., Eshtehardiha, S. and Bayati Poodeh, M. (2008). Particle swarm optimization and genetic algorithm to optimizing the pole placement controller on Cuk converter, *IEEE 2nd International Power and Energy Conference (PECon 2008)*, 1461-1465.

APPENDIX.

Table 4. Comparative Study of Closed-loop Performances

PARAMETER	TYPE-II (k-factor approach)	TYPE-II (PSO)	TYPE-II (GSA)	TYPE-III (PSO)	TYPE-III (GSA)
Maximum Overshoot (M_p)	4.52 %	0 %	0 %	0.047 %	0 %
Rise Time (t_r)	0.0050 sec	0.0047 sec	0.0043 sec	0.000273 sec	0.000245 sec
Settling Time (t_s)	0.0125 sec	0.0108 sec	0.0107 sec	0.000465 sec	0.000437 sec
Steady-State Error (E_{ss})	0	0	0	0	0
Phase Margin (PM)	67.4°	69.7°	70.9°	78°	79.3°
Gain Crossover Frequency (GCF)	391 rad/sec	567 rad/sec	544 rad/sec	6450 rad/sec	7260 rad/sec
Phase Crossover Frequency (PCF)	1210 rad/sec	2380 rad/sec	2380 rad/sec	72900 rad/sec	66500 rad/sec
Controller Gain (G_o)	1000	1243.1556	1014.0845	6.57×10^6	6.08×10^6
Controller Transfer Function (T_c)	$\frac{1000(s+1221.3)}{s(s+32324)}$	$\frac{1243.1556(s+540.9)}{s(s+16540)}$	$\frac{1014.0845(s+555.56)}{s(s+14084.50704)}$	$\frac{6.57 \times 10^6 (s+524.7)^2}{s(s+7.308 \times 10^4)^2}$	$\frac{6.08 \times 10^6 (s+500.1905)^2}{s(s^2+1.144 \times 10^5 s+4.44 \times 10^9)}$
Closed-Loop Stability	Stable	Stable	Stable	Stable	Stable

Denovo Designing, Virtual Screening and Lead Optimization of Potential Drug Candidate for Herpes Disease

Monica Sharma^{1,2*}, Puneet Rawat² and Ankita Mehta²

¹Department of Biotechnology, School of Biosciences and Biotechnology, Babasaheb Bhimrao Ambedkar University, Vidya Vihar, Raebareli Road, Lucknow, Uttar Pradesh, India

²Department of Biotechnology, Delhi Technological University, Main Bawana Road, Shahbad Daulatpur, Delhi, India

Abstract

Herpes simplex virus (HSV1, HSV 2) is a neurotropic and neuroinvasive virus which becomes latent and causes a lifelong infection. HSV-1 and 2 produce infected cell protein (ICP)-47 against MHC class I antigen presentation pathway by inhibiting the transporter associated with antigen processing (TAP). ICP 47 is also responsible for evasive nature of HSV in human immune system. Currently available antiviral drugs and vaccines only slowdowns the infection but it does not cure the infection. In present study, we have *in silico* designed a potential drug candidate against HSV ICP-47 target through de-novo pathway using eLEA3D. The derived ligand docked with the natural viral receptor ICP-47 showed the binding affinity of -4.07, but it was found toxic in FAF DRUG online ADMET tool, due to presence of high risk imine group. Further manual optimization led to generation of many bioisosteres and final lead structure showed no toxicity and a high binding affinity of -7.53. Our designed lead can act as a potential therapeutic compound against HSV.

Keywords: HSV; ICP-47; eLEA3D; Denovo designing; Bioisosteres

Introduction

Herpes simplex viruses (HSV) 1 and 2, the members of herpes virus family Herpesviridae are ubiquitous, highly contagious agents which infect humans [1,2]. They cause cold sores, herpetic keratitis and genital herpes [3-5]. An estimated 400 million people worldwide are currently infected by HSV-2 and infection of HSV-1 is spreading to developed regions like USA, Western Europe, Australia and New Zealand [WHO Fact Sheet, 2015]. HSV-1 persists in the body in dormant state by escaping the immune system and results in sporadic viral reactivation [6].

HSV evades the immune system by interfering with MHC Class I antigen presentation on the cell surface. Infected cell protein (ICP) 47 caused major histocompatibility complex (MHC) class I proteins retention in the endoplasmic reticulum (ER). MHC presents the antigen to CD⁺8 T cells that are inhibited after expression of ICP 47 in the cell [7]. ICP 47 blocks peptide (viral epitope) transport across the ER membrane by transporter associated with antigen processing (TAP) [8,9] so that MHC class I proteins remain in ER without peptides and cytotoxic T- lymphocytes activation can be stopped. This allows virus to reside for a protracted period in the host.

Due to serious threat to human population a proper treatment and cure of HSV is required. For last two decades HSV glycoprotein D, has been the predominant HSV vaccine candidate [10,11], but the outcome of clinical trials of the vaccine have been really disappointing [12]. Antiviral drugs (valacyclovir, acyclovir, famciclovir, etc.) used against HSV infection, inhibit DNA polymerases and slows down infection by reducing viral replication but does not cure the infection completely [13]. Inappropriate prescribing and wide spread uncontrolled use of antiviral drugs led to emergence of resistance in the viruses. Recently, it has been observed that natural serine protease inhibitor (serpins) like serpinantithrombin III (AT III) inhibit HSV infection during an entry event. Antithrombin III demonstrated a promising result at experimental levels but yet it is far from any therapeutic use [13,14].

Due to inaccessibility of any effective drug and vaccine there is therefore, an urgent need for an effective HSV vaccine or drug that

provides protection against infection and also thwart the virus entering a latent state [15]. Computer aided drug discovery design (CADD) has emerged as a way to significantly decrease compounds screening while retaining same level of lead compound discovery at the same time [16]. In the present manuscript we have designed lead compound by de-novo designing strategy and molecule having highest score was further optimized by virtual screening to increase its affinity to target and reduce toxicity by toxicological analysis by online ADMET profiling tools of FAF DRUG 20 online tool and ORISIS data warrior.

Methodology

Sequence retrieval

DNA sequence of ICP-47 of HSV-2 was retrieved from NCBI and it was blasted to human genomic and transcriptomic database. The structure of target protein ICP-47 was retrieved from rcsb.org in PDB (text) format (PDB I.D. 1QLO).

Denovo drug designing

After exhaustive literature survey and database searching, no ligand was found that bind to this target, so automated de-novo drug design strategy was adopted to get a hit molecule. eLEA3D program was used for denovo generation of ligand, which create new molecules by using a library of molecular fragments and by determining best combinations of molecular fragments that fit user-defined physicochemical properties

***Corresponding authors:** Monica Sharma, Department of Biotechnology, Delhi Technological University, Main Bawana Road, Shahbad Daulatpur, Delhi, India, Tel: +91-9717386785; E-mail: monashimla@gmail.com

Received September 26, 2015; **Accepted** October 17, 2015; **Published** October 24, 2015

Citation: Sharma M, Rawat P, Mehta A (2015) Denovo Designing, Virtual Screening and Lead Optimization of Potential Drug Candidate for Herpes Disease. J Microb Biochem Technol 7: 367-373. doi:10.4172/1948-5948.1000240

Copyright: © 2015 Sharma M, et al. This is an open-access article distributed under the terms of the Creative Commons Attribution License, which permits unrestricted use, distribution, and reproduction in any medium, provided the original author and source are credited.

(also called constraint function) [17]. For De-novo ligand design, PDB structure of the target protein is uploaded in the server. Binding site for the ligand is set around 17th residue (Valine) with the binding site radius of 10 angstrom. Weight in the final score and conformational search for the given ligand was set to one, also ionization of carboxylates, phosphates, and guanidiniums was allowed.

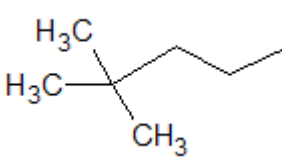
Autodocking and toxicity profiling

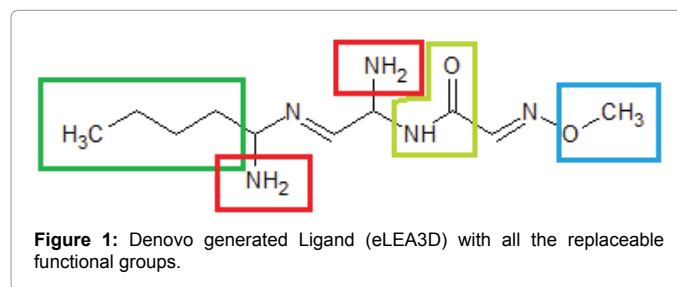
The resulting ligand was docked with natural viral receptor ICP-47 in Autodock4 [18] and toxicity profiling was done with FAF DRUG 2.0 online ADMET tool [19]. To increase its binding affinity and reduce toxicity we manually optimize the ligand by virtual combinatorial ligand optimization. The members of each class of substituent were numerated and combinatorially combined to create bioisosteres. Each functional group replacement was docked against the ICP-47 receptor taking other functional groups constant to check whether they are positively affecting the binding affinity and ADMET profile is also studied simultaneously. Threshold binding energy value is set to -4.11. All functional group possessing binding energy less than -4.11 were selected for further optimization by OVAT (One Variable at a time) method and progressive method.

Results

The blast search of the DNA sequence was performed to see whether ICP-47 of HSV showed any similarity with the human or not and it did not show significant similarity to any of the DNA/ protein sequence. Firstly, the available chemical databases were screening for their binding to the HSV ICP-47 (PDB I.D.-1QLO). No ligand was observed which had the binding affinity to target protein. Hence, automated de-novo drug design strategy was adopted to get a hit molecule.

eLEA3D (Ligand by Evolutionary Algorithm) programme was

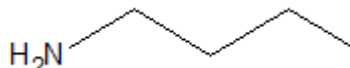
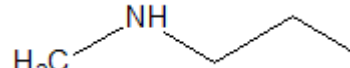
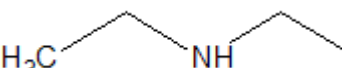




	NH ₂ replacement: On the C chain:	Binding Energy
1	HO—	-4.04
2	F—	-3.41
3	H ₃ C—	-4.19
4	HS—	-3.8
5	NH ₂ in the middle:	Binding Energy
6	HO—	-3.56
7	F—	-3.77
8	H ₃ C—	-3.94
9	HS—	-3.83
	—CH ₂ —CH ₂ —CH ₂ —CH ₃ chain replacement:	Binding Energy
10		-5.23



used for the de novo generation of the ligand was based on genetic algorithm that evolves the molecular structures generation after generation until the appearance of fitted molecules [17]. Each molecule of each generation is evaluated by fitness function (constraints) which is either molecular properties or an affinity prediction by a docking program. Submitting the query generated 10 structures of possible lead molecule along with their scores. The best structure had a maximum scoring percentage of 71.46% (Figure 1). Rest structures had the scoring percentage of 50 and hence only first result was chosen as a lead molecule for further steps.

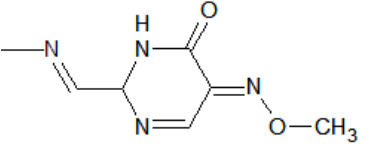
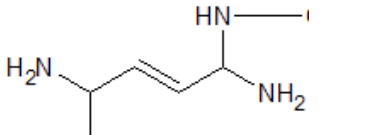
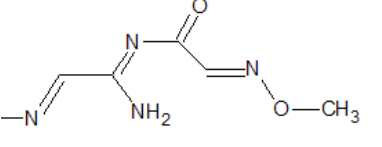
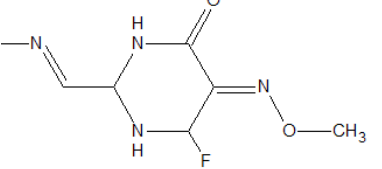
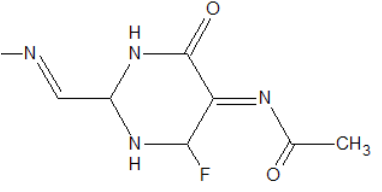
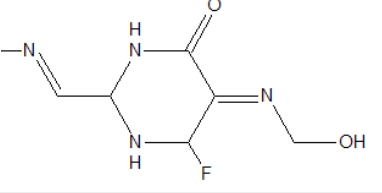
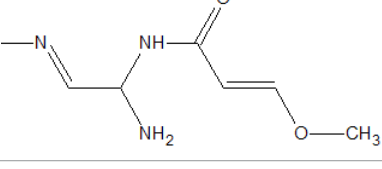
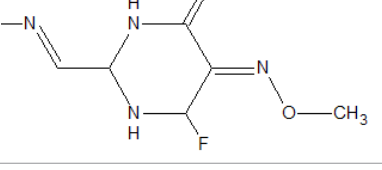
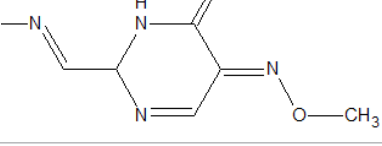
De-Novo designed lead molecule was further docked with ICP-47 and analyzed with FAF DRUG 2.0 ADMET tool. Lead molecule showed a binding affinity of -4.07 and a high risk of toxicity due to presence of imine group.

To increase binding affinity and reduce toxicity, lead compound was optimized manually by combinatorial optimization method. Due to small size of lead molecule it became possible to mark all replaceable functional groups and substitute with similar functional groups to create bioisosteres [20]. Each functional group replacement was docked with ICP-47. Out of total 57 replacements of functional groups,

11		-4.5
12		-3.3
13		-4.1
14		-3.8
15		-4.11
16		-2.84
17		-3.18

18		-3.25
19		-2.43
20		-3.02
21		-3.91
-C=O replacements:		
22		
	(Oxetane)	
23	A. Conformation 1 of oxetane	-3.1
24	B. Conformation 2 of oxetane	-3.28
25	C. Conformation 3 of oxetane	-3.94
26		-3.76
27		-3.7
28		-3.65
29		-3.43
30		-3.82
31		-4.1
32		-3.82

-O-CH₃ Replacement:		
33		-3.35
34		-3.81
35		-3.74
36		-3.08
37		-4.35
38		-4.31
39		-4.34
Replacement of the chain into cyclic compound and other replacements:		
40		-4.43
41		-4.33
42		-3.77

43		-3.41
44		-3.19
45		-3.12
46		-3.84
47		-4.04
48		-3.73
49		-3.07
50		-4.88
51		-4.89

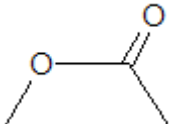
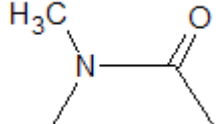
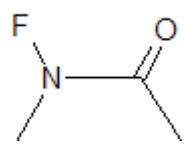

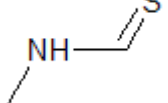
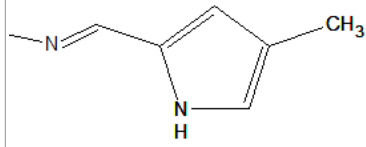
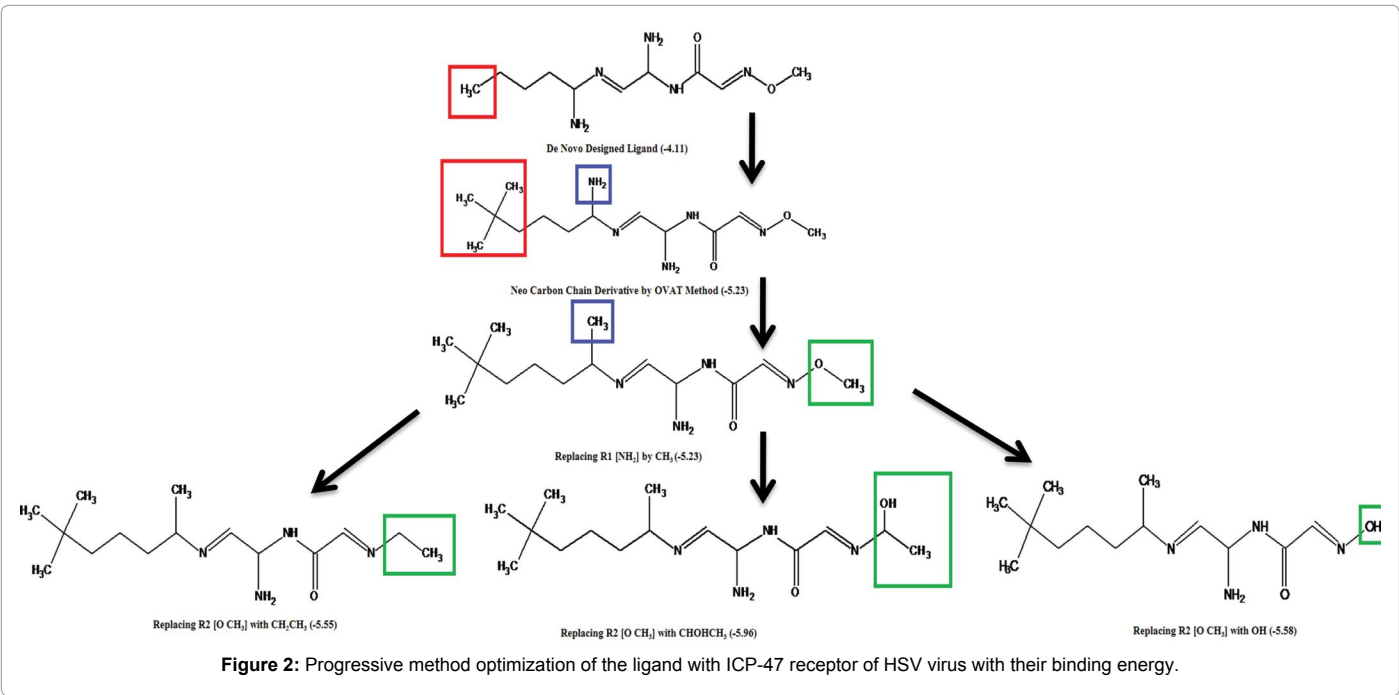
CONH ₂ Replacement:		
52		-2.71
53		-3.76
54		-4.26
55		-3.75
56		-3.06
57		-4.37

Table 1: All the functional group replacements of de-novo designed ligand and their binding affinity with ICP-47.

10 functional group were selected having better value than threshold of -4.11 (Table 1). NH₂ functional group has only one better replacement (-CH₃), so we replaced it in all further structural analysis, for the other 9 passed groups exhibiting binding energy > -4.11 (Figure 2), the OVAT method was utilized and docking with ICP-47 and ADMET profile was simultaneously studied (Table 2). Total 24 iterations were performed which showed promising results with top binding energy of -7.16, -6.6, -6.57 but toxicity still persisted (Table 3).

On analysis it is found that toxicity was being caused by the nitrogen ring replacement, so progressive method was used to generate structure excluding the ring replacements. This gave the best result of -5.96 but the toxicity was still there (Figure 2). To remove toxicity, N atoms of the ligand with the best binding energy (-7.16) were replaced by carbon one at a time and ADMET profiling was done by FAF DRUG 2.0 until any non-toxic ligand was generated. So it would be much close to natural biological compounds and toxicity of imine group and azo group can be removed.

It was further docked in Autodock 4 and finally a non-toxic lead molecule having binding energy of -7.53 (Figures 3 and 4) was obtained. The toxicity of the lead molecule is checked with FAF Drug 2.0 which categorized it non-toxic (Figure 5). Toxicity was also crosschecked with help of ORISIS data warrior which categorized final lead molecule as an irritant. The lead molecule is also checked for binding with any receptor



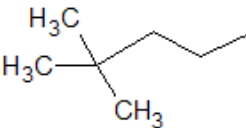
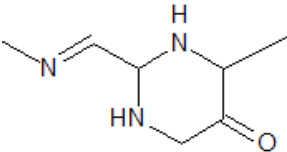

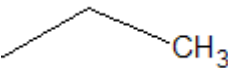
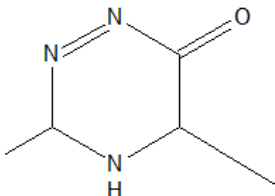
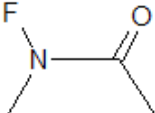
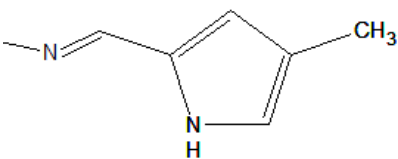
	C-C-C-C- chain (X)	O-CH ₃ replacement (Y)	CONH ₂ replacement (Z)
1.		H_3C-CH_3	
2.			
3.		$HO-$	
4.			

Table 2: All the passed functional group replacements for OVAT analysis.

S.No.	Combination of functional group	Binding energy	S. No.	Combination of functional group	Binding energy
1	X1Y1Z1	-5.82	1.	X2Y1Z1	-5.06
2	X1Y1Z2	-6.6 (2)	2.	X2Y1Z2	-5.52
3	X1Y1Z3	-5.66	3.	X2Y1Z3	-5.15
4	X1Y1Z4	-5.97	4.	X2Y1Z4	-5.07
5	X1Y1Z5	-5.56	5.	X2Y1Z5	-4.89
6	X1Y1Z6	-5.72	6.	X2Y1Z6	-4.92
1	X1Y2Z1	-6.1	1.	X2Y2Z1	-5.7
2	X1Y2Z2	-7.16 (1)	2.	X2Y2Z2	-6.06
3	X1Y2Z3	-6.38	3.	X2Y2Z3	-5.53
4	X1Y2Z4	-6.57 (3)	4.	X2Y2Z4	-5.81
5	X1Y2Z5	-6.36	5.	X2Y2Z5	-4.95
6	X1Y2Z6	-5.8	6.	X2Y2Z6	-5.12
1	X1Y3Z1	-6.49 (5)	1.	X2Y2Z1	-5.69
2	X1Y3Z2	-6.57 (4)	2.	X2Y2Z2	-5.68
3	X1Y3Z3	-5.96	3.	X2Y2Z3	-5.15
4	X1Y3Z4	-6.28	4.	X2Y2Z4	-5.35
5	X1Y3Z5	-5.74	5.	X2Y2Z5	-5.07
6	X1Y3Z6	-5.78	6.	X2Y2Z6	-4.81

Table 3: Binding affinity of the iterations made from the table 2 with ICP-47 receptor (by OVAT method).

present in human or other organism with pharmmapper server [21]. It showed some significant binding with them. Some top results of binding were retinoic acid receptor (PDB ID- 3DZY), Medium-chain specific acyl-CoA dehydrogenase, mitochondrial (PDB ID- 3MDE) and Glutathione S-transferase A1 (PDB ID- 1PL1) with binding energy of -6.39, -5.99, -7.58, respectively.

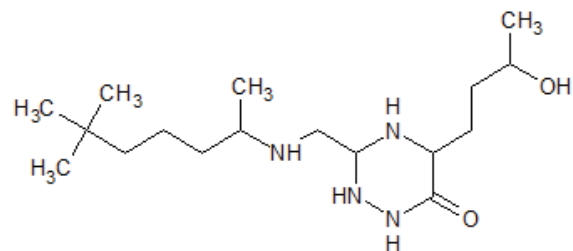


Figure 3: Structure of the ligand with no toxicity and binding energy of -7.53.

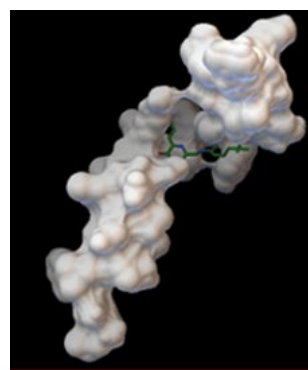


Figure 4: AUTODOCK4 results of binding of the potential drug candidate with ICP-47 receptor of Herpes virus.

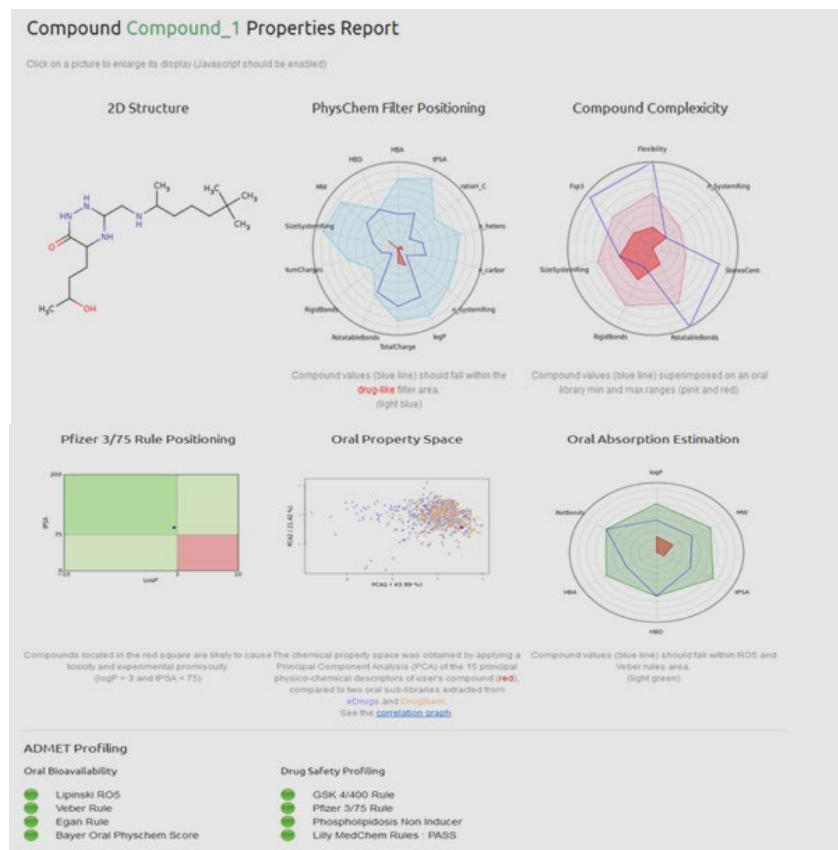


Figure 5: FAF DRUG 2.0 result of potential drug candidate.

Discussion

In recent years computer-aided drug design (CADD) approaches have revolutionized the field pharmaceutical research and many powerful standalone tools for CADD were developed, e.g., e-LEA3D, i Drug, iSMART etc. [17,22,23]. In these web servers many techniques were combined (pharmacophore mapping, similarity calculation, scoring, and target identification) to create a web interface which was more consistent and user friendly. Hartenfeller and Schneider have also emphasized that novel biologically active drug like lead molecules can be generated computationally on the basis of rule based fragment assembly [24]. Our initial hit molecule was also generated by fragment assembly method of e-LEA3D. Villoutreix et al. also generated a non enzymatic tyrosine kinase inhibitors lead by virtual screening and its ADMET profiling was done with FAF Drug 2.0. These lead molecules can be used to discover potential Anti-Allergic drugs [25]. Similarly rational drug designing was used to generate many drug like molecules e.g. cimetidine (prototypical H₂-receptor antagonist) [26], enfuvirtide [27], nonbenzodiazepines [28] and raltegravir [29].

Conclusion

The lead molecule generated by the procedure can be checked for its chemical synthesizability and can be checked for its in vivo ADMET profiling in clinical trials. Its binding with other receptors can be further analysed to access its pharmaceutical potential in other diseases. Denovo drug design and virtual lead optimization and in vitro screening can further lead to decrease the timeline of any drug development and hence holds true potential in modern pharmacology and rational drug design.

References

- Roizman B, Pellett PE (2001) The Family Herpesviridae: A Brief Introduction. In: Knipe DM, Howley PM, Fields Virology (4th edn) Lippincott, Williams and Wilkins, Philadelphia.
- Schiffer JT, Mayer BT, Fong Y, Swan DA, Wald A (2014) Herpes simplex virus-2 transmission probability estimates based on quantity of viral shedding. J R Soc Interface 11: 20140160.
- Kaye S, Choudhary A (2006) Herpes simplex keratitis. Prog Retin Eye Res 25: 355-380.
- Holdeman NR (2005) Herpes simplex virus: ocular manifestations; in Ocular therapeutics handbook: A clinical manual (2nd edn) Lippincott Williams & Wilkins, Philadelphia.
- Choudhary A, Higgins G, Kaye SB (2008) Herpes simplex keratitis and related syndromes; in Cornea and external eye disease. Springer.
- Hunsperger EA, Wilcox CL (2003) Capsaicin-induced reactivation of latent herpes simplex virus type 1 in sensory neurons in culture. J Gen Virol 84: 1071-1078.
- York IA, Roop C, Andrews DW, Riddell SR, Graham FL, et al. (1994) A cytosolic herpes simplex virus protein inhibits antigen presentation to CD8+ T lymphocytes. Cell 77: 525-535.
- Früh K, Ahn K, Djaballah H, Sempé P, van Endert PM, et al. (1995) A viral inhibitor of peptide transporters for antigen presentation. Nature 375: 415-418.
- Hill A, Jugovic P, York I, Russ G, Bennink J, et al. (1995) Herpes simplex virus turns off the TAP to evade host immunity. Nature 375: 411-415.
- Shin H, Iwasaki A (2013) Generating protective immunity against genital herpes. Trends Immunol 34: 487-494.
- Awasthi S, Friedman HM (2014) Status of prophylactic and therapeutic genital herpes vaccines. Curr Opin Virol 6: 6-12.
- Belshe RB, Leone PA, Bernstein DI, Wald A, Levin MJ, et al. (2012) Efficacy results of a trial of a herpes simplex vaccine. N Engl J Med 366: 34-43.
- Knight DA, Hejmanowski AQ, Dierksheide JE, Williams JW, Chong AS, et al. (2001) Inhibition of herpes simplex virus type 1 by the experimental immunosuppressive agent leflunomide. Transplantation 71: 170-174.
- Whitney JB, Asmal M, Geiben-Lynn R (2011) Serpin induced antiviral activity of prostaglandin synthetase-2 against HIV-1 replication. PLoS One 6: e18589.
- Bolland S, Pierce SK (2015) Ups and downs in the search for a Herpes simplex virus vaccine. Elife 4.
- Sliwoski G, Kothiwale S, Meiler J, Lowe EW Jr (2013) Computational methods in drug discovery. Pharmacol Rev 66: 334-395.
- Douguet D (2010) e-LEA3D: a computational-aided drug design web server. Nucleic Acids Res 38: W615-621.
- Morris GM, Huey R, Lindstrom W, Sanner MF, Belew RK, et al. (2009) AutoDock4 and AutoDockTools4: Automated docking with selective receptor flexibility. J Comput Chem 30: 2785-2791.
- Lagorce D, Sperandio O, Galons H, Miteva MA, Villoutreix BO (2008) FAF-Drugs2: free ADME/tox filtering tool to assist drug discovery and chemical biology projects. BMC Bioinformatics 9: 396.
- Yuya Morita (2012) Application of bioisosteres in drug design. Literature Seminar 5: 7.
- Meanwell NA (2011) Synopsis of some recent tactical application of bioisosteres in drug design. J Med Chem 54: 2529-2591.
- Thomas Sander, Joel Freyss, Modest von Korff, Christian Rufener, DataWarrior (2015) An open-source program for chemistry aware data visualization and analysis. J Chem Inf Model 55: 460-473.
- Wang X, Chen H, Yang F, Gong J, Li S, et al. (2014) iDrug: a web-accessible and interactive drug discovery and design platform. J Cheminform 6: 28.
- Chang KW, Tsai TY, Chen KC, Yang SC, Huang HJ, et al. (2011) iSMART: an integrated cloud computing web server for traditional Chinese medicine for online virtual screening, de novo evolution and drug design. J Biomol Struct Dyn 29: 243-250.
- Hartenfeller M, Schneider G (2011) De novo drug design. Methods Mol Biol 672: 299-323.
- Villoutreix BO, Laconde G, Lagorce D, Martineau P, Miteva MA, et al. (2011) Tyrosine kinase syk non-enzymatic inhibitors and potential anti-allergic drug-like compounds discovered by virtual and *in vitro* screening. PLoS One 6: e21117.
- Lipinski CA, LaMatta JL, Oates PJ (1986) Bioisosteric prototype design of biaryl imidazolyl and triazolyl competitive histamine H₂-receptor antagonists. J Med Chem 29: 2154-2163.
- Lalezari JP, Eron JJ, Carlson M, Cohen C, DeJesus E, et al. (2003) A phase II clinical study of the long-term safety and antiviral activity of enfuvirtide-based antiretroviral therapy. AIDS (London, England) 17: 691-698.
- Siriwardena AN, Qureshi Z, Gibson S, Collier S, Latham M (2006) GPs' attitudes to benzodiazepine and 'Z-drug' prescribing: a barrier to implementation of evidence and guidance on hypnotics. Br J Gen Pract 56: 964-967.

Citation: Sharma M, Rawat P, Mehta A (2015) Denovo Designing, Virtual Screening and Lead Optimization of Potential Drug Candidate for Herpes Disease. J Microb Biochem Technol 7: 367-373. doi:[10.4172/1948-5948.1000240](https://doi.org/10.4172/1948-5948.1000240)

OMICS International: Publication Benefits & Features

Unique features:

- Increased global visibility of articles through worldwide distribution and indexing
- Showcasing recent research output in a timely and updated manner
- Special issues on the current trends of scientific research

Special features:

- 700 Open Access Journals
- 50,000 editorial team
- Rapid review process
- Quality and quick editorial, review and publication processing
- Indexing at PubMed (partial), Scopus, EBSCO, Index Copernicus and Google Scholar etc
- Sharing Option: Social Networking Enabled
- Authors, Reviewers and Editors rewarded with online Scientific Credits
- Better discount for your subsequent articles

Submit your manuscript at: <http://www.editorialmanager.com/jmbt>

The International Daily Journal
ISSN 2278-69 EISSN 2278-50
© 2015 Discovery Publication. All Rights Reserved

Design and Analysis of a High Speed

Publication History

Received 28 August 2015
Accepted 20 September 2015
Published 9 October 2015

Citation

Simarpreet Singh Chawla, Swapnil Aggarwal, Anshu Ali, Siddhant Singh, and Anshu Singh. 2015. *Carry-Propagate*. In *Proceedings of the 42nd ACM SIGPLAN Conference on Programming Language Design and Implementation*, pages 1001–1011. ACM.

Design and Analysis of a High Speed Carry Select Adder

Simarpreet Singh Chawla, Swapnil Aggarwal, Anshika Nidhi Goel

Dept. of Electronics and Communication Engineering

Delhi Technological University (Formerly DCE)

chawla.simarpreet@gmail.com, swapnil.aggarwal.in@ieee.org, anshika.delhi89@gmail.com, nidhi.iitr@dce.ac.in

Abstract – An optimal high-speed and low-power VLSI architecture requires an efficient arithmetic processing unit that is optimized for speed and power consumption. Adders are one of the widely used in digital integrated circuit and system design. High speed adder is the necessary component in a data path, e.g. Microprocessors and a Digital signal processor. The present paper proposes a novel high-speed adder by combining the advantages of Carry Look Ahead Adder (CLAA) and Carry Select Adder (CSA), devising a hybrid CSA. In the proposed adder, CSA uses CLAA technology to generate the carry bits for each sum bit which are then used to select the respective multiplexer (MUX) which adds the carry bit to the sum accordingly. The proposed adder has been synthesized with bulk 40 nm standard CMOS library on Synopsys Design Compiler. Analysis has indicated the superiority of proposed adder over CLAA and CSA. As compared to CSA and CLAA, the proposed Carry Select Ahead Adder (CSAA) provides shorter average path and a simpler hardware. This has led to faster processing speed by increasing the complexity of circuit on the chip. The proposed adder finds its applications in various Arithmetic and Logic Units (ALU) of CPUs for faster arithmetic results.

Keywords – Carry Look Ahead Adder (CLAA), Carry Select Adder (CSA), Multiplexer (MUX), Carry Select Ahead Adder (CSAA), Arithmetic and Logic Unit (ALU).

I. INTRODUCTION

The latest rapid advancements in multimedia and communication systems, real time signal processing have led to an increase in the need for faster processing systems, that are able to perform complex calculations faster. Performance of large digital circuits is dependent on the speed of circuits that form various functional units.

One of the most essential units of such a functional unit is an ALU, which is a major component of the central processing unit (CPU) of a computer system. It performs all processes related to arithmetic and logic operations that need to be done on instruction words. With the increase in complexity of operations, the ALU also becomes more expensive, taking up more space in the CPU and dissipating more heat. This has augmented extensive effort to increase computation capabilities while reducing the complexity of ALU so as to ensure that the CPU is also powerful and fast enough.

Designing of high-speed and low-power VLSI architectures requires efficient arithmetic processing units that are optimized for the performance parameters, like speed and power consumption. Adders are the main component in general purpose microprocessors and digital signal processors. For adding two binary numbers there exists several adder structures based on very different design ideas. Thus if one

need to implement an addition circuit one must decide which circuit is most appropriate for its planned application.

Adders find application in many other functions such as subtraction, multiplication and division. Since addition is the base for all types of subtraction, multiplication, signal and image processing; design of an efficient adder circuit becomes necessary to realize an efficient system design. A simple, low power and area efficient addition/multiplication has always been a fundamental requirement of high performance processors and systems.

The two basic adders, i.e., Half Adder (HA) and Full Adder (FA) perform the addition of two and three bits respectively. The HA comprise of a **AND** gate, and an Exclusive OR gate. Full Adder (FA) performs the arithmetic sum of three bits. Three inputs involve two inputs plus an extra bit for an incoming carry. This is important for cascading adders together to create **N** adders. A full adder is made up of two HAs and an OR gate. Since for current applications, a two input or three input adders is not sufficient, many multiple bit adders has been proposed and consequently used as per the application requirement.

For addition of multiple bits, carry needs to be propagated from one bit position to the next bit position. The time required to propagate a carry through the adder determines the speed of addition [1]. Many different approaches have already been suggested to improve the performance of the adder. The simplest type of parallel adder to build is a ripple carry adder, which uses a chain of one bit full adder to generate its output. The Ripple Carry Adder (RCA) gives the most compact design, occupies small area but takes longer computation time. The delay of RCA is linearly proportional to number of input bits. For some input signals carry has to ripple all the way from least significant bit (LSB) to most significant bit (MSB). The propagation delay of such a circuit is defined as the worst case delay over all possible input patterns also called as critical path delay.

The time critical applications use Carry Lookahead scheme (CLAA) to derive fast results. In CLAA, for every single bit, sum and carry is independent of the previous bits. This eliminates the ripple effect making it faster than RCA but it also lead to increase in area. CLAA is fast for a design having less input bits, for higher number of bits it shows the worse delay [2]. Several modifications/improved versions have been proposed and implemented to further improve the performance of carry look ahead adders [3-7]. In contrast, a Carry Skip Adder (CSKA) uses a carry skip scheme to reduce the additional time taken to propagate the carry signal in RCA.

Thus, CSA is faster than RCA at the expense of a few simple modifications.

Another adder SCBCLA [8] which is a self-timed implementation of CAA adders based on the ϵ -section carry, has also been implemented via a semicustom ASIC design flow targeting a 130nm bulk CMOS standard cell library [9]. Unlike CLA, SCBCLA need not compute bit-wise lookahead carry signals for each and every addage. Instead SCBCLA produces the lookahead carry signal corresponding to a ϵ -section or ϵ -group of adder inputs. SCBCLA adder contains three constituent blocks: SCBCLA unit, full adder, and sum logic. Two different topologies of SCBCLA have been suggested based on the utilization of modules either solely or in conjunction with a ripple carry adder (RCA) section in the least significant adder stage.

To mitigate linear dependency of carry propagation delay, a Carry Select Adder (CSA) has been proposed that including parallelism by anticipating both possible values of the carry input i.e. 1 or 0 and evaluates the result in advance. The final sum and carry is chosen using multiplexers after the knowledge of real value of the carry. The carry bit of the preceding block of the adder acts as the select signal to the multiplexer. Though, the use of two adders and final selection multiplexers consumes more area, reduction in carry propagation delay is substantial. Thus CSA proves to be a compromise between RCA (small areas but longer delay) and CLAA (larger area with shorter delay) [10]. This has led to research in the field of CSA and varied versions of CSA have been proposed in the literature [11]-[15].

In contrast to CSA, a Carry Select Adder with Sharing (CSAS) has been proposed that uses of a fast incrementer circuit instead of adders to increment the interim sum when the input carry is obtained as logic 1 [16]. This performs each of the two additions in half of the clock cycle by using few latches. Iterative use of this concept can lead to efficient trade off of area for delay. More specifically, the delay of the proposed adder is $O(2n)$ while its area is $O((1/f)n)$, where $f < 1$.

To reduce area and power consumption with small speed penalty, a Modified Carry Select Adder (MCSA) design has also been proposed, that uses a single RCA and Binary to Excess-1 Converter (BEC) instead of using dual RCA [17]. Since BEC designing takes less number of logic gates than RCA design, reduction in area for MCSA and total power consumption is achieved.

The present paper proposes a novel parallel prefix adder that takes the advantage of both carry generating circuit of CLAA and multiplexing of CSA. The proposed CSA uses the MUXs which preselect the next four or more bits and their corresponding carry output. The proposed CSA decreases the time delay without the use of parallel multiplier circuits. A reduction in time delay has been achieved mainly due to relatively slow, which can be attributed to the fact that each full addition of four bits simultaneously instead of bit wise adder must wait for the carry bit to ripple from the previous addition. Analysis indicates that the performance of proposed full adder [18, 19]. CSA improves with increase in number of bits. Further, the performance improvement has been achieved without making any changes in the structure of conventional logic gates. The next section gives a brief overview of the three basic adders.

Section III presents the proposed adder and its result analysis. Finally, section IV concludes the proposed work.

II. PRELIMINARIES

In the simplest of operations, considering a Half Adder (HA), the output Sum is simply the XOR operation of the inputs and the output Carry (C_{out}) is the AND operation of the inputs. The more complex Full Adder (FA) also considers Carry bit (C_{in}) from the previous stage such as ALU, LU, etc., along with the two inputs. A FA is made up of two HAs. The output Sum of the first HA propagates as the input of the second HA, which receives its second input as the C_{in} from the previous stage. The resultant Sum is obtained from the Sum output of the second HA and the resultant C_{out} is obtained by performing OR operation on both the Carry outputs of the

Fig. 1. 4-bit Ripple Carry Adder [19]

It is possible to create a logical circuit using multiple 5-bit adders. Each full adder has a C_{in} input, which is the C_{out} of the previous adder. This kind of adder is called a ripple-carry adder (RCA), since each carry bit "ripples" or carries over to the next full adder. The layout of a RCA is simple, which allows for fast design time; however, RCA is

For reducing the computation time, engineers devised a faster way to add two binary numbers by using Carry Look Ahead Adder (CLAA). A CLAA improves speed by reducing the amount of time required to determine the carry bits. It can be contrasted with the simpler, but usually slower RCA for which the carry bit is calculated alongside the sum bit, and each bit must wait until the previous carry has been calculated to begin calculating its own result and carry bits respectively. The CLAA calculates one or more carry bits before the sum itself, which reduces the wait time to calculate the result of the larger value bits. CLAA is based on two principles

1. Calculating, for each position of the digit whether that position is going to propagate a carry if one comes in from the right.
2. Combining these calculated values to be able to deduce quickly whether, for each group of digits, that group is going to propagate a carry that comes in from the right.

Supposing that groups of 4 digits are chosen. Then the sequence of events goes something like this:

1. All 1-bit adders calculate their results. Simultaneously, the look-ahead units perform their calculations.
2. Suppose that a carry arises in a particular group. That carry will emerge at the left end of the group and start propagating through the group to its left.
3. If that carry is going to propagate all the way through the next group, the lookahead unit will

already have deduced this. Accordingly, the carry emerges from the next group's lookahead unit is immediately able to tell the next group to the left that it is going to receive a carry, and, at the same time, to tell the next lookahead unit to the left that a carry is on its way

Fig. 3. 16-bit Carry Select Adder [20]

The net effect is that the carries start by propagating slowly through each 4-bit group, just as in a RCA system, but then move 4 times as fast, leaping from one lookahead carry unit to the next. Finally, within each group that receives a carry, the carry propagates slowly within the digits in that group.

To determine whether a bit pair will generate a carry, the following logic works:

$$= \cdot$$

To determine whether a bit pair will propagate a carry, either of the following logic statements work:

$$= \cdot$$

Where A_i and B_i are the 4-bit inputs to the adder,

$$1 = 0 + 0 \cdot 0$$

$$2 = 1 + 1 \cdot 1$$

$$3 = 2 + 2 \cdot 2$$

$$4 = 3 + 3 \cdot 3$$

Substituting C_1 into C_2 , then C_2 into C_3 , then C_3 into C_4 yields the expanded equations:

$$1 = 0 + 0 \cdot 0$$

$$2 = 1 + 1 \cdot 0 + 0 \cdot 0 \cdot 1$$

$$3 = 2 + 2 \cdot 1 + 0 \cdot 1 \cdot 2 + 0 \cdot 0 \cdot 1 \cdot 2$$

$$4 = 3 + 3 \cdot 2 + 1 \cdot 2 \cdot 3 + 0 \cdot 1 \cdot 2 \cdot 3 + 0 \cdot 0 \cdot 1 \cdot 2 \cdot 3$$

A Carry Select Adder (CSA) is a particular way to implement an adder. CSA anticipates all possible values of input carry, i.e. 0 and 1 and evaluates the result in advance. Once the original value of carry is known, result can be selected using the multiplexer stage. Therefore the conventional CSA makes use of Dual RCAs to generate the partial sum and carry by considering input carry $C_{in} = 0$ and $C_{in} = 1$, then the final sum and carry are selected by multiplexers. The carry select adder generally consists of two RCAs and a MUX, and thus is area consuming due to the use of dual RCAs. Adding two bit numbers with a CSA is done in order to perform the calculation twice, one time with the assumption of the carry being 0 and the other assuming 1.

After the two results are calculated, the correct Sum, as well as the correct Cout, is then selected with the multiplexer once the correct carry is known. The basic building block of a CSA (4-bit) consists of two 4-bit RCAs that are multiplexed together, where the resulting Cout and Sum bits are selected by the Cin. Since one RCA assumes Cin of 0, and the other assumes a Cin of 1, select which adder had the correct assumption via the actual carry yields the desired result. A 16-bit CSA with a uniform block size of 4 can be created with 3 of these blocks and a 4-bit RCA. Since Cin is known at the beginning of computation, a carry select block is not needed for the first four bits [18, 19]. The next section explains the structure and the working of proposed CSA followed by its simulation and result analysis.

III. PROPOSED CSA

In the proposed CSA adder, several modifications have been done to decrease the computation time. In the present work, a novel architecture has been proposed that exploits the CLAA's ability to generate carry bits before computing the sum and the multiplexing ability of CSA. In a conventional adder where RCA is used in CSA, the multiplexer waits for RCA to compute the sum and propagate the carry to the next

Fig. 4. 16-bit Carry Select Ahead Adder (Modified CSA)

RCA. This renders the higher order RCAs inactive consequently leading to increase in computation time. The results for both versions of the adder, 16 bit and 32 bit have been compared taking the CSA as a standard. The following parameters of the circuit are ahead of the sum, so that all RCAs can function simultaneously and generate the sum.

- A) Area € Units: μm^2 (10^6 metre^2)
- B) Power € Units: mW (10^3 Watt)
- C) Timing € Units: ns (10^9 second)

The proposed adder is very similar to a traditional CSA, albeit different. Figure. 4 depicts the structure of proposed CSAA (say 16bit), where the operations are divided by taking 4-bits at a time. For a 16 bit addition using proposed adder, eight CLAA's and four CSA units are required, where each unit contains a 10:5 multiplexer. The initial carry bit in each CLAA is either connected to Vcc (+5V) or the ground, and each output carry is connected to the input of a 10:5 multiplexer, which then selects the required sum.

In the proposed CSA (say 16bit), the operations are divided by taking 4-bits at a time, the first 2 CLAA's are used for adding the first four bits $b[3:0]$, which only differ in the initial carry bit, i.e. 0 or 1, their sum and their output carry both selected by Cin using 10:5 Mux. The output carry C0 generated in the previous stage is similarly used for selecting the output carry and the sum of the addition of the next four bits $b[7:4]$. This same procedure takes place for both sets of bits $b[11:8]$ and $b[15:12]$ and the output carry of the $b[15:12]$ bits is the output carry (Cout) of the whole 16-bit High Speed CSA. Similarly, this same procedure can be extended for High Speed CSA or for the required number of bits.

A digital schematic for the proposed CSAA has been created using Verilog as the primary language on Xilinx Vivado Design Suite 2014.4. This has been indicated in Figure 7. The next section presents the simulation and results analysis of the proposed CSAA.

A. Result Analysis

A hardware/design schematic has been created for 16 bit and 32 bit variant of the proposed adder. The designed hardware in Verilog has been simulated using Synopsys Design Compiler. The technology used for the hardware was standard

Based on the three main performance parameters, viz., power, timing and area, a comparison analysis of the proposed adder has been done with CSA, RCA and CLAA. This has been quantitatively indicated in Table 1 and graphically depicted in Figure 5 and Figure 6. The comparison has been done for both 16-bit and 32-bit variants respectively. The result analysis clearly indicates the fast computation time achieved by proposed adder as compared to its conventional variants, CSA, CLAA and RCA.

TABLE 1: COMPARISON OF ADDERS FOR AREA, POWER AND TIMING

Word Size	Adder	Total Cell Area (μm^2)	Power (mW)	Timing (ns)
16-bit	RCA	68.947197	0.0215	1.98
	CLAA	81.421199	0.0307	1.91
	CSA	93.668399	0.0319	3.25
	Proposed CSAA	109.544398	0.0488	1.59
32-bit	RCA	137.894394	0.0436	3.92
	CLAA	163.069199	0.0621	3.93
	CSA	188.017198	0.0646	6.77
	Proposed CSAA	220.222796	0.0958	2.75

As is evident from Table 1, the High Speed CSA shows a 51.1% and a 59.4% increase in speed in the 16 and 32 bit variants w.r.t. the 16 and 32 bit variants of CSA respectively. This can be attributed to the advanced carry selection and multiplexing.

technology of the proposed CSA. Results indicate that the performance of the proposed adder improves with the increase

IV. CONCLUSION

Adders are a key component in general purpose

Fig. 5. Comparison of 16bit adders

Fig. 6. Comparison of 32bit Adders

microprocessor and digital signal processing applications. The present paper proposes a novel architecture of adder that combines CLA's ability to generate carry bits before computing the sum and the multiple ability of CSA to reduce the computation time. Hardware for the proposed adder has been created for both 16 and 32 bit variant of the adder. Thorough simulation and result analysis indicate the superiority of the proposed adder over conventional adders. Comparative analysis indicates that performance analysis improves with an increase in number of bits. The proposed adders finds its applications in the areas of real time audio, video and signal processing, where computation time is an important parameter of consideration.

V. REFERENCES

- [1] Sajesh Kumar U., Mohamed Salih K. K., Sajith K., „Design and Implementation of Carry Select Adder without Using Multiplexers..., 1st International Conference on Emerging Technology Trends in Electronics, Communication and Networking, 2012.
- [2] Behnam Amelifard, Farzan Fallah, Massoud Pedram, „Closing the Gap between Carry Select Adder and Ripple Carry Adder: A New Class of Low-power Highperformance Adders..., Proceedings of the Sixth International Symposium on Quality Electronics Design (ISQED), 2005.
- [3] G.A. Ruiz, „New static multibit carry look ahead CMOS adders,... IEEE Proc. Circuits, Devices and Systems, vol. 144, no. 6, pp.335-340, 1997.
- [4] J.B. Kuo, H.J. Liao, H.P. Chen, „A BiCMOS dynamic carry look ahead adder circuit for VLSI implementation of highspeed arithmetic unit,... IEEE J. of Solid State Circuits, vol. 28, no. 3, pp. 373-378, 1993.
- [5] G. Yang et al., „A 32bit carry look ahead adder using dual threshold logic,... IEEE Trans. on VLSI Systems, vol. 13, no. 8, pp.993-1002, 2005.
- [6] C.-C. Wang et al., „A low power highspeed 8bit pipelining CLA design using dual threshold voltage domino logic,... IEEE Trans. On VLSI Systems, vol. 16, no. 5, pp. 550-558, 2008.

in number of bits.

More importantly, it is worth noticing that with doubling the number of bits, i.e. from 16 to 32, there is an 8.3% increase in speed. This reflects better speed performance of the proposed CSAA with increase in number of bits. Though, with higher number of bits, the percentage increase in area of proposed CSAA is same as that of conventional CSA. The power reduces by 5.14%. This depicts improved power and area performance of proposed CSAA as compared to conventional CSA for higher number of bits.

Fig. 7. Digital Schematic of Proposed High Speed CSA

0010100100

- [7] R. Zlatanovici, S. Kao, B. Nikolic, „Energy delay optimization of 64bit carry-look ahead adders with a 240ps 90nm CMOS design example,... IEEE J. of Solid State Circuits, vol. 44, no. 2, pp. 5693, 2009.
- [8] K. Preethi, P. Balasubramanian, „FPGA Implementation of Synchronous Section Carry Based Carry Lookahead Adders..., 2nd International Conference on Devices, Circuits and Systems (ICDCS), 2014.
- [9] P. Balasubramanian, D.A. Edwards, W.B. Toms, „Serialized section carry based carry look ahead adders and the concept of alias logic,... Journal of Circuits, Systems and Computers, vol. 22, no. 1, pp. 13500281, 135002824, April 2013.
- [10] Y. Kim and L. S. Kim, „64bit carryselect adder with reduced area,... Electron. Lett., vol. 37, no. 10, pp. 6145, May 2001.
- [11] Tyagi, „A reduced area scheme for carryselect adders,... IEEE Trans. on Computer, IEEE Transactions on Computers, vol. 42, pp. 1163-1170, October 1993.
- [12] P. Balasubramanian, D.A. Edwards, W.B. Toms, „Serialized section carry based carry look ahead adders and the concept of alias logic,... Journal of Circuits, Systems and Computers, vol. 22, no. 1, pp. 13500281, 135002824, April 2013.
- [13] G. A. Ruiz, M. Granda, „An area efficient static CMOS carryselect adder based on a compact carry-look-ahead unit,... Microelectronics Journal, vol. 35, no. 12, pp. 933-944, 2004.
- [14] Y. He and C. H. Chang, „A Power-Delay Efficient Hybrid Carry Lookahead/Carry-Select Based Redundant Binary to Two's Complement Converter,... IEEE Trans. Circuits Syst. I, Reg. Papers, vol. 55, no. 1, pp. 336-346, Feb. 2008.
- [15] Neve, H. Schettler, T. Ludwig and D. Flandre, „Power-delay product minimization in highperformance 64bit carry-select adders, IEEE Trans. Very Large Scale Integration (VLSI) Systems, Reg. Papers, vol. 12, no. 3, pp. 235-244, March. 2004.
- [16] Samiappa Sakthikumar, S. Salivahanan, V. S. Kanchana Bhaaskaran, V. Kavinilavu, B. Brindha, C. Vinoth, „A Very Fast and Low Power Carry Select Adder Circuit..., 3rd International Conference on Electronics Computer Technology (ICECT), 2011.
- [17] Shivani Parmar, Kirat Pal Singh, „Design of high speed hybrid carry select adder..., 3rd International Advance Computing Conference (IACC), 2012.
- [18] Michael D. Ciletti, „Advanced Digital Design with the VERILOG HDL..., 2003.
- [19] Samir Palnitkar, „Verilog HDL..., 2nd ed., IEEE 1364-1 Compliant, 2003.
- [20] M. Morris Mano and Michael D. Ciletti, „Digital Design..., 4th ed



Contents lists available at ScienceDirect

Applied Surface Science

journal homepage: www.elsevier.com/locate/apsusc



Electron irradiation induced buckling, morphological transformation, and inverse Ostwald ripening in nanorod filled inside carbon nanotube

Anshika Singh^a, Reetu Kumari^a, Vinay Kumar^a, Lucky Krishnia^a, Zainab Naqvi^a,
Amrish K. Panwar^a, Umananda M. Bhatta^b, Arnab Ghosh^c, P.V. Satyam^c,
Pawan K. Tyagi^{a,*}

^a Department of Applied Physics, Delhi Technological University, Delhi, 110042

^b Centre for Emerging Technologies, Jain University, Jakkasandra, Kanakapura Taluk, Ramanagaram Dist, Karnataka, PIN 562 112, India

^c Institute of Physics, Sachivalaya Marg, Bhubaneswar 751005, India

ARTICLE INFO

Article history:

Received 7 September 2015

Received in revised form 7 November 2015

Accepted 10 November 2015

Available online xxx

Keywords:

Filled-carbon nanotube

Electron-irradiation

Nano-engineering

shape-alteration

In situ transmission electron microscopy

ABSTRACT

The present study aims to deduce the *in-situ* response of iron carbide (Fe_3C) nanorod filled inside carbon nanotube (CNT) under electron irradiation. Electron irradiation on Fe_3C filled-CNT at both high and room temperature (RT) has been performed inside transmission electron microscope. At high temperature (HT), it has been found that γ -Fe atoms in lattice of Fe_3C nanorod accumulate first and then form the cluster. These clusters follow the inverse Ostwald ripening whereas if e-irradiation is performed at RT then only the morphological changes in both carbon nanotube as well as nanorod are observed. Compression generated either by electron beam heating or by shrinkage of CNT walls is observed to be a decisive factor.

© 2015 Elsevier B.V. All rights reserved.

1. Introduction

The possibility of filling the carbon nanotube core with variety of substances has stimulated a large excitement and interest in various areas of nanotechnology such as: electro, photo and heterogeneous catalyst with high selectivity [1,2], magnetic data storage or magnetic resonance imaging [3] and nanotechnology in medicines [4–6]. This has been attributed to the fact that in filled-CNT, superior physical, chemical or electronic properties of host nanotube and filled-nanomaterials have been observed. In order to further expand the applications of filled-carbon nanotube, we need a simple technique which can modify CNT/metal interface as well as shape and position of the confined material as much as possible. In recent reports, electron irradiation performed inside transmission electron microscopy (TEM) demonstrated that it is feasible to control the shape and size of the CNTs as well as encapsulated metal by production of defect, at room [7,8] as well as high [9] temperatures. This evidenced that electron beam might be a tool which has

post-synthesis alteration capability on filled-CNTs [8,10–14]. This technique may further facilitate the reported applications of unfilled as well as fully/partially filled CNTs used as nanopipette [15], high pressure nanoextruder [16,17], diagnostic tool [18], preservative nanocell [18] and in light weight data cable [19].

Main focus of the presented work is not only to explore the practical aspects of material processing but also to study the fundamental aspects, in order to understand the electron-metal interaction in nanosize system. In past studies, irradiation-induced phenomena such as pressure build up inside CNT and carbon onions, if irradiated by both electrons and ions, have been demonstrated [16,20–22]. In these reports, high temperature has been observed to be an influencing factor. In 2007, Misra et al. performed ions (100 MeV Au^{7+}) irradiation on Ni-filled CNT and demonstrated that pressure was built up even at RT [23].

In this investigation, response of Fe_3C -filled multiwalled carbon nanotube (MWCNT) under electron irradiation at room and high temperature as well as structural related phenomena such as: shrinkage, thinning, bending and breaking of nanotube have been studied. In many cases irradiation induced changes were reported to be governed by annealing and diffusion of vacancies and interstitials [10]. In order to understand these phenomena, irradiation has specifically been performed at both room and high temperature.

* Corresponding author. Tel.: +91 8800977457.

E-mail addresses: pawantyagi@dce.edu, pawan.phy@dce.edu,
tyagi.pawan@yahoo.co.in (P.K. Tyagi).

<http://dx.doi.org/10.1016/j.apsusc.2015.11.110>

0169-4332/© 2015 Elsevier B.V. All rights reserved.

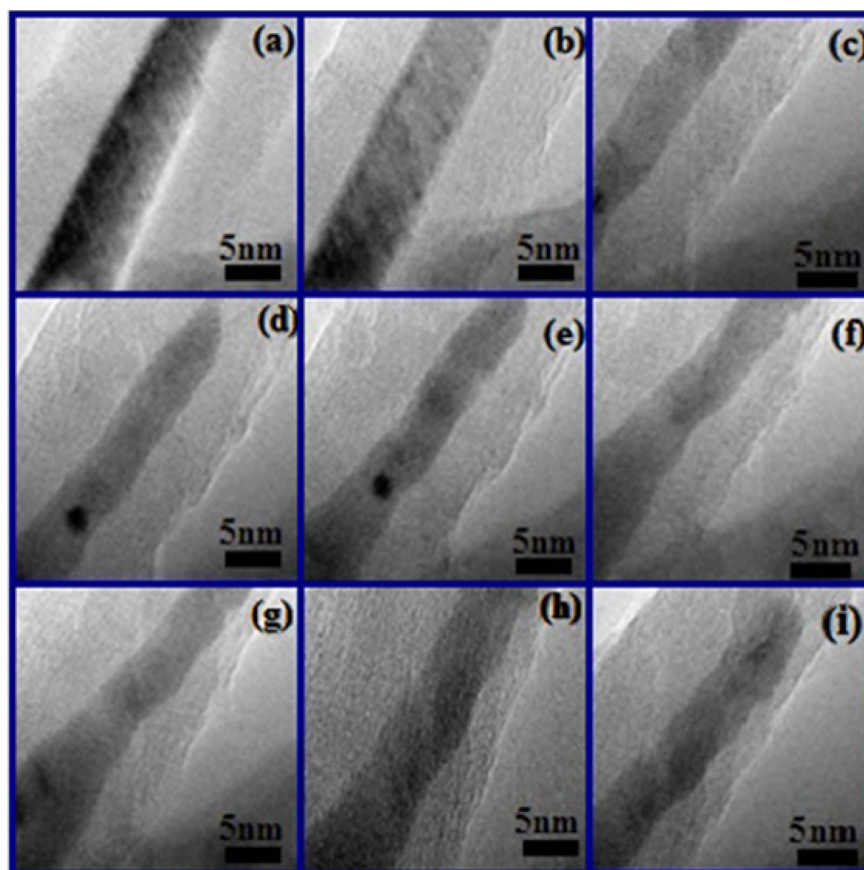


Fig. 1. TEM image of Fe_3C -filled CNT after electron irradiation at varying time intervals at RT: (a) 58 sec. (b) 1.20 min. (c) 14.00 min. (d) 15.44 min. (e) 16.56 min. (f) 21.09 min. (g) 22.25 min (h) 24.41 min. (i) 25.17 min.

2. Experimental

Filled-MWCNTs were grown by modified thermal chemical vapour deposition (Thermal CVD) technique as described previously [24]. The CNTs were found grown on the inner wall of the quartz tube. The as-grown CNTs were scratched from the tube and a very small amount of the sample was dispersed in isopropyl alcohol. After sonicating the dispersion for 10 min, one drop was casted onto uncoated copper grid of 1000 mesh for high resolution TEM imaging (JEOL JEM 2010 operated at 200 kV) for carrying out *in-situ* electron irradiation experiments and imaging. The grid was then transferred to the specimen holder for electron irradiation and microscopy measurement. Electron irradiation has been performed inside TEM operated at 200 kV and electron beam of energy 200 keV was used. A single tilt heating stage (GATAN 628UHR), equipped with tantalum furnace was used for *in-situ* heating. *In-situ* real-time measurements were carried out using a CCD camera (GATAN 832). Irradiation was carried out at current density of 100 to 300 A/cm².

3. Results and discussion

Fig. 1(a–i) shows typical low magnified bright field TEM images that were captured during the electron irradiation. The images demonstrate the morphological evolution of the MWCNT as well as nanorod. It was seen that as the electron irradiation proceed, CNT walls were gradually thinned and thickened side-selectively. This may be attributed to irradiation induced sideward sputtering of carbon atoms and subsequent re-depositing on rear-side through sideward surface diffusion [25]. As evident from Fig. 1(e)–(f), an

axial compression and expansion happened in the nanorod, particularly at thinner side of CNT. This produced a wave-like pattern along the tube axis. The periodicity and amplitude of the observed pattern decreased monotonically with the thickness or numbers of CNT wall.

Fig. 2(a) shows typical lattice image of the plane of a nanorod. The image shows that the nanorod was single crystalline with a lattice spacing of 0.208 ± 0.005 nm, which matches with d-spacing value of {121} plane of Fe_3C representing an orthorhombic structure (Pbnm space group)(PCPDF No: 89-2722) lattice constants; $a = 0.4523$ nm, $b = 0.5089$ nm and $c = 0.67428$ nm. No point defects, e.g. vacancy-interstitials, vacancy and interstitial aggregation were observed at this resolution. As e-irradiation further proceeded, impact of electrons resulted in the transfer of sufficient kinetic energy to the recoil atoms in nanorod to leave their original atomic position. As a consequence, vacancies were produced as evidenced in Fig. 2(b & d) and have been indicated by arrows. The nanotube was found to be contracting locally to “heal” holes, which had been generated due the creation of vacancies, even at RT. This was further supported by the compression in nanorod as shown in Fig. 1(i) and Fig. 2(d).

If e-irradiation was performed at high temperature ($\approx 510^\circ\text{C}$) as shown in Fig. 3, different phenomenon was observed. The nanorod which was initially confined in the core of CNT, was heavily damaged and later transformed into nanoparticle. This damage did not occur uniformly on the whole CNT. Moreover, un-filled part which was found to be more damaged than the filled part, subsequently filled with carbon nanostructures as irradiation proceeded. This filling might have happened due to the interstitials injection from unstable inner shells that followed axial diffusion through

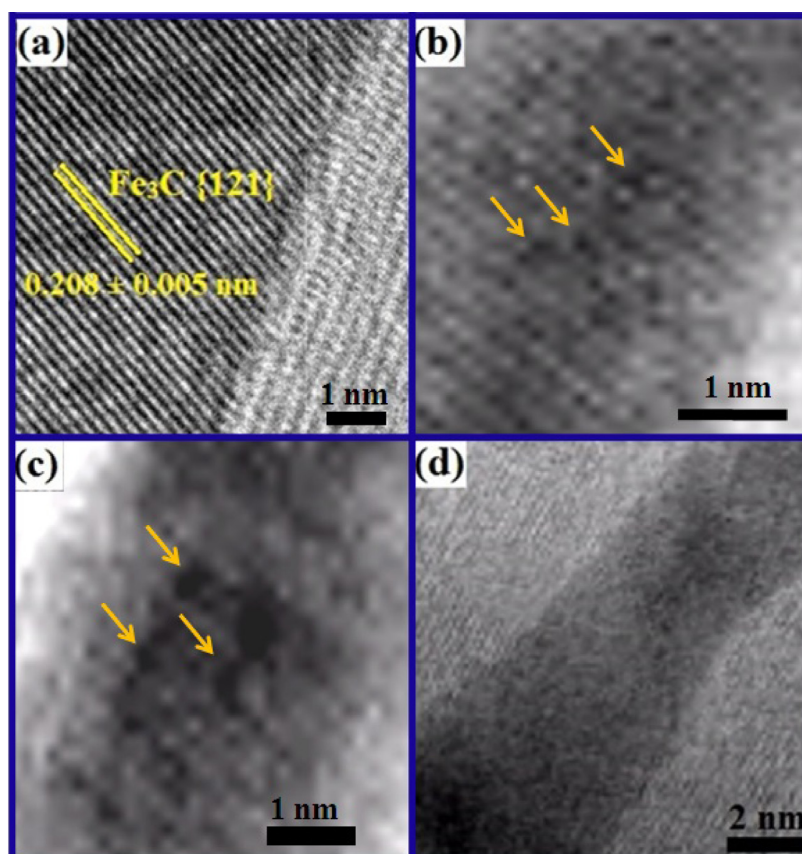


Fig. 2. HRTEM image of: (a) un-irradiated; irradiated nanotube for (b) 13.06 min (c) 19.08 min, and (d) 19.44 min at RT.

CNT core [25]. Finally, caps were formed at both the ends of the nanorod. The damage rate in the nanorod was found to be more in the direction of tube axis. Interestingly, as shown in Fig. 3(c) some clusters are clearly visible in middle of nanorod. Formation of these five clusters is attributed to the aggregation of γ -Fe atoms or Fe_3C molecules. As shown in Fig. 3(d) and (e), initially the size of these clusters increased slowly and then two of the clusters, marked 2 and 3 in Fig. 3(d), merged and formed a large one. Bigger cluster 3 moved in opposite direction towards another smaller cluster 2 whereas nearest smaller cluster 4 did not move as shown in Fig. 3(c) & (d). Thermodynamically, small clusters have been reported to be more unstable than the larger ones [26]. Thus, to attain energetically stable state, small clusters should move towards the larger one. In the present study opposite behaviour was observed. This might have happened due to the influence of irradiation which generated pressure gradient along the tube axis as reported in Ref. [27]. The observations stated above confirmed that an inverse Ostwald ripening took place. The inverse Ostwald ripening normally occurs under ion irradiation and it is associated with increased probability to sputter an atom away from large cluster. In present case, clusters were formed in the lattice of Fe_3C nanorod which was confined inside CNT. Hence, possibility to sputter an atom should be low. Recently, dislocation diffusion-assisted mass/adatom transfer in nanoparticle encapsulated inside the contracting carbon onion has been reported by Lito Sun et al. [27]. They reported that dislocation are formed in the part of nanoparticle with high pressure, and then move to the low-pressure part. This led to mass transfer from high-pressure side to low pressure side. But in present case, as evident cluster 3 at low-pressure side moved towards cluster 1 located at high-pressure side. High pressure part

can be evidenced by subsequent breakage of CNT at the side of cluster 1. Hence, in present case, mass/adatoms transfer does not seem to be dislocation-mediated, as seen in particle [27]. At 600 °C, adatoms/mass transfer in nanorod was also reported due to glide along slip planes and slips were reported to be occurred at low pressure [27]. This mechanism might have resulted in mass transfer from lower pressure part to higher pressure part depending on direction of slip plane and facilitated inverse Ostwald ripening. If electron irradiation further proceeded then nanorod was seen to transform into a spherical particle. After exposing to e-beam for ~5 min, MWCNT broke at a particular position as shown in Fig. 3(i). The broken ends of tube were quickly closed by aggregation of carbon interstitials. This resulted in formation of carbon onions at the ends of the tube. Under electron irradiation monotonic reduction in surface area of tube due to the generation of vacancies has been reported [28]. This phenomenon led to the surface tension mediated CNT/graphene sheet bending in order to eliminate the highly energetic dangling bonds caused by electron bombardment. This whole process favoured the formation of carbon onion at broken ends of tube [28]. As evidenced in Fig. 3(g-i) and Fig. 4, bending and cutting of MWCNT was only possible if it is unfilled. Hence, it can be concluded that filled-CNTs are more stable under e-irradiation. In schematic diagram (Fig. 4), steps have been described to enlighten the effect of e-irradiation on filled-CNT. Images in Fig. 5 have demonstrated the morphological transformation of nanorod into a particle.

The following steps were described to enlighten the behavior of filled-CNT under electron irradiation. At RT, if SWCNT was subjected to e-irradiation, vacancies formed and then immediately vanished by the reconstruction of lattice whereas in MWCNT

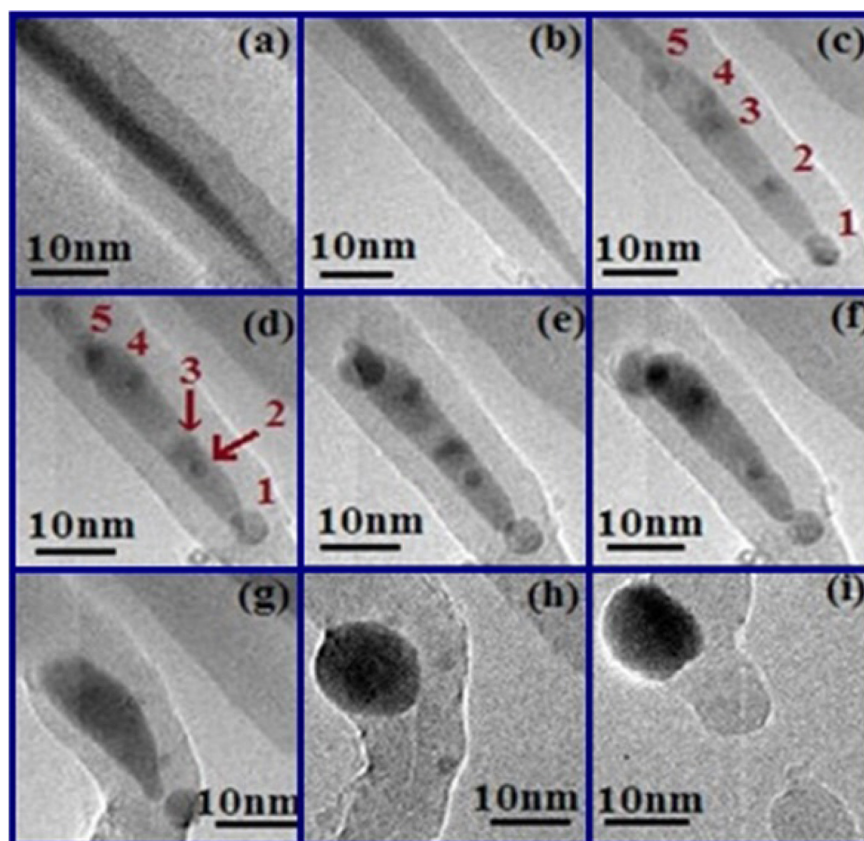


Fig. 3. TEM image of Fe_3C -filled MWCNTs after (a) 5.00 min. (b) 12.00 min. (c) 18.20 min. (d) 23.00 min. (e) 23.45 min. (f) 24.45 min. (g) 32.41 min. (h) 45.00 min., and (i) 50.00 min. electron irradiation at 510 °C.

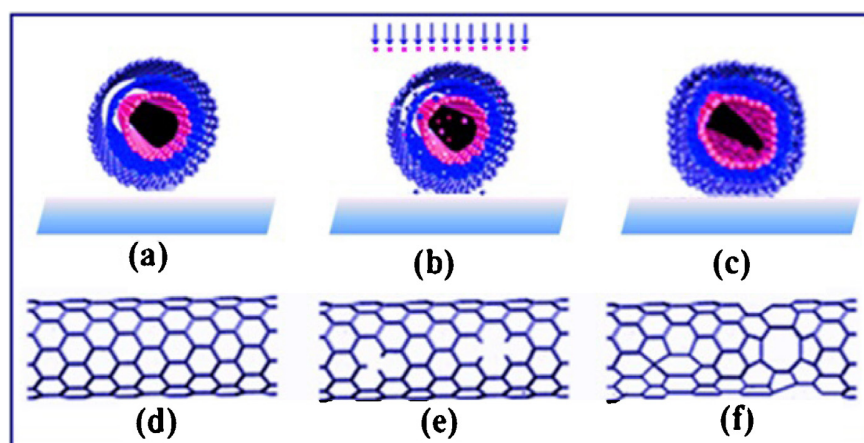


Fig. 4. (a) Fe_3C -filled MWCNT on copper grid (b) Electron-irradiation on MWCNT (c) Deformed MWCNT (d) Atomic bond structure of MWCNT (e) Creation of vacancies and interstitials in lattice of MWCNT (f) Re-arrangements of bond structure of MWCNT.

vacancies were found to be stable [29]. However, it has been reported that in situ annealing decrease the defect concentration up to 20%–50%. This reduction is due to the recombination of Frenkel pairs that exist in this state [25]. Hence, in both cases defects production is much high at RT [30]. Thus, irradiation induced damages in nanotubes can be avoided at relatively high temperature. Due to collision between energetic electron and target carbon atom, carbon atom in CNT lattice shifts from its initial position to interstitial. The threshold energy of electron beam required to shift a carbon atom by collision of electron was

reported to be 80 keV for SWCNT and 100 keV for MWCNT [31,32]. If the energy of incident electrons is greater than this threshold energy then vacancies are created, due to the removal of the carbon atoms. These carbon atoms attained low or high energy, depending on location of vacancy and e-beam energy. These low energy carbon atoms were adsorbed on the surface of CNT and diffused sideward. This results in thickening of the walls. Maximum energy transferred to carbon atom by irradiation by electron beam of energy 200 keV is calculated and found to be 43.68 eV which is greater than the threshold energy 15–20 eV required to

displace the carbon atoms in MWCNT lattice [30,31,33,34]. Hence, these energetic recoil carbon atoms can displace another atom in CNT lattice or sputtered in/out forward direction [30,31,33,34]. Deformations such as: surface reconstruction, bond rearrangement and drastic dimensional changes occurred. Under a sustained e-irradiation, electronic excitations were also generated due to significant electron-electron interaction. These excitations may be localized due to the reduction of conduction electrons [32] and transferred the energy to the nanorod lattice in picoseconds [25,35]. This might result either in strong heating of the lattice or locally melting of nanorod. It may be noted that there is a huge difference in the value of thermal expansion coefficient (CTE) (α). Values of $\alpha_{\text{Fe}_3\text{C}}$ and α_{CNT} are $4.1 \times 10^{-5} \text{ K}^{-1}$ and $0.73 \times 10^{-5} \text{ K}^{-1}$, respectively [36,37]. Here, α_{CNT} is the radial thermal expansion coefficient of the CNT of 10 nm diameter. The values of anisotropic α in cementite have been reported to be: $\alpha_a = (1.2 \pm 1.0) \times 10^{-6} \text{ K}^{-1}$, $\alpha_b = (1.4 \pm 0.7) \times 10^{-6} \text{ K}^{-1}$, $\alpha_c = (11.3 \pm 1.0) \times 10^{-6} \text{ K}^{-1}$ [38]. It is reported that this huge difference in α_{CNT} , and α_b or α_c is generating the tensile in nanorod in radial direction as well as compression along tube axis [24]. In other case, if Fe_3C nanorod melted and solidified then this difference in thermal expansion coefficients of Fe_3C and CNT generates the required compressive stress along the tube axis to produce buckling, as shown in Fig. 1(f–i). Taking into account the difference in CTEs, axial buckling has been reported in nickel nanorod confined inside MWCNT, irradiated by Au^{+7} ions of energy 100 MeV [35]. When e-irradiation took place atoms displace from its initial position and leave the vacant site as shown in Fig. 4. These carbon atoms migrated in the tube or ingested into the metals. This resulted in the surface reconstruction and formation of stable non-six-membered rings which reduced

the surface area and apparent diameter. Shrinkage of nanotube further increased the pressure inside the tube which was not uniform in whole nanotube. This facilitated the migration of clusters from higher compressive side. It was found that enough pressure was generated to control the ripening of the cluster, as shown in Fig. 3.

At high temperature (500 °C), cementite (Fe_3C) transformed into Hägg carbide (Fe_5C_2) as reported by Reetu et.al [24]. They reported that tensile stress as well as compression ($\sim 7.48 \text{ GPa}$) in nanorod were present in radial direction and along the nanotube axis, respectively. When electron irradiation was carried out, Hägg carbide decay followed by the reaction: $\text{Fe}_5\text{C}_2 \rightarrow \text{Fe}_3\text{C} + \gamma\text{-Fe}$. Blank et.al [39] suggested that this transformation might be due to the removal of carbon atoms from Fe_5C_2 lattice. However, this transformation is only possible in the presence of compression generated by the tube walls. It has also been reported that e-irradiation can generate 40 GPa of pressure inside CNT [40,41]. Excess $\gamma\text{-Fe}$ atoms aggregated and formed the cluster as shown in Fig. 3. Further, ripening of the clusters of $\gamma\text{-Fe}$ atoms was directed by the pressure. The $\gamma\text{-Fe}$ particles are known to be stable at high pressure. Thus, these clusters moved to cluster present at high compressive side as named 5 in Fig. 3.

Schematic diagram explaining and summarizing various steps during the e-irradiation on filled-CNT has been shown in Fig. 4. When irradiation of the electrons took place, carbon atoms in tube lattice got displaced from its initial position and leave the vacant site. These carbon atoms migrated in the tube and make the saturation of dangling bond. This resulted in the shrinkage of tube surface as well as encapsulated metal which produced extreme pressure in the interior region. The bond arrangement in MWCNT has also

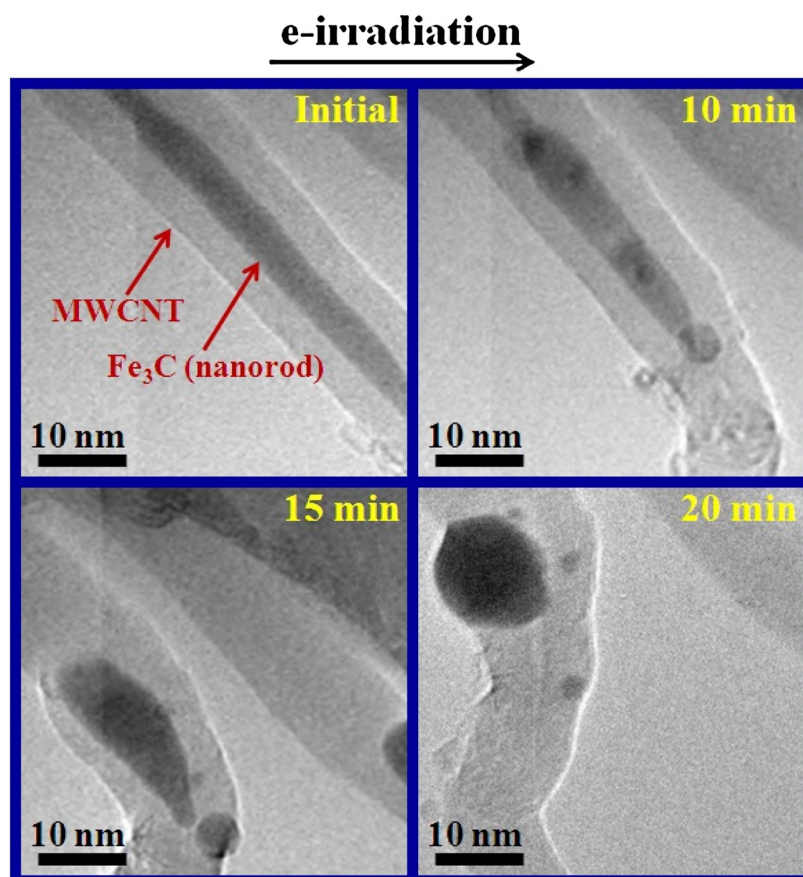


Fig. 5. MWNTs bending with irradiation time (a) initial (b) 10 min. (c) 15 min. (d) 20 min.

been shown in Fig. 4(d–f). As electron irradiation proceeded, compressive stress in both directions was developed due the removal of carbon atoms from CNT lattice and blockage of CNT core, respectively. This finally compressed the rod into particle, as shown in Fig. 5.

4. Conclusion

In the reported work, response of Fe₃C-filled carbon nanotube under electron irradiation has been studied at room as well as high temperature. This study reveals that the compression present in nanorod influenced the reverse transformation of Fe₅C₂ and ripening of the clusters. Axial buckling has been caused due to the local heating of the rod. It can be envisioned that the present studies will facilitate the post synthesis alteration in filled-CNTs, pave way for numerous applications and give insights into electron-metal interaction in confined state.

References

- [1] Q. Fu, G. Weinberg, D.S. Su, Selective filling of carbon nanotubes with metals by selective washing, *New Carbon Mater.* 23 (2008) 17–20.
- [2] Y. Yan, J. Miao, Z. Yang, F.-X. Xiao, H.B. Yang, B. Liu, Y. Yang, Carbon nanotube catalysts: recent advances in synthesis, characterization and applications, *Chem. Soc. Rev.* 44 (2015) 3295–3346.
- [3] O. Lehtinen, L. Sun, T. Nikitin, A.V. Krasheninnikov, L. Khriachtchev, J.A. Rodríguez-Manzo, M. Terrones, F. Banhart, J. Keinonen, Ion irradiation of carbon nanotubes encapsulating cobalt crystals, *Physica E* 40 (2008) 2618–2621.
- [4] U. Weissker, S. Hampel, A. Leonhardt, B. Buchner, Carbon nanotubes filled with ferromagnetic materials, *Materials* 3 (2010) 4387–4427.
- [5] A.A. Bhird, V. Patel, J. Gavard, G. Zhang, A.A. Sousa, A. Masedunskas, R.D. Leapman, R. Weigert, J.S. Gutkind, J.F. Rusling, Targeted killing of cancer cells in vivo and in vitro with EGF-directed carbon nanotube-based drug delivery, *ACS Nano* 3 (2009) 307–316.
- [6] Z. Liu, W. Cai, L. He, N. Nakayama, K. Chen, X. Sun, X. Chen, H. Dai, *In vivo* biodistribution and highly efficient tumour targeting of carbon nanotubes in mice, *Nat. Nanotechnol.* 2 (2007) 47–52.
- [7] K. Suenaga, H. Wakabayashi, M. Koshino, Y. Sato, K. Urita, S. Iijima, Imaging active topological defects in carbon nanotubes, *Nat. Nanotechnol.* 2 (2007) 358–360.
- [8] A. Hashimoto, K. Suenaga, A. Gloter, K. Urita, S. Iijima, Direct evidence for atomic defects in graphene layers, *Nature* 430 (2004) 870–873.
- [9] K. Urita, K. Suenaga, T. Sugai, H. Shinohara, S. Iijima, In-situ Observation of thermal relaxation of interstitial-vacancy pair defects in a graphite gap, *Phys. Rev. Lett.* 94 (2005) 155502–1–155502–4.
- [10] Y. Gan, J. Kotakoski, A.V. Krasheninnikov, K. Nordlund, F. Banhart, The diffusion of carbon atoms inside carbon nanotube, *New J. Phys.* 10 (2008) 023022.
- [11] A. Kis, G. Csanyi, J.-P. Salvetat, T.-N. Lee, E. Couteau, A.J. Kulik, W. Benoit, J. Brugger, L. Forro, Reinforcement of single-walled carbon nanotube bundles by intertube bridging, *Nat. Mater.* 3 (2004) 153–157.
- [12] C. Gomez-Navarro, P.J. De Pablo, J. Gomez-Herrero, B. Biel, F.J. Garcia-Vidal, A. Rubio, F. Flores, Tuning the conductance of single-walled carbon nanotubes by ion irradiation in the Anderson localization regime, *Nat. Mater.* 4 (2005) 534–539.
- [13] M. Terrones, H. Terrones, F. Banhart, J.-C. Charlier, P.M. Ajayan, Coalescence of single-walled carbon nanotubes, *Science* 288 (2000) 1226–1229.
- [14] W. Mickelson, S. Aloni, W.Q. Han, J. Cumings, A. Zettl, Packing C60 in boron nitride nanotubes, *Science* 300 (2003) 467–469.
- [15] H.J. Hwang, K.R. Byun, J.W. Kang, Carbon nanotubes as nanopipette: modeling and simulations, *Physica E* 23 (2004) 208–216.
- [16] L. Sun, F. Banhart, A.V. Krasheninnikov, J.A. Rodríguez-Manzo, M. Terrones, P.M. Ajayan, Carbon nanotubes as high-pressure cylinders and nanoextruders, *Science* 312 (2006) 1199–1202.
- [17] B.A. Kulnitskiy, V.D. Blank, I.A. Perezhogin, E.V. Polyakov, D.V. Batov, Carbon nanotubes with Co-filling: HRTEM studies, in: W. Grogger, F. Hofer, P. Polt (Eds.), *Material Science*, Verlag, 2009, pp. 173–174.
- [18] K. Varshney, Carbon nanotubes: A review on synthesis, properties and applications, *Int. J. Eng. Res. Gen. Sci.* 2 (2014) 660–677.
- [19] M.F.L.D. Volder, S.H. Tawfick, R.H. Baughman, A.J. Hart, Carbon Nanotubes: Present and future commercial application, *Science* 339 (2013) 535–539.
- [20] F. Banhart, P.M. Ajayan, Carbon onions as nanoscopic pressure cells for diamond formation, *Nature* 382 (1996) 433–435.
- [21] P. Wesolowski, Y. Lyutovich, F. Banhart, H.D. Carstanjen, H. Kronmüller, Formation of diamond in carbon onions under MeV ion irradiation, *Appl. Phys. Lett.* 71 (1997) 1948–1950.
- [22] A. Misra, P.K. Tyagi, M.K. Singh, D.S. Misra, J. Ghatak, P.V. Satyam, D.K. Avasthi, Structural damage on multiwalled carbon nanotubes and encapsulated single crystal nickel nanorods irradiated with Au⁴⁷ ions of 100 MeV, *Diamond Relat. Mater.* 15 (2006) 300–303.
- [23] K. Dharamvir, K. Jeet, C. Du, N. Pan, V.K. Jindal, Structural modifications of multiwalled carbon nanotubes by swift heavy ions irradiation, *J. Nano Res.* 10 (2010) 1–9.
- [24] R. Kumari, L. Krishnia, V. Kumar, S. Singh, H.K. Singh, R.K. Kotnala, R.R. Juluri, U.M. Bhatta, P.V. Satyam, B.S. Yadav, Z. Naqvi, P.K. Tyagi, Fe₃C-filled carbon nanotubes: permanent cylindrical nanomagnets possess exotic magnetic properties, *Article in communication*.
- [25] A.V. Krasheninnikov, K. Nordlund, Ion and electron irradiation-induced effects in nanostructured materials, *J. Appl. Phys.* 107 (2010) 071301–1–071301–70.
- [26] Ratke, Lorenz, Voorhees, W. Peter, Growth, Coarsening, Ostwald Ripening in Material Processing, Springer, Verlag Berlin Heidelberg, 2002, pp. 117–118.
- [27] Litao Sun, A.V. Krasheninnikov, T. Ahlgren, K. Nordlund, F. Banhart, Plastic deformation of single nanometer-sized crystals, *Phys. Rev. Lett.* 101 (2008) 156101.
- [28] B. Li, Y. Feng, K.-W. Ding, G. Qian, X.-B. Zhang, Y.-F. Liu, Effect of electron beam irradiation on multi-walled carbon nanotubes, *Trans. Nonferrous Met. Soc. China* 24 (2014) 764–769.
- [29] J.A. Rodríguez-Manzo, F. Banhart, Creation of individual vacancies in carbon nanotubes by using an electron beam of 1 Å diameter, *Nano Lett.* 9 (2009) 2285–2289.
- [30] A.V. Krasheninnikov, Irradiation-induced phenomena in carbon nanotubes, in: V.A. Basiuk, E.V. Basiuk (Eds.), *Chemistry of carbon nanotube*, American Scientific Publishers, Finland, 2007, pp. 1–46.
- [31] F. Banhart, Irradiation effects in carbon nanostructures, *Rep. Progr. Phys.* 62 (1999) 1181–1221.
- [32] A. Krasheninnikov, F. Banhart, Engineering of nanostructured carbon materials with electron or ion beams, *Nat. Mater.* 6 (2007) 723–733.
- [33] F. Banhart, Irradiation of carbon nanotubes with a focused electron beam in the electron microscope, *J. Mater. Sci.* 41 (2006) 4505–4511.
- [34] T.D. Yuzvinsky, W. Michelson, S. Aloni, G.E. Begtrup, A. Kis, A. Zettl, Shrinking a carbon nanotube, *Nano Lett.* 6 (2006) 2718–2722.
- [35] A. Mishra, P.K. Tyagi, P. Rai, D.R. Mahapatra, J. Ghatak, P.V. Satyam, D.K. Avasthi, D.S. Mishra, Axial buckling and compressive behavior of nickel-encapsulated multiwalled carbon nanotubes, *Phys. Rev. B* 76 (2007) 014108–14111.
- [36] F.Y. Wu, H.M. Cheng, Structure and thermal expansion of multi-walled carbon nanotubes before and after high temperature treatment, *J. Phys. D Appl. Phys.* 38 (2005) 4302–4307.
- [37] I.G. Wood, L. Vocladlo, K.S. Knight, D.P. Dobson, W.G. Marshall, G.D. Pricea, J. Brodholt, Thermal expansion and crystal structure of cementite, Fe₃C, between 4 and 600 K determined by time-of-flight neutron powder diffraction, *J. Appl. Cryst.* 37 (2004) 82–90.
- [38] N.Ya. Rokhmanov, A.F. Sirenko, S.A. Bakharev, Thermal expansion of cementite in hypereutectoid iron-carbon alloy, *Met. Sci. Heat Treat.* 39 (1997) 1–2.
- [39] V.D. Blank, B.A. Kulnitskiy, I.A. Perezhogin, Y.L. Alshevskiy, N.V. Kazennov, Decomposition of Fe₃C₂ catalyst particles in carbon nanofibers during TEM observation, *Sci. Technol. Adv. Mater.* 10 (2009) 015004.
- [40] M. Terrones, L. Sun, J.A. Rodríguez-Manzo, H. Terrones, F. Banhart, Electron irradiation effects in carbon nanostructures: surface reconstruction, extreme compression, nanotube growth and morphology manipulation, in: S. Richter, A. Schwedt (Eds.), *Materials Science*, Springer-Verlag, Berlin Heidelberg, 2008, pp. 155–156.
- [41] L. Sun, J.A. Rodríguez-Manzo, F. Banhart, Elastic deformation of nanometer-sized metal crystals in graphitic shells, *Appl. Phys. Lett.* 89 (2006) 263104.

Hybrid Dynamic MCML style (H-DyCML): A high speed Dynamic MCML style

Neeta PANDEY ^{1#}, Damini GARG^{1\$}, Kirti GUPTA ^{2^}, Bharat CHOUDHARY^{1*}

¹Dept. of Electronics and Communication Engineering, Delhi Technological University, India

²Dept. of Electronics and Communication Engineering, Bharati Vidyapeeth's College of Engineering, India

[#]n66pandey@rediffmail.com, ^{\$}daminigarg90@gmail.com, [^]kirtigupta22@gmail.com, ^{*}bharatchoudhary@dtu.ac.in

Abstract

This paper proposes hybrid dynamic current mode logic (H-DyCML) as an alternative to existing dynamic CML (DyCML) style for digital circuit design in mixed-signal applications. H-DyCML introduces complementary pass transistors for implementation of logic functions. This allows reduction in the stacked source-coupled transistor pair levels in comparison to the existing DyCML style. The resulting reduction in transistor pair levels permits significant speed improvement. SPICE simulations using TSMC 180 nm and 90 nm CMOS technology parameters are carried out to verify the functionality and to identify their advantages. Some issues related to the compatibility of the complementary pass transistor logic have been investigated and the appropriate solutions have been proposed. The performance of the proposed H-DyCML gates are compared with the existing DyCML gates. The comparison confirms that proposed H-DyCML gates are faster than the existing DyCML gates.

Keywords:

MOS current mode logic, Dynamic current mode logic, portable devices, low power

1. Introduction

There has been tremendous boost on the design and development of portable electronic goods in recent past [1-4]. As the battery life is critical in these systems, there has been a paradigm shift towards low power designs. Though the CMOS logic circuits consume negligible static power, the dynamic power consumption increases sharply as the operating high frequencies are increased [5-8]. The MOS Current Mode Logic (MCML) is a promising alternative to CMOS logic, in both reducing power consumption at high frequencies and providing high performance for mixed-signal applications [9-14]. Due to the presence of static current source, the power consumption of these circuits is high. Therefore, a new logic family called Dynamic CML [15, 16] is suggested in literature which used dynamic current source and operate on precharge evaluate method prevailing in dynamic CMOS logic. The multiple input logic realization requires stacking of transistors leading to significant delay.

In this paper, a new method to realize the logic function in DyCML gate for reducing the stacking of transistors is presented. A dynamic logic style employing the complementary pass

transistor logic (CPL) for implementing the logic functions is proposed. This new logic style is named as Hybrid Dynamic CML logic and is abbreviated as H-DyCML style. The paper first briefly describes the existing DyCML style and highlights its advantages over the MCML style in section 2. Thereafter, the architecture of the proposed H-DyCML style is presented and investigated in section 3. The power consumption of the proposed style is formulated in section 4. The functionality of the proposed H-DyCML gates and the performance comparison with the existing DyCML gates is carried out in the simulation section 5. Lastly, the conclusions are drawn in section 6.

2. Dynamic Current Mode Logic (DyCML style) [15, 16]

A DyCML gate uses dynamic current source, instead of constant current source employed in conventional CML, and achieves low power consumption. It operates on precharge and evaluate logic wherein in the output node capacitance is first precharged and subsequently evaluated according to the applied inputs. It has a pull down network (PDN) to realize the logic function, a precharge circuit operating in the precharge phase, a dynamic current source working in the evaluation phase and a latch circuit for maintaining the voltage levels at the output.

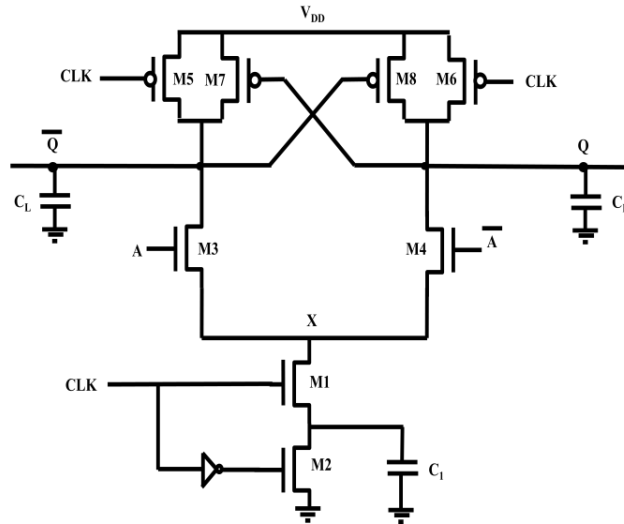


Fig.1 DyCML inverter [15, 16]

The schematic of the DyCML inverter (M1-M8) is shown in Fig. 1. In the circuit diagram, the transistors (M1, M2) and capacitor C1 forms the dynamic current source, the transistors (M3, M4) constitute the PDN, while the transistors (M5, M6) and (M7, M8) makes the precharge and the latch circuit respectively. During the precharge phase, the CLK is low, the transistors M2, M5, and M6 are ON and the transistor M1 is OFF. Both the output nodes Q and \bar{Q} are precharged to the high voltage level ($V_{OH} = V_{DD}$) through the transistors M5 and M6 respectively. Also, the capacitor C_1 is discharged to the ground potential via transistor M2. In the precharge phase, the differential input A is applied and does not cause any change in the output level as the precharge transistors M5, M6 are ON and the transistor M1 is OFF. The circuit enters in the evaluation

phase for high value of the CLK signal. The transistor M1 is ON in this phase and output is evaluated according to the input.

The DyCML gate offer significant power saving and are able to achieve smaller delays in comparison to the basic MCML gates. Also DyCML gates inherit the advantageous features such as high performance, noise immunity, and robustness to supply voltage scaling of MCML gates due to the fact that these are derived from the MCML gates [15, 16]. The circuit diagrams for different DyCML gates are shown in Fig. 2. It can be observed that the PDN consist of multiple levels of source-coupled transistor pair arranged in accordance with the series-gating approach which adds to the delay of the gate. In this paper, an alternate arrangement to reduce the delay of the DyCML gates is proposed. The new gates are built with an aim of reducing the number of source-coupled transistor pair levels in the PDN. To accomplish this, the complementary pass transistor logic is introduced in DyCML style and nomenclature hybrid dynamic CML (H-DyCML) gates is used for the resulting logic style.

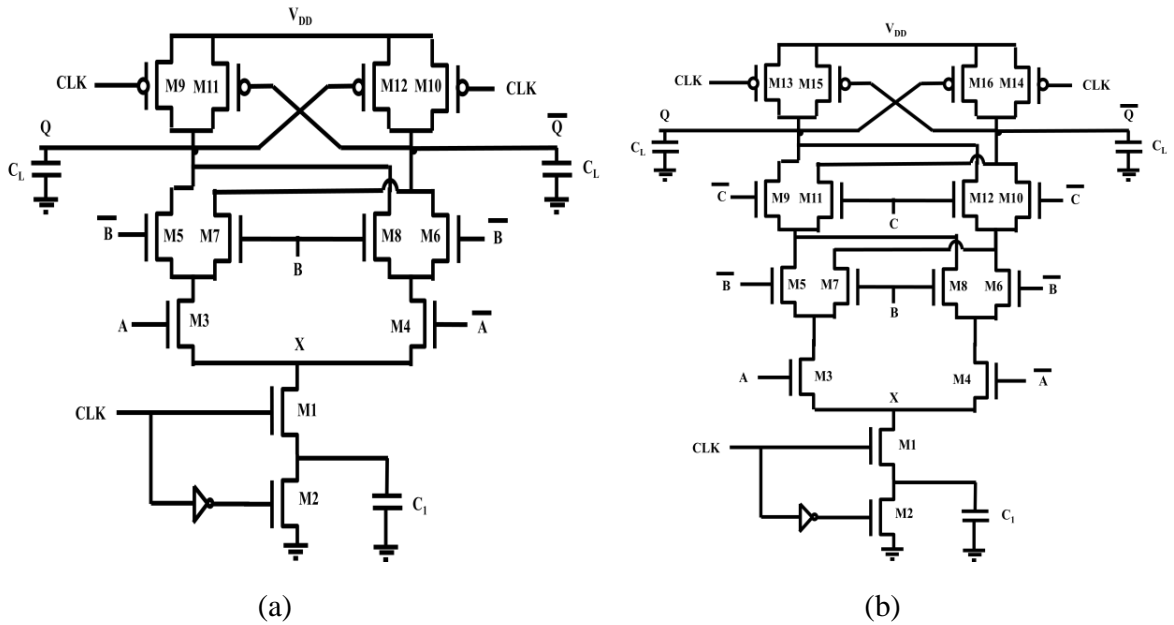


Fig 2. DyCML gate a) two input XOR b) three input XOR

3. PROPOSED HYBRID DYNAMIC CML (H-DyCML) STYLE

The basic architecture of a H-DyCML gate is shown in Fig. 3. The precharge, dynamic current source and the latch circuits are same as that of the existing DyCML gate. The only difference is in the way of realizing the logic function. The complementary pass transistor logic (CPL) is used to realize a part of functionality while the remaining part is implemented in the PDN. To illustrate the concept, the implementation of two and three input XOR gates in H-DyCML style is considered and is shown in Fig. 4. In the two input H-DyCML XOR gate (Fig. 4a), the CPL implements the XOR functionality and whose output is given as the input to the DyCML inverter. The realization of the three input XOR gate consist of two levels of stacked source-coupled transistor pair in contrast to the three levels in existing DyCML XOR gate. The input to

the lowest level is provided by the CPL logic that realizes the XOR of two inputs and the upper level is then formed by applying the series-gating approach as followed for DyCML gate. The resulting implementation is shown in Fig. 4b. Another implementation of the three input XOR gate can be obtained by realizing the complete XOR functionality in the CPL network and then connecting its output to the DyCML inverter. This implementation of the three input XOR with only single level of source coupled transistor is drawn in Fig. 4c.

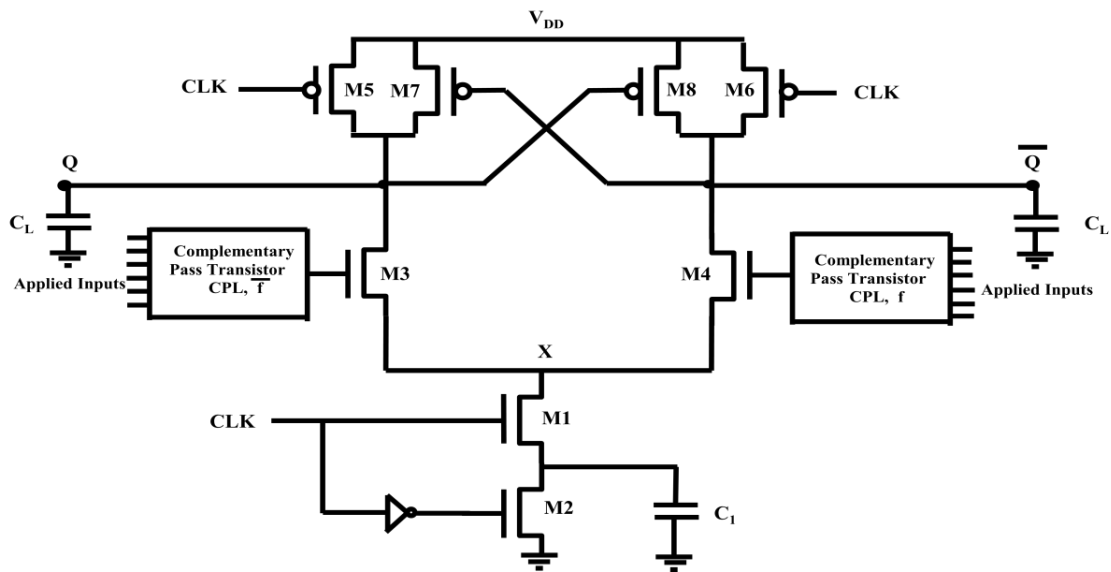
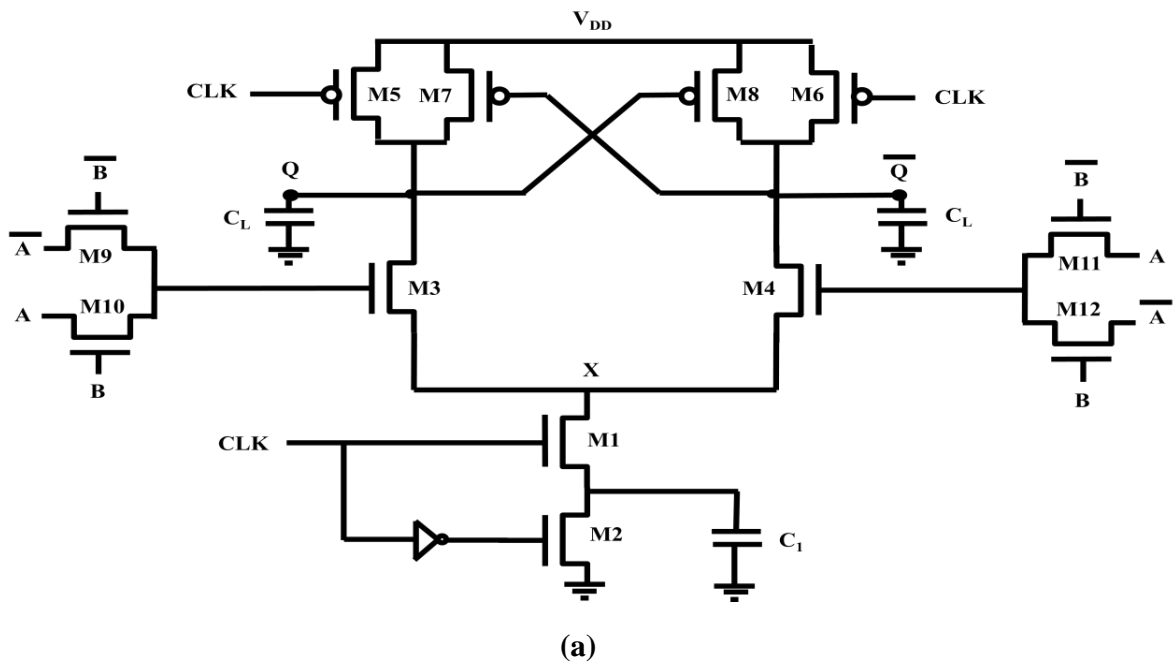
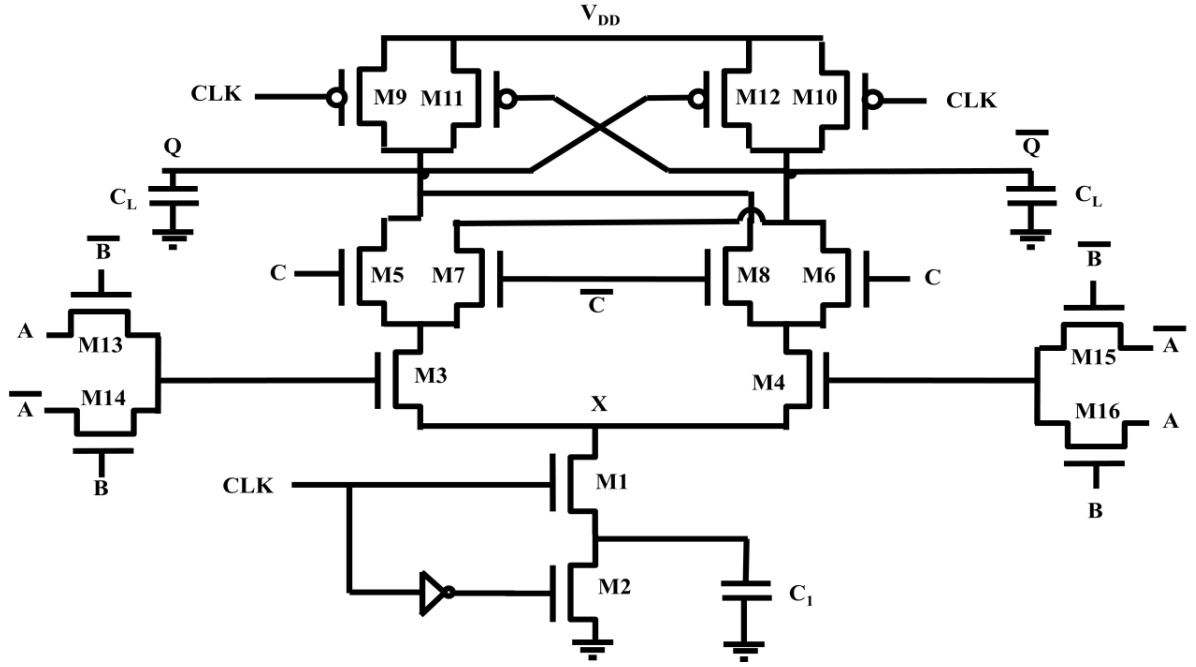
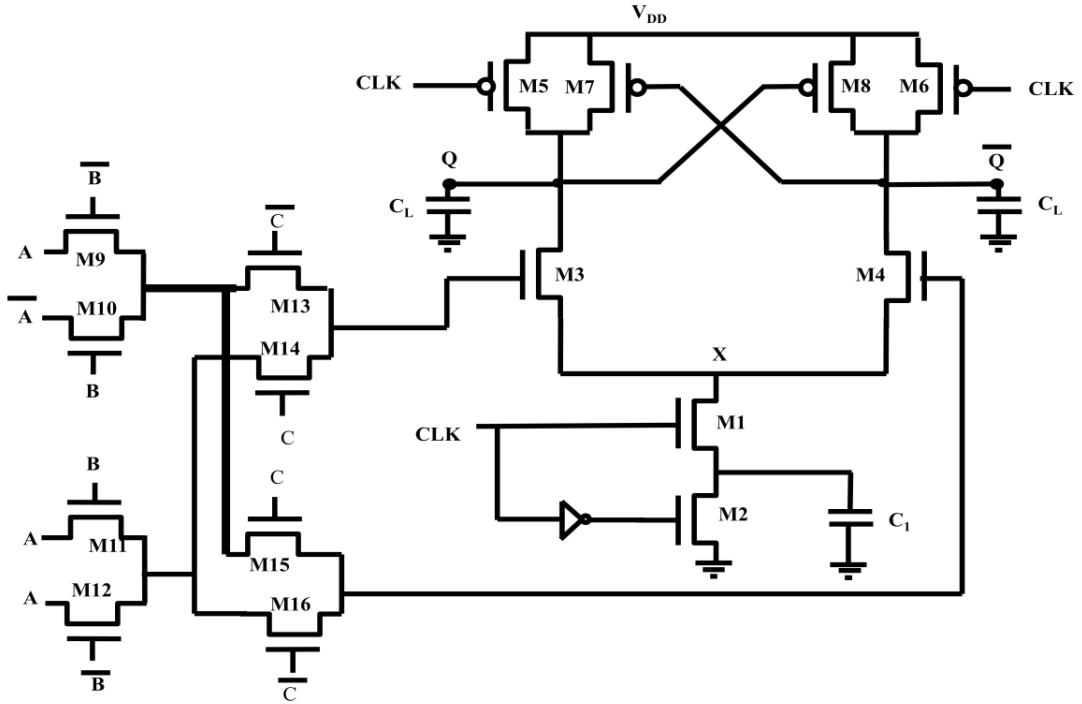


Fig. 3: Basic architecture of H-DyCML gate





(b)



(c)

Fig. 4 Proposed H-DyCML gates a) 2-input XOR gate b) 3-input XOR gate with two levels of source-coupled transistor pair in the PDN c) 3 input XOR gate with single level of source-coupled transistor pair in the PDN

It may be noted that the implementation of the logic function through the CPL approach involves the use of NMOS transistors. As already known that the maximum voltage obtained from an NMOS transistor is one threshold voltage less than the gate voltage. Therefore, if the gate potential of the NMOS ($V_{GS} = V_{DD}$) then the maximum voltage from the NMOS ($V_{OH} = V_{DD} - V_{T,n}$). This high voltage when provided as the input to the DyCML gate and may produce error in the output. So, three techniques to address the problem are proposed.

The maximum voltage obtained from the CPL can be raised by using cross-coupled PMOS transistors operating as level restorer. To illustrate the operation of a level restorer, the CPL implementation of a two input XOR gate with inputs A and B is considered and is shown in Fig. 5. Consider that the input A is high (V_{DD}) and the input B is low ($V_{DD}-V_{SWING}$) where V_{SWING} is the voltage swing of the CML gate. For this input condition, the output of the branch representing XOR functionality (f) will be high ($V_{DD} - V_{T,n}$) whereas the other branch (\bar{f}) is low ($V_{DD}-V_{SWING}$). If the gate-source voltage of the PMOS transistor M5 ($V_{SG} = V_{SWING}$) is less than the threshold voltage (V_T), it gets turned ON and raises the voltage level of the XOR function (f) to V_{DD} . The other PMOS transistor M6 will not conduct and the output of the other branch (\bar{f}) will remain low ($V_{DD}-V_{SWING}$).

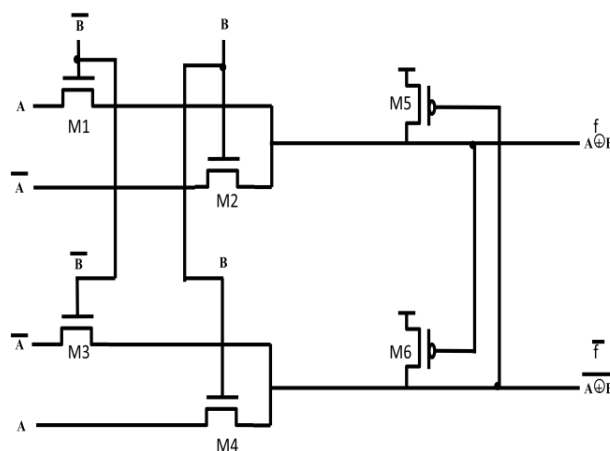


Fig. 5 CPL with level restorer

It may be noted that this technique possesses a restriction on the voltage swing V_{SWING} of the gate. This can be explained from the fact that the cross-coupled PMOS transistor M5 will be ON only if gate-source voltage is less than the threshold voltage (i.e. $V_{\text{SG}} < V_{\text{T}}$). In other words, the voltage swing of the gate should be greater than the threshold voltage ($V_{\text{SWING}} > V_{\text{T}}$). Therefore for the CML gate having lower voltage swing, this technique is not suitable. Another technique to handle the lower CML gates is presented below.

Technique 2: Use of multiple threshold voltage transistor

The above technique has the limitation on the voltage swing of the CML gate due to the threshold voltage of the transistor. Therefore, this technique suggests the use of lower threshold voltage transistors in the circuit. This can be implemented in two ways either by using lower threshold voltage NMOS transistors in the CPL network or by employing lower threshold voltage PMOS transistors in the level restorer. The same is depicted in Fig. 6 for the two input XOR gate. The transistors with bold lines denote low threshold voltage transistor. Thus, the H-DyCML gates with low voltage swing can also be implemented.

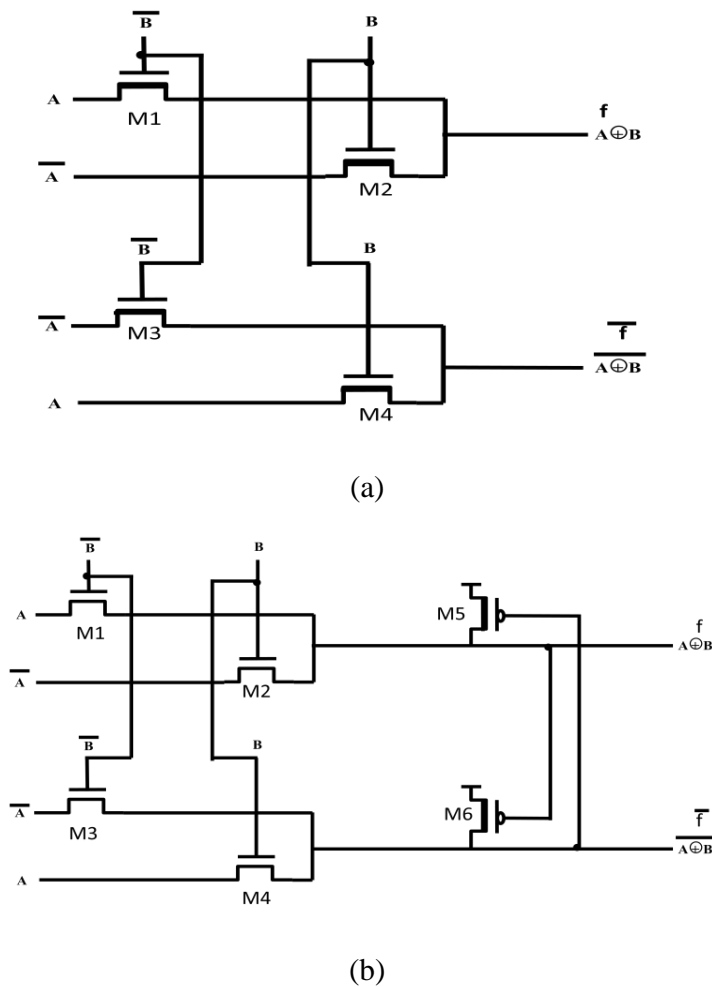


Fig. 6 CPL logic with multiple threshold voltage transistor a) NMOS transistors b) PMOS transistors

An alternate approach which does not pose any limitations on the voltage swing of the gate neither involves the use of multiple threshold voltage can also be designed and is elaborated further.

Technique 3: Use of transmission gates

The drop in the high voltage level at the output of the CPL network can be overcome by realizing the logic function through transmission gates. An implementation of the XOR gate by using transmission gate is shown in Fig. 7. Though this technique will increase the number of transistors it does not possess any restrictions on the voltage swing of the H-DyCML gate.

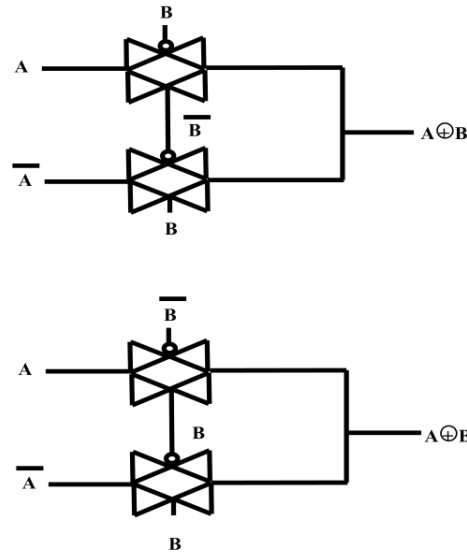


Fig. 7 XOR function realization for H-DyCML gate

4. Power Consumption of H-DyCML

In the proposed H-DyCML gate, the transistor pairs M1 and M2 (Fig. 3) never turns ON simultaneously. As a consequence, a direct path between the power supply and the ground is not established resulting in negligible static power consumption. The proposed H-DyCML gate however, consumes dynamic power due to the presence of the load capacitors. In general, the dynamic power is given by

$$P_{\text{dyn}} = \alpha C_{\text{OUT}} V_{\text{DD}} V_{\text{SWING}} f_{\text{CLK}} \quad (1)$$

where C_{OUT} is the total load capacitance at the output node which include the parasitic capacitances of the transistors and the external load capacitance C_L , f_{CLK} represents the frequency of the CLK signal, V_{DD} is the power supply, V_{SWING} and α correspond to the voltage swing and switching activity of the circuit respectively.

In H-DyCML gates, due to the inherent differential nature of the inputs, it may be noted that one of the output nodes will make a high-to-low transition which requires subsequent precharging to

V_{DD} . This observation indicates that the power consumption of the H-DyCML gate is data independent. In other words, irrespective of the differential inputs, in every clock cycle one of the output nodes will be charged. This signifies that for a H-DyCML gate, the switching activity is unity. Equation (1) reduces to (2) for power consumption of H-DyCML gates.

$$P_{\text{dynH-DyCML}} = C_{\text{OUT}} V_{DD} V_{\text{SWING}} f_{\text{CLK}} \quad (2)$$

5. Simulation Results

Different H-DyCML gates such as two input AND, two input OR, and two input XOR and three input XOR are simulated by using 180 nm and 90 nm CMOS technology parameters with a supply voltage of 1.8V. The three techniques to realize H-DyCML gates are considered. So, for the sake of fair comparison all the gates are designed to operate with a voltage swing greater than the threshold voltage of the transistor. A voltage swing of 700 mV is chosen. The other simulation settings are $C_{\text{OUT}} = 40$ fF, $f_{\text{CLK}} = 333$ MHz. The values of performance parameters such as power, delay and power-delay product are noted and are summarized in Tables I-V. The theoretical value of power consumption in H-DyCML gate is computed using (2) which is found to be 16.78 μ W and is very close to the values reported in Tables I-V.

It may be noted in Table I and II that the maximum delay reduction of 37.87% is observed for the proposed H-DyCML gates in comparison to the existing DyCML gates. Analogously, the H-DyCML two input and three input XOR gates show a delay reduction of 48.23% and 49.4% respectively as compared to existing DyCML XOR gate counterparts.

Table I: Performance Comparison of the existing DyCML and the proposed H-DyCML AND gate

<div>Style Parameter</div>	DyCML	H-DyCML (Technique 1)	H-DyCML (Technique 2)		H-DyCML (Technique 3)
			PMOS	NMOS	
Technology node 180 nm					
Delay(ps)	192.31	176.01	167.92	162.13	180.54
Power(μW)	20.31	15.57	15.58	15.02	15.58
PDP(fJ)	3.90	2.69	2.61	2.43	2.81
Technology node 90 nm					
Delay(ps)	180	156	129	164	168
Power(μW)	14.2	13.36	13.1	13.9	13.4
PDP(fJ)	2.55	2.08	1.68	2.27	2.25

Table II: Performance comparison of the existing DyCML and the proposed H-DyCML OR gate

Style Parameter	DyCML	H-DyCML (Technique 1)	H-DyCML (Technique 2)		H-DyCML (Technique 3)
			PMOS	NMOS	
Technology node 180 nm					
Delay(ps)	236.24	172.28	162.12	219.03	170.25
Power(μ W)	32.11	13.762	13.83	13.88	13.94
PDP(fJ)	7.58	2.37	2.24	3.04	2.37
Technology node 90 nm					
Delay(ps)	180	156	129	164	168
Power(μ W)	14.2	13.36	13.1	13.9	13.4
PDP(fJ)	2.55	2.08	1.68	2.27	2.25

Table III: Performance comparison of the existing DyCML and the proposed H-DyCML 2 Input XOR gate

Style Parameter	DyCML	H-DyCML (Technique 1)	H-DyCML (Technique 2)		H-DyCML (Technique 3)
			PMOS	NMOS	
Technology node 180 nm					
Delay(ps)	237.93	160.63	160.00	171.31	158.33
Power(μW)	29.28	14.84	14.84	13.23	15.20
PDP(fJ)	6.96	2.37	2.37	2.26	2.4
Technology node 90 nm					
Delay(ps)	201	143	140	145	147
Power(μW)	24	14.8	14.8	14.91	13
PDP(fJ)	4.84	2.11	2.07	2.16	1.91

Table IV: Performance comparison of the existing DyCML and the proposed H-DyCML 3 Input XOR gate with two levels of source-coupled transistors in the PDN

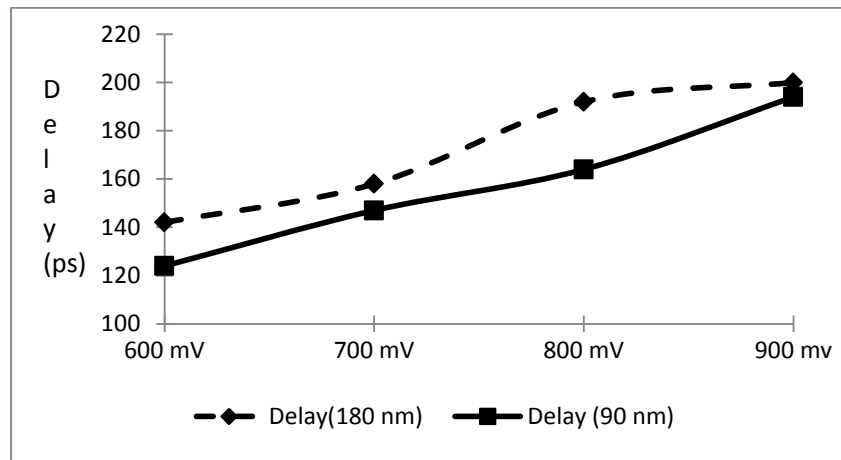
Style Parameter	DyCML	H-DyCML (Technique 1)	H-DyCML (Technique 2)		H-DyCML (Technique 3)
			PMOS	NMOS	
Technology node 180 nm					
Delay(ps)	326.39	211.02	180.00	191.31	199.05
Power(μW)	26.54	14.84	14.84	13.23	12.32
PDP(fJ)	8.66	7.35	5.56	5.69	6.37
Technology node 90 nm					
Delay(ps)	226	175	163	169	190
Power(μW)	23	16.2	16.8	18.4	16.7
PDP(fJ)	5.2	2.83	2.73	3.1	3.17

Table V: Performance comparison of the existing DyCML and the proposed H-DyCML 3 Input XOR gate with single level of source-coupled transistors in the PDN

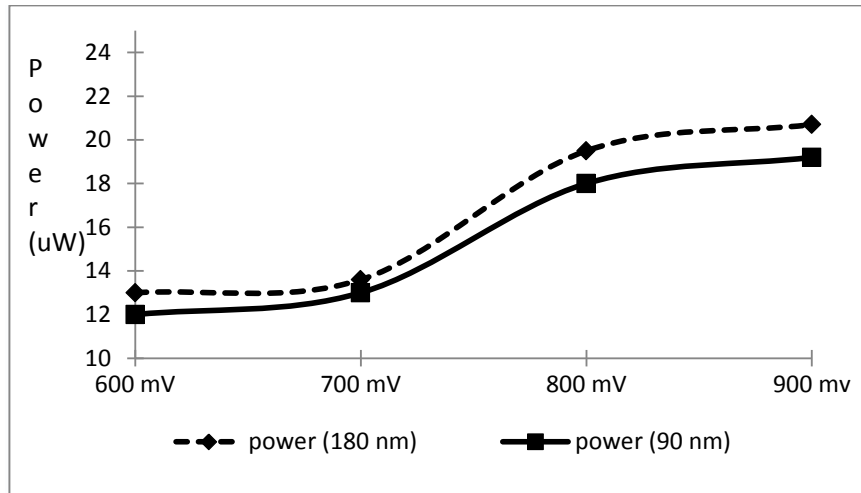
Style Parameter	DyCML	H-DyCML (Technique 1)	H-DyCML (Technique 2)		H-DyCML (Technique 3)
			PMOS	NMOS	
Technology node: 180 nm					
Delay(ps)	326.39	166	170	187	193
Power(μW)	26.54	18	17.5	19	17.6
PDP(fJ)	8.66	2.9	2.9	3.5	3.3
Technology node: 90 nm					
Delay(ps)	226	125	141	176	187
Power(μW)	23	16.2	16.8	18.4	16.7
PDP(fJ)	5.2	2.0	2.3	3.2	3.1

To include design choices as per the suggestion, the performance of the proposed H-DyCML gates is investigated through simulations for different voltage swing and aspect ratio values. The results have been summarized for a two input XOR gate based on technique 3 in Figs. 8-10. Following are the observations;

- In Fig. 8, the power consumption increases with the increase in voltage which is supported with the theoretical formulations discussed in section 4. Also, an increase in voltage swing requires more charge to be transferred from the output load capacitance making a corresponding increase in the delay as indicated in Fig. 8.
- The Fig. 9 shows the dependence of the delay on the aspect ratios of the transistors in the PDN network. There is a decreasing trend in delay with aspect ratio increase. To explain this, the transistors in the PDN can be viewed as resistor. When aspect ratios of transistors in PDN are increased it results in smaller resistance and lower delay values.
- Lastly, the power and the delay of the proposed H-DyCML gate remain almost constant for different values of aspect ratio of the transistors in the CPL network (Fig. 10). This is due to the fact that the changes in the CPL network occurs in the precharge phase which has no effect in determining the performance of the H-DyCML gate

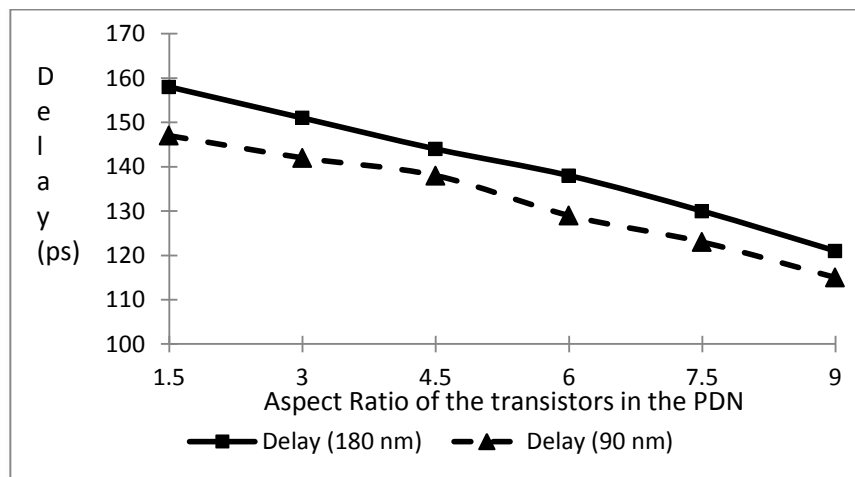


(a)

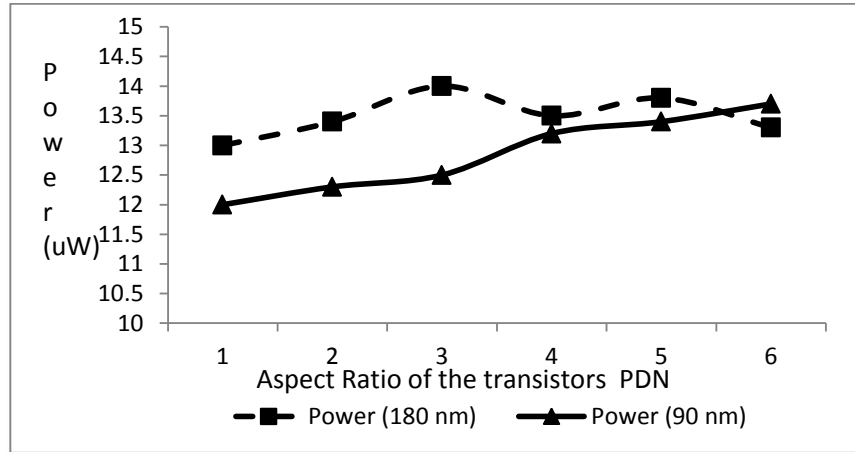


(b)

Fig. 8 Performance of the two input H-DyCML XOR gate by varying the voltage swing
a) Delay results b) Power results

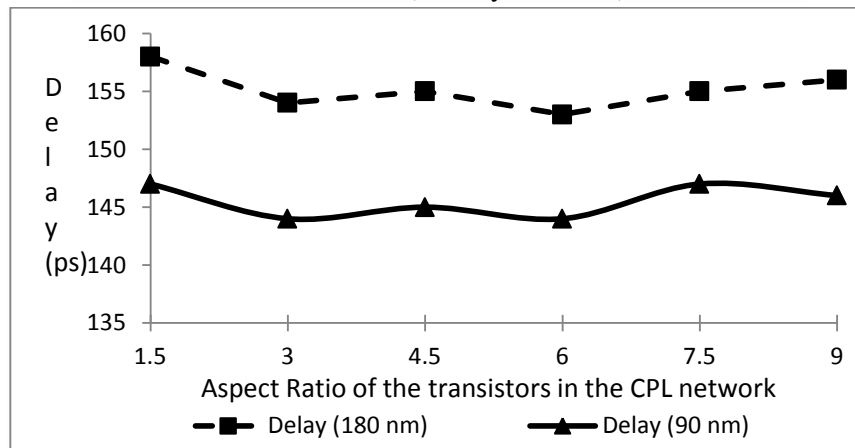


(a)

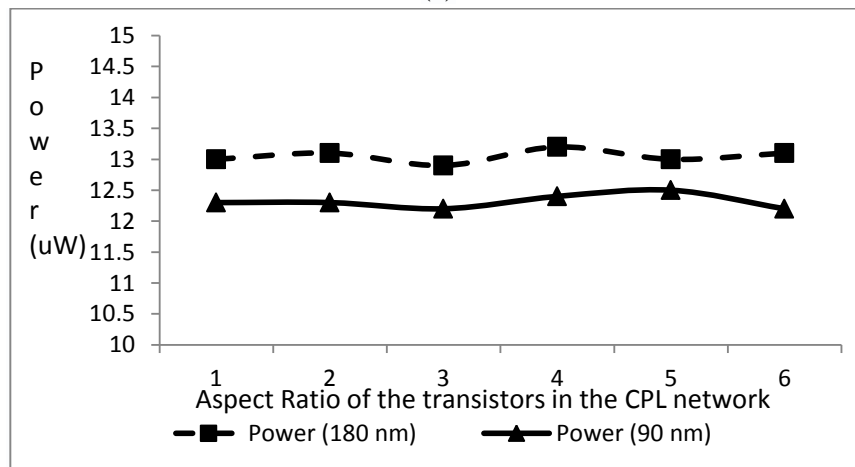


(b)

Fig. 9 Performance of the two input H-DyCML XOR gate by varying the aspect ratio of the transistors in the PDN a) Delay results b) Power results



(a)



(b)

Fig. 10 Performance of two input H-DyCML XOR gate by varying the aspect ratio of the transistors in the CPL network a) Delay results b) Power results

In order to present an application of the proposed style, a 4-bit RCA (Fig. 11) implementation is considered. The implementation requires cascading of four full adder (FA) circuits wherein the full adder is realized by cascading two half adders (HA) and an OR gate as shown in Fig. 12a. The realization of half adder uses the schematic in Fig. 12b and its H-DyCML realization is placed in Fig. 12c. The signals DC_i ($i = 1, 2$) represent voltage across capacitor C_1 of H-DyCML XOR and AND gates. In dynamic CML style, the direct cascading of various gates is not possible [16], therefore self timed buffers (STs) [16] are placed intermittently. The ST process signal $DC1$ and triggers evaluation of the gate driven by its output.

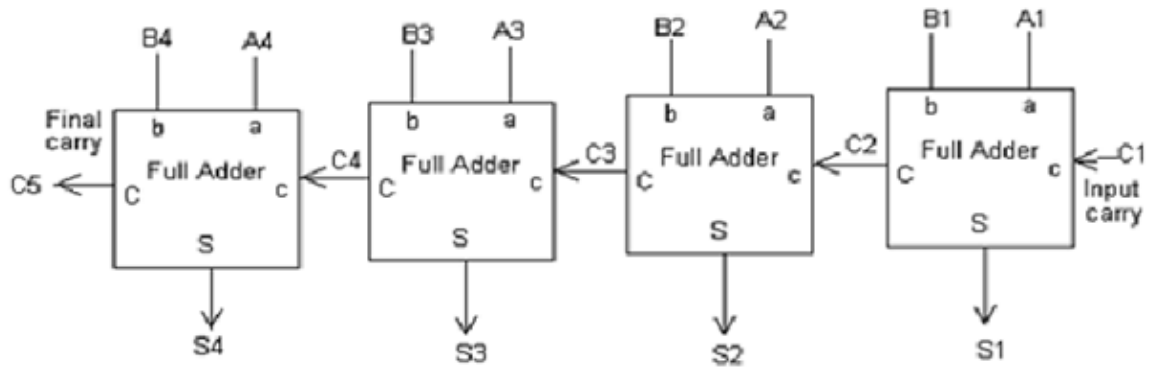
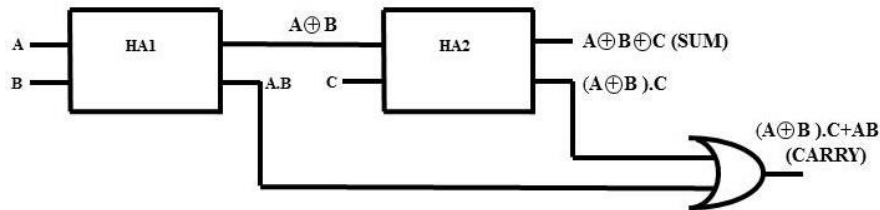
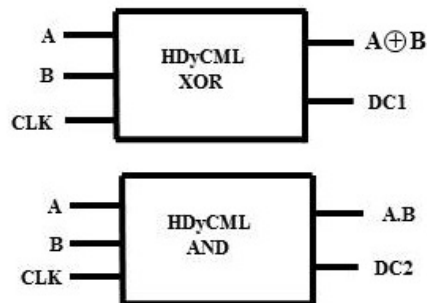


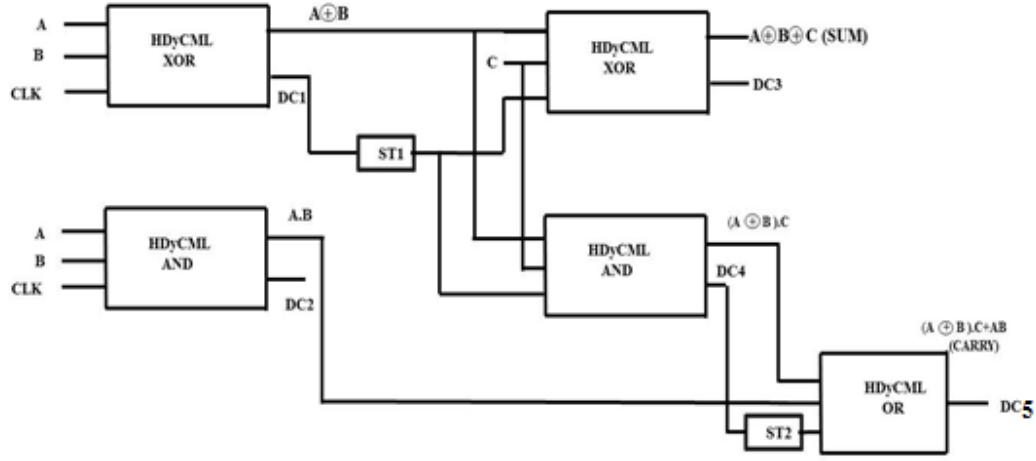
Fig. 11 Block diagram of a 4-bit RCA



(a)



(b)



(c)

Fig. 12 (a) Full Adder schematic (b) H-DyCML Half Adder schematic
(b) Complete schematic of D-HyCML full adder

The performance parameters such as power, delay and PDP are noted for the 4-bit RCA using different techniques and are noted in Table V. It may be noted that the delay is almost same for all the proposed topologies which may be attributed to the same number of total cascaded stages used for realization. Further, there is significant reduction in delay and power consumption in comparison to the existing DyCML style. The delay reduces by 63.43% in the proposed H-DyCML based design in comparison to existing DyCML RCA design.

Table V: Performance comparison of the existing DyCML and the proposed H-DyCML 4-bit RCA

Style Parameter	DyCML	H-DyCML (Technique 1)	H-DyCML (Technique 2)	H-DyCML (Technique 3)
Delay (ps)	967.74	339.57	326.39	357.08
Power (μ W)	250.88	130.362	129.52	131.11
PDP(fJ)	242.78	44.354	42.27	46.82

6. Conclusion

In this paper, a new hybrid dynamic current mode logic (H-DyCML) is presented as an alternative to the existing DyCML style. The use of complementary pass transistors in logic function realization is proposed in H-DyCML style. This is done to reduce source-coupled transistor pair levels in the PDN of the gate which results in an improvement of delay of the gate. Different gate in H-DyCML style are implemented and simulations are performed to compare their performance with the existing DyCML gates. The TSMC 180 nm and 90 nm CMOS technology parameters are used. The issues related to the compatibility of the complementary pass transistor logic with CML gates are identified and appropriate solutions have been

proposed. An application example is also taken to demonstrate the benefit of employing proposed H-DyCML gates over the existing DyCML gates. A maximum improvement of 63.43 % was observed in delay by employing proposed H-DyCML gates. Hence, it is confirmed that the proposed H-DyCML gates offer significant speed advantage over the existing DyCML gates.

References

- [1] B. Davari, R. H. Dennard and G. G. Shahidi, "CMOS Scaling for High Performance and Low Power - The Next Ten Years," Proceedings of the IEEE, Vol .83, pp.595- 606,1995.
- [2] International Technology Road Map for Semiconductors, "Radio frequency and analog/mixed signal technologies for wireless communications," ITRS, Tech. Rep., 2005.
- [3] A. Chandrakasan and R. W. Brodersen, "Low Power Digital CMOS Design", IEEE Journal of Solid State Circuits, Vol. 27, pp. 473-484,1992
- [4] P. Ng, P. T. Balsara, and D. Steiss, "Performance of CMOS differential circuits," IEEE J. Solid-State Circuits, Vol. 31, pp. 841–846,1996.
- [5] Neil H.E. Weste, David Harris, "Principles of CMOS VLSI Design: A System Perspective", (3rd ed.) Addison-Wesley, 2004.
- [6] R. H. Krambeck, C. M. Lee, H. -F.S. Law., "High-speed compact circuits with CMOS," IEEE J. Solid-State Circuits, Vol. 17, pp. 614–619, 1982
- [7] P. V. D. Meer, A. V. Staveren and A.V. Roermund, "Low-Power Deep Sub-Micron CMOS Logic: Sub-threshold Current Reduction", Springer International series in Engineering and Computer Science, 2004.
- [8] S. -Mo Kang and Y. Leblebici, "CMOS Digital Integrated Circuits", Tata McGraw-Hill Education, 2003
- [9] M. Alioto, G. Palumbo, "Power-Aware Design Techniques for Nanometer MOS Current-Mode Logic Gates: a Design Framework", IEEE Circuits and Systems Magazine, No. 4, pp. 40-59, December 2006.
- [10] M. Alioto, G. Palumbo, "Design Strategy for Source Coupled Logic Gates", IEEE Trans. on CAS part I, Vol. 50, No. 5, pp. 640-654, May 2003.
- [11] M Alioto and G Paulumbo. "Model and Design of Bipolar and MOS Current-Mode Logic, Fundamental theory and Applications" IEEE Trans. on CAS part I, vol.46, pp.1330-1341, 1999.
- [12] J.M. Musicer and J. Rabaey, "MOS current mode logic for low power, low noise CORDIC computation in mixed-signal environments," in *Proc. International Symposium on Low Power Electronics and Design*, pp. 102-107, 2000

- [13] M. Mizuno, M. Yamashina, K. Furuta, H. Igura, H. Abiko, K. Okabe, A. Ono and H. Yamada, "A GHz MOS, Adaptive Pipeline Technique Using MOS Current-Mode Logic," IEEE Journal of Solid-State Circuits, vol.31, pp.784-791, 1996.
- [14] M. Yamashina and H. Yamada, "An MOS current mode logic (MCML) circuit for low-power sub-GHz processors", IEICE Trans. Electron., Vol. E75-C, pp. 1181–1187,1992.
- [15] M.W Allam, and M.I Elmasry. "Dynamic current mode logic (Dynamic CML): A new low-power high performance logic family", Custom Integrated Circuits Conference, CICC. Proceedings of the IEEE, pp.421- 424, 2000.
- [16] M. Allam, M. Elmasry, "Dynamic Current Mode Logic (DyCML): A New Low-Power High-Performance Logic Style", IEEE Jour. of Solid-State Circuits, Vol. 36, No. 3, pp. 550-558, March 2001.

Measurement Uncertainty in Airborne Sound Insulation and Single-Number Quantities: Strategy and Implementation in Indian Scenario

N. Garg^{1,2*}, A. Kumar¹ and S. Maji²

¹CSIR - National Physical Laboratory, New Delhi 110012, India

²Delhi Technological University, Delhi 110042, India

Received: 18 June 2015 / Accepted: 12 November 2015

© Metrology Society of India 2015

Abstract: This paper presents the factors affecting the uncertainty of measurement in sound transmission loss testing and the single-number quantities (*SNQs*) used widely in building acoustics. It provides a retrospective view of the recently published work especially in European continent and standard ISO 12999-1 for interpreting and elaborating the concept of calculation of measurement uncertainty in *SNQs* particularly for the laboratories engaged in sound transmission loss testing in India by presenting case studies for different types of building materials. The study suggests that the poor low frequency sound insulation and low frequency mass-air-mass and flexural resonances inculcate a higher uncertainty in *SNQs* for building elements. It is imperative to adopt the strategy recommended in ISO 12999-1 in Indian scenario particularly with growing international trade in building materials and technology and for the recognition as well as acceptance of testing results of Indian laboratories across the globe.

Keywords: Airborne sound insulation; Single-number quantity (*SNQ*)

1. Introduction

Airborne sound insulation is a vital property of building elements characterized in terms of sound transmission loss (*STL*) or sound reduction index, *R*, which is the performance of sound insulation of a material measured in the reverberation chambers. Sound transmission class (*STC*) is an integer rating of how well a building partition attenuates the airborne sound. The method compares a family of numbered contours with one-third octave band (125–4000 Hz) *STL* data. The contour number that best fits the data gives the *STC* rating. The better the *STC* of material, the better the sound insulation it provides. This integer rating is widely used to rate interior partitions, ceilings/floors, doors, windows and exterior wall configurations in USA. The other widely used single-number quantity: weighted sound reduction index, *R_w*, calculated as per ISO 717-1 [1] in conjunction with spectrum adaptation terms for pink and traffic noise, *R_w* (*C*, *C_{tr}*) is also used by acousticians all over the world to describe the sound transmission loss of materials in terms of single-number

quantity. The sound transmission loss characteristics of building elements are measured in a specialized environment with non parallel and highly reflective walls called the reverberation chambers. The sound transmission loss is measured using two coupled rooms, one acting as a source room and other as a receiver. Two adjacent reverberation rooms are arranged with an opening in between in which the test partition is installed. An omni-directional loud-speaker is used to generate the sound field excitation in the source room. The sound field incident on the test specimen causes it to vibrate and thus creates a sound field in the adjacent receiving room. The space and time averaged sound pressure levels in the two rooms are measured using calibrated working standard (WS2P) microphones. The absorption characteristics and reverberation time of the receiving room are also measured. The sound transmission loss measurements are generally taken in 1/3rd octave bands from 100 Hz to 4 kHz and is calculated as:

$$STL = L_1 - L_2 + 10 \log (S/A) \quad (1)$$

where *L₁* and *L₂* are average sound pressure levels in the source and receiving rooms, *S* is the area of test specimen exposed in the receiving room, and *A* is sound absorption of the receiving room with test specimen in place.

*Corresponding author, E-mail: ngarg@mail.nplindia.ernet.in

The uncertainties associated with the measurement of *STL* and *SNQ* of building elements is indispensable for manufacturers, architects and researchers so as to ascertain whether a requirement is met or to compare the acoustic properties of different products. If variations and uncertainty in building acoustic measurements can be controlled, construction costs can potentially be reduced since the building will not have to be acoustically over-designed [2]. It is essential for designers, builders, consumers and authorities that they understand or know beforehand how the accuracy of building acoustic measurements is taken into account [3].

Thus, it is imperative to investigate the various aspects associated with uncertainty calculations so as to quantify the uncertainty in reporting the *SNQ*s for acoustical materials tested in laboratory with a definite confidence level. Wittstock [4] presented the analytical formulations for calculating the uncertainty in *SNQ* based on the sound transmission loss values and correlation coefficient between the frequency bands in 1/3rd octave band. The empirical correlation coefficient describes how all third-octave band uncertainties interact to give the measured uncertainty of *SNQ*. Whereas the case of full, positive correlation represents an upper limit for the uncertainty; the case of no correlation is not the lower limit since a negative correlation between the third-octave band values is observed in rare cases. Wittstock experimental investigations [4, 5] on 2000 measured spectra originating e.g. from round robins in this regard revealed that measured uncertainties are always smaller than the calculated ones when a positive correlation between the 1/3rd octave bands is associated. The use of maximum uncertainty calculated under the assumption of full correlation, or the average measured uncertainties determined from round robins is recommended. An important conclusion is that the calculation and use of uncertainties is much more meaningful if the weighted sound reduction index is calculated by taking into account decimal digits, which implies the shifting of the reference curve in steps of 0.1 dB instead of steps of 1 dB. The recently published standard ISO 12999-1:2014 [6] clearly specifies the procedure for assessing the uncertainty of measurement in sound insulation in building acoustics.

The sound transmission loss measurements can be done using the sound pressure approach as per ISO 10140 series [7] or the sound intensity approach as per ISO 15186-1 [8]. Although the sound intensity approach is described as insensitive to room mode effects in source and receiving room [9] and has been recommended to be the best approach for measurements below 200 Hz, yet the method has still not become a true alternative to the sound pressure approach [10]. The intensity method typically yields lower sound insulation values at low frequencies than the

pressure method, which can be explained by Waterhouse correction [11–13]. Dijkmans et al. [13] pointed out the systematic differences between the pressure method and intensity method are expected because of the differences in the measurement of transmitted power, increase in absorption of receiving room in the intensity method and suppression of flanking transmission in the intensity method. Sound intensity method as per ISO 15186-3:2002 [14] is also used to determine the sound reduction index at low frequencies (50–160 Hz). The method has significantly better reproducibility in a typical test facility than those of ISO 15186-1 [8] and ISO 140-3 [15]. The method differs from ISO 15186-1 in the fact that the sound pressure level in the source room is measured close to the surface of test specimen and surface opposite to the test specimen in the receiving room is highly absorbing.

In India, there are few laboratories and research institutions such as CSIR-National Physical Laboratory, Delhi (NPL); Automotive Research Association of India (ARAI), Pune; Department of Civil Engineering, IIT, Chennai etc. and some private manufacturers having in-house R&D centres engaged in sound transmission loss testing in frequency range 100 Hz to 4 kHz. Also, there are many international manufacturing units that have established in recent years in India for development and installation of sandwich dry wall constructions and other acoustical materials for noise abatement and control. However, the concept of measurement uncertainty associated with reporting of *SNQ* i.e. *STC* and R_w is at a very primitive stage. The problem is much aggravated as there has been no such participation in international round robin exercise, as a result of which there is no exact estimate of reproducibility component for calculating the measurement uncertainty. The present work thus provides a retrospective view of calculating the measurement uncertainty in sound transmission loss testing and *SNQ* based on the review of previous studies conducted in European continent especially in PTB, Germany; NRC Canada and recommendations of ISO 12999-1 standard. It is envisaged that the work shall be helpful for the Indian laboratories to understand the methodology and concept behind reporting the uncertainty of measurements until the results of participation in an international round robin exercise are not established.

2. Measurement Uncertainty

The uncertainty estimation is not an easy procedure as reported by Michalski et al. [16], since it is difficult to identify all the sources of uncertainty related to the measurand and a methodology to evidence its metrological confidence should also be applied. Reproducibility is the most important quantity to be evaluated for measuring the

uncertainty. Goydke described the reproducibility value R as: $R = 2.8\sqrt{s_r^2 + s_l^2}$ where in s_r^2 is the mean of within-laboratory variances taken over all participating laboratories and s_l^2 is between-laboratory variances taken over all participating laboratories [17]. Repeatability is the condition of measurement that includes the same measurement procedure, same operator, same measuring system, same location (i.e. laboratory) and replicate measurements over short period of time [6, 18]. The reproducibility is the value below which the absolute difference between two single test results obtained with the same method on identical test material in a different laboratory may be expected to lie with a probability of 95 % [17]. The use of reproducibility values means to characterize precision with only one single value having in view worst case situations and looking to the maximum variability in the test results [17]. The sound transmission loss is primarily affected by in-homogeneity of sound field in the reverberation chamber, background noise in the receiving room, absorption characteristics of receiving room, accuracy and precision associated with reverberation time measurements. The factors affecting the measurement uncertainty in sound insulation or sound transmission loss characteristics are assimilated in a cause and affect analysis diagram after review of previous studies [10–27] as shown in Fig. 1. Thus, various factors like different sizes or aspect ratios of test openings, different loss factors of test opening, different room geometries, different boundary conditions and remaining flanking transmission are the contributing factors towards the uncertainty estimation in sound transmission loss measurements [6]. Significant differences are observed in sound transmission loss when measured in different laboratories especially at low frequencies [13, 25–27]. The recent investigations of Wittstock [28] whereby the realistic values of standard deviation of reproducibility are derived using the results of many inter-laboratory tests is the best estimate for assessment of reproducibility in sound transmission loss. These values are published in ISO 12999-1 and are recommended to be the best estimates for the uncertainty of sound insulation measurements one can obtain today and it is proposed not to distinguish between the different constructions as light weight or heavy weight for uncertainty evaluation. The behavior of different types of test specimens is found to be similar in general even though some types of test specimens show slightly larger or smaller uncertainties than the average value in some frequency ranges. The values recommended in ISO 12999-1 are recommended to be used by laboratories, consultants and manufacturers. The measurement situation is referred as situation ‘A’ in ISO 12999-1, whereby the measurand is defined by the relevant part of ISO 10140 including all additional requirements and thus measurement results obtained in another test facility comply with this definition.

Thus, In Indian scenario, for testing laboratories engaged in sound transmission loss testing, the standard deviation of reproducibility values recommended in ISO 12999-1 (Fig. 2) can be used as it and claimed by laboratories as the measurement uncertainty in sound transmission loss testing. However, for claiming these uncertainty values, the standard recommends that the maximum standard deviation of repeatability should be less than the values described in Fig. 2. Eventually, this implies that all these laboratories have the same calibration and measurement capabilities irrespective of the size of the reverberation chambers, state of diffusion etc. Thus, for the testing laboratories in India, these values can be claimed provided:

- the reverberation chambers have adequate diffusion particularly in the low frequency ranges, reverberation time (T) ranging between, $1 \leq T \leq 2(V/50)^{2/3}$, where V is volume of reverberation chamber,
- the background sound pressure level in the receiving room should be at least 10 dB lower than the measured noise level in the receiving room,
- the structural isolation between the source and receiving room should be sufficient for suppression of flanking transmission,
- the measurement system including the microphones and analyzer is traceable to the national or international standards of sound pressure [29–32].

In case of deviation from any of these criteria's, the uncertainty contribution due to that deviation must be accounted for in the final uncertainty budget as per Guide to Expression of Uncertainty in Measurement, GUM [33] apart from the reproducibility values recommended in ISO 12999-1 to claim the final uncertainty in sound transmission loss testing. Also, the measurement considerations e.g. number of loudspeaker positions ($N \geq 2$; $N \geq (\frac{s_l}{\sigma})^2$, where s_l is the standard deviation of difference in levels and σ_l is prescribed maximum standard deviation of mean value for N loudspeaker positions e.g. for 100 Hz, σ_l is 1.4 dB and for 125 Hz, σ_l is 1.2 dB) with regard to excitation of room modes, the recommended maximum standard deviation from mean value of measured level difference for N loudspeaker positions should be in conformity to ISO 10140-5 [7].

The pre-requisite for the lowest levels of uncertainty associated with the sound transmission loss measurements is the high diffusivity in the reverberation chambers which is achieved by non-rectangular geometry, room dimensions whose ratio's are not small whole numbers, and the addition of stationary or rotary diffusers within the chamber [34]. ISO 3741 [35] recommends the maximum admissible standard deviation must not exceed the values shown in Fig. 3. The standard deviation of repeatability values of sound pressure level measurements conducted in the

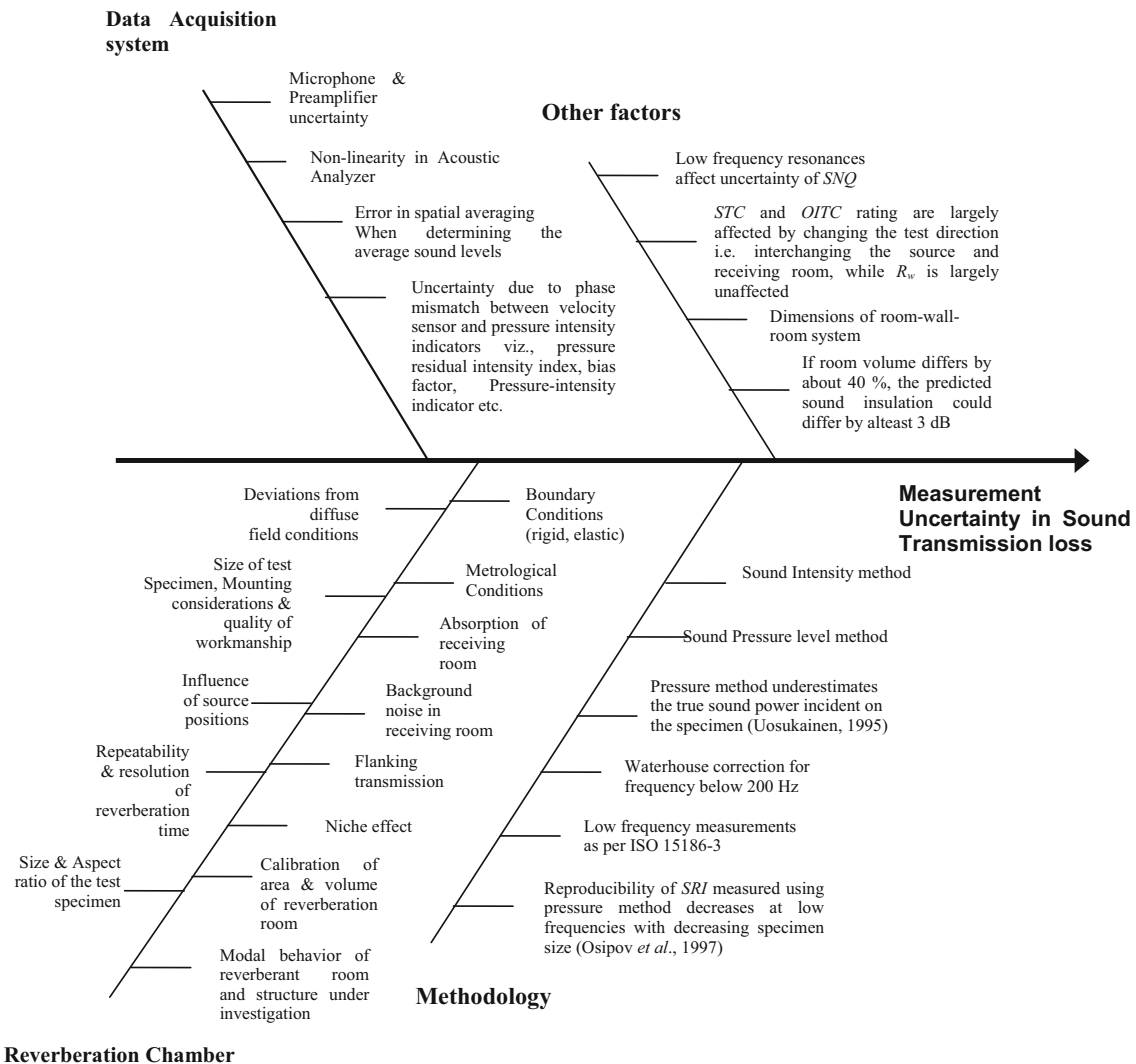
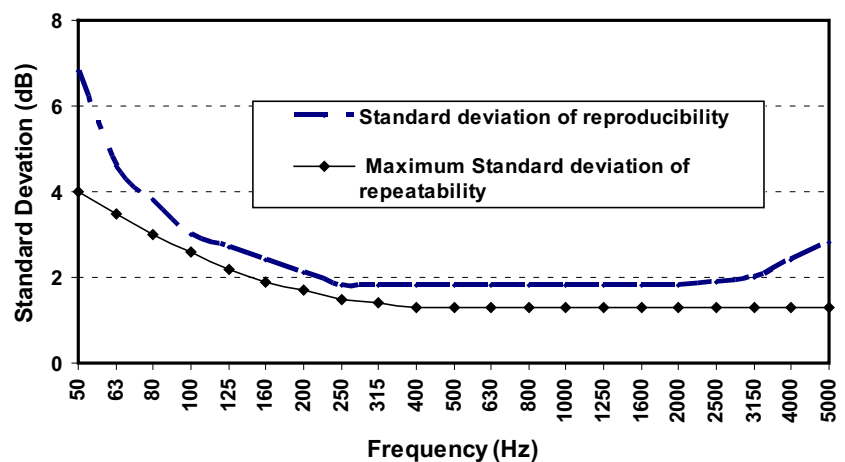


Fig. 1 Cause-and-Effect analysis diagram for factors affecting measurement uncertainty in sound transmission loss measurements

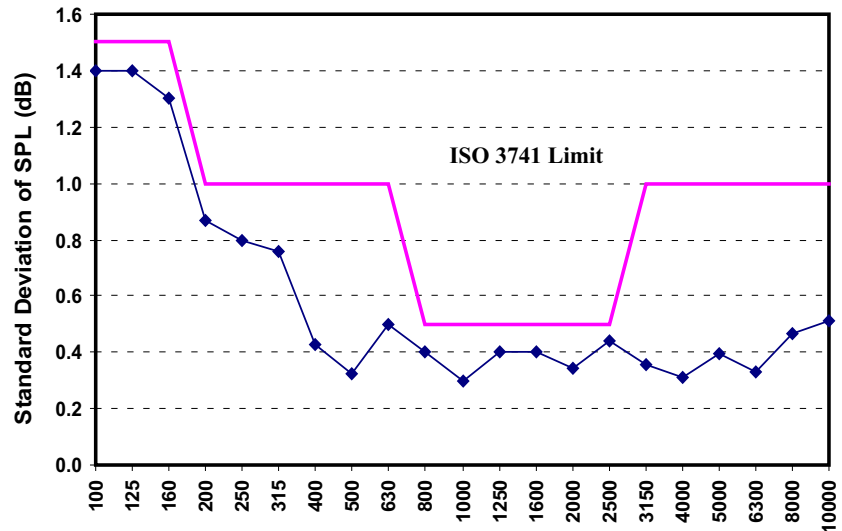
Fig. 2 Standard deviation of reproducibility, $\sigma_{R,i}$ and maximum standard deviation of repeatability recommended by ISO 12999-1:2014 [6]



reverberation chambers at NPL is compared with the recommended maximum value by ISO 3741 in Fig. 3. The construction details and other aspects pertaining to

diffusivity of reverberation chambers of NPL is discussed in details in Refs. [36, 37]. Other qualifying tests such as the measurement of variation in decay rate i.e. standard

Fig. 3 Standard deviation of sound pressure level measured in various frequencies (in Hz) in 1/3rd octave band at varied positions in reverberation room



deviation of decay rate divided by the average decay rate as described by the ASTM C423 (2009) standard and calculation of the total confidence interval (CI_{tot}) quantifier for coupled reverberation chambers as described by ASTM E90 may be exercised by Indian laboratories to ascertain the diffusivity of the reverberation room [38–40]. These investigations shall be helpful in reducing the measurement uncertainty in sound transmission loss measurements of acoustical materials in reverberation chambers [41–43].

3. Uncertainty in $SNQs$

3.1. Uncertainty in $SNQs$ in Conventional Frequency Range of 100 Hz to 4 kHz

The single-number quantities ($SNQs$) i.e. STC and R_w (C, C_{tr}) are widely used in building acoustics for characterizing the sound transmission loss value. The uncertainty calculation for $SNQs$ has been clearly specified in Wittstock (2007) work and ISO 12999-1. Two specific cases have been recommended for uncertainty calculations viz., one pertaining to no correlation between sound reduction indices in the 1/3rd octave band as [4–6] and other under the assumption of full positive correlation between the one-third octave band insulation. The uncertainty is calculated for no correlation between the 3rd octave bands as [6]:

$$u(R_w + C) = \sqrt{\sum_{i=1}^N \left[\frac{10^{(L_{ij}-R_i)/10dB}}{\sum_i 10^{(L_{ij}-R_i)/10dB}} \right]^2 u^2(R_i)} \quad (2)$$

where i is the index of third octave band, L is the reference spectrum as defined in ISO 717 and R is the measured sound reduction index in frequency band i and $u(R_i)$ is the

uncertainty of the sound reduction index. The uncertainty of R_w is calculated under the assumption of full positive correlation between the third octave band insulations by adding or subtracting the uncertainties in one-third octave band. The single-number value is determined twice for this case. In first case, all the uncertainties are added to the measured sound insulations in the one-third octave bands yielding the sum of single-number value and the standard uncertainty as:

$$R_w + C + u(R_w + C) = -10 \log \sum_i 10^{(L_i - R_i + u(R_i))/10dB} dB \quad (3)$$

In the second case, all uncertainties are subtracted from the measured sound insulation in the one-third octave bands yielding the difference between the single-number value and the standard uncertainty as:

$$R_w + C - u(R_w + C) = -10 \log \sum_i 10^{(L_i - R_i - u(R_i))/10dB} dB \quad (4)$$

The final uncertainty is thus estimated as [4–6]:

$$u(R_w) = \left(\frac{R_w + C + u(R_w + C) - [R_w + C - u(R_w + C)]}{2} \right) \quad (5)$$

Wittstock [4] derived an approximation for the uncertainty of weighted sound reduction index based on the relationship between value of the shifted reference curve at 500 Hz and sum of negative differences between the measured sound reduction curve and reference curve. Another important recommendation of the Wittstock study was to adopt the procedure of shifting the reference curve in steps of 0.1 dB instead of 1 dB as has been traditionally done so as to report the weighted sound reduction index,

R_w with one decimal digit. The newer version of ISO 717-1 [1] also recommends single-number evaluation in steps of 0.1 dB for the expression of uncertainty. Also, it was proposed that uncertainty of building acoustic quantities are typically based on round robin results rather than according to the method of GUM [4, 33]. It was proposed that measurand is inadequately defined for the estimation of the uncertainty of the calculated sound reduction index using the method of GUM. In case of full correlation (or positive correlation) between the frequency bands, the uncertainty is calculated as [4–6]:

$$u(R_w + C_j) = \left[\frac{-10 \log \sum_i 10^{(L_{ij} - R_i + u(R_i))/10} + 10 \log \sum_i 10^{(L_{ij} - R_i - u(R_i))/10}}{2} \right] \quad (6)$$

Thus, in present study, the uncertainty of calculated sound reduction index is calculated using the standard deviation of reproducibility described in ISO 12999-1:2014, wherein $u(R_i) = \sigma_{R,i}$ where $\sigma_{R,i}$ is standard deviation of reproducibility in the i th 1/3rd octave bands as shown in Fig. 2 and R_i is sound transmission loss value for i th octave band. It may be noted here that $\sigma_{R,i}$ corresponds to situation ‘A’ described in ISO 12999-1:2014 [6] which is the standard deviation of reproducibility as determined by inter-laboratory measurements. It is applicable to all the measurement results that are obtained in another test facility or building.

The expanded uncertainty of the single-number quantity is calculated as: $U(X) = k \times u(X)$ where $u(X)$ is standard uncertainty determined, k is the coverage factor and U is the expanded uncertainty calculated for a given confidence level for the two-sided test. ISO 12999-1 recommends that the chosen coverage factor shall be reported together with the information whether one sided or two sided intervals have been used. The present study utilizes $k = 1$ value for uncertainty calculations for a confidence interval of 1σ i.e.

68 % (two sided) in a Gaussian or normal distribution curve.

These equations are thus utilized to evaluate the standard uncertainty in SNQ of various building elements. Figure 4 shows the case study of double glazing with 85 mm air gap tested in reverberation chambers at NPL as discussed in Refs. [44, 45]. The corresponding value of expanded uncertainty calculated for a given confidence level for a two-sided test in dB ($k = 1$) determined in accordance with ISO 12999-1 is listed in Table 1. As an illustrative example, the weighted sound reduction index for 8 mm double glazing with 85 mm air gap is calculated as 43.7 ± 2.2 dB ($k = 1$, two sided). It may be noted here that these equations are utilized in a similar way to calculate the standard uncertainty for STC , R_w , $R_w + C$ and $R_w + C_{tr}$. Figure 5 shows another case study of the sound transmission loss characteristics of massive concrete constructions tested by Warnock et al. [46] and two sandwich dry wall constructions tested by Halliwell et al. [47]. The corresponding value of expanded uncertainty in dB ($k = 1$, two sided) determined in accordance with ISO 12999-1 is enlisted in Table 2. It can be observed that for massive concrete constructions, the uncertainty calculated in SNQ s is less as compared to sandwich gypsum constructions. These observations also suggest that the expanded uncertainty ($k = 1$, two sided) calculated for STC and R_w is not much different as observed in Tables 1 and 2. Also, the results are consistent with the Wittstock (2007a, 2015b) and Mahn et al. [48] studies in terms of arranging the SNQ s in increasing order of uncertainty as:

$$u(R_w) < u(R_w + C) \leq u(R_w + C_{tr}) \quad (7)$$

3.2. Uncertainty in SNQ s in Extended Frequency Range of 50 Hz to 5 kHz

The newly proposed airborne sound insulation (SNQ s) by Scholl et al. 2011 calculated from sound transmission loss

Fig. 4 Sound Transmission loss characteristics of various double glazed windows with 85 mm air gap tested in reverberation chambers [45]

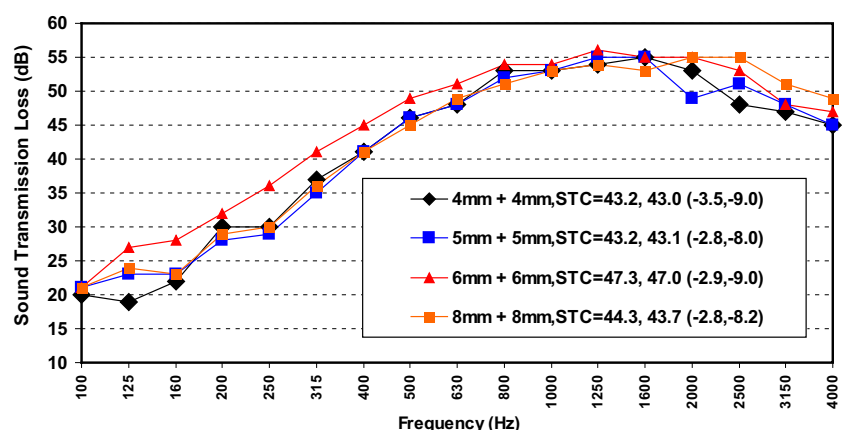
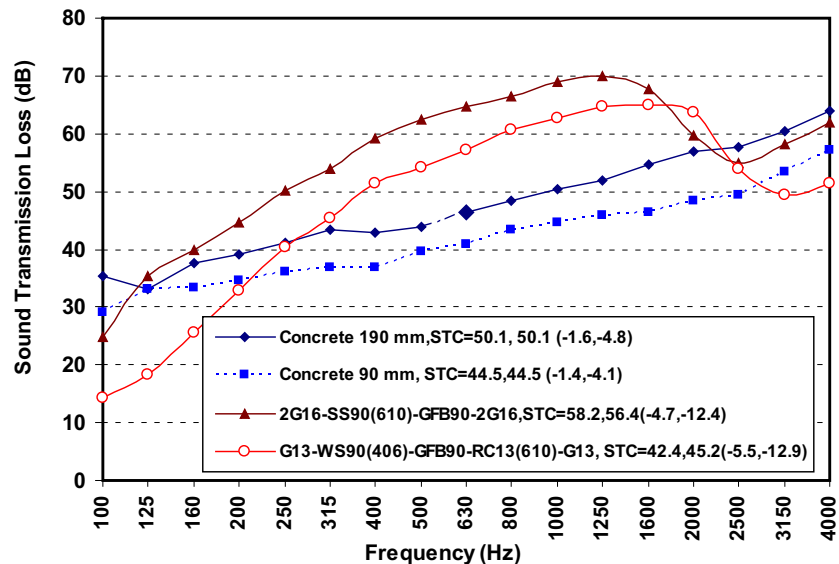


Table 1 Expanded Uncertainty in dB ($k = 1$, two sided) calculated for a given confidence level (68 %) for the two sided test in accordance with ISO 12999-1 for SNQ for various double glazing tested

Correlation between frequency bands	$U(R_w)$ (dB)	$U(STC)$ (dB)	$U(R_w + C)$ (dB)	$U(R_w + C_{tr})$ (dB)
4 mm				
No correlation	0.9	0.9	1.1	1.3
Positive correlation	2.3	2.2	2.4	2.6
5 mm				
No correlation	0.8	0.8	0.9	1.1
Positive correlation	2.1	2.1	2.2	2.4
6 mm				
No correlation	0.9	0.7	1.0	1.6
Positive correlation	2.3	2.1	2.4	2.7
8 mm				
No correlation	0.8	0.8	1.0	1.2
Positive correlation	2.2	2.1	2.3	2.5

Fig. 5 Sound Transmission loss characteristics of massive concrete constructions tested by Warnock et al. and dry wall constructions tested by Halliwell et al. [46, 47]**Table 2** Expanded Uncertainty in dB ($k = 1$, two sided) calculated for a given confidence level (68 %) for the two sided test in accordance with ISO 12999-1 for SNQ for dry wall and concrete constructions

Correlation between frequency bands	$U(R_w)$ (dB)	$U(STC)$ (dB)	$U(R_w + C)$ (dB)	$U(R_w + C_{tr})$ (dB)
Concrete 190 mm				
No correlation	0.6	0.6	0.6	0.7
Positive correlation	1.9	1.9	2.0	2.2
Concrete 90 mm				
No correlation	0.5	0.6	0.6	0.7
Positive correlation	1.9	1.9	1.9	2.1
2G16-SS90(610)-GFB90-2G16				
No correlation	1.6	1.6	1.9	2.5
Positive correlation	2.6	2.1	2.7	2.9
G13-WS90(406)-GFB90-RC13 (610)-G13				
No correlation	1.6	1.6	1.7	2.1
Positive correlation	2.7	2.5	2.8	2.9

measurements in the frequency range from 50 Hz to 5 kHz for rating of sound insulation in buildings and of building elements in many ways is simpler than the existing one [49, 50]. The transition from the old reference curve to system based on A-weighted living and traffic noise spectrum is essentially required to understand the behavior of a building material towards various noise sources. The $SNQs$ are calculated from the sound transmission loss in frequency range 50 Hz to 5 kHz as [49]:

$$X = 10 \log \left[\frac{\sum_i 10^{(L_i/10)}}{\sum_i 10^{(L_i - R_i)/10}} \right] \quad (8)$$

where X is the calculated single-number quantity, i is the index of third octave band, L is the level of reference spectrum and R is the sound reduction index. Three different reference spectrums for airborne sound insulation have been recommended for traffic noise sound reduction index, R_{traffic} (or $R_w + C_{\text{tr},50-5k}$) and the living noise sound reduction index, R_{living} (or $R_w + C_{50-5k}$) measured in 1/3rd octave bands from 50

to 5 kHz and the speech sound reduction index, R_{speech} measured in frequency range 200 to 5 kHz. Figure 6 shows the illustrative example of sandwich gypsum constructions tested by Halliwell et al. [47] in extended frequency range of 50 Hz to 5 kHz and value of corresponding $SNQs$ as proposed by Scholl et al. The corresponding value of expanded uncertainty in dB ($k = 1$, two sided) determined in accordance with ISO 12999-1 for all the $SNQs$ including that calculated from sound transmission loss in conventional frequency range and extended frequency range of 50 Hz to 5 kHz is listed in Table 3. It can be observed that these results are consistent with Mahn et al. [48] observations whereby the uncertainties (u) calculated considering correlated frequency bands (correlation coefficient, $r = +1$) in proposed $SNQs$ could be ranked as:

$$u(R_{717})_{r=+1} \leq u(R_{\text{living}})_{r=+1} \leq u(R_{\text{traffic}})_{r=+1} \quad (9)$$

where in R_{717} is single-number quantity calculated using reference spectrum of R_{living} in frequency range 100 Hz to 3.15 kHz.

Fig. 6 Effect of low frequency sound transmission loss characteristics on uncertainty ($k = 1$, two sided) in R_{traffic} and R_{living} for sandwich gypsum constructions tested by Halliwell et al. [47]

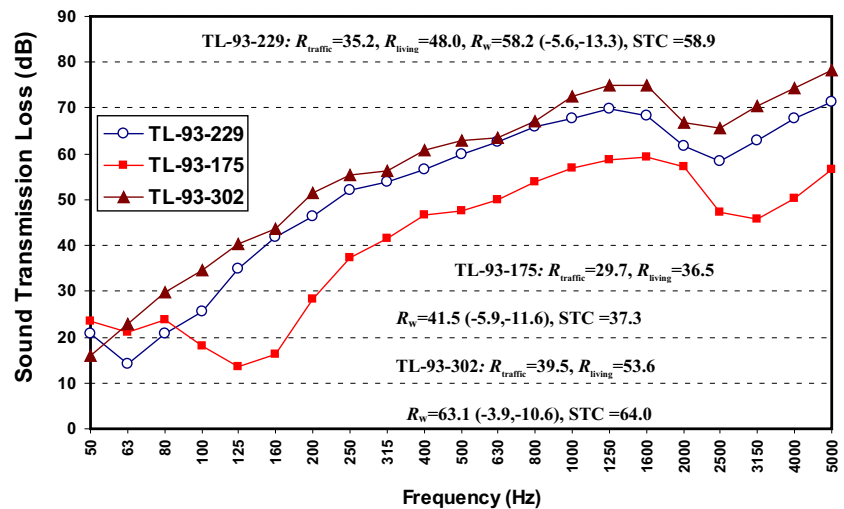


Table 3 Expanded Uncertainty in dB ($k = 1$, two sided) calculated for a given confidence level (68 %) for the two sided test in accordance with ISO 12999-1 for SNQ for various sandwich dry wall constructions tested by Halliwell et al.

Correlation between frequency bands	$U(R_w)$ (dB)	$U(STC)$ (dB)	$U(R_w + C)$ (dB)	$U(R_w + C_{tr})$ (dB)	$U(R_{\text{living}})$ (dB)	$U(R_{\text{traffic}})$ (dB)
TL-93-229						
No correlation	1.7	0.9	1.9	2.5	2.4	2.9
Positive correlation	2.6	2.2	2.7	2.9	4.0	4.5
TL-93-175						
No correlation	1.5	1.5	1.5	1.5	1.5	1.4
Positive correlation	2.5	2.5	2.5	2.6	2.6	2.8
TL-93-302						
No correlation	1.1	0.9	1.3	1.9	3.3	4.6
Positive correlation	2.4	2.2	2.5	2.8	5.1	5.9

4. Uncertainty Calculations Affected by Low Frequency Insulation

The uncertainties are affected by low frequency resonances occurring in sound transmission loss characteristics of partition panels. Poor low frequency sound insulation inculcates higher uncertainty in SNQ s of building elements as these are sensitive to the low frequency sound insulation [51, 52]. This is illustrated in Fig. 7 which shows the sound transmission loss characteristics of two sandwich gypsum constructions tested by Halliwell et al. It can be observed from Table 4 that the expanded uncertainty ($k = 1$, two sided) in R_w for partition panel TL-93-425 is higher by 0.4 dB for positive correlation case and 1.0 dB for no correlation as compared to TL-93-298. This difference in uncertainty is attributed to the poor sound transmission loss at low frequencies. This fact is substantiated on considering the sound transmission loss characteristics of sandwich concrete constructions tested by Warnock et al., 1990 as shown in Fig. 8. It can be observed from Table 4 that for partition panel TL-88-356 with comparative higher sound insulation at 100 Hz as compared to the other two partition panels, the uncertainty calculated in R_w ($k = 1$, two sided) is less. For the partition panel, TL-88-357; the sound transmission loss at low frequency 100 Hz and 125 Hz is higher as compared to TL-88-360, and thereby uncertainty calculated in R_w is less. The poor sound transmission loss characteristics of TL-88-360 at 100 Hz and 125 Hz thus cause an increase in the uncertainty value calculated. It is observed that uncertainty in R_w is 0.6 dB higher for positive correlation and 1.4 dB higher for no correlation in comparison to partition panel TL-88-357. It may be noted here that these observations can't be generalized as it can be observed from Fig. 5 showing the sound transmission loss characteristics of two sandwich dry wall constructions of 16 and 13 mm gypsum board tested by Halliwell et al.

[47]. It can be observed that 13 mm gypsum board dry wall construction although has poor sound transmission loss characteristics at low frequencies, yet the uncertainty in SNQ for both the partition panels is same. However, in majority of cases, the uncertainty values in SNQ are higher for those partition panels having poor low frequency sound transmission loss especially at 100 and 125 Hz [53].

In the extended frequency range of 50 Hz to 5 kHz also, a similar effect is observed as shown in Fig. 6. The sound transmission loss characteristics of sandwich gypsum constructions is analyzed to evaluate the uncertainty in SNQ viz., R_{living} and R_{traffic} in frequency range 50 Hz to 5 kHz. The sound transmission loss characteristic at low

Table 4 Expanded Uncertainty in dB ($k = 1$, two sided) calculated for a given confidence level (68 %) for the two sided test in accordance with ISO 12999-1 for SNQ for sandwich dry wall constructions and concrete constructions

Correlation between frequency bands	$U(R_w)$ (dB)
TL-93-298	
No correlation	0.9
Positive correlation	2.3
TL-92-425	
No correlation	1.9
Positive correlation	2.7
TL-88-357	
No correlation	0.8
Positive correlation	2.1
TL-88-360	
No correlation	2.2
Positive correlation	2.7
TL-88-356	
No correlation	0.6
Positive correlation	1.9

Fig. 7 Effect of low frequency sound transmission loss characteristics on uncertainty ($k = 1$, two sided) in R_w for sandwich gypsum constructions tested by Halliwell et al. [47]

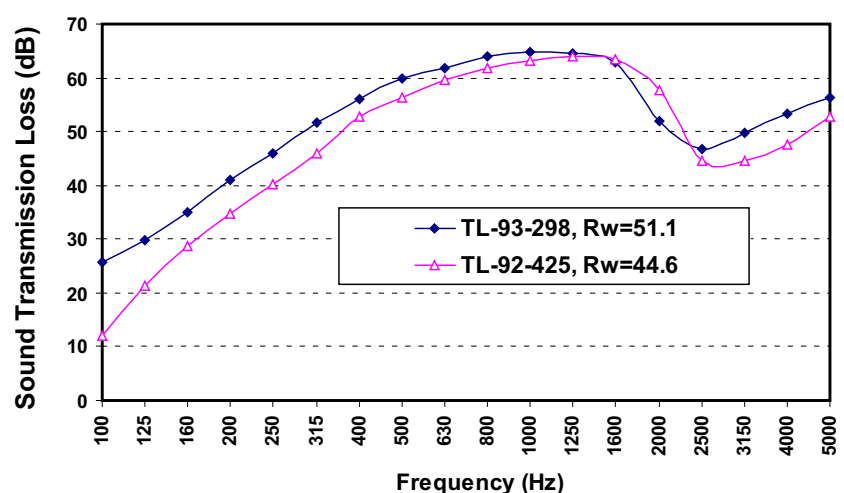
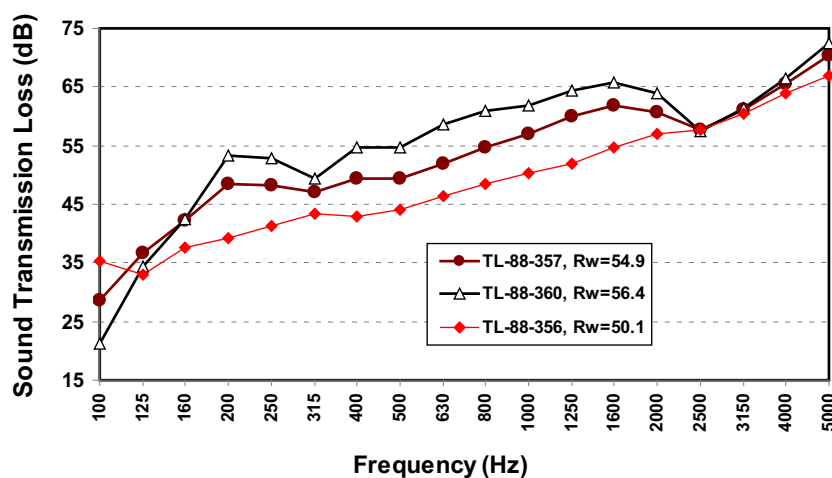


Fig. 8 Effect of low frequency sound transmission loss characteristics on uncertainty ($k = 1$, two sided) in R_w for sandwich concrete constructions tested by Warnock et al. [46]



frequency is pivotal in uncertainty calculations. Partition panel TL-93-302 having less insulation at 50 Hz in comparison to the other two partition panels as shown in Fig. 6 shows a higher uncertainty in R_{traffic} for no correlation and for positive correlation. It can be also observed that for partition panel TL-93-229 having a sharp resonance dip at 63 Hz, the uncertainty calculated is higher. Thus, these observations reveal that uncertainties are affected by poor low frequency sound insulation at 50 and 63 Hz. These observations reveal that uncertainty values are higher for partition panels having poor low frequency sound insulation particularly when mass-air-mass resonances or the flexural resonances are encountered. It may be noted here that investigations on analyzing the uncertainties in SNQ for partition panels having high frequency coincidence dip reveals that the high frequency coincidence dip has no effect on the uncertainty calculations.

5. Conclusions and Recommendations

The paper presents a retrospective view of factors affecting the measurement uncertainty in airborne sound insulation and (SNQ s) used widely in building acoustics. A case study of window glazing, sandwich drywall construction and massive concrete constructions is discussed to calculate the measurement uncertainty in SNQ in conventional frequency range of 100 Hz to 4 kHz and also in extended frequency range of 50 Hz to 5 kHz. The standard deviation of reproducibility values described in ISO 12999-1:2014 standard have been recommended in recent studies conducted at PTB, Germany to be the best estimate for the uncertainty of sound insulation measurements one can obtain today.

The following conclusions and recommendations can be derived from the present study as follows:-

- In Indian scenario, the standard deviation of reproducibility values described in ISO 12999-1 standard would be the best uncertainty for testing laboratories engaged in sound transmission loss testing provided the standard deviation of repeatability is less than the recommended values described in Fig. 2. However, these uncertainties should be claimed by laboratories in India only when there is perfect diffusion in reverberation chambers in the measurement frequency range, instrumentation used is traceable to the national standards, flanking transmission is minimal and the sound transmission loss measurements are conducted as per ISO 10140-2.
- The present investigations highlight the significance of correlation effects on uncertainty calculations of SNQ as reported by Wittstock et al. 2007. Thus, the maximum uncertainty calculated under the assumption of positive correlation between 1/3rd octave frequency bands may be reported in routine testing by laboratories in India particularly when round robin exercise can't be followed for routine testing of the partition walls.
- The present investigations also show that in majority of cases for the partition panels having poor sound insulation characteristics at low frequencies especially at 100 and 125 Hz, the uncertainty in weighted sound reduction index, R_w is higher. In case of SNQ calculated using sound transmission loss values in frequency range 50 Hz to 5 kHz, the uncertainty values are higher for partition panels having low frequency sound insulation at 50 and 63 Hz. Thus, it is obvious that the low frequency mass-air-mass and flexural resonances inculcate a higher uncertainty in SNQ s for building elements.
- The present study is consistent with Wittstock (2007) and Mahn et al., 2012 observations on the fact that the weighted sound reduction index, R_w has the smallest

uncertainty. The inclusion of spectrum adaptation terms increases the uncertainty in SNQ .

The present study should be thus helpful for Indian laboratories engaged in sound transmission loss testing to clearly understand the concept and methodology of calculating the uncertainty in SNQ s. Also, it shall be helpful for designers, architects, manufacturers of building materials and researchers for comparison of sound insulation properties of acoustical materials in terms of single-number quantity and its associated uncertainty. It is imperative to adopt the strategy recommended in ISO 12999-1 in Indian scenario particularly with growing international trade in building materials and technology and recognition as well as acceptance of testing results of Indian laboratories across the globe. It is evident that the low frequency sound transmission loss is the most affected due to deviations from diffuse field conditions, variability in sound pressure levels and reverberation time measurements. Thus, efforts should be focused to ensure that the measurement uncertainty in sound pressure level and reverberation time is reduced in low frequency range.

Future work focused on the participation in inter-laboratory comparisons in India with other laboratories shall inculcate a confidence and shall be instrumental in ascertaining the reproducibility of the sound transmission loss measurements in the entire measurement frequency range. Also, the present study considers only the sound pressure approach and its associated reproducibility in sound transmission loss measurements. Future study shall be concentrated on comparison of measurement uncertainty in sound transmission loss and SNQ comparing the sound pressure and sound intensity approach.

Acknowledgments Authors would specially acknowledge the NRC Canada reports of R.E. Halliwell (*IR 761*, 1998) and A. C. C. Warnock (*IR 586*, 1990) whose valuable data has been used for uncertainty calculations in the paper. Authors are thankful to some laboratories in India engaged in sound transmission loss testing for sharing their details and uncertainty calculations. Author also thanks Dr. Volker Wittstock, Head of Applied Acoustics Working Group, 1.72, PTB Germany and Dr. Arne Dijckmans, Department of Civil Engineering, KU Leuven, Belgium for some fruitful e-mail conversations pertaining to the topic. Part of the work was presented in Smart Technologies for Mechanical Engineering (STME 2013) Conference held at Delhi Technological University, Delhi, India, during 24th to 26th October, 2013.

Appendix

Details of the sandwich concrete and dry wall constructions used.

Nomenclature	STC	Description of sandwich configuration
Concrete constructions tested by Warnock [46] report No. IR 586		
TL-88-357	55	BLK190_WFUR40_GFB38_G16
TL-88-360	58	G16_GFB38_WFUR40_BLK190_WFUR40_G16
TL-88-356	50	BLK190
TL-88-447	44	BLK90
BLK190 is 190 mm concrete block, BLK90 is 90 mm concrete block, WFUR is 40 mm wood strapping, GFB is glass fibre batts inserted in cavity		
Sandwich gypsum constructions tested by Halliwell et al. [47] Report No. IR 761		
TL-93-298	51	G16_SS150(610)_GFB150_G16
TL-92-425	45	G13_SS90(406)_GFB90_G13
TL-93-229	59	G13_WS140(406)_GFB90_2G13
TL-93-175	43	G13_WS90(406)_CFL90_2G13
TL-93-302	64	2G16_SS65(610)_GFB65_AIR20_SS65(610)_GFB65_2G16
TL-92-369	58	2G16_SS90(610)_GFB90_2G16
TL-93-128	42	G13_WS90(406)_GFB90_RC13(610)_G13
G13 is single layer of 13 mm gypsum board, G16 is single layer of 16 mm type X gypsum board, SS 150 is 150 mm steel studs at 610 mm on centre, WS90 (406) means 90 mm wood studs at 406 mm on centre, GFB90 is 90 mm of glass fibre insulation in cavity, RC13(610) is resilient channels at 610 mm on centre		

References

- [1] ISO 717-1, Acoustics-Rating of sound insulation in Buildings and of Building elements-Part 1: Airborne sound insulation (2013).
- [2] R. Öqvist, F. Ljunggren, and A. Ågren, On the uncertainty of building acoustic measurements: case study of a cross-laminated timber construction, *Appl. Acoust.* **73** (2012) 904–912.
- [3] E. Gerresten, Interpretation of uncertainties in acoustic measurements in buildings, *Noise Control Eng. J.*, **55**(11) (2007) 50–54.
- [4] V. Wittstock, On the uncertainty of single-number quantities for rating airborne sound insulation, *Acust. United Acta Acust.*, **93** (2007) 375–386.
- [5] V. Wittstock, On the calculation of uncertainties of single number rating in building acoustics, 19th International congress on acoustics, Madrid, 2–7 September, (2007) pp 1–6.
- [6] ISO 12999-1:2014. Acoustics-determination and application of measurement uncertainties in building acoustics: Part 1: sound insulation, International organization for standardization, Geneva.
- [7] ISO 10140: Acoustics-laboratory measurement of sound insulation of building elements (all parts); Part 1-application rules for specific products, part 2-measurement of airborne sound insulation, part 3-measurement of impact sound insulation, part 4- measurement procedures and requirements and part 5-requirement for test facilities and equipments, 2010.
- [8] ISO 15186-1, Acoustics-Measurement of sound insulation in buildings and of building elements using sound intensity-Part 1: Laboratory measurements, 2000.

- [9] D.B. Pedersen, J. Roland, R. Götz, and W. Maysenhölder, Measurement of the low-frequency sound insulation of building components, *Acta Acust. United Acust.* **86** (2000) 495–505.
- [10] V. Hongisto, J. Keränen, M. Kylliäinen, and J. Mahn, Reproducibility of the present and the proposed single-number quantities of airborne sound insulation, *Acta Acust. United Acust.*, **98** (2012) 811–819.
- [11] R.V. Waterhouse, Interference patterns in reverberant sound fields, *J. Acoust. Soc. Am.*, **27**(2) (1955) 247–258.
- [12] S. Uosukainen, On the use of the Waterhouse correction, *J. Sound Vib.*, **186** (1995) 223–230.
- [13] A. Dijkmans and G. Vermeir, Numerical investigations of the repeatability and reproducibility of laboratory sound insulation measurements, *Acta Acust. United Acust.*, **99** (3) (2013) 421–432.
- [14] ISO 15186-3:2002: Acoustics-Measurement of sound insulation in buildings and of building elements using sound intensity, Part 3: Laboratory measurements at low frequencies.
- [15] ISO 140-3:1995: Acoustics—measurement of sound insulation in buildings and of building elements, Part 3: laboratory measurements of airborne sound insulation of building elements.
- [16] R. Michalski, M. Nabuco and G. Ripper, Uncertainty investigations of field measurements of airborne sound insulation, XIX IMEKO World Congress, Fundamental and Applied Metrology, September, 6–11, 2009, Lisbon, Portugal.
- [17] H. Goydke, Analysis of problems to express uncertainties of building acoustic measurements, Proceedings of 17th ICA, Rome, September, 2–7, 2001.
- [18] ISO/IEC Guide 99, International vocabulary of metrology-basic and general concepts and associated terms (VIM).
- [19] A.C.C. Warnock, Forward and reverse transmission loss measurements, The 33rd international congress and exposition on noise control engineering, proceedings of internoise, Prague, (2004) pp 22–25.
- [20] V. Wittstock, Uncertainties in applied acoustics-determination and handling, proceedings of NAG/DADA 2009, international conference on acoustics, DEGA, Rotterdam, The Netherlands, (2009) pp 22–29.
- [21] R.R. Wareing, J.L. Davy, and J.R. Pearse, Effects of sample construction, sample size and niche depth on measured sound transmission loss, Proceedings of Internoise 2014, 16–19th November (2014).
- [22] N. Garg, T.K. Saxena, A. Kumar, and S. Maji, Uncertainty evaluation and implications of spectrum adaptation terms in determining the airborne sound insulation in building elements, *Noise Control Engr. J.*, **62** (5), 333–343.
- [23] T. Bravo and S.J. Elliott, Variability of low frequency sound transmission measurements, *J. Acoust. Soc. Am.*, **115** (6) (2004) 2986–2997.
- [24] T. Wszolek, Uncertainty of airborne sound insulation index measurement in laboratory condition, *Acoustic 08*, Paris, 4486–4489.
- [25] T. Kihlman, A.C. Nilsson, The effect of some laboratory design and mounting conditions on reduction index measurements, *J. Sound Vib.*, **24** (3) (1972) 349–364.
- [26] W. Kropp, A. Pietrzyk, and T. Kihlman, On the meaning of the sound reduction index at low frequencies, *Acta Acust.*, **2** (1994) 379–392.
- [27] A. Osipov, P. Mees, and G. Vermier, Low frequency airborne sound transmission through single partitions in buildings, *Appl. Acoust.*, **53** (1997) 273–288.
- [28] V. Wittstock, Determination of measurement uncertainties in Building acoustics by Interlaboratory tests, Part 1: Airborne sound insulation, *Acta Acust. United Acust.*, **101** (2015) 88–98.
- [29] N. Garg, Establishing a traceability chain for sound pressure and vibration amplitude measurements, *NCSLI Meas. J. Meas. Sci.*, (2015) 64–74.
- [30] N. Garg and O. Sharma, Measurement accuracy of secondary standards of sound pressure in comparison to primary standards, *MAPAN- J. Metrol. Soc. India*, **27** (2012) 219–229.
- [31] N. Garg and S. Maji, Analysis of the effect of microphone parameters in reciprocity calibrations using taguchi method, *MAPAN- J. Metrol. Soc. India*, **30**(3) (2015) 179–190.
- [32] N. Garg, A. Kumar, M.A. Sanjid, K.P. Chaudhary, and S. Maji, Reaffirmation of measurement uncertainty in pressure sensitivity determination of LS2P microphones by reciprocity method, *Measurement*, **51** (2014) 281–288.
- [33] ISO/IEC Guide 98-3, Uncertainty of measurement—Part 3: guide to the expression of uncertainty in measurement (GUM, 1995).
- [34] D.T. Bradley, M. Müller-Trapel, J. Adelgren, and M. Vorländer, Effect of boundary diffusers in a reverberation chamber: Standardized diffuse field quantifiers, *J. Acoust. Soc. Am.*, **135** (2014) 1898–1906.
- [35] ISO 3741: Acoustics -Determination of sound power levels and sound energy levels of noise sources using sound pressure-Pre-cision methods for reverberation test rooms, 2010.
- [36] M. Pancholy, A.F. Chhapgar, and O. Sharma, Construction of a reverberation chamber at National Physical Laboratory of India. *J. Acoust Soc India*, **V** (2) (1977) 27–33.
- [37] N. Garg, S. Maji, Vibration induced due to acoustic excitation in diffuse field conditions, *Acoust. Aust.*, **41** (2013) 219–224.
- [38] ASTM C423, Standard test method for sound absorption and sound absorption coefficients by the reverberation room method 2002, ASTM International.
- [39] ASTM E90, Standard test method for laboratory measurement of airborne sound transmission loss of building partitions and elements, ASTM International, West Conshohocken, PA, 2009.
- [40] M. Vercammen, M. Lautenbach, Can we use standard deviation of the reverberation time to describe diffusion in a reverberation chamber? Proceedings AIA-DAGA, 2013, <http://www.peutz.nl/sites/default/files/publicaties/000666.pdf>.
- [41] N. Garg, A. Kumar, and S. Maji, Parametric sensitivity analysis of factors affecting the sound insulation of multi-layered building elements, *Achiev. Acoust.*, **39** (2), (2014) 165–176.
- [42] N. Garg, A. Kumar, and S. Maji, Practical concerns associated with use of single number ratings in describing sound transmission loss properties of partition panels, *Achiev. Acoust.*, **39**(1) 2013 115–124.
- [43] N. Garg, A. Kumar, and S. Maji, Significance and implications of airborne sound insulation criteria in building elements for traffic noise abatement, *Appl. Acoust.*, **74** (2013) 1429–1435.
- [44] M. Singh, K.K. Pujara, and V. Mohanan, Sound transmission through panels-an experimental study, *Indian J. Pure Appl. Phys.*, **39** (2001) 235–239.
- [45] N. Garg, A. Kumar, and S. Maji, Experimental investigations on sound insulation through single, double and triple window glazing for traffic noise abatement, *J. Sci. Ind. Res.*, **78** (2011), 471–478.
- [46] A.C.C. Warnock, Sound transmission loss measurement through 190 mm and 140 mm blocks with added dry wall and through cavity block walls, NRC Canada, Internal Report No. 586, (1990).
- [47] R.E. Halliwell, T.R.T. Nightingale, A.C.C. Warnock, and J.A. Birta, Gypsum board walls: transmission loss data, NRC Report No. IRC-IR-761 (1998).
- [48] J. Mahn and J. Pearse, The Uncertainty of the proposed single number ratings for airborne sound insulation, *Build. Acoust.*, **19**(3) (2012) 145–172.

- [49] W. Scholl, J. Lang, and V. Wittstock, Rating of sound insulation at present and in future. The revision of ISO 717, *Acta Acust. United Acust.*, **97** (2011) 686–698.
- [50] W. Scholl, ISO 16717-Revision of single-number quantities for sound insulation in buildings: state of discussion, *Proceedings of Internoise 2013*, 15th to 18th September, 1–10.
- [51] R.S. Smith, R. Mackenzie, R. Mackenzie, and T. Waters-Fuller, The implications of ISO 717 spectrum adaptation terms for residential buildings, In: *Proceedings of the Institute of Acoustics*, **25** (2003) Pt. 5.
- [52] N. Garg and S. Maji, On analyzing the correlations and implications of single-number quantities for rating airborne sound insulation in frequency range 50 Hz to 5 kHz, *Build. Acoust.*, **22**(1) (2015) 29–44.
- [53] N. Garg, A. Kumar, and S. Maji, Measurement Uncertainty in airborne sound insulation measurements and single-number quantities, *proceedings of international conference on smart technologies for mechanical engineering (STME 2013)*, 24th to 26th October, Delhi Technological University, Delhi, India, (2013) pp 259–266.

Modification in Weighted Clustering Algorithm for Faster Clustering Formation by Considering Absolute Attributes of Mobile Nodes and Greedy Method for Role Selection of Mobile Nodes in MANET

^aVijayanand Kumar, ^bRajesh Kumar Yadav

Department of Computer Science and Engineering, Delhi Technological University, New Delhi, India

Abstract : Wirelessly allocated mobile nodes which are configured in a geographically adjacent to each other can form cluster by applying rules on the mobile nodes. Each cluster family have different members with different assigned roles such as cluster head, cluster members, gateway members and ordinary nodes which can perform roles of any three mentioned roles as the time progresses based on absolute and relative attribute information. Absolute attributes of mobile nodes can be mobility, energy consumed and entropy of the mobile node. Relative attributes can be considered as neighbour information and sum of distances of neighbours etc. Relative attributes are the information based on neighbourhood and absolute information which can be extracted from measuring its own system parameters locally. Weighted clustering scheme uses both the information for calculating weights and delay the clustering formation process. In this paper we choose to apply greedy approach for cluster head selection and absolute weighted information for clustering to reduce the communication round which results in fast clustering formation process.

Keywords—Ad hoc networks, Clustering, Clustering Algorithms, NS-2, Weight Based Clustering, Energy Efficient, Load balancing, Cluster Creation, Cluster Formation, Fast Clustering.

I. INTRODUCTION

Clustering for mobile adhoc network is considered as hierarchical topology which is scalable for mobile nodes. Many clustering scheme has been proposed which can perform better utilisation of network properties such as bandwidth, scalability and stability etc. Network stability depends on the better clustering schemes which use absolute and relative attributes of the mobile nodes. Dynamics of the network depends in the mobile node attributes both absolute and relative. High dynamic nature shows unstable behaviour of the network. Cluster head has been selected which shows low dynamic nature in the network. Figure 1 shows general architecture of cluster with their role defined.

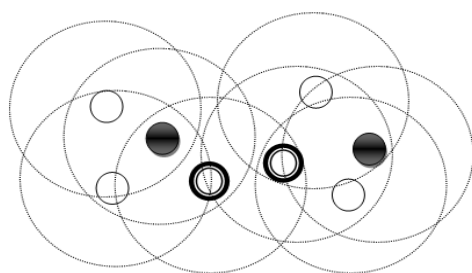


Fig 1: Cluster Architecture

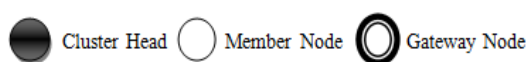


Figure 1 shows mobile nodes with equal communication range and their roles in the network formed after cluster formation process. Communication for clustering delays actual operations such as routing of information, data and packet delivery etc. Faster clustering scheme can minimise the delay and results in optimised network clustering schemes.

Section II explains about the mobile node attributes communication round requirements and uses in the weighted clustering scheme. Section III describes the proposed modification for faster cluster formation process using absolute attributes. Section IV deals with simulation environment and comparative results with the existing weight based clustering algorithms and the conclusion has been made in Section V.

II. RELATED WORK

Weighted Clustering Algorithm [1], depends on absolute and relative attributes of the mobile nodes. Steps for clustering formation for WCA [1] demands communication round for relative attributes such as degree difference and sum of distances. One round of communication to find number of neighbours along with the position of the mobile node in the neighbourhood can help in finding sum of distances. Whereas mobility and power consumed does not require communication round.

Symbol	Terms	Meanings	Attributes	Communication Round Requirements
Δ_v	Degree Difference	Difference between total number of neighbours and maximum node supported by mobile nodes	Relative attributes as information related to actual presence of neighbourhood required	Yes
D_v	Sum of Distances	Sum of all mobile nodes present in neighbourhood	Relative attributes as information required from the neighbours	Yes

M_v	Mobility	Position of mobile node at discrete time	Absolute attribute as it require its own position information at discrete time. Relative to itself	No
P_v	Consumed Battery Power	Power consumed by mobile node at discrete time	Absolute attribute as it is measure of power at mobile node end	No
Tx-Rx	Authentication	Authorised Mobile Node	Relative Attributes	Yes
Tx-Rx	Reaffiliation	Joining of other cluster	Relative Attributes	Yes
$H(s)$	Entropy	Entropy of cluster	Relative attributes as disorder measures required mobile nodes information from neighbourhood	Yes
$E(s)$	Entropy	Entropy of Mobile Nodes	Absolute attributes [Mobility, Power] required to measure disorder behaviour of mobile nodes locally	No

Table 1:- Attributes and Communication Round Information

Table 1 explains about the attributes for parameters and communication round availability for them. From above table it can be understood that relative attributes can delay the actual operations between the mobile nodes and cluster formation can take time with the addition of relative attributes. Other communications such as authentications, de-authentication, reaffiliation, association and disassociations of mobile nodes in network can be considered as relative attributes and required communication round.

Weighted Clustering Algorithm for cluster formation[1] calculate weights for each node and minimum among weights wins the cluster head election, neighbour nodes become cluster member and do not participate further in the algorithm. Equation 1 is the weighted formula used in cluster formation.

$W_v = w_1\Delta_v + w_2D_v + w_3M_v + w_4P_v$, where w_1 , w_2 , w_3 and w_4 are the weighing factors..... (1)

It's clear with equation 1 that weighted clustering scheme is combination of absolute and relative attributes for cluster formation. Relative parameters can delay network operations and consume time in cluster formations due to mutual communication.

III. PROPOSED WORK

In this section, modification of weighted clustering algorithm based on absolute attributes such as mobility, power consumed and entropy of the mobile has been proposed. Further modification by greedy approach can help in reducing the communication round in cluster formation for faster clustering formation.

Overall proposal is to faster clustering formation for minimum delay in network operations by considering greedy selection of cluster head and only considering absolute attributes for calculating weights of the mobile node. Relative attributes results in communication round and greedy selection of cluster head can reduce overall cluster formation time. Clustering algorithm which is faster helps network appears stable, communication overhead and delays are comparatively low.

$W_v = w_1M_v + w_2P_v$, where w_1 and w_2 are the weighing factors..... (2)

$W_v = w_1P_v - w_2H_v$, where w_1 and w_2 are the weighing factors..... (3)

$w_1 + w_2 = 1$; weights sum equals to 1..... (4)

Mobility, Power Consumed and Entropy of mobile node is better factors to consider while applying clustering process. Equation 2 and 3 are representation of absolute weighted parameters based on mobility, consumed power and entropy based clustering [10]. Equation 4 describes the weight factor whose sum must be equals to one. These equations have no relative parameters and do not require communication between neighbourhood mobile nodes.

Minimum weights among them will be elected as cluster head and as weighted clustering algorithm also deals with maximum supported nodes $[\delta]$ can be considered for this too. Once cluster head and cluster members are defined they will not participate further in clustering formation process [1].

Cluster formation step through greedy approach of cluster head selection to reduce communication overhead and faster clustering formation has been demonstrated further. Combined effect of selecting absolute attributes and greedy approach can result in faster and effective clustering.

Cluster Formation Steps:

Step 1: Set Up Initial Configuration

Greedy Approach for Mobile Nodes: - Initial Configuration

Received Node ID	Role	Sender Node ID	Message
MN1	Cluster Head/Cluster Member	-	-
MN2	Cluster Head/Cluster Member	-	-
MN3	Cluster Head/Cluster Member	-	-

Table 2

Initial mobile node configuration considers all mobile nodes are capable of either cluster head or cluster member. Consider case when all mobile nodes are cluster members of some arbitrary cluster. Table 2 shows the initial configuration for three mobile nodes.

Step 2: Calculate weights $[W_v]$ according to equation 2 or 3. Suppose Mobility and Power is the absolute attributes considered for this illustration. Calculation for Mobility and Power Consumed steps has been described in weighted clustering algorithm [1].

Step 3: Perform first round of communication to share weights. One round is duplex communication among nodes. Sender shares its weight and receiver compares the weight to change the role. Receiver shares this message and role. Sender remains or change its role based on shared information.

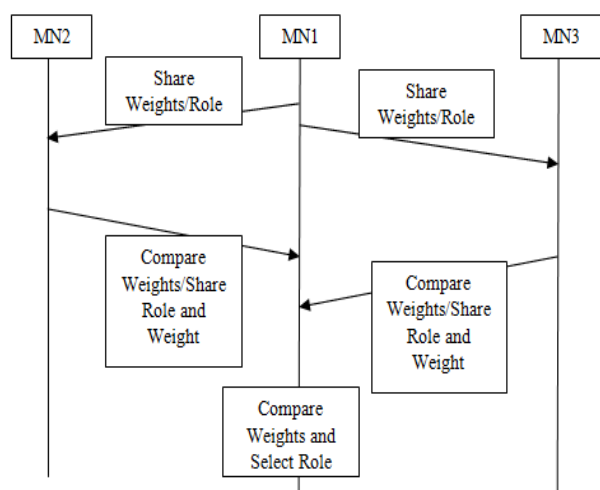


Fig 2:- Communication Round

Node ID	Weights
MN1	3
MN2	5
MN3	6

Table 3

Received Node ID	Role	Sender Node ID	Message
MN1	Cluster Head	MN2, MN3	CM2, CM3 (cluster members)
MN2	Cluster Member	MN1	CM1
MN3	Cluster Member	MN1	CM1

Table 4

Figure 2 explains the communication between mobile nodes. Mobile node 1 shares its weight with mobile node 2 and 3 along with its role. Assumed weight calculated has been shown in table 3. Mobile node 2 and 3 compares this weight and found it is less than mobile node 1 and remain as cluster member as initial consideration of role. Table 4 shows MN2 and MN3 received message from MN1 as CM1 (as initial assumption was all nodes are cluster member). MN1 receives CM2 and CM3 along with their weights shown in figure 2 after comparison made by MN2 and MN3. MN1 change its role based on this information and become cluster head shown in table 4. MN1 remains cluster member if it receives other than cluster member message i.e. either of MN2 or MN3 will be cluster head. When MN2 and MN3 receives CM1 message along with MN1 weights from figure 2 and table 4, comparison made with the weights and decides their role further this role shared with MN1.

One round of communication decides about the election of cluster head and cluster member in neighbourhood. Although one optional round to inform others about the final role by cluster head can be performed to ensure who is the cluster head elected currently. Since greedy approach already made other nodes aware about probable cluster head, it's really optional to do so. Table for further communication or neighbours table can be prepared in this round only. Clustering formation process is distributed over the network and already participated nodes will not take part in clustering. For knowing the members who has been already participated, a participation ticket flag can be introduced or assigned to the mobile nodes.

Step 4: Repeat step 2 and step 3 for all nodes till either mobile nodes become cluster head or cluster member or assigned to a cluster.

Combined effect, by (a) considering absolute attributes and (b) greedy approach for reduction of communication round relaxes clustering formation process. Mixed of result can be expected on clustering with original weighted clustering schemes in terms of cluster head selection but this method ensures that clustering formation will be faster. There were many clustering schemes which are stand alone based on mobility and power of the mobile nodes. Considering degree difference and sum of distances demands relative information of neighbourhood and do not have high significance in clustering which can be neglected. If the clustering algorithm is based on highest degree it cannot be considered as very good clustering algorithm as possibility of frequent updates can make cluster unstable.

Node ID	W_v
1	3
2	5
3	6
4	9
5	2
6	10

Table 5

Table 5 illustrates nodes and their calculated weights using equation 2 or 3. Figure 3 shows initial configuration on the network.

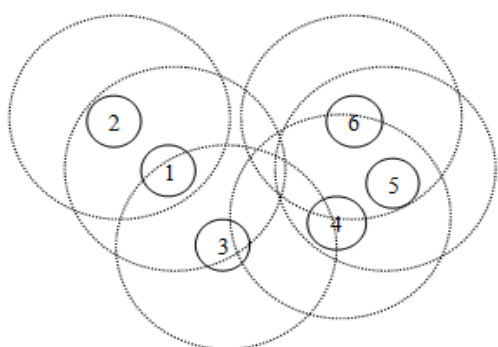


Fig 3:- Initial Mobile Nodes in the Network

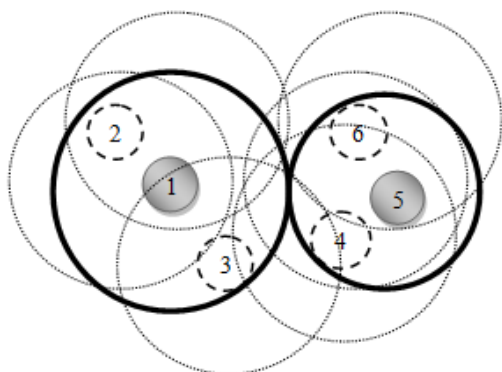


Fig 4:- Cluster formation for clustering

Figure 4 shows cluster after cluster formation process. Figure 3 and 4 is the result of cluster formation steps performed in the mentioned proposed algorithm. Cluster head election is similar to the original weighted clustering algorithm which chooses minimum weighted node as cluster head.

Difference between original weighted clustering algorithms [1] and this proposed algorithms are as follow:

- Steps for cluster formation have been reduced from the original algorithm.
- This ensures that cluster formation become faster.
- Relative attributes (degree difference and sum of distances of neighbours) have been removed from weight calculation.
- Greedy approach applied for selection of cluster head and members for faster cluster formation.

- Communication round has been reduced so that cluster formation become faster.

Results of proposed algorithm depends on network environment, it's possible that network has large congestion and band width uses that election itself get delayed. Such situation cannot be controlled but simulation must perform better result from the existing one practically as well as theoretical.

IV. SIMULATION ENVIRONMENT AND RESULTS

Simulation has been done on network simulator version ns-2.35. Weighted clustering algorithm has been implemented and further modification done for the mentioned condition.

Parameters	Meaning	Value
N	No of nodes	30
X*Y	Simulation Area	650X500
R	Transmission Range	100
Mobility Model	Random Way Point	-
Duration	Simulation time	50Sec
MD	Maximum Displacement	300-400

Table 6:- Network Environment

Table 6 describes the number of nodes, simulation area, range of the nodes and simulation time etc. Figure 5 shows time comparison between original weighted clustering algorithms [1] and modified weighted clustering with absolute attributes of mobile nodes. Further addition of greedy approach reduces the cluster formation process for the network scenarios. Comparison has been made on taking different network scenarios for average performance measure.

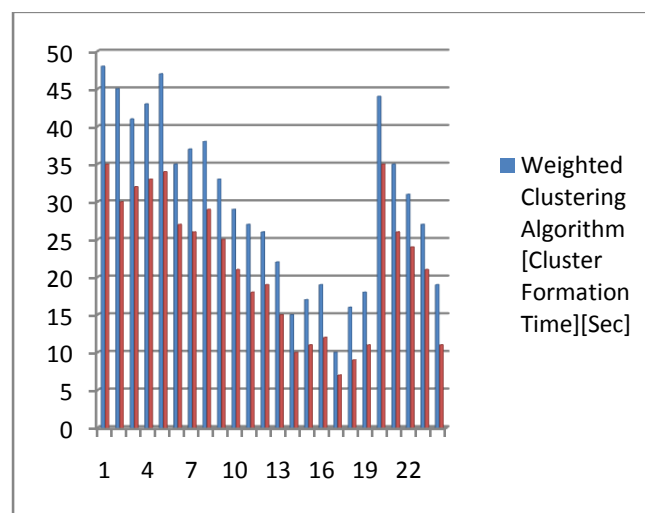


Fig 5:- Timing Comparison for Cluster Formation

Figure 5 shows significant reduction in time for cluster formation process in modified scheme. Comparison has been made by choosing different network scenarios over time. Mobile nodes are distributed over the network and algorithm started on distributed

nodes simultaneously. Mobility of nodes is also considered and nodes out of range of the nodes remains cluster members with unallocated cluster. In weighted clustering algorithm [1] nodes which are out of range become cluster head. Modified clustering with greedy approach chooses to be cluster member so there is change in result from original WCA [1] but if cluster head chosen as greedy approach then it will be same as original weighted clustering algorithm.

V. CONCLUSION

Objective of this paper is to differentiate between absolute and distributed attributes of the mobile nodes. Clustering of mobile nodes i.e. cluster formation process is highly affected by relative attributes in terms of time taken to perform task to collect the information from neighbour nodes. In this case relative attributes of the node is degree of the mobile node or number of mobile nodes present in the neighbourhood. Considering this is not important to know modified weighted clustering algorithm only used absolute attributes for cluster formation. One round of communication serves the purpose of sharing weights and knowing the neighbours from which the message received as weight value. Relative attributes require communication rounds and delay the important network operations. Cluster formation related messages must be minimised so that faster clustering can be achieved. Two methods which are considering absolute attributes of mobile nodes and greedy approach of selecting mobile node as cluster head minimised the message overhead, consumes less bandwidth or congestion control is less over the network. There is scope of improvements with the other algorithms which consider relative attributes. Timing analysis is difficult in real environment but better clustering algorithm which minimise the network congestion for clustering related messages and provide more space for non-clustering messages such as packet sharing, resource sharing or data sharing messages can be considered as effective clustering formation schemes.

REFERENCES

- i. M Chatterjee, S K Das, D Turgut, "WCA: A Weighted Clustering Algorithm for Mobile Ad Hoc Networks", *IEEE Journal of Clustering Computing* Vol.5 (2),193-204, 2002.
- ii. Jane Y. Yu and Peter H. J. Chong, "a Survey of clustering schemes for mobile ad hoc networks", *IEEE Communications Surveys*.
- iii. Vijayanand Kumar, "Relaxing weighted clustering algorithm for reduction of clusters and cluster heads", *international journal of scientific engineering and technology*. <http://ijset.com/ijset/index.php/issue-archive/v4/volume-4-issue-10>
- iv. Abdel Rahman H. Hussein, Sufian Yousef, and Omar Arabiyat, "A Load-Balancing and Weighted Clustering algorithm in Mobile Ad-Hoc Network".
- v. D. Turgut, B. Turgut, R. Elmasri, and T. V. Le, "Optimizing clustering algorithm in mobile ad hoc networks using simulated annealing," *Proc. IEEE Wireless Communication and Networking Conference*, 2003.
- vi. D. Turgut, S. K. Das, R. Elmasari, and B. Turgut, "Optimizing clustering algorithm in mobile ad hoc networks using genetic algorithm approach," *Proc. 45th IEEE Global Telecommunications Conference*, 2002.
- vii. Charalampos Konstantopoulos, Damianos Gavalas, Grammati Pantziou "Clustering in mobile ad hoc networks through neighborhood stability-based mobility prediction", *Computer Networks* 52 (2008) 1797– 1824.
- viii. Mohamed Aissa, Abdelfettah Belghith and Khalil Drira "New strategies and extensions in weighted clustering algorithms for mobile Ad Hoc networks", *The 4th International Conference on Ambient Systems, Networks and Technologies (ANT 2013)*.
- ix. Mohamed Aissa, Abdelfettah Belghith "Quality of Clustering in mobile Ad Hoc networks", *5th International Conference on Ambient Systems, Networks and Technologies (ANT-2014)*.
- x. Yu-Xuan Wang, Forrest Sheng Bao "An Entropy-based Weighted Clustering Algorithm and Its Optimization for Ad hoc Networks" originally published on *3rd IEEE Int'l Conf. on Wireless and Mobile Computing, Networking and Communications*, 2007. (WiMOB 2007)
- xi. Basagni S., "Distributed clustering for ad hoc networks," *Proceedings of International Symposium on Parallel Architectures, Algorithms and Networks*, Jun. 1999, pp. 310-315.
- xii. Basagni S., "Distributed and mobility-adaptive clustering for multimedia support in multi-hop wireless networks, *Proceedings of Vehicular Technology Conference, VTC*, vol.2, fall 1999, pp. 889-893.
- xiii. Hui Cheng, Jiannong Cao, Xingwei Wang, Sajal K. Das, *Stability-based Multi-objective Clustering in Mobile Ad Hoc Networks, The Third International Conference on Quality of Service in Heterogeneous Wired/Wireless Networks*, August7-9, 2006, Waterloo, Ontario, Canada © 2006 ACM.
- xiv. A. D. Amis and R. Prakash, "Load-Balancing Clusters in Wireless Ad Hoc Networks," in *Proc. 3rd IEEE ASSET'00*, Mar. 2000, pp. 25-32
- xv. S.K. Dhurandher & G.V. Singh, "Weight based adaptive clustering in wireless ad Hoc Networks", *IEEE International Conference on Personal Wireless Communications*, New Delhi, India, 2005, 95-100.
- xvi. D.J. Baker and A. Ephremides, "A distributed algorithm for organizing mobile Radio telecommunication networks", in: *Proceedings of the 2nd International Conference on Distributed Computer Systems*, April 1981, pp. 476-483.
- xvii. M. Gerla and J.T.C. Tsai, Multiclustet, mobile, multimedia radio network, *Wireless Networks* 1(3) (1995) 255-265.
- xviii. S. Basagni, "Distributed clustering for ad hoc networks", in: *Proceedings of International Symposium on Parallel Architectures, Algorithms and Networks*, June 1999, pp. 310-315.
- xix. S. Basagni, "Distributed and mobility-adaptive clustering for multimedia support in Multi-hop wireless networks", in: *Proceedings of Vehicular Technology Conference, VTC*, Vol. 2, 1999-Fall, pp. 889-893.
- xx. Yingpei Zeng, Jiannong Cao, Shanjing Guo, Kai Yang, Li Xie. (5-8 April, 2009). A Secure Weighted Clustering Algorithm in Wireless Ad Hoc Networks. *IEEE conference on Wireless Communication and Networking Conferences*.
- xxi. Yang Tao, Jian Wang, Ya-Li Wang, Tao Sun. (12-14 Oct. 2008). An Enhanced Maximum Stability Weighted Clustering in Ad Hoc Network. *4th International Conference on Wireless Communication, Networking and Mobile Computing*.
- xxii. Xiqing Zhao, Xifeng Guo, Zhaohao Sun, Changming Ren. (19-21 May 2009). An Intelligent Weighted Clustering Algorithm (IWCA) for Ad Hoc. *WRI World Congress on Software Engineering Volume 3*.
- xxiii. Wandee Wongsason, Chaityod Pirak and Rudolf Mathar, (2007). Distributed Maximal Weighted Independent Set Algorithm, (MWIS). *International Conference on Wireless Communication, Networking and Mobile Computing*.

Accepted Manuscript

Title: Molecular logic operations based on optical detection of sulfur mustard simulant using pyridine appended Mg-porphyrizine complex

Author: Neelam Vikram Singh Bhaskaran Shankar
Ramasamy Shanmugam Satish K. Awasthi Rinkoo D. Gupta



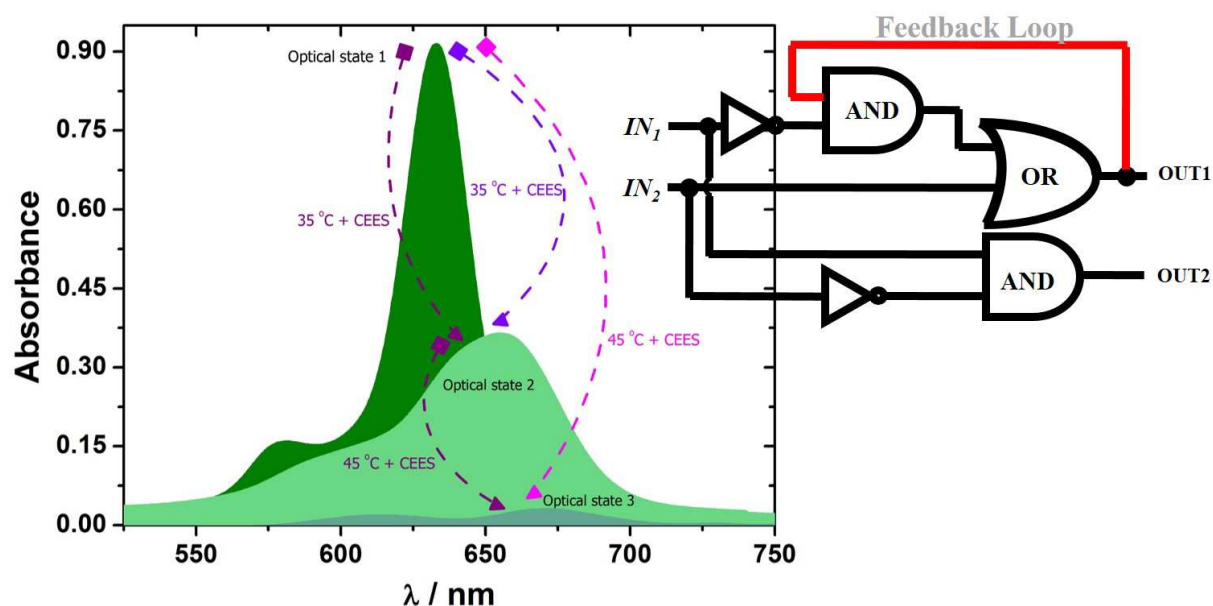
PII: S0925-4005(15)30752-8
DOI: <http://dx.doi.org/doi:10.1016/j.snb.2015.12.035>
Reference: SNB 19436

To appear in: *Sensors and Actuators B*

Received date: 21-8-2015
Revised date: 25-11-2015
Accepted date: 11-12-2015

Please cite this article as: Neelam, V. Singh, B. Shankar, R. Shanmugam, S.K. Awasthi, R.D. Gupta, Molecular logic operations based on optical detection of sulfur mustard simulant using pyridine appended Mg-porphyrizine complex, *Sensors and Actuators B: Chemical* (2015), <http://dx.doi.org/10.1016/j.snb.2015.12.035>

This is a PDF file of an unedited manuscript that has been accepted for publication. As a service to our customers we are providing this early version of the manuscript. The manuscript will undergo copyediting, typesetting, and review of the resulting proof before it is published in its final form. Please note that during the production process errors may be discovered which could affect the content, and all legal disclaimers that apply to the journal pertain.



Molecular logic operations based on optical detection of sulfur mustard simulant using pyridine appended Mg-porphyrine complex[†]

Neelam^{ab†}, Vikram Singh^{a†}, Bhaskaran Shankar^a, Ramasamy Shanmugam^c, Satish K. Awasthi^a, Rinkoo D. Gupta^{d*}

^aDepartment of Chemistry, University of Delhi, Delhi-110 007, India.

^bDepartment of Biological Chemistry, Ariel University, Ariel-40 700, Israel.

^cDepartment of Chemistry, Thiagarajar College, Madurai-625 009, India.

^dFaculty of Life Sciences and Biotechnology, South Asian University, Delhi-110 021. India.

Correspondence address:

E-mail: rdgupta@sau.ac.in;

Phone: +91 11 24122512 Fax: +91 11 24122511

Abstract: Selective detection of sulfur mustard simulant, 2-chloroethyl ethyl sulfide (CEES) is performed using specifically designed pyridine appended Mg-porphyrine complex (**1**). Interaction of CEES with pyridine units of **1** leads to perturbation/reduction in absorbance of the Q-band of **1** and the process is, thus, monitored using UV-vis spectroscopic method.

Interestingly, treating the CEES-**1** solution with KMnO_4 solution results in reappearance of Q-band of **1** and allows reuse of **1** by simple filtration. The alkylating ability of CEES and KMnO_4 oxidation of CEES-**1** appears to be playing an important role in the detection/degradation process, thereby serving the dual purpose. The chemical sensing is then used as a platform for generating different input-based combinatorial and sequential molecular logic gate(s) allowing facile information processing and as an information security system in the form of a keypad lock.

Keywords: Sulfur mustard; CEES; Chemical warfare; porphyrazine; UV-vis; Molecular logic

Introduction

Chemical warfare agents (CWAs) represent an alarming challenge in this milieu of on-going extremism in various parts of the world.¹ CWAs were extensively employed in World War I, to some extent in World War II as well as in Iran-Iraq war in 1980s.² In particular, sulfur mustard (SM) including its analogues/simulants form a dreaded class of CWAs³ and therefore, their facile, rapid and selective recognition could potentially aid in reducing their inimical effects. Two consequent reports by Anslyn *et al.* pointed towards the non-existence of optical methods for detection of SM simulant, unlike nerve agents⁴ and showed a fluorescence based SM detection methodology.⁵ Two recent papers by Farha *et al.* highlighted the importance of chemical weapon degradation and used metal-organic framework for their destruction.⁶ Nonetheless, at present, most of the methods employed (point or standoff) for SM detection/degradation involve tedious methodologies, instrumentation, and are time consuming.^{7, 8} Other methods based on conventional techniques face similar problems.⁹ In this context, swift recognition and degradation of CWAs or their decontamination becomes all the more inevitable. It should be noted that CEES are weakly electrophilic^{2a, 13}, can alkylate DNA/RNA and potential nucleophiles can either act on positively charged S-atom or β -methylene carbon unit.¹⁴ Therefore, a complementary sensing platform must be designed. For this purpose, **1** (Fig. 1) is chosen; for it is known to be highly “UV-visible active” due to extensive π -conjugation and shows an un-split Q-band in the visible region ($\lambda_{\text{max}} = \sim 650 \text{ nm}$) and B-band in the near UV region ($\lambda_{\text{max}} = \sim 383 \text{ nm}$).^{10, 11} Moreover, presence of peripheral pyridyl moiety allow **1** to be weakly nucleophilic.¹²

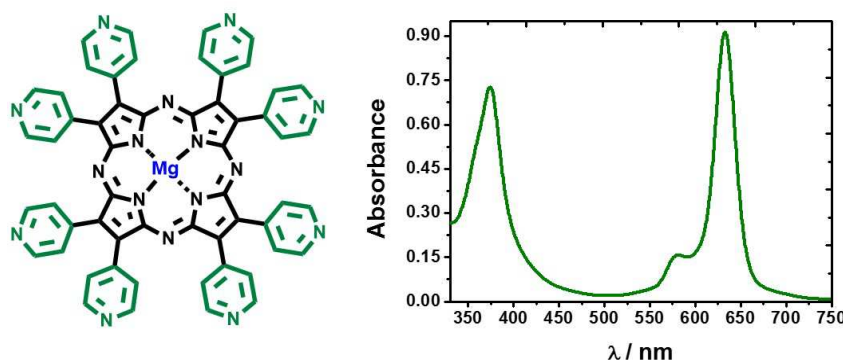


Figure 1: Representation of **1** (Left) and its UV-vis spectrum in CHCl₃/CH₃OH (Right).

Our research group is focused on the synthesis of functionalized metal complexes and fabricating their monolayer on solid substrates for varying applications including sensing of ions and molecules.¹⁵ In our previous report, we approached CEES detection using **1**-based monolayer on glass where CEES could perturb absorption bands of **1**.¹⁶ In this study, we have demonstrated that **1** in solution state can also perform CEES detection with little variation in sensitivity. The latter approach, unlike the former, affords “by-eye” CEES detection as the solution colour variations can be straight forwardly identified upon CEES-**1** interaction. Further, we made an effort to delineate CEES-**1** interaction mechanism through NMR studies and time dependent DFT calculations. A good correlation of experimental results with computational studies strengthened our hypothesis as made in the previous report.

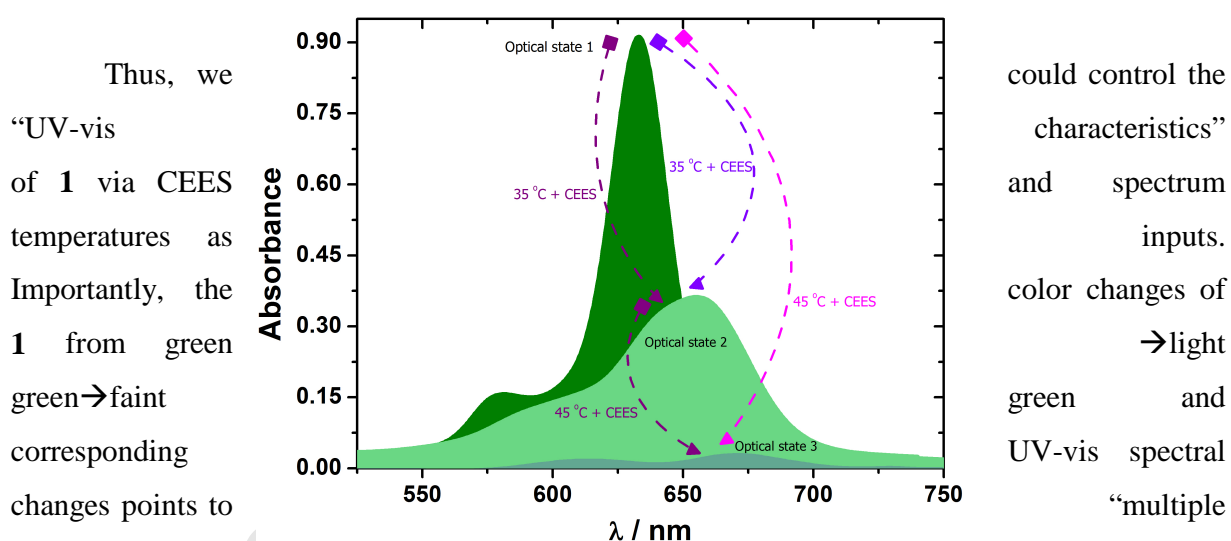
Interestingly, temperature plays a key role in the detection process and therefore, we used a stepwise rise of 10°C from 25°C to 45°C to investigate the behaviour of CEES-**1**. The reversibility of the process was studied using alcoholic KMnO₄ as the reagent of choice. The variation in temperature, introduction of CEES and reversibility by KMnO₄ resulted in “multiple optical states” of **1**, which could easily be addressed by adjusting the three “stimuli”. In addition, it is known that stimuli responsive materials can mimic the operation characteristics of logic gates and can be used for information processing at an advanced level of intricacies.¹⁷ Furthermore, logic gates based on chemical sensors allow for molecular tailoring and modulation for the optical-based output signals as well as facile realization of reversible “multi-addressable states” with different input signals (chemical, temperature, light and others).¹⁸ The idea of transforming CEES sensing by **1** into molecular logic gates allows for evaluating sensing parameters by binary reading, thereby, pondering on exact numerical values can be made redundant.

Results and Discussions

CEES exposure to 1: An addition of 5 μL of 4.3 mM CEES (~ 6 ppm) in $\text{CHCl}_3/\text{CH}_3\text{OH}$ (5:1, v/v) to a 10 μM solution of **1** in the same solvent composition was monitored using an UV-vis spectrophotometer equipped with peltier functionality in the range 300-800 nm (see ESI for details). At 25 $^\circ\text{C}$ and for up-to 60 minutes, there were no significant alterations to the UV-vis spectrum of **1**. In another experiment, a 10 $^\circ\text{C}$ rise in temperature produced reduction in optical absorption for both B- and Q-band of **1** within 5 min of CEES exposure. After 60 min of reaction time at 35 $^\circ\text{C}$, a steady, $\sim 60\%$ decline in absorbance along with $\sim +21$ nm shift was observed in the Q-band maxima [Fig. 2 and Fig. S1] with a concomitant color change from green to light green. An increase of time could not induce any further alterations in the spectra of **1**. Herein, we term initial absorption of Q-band as first “optical state” and absorption after CEES/35 $^\circ\text{C}$ input as second “optical state” of **1**. Importantly, no Q-band split was observed, which signify preservation of symmetrical nature of **1**.¹⁹ These observations strongly points to variations in the extent of π -conjugation in **1** and probably symptomatic of some intermediate formation, which is stable at the reaction temperature.

Keeping the reaction time to 60 min, we increased the temperature to 45 $^\circ\text{C}$, and observed enhanced alterations in the Q-band within 45 min and minimal changes thereafter ($\sim 96\%$ decline in absorbance in Q-band and $\sim +42$ nm shift) and faint green colored solution [Fig. 2 and Fig. S2]. Absorption at this stage is termed as third “optical state” of **1**. Along with large red shift, Q-band showed splitting and which could be attributed to either molecular aggregation or unsymmetrical structure or the phenomenon has even been observed in some symmetrically substituted **1**-like structures, e.g. symmetrically substituted Zinc phthalocyanines.¹⁹ In another experiment, reaction was first monitored at 35 $^\circ\text{C}$ and after saturation, temperature was increased to 45 $^\circ\text{C}$ and similar change was observed for **1**. Further, a first order reaction kinetics for the CEES-**1** interaction at both 35 $^\circ\text{C}$ and 45 $^\circ\text{C}$ was observed (Fig. S3) and therefore, we could calculate rate constants, $k_{35} = 2.5 \pm 0.3 \times 10^{-4} \text{ min}^{-1}$ and $k_{45} = 1.6 \pm 0.4 \times 10^{-3} \text{ min}^{-1}$) using equation $\ln[\mathbf{1}_{\text{final}}] = -kt + \ln[\mathbf{1}_{\text{initial}}]$. The k values suggest ~ 10 fold rate enhancement with increasing temperatures and are in good agreement with experimental results with activation enthalpy, E_a estimated at $\sim +15.3 \text{ KJ mol}^{-1}$ (± 0.4) calculated using Arrhenius equation.

Figure 2: Variations in Q-band absorption and band maxima ($\lambda_{\text{max}} = 634 \text{ nm}$) of **1** on interaction with 6 ppm of CEES at 35 °C and 45 °C and the corresponding “optical states”.



optical/addressable states” which could be manipulated by controlling CEES and temperature inputs.

^1H NMR and Time-dependent density functional studies (TDDFT): For the **1**-monolayer based sensing of CEES, we used solution based ^1H NMR in CD_3OD for elucidating CEES/**1** interaction at 45 °C and provided two possible binding modes (fig. 3, right; 1a and 1b).¹⁶ Herein, we will look at the ^1H NMR of CEES before (fig. 3a, left) and after (fig. 3b, left) sensing experiments. **1** has pyridine N-atoms as well as aza-N atoms and both may react with CEES.

However, aza-N atoms of such molecules have lesser reactivity to those of small aromatic amines like pyridine or pyrrole, for the stronger p - π conjugation between aza-nitrogen and **1**-ring.¹⁹ Therefore, participation of aza-N atoms can be neglected. In the ^1H NMR spectrum of CEES/**1** there seems to be a mixture of reacted and unreacted CEES, where the H(i') and H(ii') appears a little downfield then H(i) and H(ii) and this shift could be attributed to larger electron density demands of pyridinium N-atom. In principle, the lone pair on pyridine-N atoms can possibly attack the electrophilic center of CEES, that is, β -methylene carbon, thus opening up the heterocycle. These proposed events are suggestive of alkylation of **1** and simultaneous reduction of CEES by means of loss and gain of pair of electrons. Moreover, “turn-off”, that is, reduction in optical absorption, bathochromic shifts and consequent splitting of the Q-band shifts could be ascribed to quaternization/alkylation of the peripheral pyridine-N atom(s) by CEES.²⁰

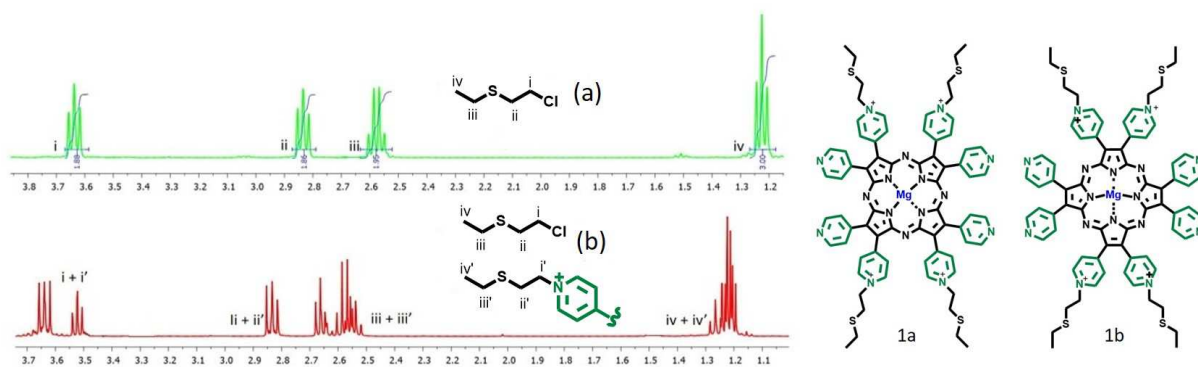


Figure 3. ^1H NMR spectrum of (a); CEES (b); **1** + CEES (spectrum region for CEES containing reacted and unreacted CEES) in CD_3OD .

To understand the nature of the different transitions, drastic changes observed in the UV-vis spectrum of **1**, and to correlate the ^1H NMR findings, DFT and TDDFT calculations were performed on optimized structures **1**, **1a** and **1b** (see ESI for details). TDDFT study suggested that the absorption spectra mainly contain three types of intense bands at three different regions for **1** and relatively less intense band at two different regions for **1a** and **1b** with complementary oscillator strength (Fig. 4; Table S1-S3 and Fig. S3-S5). The most important conclusion from the calculated UV-vis absorption spectra is, in comparison to **1**, **1a** and **1b** shows red-shifted bands with low absorption as observed during experimental studies. Observation of calculated absorption bands in the NIR region for **1a** and **1b** suggest lowering of band gap.

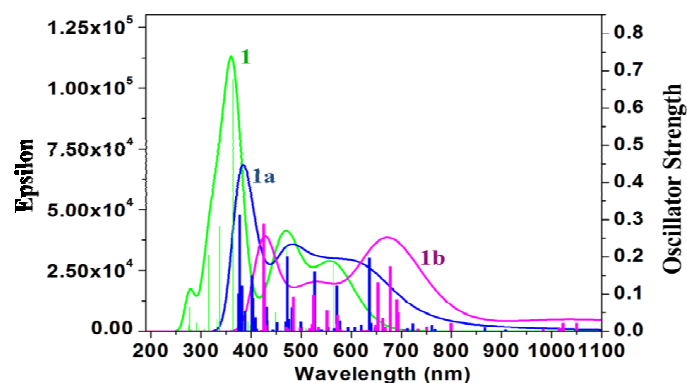


Figure 4. Calculated absorption spectra of **1** (green), **1a** (blue) and **1b** (magenta) with oscillator strengths (vertical lines).

The highest occupied molecular orbital (HOMO) and lowest unoccupied molecular orbital (LUMO) of **1** is dominated by the inner core of the porphyrazine moiety with HOMO-LUMO gap at 2.51 eV (Fig. 5). Moreover, in the HOMO of **1a** and of **1b** is located at CEES while LUMO within the porphyrazine moiety with HOMO-LUMO gap at 0.68 eV and 0.52 eV (Fig. 5).

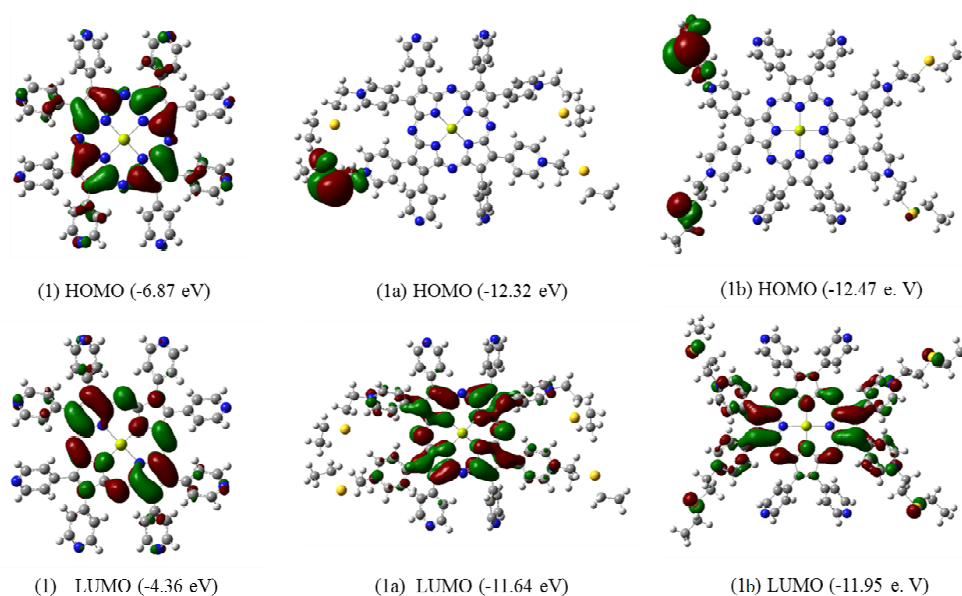


Figure 5. Molecular orbital arrangements (HOMO and LUMO) of **1**, **1a**, **1b** in the gas phase.

This lowering of HOMO-LUMO energy gap is possibly explained by the covalent linking of electron donor (**1**) and electron accepting unit (CEES)²¹, that is, quaternization of pyridine N-atoms helped in impeding $n-\pi^*$ transition of lone pair electrons in sp^2 orbit leading to enhanced conjugation over **1**-ring. This inevitably decreased HOMO-LUMO energy gap resulted in red shift of Q-band and Q-band splitting after CEES interaction relative to Q-band of **1**.¹⁹ TDDFT

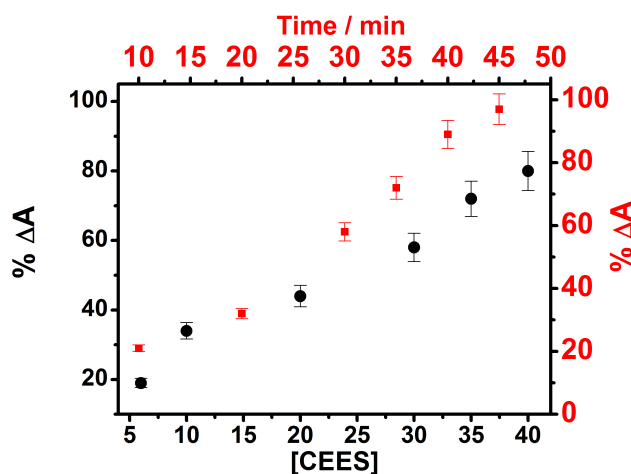
data also correlate well with the assertion that CEES coordinate to **1** and which allow for the changes in spectrum of **1** and hence for the observed multiple “optical states”.

Sensor reversibility: A prior knowledge of degradation of CEES to non-toxic chemicals by KMnO_4 was exploited to verify the NMR based description and as well as to reset the sensor to original state.²² As in our previous work we used a freshly prepared alc. KMnO_4 of 25 μM and added to both reference and **1**-CEES. UV-vis spectrum of the filtered solution was recorded after an equilibration time of ~5 min. Expectedly, Q-band was resurrected to almost original levels of absorption and band maxima, that is, “turn-on”. Thereafter, we performed five alternating sensing–recovery cycles without any significant variations in any of the optical states of **1** (fig. S6). The results are clearly comparable with **1**-based monolayer recyclability. The plausible justification seems to be detachment of CEES from **1** and further oxidation of CEES resulting in regaining of initial “optical state”. On this basis, a mechanism is proposed for **1**/CEES interaction and resetting of **1** and CEES degradation by KMnO_4 (Fig. S7). Moreover, reversibility affords **1** “ON-OFF-ON” switch characteristics, where different “optical states” can be easily addressed/maneuvered by careful management of inputs, *viz.*, CEES, temperatures and KMnO_4 .

Detection Limit: The detection range of the sensor was examined by its fixed-time exposure to $\text{CHCl}_3/\text{CH}_3\text{OH}$ (5:1, v/v) solution containing different CEES concentrations in the range 6–40 ppm. UV-vis data showed that exposure to only ~6 ppm of CEES for ~45 min at 45°C and ~60 min at 35°C is sufficient to saturate/“turn-off” the sensor (10 μM). Contrariwise, less than 6 ppm of CEES could not alter the optical absorption of **1** for as long as ~30 min and

even at elevated temperatures (upto 70°C). In addition, the optical changes in **1** were recorded as a function of time at different CEES concentrations, for assessing the response properties of the

sensor. The
that higher
CEES
reduces the
20 ppm CEES at
showed
changes in ~1
a given CEES
optical signal



relationship with time until saturation was achieved, e.g. saturation in 20 min when exposed to 40 ppm of CEES at 45°C (Fig. 6 and fig. S8).

outcome suggested
concentration of
considerably
response time, e.g.
45°C could
discernible
min. Moreover, at
concentration, the
displayed a linear

Figure 6: The percentage change in the absorption signal at $\lambda_{\max} = 634$ nm and 45 °C from the **1**-based sensor as a function of CEES concentration in the $\text{CHCl}_3 + \text{CH}_3\text{OH}$ (5:1, v/v) at a fixed exposure time of 15 min (bottom axis; black), each repeated for at least 3 times; and as a function of time at a fixed CEES concentration of 10 ppm (top axis; red).

Accuracy and selectivity: A hands-on and ready-to-use sensor system must give accurate results as well as show discriminatory behavior among potent interferences. As for the

accuracy and stability, the “turn-off” signal deviation was estimated to be just over ~7%,

calculated from three different CEES sensing experiments at 45 °C (Fig. 6). As for selectivity,

we exposed **1** to potent yet common interferences, *viz.* CO₂, water vapor (WV), petrol/diesel burn containing CO, NO_x, C_xH_y, SO₂ and cigarette smoke (CS). Some other sulfur containing compounds were also examined as well, *viz.* 3-mercaptopropionic acid (MPA) and ethyl mercaptan (EM). For selectivity, 100 ppm of CO₂, water vapor, petrol/diesel burn in real-time, cigarette smoke in real-time, 10 ppm of MPA and EM along with 10 ppm of CEES were exposed to **1** in CHCl₃/CH₃OH (5:1, v/v) either individually or as a mixture for ~30 minutes at both 35 °C and 45 °C. It was observed that none of the analytes except CEES, even in the mixture, could show any noteworthy changes to the Q-band of **1** (fig. 7 and fig. S9). Therefore, so it could be stated that **1** selectively detects CEES with or without possible interferences.

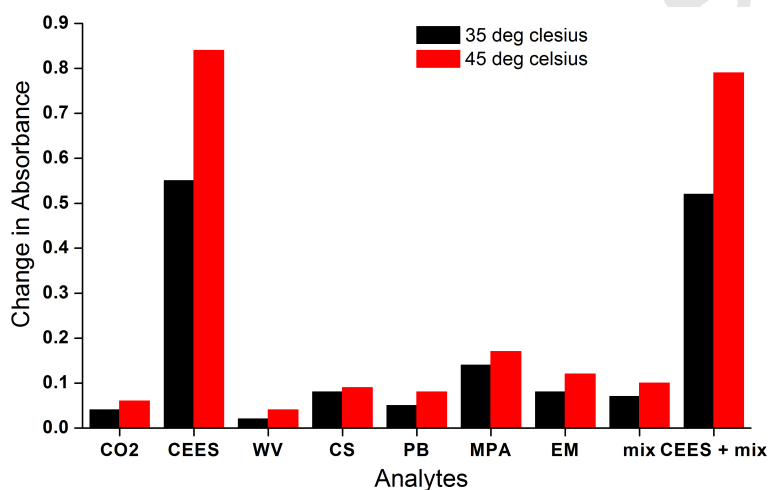


Figure 7. The absorbance change w.r.t. $\lambda_{\max} = 634$ nm after exposing the sensors to analytes for 30 min each at 35 °C (black bars) and 45 °C (red bars).

Molecular logic gates and circuits: Molecular sensors in conjunction with analytes and reaction conditions could perform information processing, where introduction of one or all could be regarded as input (*IN*) and changes in optical identity of **1** as output (*OUT*).^{17, 23} Moreover, it allows easier analysis of the results obtained during sensing process as numerical values may not be of such significance as to know whether SM is present or not. As explained *vide supra*, **1** acts as an “ON-OFF-ON” switch and show “multiple optical states” controlled by CEES and KMnO₄ (*vide supra*). The set-reset of **1** by these stimuli can process information in the form of two-input sequential and three or four-input combinatorial logic circuit.²⁴ In case of sequential logic, the output is governed by the existing state of the system and the input currently present but in case of combinatorial logic, the output depends only on the current inputs. Therefore, the former adds

extra level of complexity to such logic platforms and hence more useful to construct memory elements.¹⁷

In our investigations, the deviations in the absorbance at Q-band (OUT_1) and colour change by the naked eye (OUT_2) have been captured as the outputs. For the two-input based logic gate, the threshold value has been fixed at absorbance, $A > 0.4$. The absorbance more than the threshold values are assigned as “1” and absorbance lesser than the threshold values are assigned as “0”. The colour change from green to light green is allocated as “0” and “1” respectively. The sequential logic circuit is designed in such a way that CEES (C) behaves as IN_1 whereas $KMnO_4$ (K) functions as IN_2 (Fig. 8). When IN_1 is applied, the absorbance falls below the threshold level to give $OUT_1 = 0$ and colour change from green to light green at OUT_2 . However, successive addition of IN_2 regains its initial absorbance and colour (green). The feedback loop connects the OUT_1 back to IN_1 and ensures memory function of the circuit (fig. 6).

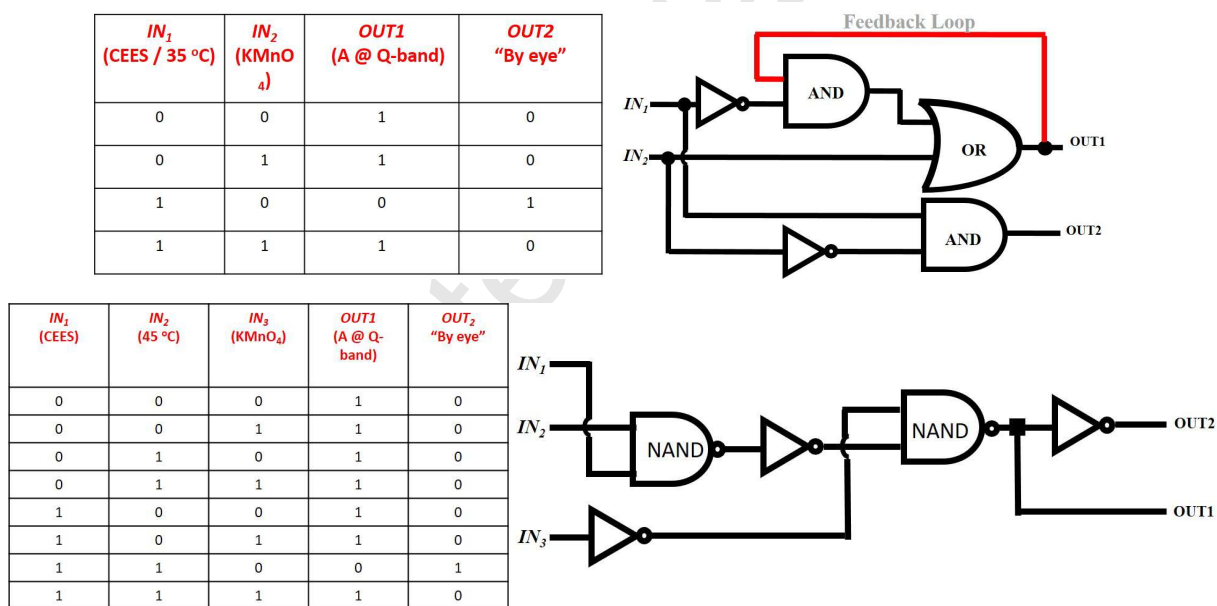


Figure 8. Truth table and sequential logic circuit displaying memory units with two inputs and two outputs in the presence of chemical inputs viz., IN_1 (CEES) and IN_2 ($KMnO_4$).

For reaction at 45°C, temperature was also considered as one input since it helps to decrease the absorbance drastically. With CEES (C) as IN_1 , $T_2 = 45^\circ C$ as IN_2 and $KMnO_4$ (K) as IN_3 , a three input combinatorial logic circuit of eight combinations was constructed with output as changes in the Q-band (OUT_1) and changes in color (OUT_2) as shown in fig. 9. In this case the

Figure 9: Truth table and sequential logic circuit displaying memory units with three inputs and two outputs in the presence of chemical inputs viz., IN_1 (CEES), IN_2 (45 °C) and IN_3 ($KMnO_4$).

absorbance threshold is considered as $A > 0.1$ and similar conditions as above were imposed for generating output.

Four input combinatorial molecular logic gates have rarely been reported and can allow generation of more complex and concatenated logic circuits.^{24c} If we consider CEES as IN_1 , $T1 = 35\text{ }^{\circ}\text{C}$ as IN_2 , $T2 = 45^{\circ}\text{C}$ as IN_3 and KMnO_4 as IN_4 , a four-input combinatorial logic circuit with sixteen input combinations can be constructed with output considered as changes in the Q-band absorption at $35\text{ }^{\circ}\text{C}$ (OUT_1) and $45\text{ }^{\circ}\text{C}$ (OUT_2) under threshold values, $A > 0.4$ for OUT_1 and $A > 0.1$ for OUT_2 . The molecular logic works under the conditions that temperature can be applied either individually (input no 3-6, 11-14; fig. 10) or one after the other (input no 7, 8, 15, 16; fig. 10). Interestingly, if we consider change in color of **1** (green \rightarrow light green \rightarrow faint green) as OUT_3 with OUT_1 , and OUT_2 as input feed from the logic circuit. OUT_3 is considered as '0' if either of OUT_1 or OUT_2 is '1' otherwise $OUT_3 = '1'$, where $OUT_3 = '0'$ implies successful sensing of CEES and $OUT_3 = '1'$ implies absence of sulfur mustard.

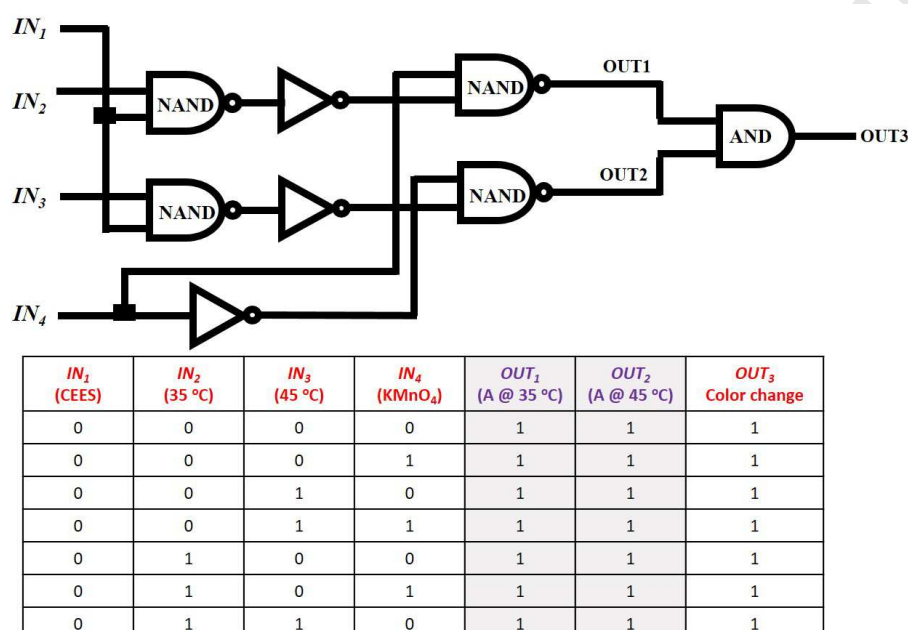


Figure 10: Truth table and sequential logic circuit displaying memory units with four inputs and two outputs in the presence of chemical inputs viz., IN_1 (CEES), IN_2 (35 °C), IN_3 (45 °C) and IN_4 (KMnO₄).

1	0	0	1	1	1	1
1	0	1	0	1	0	0
1	0	1	1	1	1	1
1	1	0	0	0	1	0
1	1	0	1	1	1	1
1	1	1	0	0	0	0
1	1	1	1	1	1	1

Further, this four input molecular logic operations could then be adopted to assemble a molecular keypad lock (fig. S10) for securing information at molecular level so that information stored cannot be seen or changed without exact inputs. In this case, the keypad can only be unlocked under the condition $OUT_3 = '0'$, that is, when either of the output, OUT_1 and OUT_2 is

'0' which will depend on choosing 4 inputs at a time from 8 possible viz., C, \bar{C} , T1, $\bar{T1}$, T2, $\bar{T2}$

K, \bar{K} inputs leading to 8^4 permutations. Inputs with bars denote *not applied* and vice-versa. Now, only three such combinations out of 8^4 total possible can open the keypad, which are $CT1\bar{T2}\bar{K}$ or $C\bar{T1}T2\bar{K}$ or $CT1T2\bar{K}$. This is very simple to explain as application of CEES (C) is must, out of T1 and T2 one of the temperature must be applied to change the color from green to light green or faint green and $KMnO_4$ if applied will revert the changes, that is, overall no change in color and hence $OUT_3 = '1'$. Keypad-lock of such complexity and difficult to think-of permutations have rarely been reported and could be of potential significance under the circumstances where chemical warfare are in action.

Conclusions

We have demonstrated that **1** can perform CEES detection equally well in solution state as it does when covalently confined on solid supports. Covalently confined molecules have lesser pre-organization energy cost and offer proper orientation of the sensing sites, therefore, sensitivity of the solution based probe is of much significance. Detection limit, accuracy, sensitivity, selectivity are of similar standards as observed in the monolayer based studies. Further, we explored the 1H NMR and time dependent density functional studies for plausible explanations for the observance of multiple “optical states” upon **1**/CEES interaction. Sensor was duly reversible and allowed addressing of various sensing parameters to be used as input for generating specific outputs and creation of molecular logic gates of higher complexities. A keypad-lock has also been demonstrated with 4096 possible input permutations and out of which only 3 possible permutations could open the lock making it a very secure molecular keypad-lock.

Note

† Dedicated to Late Prof. Dr. Tarkeshwar Gupta.

‡ Neelam and Vikram Singh made equal contributions.

Acknowledgements

This work is financially supported by the Department of Atomic Energy-Board of Research in Nuclear Sciences (DAE-BRNS)(2010/20/37P/1/BRNS/1068-1) BARC, Mumbai. Neelam

sincerely thanks DAE-BRNS for project fellowship. VS thanks UGC for fellowship. RDG thanks Department of Science and Technology (SERB/F/1424) for financial assistance.

References

1. (a) M. Dixon, D. M. Needham, *Nature*, **1946**, 158, 432; (b) R. E. Lenski, M. A. Riley, *PNAS*, **2002**, 99, 556; (c) P. A. Smith, C. R. J. Lepage, D. Koch, H. D. M. Wyatt, G. L. Hook, G. Betsinger, R. P. Erickson, B. A. Eckenrode, *TrAC*, **2004**, 23, 296; (d) N. Medvedevam, Y. Polyak, I. Kuzikova, O. Orlova, G. Zharnikov, *Environ. Res.*, **2008**, 106, 289.
2. A. Gilman, Major; F. S. Philips, 1st Lieutenant, SnC, AUS, *Science*, **1946**, 103, 2675; (b) L. F. Haber, In *The Poisonous Cloud: Chemical Warfare in the First World War*; Clarendon Press, **1986**, pp 415; (c) J. B. Tucker, In *War of nerves: chemical warfare from World War I to Al-Qaeda*. Random House LLC, **2007**.
3. J. Borak, F. R. Sidell, *Annals Emergency Med.*, **1992**, 21, 303; (b) J. C. Dacre, M. Goldman, *Pharmacol. Rev.*, **1996**, 48, 289; (c) R. N. Saladi, E. Smith, A. N. Persaud, *Clin. Exp. Dermatol.*, **2006**, 31, 1.
4. S. -W. Zhang, T. M. Swager, *J. Am. Chem. Soc.*, **2003**, 125, 3420; (b) S. Royo, R. Martinez-Manez, F. Sancenon, A. M. Costero, M. Parra, S. Gil, *Chem. Commun.*, **2007**, 4839; (c) T. J. Dale, J. Rebek, *J. Am. Chem. Soc.*, **2006**, 128, 4500; (d) B. D. De Grenu, D. Moreno, T. Torroba, A. Berg, J. Gunnars, T. Nilsson, R. Nyman, M. Persson, J. Pettersson, I. Eklind, P. Wasterby, *J. Am. Chem. Soc.*, **2014**, 136, 4125.
5. (a) V. Kumar, E. V. Anslyn, *J. Am. Chem. Soc.*, **2013**, 135, 6338; (b) V. Kumar, E. V. Anslyn, *Chem. Sci.*, **4**, 4292.
6. (a) Y. Liu, A. J. Howarth, J. T. Hupps, O. K. Farha, *Angew. Chem. Intl. Ltd.*, **2015**, 54, 9001; (b) J. E. Mondloch, M. J. Katz, W. C. Isley III, P. Ghosh, P. Liao, W. Bury, G. W. Wagner, M. G. Hall, J. B. DeCoste, G. W. Peterson, R. Q. Snurr, C. J. Cramer, J. T. Hupp, O. K. Farha, *Nat. Mater.*, **2015**, 14, 512.
7. L. M. Eubanks, T. J. Dickerson, K. D. Janda, *Chem. Soc. Rev.* **2007**, 36, 458.
8. N. R. Brletich, M. J. Waters, G. W. Bowen, M. F. Tracy, *Worldwide Chemical Detection Equipment handbook*; Chemical and Biological Defense Information Analysis Centre: Aberdeen, MD, **1995**; (b) E. Greenbaum, *Biosens. Bioelectronic.*, **2001**, 16, 439; (c) J. P. Fitch, E. Raber, D. R. Imbro, *Science*, **2003**, 302, 1350; (d) Y. Sun, K. Y. Ong, In *Detection Technologies for*

- Chemical Warfare Agents and Toxic vapors*. CRC Press, Boca Raton, FL, **2005**; (e) J. L. Gottfried, F. C. De Lucia, C. A. Munson, A. W. Miziolek, *Appl. Spectro*, **2008**, 62, 353.
- 9.** G. P. van der Schans, D. Noort, R. H. Mars-Groenendijk, A. Fidder, L. F. Chau, L. P. A. de Jong, H. P. Benshop, *Chem. Res. Toxicol.*, **2002**, 15, 21; (b) R. Bunkar, K. D. Vyas, V. K. Rao, S. Kumar, B. Singh, M. P. Kaushik, *Trasducers J.*, **2010**, 113, 41.
- 10.** M. E. Anderson, A. G. M. Barrett, B. M. Hoffman, *Inorg. Chem.*, **1999**, 38, 6143; (b) T. Hashimoto, Y. -K. Choe, H. Nakano, K. Hirao, *J. Phys. Chem. A*, **1999**, 103, 1894; (c) A. G. Montalban, W. Jarrell, E. Riguet, Q. J. McCubbin, M. E. Anderson, A. J. P. White, D. J. Williams, A. G. M. Barrett, B. M. Hoffman, *J. Org. Chem.*, **2000**, 65, 2472.
- 11.** J. W. Silbert, T. F. Baumann, D. J. Williams, A. J. P. White, A. G. M. Barrett, B. M. Hoffman, *J. Am. Chem. Soc.*, **1996**, 118, 10487; (b) P. A. Stuzhin, E. M. Bauer, C. Ercolani, *Inorg. Chem.*, **1998**, 37, 1533; (c) H. Akku, A. Gul, *Trans. Metal Chem.*, **2001**, 26, 689.
- 12.** H. K. Oh, M. H. Ku, H. W. Lee, I. Lee, *J. Org. Chem.*, **2002**, 67, 3874; (b) A. C. Spivey, S. Arseniyadis, *Angew. Chem. Intl. Ed.*, **2004**, 43, 5436.
- 13.** Q. -Q Wang, R. A. Begum, V. W. Day, K. Bowman-James, *Org. Biomol. Chem.*, **2012**, 10, 8786.
- 14.** D. B. Ludlum, P. Austin-Ritchie, M. Hagopian, T. -Q. Niu, D. Yu, *Chemico-Bio. Interac.*, **1994**, 91, 39; (b) G. P. Van der Schans, A. G. Scheffer, R. H. Mars-Groenendijk, A. Fidder, H. P. Benshop, R. A. Baan, *Chem. Res. Toxicol.*, **1994**, 7, 408; (c) Q. Li, J. Laval, D. B. Ludlum, *Carcinogenesis*, **1997**, 18, 1035; (d) D. Noort, A. G. Hulst, L.P.A. de Jong, H.P. Benshop, *Chem. Res Toxicol.*, **1999**, 12, 715.
- 15.** (a) V. Singh, P. C. Mondal, M. Chhatwal, Y. L. Jeyachandran, M. Zharnikov, *RSC Adv.*, **2014**, 4, 23168; (b) V. Singh, P.C. Mondal, Y. L. Jeyachandran, M. Zharnikov, T. Gupta, *Analyst*, **2012**, 137, 3216; (c) P. C. Mondal, V. Singh, B. Shankar, *New J. Chem.*, **2014**, 38, 2679; (d) A. Kumar, M. Chhatwal, P. C. Mondal, V. Singh, A. K. Singh, D. A. Cristaldi, R. D. Gupta, A. Gulino, *Chem. Commun.*, **2014**, 50, 3783; (e) V. Singh, P. C. Mondal, A. Kumar, Y. L. Jeyachandran, S. K. Awasthi, R. D. Gupta M. Zharnikov, *Chem. Commun.*, **2014**, 50, 11484.
- 16.** Neelam, V. Singh, T. Gupta, *Anal. Chim. Acta*, **2014**, 812, 222.
- 17.** (a) J. Andreasson, U. Pischel, *Chem. Soc. Rev.*, **2015**, 44, 1053; (b) A. P. de Silva, *Nature*, **2008**, 454, 417; (c) G. de Ruiter, M. E. van der Boom, *Acc. Chem. Res.*, **2011**, 44, 563; (d) M. Elstner, J. Axthelm, A. Schiller, *Angew. Chem. Intl. Ed.*, **2014**, 53, 7339.

18. S. Chen, Z. Guo, S. Zhu, W. Shi, W. Zhu, *ACS Appl. Mater. Interfaces*, **2013**, 5, 5623
19. (a) F. Cong, Z. Wei, Z. Huang, F. Yu, H. Lu, J. Cui, H. Yu, Z. Chu, X. Du, K. Xing, J. Lai, *Dyes Pigments*, **2015**, 120, 1; (b) M. P. Donzello, G. D. Mori, E. Viola, C. Ercolani, G. Ricciardi, A. Rosa, *Inorg. Chem.*, **2014**, 53, 8009.
20. A. A. Brimfield, A. M. Mancebo, R. P. Mason, J. J. Jiang, A. G. Siraki, M. J. Novak, *Toxicol. Appl. Pharmacol.*, **2009**, 234, 128.
21. D. F. Perepichka, M. R. Bryce, *Angew. Chem. Intl. Ed.*, **2005**, 44, 5370.
22. (a) A. Shaabani, F. T. Rad, D. G. Lee, *Syn. Commun.*, **2005**, 35, 571; (b) S. Popiel, Z. Witkiewicz, A. Szewczuk, *J. Hazard. Mater. B*, **2005**, 123, 94.
23. (a) P. C. Mondal, V. Singh, Y. L. Jeyachandran, M. Zharnikov, *ACS Appl. Mater. Interfaces*, **2015**, 7, 8677; (b) A. Kumar, M. Chhatwal, A. K. Singh, V. Singh, M. Trivedi, *Chem. Commun.*, **2014**, 50, 8488.
24. (a) A. K. Singh, R. Nagarajan, *Dalton Trans.*, **2015**, 44, 19786; (c) X. -J. Jinag, D. K. P. Ng, *Angew. Chem.*, **2014**, 53, 10481.

Biographies

Neelam received M.S. Degree in Chemistry (2004) from Indian Institute of Technology Roorkee, India and M.E. in Polymer Technology from Delhi College of Engineering, Delhi, India. She is currently pursuing her PhD with Prof. Dan Meyerstein at Department of Biological Chemistry, Ariel University, Israel. Her research interest includes Surface-mediated bio-inorganic chemistry and polyoxometalate based sol-gel processes.

Vikram Singh obtained M.S. Degree and PhD in Chemistry from University of Delhi, India and currently a post-doctoral fellow in South Korea. His research interest includes Surface-mediated bio-inorganic chemistry, in general and development of artificial nucleases immobilized on solid supports, in particular.

Bhaskaran Shankar received M.S. Degree (Chemistry) from Vivekananda College (Madurai Kamaraj University), Madurai, India in 2007 and PhD degree in Chemistry from the University of Delhi in 2013. Presently he is D. S. Kothari Postdoctoral fellow under the guidance of Dr. M. Sathiyendiran at School of Chemistry, University of Hyderabad, India. His research interests on functional Supramolecular coordination chemistry.

Ramasamy Shanmugam, received his M.S. Degree in Chemistry (2010) from Madurai Kamaraj University, Madurai, India. Currently he is working as a Senior Research Fellow under the guidance of Dr. A. Tamaraichelvan at Thiagarajar College, Madurai, India. His research focuses on CO₂ activation on catalytic surfaces.

Dr. Satish K. Awasthi obtained his D.Phil from Allahabad University, Allahabad, India in 1991. He is currently working as an Associate Professor in the Department of Chemistry, University of Delhi, Delhi. His research interests Drug Discovery, Parallel Peptide-nucleic acid (PNA) /peptide synthesis, peptide chemistry (Boc and Fmoc), peptidomimetic synthesis, Peptide-nucleic acid (PNA), combinatorial synthesis, synthesis of kinase inhibitor and screening, synthesis of

heterocyclic compounds. Synthesis and characterization of nucleobases, development of new protecting group for nucleobases, cell culture, cellular uptake, PNA-peptide conjugation

Dr. Rinkoo D. Gupta obtained her Ph.D. degree in Histopathology from Department of Zoology, Banaras Hindu University, Varanasi, India in 2005. She was a Post-Doctoral Fellow in the Department of Biological Chemistry, in Weizmann Institute of Sciences, Israel from 2006 to 2009. She worked in Institute of Genomics and Integrative Biology, Delhi from 2010-2011. She is working as an Assistant Professor in the Faculty of Life Sciences and Biotechnology, South Asian University, New Delhi since 2011. Her research interests focus on the Protein Engineering for the development of new therapeutic proteins and drug discovery. She has more than 30 publications in peer-reviewed journals including Nature Chemical Biology, Nature Methods, and Chemical Communications.

Biographies

Neelam received her M.S. Degree in Chemistry (2004) from Indian Institute of Technology Roorkee, India and M.E. in Polymer Technology from Delhi College of Engineering, Delhi, India. She is currently pursuing her Ph.D. with Prof. Dan Meyerstein at Department of Biological Chemistry, Ariel University, Israel. Her research interest includes Surface-mediated bioinorganic chemistry and polyoxometalate based sol-gel processes.

Vikram Singh obtained M.S. Degree and Ph.D. in Chemistry from University of Delhi, India and currently a post doctoral fellow in South Korea. His research interest includes Surface-mediated bio-inorganic chemistry, in general and development of artificial nucleases immobilized on solid supports, in particular.

Bhaskaran Shankar received his M.S. (Chemistry) from Vivekananda College (Madurai Kamaraj University), Madurai, India in 2007 and Ph.D. degree in Chemistry from the University of Delhi in 2013. Presently he is D. S. Kothari Postdoctoral fellow under the guidance of Dr. M. Sathiyendiran at School of Chemistry, University of Hyderabad, India. His research interests on functional Supramolecular coordination chemistry.

Ramasamy Shanmugam received his M.S. degree in Chemistry (2010) from Madurai Kamaraj University, Madurai, India. Currently he is working as a Senior Research Fellow under the guidance of Dr. A. Thamaraichelvan at Thiagarajar College, Madurai, India. His research focuses on CO₂ activation on catalytic surfaces.

Dr. Satish K. Awasthi obtained his D.Phil. from Allahabad University, Allahabad, India in 1991. He is currently working as an Associate Professor in the Department of Chemistry, University of Delhi, Delhi, India. His research

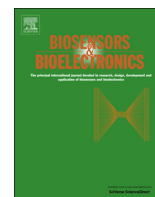
interests Drug Discovery, Parallel Peptide-nucleic acid (PNA) /peptide synthesis, peptide chemistry (Boc and Fmoc), peptidomimetic synthesis, Peptide-nucleic acid (PNA), combinatorial synthesis, synthesis of kinase inhibitor and screening, synthesis of heterocyclic compounds. Synthesis and characterization of nucleobases, development of new protecting group for nucleobases, cell culture, cellular uptake, PNA-peptide.

Dr. Rinkoo D. Gupta obtained her Ph.D. degree in Histopathology from Department of Zoology, Banaras Hindu University, Varanasi, India in 2005. She was a Post-Doctoral Fellow in the Department of Biological Chemistry, in Weizmann Institute of Sciences, Israel from 2006 to 2009. She worked in Institute of Genomics and Integrative Biology, Delhi from 2010-2011. She is working as an Assistant Professor in the Faculty of Life Sciences and Biotechnology, South Asian University, New Delhi since 2011. Her research interests focus on the Protein Engineering for the development of new therapeutic proteins and drug discovery. She has more than 30 publications in peer-reviewed journals including Nature Chemical Biology, Nature Methods, and Chemical Communications.



Contents lists available at ScienceDirect

Biosensors and Bioelectronics

journal homepage: www.elsevier.com/locate/bios

Nanostructured zirconia decorated reduced graphene oxide based efficient biosensing platform for non-invasive oral cancer detection



Suveen Kumar, Jai Gopal Sharma, Sagar Maji, Bansi Dhar Malhotra *

Nanobioelectronics Laboratory, Department of Biotechnology, Delhi Technological University, Delhi 110042, India

ARTICLE INFO

Article history:

Received 15 September 2015

Received in revised form

13 November 2015

Accepted 27 November 2015

Available online 30 November 2015

Keywords:

Biosensor

Zirconia

Reduced graphene oxide

CYFRA-21-1

Oral cancer

ABSTRACT

We report results of the studies relating to fabrication of a non-invasive, label-free and an efficient biosensing platform for detection of the oral cancer biomarker (CYFRA-21-1). One step hydrothermal process was used for uniform decoration of nanostructured zirconia (average particle size 13 nm) on reduced graphene oxide (ZrO₂-RGO) to avoid coagulation of the zirconia nanoparticles and to obtain enhanced electrochemical performance of ZrO₂-RGO nanocomposite based biosensor. Further, ZrO₂-RGO has been functionalized using 3-aminopropyl triethoxy saline (APTES) and electrophoretically deposited on the indium tin oxide coated glass substrate at a low DC potential. The APTES/ZrO₂-RGO/ITO electrode exhibits improved heterogeneous electron transfer (more than two times) with respect to that of the APTES/ZrO₂/ITO electrode indicating faster electron transfer kinetics. The -NH₂ containing APTES/ZrO₂-RGO/ITO platform is further biofunctionalized with anti-CYFRA-21-1. The structural and morphological investigations of the ZrO₂-RGO based biosensing platform have been accomplished using X-ray diffraction (XRD), electrochemical, transmission electron microscopy (TEM), atomic force microscopy (AFM) and Fourier transform infrared spectroscopy (FT-IR) studies. This immunosensor exhibits a wider linear detection range (2–22 ng mL⁻¹), excellent sensitivity (0.756 μA mL ng⁻¹) and a remarkable lower detection limit of 0.122 ng mL⁻¹. The observed results have been validated via enzyme linked immunosorbent assay (ELISA).

© 2015 Elsevier B.V. All rights reserved.

1. Introduction

Non-invasive detection strategy is considered to be a promising alternative for detection of human diseases (Guilbault et al., 1995). To accomplish this, saliva, tear, urine and sweat have been proposed as interesting for desired biomedical investigations (Chen et al., 2011; Tille, 2013). Among these, saliva based clinical testing has many advantages due to easier saliva collection, low cost of storage and easy transport (Lawrence, 2002). Further, the non-invasive saliva based collection techniques can dramatically reduce anxiety and discomfort for monitoring disease and general health of a patient. Saliva is a useful non-invasive body fluid that can be used for biomarker detection. Besides this, it is one of the simplest and easily accessible body fluid that can be utilized for a wide range of applications including early detection and monitoring of diseases including oral cancer (Lawrence, 2002; Tille, 2013).

Oral cancer (OC) is currently the sixth most common cancer and is caused by uncontrolled growth of cells in the floor of

mouth, lips, sinuses, tongue, cheeks, throat etc. (Kujan et al., 2006; Kumar et al., 2015a). The main reasons behind this cancer are chewing of tobacco, smoking, alcohol consumption, gastro-esophageal reflux disease, human papillomavirus and exposure to chemicals (e.g. formaldehyde and asbestos) (Gorschinski et al., 2009). These high risk factors may alter the expression of p16, APC and p53 genes resulting in the origin of oral cancer (Gonzalez et al., 1997). This cancer can be life threatening if not detected and is not treated at an early stage. For diagnosis of the oral cancer, laser-capture micro-dissection, visualization adjuncts, cytopathology and biopsy techniques can be used and these techniques require tissue specimens that are highly painful to obtain (Mehrotra and Gupta, 2011; Patton et al., 2008; Scully et al., 2008). Besides this, these methods are highly expensive, time consuming and require skilled personnel for specimen collection. However, the non-invasive biosensing is attractive, cost effective, accurate and easier to use for oral cancer detection (Malhotra et al., 2012; Mehrotra and Gupta, 2011; Scully et al., 2008).

The salivary biomarkers such as Interleukin-8 (IL-8), Interleukin-6 (IL-6), Interleukin-1 (IL-1), Interleukin-1β (IL-1β), TNFα-1, Endotheline-1 (ET-1), HNP-1, hsa-miR-200a can be used for early diagnosis and prognosis of the oral cancer (Malhotra et al., 2010; Pickering et al., 2007; Punyani and Sathawane, 2013). However,

* Corresponding author.

E-mail address: bansi.malhotra@gmail.com (B.D. Malhotra).

only a few reports are available for detection of salivary biomarkers using biosensing technique. Most of these biomarkers are secreted in very low amount (pg mL^{-1}) (Malhotra et al., 2012, 2010; Mehrotra and Gupta, 2011). CYFRA-21-1, a proteinaceous biomarker (also known as cytokeratin-19) is a member of keratin family that is known to maintain structural integrity of the epithelial cells. It is a 40 kDa molecule encoded by *KRT19* gene. In saliva of oral cancer patients, it is secreted in higher concentration ($17.46 \pm 1.46 \text{ ng mL}^{-1}$) (Nagler et al., 2006; Rajkumar et al., 2015).

Transducers are known to play an important role towards the fabrication of an efficient biosensor. It provides an interactive platform for the immobilization of biomolecules on desired substrate and can be used for monitoring of an electrical signal resulting due to an electrochemical reaction at an electrode surface, usually as a result of an imposed potential, current or frequency. The unique properties of a transducer can be helpful in improving the characteristics of a biosensor (Roushani and Valipour, 2016; Solanki et al., 2011). Nanostructured metal oxides (NMOs) have been found to have interesting optical and electrical properties due to electron and phonon confinement, high surface-to-volume ratio, modified surface work function, high surface reaction activity, high catalytic efficiency and strong adsorption ability. The NMOs can thus be utilized for increased loading of desired biomolecules per unit mass of particles. Among the various NMOs, zirconia has been found to have interesting physiochemical as well as biosensing characteristics (Das et al., 2011). Biocompatibility, excellent electrical and surface charge properties, oxygen moieties in ZrO_2 make it a promising material as a transducer in the fabrication of a biosensor (Das et al., 2011; Liu and Lin, 2005; Kumar et al., 2015a). In this context, it has been reported that zirconia nanoparticles tend to aggregate and form large clusters (Kumar et al., 2015a; Zhao et al., 2006). To overcome these problems, a substrate material with a high surface area and good conductivity is crucial for increasing the physiochemical and biosensing activity of zirconia nanoparticles.

The chemically reduced graphene oxide (GO) has recently been found to be a promising substrate for uniform distribution of metal oxide nanoparticles (Dong et al., 2012; Sawangphruk et al., 2013; Wei et al., 2011). The reduced graphene oxide (RGO) has been demonstrated to have excellent electrochemical conductivity due to rapid heterogeneous electron transport (HET), superior mechanical flexibility and remarkable stability that can be helpful for the fabrication of an efficient biosensing platform (Ali et al., 2014). Gong et al. (2012) proposed a facile electrochemical approach for synthesis of zirconia-reduced graphene oxide nanosheets for application in enzyme less methyl parathion sensor. Efforts have also been made to detect hydroquinone and catechol using RGO- ZrO_2 based sensor (Vilian et al., 2014).

We report for the first time results of the studies relating to application of zirconia decorated reduced graphene oxide nanocomposite as a transducer for development of an immunosensor. This immunosensor can be used for non-invasive, label-free and efficient detection of oral cancer biomarker (CYFRA-21-1) and it covers the entire physiological range (3.8 to $17.46 \pm 1.46 \text{ ng mL}^{-1}$) secreted in saliva of oral cancer patients. The results obtained have been validated via enzyme linked immunosorbent assay (ELISA).

2. Materials and methods

2.1. Chemicals

Zirconium ethoxide, natural graphite flakes and 1-(3-(dimethylamino)-propyl)-3-ethylcarbodiimide hydrochloride (EDC) were purchased from Sigma-Aldrich. Sodium hydroxide, cetyltrimethylammonium bromide (CTAB), sodium monophosphate,

sodium diphosphate dihydrate and N-hydroxysuccinimide (NHS) were purchased from Fisher Scientific. 3-aminopropyl triethoxy saline (APTES) was purchased from Alfa-aesar. All the chemicals were of analytical grade and used without any further purification. Electrochemical studies were performed using 0.05 M phosphate buffer solution (PBS) prepared using sodium monophosphate and sodium diphosphate dihydrate. All solutions prepared using milli-Q water having resistivity of $18 \text{ M}\Omega \text{ cm}$ were stored at 4°C . CYFRA-21-1 antigen and anti-CYFRA-21-1 antibodies were purchased from Ray Biotech, Inc., India. These biomolecules were further diluted by using PBS buffer of pH 7.0. CYFRA-21-1 ELISA Kit was purchased from Kinesis DX, USA.

2.2. Fabrication of biosensing platform

Nanostructured ZrO_2 decorated RGO was prepared and functionalized with APTES (please see Supporting Information). 20 mg of functionalized nanocomposite (APTES/ ZrO_2 -RGO) was dispersed in 50 mL of acetonitrile by mild ultrasonication. The electrophoretic deposition (EPD) technique was used to deposit thin film of APTES/ ZrO_2 -RGO onto prehydrolyzed ITO glass that worked as an anode and platinum wire as cathode, placed parallelly at a separation distance of 1 cm in glass cell. These were dipped in the prepared colloidal solution and electrophoretically deposited at an optimized DC potential (15 V) for about 3 min using electrophoretic deposition unit (Genetix, GX300C). This APTES/ ZrO_2 -RGO/ITO film was washed with deionized water and dried at room temperature (25°C) over night. Next, a stock solution ($50 \mu\text{g mL}^{-1}$) of anti-CYFRA-21-1 was prepared in PBS (pH=7.0). For activation of the $-\text{COOH}$ groups of antibodies, EDC-NHS chemistry was used where EDC (0.2 M) worked as a coupling agent and NHS (0.05 M) as an activator. A solution mixture of anti-CYFRA-21-1, EDC and NHS in 2:1:1 ratio was made and kept at room temperature (25°C) for 30 min. Further, $30 \mu\text{L}$ of activated antibody solution was uniformly spread over APTES/ ZrO_2 -RGO/ITO electrode and kept in a humid chamber at room temperature (25°C) during the next 3 h. Thereafter, it was washed with PBS to remove any unbound antibody molecules. $20 \mu\text{L}$ of BSA (2 mg dL^{-1}) was used for blocking the non-specific active sites. The fabricated BSA/anti-CYFRA-21-1/APTES/ ZrO_2 -RGO/ITO immunoelectrode was washed with PBS and stored at 4°C until further use.

2.3. Sample collection and processing

Saliva samples of eight OC patients were collected from Rajiv Gandhi Cancer Institute and Research Centre (RGCIRC), Delhi (India) after written consent by the patients. Prior to this, we took ethical approval of the Institutional Review Board of RGCIRC and Institutional Ethical and Biosafety Committee, DTU. We collected un-stimulated saliva samples after rinsing the mouth with 5 mL deionized water and thereafter expectorated into sterilized tube. These samples were centrifuged at 2800 rcf (25°C) for 30 min. the supernatant was collected in sterilized eppendorf and stored at -20°C until further use (Rajkumar et al., 2015). All the samples were collected, processed and stored in a similar fashion.

3. Results and discussion

3.1. X-ray diffraction (XRD) and Electron microscopy studies

Fig. 1a shows the XRD pattern obtained for the hydrothermally synthesized ZrO_2 -RGO nanocomposite. The peak observed at 24.2° is due to merging of the ZrO_2 (110) and RGO (002) planes. Further, the relatively lower intensity broad peak is observed at 43.0°

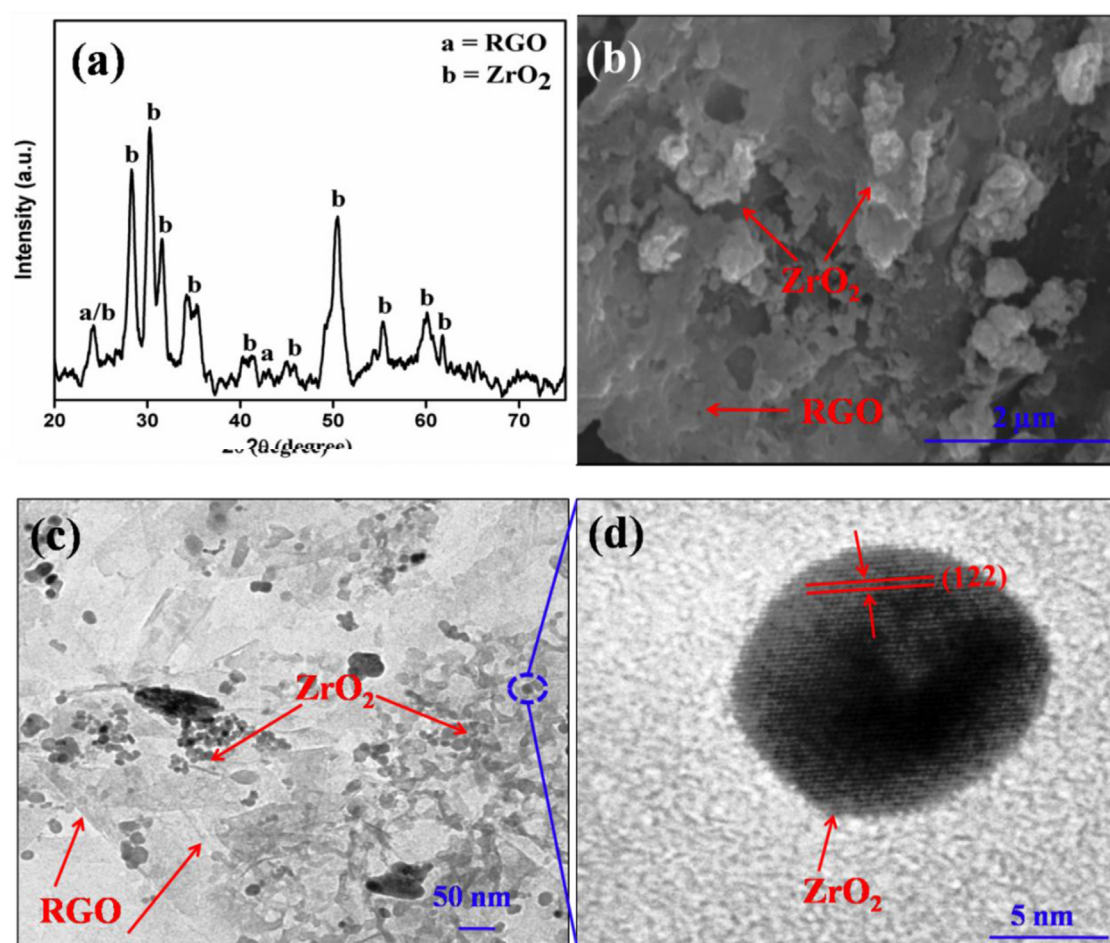


Fig. 1. (a) XRD pattern (b) SEM and (c) TEM image of ZrO₂ grafted reduced graphene oxide (d) HR-TEM image of individual ZrO₂.

indicating RGO planes of (001) (Srivastava et al., 2013). The other reflection peaks observed at 28.34° , 30.28° , 31.6° , 34.2° , 35.4° , 40.3° , 44.9° , 50.4° , 55.3° , 60.1° and 61.8° correspond to (111), (111), (-111), (022), (200), (-102), (-211), (122), (013), (302) and (-113) planes. These results indicate grafting of the pure monoclinic phase of ZrO₂ (Kumar et al., 2015a) on the surface of RGO sheet. The average grain size (D) of the grafted zirconia on RGO surface is found to be 13 nm, calculated using Scherrer formula i.e. $D = 0.94\lambda / \beta \cos \theta$, where λ ($= 1.54060 \text{ \AA}$) is the X-ray wavelength, β is the full width at half maximum and θ is the Bragg angle.

Fig. 1b–d shows SEM, TEM and HR-TEM images of the synthesized ZrO₂–RGO nanocomposite. A well dispersed solution of ZrO₂–RGO nanocomposite is prepared in milli-Q water and dropped onto 50 mesh carbon coated gold grid and dried at room temperature for the TEM studies. It appears that spherical ZrO₂ nanoparticles are uniformly grafted on the RGO sheet (Fig. 1b and c). Fig. 1d shows an individual spherical ZrO₂ nanoparticle present at the RGO sheet indicating a crystal lattice spacing of 0.179 nm corresponding to the inter-spacing of the (122) plane with an average grain size of 13 nm. The calculated grain size of ZrO₂ is in

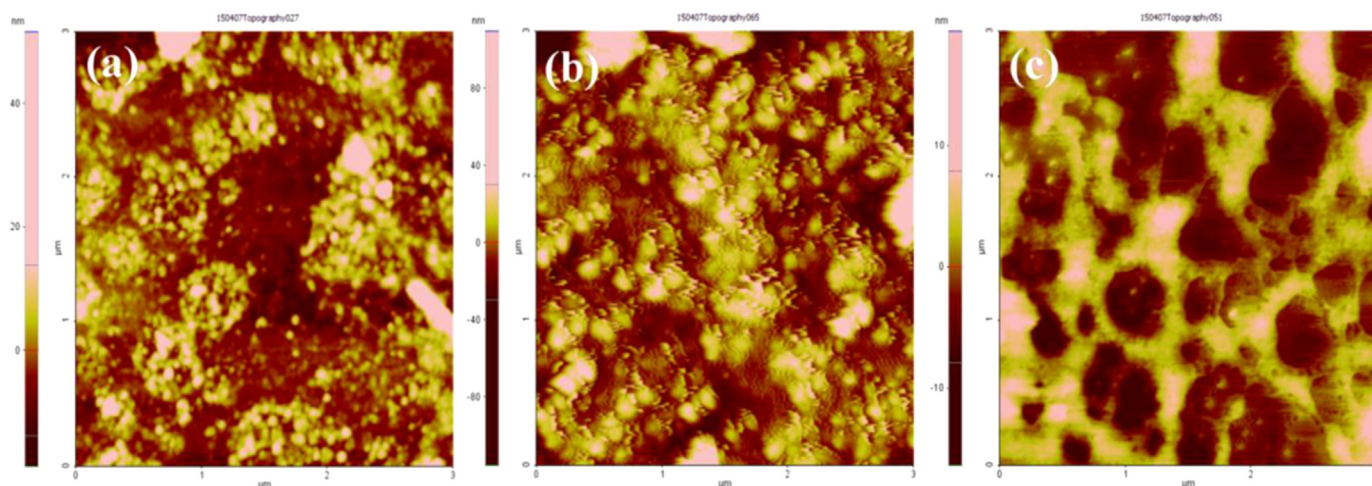


Fig. 2. Atomic force microscopic images of (a) APTES/ZrO₂–RGO/ITO (b) anti-CYFRA/APTES/ZrO₂–RGO/ITO and (c) BSA/anti-CYFRA/APTES/ZrO₂–RGO/ITO electrodes.

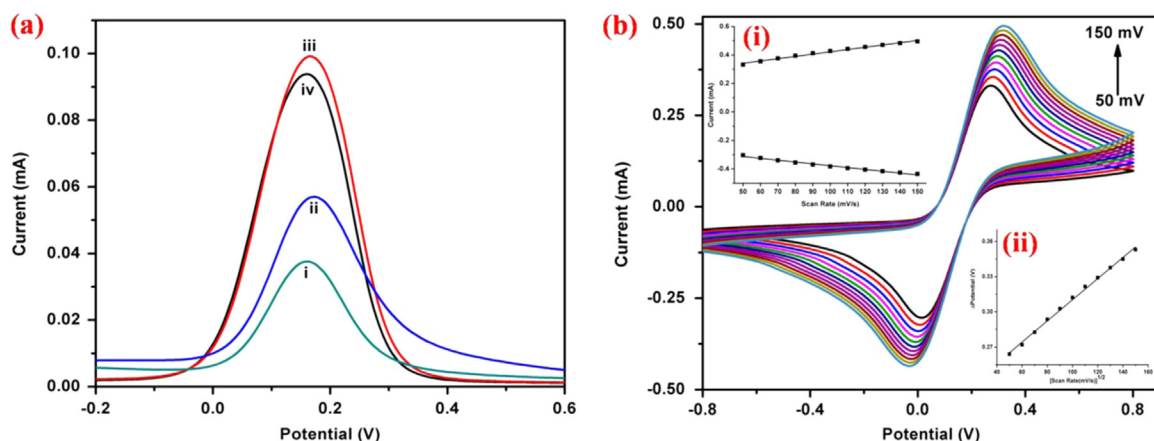


Fig. 3. (a) Electrode response study of APTES/ZrO₂/ITO (curve i), APTES/ZrO₂-RGO/ITO (curve ii), anti-CYFRA-21-1/APTES/ZrO₂-RGO/ITO (curve iii) and BSA/anti-CYFRA-21-1/APTES/ZrO₂-RGO/ITO (curve iv) and (b) scan rate studies of BSA/anti-CYFRA-21-1/APTES/ZrO₂-RGO/ITO [inset (a) magnitude of oxidation and reduction current generated as response of scan rate (mV/s), inset (b) potential as function of scan rate] electrodes.

support of the results of X-ray diffraction studies (Fig. 1a)

3.2. Atomic force microscopic (AFM) studies

Fig. 2 shows AFM image of (a) APTES/ZrO₂-RGO/ITO, (b) anti-CYFRA-21-1/APTES/ZrO₂-RGO/ITO and (c) BSA/anti-CYFRA-21-1/APTES/ZrO₂-RGO/ITO obtained in the non-contact mode. The average roughness of APTES/ZrO₂-RGO/ITO electrode is observed to be 4.256 nm with granular topography, indicating uniform electrophoretic deposition of functionalized ZrO₂-RGO film on ITO coated glass electrode. After covalent immobilization of anti-CYFRA-21-1, topography of the electrode changes from granular to globular as shown in Fig. 2 (b). The average roughness increases to 27.803 nm and the observed globular topography reveals successive immobilization of biomolecules on the APTES/ZrO₂-RGO/ITO electrode. Fig. 2(c) shows that the average roughness of the electrode decreases to 1.521 nm after BSA immobilization. This can be attributed to blocking of the non-specific binding sites and formation of highly uniform immunoelectrode surface.

3.3. Fourier transform infrared spectroscopy (FT-IR)

FT-IR studies have been carried out to investigate the presence of functional groups on fabricated APTES/ZrO₂-RGO/ITO electrode and bond formation after immobilization on anti-CYFRA-21-1. Fig. S1 (Supplementary information) shows FT-IR spectra of (i) APTES/ZrO₂-RGO/ITO and (ii) anti-CYFRA-21-1/APTES/ZrO₂-RGO/ITO. In spectra (i) the peak at 1099 cm⁻¹ is due to the C–OH stretching vibration present on the RGO sheet. The band found at 1557 cm⁻¹ is due to the bending vibration mode of the secondary amide groups. The bands present at 1641 cm⁻¹ and 3350 cm⁻¹ are due to bending mode of primary amide groups indicating presence of the free –NH₂ groups on surface of APTES/ZrO₂-RGO/ITO electrode. The additional peaks observed at 2852 cm⁻¹ and 2922 cm⁻¹ are attributed to C–H bonds of alkanes and aldehydes groups present on the APTES molecules as well as on RGO sheet (Ali et al., 2014). In spectra (ii) an additional broad band is observed between 1220 and 1300 cm⁻¹ indicating amide bond (C–N) formation between –NH₂ groups present on APTES/ZrO₂-RGO/ITO electrode and –COOH groups present in Fc region of anti-CYFRA-21-1 biomolecules revealing successful covalent immobilization of the anti-CYFRA-21-1 (Ali et al., 2014). The peaks seen at 1269 cm⁻¹, 1452 cm⁻¹, 1562 cm⁻¹, 1641 cm⁻¹ and 2712 cm⁻¹ can be assigned to C–O, C=C, –NH₂ (primary amine), –NH–R (secondary amine) and C–H groups of aldehydes, respectively (Ali

et al., 2014; Pasternack et al., 2008; Vasudev et al., 2013). In both spectra (i) and (ii), a sharp peak with the same intensity is observed at 2360 cm⁻¹ due to presence of O–H groups of carboxylic acid present on RGO. This indicates that anti-CYFRA-21-1 is not bound with carboxylic acid of RGO present on APTES/ZrO₂-RGO/ITO electrodes.

3.4. Electrochemical studies

Fig. S2 shows the effect of [Fe(CN)₆]^{3-/4-} on CV of APTES/ZrO₂-RGO/ITO and BSA/anti-CYFRA-21-1/APTES/ZrO₂-RGO/ITO electrodes. It can be seen (Fig. S2(a) and (b)) that in the presence of [Fe(CN)₆]^{3-/4-}, cyclic voltammogram shows oxidation as well as reduction peaks. In the absence of [Fe(CN)₆]^{3-/4-}, we did not observe any redox peak current in case of the APTES/ZrO₂-RGO/ITO and BSA/anti-CYFRA-21-1/APTES/ZrO₂-RGO/ITO electrodes. In the present studies, [Fe(CN)₆]^{3-/4-} was used as an electron mediator that provides electronic amplification, facilitating high-sensitivity as a result of occurrence of each of the biomolecular complexation event.

Fig. S3 shows electrochemical response of the BSA/anti-CYFRA-21-1/APTES/ZrO₂-RGO/ITO immunoelectrode as a function of pH (6.0 to 8.0) in PBS buffer (50 mM, 0.9% NaCl) containing [Fe(CN)₆]^{3-/4-} (5 mM) ions using differential pulse voltammetry (DPV) technique. The DPV shows maximum peak current at pH 7.0. This is because at neutral pH, structure of the biological molecule is preserved (Liu and Lin, 2005). Thus PBS buffer with pH 7.0 was used for the electrochemical studies.

Fig. 3a shows DPV response of (i) APTES/ZrO₂/ITO (ii) APTES/ZrO₂-RGO/ITO (iii) anti-CYFRA-21-1/APTES/ZrO₂-RGO/ITO and (iv) BSA/anti-CYFRA-21-1/APTES/ZrO₂-RGO/ITO electrode at a scan rate of 50 mV/s in the potential range, –0.2 to 0.6 V. It is found that APTES/ZrO₂/ITO electrode exhibits a peak current of 0.037 mA and is 0.057 mA in case of the APTES/ZrO₂-RGO/ITO electrode. This is attributed to the excellent electrochemical properties of the reduced graphene oxides sheets present in the RGO–ZrO₂ composite. After immobilization of the antibodies, the anti-CYFRA-21-1/APTES/ZrO₂-RGO/ITO electrode shows increased peak current of 0.10 mA. The observed increase in the peak current after immobilization of anti-CYFRA-21-1 on APTES/ZrO₂-RGO/ITO electrode is due to presence of the ZrO₂-RGO matrix that acts as a mediator at the electrode surface (ITO) resulting in significant decrease of the electron tunneling distance between the antibodies and the electrode (Anusha et al., 2014; Vasudev et al., 2013). Besides this, presence of the electrostatic interaction between the free site of the antibodies (–NH₂ terminal) and the

redox species results in faster electron diffusion towards the immunoelectrode (Kumar et al., 2015b). BSA has been used for blocking the non-specific active sites of the anti-CYFRA-21-1/APTES/ZrO₂-RGO/ITO immunoelectrode. After BSA immobilization, magnitude of the peak current further decreases to 0.094 mA due to insulating nature of the BSA molecules (Kumar et al., 2015; Vilian et al., 2014). Further, impedance spectrum was measured in the frequency range, 100 kHz–100 mHz, with varying potential from 10 to 100 mV (Fig. S4). It is found that the impedance spectra changes shape as the voltage increases and with increase in the voltage there is a decrease in the charge transfer resistance (R_{ct}) value after 20 mV. Thus, 20 mV was selected as the optimized voltage for all the impedance measurements. To investigate the heterogeneous electron transport (HET) of APTES/ZrO₂/ITO and APTES/ZrO₂-RGO/ITO electrodes, electrochemical impedance spectroscopy (EIS) studies were conducted at 20 mV/s (Fig. S5). The HET ($6.624 \times 10^{-6} \text{ cm s}^{-1}$) of APTES/ZrO₂/ITO electrode is found to increase by more than two times ($14.49 \times 10^{-6} \text{ cm s}^{-1}$) when RGO is incorporated in APTES/ZrO₂-RGO/ITO electrode facilitating faster electron transfer.

The cyclic voltammogram (CV) of APTES/ZrO₂-RGO/ITO and BSA/anti-CYFRA-21-1/APTES/ZrO₂-RGO/ITO electrodes were recorded as a function of scan rate (50–150 mV/s) (Figs. S6 and 3b). The magnitudes of both anodic (I_{pa}) and cathodic (I_{pc}) peak currents exhibit a linear relationship with scan rate (Figs. S6 and 3b, inset a) indicating that the electrochemical reaction is a diffusion-controlled process (Vasudev et al., 2013) and follows Eqs. (1)–(4):

$$I_{pc(\text{APTES/ZrO}_2\text{-RGO/ITO})} = [1.43 \times 10^{-9} \text{ A(s/mV)} \times (\text{scan rate[mV/s]})^{1/2}] + 2.31 \times 10^{-7} \text{ A}, R^2 = 0.99, \text{ SD} = 4.53 \times 10^{-6} \quad (1)$$

$$I_{pa(\text{APTES/ZrO}_2\text{-RGO/ITO})} = -[1.25 \times 10^{-9} \text{ A (s/mV)} \times (\text{scan rate[mV/s]})^{1/2}] - 2.05 \times 10^{-7} \text{ A}, R^2 = 0.99, \text{ SD} = 4.11 \times 10^{-6} \quad (2)$$

$$I_{pc(\text{BSA/anti-CYFRA-21-1/APTES/ZrO}_2\text{-RGO/ITO})} = [1.60 \times 10^{-9} \text{ A(s/mV)} \times (\text{scan rate[mV/s]})^{1/2}] + 2.61 \times 10^{-7} \text{ A}, R^2 = 0.99, \text{ SD} = 4.53 \times 10^{-6} \quad (3)$$

$$I_{pa(\text{BSA/anti-CYFRA-21-1/APTES/ZrO}_2\text{-RGO/ITO})} = -[1.29 \times 10^{-9} \text{ A (s/mV)} \times (\text{scan rate[mV/s]})^{1/2}] - 2.48 \times 10^{-7} \text{ A}, R^2 = 0.99, \text{ SD} = 4.11 \times 10^{-6} \quad (4)$$

Further it is observed that with increasing scan rate, the oxidation peak shifts towards higher potential and the reduction peak shifts towards lower potential. The linearity is obtained between the difference in magnitude of the oxidation peak potential and reduction peak potential ($\Delta V = V_{pa} - V_{pc}$, V_{pa} is anodic peak potential and V_{pc} is cathodic peak potential) as a function of scan rate (Fig. S6 and 3b, inset b), indicating facile charge transfer kinetics between medium to electrode (Kumar et al., 2015a) and follows Eqs. (5) and (6) :

$$\Delta V_{(\text{APTES/ZrO}_2\text{-RGO/ITO})} = [1.70 \times 10^{-3} \text{ V(s/mV)} \times (\text{scan rate[mV/s]})^{1/2}] + 0.346 \text{ V}, R^2 = 0.99, \text{ SD} = 4.79 \times 10^{-3} \quad (5)$$

$$\Delta V_{(\text{BSA/anti-CYFRA-21-1/APTES/ZrO}_2\text{-RGO/ITO})} = [0.90 \times 10^{-3} \text{ V(s/mV)} \times (\text{scan rate[mV/s]})^{1/2}] + 0.220 \text{ V}, R^2 = 0.99, \text{ SD} = 1.75 \times 10^{-3} \quad (6)$$

where R is the correlation coefficient and SD is the standard deviation. The diffusion coefficient (D) of BSA/anti-CYFRA-21-1/APTES/ZrO₂-RGO/ITO immunoelectrode has been determined to be $1.12 \times 10^{-3} \text{ cm}^2 \text{ s}^{-1}$ using Randle Sevcik equation (Sharma et al., 2012):

$$I_p = (2.69 \times 10^5) n^{3/2} A D^{1/2} C v^{1/2} \quad (7)$$

where I_p is the peak current of immunoelectrode, n is the number of electrons (1) transferred, A is the active surface area of the immunoelectrode (0.25 cm^2), D is the diffusion coefficient, C is the concentration of redox species ($5 \times 10^{-3} \text{ mol cm}^{-2}$) and v is the scan rate (50 mV/s).

The surface concentration of BSA/anti-CYFRA-21-1/APTES/ZrO₂-RGO/ITO immunoelectrode has been calculated to be $8.03 \times 10^{-9} \text{ mol cm}^{-2}$ by using Laviron's theory (Sharma et al., 2012):

$$I_p = n^2 F^2 \gamma A \nu (4RT)^{-1} \quad (8)$$

where I_p represents the peak current of immunoelectrode, n is the number of electrons (1) transferred, F is the Faraday constant ($96,485 \text{ C mol}^{-1}$), γ is the surface concentration of the absorbed electro-active species, A is the surface area of the electrode, ν is the scan rate (V/s), R is the gas constant ($8.314 \text{ J mol}^{-1} \text{ K}^{-1}$) and T is room temperature (25°C or 298 K).

3.5. Response studies

Differential pulse voltammetry (DPV) technique has been utilized to investigate electrochemical response of the fabricated BSA/anti-CYFRA-21-1/APTES/ZrO₂-RGO/ITO immunoelectrode as a function of CYFRA-21-1 concentration in PBS buffer (50 mM, 0.9% NaCl) containing $[\text{Fe}(\text{CN})_6]^{3-/4-}$ (5 mM) (Fig. 4b). It has been found that magnitude of the anodic peak current increases after formation of antigen–antibody complex between CYFRA-21-1 and anti-CYFRA-21-1 on the electrode surface. To investigate the reasons behind increased peak current, we analyzed the sequence of CYFRA-21-1 (Cytokeratin 19 fragments, *Homo sapiens*) obtained from NCBI protein database (Accession: AAF27048.1, shown in Fig. S7). It can be seen that CYFRA-21-1 protein contains 14 residues of tyrosine (Y) molecules. During an electrochemical reaction these tyrosine molecules undergo oxidation and release electrons (as shown in Scheme S1) resulting in increased peak current. (Okuno et al., 2007, Wei et al., 2012, Palecek et al., 2015) The increased concentration of amino acids due to increased concentration of CYFRA-21-1 antigen is likely to result in enhanced antigen–antibody interaction onto APTES/ZrO₂-RGO/ITO electrode leading to increased peak current. Alternatively, it may perhaps be attributed to both the conformation changes in the BSA/anti-Cyfra-21-1/APTES/ZrO₂-RGO matrix and the strong affinity of CYFRA-21-1 antigen towards the spatially oriented antibodies that are likely to provide easy conducting paths for electron transfer to the BSA/anti-CYFRA-21-1/APTES/ZrO₂-RGO/ITO electrode leading to improved sensing characteristics such as linearity, faster response time and shelf life (Wan et al., 2013, Okuno et al., 2007, Kaushik et al., 2009, Viswanathan et al., 2006, Zhang et al., 2008, Kumar et al., 2015b). The magnitude of anodic current increases with increasing concentration of CYFRA-21-1 from 2 to 22 ng mL^{-1} (Fig. 4d) after which the current tends to saturate at higher concentrations. All the experiments were repeated three times at each concentration. Results of the response studies

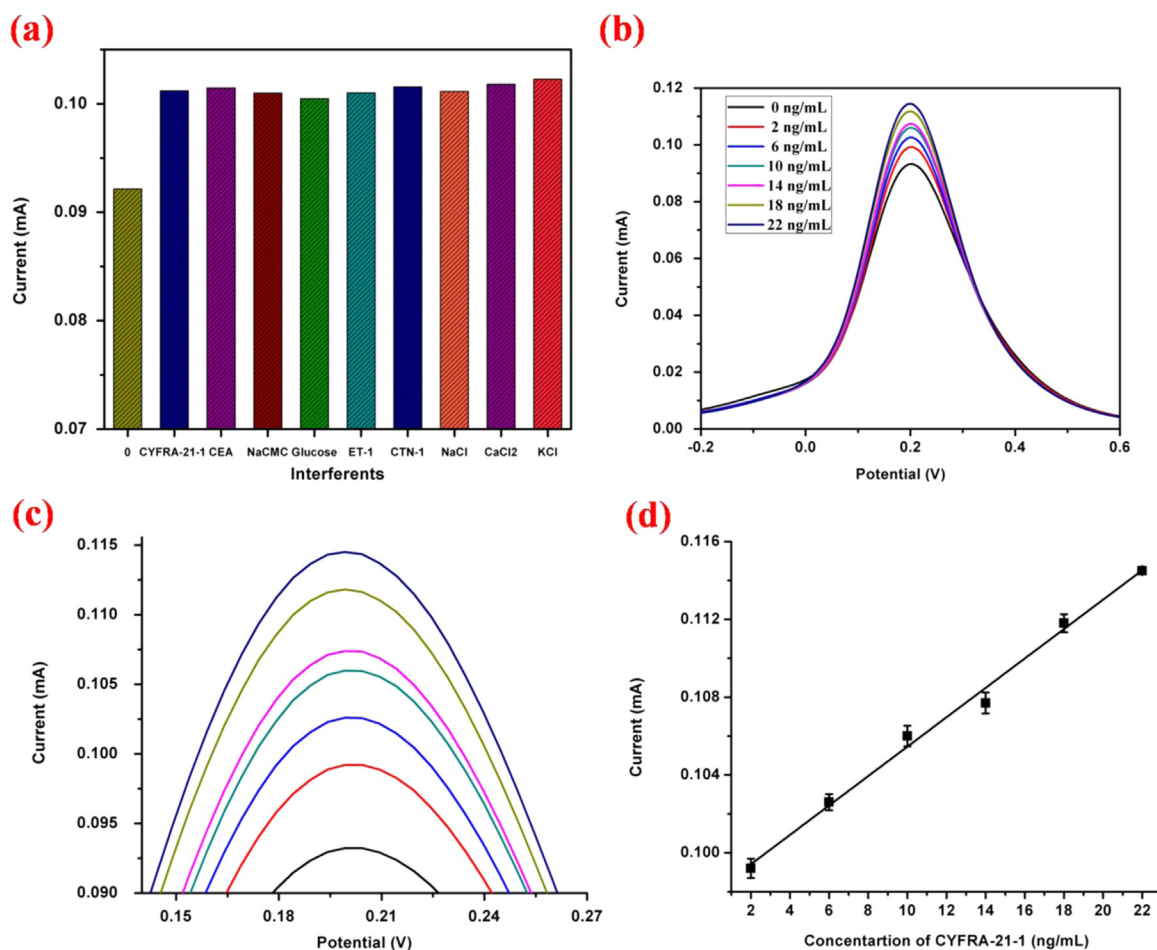


Fig. 4. (a) Interferents studies of BSA/anti-CYFRA-21-1/APTES/ZrO₂-RGO/ITO immunoelectrode (b) electrochemical response studies of BSA/anti-CYFRA-21-1/APTES/ZrO₂-RGO/ITO immunoelectrode as a function of CYFRA-21-1 concentration (2–22 ng/mL) (c) magnified view of oxidation peak current (d) a calibration curve has been plotted between peak current and CYFRA-21-1 concentration.

indicate that BSA/anti-CYFRA-21-1/APTES/ZrO₂-RGO/ITO immunoelectrode can be used to detect CYFRA-21-1 in the range of 2–22 ng mL⁻¹ ($R^2=0.99$). The sensitivity of the fabricated immunoelectrode can be estimated by the slope of the curve and is found to be 0.756 $\mu\text{A mL ng}^{-1}$. The standard deviation and limit of detection (LOD) for the immunoelectrode are obtained to be 3.08×10^{-5} and 0.122 ng mL⁻¹, respectively. The limit of detection has been calculated using the standard Eq. (9):

$$\text{Limit of detection} = 3 \sigma / \text{Sensitivity} \quad (9)$$

where σ is standard deviation of the BSA/anti-CYFRA-21-1/APTES/ZrO₂-RGO/ITO immunoelectrode.

We conducted a control experiment using covalently immobilized anti-CYFRA-21-1 onto electrophoretically deposited RGO on ITO electrode. Fig. S8(a) shows the electrochemical response of the fabricated BSA/anti-CYFRA-21-1/RGO/ITO immunoelectrode as a function of CYFRA-21-1 concentration in PBS buffer (50 mM, 0.9% NaCl) containing $[\text{Fe}(\text{CN})_6]^{3-/4-}$ (5 mM). It can be seen that the electrochemical response increases as a function of CYFRA-21-1 concentration (Fig. S8b). Similar behavior is observed in case of the APTES/ZrO₂ based immunosensor (Kumar et al., 2015b). And it may be noted that the observed results obtained in case of BSA/anti-CYFRA-21-1/RGO/ITO, BSA/anti-CYFRA-21-1/ZrO₂/ITO and BSA/anti-CYFRA-21-1/ZrO₂-RGO/ITO immunoelectrodes are repeatedly obtained.

And another control experiment was conducted to investigate the electrochemical response of APTES/ZrO₂-RGO/ITO electrode towards

CYFRA-21-1 without using anti-CYFRA-21-1 (Fig. S9). We did not observe any significant changes in magnitude of the peak current with respect to different concentration of CYFRA-21-1. This result indicates that the sensor response is likely to be due to the immunoreaction between anti-CYFRA-21-1 and CYFRA-21-1 molecules.

3.6. Interferents studies

Saliva is known to be saturated with a large number of organic, inorganic and biological analytes such as carcinoembryonic antigen (CEA) [4–16 ng mL⁻¹], cardiac troponin I (CTN-I) [0.19 ng mL⁻¹], sodium carboxymethyl cellulose (NaCM) [10 mg mL⁻¹], glucose [7 mg mL⁻¹], endothelin 1 protein, NaCl (20 mM), CaCl₂ (1.13 mM), KCl (8.38 mM) etc. These analytes may interfere with the electrochemical response of a BSA/anti-CYFRA-21-1/APTES/ZrO₂-RGO/ITO immunoelectrode. To investigate the effect of these analytes on electrochemical response, we conducted the interferent studies (Fig. 4a) in PBS buffer (pH 7.0, 50 mM, 0.9% NaCl) containing $[\text{Fe}(\text{CN})_6]^{3-/4-}$ (5 mM). First we added 2 ng mL⁻¹ concentration of CYFRA-21-1. After a defined incubation time the peak current increased to 0.10 mA. On addition of the various analytes we observed that the maximum peak current change occurred in the presence of glucose and KCl with %RSD as 0.60% and 0.75% respectively. The mean %RSD due to all the interferents is 0.32% which is very low and has no significant effect on the peak current of electrochemical response. These results reveal that BSA/anti-CYFRA-21-1/APTES/ZrO₂-RGO/

Table 1

Determination of CYFRA-21-1 concentration in saliva samples using BSA/anti-CYFRA-21-1/APTES/ZrO₂-RGO/ITO bioelectrode.

S. No.	CYFRA-21-1 concentration determined using ELISA (in ng mL ⁻¹)	Peak current (mA) obtained for standard CYFRA-21-1 samples	Peak current samples (mA) obtained with saliva	%RSD (%)
1.	15.35	0.1095	0.1071	1.51
2.	13.35	0.1080	0.1035	3.35
3.	13.50	0.1082	0.1065	1.12
4.	14.15	0.1086	0.1048	2.52
5.	12.50	0.1074	0.1071	0.20
6.	14.15	0.1086	0.1053	2.18

ITO immunoelectrode is highly selective for the detection of CYFRA-21-1 antigen.

3.7. Real sample analysis

Enzyme linked immunosorbent assay (ELISA) was used for quantitative determination of CYFRA-21-1 in saliva samples of six oral cancer patients. We performed double-antibody sandwich ELISA in anti-CYFRA-21-1 coated 96 microtiter wells plate. Both the standard and the patient's samples were used in triplicate. Colorimetric reactions were recorded at 450 nm by ELISA plate reader (iMark, Bio red, USA). After determination of the CYFRA-21-1 concentration in the saliva of oral cancer patients by ELISA, the BSA/anti-CYFRA-21-1/APTES/ZrO₂-RGO/ITO electrode was used to record the DPV response towards different concentrations of the real samples. A reasonable agreement between the response current was obtained (Table 1) for real samples and the standard samples with acceptable %RSD. These results reveal high accuracy of the fabricated immunosensor for the determination of CYFRA-21-1 in clinical patient samples.

3.8. Stability and response time studies

The stability of the BSA/anti-CYFRA-21-1/APTES/ZrO₂-RGO/ITO immunoelectrode was determined by DPV studies at a regular interval upto 10 weeks (Fig. S10). The immunoelectrode was stored at 4 °C when not in use. It was observed that magnitude of the peak current exhibited 94% response upto 8 weeks after which the peak current decreased rapidly indicating that stability of the fabricated immunoelectrode is upto 8 weeks. The response time of the BSA/anti-CYFRA-21-1/APTES/ZrO₂-RGO/ITO immunoelectrode was determined by measuring DPV current response by varying the incubation period from 1 to 30 min (Fig. S11). It was found that the biosensor reached maximum peak current after 16 min of incubation revealing sufficient attachment of the antigens to the immunoelectrode surface. The sensing characteristics of the proposed BSA/anti-CYFRA-21-1/APTES/ZrO₂-RGO/ITO immunosensor are summarized in Table 2.

4. Conclusions

In summary, a non-invasive, label free and efficient immunosensor based on nanostructured zirconia decorated reduced graphene oxide has been fabricated to detect CYFRA-21-1 biomarker in saliva of oral cancer patients. The ZrO₂-RGO nanocomposite has been prepared through one step low temperature hydrothermal process and silanized with APTES. Further, the electrophoretic deposition (EPD) technique has been used for formation of the thin film of APTES/ZrO₂-RGO on ITO coated glass substrate. The APTES/ZrO₂-RGO/ITO electrode surface has been

Table 2
Characteristics of the various detection techniques used for oral cancer detection.

Method	Detection technique	Invasive/non-invasive	Label	Sample	Biomarker	Platform	Concentration range of biomarker	Sensitivity	Linear detection range	Response time	Shelf Life	Reference
Cytopathology	Staining	Invasive	-	Cells	-	-	-	-	-	-	-	Rosenberg and Cretin (1989)
Biopsy	Cell culture	Invasive	-	Tissue	-	-	-	-	-	2–3 Weeks	-	Patton et al. (2008)
Visualization adjuncts	Staining	Invasive	-	Tissue	-	-	-	-	-	1 Week	-	Patton et al. (2008)
Biosensor	Amperometric	Invasive	Yes	Serum	IL-6 (Protein)	-	≤ 6 pg mL ⁻¹ to ≥ 20 pg mL ⁻¹	19.3 nA mL pg ⁻¹ cm ⁻²	0.5–30 pg mL ⁻¹	-	-	Malhotra et al. (2010)
	DPV	Invasive	Yes	Serum	IL-6 (Protein)	-	< 6 pg mL ⁻¹ to > 20 pg mL ⁻¹	-	0.002–20 ng mL ⁻¹	-	4 Weeks	Li and Yang (2011)
	CV	Non invasive	Yes	Saliva	has-miR-200a (miRNA)	-	-	-	1 aM–10 fM	-	-	Wang et al. (2013)
	CV	Non invasive	No	Saliva	CYFRA-21-1 (Protein)	BSA/anti-CYFRA-21-1/APTES/ZrO ₂ /ITO	0–18 ng mL ⁻¹	2.2 μA mL ng ⁻¹	2–16 ng mL ⁻¹	20 min	6 Weeks	Kumar et al. (2015b)
	DPV	Non invasive	No	Saliva	CYFRA-21-1 (Protein)	BSA/anti-CYFRA-21-1/APTES/ZrO ₂ -RGO/ITO	0–18 ng mL ⁻¹	0.756 μA mL ng ⁻¹	2–22 ng mL ⁻¹	16 min	8 Weeks	Present work

functionalized with anti-CYFRA-21-1 antibodies and BSA molecules. The fabricated immunoelectrode (BSA/anti-CYFRA-21-1/APTES/ZrO₂-RGO/ITO) exhibits higher sensitivity (0.756 μ A mL ng⁻¹), wider linear detection range (2–22 ng mL⁻¹) and remarkable low detection limit (0.122 ng mL⁻¹). The shelf life of this immunoelectrode has been found to be 8 weeks and results of the sensing studies have been validated through ELISA. Efforts should be made to utilize this immunosensor for detection of other cancer biomarkers and it should be interesting to investigate the effect of the ZrO₂ nanoparticle and the role of antigen-antibody interactions on the performance of this immunosensor.

Acknowledgments

We thank Prof. Yogesh Singh, Vice Chancellor Delhi Technological University, Delhi (India) for providing the research facilities. We thank Dr. A.K. Dewan, Dr. D.C. Dovel and Dr. Birendra Kumar Yadav of Rajiv Gandhi Cancer Institute & Research Centre for valuable discussions. Suveen Kumar is thankful to DTU for the award of financial assistance, nanofabrication laboratory of DTU for the AFM facilities, Sandeep Mishra for XRD, Dr. Laxman S. Meena, Institute of Genomics and Integrative Biology, Delhi (India) for TEM studies and Dr. Saurabh Srivastava, Department of Applied Physics and Saroj Kumar, DTU for valuable scientific discussions.

Appendix A. Supplementary material

Supplementary data associated with this article can be found in the online version at <http://dx.doi.org/10.1016/j.bios.2015.11.084>.

References

- Ali, M.A., Kamil Reza, K., Srivastava, S., Agrawal, V.V., John, R., Malhotra, B.D., 2014. Lipid–lipid interactions in aminated reduced graphene oxide interface for biosensing application. *Langmuir* 30 (14), 4192–4201.
- Anuska, J., Kim, H.-J., Fleming, A.T., Das, S.J., Yu, K.-H., Kim, B.C., Raj, C.J., 2014. Simple fabrication of ZnO/Pt/chitosan electrode for enzymatic glucose biosensor. *Sens. Actuators B: Chem.* 202, 827–833.
- Chen, J., Zhang, J., Guo, Y., Li, J., Fu, F., Yang, H.-H., Chen, G., 2011. An ultrasensitive electrochemical biosensor for detection of DNA species related to oral cancer based on nuclease-assisted target recycling and amplification of DNzyme. *Chem. Commun.* 47 (28), 8004–8006.
- Das, M., Dhand, C., Sumana, G., Srivastava, A., Vijayan, N., Nagarajan, R., Malhotra, B., 2011. Zirconia grafted carbon nanotubes based biosensor for M. Tuberculosis detection. *Appl. Phys. Lett.* 99 (14), 143702.
- Dong, X.-C., Xu, H., Wang, X.-W., Huang, Y.-X., Chan-Park, M.B., Zhang, H., Wang, L.-H., Huang, W., Chen, P., 2012. 3D graphene–cobalt oxide electrode for high-performance supercapacitor and enzymeless glucose detection. *ACS Nano* 6 (4), 3206–3213.
- Gong, J., Miao, X., Wan, H., Song, D., 2012. Facile synthesis of zirconia nanoparticles-decorated graphene hybrid nanosheets for an enzymeless methyl parathion sensor. *Sens. Actuators B: Chem.* 162 (1), 341–347.
- Gonzalez, M., Artime, M., Rodrigo, L., Lopez-Larrea, C., Menendez, M., Alvarez, V., Perez, R., Fresno, M., Perez, M., Sampedro, A., 1997. Mutation analysis of the p53, APC, and p16 genes in the Barrett's oesophagus, dysplasia, and adenocarcinoma. *J. Clin. Pathol.* 50 (3), 212–217.
- Gorschinski, A., Khelashvili, G., Schild, D., Habicht, W., Brand, R., Ghafari, M., Bönnemann, H., Dinjus, E., Behrens, S., 2009. A simple aminoalkyl siloxane-mediated route to functional magnetic metal nanoparticles and magnetic nanocomposites. *J. Mater. Chem.* 19 (46), 8829–8838.
- Guilbault, G.G., Palleschi, G., Lubrano, G., 1995. Non-invasive biosensors in clinical analysis. *Biosens. Bioelectron.* 10 (3), 379–392.
- Kaushik, A., Solanki, P.R., Pandey, M., Ahmad, S., Malhotra, B.D., 2009. Cerium oxide-chitosan based nanobiocomposite for food borne mycotoxin detection. *Appl. Phys. Lett.* 95 (17), 173703.
- Kujan, O., Glenny, A.M., Oliver, R., Thakker, N., Sloan, P., 2006. Screening Programmes for the Early Detection and Prevention of Oral Cancer. John Wiley & Sons, Ltd., The Cochrane Library, New York.
- Kumar, S., Kumar, S., Srivastava, S., Yadav, B.K., Lee, S.H., Sharma, J.G., Doval, D.C., Malhotra, B.D., 2015a. Reduced graphene oxide modified smart conducting paper for Cancer biosensor. *Biosens. Bioelectron.* 73, 114–122.
- Kumar, S., Kumar, S., Tiwari, S., Srivastava, S., Srivastava, M., Yadav, B.K., Tran, T.T., Dewan, A.K., Mulchandani, A., Sharma, J.G., Maji, S., Malhotra, B.D., 2015b. Biofunctionalized nanostructured zirconia for biomedical application: a smart approach for oral cancer detection. *Adv. Sci.* 2 (8), 1500048.
- Lawrence, H.P., 2002. Salivary markers of systemic disease: noninvasive diagnosis of disease and monitoring of general health. *J. Can. Dent. Assoc.* 68 (3), 170–175.
- Li, T., Yang, M., 2011. Electrochemical sensor utilizing ferrocene loaded porous polyelectrolyte nanoparticles as label for the detection of protein biomarker IL-6. *Sensors and Actuators B: Chemical* 158 (1), 361–365.
- Liu, G., Lin, Y., 2005. Electrochemical sensor for organophosphate pesticides and nerve agents using zirconia nanoparticles as selective sorbents. *Anal. Chem.* 77 (18), 5894–5901.
- Malhotra, R., Patel, V., Vaqu , J.P., Gutkind, J.S., Rusling, J.F., 2010. Ultrasensitive electrochemical immunosensor for oral cancer biomarker IL-6 using carbon nanotube forest electrodes and multilabel amplification. *Anal. Chem.* 82 (8), 3118–3123.
- Malhotra, R., Patel, V., Chikkaveeraiah, B.V., Munge, B.S., Cheong, S.C., Zain, R.B., Abraham, M.T., Dey, D.K., Gutkind, J.S., Rusling, J.F., 2012. Ultrasensitive detection of cancer biomarkers in the clinic by use of a nanostructured microfluidic array. *Anal. Chem.* 84 (14), 6249–6255.
- Mehrotra, R., Gupta, D.K., 2011. Exciting new advances in oral cancer diagnosis: avenues to early detection. *Head Neck Oncol.* 3 (1), 1–9.
- Nagler, R., Bahar, G., Shpitzer, T., Feinmesser, R., 2006. Concomitant analysis of salivary tumor markers—a new diagnostic tool for oral cancer. *Clin. Cancer Res.* 12 (13), 3979–3984.
- Okuno, J., Maehashi, K., Kerman, K., Takamura, Y., Matsumoto, K., Tamiya, E., 2007. Label-free immunosensor for prostate-specific antigen based on single-walled carbon nanotube array-modified microelectrodes. *Biosens. Bioelectron.* 22, 2377–2381.
- Pasternack, R.M., Rivillon Amy, S., Chabal, Y.J., 2008. Attachment of 3-(aminopropyl) triethoxysilane on silicon oxide surfaces: dependence on solution temperature. *Langmuir* 24 (22), 12963–12971.
- Patton, L.L., Epstein, J.B., Kerr, A.R., 2008. Adjunctive techniques for oral cancer examination and lesion diagnosis: a systematic review of the literature. *J. Am. Dent. Assoc.* 139 (7), 896–905.
- Pickering, V., Jordan, R.C., Schmidt, B.L., 2007. Elevated salivary endothelin levels in oral cancer patients—a pilot study. *Oral Oncol.* 43 (1), 37–41.
- Punyani, S.R., Sathawane, R.S., 2013. Salivary level of interleukin-8 in oral precancer and oral squamous cell carcinoma. *Clin. Oral Investig.* 17 (2), 517–524.
- Rajkumar, K., Ramya, R., Nandhini, G., Rajashree, P., Ramesh Kumar, A., Nirmala Anandan, S., 2015. Salivary and serum level of CYFRA 21-1 in oral precancer and oral squamous cell carcinoma. *Oral Dis.* 21 (1), 90–96.
- Roushani, M., Valipour, A., 2016. Using electrochemical oxidation of Rutin in modeling a novel and sensitive immunosensor based on Pt nanoparticle and graphene–ionic liquid–chitosan nanocomposite to detect human chorionic gonadotropin. *Sens. Actuators B: Chem.* 222, 1103–1111.
- Sawangphruk, M., Srimuk, P., Chiochan, P., Kritayavathananon, A., Luanwuthi, S., Limtrakul, J., 2013. High-performance supercapacitor of manganese oxide/reduced graphene oxide nanocomposite coated on flexible carbon fiber paper. *Carbon* 60, 109–116.
- Scully, C., Bagan, J.V., Hopper, C., Epstein, J.B., 2008. Oral cancer: current and future diagnostic techniques. *Am. J. Dent.* 21 (4), 199–209.
- Sharma, A., Pandey, C.M., Sumana, G., Soni, U., Sapra, S., Srivastava, A., Chatterjee, T., Malhotra, B.D., 2012. Chitosan encapsulated quantum dots platform for leukemia detection. *Biosens. Bioelectron.* 38 (1), 107–113.
- Solanki, P.R., Kaushik, A., Agrawal, V.V., Malhotra, B.D., 2011. Nanostructured metal oxide-based biosensors. *NPG Asia Mater.* 3 (1), 17–24.
- Srivastava, S., Kumar, V., Ali, M.A., Solanki, P.R., Srivastava, A., Sumana, G., Saxena, P. S., Joshi, A.G., Malhotra, B., 2013. Electrophoretically deposited reduced graphene oxide platform for food toxin detection. *Nanoscale* 5 (7), 3043–3051.
- Tille, P., 2013. Bailey & Scott's Diagnostic Microbiology. Elsevier Health Sciences, United States.
- Vasudev, A., Kaushik, A., Bhansali, S., 2013. Electrochemical immunosensor for label free epidermal growth factor receptor (EGFR) detection. *Biosens. Bioelectron.* 39 (1), 300–305.
- Vilian, A.E., Chen, S.-M., Huang, L.-H., Ali, M.A., Al-Hemaid, F.M., 2014. Simultaneous determination of catechol and hydroquinone using a Pt/ZrO₂-RGO/GCE composite modified glassy carbon electrode. *Electrochim. Acta* 125, 503–509.
- Viswanathan, S., Wu, L.C.M., Huang, R., Ho, J.A., 2006. Electrochemical immunosensor for cholera toxin using liposomes and poly(3,4-ethylenedioxythiophene)-coated carbon nanotubes. *Anal. Chem.* 78, 1115–1121.
- Wan, Y., Su, Y., Zhu, X., Liu, G., Fan, C., 2013. Development of electrochemical immunosensors towards point of care diagnostics. *Biosens. Bioelectron.* 47, 1–11.
- Wang, J.H., Wang, B., Liu, Q., Li, Q., Huang, H., Song, L., Sun, T.Y., Wang, H., Yu, X.F., Li, C., 2013. Bimodal optical diagnostics of oral cancer based on Rose Bengal conjugated gold nanorod platform. *Biomaterials* 34 (17), 4274–4283.
- Wei, J., Qiu, J., Li, L., Ren, L., Zhang, X., Chaudhuri, J., Wang, S., 2012. A reduced graphene oxide based electrochemical biosensor for tyrosine detection. *Nanotechnology* 23 (33), 335707.
- Wei, Y., Gao, C., Meng, F.-L., Li, H.-H., Wang, L., Liu, J.-H., Huang, X.-J., 2011. SnO₂/reduced graphene oxide nanocomposite for the simultaneous electrochemical detection of cadmium (II), lead (II), copper (II), and mercury (II): an interesting favorable mutual interference. *J. Phys. Chem. C* 116 (1), 1034–1041.
- Zhang, S., Zheng, F., Wu, Z., Shen, G., Yu, R., 2008. Highly sensitive electrochemical detection of immunospecies based on combination of Fc label and PPD film/gold nanoparticle amplification. *Biosens. Bioelectron.* 24, 129–135.
- Zhao, N., Pan, D., Nie, W., Ji, X., 2006. Two-phase synthesis of shape-controlled colloidal zirconia nanocrystals and their characterization. *J. Am. Chem. Soc.* 128 (31), 10118–10124.

New Generation Antibiotics/Antibacterials: Deadly Arsenal for Disposal of Antibiotic Resistant Bacteria

Monica Sharma^{*1,2}, Shashank Singh² and Sidharth Sharma²

¹Department of Biotechnology, School of Biosciences and Biotechnology, Babasaheb Bhimrao Ambedkar University, Vidya Vihar, Raebareli Road, Lucknow, Uttar Pradesh, India

²Department of Biotechnology, Delhi Technological University, Main Bawana Road, Shahbad Daultpur, Delhi, India

Abstract

Inappropriate prescribing, lack of compliance in taking medicines and wise spread uncontrolled use of drugs led to emergence of multidrug resistance in clinically important infectious agents. Over 480000 new cases of multidrug-resistant tuberculosis (MDR-TB) were reported by WHO in the year 2013 in hundred countries world wide. Therefore, there is an urgent need for new generation antibacterial which can effectively and precisely act on drug resistant bacteria. Different strategies of development of resistance in bacteria involve the changes at molecular level like mutations, over expression of enzymes and efflux. So, the strategies of antibiotics development can include methods which can counteract at molecular level like antisense antibacterial and inhibition of quorum sensing. Bacterial gene *rpoD* found in *Staphylococcus* species is highly conserved and became basis in creation of antisense antibacterial against it. Lipid II class of antibiotics including teixobactin and antimicrobial peptides (AMPs), i.e. produced synthetically, have also shown promising results against the resistant bacterial strains. The present review summarizes the current scenario on research and development of new age antibiotics and techniques to tackle drug resistant bacterial infection.

Keywords: Teixobactin; Anti-microbial peptides; Ctriporin; Beta-Lactum

Introduction

The last century saw the emergence of antibiotics as wonder drugs which not only saved million lives but also revolutionised the arena of advanced medical sciences. These drugs have not only reduced the mortality during routine surgery and childbirth to negligible, and but also reduced the stigma associated with HIV which was once considered as deadly disease. In recent times due to exposure to various xenobiotics/drugs, bacteria are evolving so rapidly that they have developed resistant against antibiotics/antibacterial and hence pose serious threat to health [1]. Resistance development limits the use of antibacterials and this increases the demand of introduction of new compounds [2,3]. When early resistance to penicillin was observed, second generation antibiotics, methicillin, cephalothin and imipenem were already developed [4]. In 1961, a methicillin resistant strain of *S. aureus* (MRSA) was observed [5] and at present worldwide, an estimated 2 billion peoples carry some form of *S. aureus* and of these up to 53 million (2.7% of carriers) are thought to carry MRSA [6]. Over the years it has become clear that bacteria can develop resistance to almost any antibiotic. Except a few antibiotics, for instance erythromycin and vancomycin, resistance was developed against majority of antibacterials only a few years after their introduction into clinical use [7,8].

The mechanism of development of resistance in bacteria is mainly consisting of three strategies- (i) overexpression of enzymes that can modify the antibiotic drug rendering the antibiotic inactive; (ii) mutation of the bacterial target site that allows the target site to maintain its functional role yet abrogates binding of drug to the target or transverse of the antibiotic across the bacterial cell wall; (iii) export of antibiotic drugs to the extracellular media via multidrug-resistant (MDR) efflux pumps or loss of porin channels resulting in lower permeability of antibiotics (Figure 1) [9]. For example-drugs such as β -lactams, are inactivated via the over expression of β -lactamases, which hydrolyze the antibiotics [10], antibiotics such as linezolidare

and the streptogramin class rendered ineffective via the modification of 23S ribosomal RNA [11] and efflux pump proteins such as AcrB in *E. coli* [12] export antibiotics such as ciprofloxacin and tetracycline out of bacterial cells.

The aim of this review is to explore the current status of research and development of antibacterial compounds and techniques to tackle the bacterial infection.

Teixobactin

Teixobactin is the first of its kind of antibiotic that provides a

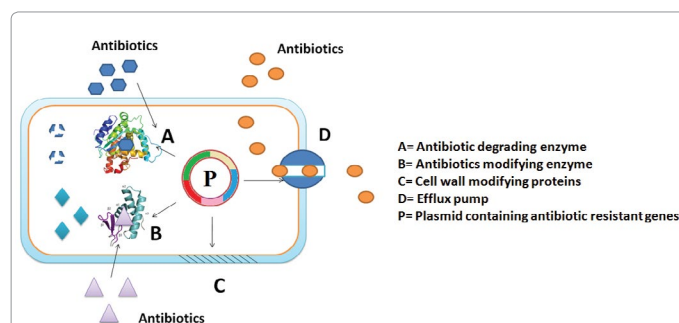


Figure 1: General mechanism of developing antibiotic resistance in bacteria.

***Corresponding authors:** Monica Sharma, Department of Biotechnology, Delhi Technological University, Main Bawana Road, Shahbad Daultpur, Delhi, India, Tel: +91-9717386785; E-mail: monashimla@gmail.com

Received September 26, 2015; **Accepted** October 20, 2015; **Published** October 27, 2015

Citation: Sharma M, Singh S, Sharma S (2015) New Generation Antibiotics/Antibacterials: Deadly Arsenal for Disposal of Antibiotic Resistant Bacteria. J Microb Biochem Technol 7: 374-379. doi:10.4172/1948-5948.1000241

Copyright: © 2015 Sharma M, et al. This is an open-access article distributed under the terms of the Creative Commons Attribution License, which permits unrestricted use, distribution, and reproduction in any medium, provided the original author and source are credited.

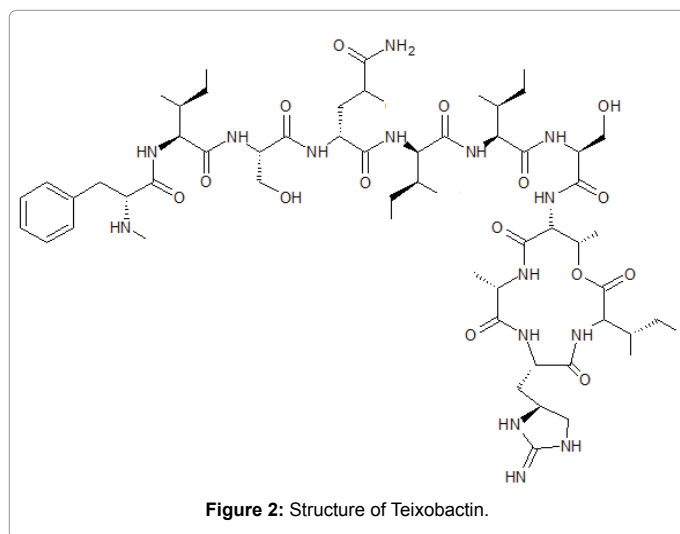


Figure 2: Structure of Teixobactin.

maiden entry to a more promising lipid II class of antibiotics (Figure 2). It is different from other known antibiotics like glycopeptides, lantibiotics and defensins in both its mode of action and structure [13-15]. Teixobactin is light of new hope in this era of incessantly growing antibiotics resistance; it is found out to be effective against a number of drug-resistant pathogenic microbes in some animal models of infection. Attack of teixobactin involves its binding to the wall of teichoic acid precursor that leads to the efficient lysis of cells and also the killing of cells by action of liberated autolysins [16]. Action of teixobactin is similar to the one other naturally occurring compound with a competent killing ability, 'acyldepsipeptide'. It converts the ClpP protease into a non-specific hydrolase which finally digests the cell [17]. Multiple targets are involved in the action of teixobactin out of which none of them is a protein.

Gram positive bacteria possess easily accessible lipid II which are poly prenyl precursors coupled to cell envelop and they represent a deadly weakness for antibiotic attack [18]. Among eubacteria pyrophosphate-sugar moiety of teixobactin target molecules is highly conserved. Gram-negative bacterium is one of those producers and its external membrane protects the bacterium from the re-entry of the compound. Henceforth, it is suggested by the study that the producer does not hire an alternative pathway for the synthesis of cell wall that would protect it from teixobactin. Therefore other bacteria couldn't borrow it. Horizontal transmission of a confrontation mechanism could sooner or later arise from some soil bacterium. The highly conserved teixobactin binding motif can take the form of an antibiotic modifying enzyme. Beta-lactams or aminoglycosides are those common antibiotics that codes for enzymes which attacks recurrently and they are unidentified for the vancomycin.

Newly discovered teixobactin is even less common than vancomycin. After its introduction into the clinic, it took years for vancomycin resistance to appear [19]. The lipid II modification pathway leading to vancomycin resistance possibly originated in the producer of vancomycin, *Amycolatopsis orientalis* [20]. Perhaps this could take even longer for resistance to better-protected teixobactin to emerge. The properties of teixobactin suggest that it evolved to minimize resistance development by target microorganisms. It is expected that additional natural compounds with similarly low susceptibility to resistance are present in nature and are waiting to be discovered [21]. However, teixobactin is not active against bacteria with an outer

membrane like gram negative pathogens, particularly carbapenem resistant enterobacteriaceae, or those with New Delhi metallo-beta-lactamase 1 [22].

Antisense Antibacterial

Antisense antibacterials are short (about 10 to 20 bases), synthetic DNA analogs that constrains the essential genes expression at mRNA level in a sequence-specific manner [23]. Thereafter, antisense inhibition leads to bacteriocidal or bacteriostatic effect or restoration of bacterial susceptibility, which relies on the role of targeted gene. Synthetic antisense oligomers, particularly phosphorodiamidate morpholino (PMO) [24] and peptide nucleic acid (PNA) [25], possess favorable properties in light of antisense antibacterial application. It also includes enhanced biological stability, targeting specificity, binding affinity and access to an array of chemical modifications. Meanwhile, instead of simple mixture, cell penetrating peptides (CPP) can be covalently attached or conjugated at the end of PNA or PMO chain to upgrade cellular uptake of antisense oligodeoxynucleotides (ASODNs) without affecting Watson-Crick base pairing between antisense oligomers and targeted RNAs [26]. Synthetic peptide- PNA or peptide-PMO conjugates targeting growth-essential genes shown to inhibit bacterial progression in pure culture and in infected tissue culture too. Therefore, a range of functional genes have been identified as potential targets [27]. However, only a few initial reports provided preliminary proof-of-principle support on antisense targeting of *S. aureus* genes for growth inhibitory effect (i.e., peptide-PNA targeting fabI [28] and phoB, fmhB, gyrA, plus hmrB).

Bacterial DNA-dependent RNA polymerase (RNAP) plays a vital role in transcription regulation and gene expression. Function of which requires coordination of a core enzyme (comprising five subunits α_2 , β , β' and Ω) and an independent σ subunit that is reversibly employed by core enzyme [29]. The RNAP core enzyme is accountable for transcription elongation whereas different σ s bind to different promoters to initiate transcription of genes of varied function. This irreversible inhibition of RNAP thereby causes cell death. It has engrossed much exploration for developing specific RNAP inhibitors (e.g., the rifamycins with fundamental clinical significance). The most developed $\sigma 70$ family of σ s, especially the primary $\sigma 70$, is essential for initiating transcription of multiple genes in exponential growth cells [30], which to our knowledge has not previously been demonstrated for antisense target validation in *S. aureus*. The primary $\sigma 70$ s are found to be unique in structure, function as well as homology. The core regions of bacterial and eukaryotic RNAPs share structural and functional similarities, but the sequences of encoding genes are only partially homologous. Specifically, bacterial gene rpoD (encoding the primary $\sigma 70$ of RNAP) shares the least homology in sequence with eukaryotic rpoD. Hence, in contrast to more conserved molecules, sequence-based drugs targeting rpoD products, including mRNAs, are less likely to cross react with host molecules. Most importantly, bacterial gene rpoD is highly conserved in identity and homologous in sequence among different pathogenic *Staphylococcus* species [31]. Such features are of distinctive advantages for developing narrow-spectra of anti-MRSA antisense agents.

Antimicrobial Peptides (AMPs)

In year 1939 Dubas discovered antimicrobial peptides [32]. Both Dubos and Hotchkiss identified an AMP in the following year which was named as gramicidin [33]. It was found to be very effective for topical treatment of wounds and ulcers [34]. AMPs, the major components of

innate immune system play a vital role in the host defense mechanism against environmental microorganisms. They are well versed in nature, existing in organisms from insects to plants and from microorganisms to mammals. AMPs have broad spectra of activity against infectious agents that includes Gram-negative and Gram-positive bacteria, fungi, viruses, and parasites too and rapid action. Cationic peptides are not affected by many antibiotic resistance mechanisms that now bound the use of other antibiotics [35,36]. Furthermore, in some of the cases, certain AMPs have been reported to kill antibiotic resistant bacteria e.g., both nisin (an AMP) and vancomycin (an antibiotic) kill bacteria by blocking their cell wall synthesis. However, MRSA (methicillin resistant *Staphylococcus aureus*) strain was reported to be resistant to vancomycin, while it was still sensitive to nisin [37].

In total, more than 5,000 AMPs have been discovered or synthesized up to date [38]. Natural AMPs can be found in both prokaryotes (e.g., bacteria) and eukaryotes (e.g., protozoan, fungi, plants, insects, and animals) [39-42] whereas in animals, AMPs are mostly found in the tissues and organs that are exposed to airborne pathogens. They are believed to be the first line of the innate immune defense [43,44] against viruses, bacteria, as well as fungi [40].

Most AMPs reported till date can be characterized on the basis of their secondary structures and classified into four types: β -sheet, α -helix, extended, and loop. Among these structural elements, α -helix and β -sheet structures are more common [45] and α -helical peptides are the most extensively studied AMPs (Table 1). In α -helix conformation the distance between two adjacent amino acids is around 0.15 nm and the angle between them with regard to the center is around 100 degree from the top view. The best known examples of α -helical AMPs are magainin, protegrin, cyclic indolicin and coiled indolicin [46]. β -sheet peptides are composed of at least two β -strands with disulfide bonds between these strands [47].

Researchers have identified, cloned and characterized a novel antimicrobial peptide from the venom of the scorpion *Chaerilus tricostatus* and named it as ctriporin [58]. The mature peptide of ctriporin was composed of 19 amino acid residues and possessed amidated C terminus. At low concentrations Ctriporin showed potent growth-inhibitory activity against standard *Candida albicans* and Gram-positive bacteria. Moreover, the *in vitro* treatment of clinically isolated pathogenic strains exhibited that ctriporin can also restrain antibiotic-resistant pathogens, including MRSA, methicillin-resistant coagulase-negative *Staphylococcus* (MRCNS), and penicillin-resistant *Staphylococcus epidermidis* (PRSE) strains. Ctriporin antimicrobial activity was explored in *in vivo* ointment application in topical treatment of mouse skin infection model. Finally, a standard Gram-positive bacterium, *S. aureus*, as a model bacterial strain is chosen to further explore the antimicrobial mechanism of ctriporin. All research about Ctriporin indicate it as an effective promising antimicrobial agent which act via the bactericidal mechanism of the rapid cell lysis [58].

S.No	Classes of AMPs	Examples
1.	Antiviral Peptides [48,49]	Heparan Sulfate (glylicosaminoglycan) Lactoferrin (cationic peptides)
2.	Antibacterial Peptides [37,50-52]	Buforin Drosocin, Pyrrocoricin & Apidaecin Nisin
3.	Antifungal Peptides [53-55]	α helical(D-V 13K and P18) β sheet (Defensins) Indolicin
4.	Antiparasitic Peptides [56,57]	Magainin Cahelicidin

Table 1: Classifications of AMPs.

Inhibition of Quorum Sensing

Quorum sensing is a communication services or a system of communication between bacterial cells, whereby bacterial cells secrete and receipt signaling molecules from the local environment. A sufficient amount of inducer molecules is required to trigger the expression or suppression of specific genes responsible for bacterial activities like virulence gene expression, biofilm formation and resistance against antibiotic treatment [9]. Almost all quorum-sensing processes use micro molecules, known as autoinducers (AIs). Most frequently studied autoinducers belong to one of the following classes: acylated homoserine lactones (AHLs) used by Gram-negative bacteria (also sometimes called autoinducer-1 [AI-1]); peptide signals used by Gram-positive bacteria; and autoinducer-2 (AI-2) used by both Gram-negative and Gram-positive bacteria [59].

Inhibition of Quorum Sensing is one of the latest therapeutics development technologies that aim at targeting functions that are important for the infection. This technique has various potential benefits that include increase in range of bacterial targets, exertion of less selective stress and preservation of the host endogenous microbiome, which could ultimately result into the decreases resistance [60]. Several measures that were taken to inhibit regulation of virulence factors have engrossed on their interference with QS. Various efforts have been taken to discover the compounds along with inhibitory QS systems due to the vital role of QS in modulation and regulation of hundreds of virulence factors in bacteria. These compounds shall inhibit the synchronized expressions of virulence determinants without prying with bacterial growth because they could stay along with the base of an anti-pathogenic strategy and this would ultimately generate less resistance [61]. Some bacteria species can produce enzymes called lactonases that can target and inactivate AHLs. Researchers have developed novel molecules which block the signaling receptors of bacteria, mBTL is a compound that has been shown to inhibit quorum sensing [62]. Furthermore, several research groups are analyzing and developing some compounds of natural origin (such as caffeine) as potential quorum sensing inhibitors [63].

Broadening the Spectrum of Beta-Lactam Antibiotics

The resistance of MRSA strain to all Beta-lactam class antibiotics limits treatment recourse for serious ailments caused by this organism. Researchers discover new agents that restore the activity of beta-lactams against MRSA, an approach that has led to the discovery of two classes of natural product antibiotics, a cyclic depsipeptide (krisynomycin) and a lipoglycopeptide (actinocarbasin) [64], which potentiate the activity of imipenem against MRSA strain COL. Researchers reported that these imipenem synergists are inhibitors of the bacterial type I signal peptidase SpsB, a serine protease that is required for the secretion of proteins that are exported through the Sec and Tat systems [65]. A synthetic derivative of actinocarbasin, M131, synergized with imipenem was prepared and exhibited both *in vitro* and *in vivo* potent efficacy. The *in vitro* activity of M131 extends to clinical isolates of MRSA but not to a methicillin-sensitive strain (Figure 3).

Synergy is restricted to beta-lactam antibiotics and is not observed with other antibiotic classes. The current propose is that the SpsB inhibitors synergize with beta-lactams by preventing the signal peptidase-mediated secretion of proteins required for beta-lactam resistance. Combinations of SpsB inhibitors and beta-lactams may expand the utility of these widely prescribed antibiotics to treat MRSA

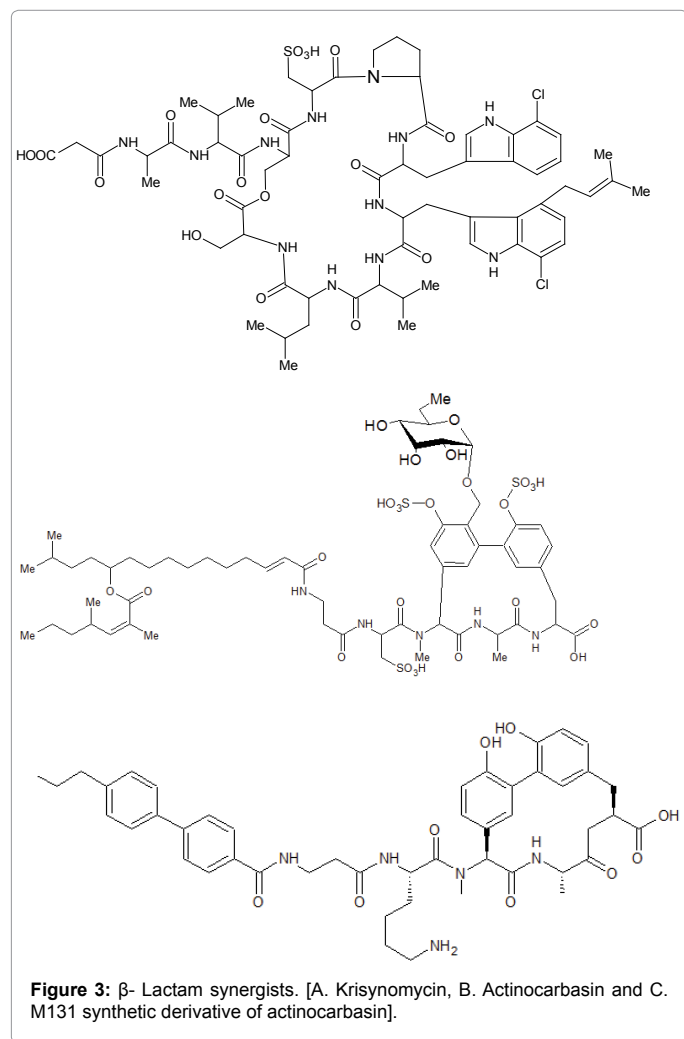


Figure 3: β -Lactam synergists. [A. Krisynomycin, B. Actinocarbasin and C. M131 synthetic derivative of actinocarbasin].

infections, analogous to beta-lactamase inhibitors which restored the utility of this antibiotic class for the treatment of resistant Gram-negative infections [64].

Nano Metals as Antibacterial Agents

Metals possess good thermal, electrical conductivity and chemical reactivity owing to their large crystallographic surface area to volume ratio, hence can be potentially very toxic to the microbes. Due to their antimicrobial activity humans are using some metals since ages as antimicrobial agents in agriculture and medical uses e.g., silver has potential antimicrobial activity at unusual low concentrations [66]. Recently developed approaches in the domains of nanotechnology, especially the capability to produce metal oxide nanomaterials of definite size and shape, are liable to lead the development of new antibacterial agents [67]. Nanoparticles have received great attention due to their unique physical, chemical, and effective biological properties in various fields, including medicine. Considering these unique properties, nano-sized organic and inorganic particles are being generated for ultimate use in medical practices, such as metal oxides of zinc, copper, and iron in biomedical research [68,69].

Silver nanoparticles manifested biocide effect by anchoring and penetrating the bacterial cell wall and interact with sulfur- and phosphorus-containing biomolecules like DNA and silver ions

strongly interacts with thiol groups of vital enzymes and inactivates them [70,71]. Silver exhibited more pronounced action against gram-negative organisms than gram-positive bacteria and can inhibit growth of approximately 650 disease-causing agents. Silver nanoparticle-based biocide showed that its antimicrobial effect is independent of acquisition of resistance against antibiotics [72]. Necessary metals such as copper also show similar properties but above some threshold levels [73,74]. The mode of action of the biocide activity is based on specific properties of metals and it can be activated by the metal reduction potential and the metal donor atom selectivity and/or speciation [66]. In addition, nanoparticles with smaller particle size have been reported to show good antimicrobial activity [75]. Antimicrobial activity of nanoparticles has largely been studied with human pathogenic bacteria such as *Escherichia coli* [76] and *Staphylococcus aureus* [77]. Moreover, these microbes seem to be highly sensitive to ZnO and CuO nanoparticles [75,78]. The cell can directly incorporate nanoparticles via endocytotic mechanisms and afterwards the cellular uptake of ions increases as ionic species are subsequently released within the cells by nanoparticle dissolution, a process often referred to as “the Trojan horse mechanism”. This high intracellular concentration gained after nanoparticle dissolution within the cell likely results in massive oxidative stress [79-81]. Recently bioactive glass BAG-S53P4 was reported to have anti-biofilm-forming activity against MDR bacterial strains [82,83].

Conclusion

According to an estimate the number of deaths caused by bacterial infection is highest in the world. There is an urgent need of novel antimicrobial drugs to fight against infection because bacteria are evolving and developing with a greater pace. We are surrounded by endless possibilities to fight against bacterial infection but only some of them are explored yet. Out of all existent antimicrobial drugs only a few have been taken to the clinical trials only a very few reached to the market for public use.

Teixobactin is a very effective drug against many pathogenic microorganisms which are resistant to the drugs currently in market. But it has some limitations for gram-negative bacteria. Anti-microbial peptides (AMPs) being a module of immune system though, can be synthesized for use as antibiotics, which are very effective especially in topical treatment of ulcer etc. Cloned AMP cecropin is a good example which has a very effective role in inhibiting MRSA, MRCNS and PRSE. Molecular methods have also been employed for bacterial infection treatment involving antisense antibacterial and quorum sensing inhibitions which can easily overcome the resistance developed by micro-organisms and are very specific to its target. This can be a very sincere step in developing new antimicrobials.

References

1. Arias CA, Murray BE (2009) Antibiotic-resistant bugs in the 21st century—a clinical super-challenge. N Engl J Med 360: 439-443.
2. Spellberg B, Shlaes D (2014) Prioritized current unmet needs for antibacterial therapies. Clin Pharmacol Ther 96: 151-153.
3. Bush K, Courvalin P, Dantas G, Davies J, Eisenstein B, et al. (2011) Tackling antibiotic resistance. Nat Rev Microbiol 9: 894-896.
4. von Nussbaum F, Brands M, Hinzen B, Weigand S, Häbich D (2006) Antibacterial natural products in medicinal chemistry—exodus or revival? Angew Chem Int Ed Engl 45: 5072-5129.
5. Jevons MP (1961) ‘Celbenin’-resistant *Staphylococci*. Br Med J 1: 124-125.
6. Singh SK, Anwar S, Sharma HK, Chaudhary U, Verma SK (2014) FemA gene in Indian isolates of methicillin-resistant *Staphylococcus aureus*, isolation and amplification through real time PCR. Euro J Exp Bio 4: 90-94.

7. Shlaes DM, Marino J, Jacobs MR (1984) Infection caused by vancomycin-resistant *Streptococcus sanguis* II. Antimicrob Agents Chemother 25: 527-528.
8. Uttley AH, Collins CH, Naidoo J, George RC (1988) Vancomycin-resistant enterococci. Lancet 1: 57-58.
9. Sintim HO, Smith JA, Wang J, Nakayama S, Yan L (2010) Paradigm shift in discovering next-generation anti-infective agents: targeting quorum sensing, c-di-GMP signaling and biofilm formation in bacteria with small molecules. Future Med Chem 2: 1005-1035.
10. Sanders CC, Sanders WE Jr (1979) Emergence of resistance to cefamandole: possible role of cefoxitin-inducible beta-lactamases. Antimicrob Agents Chemother 15: 792-797.
11. Gonzales RD, Schreckenberger PC, Graham MB, Kelkar S, DenBesten K, et al. (2001) Infections due to vancomycin-resistant *Enterococcus faecium* resistant to linezolid. Lancet 357: 1179.
12. Sulavik MC, Houseweart C, Cramer C, Jiwani N, Murgolo N, et al. (2001) Antibiotic susceptibility profiles of *Escherichia coli* strains lacking multidrug efflux pump genes. Antimicrob Agents Chemother 45:1126-1136.
13. Wiedemann I, Breukink E, van Kraaij C, Kuipers OP, Bierbaum G, et al. (2001) Specific binding of nisin to the peptidoglycan precursor lipid II combines pore formation and inhibition of cell wall biosynthesis for potent antibiotic activity. J Biol Chem 276: 1772-1779.
14. Hasper HE, Kramer NE, Smith JL, Hillman JD, Zachariah C, et al. (2006) An alternative bactericidal mechanism of action for lantibiotic peptides that target lipid II. Science 313: 1636-1637.
15. Schneider T, Kruse T, Wimmer R, Wiedemann I, Sass V, et al. (2010) Plectasin, a fungal defensin, targets the bacterial cell wall precursor Lipid II. Science 328: 1168-1172.
16. Ling LL, Schneider T, Peoples AJ, Spoering AL, Engels I, et al. (2015) Erratum: A novel antibiotic kills pathogens without detectable resistance. Nature 520: 388.
17. Conlon BP, Nakayasu ES, Fleck LE, LaFleur MD, Isabella VM, et al. (2013) Activated ClpP kills persisters and eradicates a chronic biofilm infection. Nature 503: 365-370.
18. Schneider T, Sahl HG (2010) An oldie but a goodie - cell wall biosynthesis as antibiotic target pathway. Int J Med Microbiol 300: 161-169.
19. Leclercq R, Derlot E, Duval J, Courvalin P (1988) Plasmid-mediated resistance to vancomycin and teicoplanin in *Enterococcus faecium*. N Engl J Med 319: 157-161.
20. Marshall CG, Broadhead G, Leskiw BK, Wright GD (1997) D-Ala-D-Ala ligases from glycopeptide antibiotic-producing organisms is highly homologous to the enterococcal vancomycin-resistance ligases VanA and VanB. Proc Natl Acad Sci USA 94: 6480-6483.
21. Ling LL, Schneider T, Peoples AJ, Spoering AL, Engels I, et al. (2015) A new antibiotic kills pathogens without detectable resistance. Nature 517: 455- 459.
22. Stone J (2015) Teixobactin and ichip promise hope against antibiotic resistance. Forbes.
23. Rasmussen LC, Sperling-Petersen HU, Mortensen KK (2007) Hitting bacteria at the heart of the central dogma: sequence-specific inhibition. Microb Cell Fact 6: 24.
24. Geller BL (2005) Antibacterial antisense. Curr Opin Mol Ther 7: 109-113.
25. Hatamoto M, Ohashi A, Imachi H (2010) Peptide nucleic acids (PNAs) antisense effect to bacterial growth and their application potentiality in biotechnology. Appl Microbiol Biotechnol 86: 397-402.
26. Good L, Awasthi SK, Dryselius R, Larsson O, Nielsen PE (2001) Bactericidal antisense effects of peptide-PNA conjugates. Nat Biotechnol 19: 360-364.
27. Bai H, Zhou Y, Hou Z, Xue X, Meng J, et al. (2011) Targeting bacterial RNA polymerase: promises for future antisense antibiotics development. Infect Disord Drug Targets 11: 175-187.
28. Ji Y, Yin D, Fox B, Holmes DJ, Payne D, et al. (2004) Validation of antibacterial mechanism of action using regulated antisense RNA expression in *Staphylococcus aureus*. FEMS Microbiol Lett 231: 177-184.
29. Borukhov S, Nudler E (2008) RNA polymerase: The vehicle of transcription. Trends Microbiol 16: 126-134.
30. Paget MS, Helmann JD (2003) The sigma70 family of sigma factors. Genome Biol 4: 203.
31. Lane WJ, Darst SA (2010) Molecular evolution of multisubunit RNA polymerases: sequence analysis. J Mol Biol 395: 671-685.
32. Dubos RJ (1939) Studies on a bactericidal agent extracted from a soil bacillus: II. Protective effect of the bactericidal agent against experimental pneumococcus infections in mice. J Exp Med 70: 11-17.
33. Hotchkiss RD, Dubos RJ (1940) Fractionation of the bactericidal agent from cultures of a soil Bacillus. J Biol Chem 132: 791-792.
34. Van Epps HL (2006) René Dubos: unearthing antibiotics. J Exp Med 203: 259.
35. Hirsch JG (1956) Phagocytin: a bactericidal substance from polymorphonuclear leucocytes. J Exp Med 103: 589-611.
36. Scott MG, Gold MR, Hancock RE (1999) Interaction of cationic peptides with lipoteichoic acid and gram-positive bacteria. Infect Immun 67: 6445-6453.
37. Brumfitt W, Salton MRJ, Hamilton-Miller JMT (2002) Nisin, alone and combined with peptidoglycan-modulating antibiotics: activity against methicillin-resistant *Staphylococcus aureus* and vancomycin-resistant Enterococci. J Antimicrob Chemother 50: 731-734.
38. Zhao X, Wu H, Lu H, Li G, Huang Q (2013) LAMP: A Database Linking Antimicrobial Peptides. PLoS One 8: e66557.
39. Conlon JM, Sonnevend A, Davidson C, Smith DD, Nielsen PF (2004) The ascaphins: A family of antimicrobial peptides from the skin secretions of the most primitive extant frog, *Ascaphus truei*. Biochem Biophys Res Commun 320: 170-175.
40. Radek K, Gallo R (2007) Antimicrobial peptides: Natural effectors of the innate immune system. Semin Immunopathol 29: 27-43.
41. Peters BM, Jabra-Rizk MA, O'May GA, Costerton JW, Shirliff ME (2012) Polymicrobial interactions: impact on pathogenesis and human disease. Clin Microbiol Rev 25: 193-213.
42. Leippe M (1999) Antimicrobial and cytolytic polypeptides of amoeboid protozoa-effector molecules of primitive phagocytes. Dev Comp Immunol 23: 267-279.
43. Zasloff M (2002) Antimicrobial peptides of multicellular organisms. Nature 415: 389-395.
44. Schaubert J, Gallo RL (2008) Antimicrobial peptides and the skin immune defense system. J Allergy Clin Immunol 122: 261-266.
45. Powers JP, Hancock RE (2003) The relationship between peptide structure and antibacterial activity. Peptides 24: 1681-1691.
46. Huang Y, Huang J, Chen Y (2010) Alpha-helical cationic antimicrobial peptides: Relationships of structure and function. Protein Cell 1: 143-152.
47. Bulet P, Stöcklin R, Menin L (2004) Anti-microbial peptides: From invertebrates to vertebrates. Immunol Rev 198: 169-184.
48. Laquerre S, Argnani R, Anderson DB, Zucchini S, Manservigi R, et al. (1998) Heparan sulfate proteoglycan binding by herpes simplex virus type 1 glycoproteins B and C, which differ in their contributions to virus attachment, penetration, and cell-to-cell spread. J Virol 72: 6119-6130.
49. Andersen JH, Jenssen H, Sandvik K, Gutteberg TJ (2004) Anti-HSV activity of lactoferrin and lactoferricin is dependent on the presence of heparan sulphate at the cell surface. J Med Virol 74: 262-271.
50. Park CB, Kim HS, Kim SC (1998) Mechanism of action of the antimicrobial peptide buforin II: Buforin II kills microorganisms by penetrating the cell membrane and inhibiting cellular functions. Biochem Biophys Res Commun 244: 253-257.
51. Otvos L Jr, O I, Rogers ME, Consolvo PJ, Condie BA, et al. (2000) Interaction between heat shock proteins and antimicrobial peptides. Biochemistry 39: 14150-14159.
52. Kragol G, Lovas S, Varadi G, Condie BA, Hoffmann R, et al. (2001) The antibacterial peptide pyrrolicin inhibits the ATPase actions of DnaK and prevents chaperone-assisted protein folding. Biochemistry 40: 3016-3026.
53. Jiang Z, Vasil AI, Hale JD, Hancock RE, Vasil ML, et al. (2008) Effects of net charge and the number of positively charged residues on the biological activity of amphipathic alpha-helical cationic antimicrobial peptides. Biopolymers 90: 369-383.

54. Lee DG, Hahm KS, Shin SY (2004) Structure and fungicidal activity of a synthetic antimicrobial peptide, P18, and its truncated peptides. Biotechnol Lett 26: 337-341.
55. Lee DG, Kim HK, Kim SA, Park Y, Park SC, et al. (2003) Fungicidal effect of indolicidin and its interaction with phospholipid membranes. Biochem Biophys Res Commun 305: 305-310.
56. Zasloff M (1987) Magainins, a class of antimicrobial peptides from *Xenopus* skin: isolation, characterization of two active forms, and partial cDNA sequence of a precursor. Proc Natl Acad Sci U S A 84: 5449-5453.
57. Park Y, Jang SH, Lee DG, Hahm KS (2004) Antinematodal effect of antimicrobial peptide, PMAP-23, isolated from porcine myeloid against *Caenorhabditis elegans*. J Pept Sci 10: 304-311.
58. Fan Z, Cao L, He Y, Hu J, Di Z, et al. (2011) Ctriporin, A new anti-methicillin-resistant *Staphylococcus aureus* peptide from the venom of the scorpion *Cherilus tricotatus*. Antimicrob Agents Chemother 55: 5220-5229.
59. LaSarre B, Federle MJ (2013) Exploiting quorum sensing to confuse bacterial pathogens. Microbiol Mol Biol Rev 77: 73-111.
60. Cotar AL (2013) Quorum sensing inhibitors as anti-pathogenic drugs in the fight against *Pseudomonas aeruginosa* infections. Clin Microbiol 2.
61. Smith RS, Iglewski BH (2003) *P. aeruginosa* quorum-sensing systems and virulence. Curr Opin Microbiol 6: 56-60.
62. O'Loughlin CT, Miller LC, Sityaporn A, Drescher K, Semmelhack MF, et al. (2013) A quorum-sensing inhibitor blocks *Pseudomonas aeruginosa* virulence and biofilm formation. Proc Natl Acad Sci U S A 110: 17981-17986.
63. Norizan SN, Yin WF, Chan KG (2013) Caffeine as a potential quorum sensing inhibitor. Sensors (Basel) 13: 5117-5129.
64. Therien AG, Joann L, Huber B, Kenneth E, Wilson B, et al. (2012) Broadening the spectrum of lactam antibiotics through inhibition of signal peptidase type I. Antimicrob Agents and Chemother 56: 4662-4670.
65. Paetzel M, Karla A, Strynadka NC, Dalbey RE (2002) Signal peptidases. Chem Rev 102: 4549-4580.
66. Lemire JA, Harrison JJ, Turner RJ (2013) Antimicrobial activity of metals: Mechanisms, molecular targets and applications. Nat Rev Microbiol 11: 371-384.
67. Azam A, Ahmed AS, Oves M, Khan MS, Memic A (2012) Size-dependent antimicrobial properties of CuO nanoparticles against Gram-positive and -negative bacterial strains. Int J Nanomedicine 7: 3527-3535.
68. Mahapatra O, Bhagat M, Gopalakrishnan C, Arunachalam KD (2008) Ultrafine dispersed CuO nanoparticles and their antibacterial activity. J Exp Nanosci 3: 185-193.
69. Tran N, Mir A, Mallik D, Sinha A, Nayar S, et al. (2010) Bactericidal effect of iron oxide nanoparticles on *Staphylococcus aureus*. Int J Nanomedicine 5: 277-283.
70. Matsumura Y, Yoshikata K, Kunisaki S, Tsuchido T (2003) Mode of bactericidal action of silver zeolite and its comparison with that of silver nitrate. Appl Environ Microbiol 69: 4278-4281.
71. Gupta A, Maynes M, Silver S (1998) Effects of halides on plasmid-mediated silver resistance in *Escherichia coli*. Appl Environ Microbiol 64: 5042-5045.
72. Singh M, Singh S, Prasad S, Gambhir IS (2008) Nanotechnology in medicine and antibacterial effect of silver nanoparticles. Dig J Nanomater Bios 3: 115-122.
73. Gunawan C, Teoh WY, Marquis CP, Amal R (2011) Cytotoxic origin of copper(II) oxide nanoparticles: comparative studies with micron-sized particles, leachate, and metal salts. ACS Nano 5: 7214-7225.
74. Chatterjee AK, Chakraborty R, Basu T (2014) Mechanism of antibacterial activity of copper nanoparticles. Nanotechnology 25: 135101.
75. Jones N, Ray B, Ranjit KT, Manna AC (2008) Antibacterial activity of ZnO nanoparticle suspensions on a broad spectrum of microorganisms. FEMS Microbiol Lett 279: 71-76.
76. Yoon KY, Hoon Byeon J, Park JH, Hwang J (2007) Susceptibility constants of *Escherichia coli* and *Bacillus subtilis* to silver and copper nanoparticles. Sci Total Environ 373: 572-575.
77. Ruparelia JP, Chatterjee AK, Duttagupta SP, Mukherji S (2008) Strain specificity in antimicrobial activity of silver and copper nanoparticles. Acta Biomater 4: 707-716.
78. Heinlaan M, Ivask A, Blinova I, Dubourguier HC, Kahru A (2008) Toxicity of nanosized and bulk ZnO, CuO and TiO₂ to bacteria *Vibrio fischeri* and crustaceans *Daphnia magna* and *Thamnocephalus platyurus*. Chemosphere 71: 1308-1316.
79. Studer AM, Limbach LK, Van Duc L, Krumeich F, Athanassiou EK, et al. (2010) Nanoparticle cytotoxicity depends on intracellular solubility: comparison of stabilized copper metal and degradable copper oxide nanoparticles. Toxicology Lett 197: 169-174.
80. Cronholm P, Midander K, Karlsson HL, Elihn K, Wallinder IO, et al. (2011) Effect of sonication and serum proteins on copper release from copper nanoparticles and the toxicity towards lung epithelial cells. Nanotoxicology 5: 269-281.
81. Wang J, Sun P, Bao Y, Dou B, Song D, et al. (2012) Vitamin E renders protection to PC12 cells against oxidative damage and apoptosis induced by single-walled carbon nanotubes. Toxicol In Vitro 26: 32-41.
82. Drago L, Vassena C, Fenu S, De Vecchi E, Signori V, et al. (2014) *In vitro* antibiofilm activity of bioactive glass S53P4. Future Microbiol 9: 593-601.
83. Bortolin M, De Vecchi E, Romanò CL, Toscano M, Mattina R, et al. (2015) Antibiofilm agents against MDR bacterial strains: is bioactive glass BAG-S53P4 also effective? J Antimicrob Chemother.

Citation: Sharma M, Singh S, Sharma S (2015) New Generation Antibiotics/Antibacterials: Deadly Arsenal for Disposal of Antibiotic Resistant Bacteria. J Microb Biochem Technol 7: 374-379. doi:[10.4172/1948-5948.1000241](https://doi.org/10.4172/1948-5948.1000241)

OMICS International: Publication Benefits & Features

Unique features:

- Increased global visibility of articles through worldwide distribution and indexing
- Showcasing recent research output in a timely and updated manner
- Special issues on the current trends of scientific research

Special features:

- 700 Open Access Journals
- 50,000 editorial team
- Rapid review process
- Quality and quick editorial, review and publication processing
- Indexing at PubMed (partial), Scopus, EBSCO, Index Copernicus and Google Scholar etc
- Sharing Option: Social Networking Enabled
- Authors, Reviewers and Editors rewarded with online Scientific Credits
- Better discount for your subsequent articles

Submit your manuscript at: <http://www.editorialmanager.com/jmbt>

Accepted Manuscript

Non-invasive topical delivery of plasmid DNA to the skin using a peptide carrier

Manika Vij, Poornemaa Natarajan, Bijay Ranjan Pattnaik, Shamshad Alam, Nidhi Gupta, Deenan Santhiya, Rajpal Sharma, Archana Singh, Kausar M. Ansari, Rajesh S. Gokhale, Vivek T. Natarajan, Munia Ganguli

PII: S0168-3659(15)30269-8
DOI: doi: [10.1016/j.jconrel.2015.12.017](https://doi.org/10.1016/j.jconrel.2015.12.017)
Reference: COREL 8016

To appear in: *Journal of Controlled Release*

Received date: 1 July 2015
Revised date: 25 November 2015
Accepted date: 12 December 2015



Please cite this article as: Manika Vij, Poornemaa Natarajan, Bijay Ranjan Pattnaik, Shamshad Alam, Nidhi Gupta, Deenan Santhiya, Rajpal Sharma, Archana Singh, Kausar M. Ansari, Rajesh S. Gokhale, Vivek T. Natarajan, Munia Ganguli, Non-invasive topical delivery of plasmid DNA to the skin using a peptide carrier, *Journal of Controlled Release* (2015), doi: [10.1016/j.jconrel.2015.12.017](https://doi.org/10.1016/j.jconrel.2015.12.017)

This is a PDF file of an unedited manuscript that has been accepted for publication. As a service to our customers we are providing this early version of the manuscript. The manuscript will undergo copyediting, typesetting, and review of the resulting proof before it is published in its final form. Please note that during the production process errors may be discovered which could affect the content, and all legal disclaimers that apply to the journal pertain.

REVISED MANUSCRIPT

Non invasive topical delivery of plasmid DNA to skin using a peptide carrier

^{1,5}Manika Vij, ¹Poornemaa Natarajan, ¹Bijay Ranjan Pattnaik, ²Shamshad Alam, ³Nidhi Gupta, ³Deenan Santhiya, ^{1,5}Rajpal Sharma, ¹Archana Singh, ²Kausar M. Ansari, ^{1,4}Rajesh S. Gokhale, ¹Vivek T. Natarajan, ^{1,5*}Munia Ganguli.

¹Department of Structural Biology, CSIR- Institute of Genomics and Integrative Biology, South Campus, Mathura Road, New Delhi - 110020 (INDIA).

²Environmental Carcinogenesis Division, CSIR- Indian Institute of Toxicology Research, Post Box No.80, Mahatma Gandhi Marg, Lucknow, Uttar Pradesh - 226001 (INDIA).

³Delhi Technological University, Shahbad Daultpur, Main Bawana Road, New Delhi - 110042 (INDIA).

⁴National Institute of Immunology, New Delhi - 110067 (INDIA).

⁵Academy of Scientific and Innovative Research (AcSIR), Anusandhan Bhawan, 2 Rafi Marg, New Delhi - 110001 (INDIA).

* To whom correspondence should be addressed:

Tel. No.: +91-11-29879225 / +91-9871607437; Fax: 001-27667471;

Email id: mganguli@igib.res.in, mganguli@igib.in;

Present Address: Dr. Munia Ganguli, Room No. 225/ Lab No. 219, Department of Structural Biology, CSIR-Institute of Genomics and Integrative Biology, South Campus, Mathura Road, New Delhi, 110020 (INDIA).

ABSTRACT

Topical delivery to skin is an essential step in non-invasive application of nucleic acid therapeutics for cutaneous disorders. The barrier posed by different layers of skin - stratum corneum on top followed by the viable epidermis below - makes it extremely challenging for large hydrophilic molecules like nucleic acids to efficiently enter the uncompromised skin. We report an amphipathic peptide Mgpe9 (CRRLRHLRHHYRRRWHRFRC) that can penetrate the uncompromised skin, enter skin cells and deliver plasmid DNA efficiently as nanocomplexes in vitro and in vivo without any additional physical or chemical interventions prevalent currently. We observe efficient gene expression up to the highly proliferating basal layer of the skin without observable adverse reactions or toxic effects after delivery of reporter plasmids. The entry mechanism of nanocomplexes possibly involves reversible modulation of junction proteins accompanied by transient changes in skin structure. This peptide holds potential to be used as an efficient transporter of therapeutic nucleic acids to skin.

Keywords

Cell penetrating peptide, Topical, Nucleic acid delivery, Skin penetration, Dermatology, Transfection

INTRODUCTION

Skin, by virtue of its large size and easy accessibility, can be explored for therapeutic interventions. It has been shown to be a favorable target for both topical as well as transdermal delivery of different small molecule drugs [1-3]. Usually substances that are small in size (<500Da) with high or moderate lipid solubility penetrate/permeate skin more easily as compared to large hydrophilic molecules whose diffusion is slow and inefficient. The stratum corneum containing dead keratinocytes, tight junctions called desmosomes and different cellular barriers pose difficulty for facile delivery of such molecules to skin. Strategies have been designed to aid delivery of macromolecules like proteins, nucleic acids and glycosaminoglycans to the skin [4-6]. Delivery methods usually involve harsh physical procedures e.g. electroporation and microneedle injections, treatments with chemical enhancers or use of vesicles like liposomes, ethosomes and transferosomes [7-11]. These methods other than ethosomes which have been used for dermal and transdermal delivery in clinic [4], compromise the integrity of the skin structure to an extent and may have other side effects if intended to be used in a diseased condition where the structure of the skin could be even more fragile. In recent times, natural and synthetic peptides have emerged as potential transporters of large biomolecules like proteins and plasmid DNA to cells [12-14]. Peptides are easy to synthesize, diverse in chemistry and can be modified for cellular targeting. Peptides like TAT, polyarginine, magainin and penetratin can penetrate the stratum corneum and have been used for efficient transdermal delivery of small molecules in skin [15,16]. Recently TD-1, a cyclic peptide, has been shown to enhance transdermal delivery of hydrophilic macromolecular proteins like insulin [17]. Another phage display derived peptide SPACE has been used for siRNA delivery across intact skin [18]. Peptide mediated HIF α ODD plasmid DNA delivery has been successful in stimulating wound healing in integrity compromised skin [19]. In another report cysteine flanked arginine-rich peptide has been shown to deliver luciferase plasmid through intradermal injection in skin [20]. Also many fusion proteins such as TAT-epidermal growth factor, Chaperon-epidermal growth factor, TAT and R9 fused anti-oxidative enzymes, and non-covalently associated cargo such as TAT-EGFP have been shown to enter skin in an efficient manner [21-23]. However none of these peptide transporters has been used alone for simple topical delivery of plasmid DNA to uncompromised skin without additional intervention. We have investigated whether a novel cell penetrating peptide Mgpe9 can potentially be used as a non-invasive and non-toxic topical delivery system for plasmid DNA delivery to intact human skin in unaided manner. We have also analyzed if the plasmid delivered is functionally potent, shows efficient gene expression throughout the skin tissue and the expression is retained for a long duration thereby indicating its usefulness for future clinical applications.

MATERIAL AND METHODS

Chemicals and Cell lines

All the peptides (either labeled with Fluorescein Isothiocyanate (FITC) or used without any fluorophore label) used in this study were custom synthesized (>98% purity) by Beijing SBS Genetech Co., Ltd.(Beijing, China). FITC-labeled peptides were used for partition coefficient analysis [24,25], peptide uptake studies in either cell lines [25] or tissue [26-28], to study the role of junction proteins upon peptide treatment on skin [29] as well as skin integrity assessment using dye penetration assay [30]. For all other experiments, unlabeled peptide was used. However stability of the FITC peptide under test conditions has not been studied. The plasmids pEGFP-C1, 4.7kb (Clontech) and pMIR- REPORT™ Luciferase, 6.47kb (Ambion) were cultured using Escherichia coli DH5α strain and isolated using GenElute HP Endotoxin-Free Plasmid MaxiPrep kit (Sigma). pMIR-REPORT™ Luciferase plasmid was used to prepare nanocomplexes in those cases where the luciferase gene was transfected. In all other experiments pEGFP-C1 plasmid was used to prepare the nanocomplexes. All the chemicals and culture media used were obtained from Sigma unless mentioned otherwise. The luciferase assay kit and CellTiter Glo viability assay kit were purchased from Promega. Label IT® Tracker Fluorescein kit for labeling plasmid DNA was obtained from Mirus Bio Corp. HaCaT, which is an adult keratinocyte cell line, was obtained as a gift from Dr. Sudhir Krishna, NCBS, Bangalore, India. WM266-4 melanoma cells were obtained from NCCS cell repository, Pune, India.

Partition coefficient estimation

Partition coefficient of the peptides (Mgpe9 and control peptides TAT, Penetratin) was estimated using pentanol:water (1:1, v/v) system with slight modification of protocol [24,25] wherein 500μl of pentanol was mixed with 500μl of water and vortexed for 1min, followed by addition of 200μg FITC- labeled peptides. The solution was again vortexed for 2-3 minutes and left undisturbed at room temperature. After 24h, fluorescence was measured in 100μl of solution from pentanol phase and water phase respectively in independent experiments using microplate reader (Infinite 200 Pro, Tecan). Sampling from the interface of two solutions was avoided to get proper distribution of peptide between the two separate phases. Hydrophobicity index for all the peptides was calculated using HELIQUEST software.

Pre-processing of human skin tissue

Human foreskin tissue (discarded sample, collected and studies approved by institutional human ethics committee [Approval Number:IGIB/HEC/09/13]) obtained in transportation media (Hank's Balanced Salt Solution or HBSS from Invitrogen) was washed three times alternately with 1X phosphate buffered saline (PBS) and 70% alcohol solution to clear the contamination if any. For skin penetration and integrity tests,

tissue was pre-soaked for 24h in 1X phosphate buffered saline solution before conducting the study whereas for ex vivo experiments, tissue was processed into small pieces of 0.5cm x 0.5cm using sterile scalpel and plated in small inserts (to cover the base area completely and avoid sideways contamination owing to movement during treatment) in a 24 well plate with 300µl of Keratinocyte-Serum Free medium (K-SFM from Invitrogen) in the outer well such that only the dermis remained submerged in media whereas epidermis was exposed for the topical treatment.

Peptide skin penetration test

The penetration ability of peptides (labeled with FITC) across human skin was assessed using peptide skin penetration test with slight modification of protocols [26,27]. Equilibrated skin tissue was placed in between the two compartments of Franz apparatus held together by means of spring clips where receptor compartment was pre-filled with 20ml of 1X phosphate buffered saline (PBS) solution (pH=7.4) along with a magnetic bead in it to allow continuous stirring to take place while the experiment is being performed. Following this set up, 200µl of 1µg/µl FITC labeled peptide solution (Mgpe9 and control peptide TAT) was added from the opening provided in donor compartment present on top of the tissue. Application was made on the dorsal surface of exposed epidermis of skin tissue and system was kept under constant agitation at 250rpm at room temperature. Tissues were taken out after 4h and also after 24h (in independent experiments), followed by three washes with ice cold 1X phosphate buffered saline (PBS) having heparin salt (1mg/ml) to remove the unbounded fraction if any. Fixation of samples was done using 4% paraformaldehyde for 30minutes and immediate cryosectioning in each case to obtain thin tissue sections (6 microns) that were visualized using inverted DMI6000B fluorescence microscope (Biomedical Research Leica).

Cellular uptake of peptides

Cells were seeded in a 24 well plate at density of 60,000 cells per well for HaCaT and 80,000 cells per well for WM266-4 melanoma respectively. After 24h (when 70% confluency was attained), complete media was replaced with 300µl of Opti-MEM (Invitrogen) in each well. Following this, 100µl of FITC- labeled peptides Mgpe9, TAT and Penetratin (with final concentration 5µM per well) were added to the cells. After 4h of incubation at 37°C, cells were washed twice with ice cold 1X phosphate buffered saline (PBS) containing 1mg/ml heparin salt followed by single wash with 100µl of 0.4% trypan blue in 1X phosphate buffered saline (PBS) [1:1; v/v ratio] in order to quench extracellular fluorescence. Cells were obtained by trypsinization (100µl of 0.25% trypsin) and centrifuged at a speed of 2000rpm for 5 minutes at 4°C. The pellet was resuspended in 500µl of ice cold 1X phosphate buffered saline (PBS) and kept in ice. Flow cytometry measurements were performed using FACS Caliber (Becton Dickinson) to assay for the presence of fluorescently labeled peptides in the cells.

Peptide-DNA nanocomplex formation

Nanocomplexes were prepared at different N/P ratios (Z (+/-)) of 5 and 10 where N/P refers to the ratio between total number of amines of a peptide and total number of phosphates of a plasmid DNA. Nanocomplexes were formed by gradual addition of 100 μ l plasmid DNA (40ng/ μ l) to 100 μ l of peptide solution of appropriate concentration (68.97 μ M for charge ratio 10, 34.49 μ M for charge ratio 5) in a drop-wise manner accompanied by constant vortexing. The nanocomplexes were left undisturbed for 1h at room temperature before performing any biophysical study or addition to cells or tissue. For *ex vivo* and *in vivo* studies nanocomplexes were prepared such that overall volume was either 80 or 100 μ l keeping the peptide:DNA ratio constant to maintain same concentrations during treatments.

Atomic Force Microscopy for observing morphology of nanocomplexes

Briefly, 4 μ l of the Mgpe9 nanocomplexes prepared at charge ratio 10 (as described earlier) were deposited on mica and spray-dried following which imaging was carried out with 5500 scanning probe microscope (Agilent Technologies, Inc., AZ) using Picoview software 1.4.4. Images were taken in AAC mode in air with silicon cantilevers having resonance frequency of 75 kHz and force constant of 2.8N/m. Scan speed was 1 line/s. Minimum image processing was employed and image analysis was done using Picoview software.

FITC labeling of plasmid DNA

FITC labeled plasmid DNA was used to prepare nanocomplexes for cellular uptake studies. Briefly plasmid DNA (pEGFP-C1) was labeled with FITC using Label IT® Tracker Fluorescein kit (Mirus Bio Corp.) at a ratio of 0.75:1 (v:w) i.e. 0.75 μ l of labeling reagent/ μ g of DNA according to manufacturer's protocol.

Cellular uptake of nanocomplexes

HaCaT cells were seeded in small dishes (Ibidi) at density of 1×10^5 cells per dish. After 24h (when 70% confluency was attained), complete media was replaced with 800 μ l of Opti-MEM (Invitrogen) in each well. Following this, 200 μ l of FITC labeled nanocomplexes prepared using FITC labeled plasmid DNA and unlabeled peptide at charge ratio 10 were added to the cells. After 4h of incubation at 37°C, cells were washed twice with ice cold 1X phosphate buffered saline (PBS) containing 1mg/ml heparin salt followed by single wash with 500 μ l of 0.4% trypan blue in 1X phosphate buffered saline (PBS) [1:1; v/v ratio] in order to quench extracellular fluorescence. Following this, cells were again washed with 500 μ l of ice cold 1X phosphate buffered saline (PBS) and nuclei were stained using DAPI. Cells were then visualized at 100x magnification using inverted DMI6000B fluorescence microscope (Biomedical Research Leica).

Transmission Electron Microscopy to locate nanocomplexes in skin

Transmission Electron Microscopy was performed to check the presence of nanocomplexes in skin [31]. Tissue was topically treated with 100µl of Mgpe9 nanocomplexes consecutively for 3days (1 application per day with 4µg of plasmid DNA per application) followed by pre-processing for TEM imaging after 24h. Pre-processing involved tissue fixation in 2.5% glutaraldehyde and 4% paraformaldehyde, osmication in 1 % osmium tetroxide, dehydration in graded series of alcohol followed by infiltration with Epon 812 resin. Ultrathin sections of 70nm were cut on RMC ultramicrotome, collected on copper grids and stained with uranyl acetate and lead citrate. Samples were then visualized on Tecnai G2 20 twin (FEI) Transmission Electron Microscope at respective magnifications of 170x, 220x, 800x, 1100x and 5000x. Untreated and Milli-Q treated skin tissue samples were taken as experimental controls.

Plasmid DNA delivery in skin cell lines

HaCaT and WM266-4 melanoma cells were seeded in a 24 well plate as described in cellular uptake of nanocomplexes. 200µl of nanocomplexes (Mgpe9 and control peptides TAT, Penetratin) was prepared either using pMIR luciferase plasmid (40ng/µl) or EGFP-C1 plasmid (40ng/µl) and 100µl of nanocomplexes was added to each well (2µg plasmid DNA per well). After 4h of incubation at 37°C, the incomplete media was replaced by complete media and kept for further incubation. After 24h of treatment, luciferase activity was assessed in the cell lysate according to the standard protocol (Promega) in case of pMIR. For EGFP analysis, cells were washed with ice cold 1X phosphate buffered saline (PBS) followed by trypsinization (100µl of 0.25% trypsin) and centrifugation at speed of 2000rpm for 5 minutes at 4°C. The pellet was resuspended in 500µl of ice cold 1X phosphate buffered saline (PBS) and kept in ice. Flow cytometry measurements were performed using FACS Caliber (Becton Dickinson). EGFP expression was visualized before processing for flow cytometry in intact cells seeded in the plate using inverted DMI6000B fluorescence microscope (Biomedical Research Leica). Statistical significance for transfection data was calculated using two-tailed student's t-test (unpaired) in GraphPad Prism.

Plasmid DNA delivery in human foreskin tissue

After 24h of skin tissue pre-processing (described previously), 200µl of nanocomplexes (Mgpe9, control peptide TAT and commercial agent Lipofectamine 2000TM) was prepared at charge ratio 10 using EGFP-C1 plasmid (80ng/µl) and 100µl of the complex was added topically on the tissue in each well. This treatment was repeated for 3 days consecutively with a single such application per day (4µg plasmid DNA per application) along with intermittent washing of the tissue using 1X phosphate buffered saline (PBS) before each of the fresh applications. 24h after the final application the tissue was again washed in similar manner, fixed using 4% paraformaldehyde for 30 minutes and transferred to 20% sucrose solution having 0.01%

sodium azide to be stored at 4°C until further processing was done. For cryosectioning (24h post-fixation), the tissue was embedded in an OCT compound and sections of 6µm thickness were obtained which was visualized as green fluorescence of EGFP using inverted DMI6000B fluorescence microscope (Biomedical Research Leica). For quantification of EGFP fluorescence in the epidermis, the epidermis was removed from the full thickness skin tissue using overnight Dispase (0.25%) treatment followed by incubation of the epidermis with 200µl of trypsin (0.25%) solution for 20 minutes at 37°C to allow cell separation to occur. The dissociated cells obtained were suspended in ice-cold 1X phosphate buffered saline (PBS) and centrifuged at a speed of 2000rpm for 5 minutes at 4°C. After centrifugation, the pellet obtained was resuspended in 200µl of 1X phosphate buffered saline (PBS) for further analysis. The flow cytometry measurements were then performed using FACS Caliber (Becton Dickinson) to quantify the cellular fluorescence. Statistical significance for quantitative data obtained was calculated using two-tailed student's t-test (unpaired) in GraphPad Prism.

Immunostaining and Co-localization studies in human foreskin tissue

Full thickness human foreskin tissue was processed, plated and treated topically as described in previous section of plasmid DNA delivery in human foreskin tissue. Post treatment tissue cryosections were obtained in a similar manner as mentioned before and rehydrated using wash buffer (1X phosphate buffered saline with 0.1% Triton X-100) for 15 minutes followed by 1h of blocking in 5% BSA (bovine serum albumin) at room temperature. Primary antibody, anti-EGFP or anti-Keratin, was applied to the tissues at dilution of 1:200 and incubated overnight at 2-8°C. The tissues were then given 3 washes of 15 minutes each in wash buffer before addition of TRITC labeled secondary antibody, anti-rabbit IgG against EGFP or ALEXA FLUOR 488 labeled secondary antibody, anti- mouse IgG against Keratin 14 at dilution of 1:250 for 1h, at room temperature. The washing was repeated along with the final rinsing using 1X phosphate buffered saline (PBS). The mounting of tissues was done with DAPI-antefade reagent (Invitrogen) and results were recorded using inverted LSM510 META laser scanning microscope (Carl Zeiss) and TCS SP8 confocal microscope (Leica). The correlation coefficient calculation was performed using Zen software and 3-D model of skin was generated using Zen BlueLite software to analyze the depth of fluorescence expression as seen in µm along the x-axis.

Effect of dose, time and mode of application on nanocomplex delivery in skin

For dose response study, the nanocomplexes were formed with varying amount of plasmid DNA (2µg, 4µg, 8µg) and administered topically as single application on the tissues, and sections were analyzed 24h after treatment. For time dependent study same amount of plasmid DNA (4µg) was administered as 3 consecutive applications (once per day for 3 days) and sections were analyzed after 24h, 48h and 72h. Moreover to study the effect of mode of application, the entire plasmid amount (12µg) was applied topically

either as single application or in form of 3 consecutive applications for 3 days with equal amount of plasmid DNA (4 μ g) in each application and sections were analyzed 24h post-treatment. To visualize the EGFP expression in all the three different treatments, cryosectioning was done to obtain 6 μ m sections and immunostaining was performed in a similar manner as mentioned in previous section where tissues were treated with only single primary antibody i.e. anti-EGFP followed by addition of TRITC labeled secondary antibody anti-rabbit IgG against it and results were recorded as red fluorescent signals using TCS SP8 confocal microscope (Leica).

In vivo transfection study

Entire animal studies were performed using 2-4 weeks old hairless mice SKH-1 (irrespective of gender) and animal usage was in line with the approval by Institutional animal ethics committee [Approval Number: IITR/IAEC/47/13]. Each study was done in two groups where each group comprised of 3 mice (n=6). For peptide uptake, mice were topically treated with FITC labeled bare peptide Mgpe9 and for nanocomplex transfection, mice were topically treated with Mgpe9 nanocomplexes prepared at charge ratio 10 along with respective controls in independent experiments. In each case the treatment consisted of three applications on three consecutive days where a single application per day involved administering 5 μ M bare peptide per application and 4 μ g plasmid DNA in case of nanocomplex per application on the dorsal surface of mice in form of a solution (80 μ l) added into a circular plastic well (diameter=1cm) pre-adhered to mice skin and covering area of 3.14cm² along with the washing of skin surface before each fresh application using 1X phosphate buffered saline (PBS). The mice were sacrificed 24h after final application and skin tissue was obtained. Following this, the tissue was washed using 1X phosphate buffered saline, fixed using 4% paraformaldehyde for 30 minutes and transferred to 20% sucrose solution having 0.01% sodium azide to be stored at 4°C until further processing was done. For cryosectioning (24h post-fixation), the small piece of tissue from application site was embedded in an OCT compound and sections of 6 μ m thickness were obtained which were further processed for immunostaining. Initially tissue sections were rehydrated using wash buffer (1X Phosphate buffered saline and 0.1% Triton X-100) for 15 minutes followed by 1h of blocking in 5% BSA (bovine serum albumin) at room temperature. Primary antibody, anti-EGFP was applied to the tissues at dilution of 1:200 and incubated overnight at 2-8°C. The tissues were then given 3 washes of 15 minutes each in wash buffer before addition of TRITC labeled secondary antibody, anti-rabbit IgG against EGFP at dilution of 1:250 for 1h, at room temperature. The washing was repeated along with the final rinsing using 1X phosphate buffered saline (PBS). The mounting of tissues was done with DAPI-antefade reagent (Invitrogen) and results were recorded using inverted LSM510 META laser scanning microscope (Carl Zeiss). For luciferase estimation 24h after completion of last application, the tissue was homogenized in liquid nitrogen using mortar- pestle and enzyme activity was assessed in the obtained lysate according to the standard protocol (Promega). Statistical significance for luciferase transfection data was calculated using two-tailed student's t-test (unpaired) in GraphPad Prism.

Mechanism of tissue entry

i) FTIR study

Stratum corneum (SC) was obtained by standard heat separation method. SC membrane samples were cut into 0.5cm x 0.5cm pieces and Fourier transform infrared (FTIR) spectra were recorded on the samples before and after interaction with 18 μ M of unlabeled bare peptide Mgpe9 as single application for different time points of 4h and 24h in independent experiments. FTIR spectra was recorded using the Thermo scientific model NICOLET 380 FTIR operating in the range of 400–4000 cm^{-1} with the resolution of 4 cm^{-1} and averaged over 400 scans.

ii) Role of junction proteins

Tissue was plated and treated with 18 μ M of FITC labeled Mgpe9 peptide applied as single topical application. Post treatment samples were given single wash using 1X phosphate buffered saline (PBS) followed by its fixation in 4% paraformaldehyde for 30 minutes at different time intervals of 4h, 10h and 24h respectively to perform a time lapse study. It was then cryosectioned (24h post-fixation) and processed for immunostaining followed by treatment with primary antibody against occludin proteins of tight junctions in skin at a dilution of 1:200 with overnight incubation at 2-8°C. After three washings using 1X phosphate buffered saline (PBS), TRITC labeled anti-rabbit IgG secondary antibody was added at a dilution of 1:250 and incubated for 1h at room temperature in dark. Finally DAPI antifade was used to stain the nuclei. Direct visualization of fluorescence in the samples was then performed at 20x and 63x magnification using TCS SP8 confocal microscope (Leica) and inverted fluorescence microscope (Leica SPE LSI-Germany) respectively. Higher resolution zoomed (4 times) images were obtained from 20x magnification image for better clarity of results.

Pathway analysis for cellular entry of nanocomplexes

HaCaT cells were seeded at density of 60,000 cells per well in a 24 well plate and complete media was replaced with 200 μ l Opti-MEM (Invitrogen) after 24h when 70% confluency was achieved. Before addition of nanocomplexes cells were pre-incubated with 100 μ l of different pathway inhibitors i.e. Chlorpromazine (10 μ g/ml), Genistein (200 μ M), 5-(N,N-Dimethyl)amiloride hydrochloride (200 μ M), Methyl- β -cyclodextrin (2mM) and deoxy-D-glucose (5mM) for 1h. Following this, 100 μ l of FITC-labeled nanocomplexes formed using FITC labeled plasmid DNA was added to the cells (2 μ g plasmid DNA per well). For 4°C treatment cells were incubated with nanocomplexes for 1h only to avoid excessive cell death. After 4h of incubation at 37°C, cells were processed as mentioned in cellular uptake protocol followed by flow cytometry measurements using FACS Caliber (Becton Dickinson). Statistical significance of the data obtained was calculated using two-tailed student's t-test (unpaired) in GraphPad Prism.

Cell viability assay for bare peptide and nanocomplexes

Cells were seeded in a 96 well plate at density of 3000 cells per well for HaCaT and 5000 cells per well for WM266-4 melanoma respectively. After 24h when 70% confluency was attained, complete media was replaced with 50 μ l of Opti-MEM (Invitrogen) in each well. Following this 50 μ l of bare peptides (with final concentrations (5 μ M, 10 μ M and 15 μ M) or nanocomplexes (with final DNA concentration of 200ng/well) were added to the cells. Cell viability was analyzed after 4h and 24h of incubation at 37°C (in the latter case media was replaced with complete media after 4h) according to manufacturer's protocol. Measurements were recorded using microplate reader (Infinite 200 Pro Tecan) and plotted as percentage cell viability.

Skin integrity test

For checking the effect of bare peptide and nanocomplex on skin integrity, skin permeability test was performed using equilibrated full thickness human foreskin tissue processed according to protocol described previously. 100 μ l of nanocomplexes (formed using unlabeled Mgpe9 or Lipofectamine 2000TM with 4 μ g of plasmid DNA) or 5 μ M of FITC labeled bare Mgpe9 peptide was added to the donor compartments of independent experiments along with 100 μ l of 2 μ g/ μ l Rhodamine (430Da) solution and 100 μ l of 1mM Dextran (3000Da) in all the set ups. The system was kept under constant agitation at 250rpm at room temperature and 1ml of sample volume was collected at different time intervals (i.e. 0h or time of application, 1h, 2h, 3h, 4h, 5h, 18h and 24h). The volume of receptor compartment was maintained constant by re-addition of 1ml 1X phosphate buffered saline (PBS). Rhodamine fluorescence was recorded in the collected samples at emission wavelength of 543nm using microplate reader (Infinite 200 Pro Tecan). Dextran was assessed by anthrone test for carbohydrates.

RESULTS

Entry of Mgpe9 peptide and nanocomplexes in skin.

Mgpe9 is a secondary amphipathic peptide (CRRLRHLRHYYRRRWHRFRC, Figure 1a) developed in our laboratory containing both arginines and hydrophobic residues [32]. It remains unstructured in water but adopts an alpha-helical conformation in hydrophobic environment as shown earlier through Circular Dichroism spectroscopy [32]. To study its affinity for a lipid-rich environment like that in skin, we analyzed the pentanol-water partitioning of FITC-labeled Mgpe9 (Figure 1b) [24,25]. In spite of being water soluble, some retention of the peptide (~7% of total fluorescence recorded) is noted in pentanol phase as well. Comparison with peptides used for cargo delivery to skin and otherwise, such as TAT and penetratin, reveals that TAT is almost completely retained in water and penetratin shows slightly higher retention in pentanol. The hydrophobicity index of Mgpe9 is found to be between that of TAT and penetratin (Figure 1b).

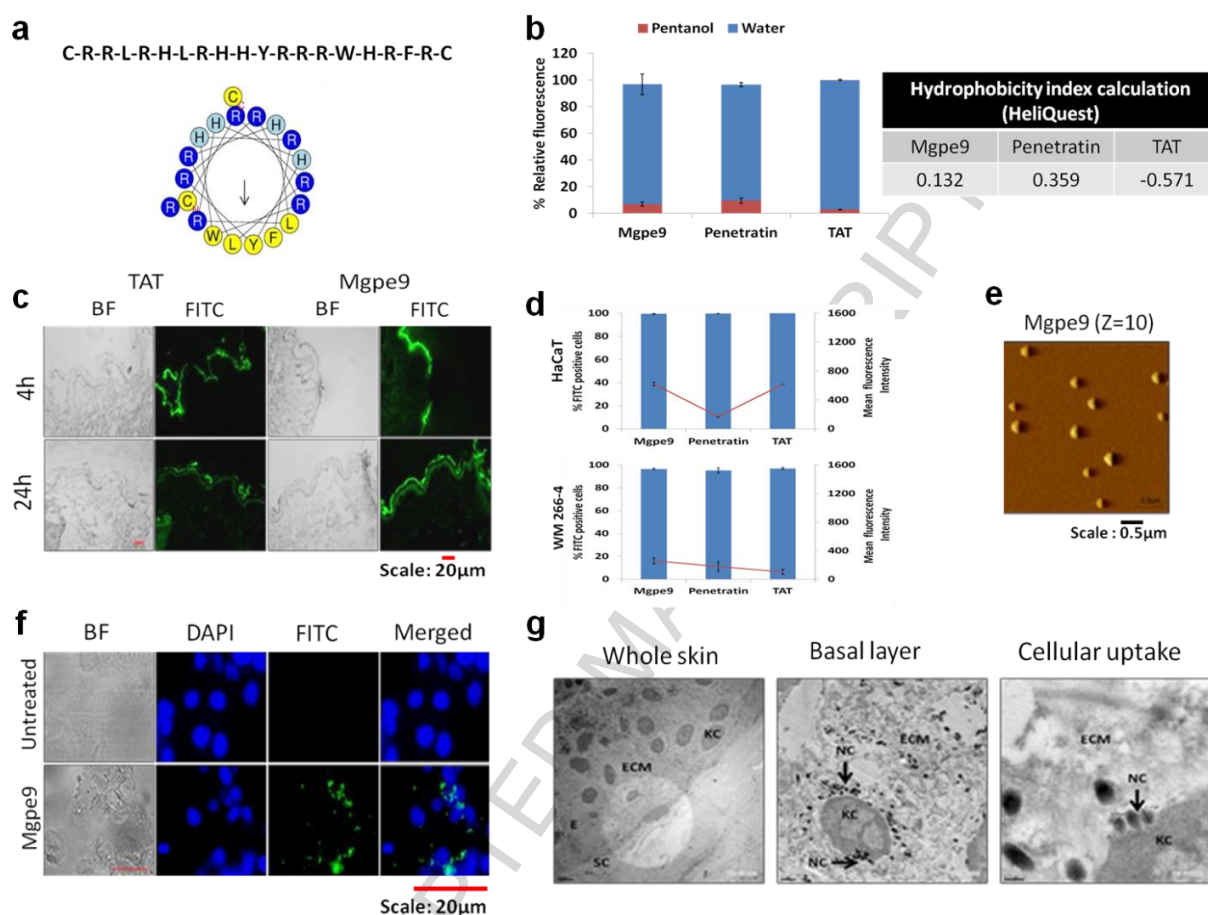


Figure 1. Entry of Mgpe9 peptide and nanocomplexes in skin. **a)** Sequence of Mgpe9 peptide is shown. The helical wheel diagram represents the top-down view of the peptide along the helical axis when it forms a secondary structure. **b)** Pentanol-water partitioning of Mgpe9 and control peptides (Penetratin and TAT) was studied using fluorescence estimation method. The percentage relative fluorescence (bars) in each phase (Red bars indicate hydrophilic phase, Blue bars indicate hydrophobic phase) was recorded after 24h of peptide treatment. Hydrophobicity index calculation for all the peptides was carried out using HELIQUEST software. **c)** Human skin penetration ability of FITC labeled peptides (Mgpe9 and TAT) 4h and 24h after application was studied using peptide skin penetration test in independent experiments. Direct visualization of FITC fluorescence was performed after single topical application of peptides using fluorescence microscopy at 10x magnification. Scale bar: 20µm. **d)** Cellular uptake of peptides (labeled with FITC) was investigated using flow cytometry in skin cell lines. The percentage of FITC positive cells (bars) and the mean fluorescence intensity (line) were recorded after 4h. The data are shown as Mean±SD. **e)** Atomic Force Microscopy was carried out to show the formation of nanocomplexes (<100nm) between Mgpe9 and plasmid DNA at charge ratio 10. Scale bar: 0.5µm. **f)** Cellular uptake of labeled Mgpe9 nanocomplexes (formed using FITC labeled plasmid DNA and unlabeled peptide) in HaCaT cells was studied using fluorescence microscopy. Cells were imaged at 100x magnification and uptake of nanocomplexes was visualized as green fluorescence inside the cells. DAPI (blue) has been used to stain the cellular nuclei. Scale bar: 20µm. **g)** Transmission Electron Microscopy was carried out to demonstrate the entry of nanocomplexes across stratum corneum and into the viable epidermal cells of skin. Imaging was performed at magnifications of 170x, 800x and 5000x respectively to locate the nanocomplexes in skin. Scale bar: 5µm, 1µm, 0.2µm respectively. SC denotes stratum corneum; E denotes epidermis; KC denotes keratinocytes; ECM denotes extracellular matrix, NC denotes Mgpe9 nanocomplexes.

A peptide skin penetration test was performed on human skin at two time points (4h and 24h) using fluorescently labeled peptides (as described in Material and Methods) to analyze penetration ability of Mgpe9 (Figure 1c). Fluorescence is observed on the stratum corneum even 4h post treatment. Increased fluorescence is seen at 24h indicating increase in peptide entry into the skin. TAT peptide also shows a similar pattern. We next studied entry of bare Mgpe9 in HaCaT and WM266-4 cell lines. FITC labeled Mgpe9 can enter more than 90% cells. Both the percentage fluorescent cells and the mean intensity of fluorescence are equivalent to or better than that obtained with TAT and penetratin (Figure 1d). It is known that for efficient DNA delivery to cells, the peptide has to be able to efficiently condense the plasmid DNA. Atomic Force Microscopy indicates that Mgpe9 can form completely condensed nanocomplexes which are less than 100nm in size with a 4.7kb plasmid DNA at charge ratio 10 (Figure 1e) which is in concurrence with Dynamic Light Scattering measurements as shown by us in a previous report [32]. To check if it can also assist in efficient entry of nanocomplexes in skin cell lines, we analyzed the cellular entry of Mgpe9 nanocomplexes containing FITC labeled plasmid DNA. The labeled nanocomplexes entered HaCaT cells 4h after treatment (Figure 1f). Further, entry of these nanocomplexes up to the basal layer of the epidermis in uncompromised human skin 24h after topical treatment was confirmed using Transmission Electron Microscopy where untreated and Milli-Q treated control skin tissues do not show the presence of nanocomplexes (Figure 1g; Supplementary Information Figure S1). Hence Mgpe9 either in bare form or as a part of a nanocomplex can enter skin cells and tissue.

Plasmid DNA delivery *in vitro* and *in vivo* using Mgpe9.

Efficiency of Mgpe9 to deliver plasmid DNA encoding luciferase (Figure 2a) and EGFP (Supplementary Information Figure S2a, Supplementary Information Figure S2b) was studied next in independent experiments. Transfection efficiency (measured through luciferase activity, Figure 2a) of Mgpe9 is higher than that of penetratin and TAT. Efficiency of delivery of the plasmid encoding EGFP using Mgpe9 (measured as percentage fluorescence positive cells, Supplementary Information Figure S2b) is also higher than that observed with the peptides mentioned above. Comparison with the commercial transfection agent Lipofectamine 2000TM shows that Mgpe9 is not as efficient in cellular transfection. However, we observed that Mgpe9 efficiently delivers the plasmid encoding EGFP to human skin tissue with transfection efficiency comparable to that of Lipofectamine 2000TM (30% EGFP positive cells; Supplementary Information Figure 2c, Supplementary Information Figure 2d). While we observed gene expression 24h after delivery of single dose comprising 4µg of plasmid DNA in the nanocomplex, the expression increased further with addition of higher amounts as observed visually using confocal microscopy (Supplementary Information Figure S3). Optimal expression is obtained on 3 consecutive applications (24, 48 and 72h) of same dose of plasmid DNA (4µg) (Supplementary Information Figure S4)

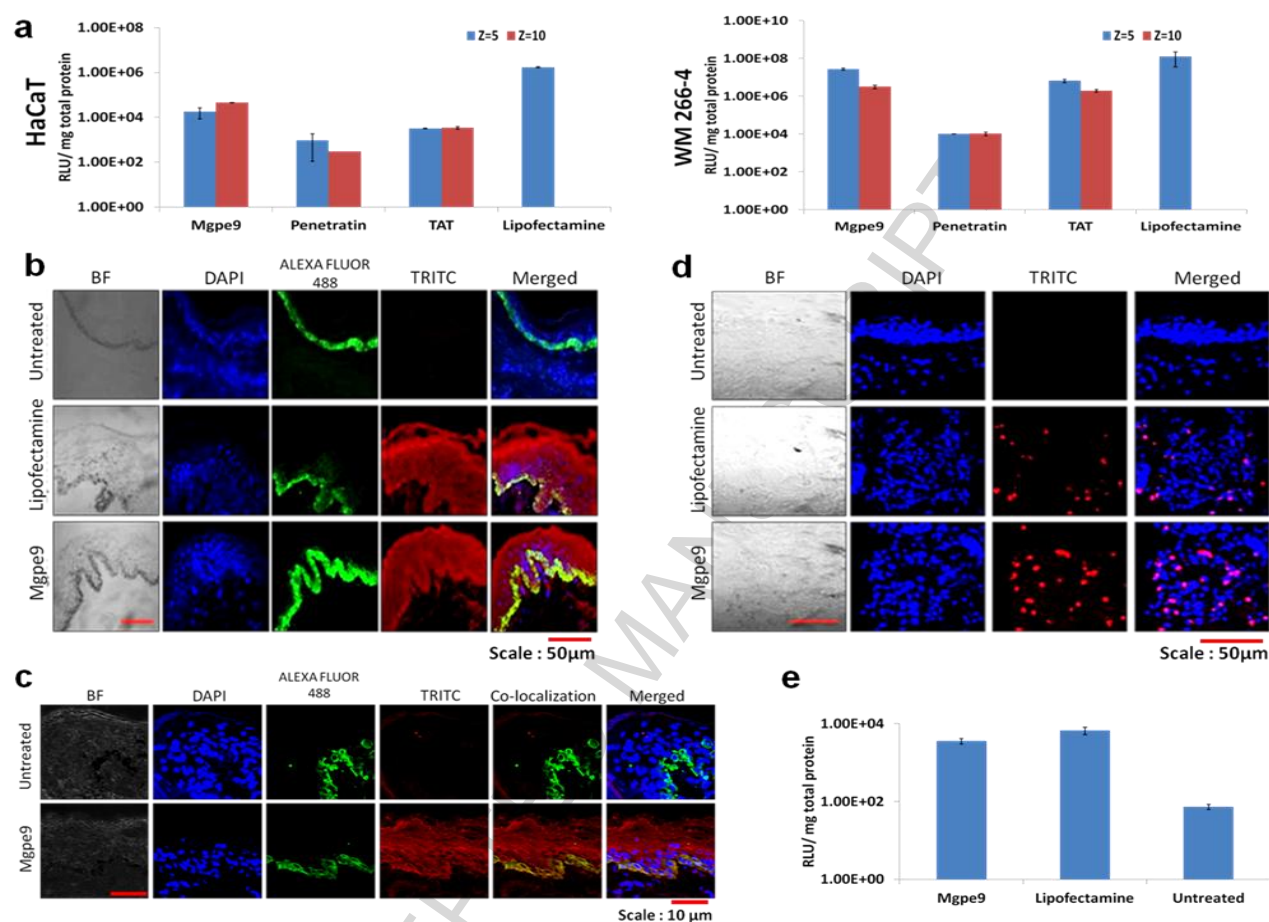


Figure 2. Plasmid DNA delivery in vitro and in vivo using Mgpe9. **a)** Transfection efficiency of nanocomplexes (prepared with the respective unlabeled peptide and DNA) was investigated 24h post-application using Luciferase assay in skin cell lines. Transfection efficiency of commercial agent Lipofectamine 2000TM was also estimated for comparison. Transfection efficiency at charge ratio 5 is indicated by blue bars and at charge ratio 10 by red bars. The data are shown as Mean \pm S.D. RLU (Relative Light Units). $p < 0.0001$ for all the observations in both cell lines except TAT and Lipofectamine 2000TM in WM 266-4 where $p < 0.005$. (Experiment was done in triplicates and $n=6$ values) **b)** Co-localization study was performed to investigate the depth of EGFP expression in human skin after topical application of Mgpe9 nanocomplexes for 3 consecutive days (1 application per day with 4µg plasmid DNA per application). Immunostaining was carried out (to avoid autofluorescence artifact) followed by confocal imaging at 63x magnification. Green signal of ALEXA FLUOR 488 indicates basal layer of skin; Red signal of TRITC indicates EGFP expression in skin. DAPI dye (blue) was used to stain the nuclei. Also comparison with commercial agent Lipofectamine 2000TM has been shown. Scale bar: 50µm. **c)** High resolution confocal microscopy images to depict co-localization between EGFP expression and basal layer of human skin after topical application of Mgpe9 nanocomplexes. Green signal of ALEXA FLUOR 488 indicates basal layer of skin; Red signal of TRITC indicates EGFP expression in skin. DAPI dye (blue) was used to stain the nuclei. Scale bar: 10µm **d)** Confocal microscopy was carried out to illustrate the EGFP expression in SKH-1 mice skin tissue through immunostaining. DAPI (blue) has been used as nuclear stain to show proper tissue integrity. TRITC (red) indicates the EGFP expression. Also comparison with commercial agent Lipofectamine 2000TM has been shown. Scale bar: 50µm. **e)** Transfection efficiency of Mgpe9 in SKH-1 mice was assessed by Luciferase assay. Also comparison with commercial agent Lipofectamine 2000TM was done. The data are shown as Mean \pm S.D. RLU (Relative Light Units). $p < 0.0001$ for all the observations. (Experiment was done in duplicates and $n=6$ values).

and is sustained for at least 48h (Supplementary Information Figure S5). However delivery of the total amount of plasmid DNA (12µg) as a single application leads to lower EGFP expression (Supplementary Information Figure S5). In comparison to Mgpe9, TAT does not have demonstrable DNA delivery property in skin tissue (10% EGFP positive cells) (Supplementary Information Figure 2c, Supplementary Information Figure 2d) although TAT peptide by itself shows better tissue entry (Supplementary Information Figure S6a, Supplementary Information Figure S6b). Penetratin on the other hand is unable to enter skin tissue in an independent manner (Supplementary Information Figure S6a, Supplementary Information Figure S6b) and is thus not expected to show significant plasmid DNA delivery either.

Moreover no fluorescence is observed upon treatment of the skin either with unlabeled bare peptides (thereby ruling out fluorescence related artifacts) or bare EGFP plasmid DNA (emphasizing the importance of the carrier Mgpe9) (Supplementary Information Figure S6c, Supplementary Information Figure S6d). Next we wanted to explore the extent of penetration of the nanocomplexes in skin. We topically applied the nanocomplexes on human skin tissue using similar dosage as described above and studied co-localization of EGFP expression (indicated by TRITC label) with the ALEXA FLUOR 488 labeled antibody against Keratin 14 marker; a protein which is specific to the basal layer of human skin. Strong EGFP expression is observed with Mgpe9 throughout the viable layers of skin tissue up to the highly proliferating basal layer (Figure 2b, Figure 2c) and visually stronger than that observed with the commercial agent Lipofectamine 2000TM (Figure 2b). This was also analyzed using the 3-D simulation of the skin tissue which shows expression up to 150µm below the stratum corneum with the correlation coefficient value of 0.59 for co-localization of signals (Supplementary Information Figure S7a, Supplementary Information Figure S7b). When compared to TAT the EGFP expression is much stronger for Mgpe9. In skin, follicular pathway is the commonly predicted route of entry for majority of hydrophilic molecules. The high expression of Mgpe9 nanocomplexes in skin prompted us to investigate if it can also adopt non-follicular pathways of entry. We selected hairless model of mice SKH-1 where the follicles are completely absent and checked the skin entry of bare Mgpe9 (Supplementary Information Figure S8a) as well as its ability to deliver plasmid DNA (Figure 2d, Figure 2e, Supplementary Information Figure S8b) on topical application *in vivo*. Strong EGFP expression was observed through confocal imaging (analyzed by immunostaining using anti-EGFP antibody) which indicates efficient DNA delivery. Quantitative analysis for delivery of luciferase plasmid DNA to skin tissue reveals that Mgpe9 exhibits significant transfection efficiency which is comparable to Lipofectamine 2000TM (Figure 2e).

Mechanism of entry of Mgpe9 in skin tissue and cells.

We next explored the possible underlying mechanism of Mgpe9 nanocomplex entry in skin. FTIR spectroscopy was carried out on the stratum corneum of human skin treated with Mgpe9 for 4h and 24h in independent experiments (Figure 3a). The major signatures in the region of 2800-3400 cm⁻¹ (from -CH₂ vibrations arising from skin lipids and -OH vibrations arising from water) and in the region of 1600-1700 cm⁻¹

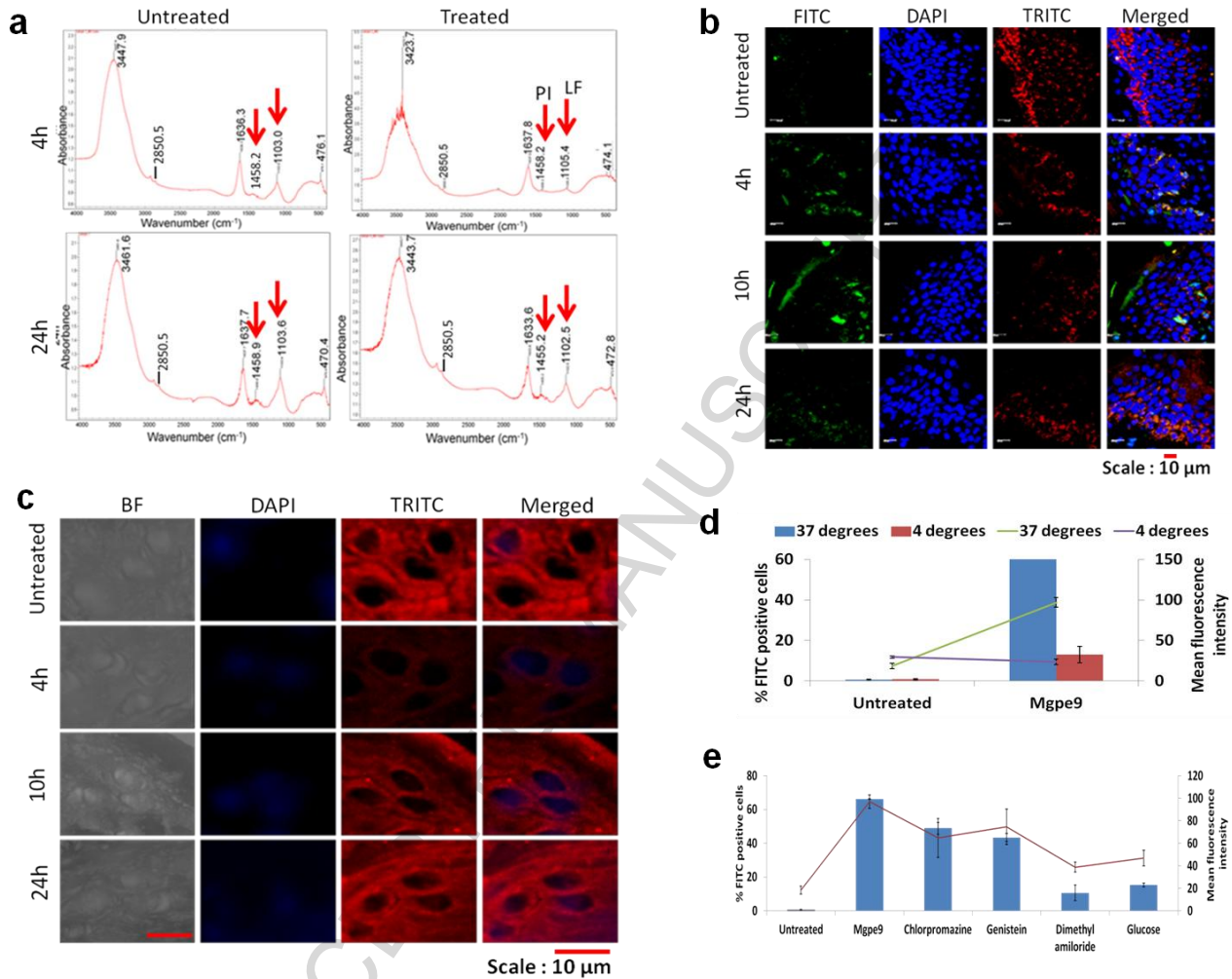


Figure 3. Mechanism of entry of Mgpe9 in skin tissue and cells. **a)** FTIR spectroscopy was carried out on stratum corneum of human skin (untreated and pre-treated with Mgpe9 peptide) at two time points of 4h and 24h to predict the interaction of skin with Mgpe9. **PI** : Protein Interaction; **LF**: Lipid fluidization. Red arrows indicate critical peaks. **b)** Expression of occludin proteins in human skin was checked using immunostaining study post treatment with the FITC labeled Mgpe9 peptide at different time points of 4h, 10h and 24h. Red fluorescence of TRITC indicates Occludin expression in skin. DAPI (blue) has been used to stain the nuclei. The sections were visualized using confocal microscope at 63x magnification. Scale bar: 10μm. **c)** Zoomed images to illustrate expression of occludin proteins in human skin post treatment with Mgpe9 peptide at different time points of 4h, 10h and 24h. Red fluorescence of TRITC indicates Occludin expression in skin. DAPI (blue) has been used to stain the nuclei. The sections were visualized using confocal microscope at 20x magnification. Scale bar: 10μm. **d)** Mode of transport of cellular entry of nanocomplexes was investigated in HaCaT cells at different temperatures (4°C and 37°C) 4h post treatment using flow cytometry. Percentage FITC positive cells (bars) and the mean fluorescence intensity (line) was recorded. The data are shown as Mean±S.D. $p < 0.0001$ is observed for all except for mean intensity value at 4°C of untreated sample where $p < 0.005$ (Experiment was done in triplicates and $n = 6$ values) **e)** Pathway of cellular entry of nanocomplexes were investigated with different endocytotic inhibitors using flow cytometry. Percentage FITC positive cells (bars) and the mean fluorescence intensity (line) was recorded after 4h using flow cytometry. The data are shown as Mean±S.D. $p < 0.0001$ is observed for all except mean intensity value of Chlorpromazine and Genistein where $p < 0.005$ (Experiment was done in duplicates and $n = 6$ values).

¹ (from the amide I band) are nearly unaltered between the treated and untreated samples at 4h. However, the fluidity of the lipid and the changes in the nature of lipid packing can also be assessed by the bands in the region 1000-1400 cm^{-1} [33-34]. The peak at around 1100 cm^{-1} reduces in intensity at 4h possibly indicating changes in the lipid organization like fluidization which is restored by 24h indicating that the changes in lipid organization, if any, could be transient. Also the region around 1450 cm^{-1} is the amide II region which indicates C-H scissoring vibrations of the protein corneocytes [33]. We do observe mild change in the intensity of peaks in this region in the 4 h treated sample as compared to the 24h treated sample and this can be indicative of the transient interactions with the stratum corneum proteins. We further checked if the peptide could be transiently disrupting the tight junctions of skin by checking the alteration of occludin protein expression in skin (Figure 3b, Figure 3c). The expression of occludin decreases at 4h and 10h but is restored by 24h as observed through immunostaining (Figure 3b, Figure 3c). This might indicate reversible modulation of junction protein by Mgpe9 causing transient openings in the skin facilitating entry of these nanocomplexes. Further, the cellular entry mechanism of these nanocomplexes in skin keratinocytes was studied at two different temperatures and in presence of different endocytosis pathway inhibitors. It exhibits an active transport mechanism (through comparison of entry at 4°C and 37°C) (Figure 3d) and cellular entry is primarily through macropinocytosis (Figure 3e). This is particularly interesting because nanocomplexes going through macropinocytosis pathway may avoid the lysosomal entrapment or degradation through lysosomal enzymes; thus resulting in overall enhancement of their cellular bioavailability as well as transfection efficiency.

Cytotoxicity and tissue integrity analysis for skin penetrating peptide Mgpe9.

Skin is the first line of defense against microbial invasion and any disturbance to this barrier integrity may increase the susceptibility to other infections. We wanted to check whether Mgpe9 causes any deleterious effects on skin either at tissue or cellular level. We carried out cytotoxicity analysis by assessing the ATP production from cells in presence of free peptide (Figure 4a, Figure 4b) and nanocomplexes (Figure 4c, Figure 4d). Nearly 80% cells are viable up to the highest peptide concentration (15 μM) till 24h. We also performed a skin permeability test through dye penetration assay (using low molecular weight Rhodamine and high molecular weight Dextran) across skin in order to assess the adverse effect if any at the tissue level (Figure 4e). Any recordable presence of these dyes in the receptor solution of Franz apparatus on co-administration with Mgpe9 or the nanocomplex would indicate compromise in skin tissue integrity. We observe that Mgpe9/nanocomplex, does not allow dye penetration indicating uncompromised skin integrity (Figure 4e) and absence of tissue damage unlike what is observed with Lipofectamine 2000TM.

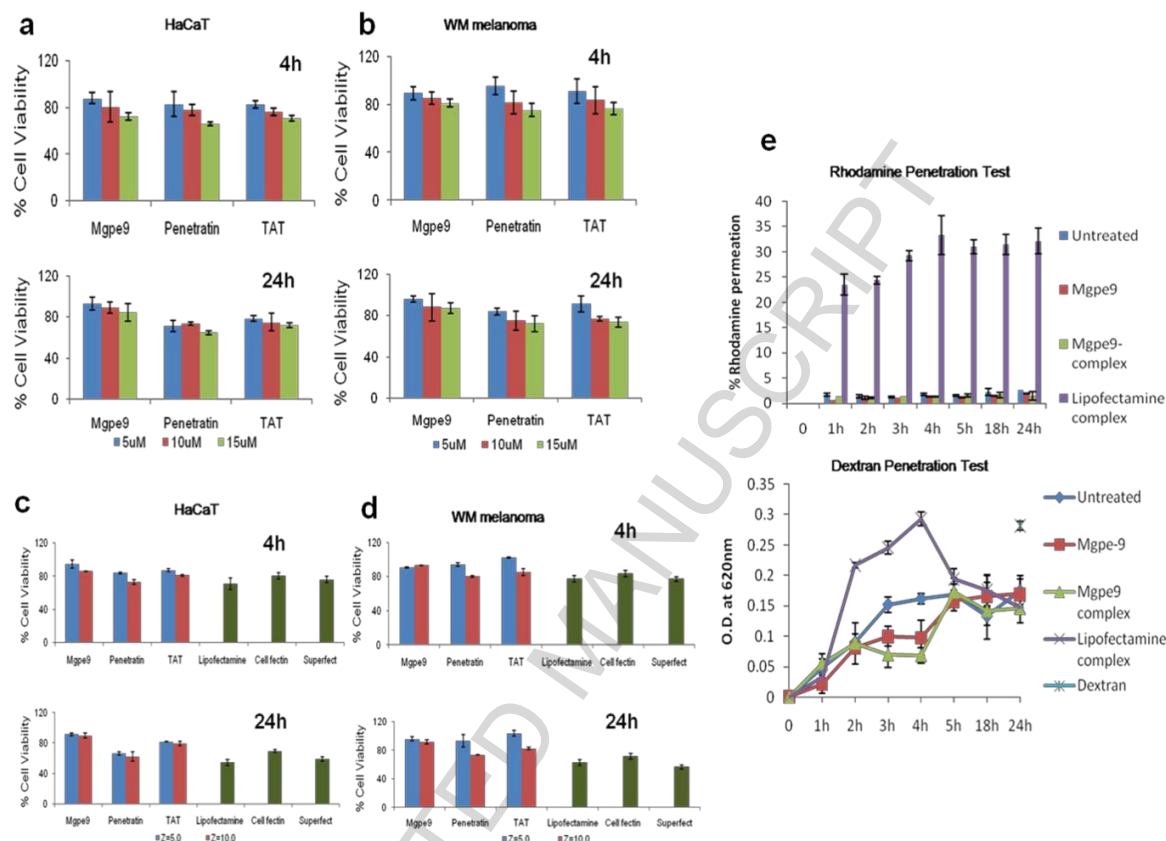


Figure 4. Cytotoxicity and tissue integrity analysis for skin penetrating peptide Mgpe9. **a)** Cell viability in presence of different concentrations of bare peptides (Mgpe9 and control peptides TAT and Penetratin; 5μM, 10μM, 15μM) was assessed using CellTitre Glo Luminescent Cell Viability assay for 4h and 24h in HaCaT cells. Untreated cells were taken as 100% viable (Blue bars indicate % cell viability at 5μM, Red bars indicate % cell viability at 10μM, Green bars indicate % cell viability at 15μM). **b)** Cell viability in presence of different concentrations of bare peptides (Mgpe9 and control peptides TAT and Penetratin; 5μM, 10μM, 15μM) was assessed using CellTitre Glo Luminescent Cell Viability assay for 4h and 24h in WM266-4 melanoma cells. Untreated cells were taken as 100% viable (Blue bars indicate % cell viability at 5μM, Red bars indicate % cell viability at 10μM, Green bars indicate % cell viability at 15μM). **c)** Cell viability in presence of nanocomplexes at different charge ratios 5 and 10 (Mgpe9 and control peptides TAT and Penetratin) was assessed using CellTitre Glo Luminescent Cell Viability assay for 4h and 24h in HaCaT cells. Also comparison with commercial agents Lipofect amine 2000TM, Cellfectin and Superfect was done. Untreated cells were taken as 100% viable. (Blue bars indicate % cell viability at charge ratio 5, Red bars indicate % cell viability at charge ratio 10, Green bars indicate % cell viability for commercial agents). **d)** Cell viability in presence of nanocomplexes at different charge ratios 5 and 10 (Mgpe9 and control peptides TAT and Penetratin) was assessed using CellTitre Glo Luminescent Cell Viability assay for 4h and 24h in WM266-4 melanoma cells. Also comparison with commercial agents Lipofectamine 2000TM, Cellfectin and Superfect was done. Untreated cells were taken as 100% viable. (Blue bars indicate % cell viability at charge ratio 5, Red bars indicate % cell viability at charge ratio 10, Green bars indicate % cell viability for commercial agents). **e)** Skin integrity was assessed by skin permeability test using dye penetration assay. Lipofectamine 2000TM was used as a positive control for comparison studies. The data are shown as Mean±S.D. Dextran alone indicates the amount of absorbance obtained upon complete penetration of 1mM Dextran in the 20ml receptor solution

DISCUSSION

We rationalized that a peptide that can efficiently deliver plasmid DNA to skin should possess characteristics that allow efficient penetration through the stratum corneum into viable epidermal cells. It should also efficiently condense plasmid DNA into stable nanocomplexes that can enter skin cells in the epidermis/dermis *in vivo*, show endosomal release and deliver DNA at the intracellular site of action without exhibiting toxicity. Based on this, we investigated whether a novel cell penetrating peptide Mgpe9 possessing secondary amphipathicity and has been earlier shown to deliver plasmid DNA efficiently to cells of different origins can be used to deliver plasmid DNA to skin. As observed through Circular Dichroism study in our previous report, the tendency of Mgpe9 to acquire alpha helical conformation in presence of hydrophobic environment resembles many anti-microbial peptides found in skin e.g. dermcidin, cathelicidin, LL-37 and other known skin penetrating systems such as magainin whose helical form has been reported previously to allow enhanced transdermal delivery [35,36]. Moreover the presence of 9 arginines, 4 histidines, 5 hydrophobic amino acid residues and 2 terminal cysteines in Mgpe9 sequence can allow stable complexation of the plasmid DNA into nanocomplexes through peptide-DNA electrostatic interactions, easy tissue penetration and cellular internalization, efficient endosomal escape through proton sponge effect of the histidines and release of the plasmid DNA at designated site within the cell. This is likely to account for the high transfection efficiencies observed with Mgpe9 nanocomplexes at both cellular and tissue level in our study. Since the peptide has characteristics that help skin penetration, it can be possibly used for delivery of different cargoes through conjugation as well as complexation strategies. Moreover, its ability to overcome the barrier of stratum corneum without any obvious physical damage unlike other methods like derma-abrasion, can make it a potential carrier for non invasive topical delivery. Optimization of the dose, time and number of applications in order to attain efficient delivery in skin helped us to highlight the benefits of small repeated doses in skin over a single topical application of higher dose. Although the intensity of EGFP expression in skin increases in a dose dependant manner (as shown by repeated administrations of 4µg plasmid DNA in every dose) still in contrast to the above lower EGFP expression was observed upon administration of larger amounts of plasmid DNA (12µg) as a single dose. This could possibly be due to the saturation effect which leads to slow movement of nanocomplexes across skin and occlusion of entry routes by the ones migrating faster. Another factor that could be contributing to this low transfection efficiency is the slight increase in size of the nanocomplexes impeding their entry in skin. Three consecutive applications of 4µg plasmid DNA was thus a more effective way of administering these nanocomplexes in skin. Moreover the ability of Mgpe9 to deliver a functionally potent plasmid DNA up to the highly proliferating basal layer of the epidermis indicates its possible future applications. The presence of nanocomplexes in deeper layers of skin along with sustainable expression of plasmid DNA till 48hrs may help in delivery of therapeutics to skin in future.

We have also attempted to elucidate the precise mechanism of entry of Mgpe9 in skin. Previous reports emphasize three primary routes by which molecules can enter skin: a.transcellular route which involves

diffusion across the corneocytes, b.intercellular route through interstitial lipids and c. transappendageal /transfollicular route which consists of sweat and sebaceous glands. The transappendageal /transfollicular route covers <0.1% area of skin but is considered to act as a major reservoir for hydrophilic molecules in particular [37-39]. However, entrapment of such molecules causes them to enter in therapeutically insufficient amounts. Mgpe9 seem to enter skin through mild fluidization of lipids, transient alterations in lipid packaging as well as interaction with skin proteins as seen through FTIR and transient disruption of tight junctions of skin as seen through time dependent microscopy analysis. Such entry through non follicular pathways can help in the development of this carrier for macromolecule delivery to different skin types. This is also evident from efficient gene expression in SKH-1 hairless mice. In addition to this advantage we have also seen from peptide skin penetration test that in case of Lipofectamine 2000TM, there is indication of major loss of skin integrity as compared to Mgpe9 nanocomplexes which are largely nontoxic to cells and the tissue. This can help in high retention of Mgpe9 nanocomplexes in the skin. Although skin permeability alterations can take place during cargo delivery to skin still it needs to be mild and transient for both topical and transdermal delivery in order to avoid undesirable entry of pathogens or any other external allergens. Hence we speculate that the lack of skin integrity and loss of cell viability in case of Lipofectamine 2000TM make it less attractive a carrier as compared to Mgpe9 which possesses better potential to be used for delivery of nucleic acid to skin [40].

CONCLUSION

In conclusion we describe a peptide that can penetrate skin, enter skin cells and deliver plasmid DNA efficiently *in vitro* and *in vivo* without toxicity or compromise of skin integrity unlike commercial agents such as Lipofectamine 2000TM. Entry of this peptide Mgpe9 in skin via non-follicular pathways is likely to make it suitable for delivery in multiple skin types. This peptide shows potential for non invasive delivery of therapeutic nucleic acids to skin in an easy manner and has possibility for cell-specific delivery in skin after modification with targeting moieties.

ACKNOWLEDGEMENT

We acknowledge Council of Scientific and Industrial Research (CSIR), New Delhi, India (Network Project TOUCH: BSC0302) for providing financial support to conduct this work. We also thank Dr. S. Ghosh and A. Jain (Vyome Biosciences Pvt Ltd), Dr. B. Ghosh and V. Negi (CSIR-IGIB) and Mr. M. Kumar (CSIR-IGIB) for experimental support.

FUNDING

This work was supported by Council of Scientific and Industrial Research (CSIR), New Delhi, India (Network Project TOUCH: BSC0302).CSIR research fellowships to [M.V., R.S. and S .A.]. CSIR project

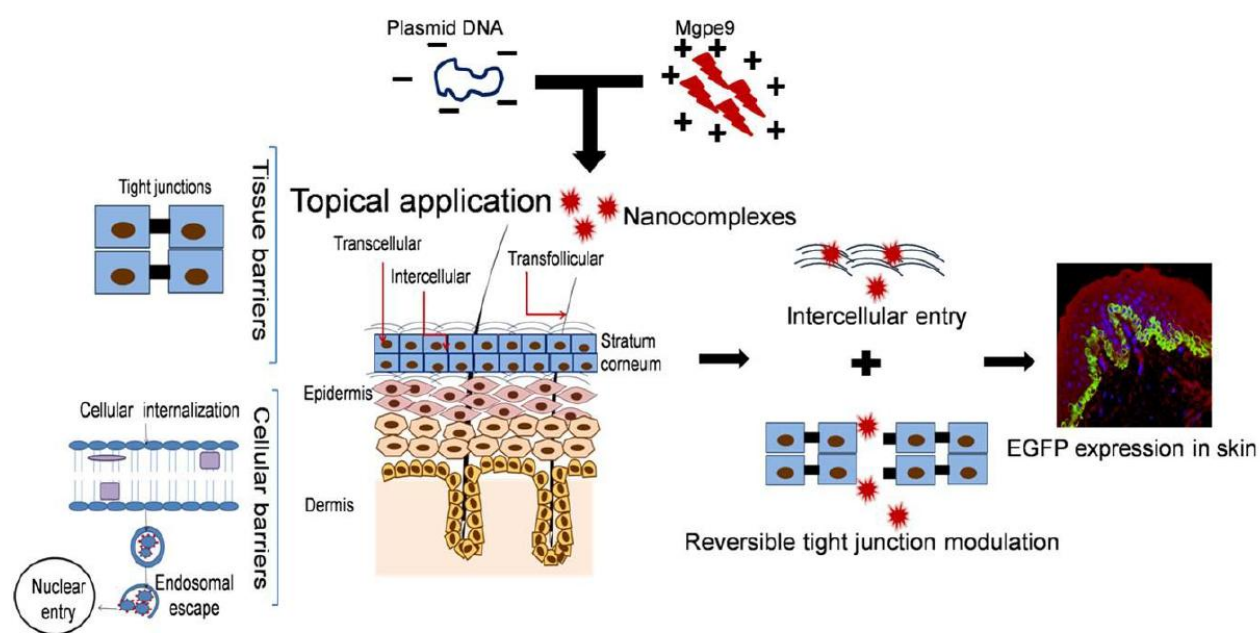
fellowships to [P.N. and B.R.P.] TOUCH network project support to [M.G., V.T.N., K.M.A., R.S.G. and A.S.].

REFERENCES

1. Prausnitz, MR., Mitragotri, S. and Langer, R. (2004) Current status and future potential of transdermal drug delivery. *Nat. Rev. Drug Discov.*, 3,115-124.
2. Rothbard, JB., Garlington, S., Lin, Q., Kirschberg, T., Kreider, E., McGrane, PL., Wender, PA. and Khavari, PA. (2000) Conjugation of arginine oligomers to cyclosporine A facilitates topical delivery and inhibition of inflammation. *Nat. Med.*, 6, 1253-1257.
3. Prausnitz, MR. and Langer, R. (2008) Transdermal drug delivery. *Nat. Biotechnol.*, 26,1261-1268.
4. Chen, M., Gupta, V., Anselmo, AC., Muraski, JA. and Mitragotri, S. (2014) Topical delivery of hyaluronic acid into skin using SPACE-peptide carriers. *J. Control Release*, 173, 67-74.
5. Mikszta, JA., Alarcon, JB., Brittingham, JM., Sutter, DE., Pettis, RJ. and Harvey, NG. (2002) Improved genetic immunization via micromechanical disruption of skin-barrier function and targeted epidermal delivery. *Nat. Med.*, 8, 415-419.
6. Siu, KS., Chen, D., Zheng, X., Zhang, X., Johnston, N., Liu, Y., Yuan, K., Koropatnick, J., Gillies, ER. and Min, WP. (2014) Non covalently functionalized single walled carbon nanotube for topical siRNA delivery into melanoma. *Biomaterials*, 35, 3435-3442.
7. Wermeling, DP., Banks, SL., Hudson, DA., Gill, HS., Gupta, J., Prausnitz, MR. and Stinchcomb, AL. (2008) Microneedles permit transdermal delivery of a skin-impermeant medications to humans. *Proc. Natl. Acad. Sci. U S A*, 105, 2058-2063.
8. Steinstraesser, L., Lam, MC., Jacobsen, F., Porporato, PE., Chereddy, KK., Becerikli, M., Stricker, I., Hancock, RE., Lehnhardt, M., Sonveaux, P. et al. (2014) Skin Electroporation of a Plasmid Encoding hCAP-18/LL-37 Host Defense Peptide Promotes Wound Healing, *Mol. Ther.*, 22, 734-742.
9. Dou, C., Lay, F., Ansari, AM., Rees, DJ., Ahmed, AK., Kovbasnjuk, O., Matsangos, AE., Du, J., Hosseini, SM., Steenbergen, C. et al. (2014) Strengthening the skin with topical delivery of Keratinocyte Growth Factor 1 using a novel DNA plasmid, *Mol. Ther.*, 22, 752-761.
10. Karande, P., Jain, A. and Mitragotri, S. (2004) Discovery of transdermal penetration enhancers by high throughput screening. *Nat. Biotechnol.*, 22, 192-197.
11. Desai, P., Patlolla, RR. and Singh, M. (2010) Interaction of nanoparticles and cell penetrating peptides with skin for transdermal drug delivery. *Mol. Membr. Biol.*, 27, 247-259.
12. Margus, H., Padari, K. and Pooga, M. (2012) Cell penetrating peptides as versatile vehicles for Oligonucleotide delivery, *Mol. Ther.*, 20, 525-533.
13. Joliot, A. and Prochiantz, A. (2004) Transduction peptides: from technology to physiology. *Nat. Cell Biol.*, 6, 189-196.
14. Mann, A., Thakur, G., Shukla, V. and Ganguli, M. (2008) Peptides in DNA delivery: current insights and future directions. *Drug Discov. Today*, 13, 152-160.
15. Patlolla, RR., Desai, PR., Belay, K. and Singh, MS. (2010) Translocation of Cell Penetrating Peptide Engrafted Nanoparticles Across Skin Layers. *Biomaterials*, 31, 5598-5607.

16. Barua, S. and Mitragotri, S. (2014) Challenges associated with penetration of nanoparticles across cell and tissue barriers: A review of current status and future prospects. *Nano Today*, 9, 223-243.
17. Chen, Y., Shen, Y., Guo, X., Zhang, C., Yang, W., Ma, M., Liu, S., Zhang, M. and Wen, LP. (2006) Transdermal protein delivery by a co-administered peptide identified via phage display. *Nat. Biotechnol.*, 24, 455-460.
18. Hsu, T. and Mitragotri, S. (2011) Delivery of siRNA and other macromolecules into skin and cells using a peptide enhancer. *Proc. Natl. Acad. Sci. U S A*, 108, 15816-15821.
19. Trentin, D., Hall, H., Wechsler, S. and Hubbell, JA. (2006) Peptide matrix mediated gene transfer of an oxygen –insensitive hypoxia inducible factor -1 alpha variant for local induction of angiogenesis, *Proc. Natl. Acad. Sci. U S A*, 103, 2506-2511.
20. Siprashvili, Z., Scholl, FA., Oliver, SF., Adams, A., Contag, CH., Wender, PA. and Khavari, PA. (2003) Gene transfer via Reversible Plasmid condensation with cysteine flanked, internally spaced arginine rich peptides. *Human Gene Therapy*, 14, 1225-1233.
21. Hou, YW., Chan, MH., Hsu, HR., Liu, BR., Chen, CP., Chen, HH. and Lee, HJ. (2007) Transdermal delivery of proteins mediated by non-covalently associated arginines rich intracellular delivery peptides. *Exp.Dermatol.*, 16, 999-1006.
22. Ruan, RQ., Wang, SS., Wang, CL., Zhang, L., Zhang, YJ., Zhou, W., Ding, WP., Jin, PP., Wei, PF., Man, N. et al. (2013) Transdermal delivery of human epidermal growth factor facilitated by a peptide chaperon. *Eur. J. Med. Chem.*, 62, 405-409.
23. Zhao, B., Guo, Y. and Fu, A. (2012) Genetically engineered epidermal growth factor conjugate crosses cell membrane. *Appl. Biochem. Biotechnol.*, 166, 463-471.
24. Chaires, J.B., Dattagupta, N., Crothers, D.M. (1982) Studies on interaction of anthracycline antibiotics and deoxyribonucleic acid: equilibrium binding studies on the interaction of daunomycin with deoxyribonucleic acid. *Biochemistry*, 21, 3933–3940.
25. Patil, KM., Naik, RJ., Rajpal, Fernandes, M., Ganguli, M. and Kumar, VA. (2012) Highly Efficient (R-X-R)- Type Carbamates as Molecular Transporters for Cellular Delivery. *J. Am. Chem. Soc.*, 134, 7196-7199.
26. Do, N., Weindl, G., Grohmann, L., Salwiczek, M., Kokscho, B., Korting, H.C. and Sch€afer-Korting, M. (2014) Cationic membrane-active peptides – anticancer and antifungal activity as well as penetration into human skin. *J. Expt. Dermatol.*, 23, 326-331.
27. Chai, H., Li, J., Huang, H., Li, T., Chan, Y., Shiao, C. and Wu, C.(2010) Effects of Sizes and Conformations of Fish-Scale Collagen Peptides on Facial Skin Qualities and Transdermal Penetration Efficiency. *Journal of Biomedicine and Biotechnology*, 2010, 1-9.
28. Abe, R., Donnelly, S.C.,Peng, T., Bucala, R. and Metz, C.N. (2001) Peripheral Blood Fibrocytes: Differentiation Pathway and Migration to Wound Sites. *J. of Immunology*, 166, 7556-7562.
29. Uchida, T.,Kanazawa, T., Takashima, Y. and Okada, H. (2011) Development of an Efficient Transdermal Delivery System of Small Interfering RNA Using Functional Peptides, Tat and AT-1002. *Chem. Pharm. Bull.*, 59, 196-201.
30. Bartosova, L. and Bajgar, J. (2012) Transdermal Drug Delivery In Vitro Using Diffusion Cells. *Current Medicinal Chemistry*, 19, 4671-4677.

31. Graham, L. and Orenstein, JM. (2007) Processing tissue and cells for transmission electron microscopy in diagnostic pathology and research. *Nat. Protoc.*, 2, 2439-2450.
32. Sharma, R., Nisakar, D., Shivpuri, S. and Ganguli M. (2014) Contrasting effects of cysteine modification on the transfection efficiency of amphipathic peptides. *Biomaterials*, 35, 6563-6575.
33. Barry, B.W., Edwards, H.G.M., Williams, A.C.(1992) Fourier Transform Raman and Infrared Vibrational Study of Human Skin: Assignment of Spectral Bands. *J. Raman Spectroscopy*, 23, 641-645.
34. Karande, P., Jain, A., Ergun, K., Kispersky, V. and Mitragotri, S.(2005) Design principles of chemical penetration enhancers for transdermal drug delivery. *Proc. Natl. Acad. Sci. U S A*, 102, 4688-4693.
35. Kim, YC., Ludovice, PJ. and Prausnitz, MR. (2007) Transdermal delivery enhanced by magainin pore forming peptide. *J Control Release*, 122, 375-383.
36. Kim, YC., Ludovice, PJ. and Prausnitz, MR. (2010) Transdermal delivery enhanced by antimicrobial peptides. *J Biomed. Nanotechnol.*, 6, 612-620.
37. Li, L. and Hoffman, RM. (1995) The feasibility of targeted selective gene therapy of the hair follicle. *Nat. Med.*, 1, 705-706.
38. Lauer, AC., Lieb, LM., Ramachandran, C., Flynn, GL. and Weiner, ND. (1995) Transfollicular drug delivery. *Pharm. Res.*, 12, 179-186.
39. Agarwal, R., Katare, OP. and Vyas, SP. (2000) The pilosebaceous unit: a pivotal route for topical drug delivery. *Methods Find. Exp. Clin. Pharmacol.*, 22,129-133.
40. Zakrewsky, M., Kumar, S. and Mitragotri, S. (2015) Nucleic acid delivery into skin for the treatment of skin disease: Proofs-of-concept, potential impact, and remaining challenges. *J Control Release.*, 219, 445-56.



Graphical abstract

OTRA BASED R-2R LADDER AND WEIGHTED RESISTOR DAC REALIZATIONS

Rohan Chandra¹, Ravi Teja², Neeta Pandey³, Rajeshwari Pandey⁴

*^{1, 2, 3, 4} Dept. of Electronics and Communication Engg, Delhi Technological University,
New Delhi (India)*

ABSTRACT

This paper presents realization of R-2R ladder and weighted resistor digital to analog converters (DACs) using the Operational Trans Resistance Amplifiers (OTRA). These circuits use a single OTRA and are therefore power efficient. The functionality of the proposed converters is verified through SPICE simulations using CMOS based implementation of the OTRA. The circuits are shown to be 3-bit accurate using DNL and INL analysis. Other parameters like offset have also been computed. Through DNL and INL analysis, monotonicity of both configurations has been preserved.

Keywords: CMOS based OTRA, Digital-to-Analog Conversion, OTRA, Resistive Ladders, Weighted Resistors

I. INTRODUCTION

Digital to Analog converters (DACs) are used in wide range of applications. It is employed - in audio amplifier to produce DC voltage gain with microcontroller commands; to provide dynamic calibration for gain and voltage offset for accuracy in test and measurement system; to change voltage dynamically during operation of the system circuits that convert digital input to analog signals and in digital potentiometers. The DACs are typically realized with operational amplifier which has constant gain-bandwidth product and lower slew rate therefore their high frequency operations are limited. The current mode active blocks on the other hand possess gain independent of gain and better slew rate. The research therefore has gained momentum towards developing applications based on current mode active blocks.

The OTRA inherits all the advantages offered by current mode techniques, and has emerged as an alternate analog building block for developing various applications [1-8]. The OTRA is a high gain current input voltage output device. Due to low impedance input and output terminals, limitations on the response by the time constants of the capacitors are reduced. The device is unaffected by stray capacitances due to virtually grounded inputs [3]. Ideally, the Transresistance gain of OTRA approaches infinity and external negative feedback must be used which forces the input currents to be equal. The OTRA has not been used for realization of DAC to the best of authors' exposure in the field.

This paper aims at putting forward OTRA based DAC realizations. The paper is arranged in five sections. The terminal properties and its CMOS schematic is briefly discussed first in section 2 and is followed by proposed DAC configurations. Simulation results for functional verification and performance are given in section 3 and conclusions are drawn in section 4.

II. CIRCUIT DESCRIPTION

The OTRA is a three terminal current mode analog device with two low-impedance input terminals and one low-impedance output terminal. The input terminals of the OTRA are virtually grounded. The input and output terminal of an OTRA can be characterized by the matrix of (1)

$$\begin{bmatrix} V_p \\ V_n \\ V_o \end{bmatrix} = \begin{bmatrix} 0 & 0 & 0 \\ 0 & 0 & 0 \\ R_m & -R_m & 0 \end{bmatrix} \begin{bmatrix} I_p \\ I_n \\ I_o \end{bmatrix} \quad (1)$$

Where R_m is the Transresistance gain of the ideal OTRA. Ideally the value of the R_m gain is very high; therefore the OTRA has to be used in negative feedback configuration for linear applications

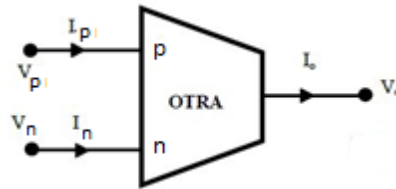


Fig.1 the OTRA block

The CMOS based schematic of OTRA [6] is shown in Fig. 2. The transistors M1 – M13 form current differencing circuit and provide a virtual ground at p and n terminals whereas common source amplifier (M14) provides high gain.

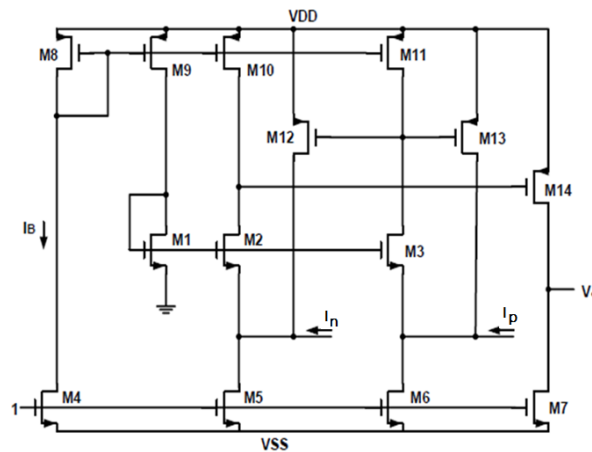


Fig.2 OTRA Block using CMOS implementation [6]

The proposed OTRA based R-2R and weighted resistor 3 – bit DAC realizations are shown in Fig. 3. Both the circuits use single OTRA and three switches. The number of resistors in proposed R-2R DAC and weighted resistor DAC are eight and four respectively. The output voltage V_o for Fig. 3a is computed as:

$$V_o = i_{total} \cdot R_f \quad (2)$$

Where i_{total} is, the sum of currents entering at p terminal of OTRA, selected by the digital input given by

$$i_{total} = \sum_{k=0}^{N-1} D_k \cdot \frac{V_{in}}{2^{N-k}} \cdot \frac{1}{2R} \quad (3)$$

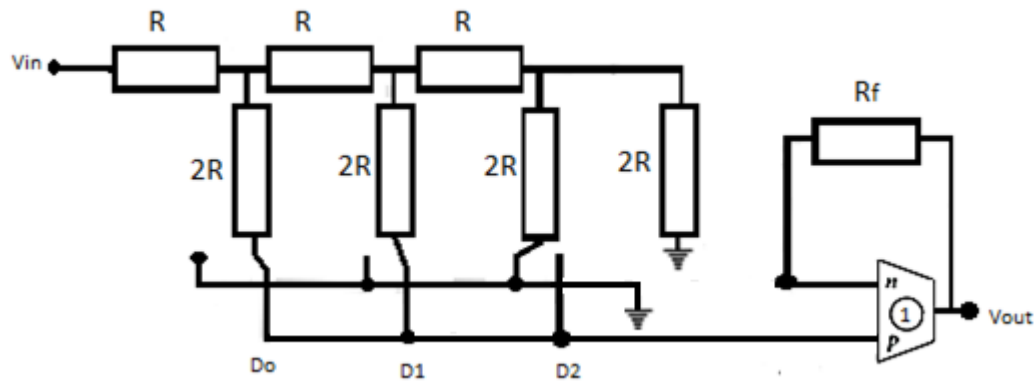
Where D_k is the k^{th} bit of the input word that is either 0 or 1.

The output voltage V_o for Fig. 3b can be computed as:

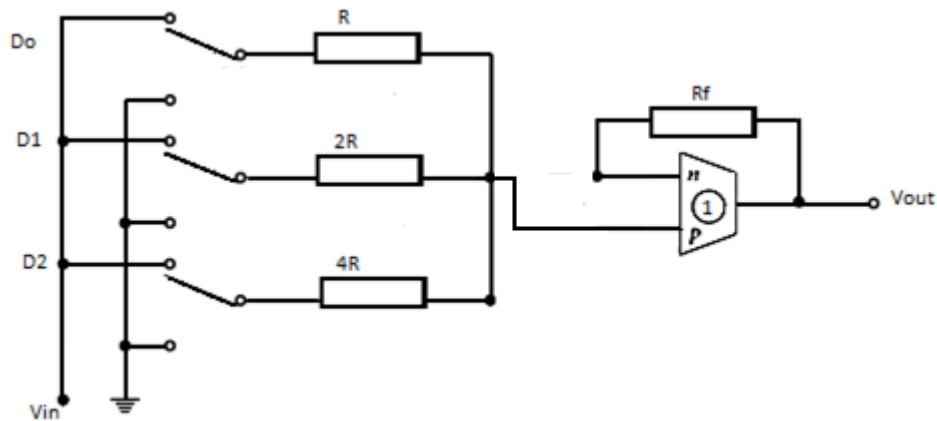
$$V_o = i_{total} \cdot R_f \quad (4)$$

Where,

$$i_{total} = \sum_{k=0}^{N-1} D_k \cdot \frac{V_{in}}{2^{N-k-1}} \cdot \frac{1}{R} \quad (5)$$



(a)



(b)

Fig.3 Proposed OTRA based (a) R-2R and (b) weighted resistor DAC realizations.

Further, we delineate the differences between the weighted DAC and the R-2R realizations. It can be seen that while both circuits make use of one active block each, the weighted DAC comprises of fewer passive components. Both converters being monotonic, the weighted DAC has a higher error in output value than its R-2R counterpart circuit. While the weighted DAC is an optimum choice of converter for low bit circuits, for high number of bits it has the problem of a wide range of resistor values R to $2^{N-1} \cdot R$ with required precision and

also which tracks over a wide temperature range. The R-2R in general, takes care of this problem by only employing resistors of two values- R and 2R.

III. SIMULATION RESULTS

The operation and performance of proposed DAC realizations of Fig 3 are verified through SPICE simulation using 0.5 μm CMOS technology parameters and power supply of $\pm 1.5\text{V}$. The proposed circuit is shown as 3-bit accurate after careful analysis of DNL and INL parameters. Offset for both the R-2R and weighted resistor circuits have also been calculated to be near negligible. The component values for the R-2R circuit are $R = 1\text{k}\Omega$, $R_f = 2\text{k}\Omega$, $V_{in} = 5\text{V}$ and the component values for the weighted resistor DAC are $R = 1\text{k}\Omega$, $R_f = 2.5\text{k}\Omega$, $V_{in} = 5\text{V}$. The theoretical, simulated output voltage and relative error for both proposed DACs have been recorded in Tables 1 and 2. Output voltages have also been plotted in Figs. 4 (a) and (b). As can be seen from Tables 1 and 2 that the error percentage is less than 0.1 % for the R-2R DAC and less than 1% for the weighted DAC.

Table 1: Output voltage for proposed R-2R DAC circuit

Digital Input	V_{OUT} (Theoretical)	V_{OUT} (Simulated)	%Error
000	0	10^{-30}	Negligible
001	0.625	0.624701	0.04
010	1.25	1.2494	0.04
011	1.875	1.8739	0.05
100	2.5	2.4988	0.04
101	3.125	3.1230	0.06
110	3.75	3.7477	0.06
111	4.375	4.3720	0.06

Table 1: Output voltage for proposed weighted resistor DAC circuit

Digital Input	V_{OUT} (Theoretical)	V_{OUT} (Simulated)	%Error
000	0	10^{-30}	Negligible
001	3.125	3.1212	0.12
010	6.25	6.2425	0.12
011	9.375	9.3635	0.12
100	12.5	12.485	0.12
101	15.625	15.606	0.12
110	18.75	18.7275	0.12
111	21.875	21.8485	0.12

DNL analysis has also been done and has been shown in fig 5. Both the R-2R and weighted resistor configurations have a DNL of the order of 10^{-3} and 10^{-4} respectively. INL analysis has also been done and has been shown in fig 6. Both the R-2R and weighted resistor configurations have an INL of the order of 10^{-3} .

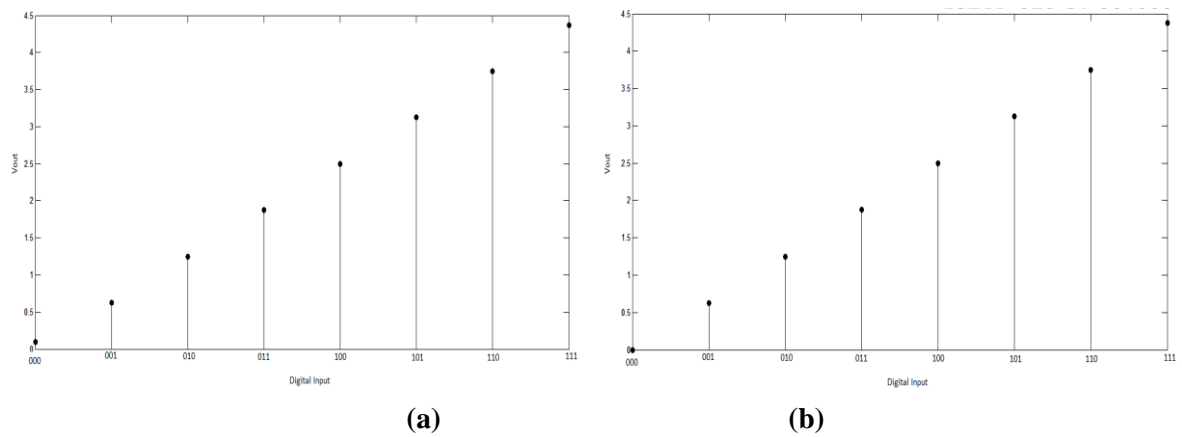


Fig. 4 Output voltages for proposed (a) R-2R and (b) weighted resistor DAC

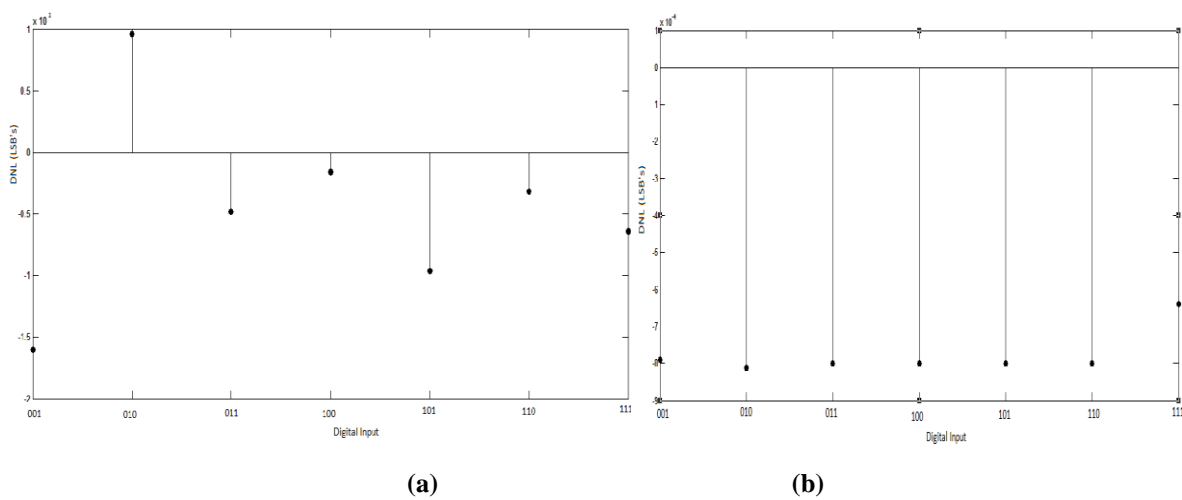


Fig. 5 DNL for proposed (a) R-2R and (b) weighted resistor DAC

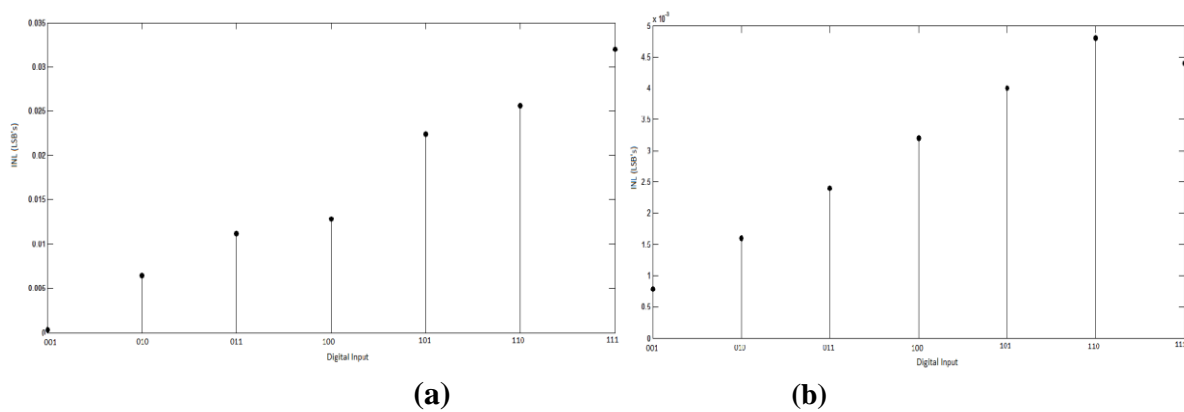


Fig. 6 INL for proposed (a) R-2R and (b) weighted resistor DAC

IV. CONCLUSION

New realizations of OTRA based R-2R and weighted DAC's have been presented. Both configurations are shown to be 3-bit accurate. They are monotonic through DNL and INL analysis. They provide advantages over existing circuits in the form of improved DNL and INL measurements. By using the OTRA, gain-bandwidth independence is achieved. We are also able to achieve optimum slew rate and negligible parasitic effects.

REFERENCES

- [1] K. N. Salama and A. M. Soliman, "Novel Oscillators using Operational Transresistance Amplifier," *Microelectron. J.* vol. 31, pp. 39–47, 2000.
- [2] Y.K. Lo, H.C. Chien and H.J. Chiu, "Current-Input OTRA Schmitt Trigger with Dual Hysteresis Modes," *International Journal of Circuit Theory and Applications* vol. 38, pp. 739-746, 2009.
- [3] H.C. Chien, "New Realizations of Single OTRA-Based Sinusoidal Oscillators" Hindawi Publishing Corporation, vol 2014, Article ID 938987, 12 pages
- [4] R. Pandey, N. Pandey, B. Sriram and S. K. Paul, "Single OTRA Based Analog Multiplier and Its Applications", *ISRN Electronics*, vol.2012, 7 pages
- [5] U. Çam, F. Kaçar, O. Cicekoglu, H. Kuntman and A. Kuntman, "Novel Grounded Parallel Immittance Simulator Topologies Employing Single OTRA" ", *International Journal of Electronics and Communications (AEU)*, 57 No. 4, pp. 287–290, 2003
- [6] H. Mostafa and A. M. Soliman, "A Modified CMOS Realization of the Operational Transresistance Amplifier (OTRA)" *Frequenz*, vol. 60, pp. 3-4, 2006
- [7] K. N. Salama and A. M. Soliman, "CMOS operational Transresistance amplifier for analog signal processing applications," *Microelectron. J.*, vol. 30, pp. 235–245, 1999
- [8] J. Chen, H. Tsao, S. Liu and W. Chui, "Parasitic Capacitance Insensitive Current-Mode Filters Using Operational Transresistance Amplifier," *Proc. IEE Circuit Devices Syst.*, vol. 142, no. 3, pp. 186–192, 1995.
- [9] B. Greenley, R.Veith, D.Y. Chang, and U.K. Moon, "A Low-Voltage 10-Bit CMOS DAC in 0.01- μm^2 Die Area" *IEEE Transactions on Circuits and Systems—II: Express Briefs*, Vol. 52, No. 5, May 2005
- [10] B. Vargha, I. Zoltán, "Calibration Algorithm for Current-Output R-2R Ladders", XVI IMEKO World Congress, Measurement - Supports Science - Improves Technology - Protects Environment ... and Provides Employment - Now and in the Future, Vienna, AUSTRIA, 2000, September 25-28
- [11] M.P Kennedy, "On the robustness of R-2R ladder DACs", *IEEE Transactions on Circuits and Systems I: Fundamental Theory and Applications*, 47(2), pp.109-116. doi: 10.1109/81.828565

Oxygen stress: impact on innate immune system, antioxidant defence system and expression of HIF-1 α and ATPase 6 genes in *Catla catla*

Samar Pal Singh · JaiGopal Sharma ·
Tauqueer Ahmad · Rina Chakrabarti

Received: 12 December 2014 / Accepted: 13 November 2015
© Springer Science+Business Media Dordrecht 2015

Abstract *Catla catla* catla (2.28 ± 0.1 g) were exposed to six different levels of dissolved oxygen: 1 (DO-1), 3 (DO-3), 5 (DO-5), 7 (DO-7), 9 (DO-9) and 11 (DO-11) mg/L. DO-5 served as control. In DO-1 and DO-3, the number of red blood cells (RBC), lysozyme, respiratory burst activity and nitric oxide synthase were significantly ($p < 0.05$) lower compared to the control one. In DO-7 and DO-9, RBC and lysozyme were significantly ($p < 0.05$) higher compared to the control one. Thiobarbituric acid reactive substances was significantly ($p < 0.05$) higher in catla exposed at low (1 and 3 mg/L) and high (9 and 11 mg/L) dissolved oxygen compared to others. In muscles and hepatopancreas, reduced glutathione was significantly ($p < 0.05$) higher in DO-5 and DO-7 and in gills of DO-5 compared to others after 1 h. In muscles, glutathione *S*-transferase (GST) was significantly ($p < 0.05$) lower in DO-5 and DO-7 compared to others. In hepatopancreas, GST and glutathione peroxidase (GPx) were significantly ($p < 0.05$) higher in DO-1 and DO-3 compared to others. In gills, GPx was higher in DO-9 and DO-11 after 48 h. In brain,

hypoxia-inducible factor (HIF)-1 α mRNA level was induced in DO-1 and DO-3 compared to others after 1 h of exposure. In gills and hepatopancreas, HIF-1 α mRNA level was significantly ($p < 0.05$) higher in DO-1 compared to others after 1 h. The ATPase 6 mRNA level was significantly ($p < 0.05$) higher in brain and hepatopancreas of DO-1 after 1 h and in gills and hepatopancreas of DO-3 and DO-9, respectively, after 48 h compared to others.

Keywords *Catla catla* · Lysozyme · Nitric oxide synthase · Antioxidant enzymes · Hypoxia-inducible factor (HIF)-1 α · ATPase 6

Introduction

The availability of ambient dissolved oxygen has been considered as one of the most important parameters for survival and growth of aquatic organisms. In the aquatic environment, dissolved oxygen level varies considerably because of the photoperiod and respiration cycles. Fish may be exposed to transient hyperoxia in their natural habitats during the daylight hours of summer as a result of the production of oxygen by algae under intensive solar irradiation (Halliwell and Gutteridge 1989). Hyperoxic condition is also encountered during transportation of live fish under an oxygen atmosphere. The diel-cycling hypoxia often found in high biomass aquatic ecosystems during the dark

S. P. Singh · T. Ahmad · R. Chakrabarti (✉)
Aqua Research Lab, Department of Zoology, University
of Delhi, Delhi 110007, India
e-mail: aquaresearchlab@yahoo.co.in

J. Sharma
Department of Biotechnology, Delhi Technological
University, Delhi 110042, India

cycle when the oxygen consumption rate of organisms exceeds oxygen production (D'Avanzo and Kremer 1994; Graham 1990). This phenomenon is particularly obvious during the summer months in shallow water bodies (Grecay and Stierhoff 2002; Stierhoff et al. 2003). Moreover, global climate change especially rise in summer water temperature possesses threat to the aquatic organisms that leads to decrease in dissolved oxygen level in the aquatic system. Environmental hypoxia may have negative effect on fish, even leading to death (Secor and Gunderson 1998). Within a physiological temperature range, oxygen consumption of fish increases more than twofold with every 10 °C increase in temperature (Hochachka and Somero 2002). The recommended minimum dissolved oxygen requirements for cold water, tropical freshwater and tropical marine fishes are 6, 5 and 5 mg/L, respectively (Mallya 2007). Most fish species will tolerate a drop below these minimum values for a short period of time, probably the cold water species are likely to tolerate a lower level than tropical fish.

Many studies show that transitions between hypoxia/anoxia and normoxia and/or between normoxia and hyperoxia may result in oxidative stress (Hermes-Lima 2004; Sies 1991; Storey 1996). Oxidative stress is a situation when steady-state reactive oxygen species (ROS) concentration is transiently or chronically enhanced, disturbing cellular metabolism and its regulation and damaging cellular constituents (Janssens et al. 2000; Lushchak 2011). It directly influences physiology, welfare and behaviour of the organisms. The deleterious effects of free radicals may be controlled by specific antioxidant systems. Many freshwater animals appear to be well-adapted to deal with such periodic fluctuations in oxygen levels. Some species maintain high antioxidant defences at all times, whereas others use an anticipatory strategy. In this process, the organism enhances antioxidant capacity during the hypoxic/anoxic state in order to prepare for oxidative stress that will occur when oxygen levels rise again (Hermes-Lima and Zenteno-Savin 2002; Lushchak et al. 2001). This latter phenomenon has been found in goldfish *Carassius auratus* (Lushchak et al. 2001) and in common carp *Cyprinus carpio* (Vig and Nemcsok 1989). Hypoxia induces primary, secondary and tertiary stress responses in fish. Kvamme et al. (2013) studied the effect of hypoxia on innate

immune responses in Atlantic salmon (*Salmo salar*). But the appearance of immune parameters and defensive competence varies greatly from species to species (Schröder et al. 1998).

Hypoxia also induced the expression of genes. Gene expression analyses in gonads of mature zebrafish (*Danio rerio*) maintained under normoxia (3 mg/L) and hypoxia (1 mg/L) following short-term (4 days) and long-term (14 days) exposures showed differential expression of genes associated with initial adaptive response and a suite of genes belonging to different ontology categories related with lipid metabolism, steroid synthesis and immune response which could lead to reproductive impairment (Martinovic et al. 2009). Zebrafish embryos were able to survive in absence of oxygen and their embryonic development ceased and the embryos entered a state of suspended animation (Padilla and Roth 2001). However, the molecular basis of the zebrafish response to hypoxic stress has not been clarified. The over expressions of CYP 1A (cytochrome P450 gene family 1) were found in liver of Amur sturgeon *Acipenser schrenckii* in hypoxia stress (Ni et al. 2014). Understanding how hypoxia alters gene expression will likely contribute to our knowledge of how vertebrates in general respond to hypoxia and will illustrate the dynamic interactions between genes and environment.

India is the second largest inland fish producing country in the world. Aquaculture has been playing significant role in the economy of the country. Carps contributed around 82 % of the aquaculture production. In pond culture, low dissolved oxygen availability resulted in respiratory stress of carps leading to poor growth. Carp gulping for air at the surface is found particularly in the early morning is a sign of oxygen deficiency in the culture pond. Mass mortality may occur due to prolonged oxygen deficiency of water (ICAR 2013). Being a tropical country, climate change will influence the aquaculture production in India. There is a wide scientific consensus that changes in the composition of the atmosphere will lead to significant changes in global climate (IPCC 2007; Brander 2010). The most important changes caused by climate change are the shortening of winter period and a rise in summer water temperatures (Magnuson et al. 1979; Huttula et al. 1992). This will influence the dissolved oxygen level of aquatic environment.

Catla catla is an economically important, surface dwelling carp species and extensively used in composite culture. The aim of the present investigation was to study the effect of both hypoxia and hyperoxia on the immune system, lipid peroxidation and enzymatic and non-enzymatic antioxidant systems of catla exposed to various concentrations of dissolved oxygen. The mRNA level of hypoxia-inducible factor (HIF)-1 α and mitochondrial (MT) ATPase genes were also quantified. Serum lysozyme is a cationic enzyme that attacks the β -1, 4 glycosidic bond between *N*-acetylmuramic acid and *N*-acetylglucosamine in the peptidoglycan of bacterial cell walls. This enables lysozyme to lyse certain gram-positive bacteria and gram-negative bacteria (Alexander and Ingram 1992). Reduced glutathione (GSH) is low molecular mass tripeptide (Glu-Cys-Gly) described as non-enzymatic antioxidant. They are usually known as free radical scavengers (Pamplona and Costantini 2011). High molecular mass antioxidant group consists of enzymatic antioxidants like superoxide dismutases (SOD), catalases, Se-dependent glutathione peroxidases (GPx) and glutathione *S*-transferase (GST).

One of the pivotal mediators of the cellular response to hypoxia is hypoxia-inducible factor (HIF), a transcription factor (Benita et al. 2009). HIF-1 α is a master regulator of hypoxia-induced gene responses that allows rapid adaptation to oxygen availability. This effect is mediated through key regulators of bioenergetics and growth. The mitochondrial (MT) ATP 6 gene provides information for making a protein that is essential for normal mitochondrial function. The MT-ATP 6 protein forms one part of a large enzyme called ATP synthase (F₀F₁-ATPase). This enzyme is responsible for the final step of oxidative phosphorylation. Specifically, one segment of ATP synthase allows positively charged particles, called protons, to flow across a specialized membrane inside mitochondria. Another segment of the enzyme uses the energy created by this proton flow to convert a molecule called adenosine diphosphate (ADP) to ATP. Present investigation is the first study with this freshwater carp challenged with various dissolved oxygen levels. The information related to the physiological responses to hypoxia and hyperoxia induced stresses is most essential for the assessment of the health status of the cultivable organisms. This will help in the development of proper husbandry for this economically important species.

Materials and methods

Fish maintenance

Catla catla catla (2.28 ± 0.12 g) were collected from local fish farm and transported to the wet laboratory facility. Fish were randomly distributed in eighteen aquaria (50 L each). Each aquarium was connected with one filtration unit (Sera fil bioactive 130, Germany). This helped to maintain the water quality in the aquarium. Each aquarium was covered with transparent fibreglass sheet having two holes at two ends for the connection of filtration unit and gas pipes. These pipes were fitted tightly. This arrangement helped to maintain the desirable dissolved oxygen level in the aquarium. Prior to the start of the experiment, fish were acclimated to experimental conditions under 12:12 h light/dark photoperiod for 21 days. Water temperature was maintained at 25 ± 0.50 °C, and the dissolved oxygen was kept at 5 ± 0.15 mg/L. During the acclimation and experimental period, pelleted feed (containing 40 % of crude protein) was provided two times (9.00 a.m. and 5.00 p.m.) daily at a feeding rate of 5 % of body weight per day.

Experimental design

Fish were exposed to six different levels of dissolved oxygen: 1 (DO-1), 3 (DO-3), 5 (DO-5), 7 (DO-7), 9 (DO-9) and 11 (DO-11) mg/L. Each level had three replicates. The oxygen tension in DO-1 and DO-3 treatments was regulated through the pumping of nitrogen (Laser Gases, India), whereas in DO-9 and DO-11 through the pumping of oxygen gas (Laser Gases, India). The bubbling rate of gas was adjusted by mechanical controller to keep the dissolved oxygen concentration stable. The dissolved oxygen levels of 5 and 7 mg/L treatments were maintained using continuous aeration (Rocker 320 aerator, Taiwan). The exact time of reaching desirable dissolved oxygen concentration in each aquarium was recorded. It required 45 min to 3 h to reach the desirable oxygen concentration of water from the acclimation dissolved oxygen condition (5 mg/L). Water temperature was continuously monitored in individual aquarium. pH, and oxygen concentrations were measured using digital oximeter (HACH 40 D, USA). Dissolved oxygen concentration in each aquarium was measured thrice

daily during the exposure of fish, and variations between the desirable and actual dissolved oxygen concentrations for individual aquarium were recorded (Table 1). During the experimental period, the water temperature of experimental aquarium was 25 ± 0.50 °C and pH ranged from 7.85 to 8.02.

Blood and tissue sampling

Blood and tissue samples were collected from individual fish exactly after 1 and 48 h of reaching the desirable dissolved oxygen level. Fish were anesthetized with MS 222 (Sigma, USA) and weighed. Blood samples were taken gently from the caudal vein by 1-mL plastic syringe (Hindustan Syringes and Medical Devices Ltd., India) within 1 min and the whole process of blood sampling required <2 min for individual fish after netting. Two different aliquots of blood were used for different analyses. The first aliquot was transferred to a plastic tube coated with ethylene diamine tetraacetate (EDTA) as anticoagulant and was used for respiratory burst activity estimation. A second aliquot was transferred to a plastic tube without EDTA, clot at 4 °C, centrifuged at $1500 \times g$ for 10 min and collected serum was stored at -20 °C for analyses.

Tissues—muscles, gills and hepatopancreas were immediately frozen with liquid nitrogen and stored at -80 °C for further assays. For the study of nitric oxide synthase, antioxidant system (reduced glutathione) and antioxidant enzymes (glutathione *S*-transferase and glutathione peroxidase), one gram of tissue (10 %) was homogenized in chilled 10 ml phosphate buffer (0.1 M, pH 7.4) using glass/Teflon

tissue grinder. The homogenate was centrifuged at $10,500 \times g$ for 20 min; the supernatant was used for assay. All assays were carried out using Microplate Reader (BioTek, Synergy HT, NY, USA). For gene expression study, brain, gills and hepatopancreas were collected aseptically after 1 and 48 h of reaching the desirable dissolved oxygen level and immediately stored in RNAlater (Sigma-Aldrich, USA) at -20 °C for extraction of total RNA. For all parameters, three replicates were used.

Abundance of red blood cells

Total erythrocyte counting was performed using an improved Neubauer-ruled hemocytometer (Tripathi et al. 2004). Briefly, blood sample was diluted (1:200) in Hayem's fluid. Then the fluid was allowed to stand in the pipette for 8–10 min before charging into the Neubauer's chamber. Total numbers of red blood cells (RBC) were counted in five secondary square of the centre primary square.

$$\text{RBC}/\mu\text{L} = n \times 10,000$$

where, n = number of RBCs observed in the secondary squares, 10,000 = (200, dilution factor and 50 = volume of fluid in RBC's secondary squares).

Cells were observed in both chambers of the hemocytometer ($\times 40$ objective in compound microscope, Carl Zeiss, Germany), and the number was averaged to produce the raw RBC count to reduce analytical variation.

Lysozyme

For lysozyme assay, bacteria *Micrococcus lysodeikticus* (MTCC No *106) was cultured in *Staphylococcus* broth (Himedia, Mumbai, India) containing 1 % D-glucose. After 24 h of incubation, the culture was centrifuged and the bacterial pellet was lyophilized. Lysozyme was determined by incubating 10 μL of serum with 1 mL of *Micrococcus lysodeikticus* (20 mg/100 mL) suspended in acetate buffer (0.02 M, pH 5.5) for 60 min at room temperature. The initial absorbance was recorded immediately after addition of sample at 450 nm. The final absorbance was recorded after 60 min of incubation. The standard curve was prepared using hen egg lysozyme (1 mg/mL).

Table 1 Expected and recorded dissolved oxygen levels (\pm SE) in each treatment during experiment

Treatment	Expected DO (mg/L)	Recorded DO (mg/L)
DO-1	1	0.93 ± 0.02
DO-3	3	2.85 ± 0.02
DO-5	5	5.15 ± 0.08
DO-7	7	7.39 ± 0.03
DO-9	9	8.81 ± 0.03
DO-11	11	11.23 ± 0.02

DO-1, 1 mg/L dissolved oxygen; DO-3, 3 mg/L dissolved oxygen; DO-5, 5 mg/L dissolved oxygen; DO-7, 7 mg/L dissolved oxygen; DO-9, 9 mg/L dissolved oxygen; DO-11, 11 mg/L dissolved oxygen

Respiratory burst activity

The fresh blood with EDTA powder was processed for measurement of nitroblue tetrazolium (NBT) within 1 h of collection following the method of Anderson and Siwicki (1995). Reactive oxygen radical production by neutrophils during respiratory burst activity was assayed by the reduction of nitroblue tetrazolium to formazan. Briefly, the blood was mixed with equal volume of 0.2 % NBT (Himedia) and incubated at 25 °C for 30 min. In 25 µL of this mixture, 500 µL of dimethyl formamide (Merck, India) was added to solubilize the reduced formazan product. Then it was centrifuged at 2000×*g* for 5 min and the supernatant was taken. The extent of NBT reduced was measured at 540 nm. Dimethyl formamide was used as the blank.

Nitric oxide synthase

Inducible nitric oxide synthase (iNOS) level of muscles was measured using the method of Lee et al. (2003). The supernatant (100 µL) was mixed with equal volume of Griess reagent (1 % sulphanilamide and 0.1 % naphthylethylenediamine in 5 % phosphoric acid) and incubated at room temperature for 10 min. The absorbance was recorded at 540 nm. The nitrite concentration was determined from the nitrite standard curve and expressed as mmol/mg tissue.

Thiobarbituric acid reactive substances

Thiobarbituric acid reactive substances (TBARS) were measured following the method of Ohkawa et al. (1979). In this process, the end product of lipid peroxidation, the MDA reacts with thiobarbituric acid (TBA). One gram of muscles was homogenized in 9 ml of KCl (1.15 %), and the sample was incubated in 0.6 % TBA (pH 3.5) containing SDS (0.45 %) for 1 h at 100 °C. After cooling, the sample was centrifuged at 825×*g* for 15 min and the absorbance of the supernatant was measured at 532 nm. The standard curve was prepared using 1, 1, 3, 3-tetramethoxy propane, and the result was expressed as µmol MDA/mg protein.

Reduced glutathione

Reduced glutathione (GSH) for muscles, hepatopancreas and gills was determined using the method of Jollow et al. (1974). The collected supernatant was

precipitated with 4 % sulfosalicylic acid (Himedia) in 1:1 ratio. The samples were kept at 4 °C for 1 h and then centrifuged at 1500×*g* for 15 min at 4 °C. This supernatant was used for GSH assay. The assay mixture (200 µL) consisted of supernatant, 0.1 M phosphate buffer (pH 7.4) and 5-5-dithiobis-2-nitrobenzoic acid (DTNB, Himedia). Optical density was measured at 412 nm and expressed as nmol GSH/g tissue.

Glutathione S-transferase

Glutathione S-transferase (GST) activity of muscles and hepatopancreas was measured (Habig et al. 1974). The reaction mixture consisted of 0.1 M phosphate buffer (pH 7.4), 0.60 mM 1-chloro-2-dinitrobenzene (CDNB, Sigma, USA) and 10 mM reduced glutathione (GSH, Himedia). Absorbance was monitored at 340 nm kinetic mode at 25 °C. Activity was expressed as nmol of CDNB/mg protein/min. The molar extinction coefficient is 9.6×10^3 /M cm.

Glutathione peroxidase

Glutathione peroxidase (GPx) activity of gills and hepatopancreas was measured following the method of Mohandas et al. (1984). The assay mixture consisted of 0.05 M phosphate buffer (pH 7.4), 1 mM (EDTA, Himedia), 1 mM sodium azide (Himedia), 1 U/mL glutathione reductase (Sigma, USA), 1 mM reduced glutathione (GSH, Sigma), 0.2 mM nicotinamide adenine dinucleotide (NADPH, Sigma) and 0.25 mM hydrogen peroxide (H₂O₂, Sigma). The decrease in absorbance was recorded at 340 nm. Activity was expressed as nmol of NADPH/mg protein/min. The molar extinction coefficient is 6.22×10^3 M cm.

Gene expression study

RNA isolation and first-strand cDNA synthesis

Total cellular RNA from different tissues of fish (brain, gills and hepatopancreas) was extracted with TRIzol reagent (Invitrogen, USA). RNA concentration was measured with Nanodrop ND-1000 spectrophotometer (Thermo Scientific, USA), and the integrity was assessed by observing the band intensity of RNA on 1 % agarose gel. For the first-strand cDNA synthesis, 1 µg of total RNA was treated with 1 U of

DNase I (Sigma-Aldrich, USA), and reverse transcription was carried out using ProtoScript M-MuLV first-strand cDNA synthesis kit (New England Biolabs, USA). The constitutively expressed housekeeping gene, β -actin, was used both as a positive control and for sample normalization.

Real-time PCR analysis

Quantitative real-time PCR was performed in MicroAmp® Fast Optical 96-well reaction plates with optical adhesive cover in the ViiA-7™ real-time PCR system (Applied Biosystems, USA). Primers for HIF-1 α , ATPase 6 and β -actin were designed using Primer 3 software (Table 2). In real-time PCR, amplifications were carried out, in 10 μ L reaction volume containing 1 μ L of cDNA, 0.25 μ L of FW and RV primers (2.5 μ M each), 5 μ L of 2X Power SYBR® Green PCR Master Mix and 3.5 μ L of PCR-grade H₂O. The PCR amplification was performed under the following conditions: 50 °C for 2 min, initial denaturation at 95 °C for 10 min, followed by 45 cycles of 95 °C/15 s, 55 °C/1 min. The reaction carried out without cDNA was used as a negative control. The PCR efficiencies were determined by analysis of serial dilutions of cDNA, and efficiencies were close to 100 % allowing the use of the $2^{-\Delta\Delta CT}$ method for calculation of relative gene expression (Livak and Schmittgen 2001). Specificity of the amplification reaction was analysed using dissociation curves with a temperature range from 60 to 95 °C. The correct size and single-band amplification were confirmed by running the real-time PCR products (8 μ L) in agarose gels (1 %) using ethidium bromide.

Statistical analysis

All data were presented as mean \pm standard error. Data were analysed using one-way analysis of

variance, ANOVA (SPSS 13.0) and Duncan's multiple range (DMR) test (Montgomery 1984). The significance level was accepted at $p < 0.05$.

Results

Catla were acclimated at 5 ± 0.05 mg/L dissolved oxygen and then exposed to both low (1 and 3 mg/L) and high (7, 9 and 11 mg/L) levels of dissolved oxygen. Therefore, 5 ± 0.05 mg/L dissolved oxygen treatment was considered as the normal/control (acclimation) condition. Response of catla to low and high levels of dissolved oxygen was compared with this control one. There was no mortality of fish during experimental period.

Abundance of red blood cells

The number of red blood cells (RBC) decreased in catla exposed at 1 and 3 mg/L dissolved oxygen compared to the control 5 mg/L treatment (Fig. 1) after 1 h of exposure. The number of RBC increased 1.5–1.75-fold in 7–11 mg/L dissolved oxygen treatments compared to the control one after 1 h of exposure. The abundance of RBC reduced significantly in 7, 9 and 11 mg/L dissolved oxygen treatments after 48 h of exposure compared to 1 h exposed fish in respective treatment. There was no significant difference in RBC number in 1, 3 and 5 mg/L treatments after 48 h compared to the 1 h exposed fish in respective treatment.

Lysozyme

Serum lysozyme level reduced significantly after 1 h of exposure of catla in 1 and 3 mg/L dissolved oxygen treatments compared to the control condition (DO-5). The lysozyme activity was 3.50 ± 0.06 mg/mL in

Table 2 Primer sequences used for real-time PCR analysis

Target gene	Primer name	Primer sequence (5'–3')	Accession number
HIF-1 α	HIF 1 α Fw	GGAAAGGAGTCTGAGGTATTCT	EF222026.1
	HIF 1 α Rv	ACTCTCCAGTTCGTTCTCCTTG	
ATPase 6	ATPase 6 Fw	CCAATTTCGCAAGCCCATCAT	JN859669.1
	ATPase 6 Rv	AGGGGGGAGTAGCAGTTGGT	
β -actin	β -actin Fw	AGACCACCTTCAACTCCATCATG	JQ991014.1
	β -actin Rv	CCGATCCAGACAGAGTATTACG	

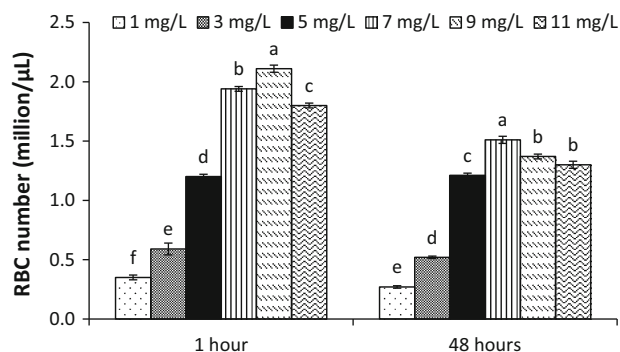


Fig. 1 Abundance of red blood cells in *Catla catla* exposed to various levels of dissolved oxygen. Vertical bars with different superscripts are significantly ($p < 0.05$) different ($n = 3$)

control fish at this period. The activity was significantly higher in catla exposed at high levels (7–9 mg/L) of dissolved oxygen compared to the control one. Lysozyme activity increased significantly in all treatments (except DO-5) after 48 h exposure compared to the 1 h exposed fish in the respective treatment (Fig. 2). Significantly lower activity was also found in DO-1 and DO-3 treatments compared to others after 48 h exposure.

Respiratory burst activity

The respiratory burst activity was significantly lower in 1 and 3 mg/L treatments compared to the control catla (DO-5) after 1 h of exposure. The activity increased in fish exposed at high levels of dissolved oxygen compared to the control one. The activity was significantly higher in DO-9 and DO-11 compared to the other treatments in both samples (Fig. 3).

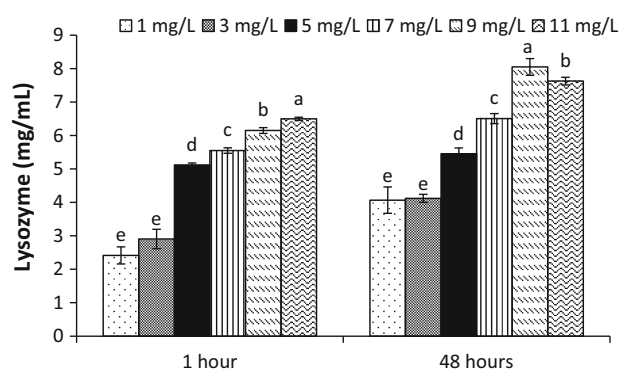


Fig. 2 Serum lysozyme levels of *Catla catla* exposed to various levels of dissolved oxygen. Vertical bars with different superscripts are significantly ($p < 0.05$) different ($n = 3$)

Respiratory burst activity reduced 6.8–32.0 % in 48 h exposed fish in 1, 3, 9 and 11 mg/L dissolved oxygen treatments compared to the 1 h exposed fish in the same treatment. The activity was 3.5 % higher in both 5 and 7 mg/L treatments after 48 h of exposure compared to the 1 h exposed fish in the same treatment.

Nitric oxide synthase

This was interesting to observe that nitric oxide synthase (iNOS) level was significantly higher in DO-11 treatment compared to others after 1 and 48 h of exposures. A direct relationship was found between the dissolved oxygen level of water and nitric oxide synthase level in both samples (Fig. 4). Nitric oxide synthase levels in all treatments were significantly higher after 48 h exposure compared to the 1 h exposed fish in the respective treatment.

Thiobarbituric acid reactive substances

Thiobarbituric acid reactive substances (TBARS) level is an indicator of lipid peroxidation of tissues. Significantly lower TBARS was found in DO-5 and DO-7 treatments compared to others. Exposure of catla to low (1 and 3 mg/L) and high (9 and 11 mg/L) levels of dissolved oxygen resulted into higher level of TBARS in the muscles of catla (Fig. 5). TBARS level increased significantly in all 48 h exposed fish regardless of treatments (except DO-5 and DO-7) compared to 1 h exposed fish in respective treatment.

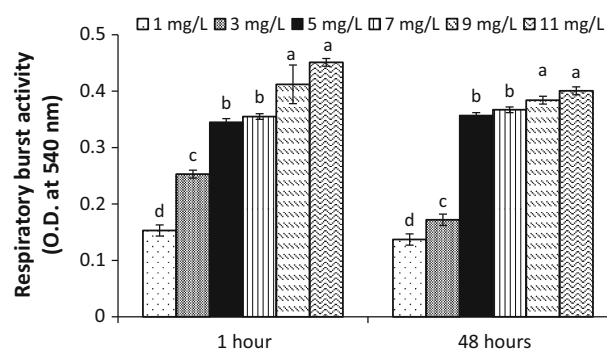


Fig. 3 Respiratory burst activity found in *Catla catla* exposed to various levels of dissolved oxygen. Vertical bars with different superscripts are significantly ($p < 0.05$) different ($n = 3$)

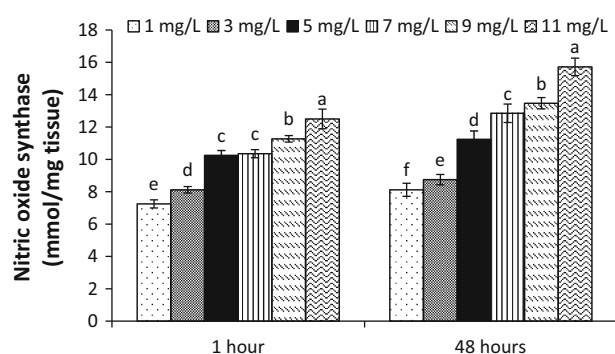


Fig. 4 Nitric oxide synthase levels found in *Catla catla* exposed to various levels of dissolved oxygen. Vertical bars with different superscripts are significantly ($p < 0.05$) different ($n = 3$)

Reduced glutathione

Reduced glutathione (GSH) was assayed in muscles, hepatopancreas and gills (Fig. 6a–c). In muscles of catla, reduced glutathione level was significantly higher in DO-5 and DO-7 treatments compared to others after 1 h of exposure. Similar trend was found after 48 h of exposure, except in DO-7. The level was significantly lower in this treatment compared to DO-5. In muscles, GSH level reduced significantly in fish exposed at 7–9 mg/L dissolved oxygen after 48 h compared to the 1 h exposed fish in the respective treatment. Like muscles, GSH level was significantly higher in hepatopancreas of catla exposed at 5 and 7 mg/L of dissolved oxygen compared to the other treatments after 1 h exposure. The level was significantly lower after 48 h of exposure compared to 1 h in all treatments, except DO-5. In gills, GSH level was significantly higher in DO-5 compared to others in

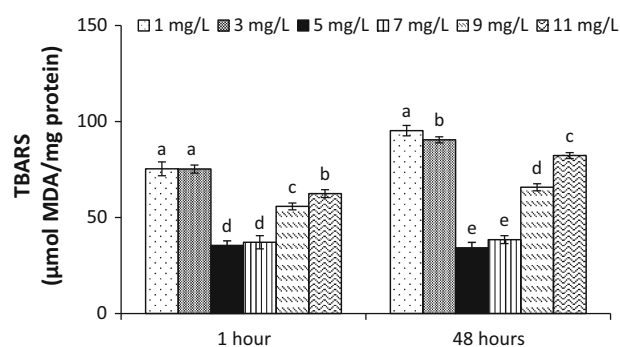


Fig. 5 Effect of various levels of dissolved oxygen on the thiobarbituric acid reactive substances (TBARS) of *Catla catla* after 1 and 48 h of exposure. Vertical bars with different superscripts are significantly ($p < 0.05$) different ($n = 3$)

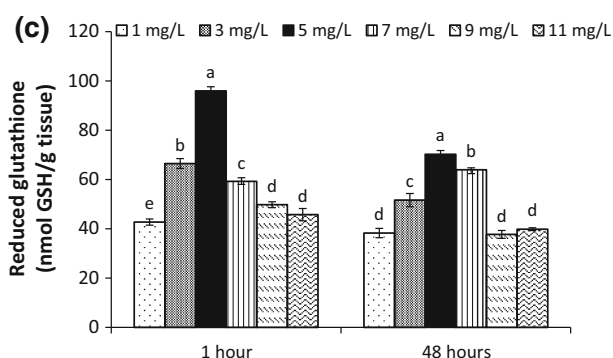
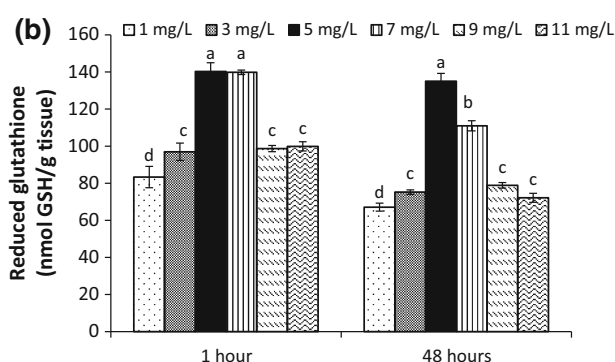
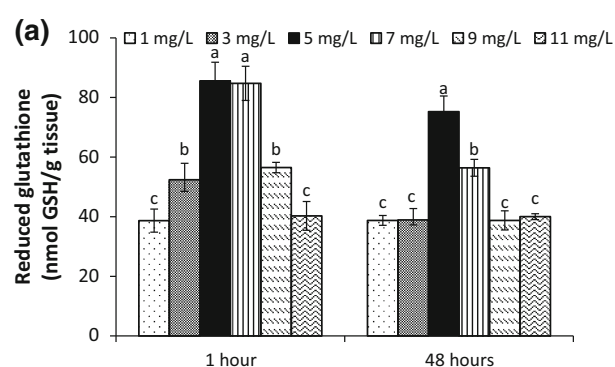


Fig. 6 Effect of various levels of dissolved oxygen on reduced glutathione levels of **a** muscles, **b** hepatopancreas and **c** gills of *Catla catla* after 1 and 48 h of exposure. Vertical bars with different superscripts are significantly ($p < 0.05$) different ($n = 3$)

both samples. In gills, GSH level reduced after 48 h exposure compared to the 1 h exposed fish regardless of treatment.

Glutathione S-transferase

Glutathione S-transferase (GST) level in muscles of catla (Fig. 7a) was significantly lower in DO-5 and DO-7 compared to other treatments after 1 h of exposure. There was no significant difference between DO-5 and DO-7 during this period. In muscles, GST level was significantly higher in DO-1 and DO-3 after

48 h of exposure compared to the 1 h exposed fish in the respective treatment. In hepatopancreas of catla, GST level (Fig. 7b) was significantly higher in DO-1 and DO-3 treatments compared to others after 1 and 48 h of exposure. In hepatopancreas, GST level was significantly higher in all treatments (except DO-5 and DO-7) after 48 h of exposure compared to the respective 1 h exposed fish.

Glutathione peroxidase

In hepatopancreas of catla, glutathione peroxidase (GPx) level was significantly higher in DO-1 and DO-3 treatments compared to DO-5 after 1 h of exposure. There was no significant difference in GPx level between the high dissolved oxygen treatments and the control one (Fig. 8a) during this period. GPx level increased in fish exposed at 9 and 11 mg/L dissolved oxygen treatments after 48 h of exposure compared to the control one. GPx level in hepatopancreas was 7.37–65.78 % higher in 48 h exposed fish compared to 1 h exposed one regardless of treatment (except DO-5). In gills, GPx level was significantly higher in fish

exposed at 1 mg/L dissolved oxygen compared to the control one in both samples (8b). The level increased significantly in 48 h exposed catla compared to the 1 h exposed fish in all treatments, except DO-5 and DO-7.

Gene expression

The mRNA level of hypoxia-inducible factor (HIF)-1 α was studied in brain, gill and hepatopancreas of catla exposed to six different dissolved oxygen (Fig. 9a, b). In brain, HIF-1 α mRNA was increased in 1 and 3 mg/L dissolved oxygen treatments compared to others after 1 h of exposure. In gill and hepatopancreas, HIF-1 α mRNA level was significantly higher in DO-1 treatment compared to others after 1 h exposure. The mRNA level was reduced in hepatopancreas of all treatments (except DO-1) compared to DO-5. After 48 h of exposure, HIF-1 α mRNA level was significantly higher in gills of DO-3 treatment compared to others. This treatment was followed by DO-11 treatment. The mRNA level was lower in hepatopancreas of all treatments compared to DO-5.

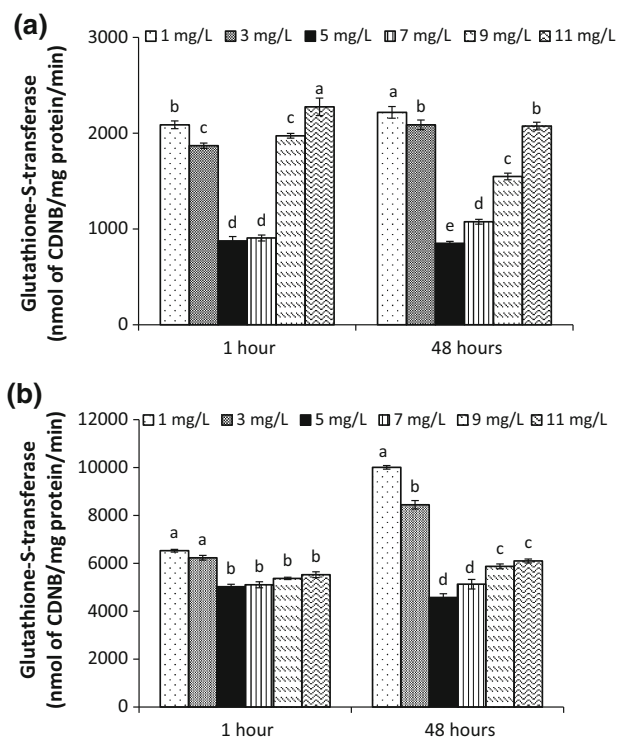


Fig. 7 Glutathione S-transferase levels found in **a** muscles and **b** hepatopancreas of *Catla catla* exposed to various levels of dissolved oxygen. Vertical bars with different superscripts are significantly ($p < 0.05$) different ($n = 3$)

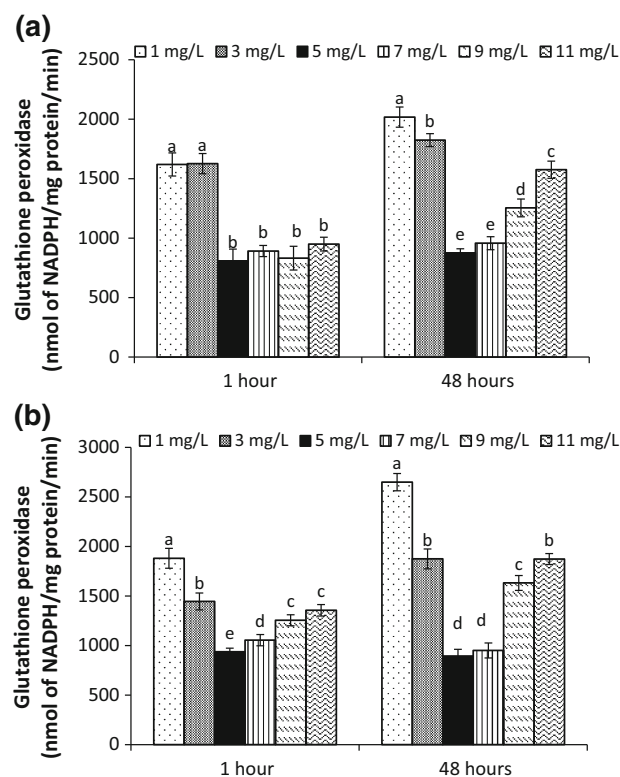


Fig. 8 Glutathione peroxidase level found in **a** hepatopancreas and **b** gills of *Catla catla* exposed to various levels of dissolved oxygen after 1 and 48 h. Vertical bars with different superscripts are significantly ($p < 0.05$) different ($n = 3$)

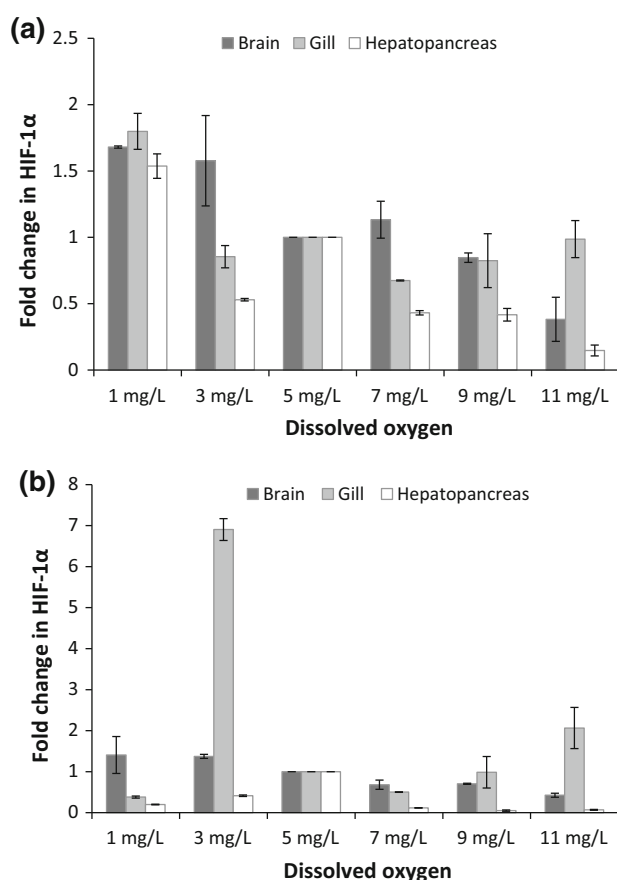


Fig. 9 HIF-1 α mRNA levels in brain, gill and hepatopancreas of *Catla catla* exposed to different levels of dissolved oxygen for **a** 1 h and **b** 48 h. The relative expression of the target gene HIF-1 α was normalized to the expression of β -actin (internal control) and expressed as fold changes relative to the control group (5 mg/L)

The mRNA level of ATPase 6 was significantly higher in brain and hepatopancreas of DO-1 treatment compared to others after 1 h exposure. This treatment was followed by DO-3. The mRNA level of ATPase 6 was decreased in gills of catla regardless of treatments (Fig. 10a). After 48 h of exposure, mRNA level was significantly higher in gill and hepatopancreas of DO-3 and DO-9 treatment, respectively compared to others. In 11 mg/L dissolved oxygen treatment, the mRNA level of ATPase 6 was induced compared to 5 mg/L dissolved oxygen treatment (Fig. 10b).

Discussion

Availability of dissolved oxygen is a critical parameter. The optimum recommended oxygen level for

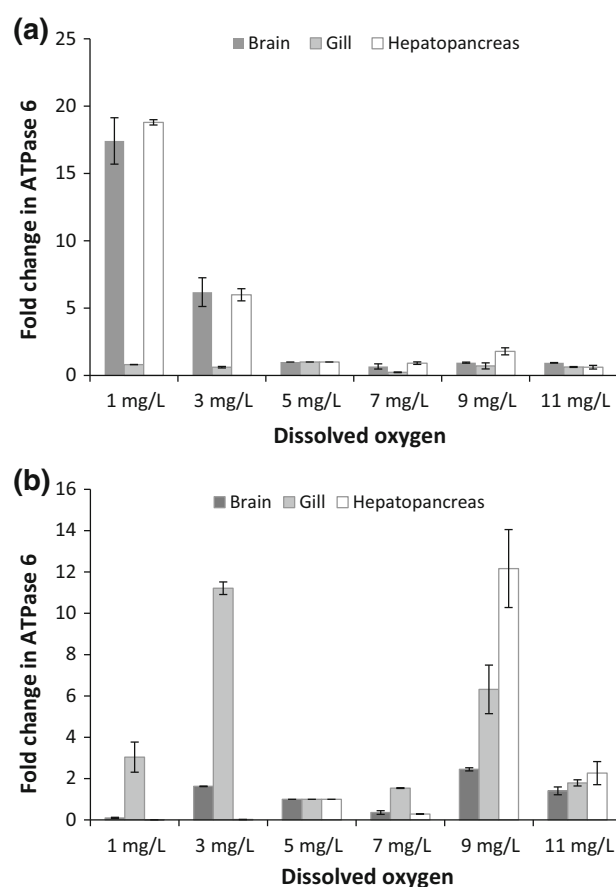


Fig. 10 ATPase 6 mRNA levels in brain, gill and hepatopancreas of *Catla catla* exposed to different levels of dissolved oxygen for **a** 1 h and **b** 48 h. The relative expression of the target gene ATPase 6 was normalized to the expression of β -actin (internal control) and expressed as fold changes relative to the control group (5 mg/L)

tropical freshwater fish is 5 mg/L (Mallya 2007). In the present study, the exposure of catla at above and below this level showed physiological stress in this species. The number of red blood cells (RBC) is an important parameter as these are associated with the oxygen carrying capacity of the blood. The number of RBC reduced in fish challenged with low dissolved oxygen after 1 h. The abundance of red blood cell increased as the fish was exposed to higher levels of dissolved oxygen during this period. But there was change in the abundance of RBC after 48 h of exposure. In normoxic (5 mg/L) and hypoxic (1 and 3 mg/L) conditions, there was no significant change in RBC abundance between 1 and 48 h samples of same treatment. But in hyperoxic (7–11 mg/L) treatments, there was significant reduction in RBC number after

48 h exposure compared to the sample of 1 h in the same treatment. In juvenile turbot *Scophthalmus maximus*, the number of RBC was higher in 14 mg/L dissolved oxygen treatment compared to the control (7 mg/L) one after 7 days of exposure, but the number reduced significantly in the former after 28 days of exposure (Wu et al. 2014). Both these studies indicated the time-dependent variation in RBC number with response to oxygen stress. In catla, the reduction of number of RBC in 7–11 mg/L treatments after 48 h exposure might be related to less requirement of oxygen transport in fish. This is opposite to the hypoxic conditions. Under hypoxia conditions, increasing the RBC level may help to acquire more oxygen and increase gas transport capacity of the fish blood (Wu et al. 2014). In Amur sturgeon *A. schrenckii*, the abundance of white blood cells and red blood cells increased after 0.5 and 1.5 h exposure at 1 mg/L dissolved oxygen, but there was no significant difference 3 h after hypoxia (Ni et al. 2014). In the present study, the number of RBC was counted at 1 and 48 h. The increase in abundance of RBC was not recorded might be due to the difference in sampling time in the present study. This also might be species-specific response. Rees et al. (2001) found in zebrafish *D. rerio*, the magnitude of the acclimation to hypoxia depended upon the sex of the fish. In hyperoxic condition, RBC abundance reduced after 48 h of exposure. Further study may require to understand the impact of longer duration exposure in hypoxic condition on the abundance of RBC in catla.

The reduced level of serum lysozyme and respiratory burst activity in fish challenged at 1 and 3 mg/L dissolved oxygen were indicators of poor immune system in these treatments. A direct relationship was found between the dissolved oxygen and both parameters, except the serum lysozyme level in 11 mg/L treatment after 48 h of exposure. Fish lysozymes possess a high potential for bacteriocidal or bacteriolytic activity. This plays an important role in the bio-defence system against gram-positive and gram-negative bacteria (Saurabh and Sahoo 2008). Lowest level of nitric oxide synthase (iNOS) also showed the impaired immune system of catla exposed at 1 and 3 mg/L dissolved oxygen levels. NOS are a family of enzymes that catalyse the production of cellular signalling molecule nitric oxide. This nitric oxide plays vital role in many biological processes. The inducible isoform iNOS produces large amount of

nitric oxide as a defence mechanism. The young fish use innate mechanisms during the first weeks/months of their development, and this may find application for the defence of farmed fish against pathogens at early age (Rombout et al. 2005). In the present study, the elevated levels of lysozyme, respiratory burst activity and NOS indicated the improved defence system of catla in higher dissolved oxygen treatments. But respiratory burst activity reduced in these treatments after 48 h exposure compared to the 1 h exposed fish in the same treatment. In sea bass *Dicentrarchus labrax*, hyperoxygenation of sea water resulted in a twofold increase in immunoglobulins (Scapigliati et al. 1999). The oxygen levels in the environment may modulate the immune response; hypoxia depresses the respiratory burst activity of macrophages and lowers the levels of circulating antibodies, which in turn are elevated by hyperoxia (Watts et al. 2001; Bowden 2008).

Fish maintained at 5 and 7 mg/L dissolved oxygen had less lipid peroxidation compared to the other treatments as the level of TBARS was low in these two treatments. Lipid peroxidation is a well-established mechanism of oxidative damage caused by ROS such as superoxide (O_2^-), OH and hydrogen peroxide (H_2O_2), and the measurement of malondialdehyde (MDA) provides a convenient index of lipid peroxidation (Devasena et al. 2001). Fish challenged with low and high levels of dissolved oxygen (compared to the control condition) were prone to lipid peroxidation in the present study. Lipid peroxidation may bring about protein damage by its end products, MDA and 4-hydroxynonenal (Bhor et al. 2004). Fish tissue contains large quantities of polyunsaturated fatty acids (PUFAs) essential for membrane function (Martinez-Alvarez et al. 2005). Lipid peroxidation is the process of oxidative degradation of PUFA, and its occurrence in biological membranes causes impaired membrane function, structural integrity and inactivation of several membrane-bound enzymes (Goel et al. 2005). Lushchak et al. (2005a) reported that in common carp, TBARS level increased three-fold in hepatopancreas during hypoxic condition. In vitro exposure of rainbow trout plasma and red blood cells to hyperoxia for 5 min resulted in more marked changes in TBARS content (Ritola et al. 2002a, b). In the present study, 48 h exposure resulted in higher lipid peroxidation compared to the 1 h exposed fish in all treatments except DO-5 and DO-7.

It is suggested that increased dissolved oxygen levels increase ROS generation due to enhanced probability of electrons escaped from electron-transport chains to combine with molecular oxygen. However, organisms possess specific adaptive mechanisms to prevent negative consequences of high environmental oxygen levels. In catla, decrease and increase in dissolved oxygen level of water from the control condition (5 mg/L) resulted into lower level of reduced glutathione after 1 and 48 h exposure in all tissues (muscles, hepatopancreas and gills), except muscles of DO-7 treatment after 1 h of exposure. Therefore, it is clear that both decreased and increased levels of external oxygen are an inducer of oxidative stress in catla. The exposure to hyperoxia induced oxidative stress in goldfish (Lushchak et al. 2005b), Atlantic salmon *S. salar* (Olsvik et al. 2005) and Senegal sole *Solea senegalensis* (Salas-Leiton et al. 2009). Maintenance of GSH levels is crucially important in preventing damage to cells exposed to conditions that promote oxidative stress. The cysteine thiol moiety of GSH imparts the antioxidant activity of this molecule. GSH can directly reduce a number reactive oxygen species including $^1\text{O}_2$, HO^\cdot , and O_2^- and GSH are oxidized to GSSG in this process. Glutathione may serve as a co-factor for antioxidant enzymes such as glutathione-dependent peroxidases or glutathione *S*-transferases, a second-phase detoxification enzyme (Lushchak 2011). Thus, the depletion of GSH during oxidative stress could have a significant impact on the antioxidant potential of cell (Pompella et al. 2003; Masella et al. 2005).

Glutathione *S*-transferases (GST) represent a major group of detoxification enzymes that catalyses intracellular detoxification reactions, including the inactivation of electrophilic carcinogens by catalysing their conjugation with glutathione (Henderson et al. 1998). In addition, GSTs have endogenous substrates, such as lipid and nucleic acid hydroperoxides and alkenals, which result from the decomposition of lipid hydroperoxides (Coles and Kadlubar 2003). Significantly higher level of GST was found in catla exposed at lower and higher levels of dissolved oxygen compared to the control condition. GST level was higher in hepatopancreas compared to the muscles of respective treatment. Oehlers et al. (2007) found that in medaka *Oryzias latipes* hypoxia increased glutathione *S*-transferase level. Elevated levels of GST in hepatopancreas of catla in all treatments (except DO-5 and

DO-7) after 48 h of exposure compared to the 1 h exposed fish of the respective treatment indicated higher detoxification mechanism in the tissue to overcome the adverse conditions. This may result into better immune system in fish exposed at elevated dissolved oxygen levels.

Glutathione peroxide (GPx) is a tetrameric enzyme that catalyses the oxidation of glutathione. The enzyme is found in both selenium-containing and selenium-independent forms in the cytosol and mitochondria of animal tissues (Halliwell and Gutteridge 1999). Exposure of catla at low dissolved oxygen resulted in higher value of glutathione peroxidase in hepatopancreas and gills. Longer (48 h) duration exposure caused chronic stress as the GPx level increased in fish maintained above 5 mg/L oxygen level. The level was higher in hepatopancreas compared to gills of respective treatments. This showed tissue-specific expression pattern. The responses of oxidative stress in fishes were highly tissue specific. White muscles have low content of mitochondria and low-intensive oxidative metabolism (Lushchak et al. 2005b). Therefore, it often shows a slight response to oxidative/reductive conditions. On the other hand, aerobic tissues, brain and especially hepatopancreas possess high potential for ROS generation, which seems to be efficiently counter balanced by powerful protective mechanisms to detoxify and repair damaged lipids and proteins.

This study clearly showed that after 48 h of exposure of fish was more stressful for fish compared to the 1 h exposed fish in the same treatments as TBARS levels were elevated in muscles of all treatments, except DO-5. Simultaneously, elevation of GPx level in hepatopancreas of fish in all these treatments indicated stress. This GPx virtually reduced the amount of GSH in most of these treatments. A close connection between oxidized lipids and antioxidant enzymes is proven by time dynamics of these parameters in response to stress. Elevation of lipid peroxidation is often the first reaction to increase ROS generation, but an induction in antioxidant defences, GPx and GST being the main enzymatic ones, causes a quick return of oxidized products to initial level (Lushchak and Bagnyukova 2006). Better detoxification mechanisms at elevated oxygen levels improved immune system of catla. Oxygen free radicals reportedly play a decisive role in the regulation of defence systems. Levels of these oxygen free radicals were

found to be increased in immunocytes during immune responses and the killing of pathogens by phagocytes (Jones et al. 1991). However, reports exploring the effects of generation of oxygen free radicals on immune response are limited. It was revealed that oxygen free radicals may contribute to the immunomodulation and indicated the possible link between oxygen free radicals generation and suppressed immune system during oxidative stress (Koner et al. 1997). Levels of TBARS, reduced glutathione and the activities of antioxidant enzymes clearly showed development of mild oxidative stress under hypoxic conditions in the present study. Glutathione is one more potential candidate because its biosynthesis is stimulated under mild oxidative stress owing to increased expression of glutamate cysteine ligase, a key enzyme for its biosynthesis (Lushchak 2014).

Most studies suggested that HIF levels are regulated via oxygen-dependent breakdown; studies on hypoxia-tolerant vertebrates suggested that HIF mRNA levels may be regulated (Shams et al. 2005; Law et al. 2006; Rissanen et al. 2006). In normoxia- and hypoxia-grown zebra fish *D. rerio*, highest HIF-1 α mRNA levels were found in tissues like brain, gill and heart that are important for hypoxic survival (Rytönen et al. 2014). In the present study, the mRNA level of HIF-1 α increased in brain of catla exposed at 1 and 3 mg/L dissolved oxygen after 1 h of exposure. In gill and hepatopancreas of catla, mRNA level of HIF-1 α increased in 1 mg/L dissolved oxygen. The mRNA level of HIF-1 α increased in gill of catla exposed at 3 and 11 mg/L dissolved oxygen level after 48 h of exposure. This showed tissue-specific expression pattern. Brain is most sensitive to hypoxic condition (≤ 3 mg/L). The detoxification capacity of hepatopancreas was confirmed from this result. In DO-3 and DO-11 treatments, mRNA level of HIF-1 α in gills required longer duration exposure (48 h) for its expression. Gracey et al. (2001) reported tissue-specific patterns of expression reflect the different metabolic roles of tissues during hypoxia in goby fish, *Gillichthys mirabilis*. This was also important to record that like hypoxia, hyperoxic condition was also stressful to catla.

Several studies showed the adaptive response of fish to low oxygen levels. In crucian carp *Carassius carassius*, HIF-1 DNA binding activity and HIF-1 expression in normoxia and hypoxia (0.7 mg/L O₂) were studied at temperatures of 26, 18 and 8 °C

(Rissanen et al. 2006). Temperature had a marked influence on HIF-1 in normoxia. Tissue-specific expression pattern was recorded in heart, gills and kidney. HIF is a key transcriptional activator in responses to hypoxia and primary regulator of the production of red blood cells through mediation of the expression of erythropoietin gene (Zhao and Wu 2013). In the present study the mRNA level of HIF-1 α increased after 1 h, while the RBC number decreased. This possibly indicates that during hypoxic conditions longer time was required for erythropoiesis as there was no increase in RBC number at least up to 48 h of exposure.

A defence promoting process in hypoxic condition is a drastic suppression of ATP demand, including shutting down energy costly processes like protein synthesis, cell division and ion pumping activity. Another hypoxia defence strategy involves reorganization of metabolic pathways by switching from aerobic oxidation to the glycolytic pathway (Ton et al. 2003). Hypoxia also induced the expression of hepatopancreas genes needed for enhanced anaerobic ATP production of gluconeogenesis. These responses represented an important adaptive strategy enabling *G. mirabilis* to survive under natural conditions of environmental hypoxia (Gracey et al. 2001). In the present study, though initially the mRNA level of ATPase 6 increased in hepatopancreas of catla exposed at DO-1 and DO-3 treatments compared to control one, the mRNA level reduced after 48 h of exposure. These results are comparable with the results of Busk and Boutilier (2005). They observed that anoxia exposure of hepatocytes of eel *Anguilla anguilla* caused an initial decrease in ATP, followed by a stabilization at a new, lower level. In contrast, Krumschnabel et al. (1997) demonstrated that exposure of goldfish hepatocytes to anoxia did not result in a decrease in ATP. In the present study, increased mRNA level of ATPase 6 gene in hepatopancreas after 1 h and decreased mRNA level after 48 h exposure can be considered as the compensatory mechanism to fulfil the ATP requirement needed in various metabolic processes. In the present study, long duration (48 h) exposure of fish to higher levels of dissolved oxygen (DO-9) resulted in up-regulation of ATPase 6 in hepatopancreas. The increase in ATP production must be achieved by coordinate expression of associated proteins encoded by mitochondrial and nuclear genes (Anderson et al. 1981). Carp acclimated at 10 °C

showed two-fold higher ATPase mRNA levels compared to the carp acclimated at 30 °C (Itoi et al. 2003). The present study showed the of ATP metabolism character of the brain, gills and hepatopancreas. Brain is the most sensitive to hypoxic condition as its metabolism relies on majority of ATP formed in the mitochondria through oxidative phosphorylation of adenosine diphosphate (ADP) catalysed by the enzyme ATPase.

Conclusions

The exposure of tropical freshwater fish catla below recommended dose of dissolved oxygen 5 mg/L impaired immune system. This was reflected in the lower values of respiratory burst activity and nitric oxide synthase, whereas lipid peroxidation was higher in fish exposed below and above the 5 mg/L level of dissolved oxygen. In catla, decrease and increase in dissolved oxygen level of water from the control condition resulted into lower level of GSH and increased levels of GST and GPx. Maintenance of GSH levels is crucially important in preventing damage to cells exposed to conditions that promote oxidative stress. The mRNA level of HIF-1 α and ATPase increased in treatments with ≤ 5 mg/L dissolved oxygen just 1 h after exposure. This showed immediate stress effect. Tissue-specific expression showed the different metabolic roles of tissues during hypoxia and hyperoxia in carps. This is clear from the present study that both decreased and increased levels of oxygen in the culture system induced oxidative stress in catla.

Acknowledgments Authors are thankful to Indian Council of Agricultural Research, ICAR, New Delhi, for providing financial support in the form of NFBSFARA project (AS-2001/2010-11) to carry out the research work.

References

- Alexander JB, Ingram GA (1992) Noncellular nonspecific defence mechanisms of fish. *Annu Rev Fish Dis* 2:249–279
- Anderson DP, Siwicki AK (1995) Basic haematology and serology for fish health programs. In: Shariff M, Arthur JR, Subasinghe RP (eds) *Diseases in Asian Aquaculture II*. Manila, Fish Health Section, Asian Fisheries Society
- Anderson S, Bankier AT, Barrell BG, de Bruijn MHL, Coulson AR, Drouin J, Eperon IC, Nierlich DP, Roe BA, Sanger F, Schreier PH, Smith AJ, Staden R, Young IG (1981) Sequence and organization of the human mitochondrial genome. *Nature* 290:457–465
- Benita Y, Kikuchi H, Smith AD, Zhang MQ, Chung DC, Xavier RJ (2009) An integrative genomics approach identifies Hypoxia Inducible Factor-1 (HIF-1)-target genes that form the core response to hypoxia. *Nucleic Acids Res* 37:4587–4602
- Bhor VM, Raghuram N, Sivakami S (2004) Oxidative damage and altered antioxidant enzyme activities in the small intestine of streptozotocin-induced diabetic rats. *Int J Biochem Cell Biol* 36:89–97
- Bowden TJ (2008) Modulation of the immune system of fish by their environment. *Fish Shellfish Immunol* 25:373–383
- Brander K (2010) Impacts of climate change on fisheries. *J Mar Syst* 79:389–402
- Busk M, Boutilier RG (2005) Metabolic arrest and its regulation in anoxic eel hepatocytes. *Physiol Biochem Zool* 78:926–936
- Coles BF, Kadlubar FF (2003) Detoxification of electrophilic compounds by glutathione *S*-transferase catalysis: determinants of individual response to chemical carcinogens and chemotherapeutic drugs? *BioFactors* 17:115–130
- D'Avanzo C, Kremer JN (1994) Diel oxygen dynamics and anoxic events in an eutrophic estuary of Waquoit Bay, Massachusetts. *Estuaries* 17:131–139
- Devasena T, Lalitha S, Padma K (2001) Lipid peroxidation, osmotic fragility and antioxidant status in children with acute post-streptococcal glomerulonephritis. *Clin Chim Acta* 308:155–161
- Goel A, Dani V, Dhawan DK (2005) Protective effects of zinc on lipid peroxidation, antioxidant enzymes and hepatic histoarchitecture in chlorpyrifos-induced toxicity. *Chem Biol Interact* 156:131–140
- Gracey AY, Troll JV, Somero GN (2001) Hypoxia-induced gene expression profiling in the euryoxic fish *Gillichthys mirabilis*. *Proc Natl Acad Sci USA* 98:1993–1998
- Graham JB (1990) Ecological, evolutionary, and physical factors influencing aquatic animal respiration. *Am Zool* 30:137–146
- Grecay PA, Stierhoff KL (2002) A device for simultaneously controlling multiple treatment levels of dissolved oxygen in laboratory experiments. *J Exp Mar Biol Ecol* 280:53–62
- Habig WH, Pabst MJ, Jakoby WB (1974) Glutathione *S*-transferases the first enzymatic step in mercapturic acid formation. *J Biol Chem* 249:7130–7139
- Halliwell B, Gutteridge JMC (1989) *Free radicals in biology and medicine*, 2nd edn. Clarendon Press, Oxford
- Halliwell B, Gutteridge JMC (1999) *Free radicals in biology and medicine*, 3rd edn. Clarendon Press, Oxford
- Henderson CJ, Smith AG, Ure J, Brown K, Bacon EJ, Wolf CR (1998) Increased skin tumorigenesis in mice lacking pi class glutathione *S*-transferases. *Proc Natl Acad Sci USA* 95:5275–5280
- Hermes-Lima M (2004) Oxygen in biology and biochemistry: role of free radicals. In: Storey KB (ed) *Functional metabolism: regulation and adaptation*. Wiley, New Jersey, pp 319–368
- Hermes-Lima M, Zenteno-Savín T (2002) Animal response to drastic changes in oxygen availability and physiological oxidative stress. *Comp Biochem Physiol C: Toxicol Pharmacol* 133:537–556

- Hochachka PW, Somero GN (2002) Biochemical adaptation: mechanism and process in physiological evolution, 1st edn. Oxford University Press, New York
- Huttula T, Peltonen A, Bilaletdin A, Saura M (1992) The effects of climatic change on lake ice and water temperature. *Aqua Fenn* 22:129–142
- Indian Council of Agricultural Research (2013) Handbook of Fisheries And aquaculture, 2nd edn. Indian Council of Agricultural Research, New Delhi, p 1116
- Intergovernmental Panel on Climate Change (2007) Climate change 2007: the scientific basis. In: Solomon S et al (eds) Contribution of working group I to the fourth assessment report of the intergovernmental panel on climate change. Cambridge University Press, New York
- Itoi S, Kinoshita S, Kikuchi K, Watabe S (2003) Changes of carp F_0F_1 -ATPase in association with temperature acclimation. *Am J Physiol Regul Integr Comp Physiol* 284:R153–R163
- Janssens BJ, Childress JJ, Baguet F, Rees J-F (2000) Reduced enzymatic antioxidative defense in deep-sea fish. *J Exp Biol* 203:3717–3725
- Jollow DJ, Mitchell JR, Zampaglione N, Gillette JR (1974) Bromobenzene-induced liver necrosis. Protective role of glutathione and evidence for 3, 4-bromobenzene oxide as the hepatotoxic metabolite. *Pharmacology* 11:151–169
- Jones OTG, Hancock JT, Henderson LM (1991) Oxygen radical production by transformed B lymphocytes. *Mol Aspects Med* 12:87–92
- Koner BC, Banerjee BD, Ray A (1997) Effects of in vivo generation of oxygen free radicals on immune responsiveness in rabbits. *Immunol Lett* 59:127–131
- Krumschnabel G, Schwarzbaum PJ, Biasi C, Dorigatti M, Wieser W (1997) Effects of energy limitation on Ca^{2+} and K^{+} homeostasis in anoxia-tolerant and anoxia-intolerant hepatocytes. *Am J Physiol Regul Integr Comp Physiol* 273:R307–R316
- Kvamme BO, Gadan K, Finne-Fridell F, Niklasson L, Sundh H, Sundell K, Taranger GL, Evensen Ø (2013) Modulation of innate immune responses in Atlantic salmon by chronic hypoxia-induced stress. *Fish Shellfish Immunol* 34:55–65
- Law SH, Wu RS, Ng PK, Richard MK, Kong RY (2006) Cloning and expression analysis of two distinct HIF- α isoforms—gcHIF-1 α and gcHIF-4 α —from the hypoxia-tolerant grass carp, *Ctenopharyngodon idellus*. *BMC Mol Biol* 7:15. doi:10.1186/1471-2199-7-15
- Lee D-U, Kang YJ, Park MK, Lee YS, Seo HG, Kim TS, Kim CH, Chang KC (2003) Effects of 13-alkyl-substituted berberine alkaloids on the expression of COX-II, TNF- α , iNOS, and IL-12 production in LPS-stimulated macrophages. *Life Sci* 73:1401–1412
- Livak KJ, Schmittgen TD (2001) Analysis of relative gene expression data using real-time quantitative PCR and the $2^{-\Delta\Delta CT}$ method. *Methods* 25:402–408
- Lushchak VI (2011) Environmentally induced oxidative stress in aquatic animals. *Aquat Toxicol* 101:13–30
- Lushchak VI (2014) Free radicals, reactive oxygen species, oxidative stress and its classification. *Chem Biol Interact* 224:164–175
- Lushchak VI, Bagnyukova TV (2006) Effects of different environmental oxygen levels on free radical processes in fish. *Comp Biochem Physiol B: Biochem Mol Biol* 144:283–289
- Lushchak VI, Lushchak LP, Mota AA, Hermes-Lima M (2001) Oxidative stress and antioxidant defenses in goldfish *Carassius auratus* during anoxia and reoxygenation. *Am J Physiol Regul Integr Comp Physiol* 280:R100–R107
- Lushchak VI, Bagnyukova TV, Lushchak OV, Storey JM, Storey KB (2005a) Hypoxia and recovery perturb free radical processes and antioxidant potential in common carp (*Cyprinus carpio*) tissues. *Int J Biochem Cell Biol* 37:1319–1330
- Lushchak VI, Bagnyukova TV, Husak VV, Luzhna LI, Lushchak OV, Storey KB (2005b) Hyperoxia results in transient oxidative stress and an adaptive response by antioxidant enzymes in goldfish tissues. *Int J Biochem Cell Biol* 37:1670–1680
- Magnuson JJ, Crowder LB, Medvick PA (1979) Temperature as an ecological resource. *Am Zool* 19:331–343
- Mallya YJ (2007) The effect of dissolved oxygen on fish growth in aquaculture. Kingolwira National Fish Farming Centre, Fisheries Division Ministry of Natural Resources and Tourism, Tanzania
- Martinez-Alvarez RM, Morales AE, Sanz A (2005) Antioxidant defenses in fish: biotic and abiotic factors. *Rev Fish Biol Fisher* 15:75–88
- Martinovic D, Villeneuve DL, Kahl MD, Blake LS, Brodin JD, Ankley GT (2009) Hypoxia alters gene expression in the gonads of zebrafish (*Danio rerio*). *Aquat Toxicol* 95:258–272
- Masella R, Di Benedetto R, Vari R, Filesi C, Giovannini C (2005) Novel mechanisms of natural antioxidant compounds in biological systems: involvement of glutathione and glutathione-related enzymes. *J Nutr Biochem* 16:577–586
- Mohandas J, Marshall JJ, Duggin GG, Horvath JS, Tiller DJ (1984) Differential distribution of glutathione and glutathione-related enzymes in rabbit kidney: possible implications in analgesic nephropathy. *Biochem Pharmacol* 33:1801–1807
- Montgomery DC (1984) Design and analysis of experiments. Wiley, New York
- Ni M, Wen H, Li J, Chi M, Bu Y, Ren Y, Zhang M, Song Z, Ding H (2014) The physiological performance and immune responses of juvenile Amur sturgeon (*Acipenser schrenckii*) to stocking density and hypoxia stress. *Fish Shellfish Immunol* 36:325–335
- Oehlers LP, Perez AN, Walter RB (2007) Detection of hypoxia-related proteins in medaka (*Oryzias latipes*) brain tissue by difference gel electrophoresis and *de novo* sequencing of 4-sulfophenyl isothiocyanate-derivatized peptides by matrix-assisted laser desorption/ionization time-of-flight mass spectrometry. *Comp Biochem Physiol C: Toxicol Pharmacol* 145:120–133
- Ohkawa H, Ohishi N, Yagi K (1979) Assay for lipid peroxides in animal tissues by thiobarbituric acid reaction. *Anal Biochem* 95:351–358
- Olsvik PA, Kristensen T, Waagbø R, Rosseland BO, Tollefsen KE, Bæverfjord G, Berntsen MHG (2005) mRNA expression of antioxidant enzymes (SOD, CAT and GSH-Px) and lipid peroxidative stress in liver of Atlantic salmon (*Salmo salar*) exposed to hyperoxic water during smoltification. *Comp Biochem Physiol C: Toxicol Pharmacol* 141:314–323

- Padilla PA, Roth MB (2001) Oxygen deprivation causes suspended animation in the zebrafish embryo. *Proc Natl Acad Sci USA* 98:7331–7335
- Pamplona R, Costantini D (2011) Molecular and structural antioxidant defenses against oxidative stress in animals. *Am J Physiol Regul Integr Comp Physiol* 301:R843–R863
- Pompella A, Visvikis A, Paolicchi A, deTata V, Casini AF (2003) The changing faces of glutathione, a cellular protagonist. *Biochem Pharmacol* 66:1499–1503
- Rees BB, Sudradjat FA, Love JW (2001) Acclimation to hypoxia increases survival time of zebrafish, *Danio rerio*, during lethal hypoxia. *J Exp Zool* 289:266–272
- Rissanen E, Tranberg HK, Sollid J, Nilsson GE, Nikinmaa M (2006) Temperature regulates hypoxia-inducible factor-1 (HIF-1) in a poikilothermic vertebrate, crucian carp (*Carassius carassius*). *J Exp Biol* 209:994–1003
- Ritola O, Livingstone DR, Peters LD, Lindström-Seppä P (2002a) Antioxidant processes are affected in juvenile rainbow trout (*Oncorhynchus mykiss*) exposed to ozone and oxygen-supersaturated water. *Aquaculture* 210:1–19
- Ritola O, Tossavainen K, Kiuru T, Lindström-Seppä P, Molsa H (2002b) Effects of continuous and episodic hyperoxia on stress and hepatic glutathione levels in one-summer-old rainbow trout (*Oncorhynchus mykiss*). *J Appl Ichthyol* 18:159–164
- Rombout J, Huttenhuis HBT, Picchiatti S, Scapigliati G (2005) Phylogeny and ontogeny of fish leucocytes. *Fish Shellfish Immunol* 19:441–455
- Rytkönen KT, Prokkola JM, Salonen V, Nikinmaa M (2014) Transcriptional divergence of the duplicated hypoxia-inducible factor alpha genes in zebrafish. *Gene* 541:60–66
- Salas-Leiton E, Cánovas-Conesa B, Zerolo R, López-Barea J, Cañavate JP, Albama J (2009) Proteomics of juvenile Senegal sole (*Solea senegalensis*) affected by gas bubble disease in hyperoxygenated ponds. *Mar Biotechnol* 11:473–487
- Saurabh S, Sahoo PK (2008) Lysozyme: an important defence molecule of fish innate immune system. *Aquac Res* 39:223–239
- Scapigliati G, Scalia D, Marras A, Meloni S, Mazzini M (1999) Immunoglobulin levels in the teleost sea bass *Dicentrarchus labrax* (L.) in relation to age, season, and water oxygenation. *Aquaculture* 174:207–212
- Schrøder MB, Villena AJ, Jørgensen TØ (1998) Ontogeny of lymphoid organs and immunoglobulin producing cells in Atlantic cod (*Gadus morhua* L.). *Dev Comp Immunol* 22:507–517
- Secor DH, Gunderson TE (1998) Effects of hypoxia and temperature on survival, growth, and respiration of juvenile Atlantic sturgeon, *Acipenser oxyrinchus*. *Fish Bull* 96:603–613
- Shams I, Nevo E, Avivi A (2005) Ontogenetic expression of erythropoietin and hypoxia-inducible factor-1 alpha genes in subterranean blind mole rats. *FASEB J* 19:307–309
- Sies H (1991) Role of reactive oxygen species in biological processes. *Klin Wochenschr* 69:965–968
- Stierhoff KL, Targett TE, Greco PA (2003) Hypoxia tolerance of the mummichog: the role of access to the water surface. *J Fish Biol* 63:580–592
- Storey KB (1996) Oxidative stress: animal adaptations in nature. *Braz J Med Biol Res* 29:1715–1733
- Ton C, Stamatidou D, Liew C-C (2003) Gene expression profile of zebrafish exposed to hypoxia during development. *Physiol Genomics* 13:97–106
- Tripathi NK, Latimer KS, Burnley VV (2004) Hematologic reference intervals for koi (*Cyprinus carpio*), including blood cell morphology, cytochemistry, and ultrastructure. *Vet Clin Pathol* 33:74–83
- Vig E, Nemcsok J (1989) The effects of hypoxia and paraquat on the superoxide dismutase activity in different organs of carp, *Cyprinus carpio* L. *J Fish Biol* 35:23–25
- Watts M, Munday BL, Burke CM (2001) Immune responses of teleost fish. *Aust Vet J* 79:570–574
- Wu Z, You F, Wen A, Ma D, Zhang P (2014) Physiological and morphological effects of severe hypoxia, hypoxia and hyperoxia in juvenile turbot (*Scophthalmus maximus* L.). *Aquac Res*. doi:10.1111/are.12483
- Zhao S, Wu J (2013) Hypoxia inducible factor stabilization as a novel strategy to treat anemia. *Curr Med Chem* 20:2697–2711

Performance Evaluation Of Bandwidth Scheduling Techniques In Passive Optical Networks

Dr. Vibhakar Shrimali¹, Dr. Manoj Kumar Taneja², Mr. Abhishek Gaur³

¹(Associate Professor & Head, Ece Deptt. Gb Pant Govt. Engg. College, Delhi, India)

²(Associate Professor, Usict, Guru Gobind Singh Indraprastha University, Delhi, India)

³(Assistant Professor, Ece Deptt., Gb Pant Govt. Engg. College, Delhi, India)

Abstract—Passive Optical Networks are thought to be the next step in the development of Access Networks and providing broadband access in the "last mile" area. Ethernet PONs (EPON) gain the most attention from the industry as they offer highly flexible, cost effective solution. In this paper we propose algorithms that provide Dynamic Bandwidth Allocation and shift the burden of queue management from the customer to the network, this results in less complicated and more generic equipment used on the customer's premises. We show the results of simulations to validate the effectiveness of algorithms presented.

I. Introduction

With the increasing popularity of the Internet the traffic generated by domestic and small business users has been growing constantly over the last couple of years. Various technologies have been deployed to provide broadband access to the network in the area known as the "last mile". As network operators strive for cost efficiencies, Passive Optical Network (PON) seem to be the next step in the development of Access Networks (AN).

A PON is a point-to-multipoint all optical network with no active elements in the path between the signal source and the destination. On the network side there is an Optical Line Terminator (OLT) unit. The OLT is usually placed in the local exchange and it acts as a point of access to the Wide or Metropolitan Area Network. On the customer's side there is an Optical Network Unit (ONU). An ONU can be placed either in the curb, building or home and its primary task is to convert data between optical and electrical domains.

Two protocols, Asynchronous Transfer Mode (ATM) and Ethernet, have been proposed as the transmission protocol in PONs. In recent years EPONs have gained more attention from the industry. The architecture of an Ethernet network is simple yet extremely efficient. Interoperability between old and new networks can easily be maintained and legacy solutions can be used as EPON data is carried in standard Ethernet frames.

Typically EPON networks are connected in a tree topology with multiple ONUs attached to a single OLT by means of optical splitters as shown in Figs. 1 and 2. In a downstream (network→user) transmission the OLT uses all the available bandwidth to broadcast

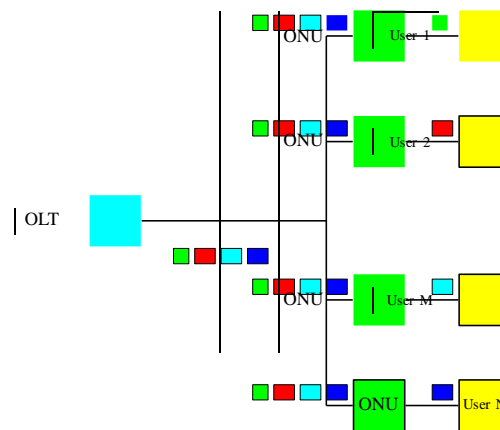


Fig. 1. Downstream transmission in EPON.

packets through the splitter/coupler to every ONU. Each ONU extracts packets from the stream based on the Medium Access Control (MAC) address.

In the upstream direction packets sent by an ONU can only reach the OLT as optical splitter prevents an ONU from receiving packets from other ONUs. In order to avoid collisions between frames from different ONUs at the optical splitter available bandwidth must be shared among all ONUs. The OLT is responsible for assigning a non-overlapping time-slot to each ONU, and ONUs can only transmit during that time-slot. During an off period packets are buffered and when the time arrives send in a burst using all the available bandwidth.

One of the key features of EPON networks is their ability to support Differentiated Services (DiffServ) [1] architecture and offer various levels of quality of service (QoS). Generally three classes of traffic can be distinguished: Expedited Forwarding (EF), Assured Forwarding (AF), and Best Effort (BE). EF services (primarily voice and video) have very strict requirements and demand a constant, low end-to-end delay and jitter. AF services tend to be less sensitive to packet delay but require a guaranteed amount of bandwidth. BE traffic is generated by applications that have no strong requirements regarding traffic properties.

In this paper we analyze various Dynamic Bandwidth Allocation (DBA) algorithms that support

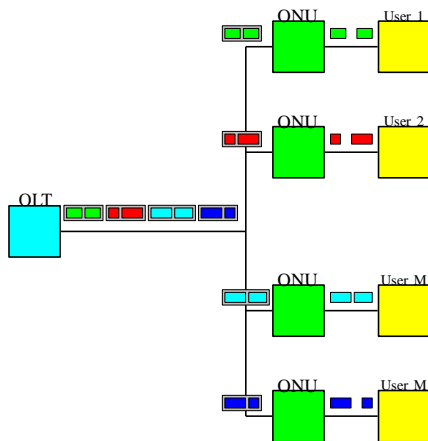


Fig. 2. Upstream transmission in EPON.

DiffServ architecture. In comparison to algorithms already presented in literature, the OLT should be responsible for granting time on a per class rather than per ONU basis, so no intra-ONU scheduling exists. This ensures that the equipment on the customer's side is kept as simple and inexpensive as possible.

II. Background

In EPON networks ONUs cannot transmit at the same time. It is the OLT's responsibility to divide the available bandwidth between ONUs. To achieve that the OLT assigns a non overlapping time-slot to every ONU. In a static bandwidth allocation (SBA) a fixed amount of time is assigned to every ONU. Algorithms with and without support for differentiated services based on a static bandwidth allocation were studied in [2], [3]. The obvious disadvantage of SBA is that bandwidth cannot be utilized efficiently. This is especially true in the case where the difference between bandwidth requested by and bandwidth assigned to the source is large.

In [4], a DBA algorithm called "Interleaved Polling with Adaptive Cycle Time (IPACT)" was presented. This algorithm allocates time slots based on information received from ONUs during a polling cycle. IPACT provides statistical multiplexing and gives good bandwidth utilization but due to a variable polling cycle, delay sensitive services are hampered.

Dynamic bandwidth allocation combined with priority scheduling algorithms were studied in [4], [5]. In both papers OLT is responsible for granting time slots to ONUs. Every ONU assigns packets to different queues based on their QoS demands. The main disadvantage of this approach is that to fully support DiffServ, an ONU has to have knowledge about the SLA between a customer and the network provider. Here, we propose a different approach where all packet scheduling is done at the OLT and the ONU's functionality is limited to the minimum. The bandwidth is allocated per class of traffic rather than per ONU. For every class the OLT informs an ONU about

the allocated transmission window with a Multi-Point Control Protocol (MPCP) [6] GATE message.

Removing the scheduling mechanism from an ONU has two benefits. Firstly the ONU becomes a very simple unit that is easy to manufacture and is inexpensive to maintain. Secondly greater flexibility is achieved as the ONU becomes independent from the OLT. Various scheduling algorithms can be deployed on the OLT without any modifications at the client side. Hence Service Level Agreements (SLA) can be introduced, changed and modified at any time.

III. Dynamic Bandwidth Allocation with DiffServ Support

An efficient bandwidth allocation algorithm is the key to enabling PONs that support DiffServ. Before transmission windows are assigned, various parameters must be taken into account. As for the EF class, delay and jitter are the priority. AF class usually demands various levels of certainty that packets reach the destination and BE class has no strong requirements regarding QoS. The algorithm must balance these factors to achieve the optimal utilization of available bandwidth.

Two MPCP messages are involved in the exchange of control information. The REPORT message is used by an ONU to periodically inform the OLT about the length of its queues. On the other side the OLT issues GATE messages to notify each ONU about transmission times assigned to every class.

A granting cycle is a time in which all active ONUs should have a chance to transmit their data. An increase in the duration of a granting cycle leads to larger delays experienced by packets, as ONU must wait for a longer period of time for its opportunity to send its data. Conversely making a granting cycle too short leads to more bandwidth being wasted to guard intervals that are necessary to separate transmission from two ONUs.

There are two categories of bandwidth allocation algorithms. In static allocation every ONU/class is assigned its fixed share of bandwidth. In dynamic allocation bandwidth is assigned proportionally to the reported queue length. Data that can't be sent during a granting cycle has to wait for the next opportunity.

Here, we want to present new algorithms that could be used with EPONs supporting different classes of service. Let the system have N ONUs with q queues at each ONU. Also, let $B_{n,q}$ be a percent of the total bandwidth requested/assigned to a queue q at ONU n .

A. DBA with Priority Transmission Order - DBA-P

In this algorithm at the first stage every class is assigned bandwidth that is proportional to the bandwidth requested.

$$B_{n,q}^{\text{assigned}} = \frac{B_{n,q}^{\text{request}}}{\sum_{n,q} B_{n,q}^{\text{request}}}$$

(1)

To improve the performance of this algorithm for high priority traffic every ONU has a chance to transmit its EF packets at the beginning of the granting cycle.

B. DBA with a Guaranteed Minimum bandwidth - DBA-GM

This approach is a tradeoff between static and dynamic allocation schemes. Every class is assigned some minimal amount of bandwidth that was agreed in the SLA between the network provider and a customer. The amount of bandwidth assigned is dependent on the priority of the traffic.

$$B^{min} = \sum_{n,q} B^{min}_{n,q} \text{ and } B^{min} < 1 \quad (2)$$

The remaining bandwidth is assigned to all classes proportionally to the bandwidth required.

$$B^{avail} = 1 - B^{min} \quad (3)$$

$$B^{excess} = \sum B^{request}_{n,q} - B^{min}_{n,q} \quad (4)$$

$$B^{assigned}_{n,q} = B^{min}_{n,q} + B^{avail} \cdot B^{access}(B^{request}_{n,q} - B^{min}_{n,q}) \quad (5)$$

As in DBA-P in order to minimize the delay and jitter experienced by EF classes, these classes are assigned bandwidth at the beginning of the granting cycle. The modified version of DBA-GM scheme is shown as DBA-GM-P.

IV. Performance Evaluation

To measure the performance of each bandwidth allocation algorithm we designed an event-driven C++ based EPON simulator. In our research we used 16

ONUs connected in a tree topology to a single OLT operating at a speed of 1Gb/s. Each ONU has three queues with an independent buffering space. The guard time between transmissions from different ONUs is set to 1μs and the value of Inter-Frame Gap (IFG) between Ethernet packets is 96 bits. In our simulator the length of a granting cycle stays the same throughout the simulation.

It has been shown that most network traffic (i.e., http, ftp and VBR services) is best characterized by self-similarity and long-range dependence [7]. To model a high priority EF class of traffic (e.g., voice applications) a Poisson distribution is generally used. In our simulator we used a class of a high priority traffic with a fixed packet length of 70 bytes. A length of packets for AF and BE classes was uniformly distributed between 64 and 1518 bytes. We ran our simulations for various proportions in the volume of EF, AF and BE traffic. Average and maximum packet delay were measured during experiments.

We compared the performance of algorithms proposed in this paper with the performance of SBA and DBA algorithms. The results for 20% of EF, 40% of

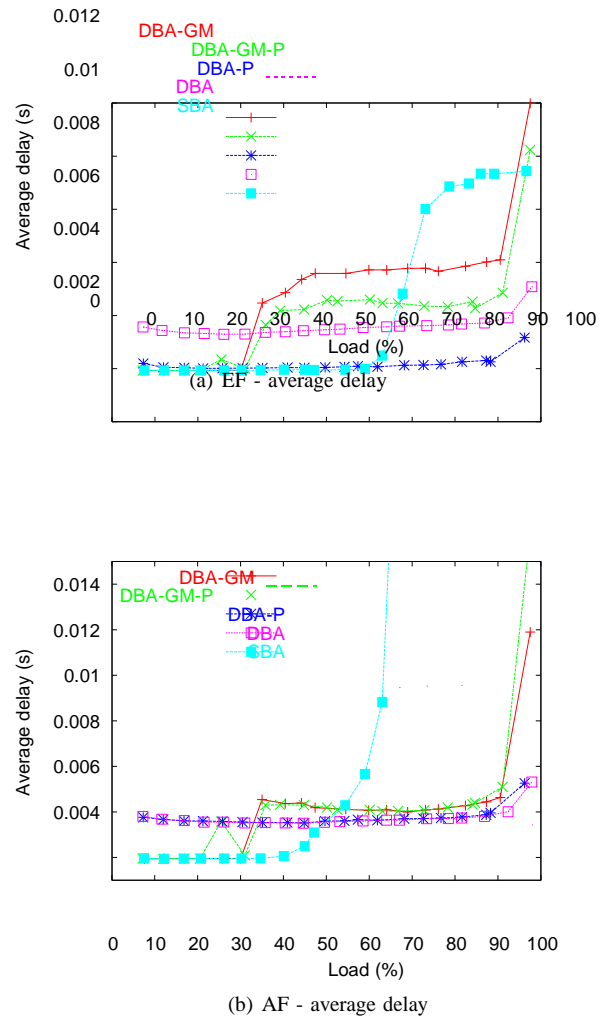
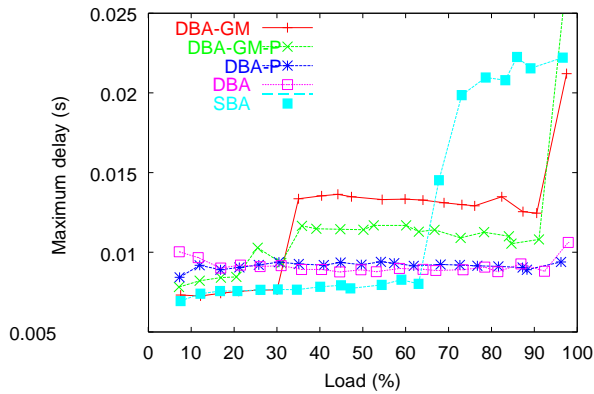


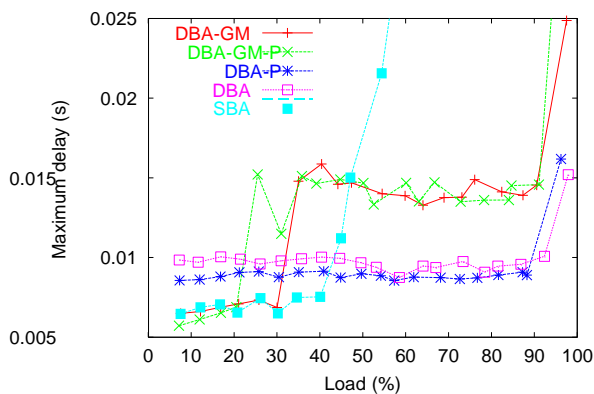
Fig. 3. Algorithms performance comparison. EF - 20%, AF - 40% and BE- 40%.

AF and 40% of BE traffic are presented in Figs. 3 and 4, and for 30% of EF, 60% of AF and 10% of BE in Fig. 5. For light loads the SBA scheme showed better performance compared to other algorithms. On the other hand for heavy loads average and maximum delays are much longer than for other algorithms. DBA algorithm showed a steady performance under various conditions and the difference in the average delay for small and large loads was not larger than 2ms. The DBA-P scheme gave good results for both EF and AF classes of traffic. The values of an average delay for light loads are similar to SBA. For heavy loads DBA-P outperforms all other algorithms. The DBA-GM algorithm showed properties of both static and dynamic allocation. Under low traffic conditions the average delay was as low as for the SBA. If traffic offered was average or heavy it behaved as DBA, although its performance was worse as some bandwidth was statically allocated.

The improved versions of those algorithms (DBA-GM-P) produced better results, due to the fact that high priority packets were sent at the beginning of every granting cycle in passive optical networks.

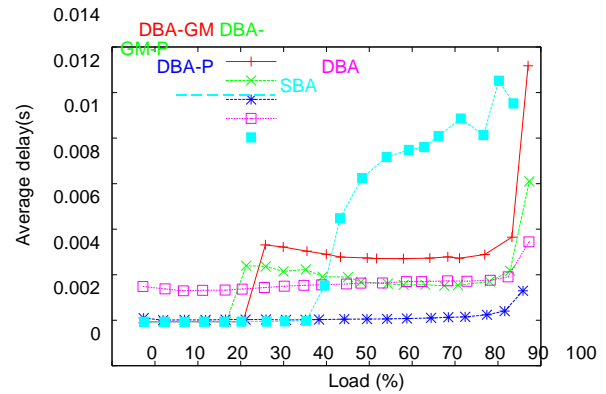


(a) EF - maximum delay

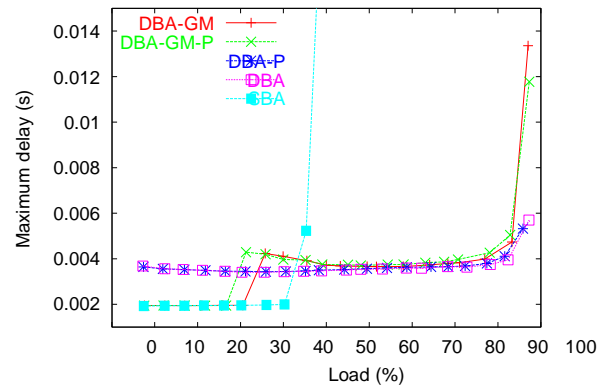


(b) AF - maximum delay

Fig. 4. Algorithms performance comparison. EF - 20%, AF - 40% and BE- 40%.



(a) EF



(b) AF

Fig. 5. Average delays comparison for EF - 20%, AF - 60% and BE- 10%.

V. Conclusion

In this paper we addressed the problem of the support for DiffServ in EPON. We proposed algorithms that shifted the responsibility of Access Control and queue management from the ONU to the OLT, as this creates a possibility of developing more generic, less complicated hence cheaper equipment.

We introduced new algorithms that supported that scheme. We ran detailed simulation experiments to analyze their performance.

A novel DBA-P scheme showed the best performance for EF and AF class of traffic. The disadvantage of this approach was that as the bandwidth was assigned proportionally to the reported length of queues there was no mechanism to guarantee that the user was allocated as much bandwidth as it was promised in the SLA.

We addressed that problem and proposed an DBA-GM algorithm, where a protection of parameters was achieved by static assignment of a certain amount of bandwidth agreed in the SLA. The results showed that DBA-GM performance was comparable but not as good as the DBA scheme. Considerable improvement in the values of average delay for EF classes was achieved when a mechanism of priority transmission was applied.

References

- [1] S. Blake, D. Black, M. Carlson, E. Davies, Z. Wang, and W. Weiss, "RFC-2475 - An Architecture for Differentiated Services," 1998, <http://www.ietf.org/rfc/rfc2475.txt>.
- [2] G. Kramer, B. Mukherjee, and A. Maislos, "Ethernet Passive Optical Networks (EPON): a missing link in an end-to-end optical internet," S. Dixit, Ed. John Wiley & Sons, Inc, Mar. 2003, ch. 8.
- [3] G. Kramer and B. Mukherjee, "Ethernet PON: design and analysis of an optical access network," *Photonic Network Communication*, vol. 3, no. 3, pp. 307–319, July 2001.
- [4] G. Kramer, B. Mukherjee, S. Dixit, Y. Ye, and R. Hirth, "On supporting differentiated classes of service in EPON-based access network," *OSA Journal of Optical Networking*, vol. 1, no. 8/9, pp. 280–298, 2002.
- [5] Ch. M. Assi, Y. Ye, S. Dixit, and M. A. Ali, "Dynamic Bandwidth Allocation for Quality-of-Service Over Ethernet PONs," *IEEE Journal on Selected Areas in Communications*, vol. 21, no. 9, pp. 1467–1477, Nov. 2003.
- [6] "IEEE 802.1Q," 1998.
- [7] W. Leland, M. Taqqu, W. Willinger, and D. Wilson, "On the Self-Similar Nature of Ethernet Traffic (extended version)," *IEEE/ACM Transactions on Networking*, vol. 2, no. 1, pp. 1–15, Feb. 1994.

VI. BIOGRAPHIES

Dr. Vibhakar Shrimali(vibhakar.shrimali@gmail.com) graduated in Electronics and Communication Engineering from MBM Engineering College, Jodhpur, India, in 1987, and received his Masters' degree in Electronics and Communication Engineering from Delhi College of Engineering, Delhi India. His research interest includes image processing, signal processing, microprocessors & wireless communication. He is member of Institute of Electrical and Electronics Engineers (IEEE).

cs Engineers (IEEE), USA, Society of Engineering in Medicine and Biology, Society (EMBS), USA, a fellow member of Institute of Electronics and Telecommunication Engineers (IETE), India, Institute of Engineering (IE), India and Life member of Computer Society of India (CSI). He got selection from Union Public Service Commission (UPSC) in the year 2014 in G.B Pant Govt. Engg. College for the post of Associate Professor in ECE Deptt.

Dr. Manoj Kumar Taneja(manojtaneja@ipu.ac.in) is working as an Associate Professor in USICT (ECE), GGSIPU, Dwarka, New Delhi. He has experience of 11 years in teaching and research. He has also worked as an Assistant Professor in Chaudhary Devi Lal Govt. Engineering College, Panniwala Mota, Sirsa, Haryana. He has completed Ph.D from Department of Electronics & Communication Engineering, GJUST, Hisar. He has published 25 research papers in International/National journals. He has also published more than 30 research papers in International/National conference. He has guided 25 M. Tech students and presently one Ph. D student is working under his guidance. His research interests include integrated circuit design, low power CMOS system and microelectronics for communication systems. He is a Life Member of IETE (India), ISTE (India) and Semiconductor Society of India.

ABHISHEK GAUR (a.abhishekgaur@rediffmail.com) received his B.Tech degree in Electronics & Communication Engineering and M.Tech degree in Digital Communication from Guru Gobind Singh Indraprastha University, Delhi, India in 2010 & 2012 respectively. He is currently working as an Asst. Professor in G.B Pant Govt. Engineering. College, Delhi, India in Deptt. of Electronics & Communication Engineering. He is also pursuing his doctorate degree in the field of optical-wireless convergence from Galgotias University, India. His research interests includes Optical Networks, Wireless Networks , Digital Communication, Consumer Electronics, Heterogeneous Networks (HETNET), LTE Networks, Control Systems, Microwaves, Electromagnetic, Micro strip Antennas and Wireless Backhauling.

Social CRM: An Emerging Medium

Anurag Tiruwa¹ and Rajan Yadav²

^{1,2}DSM, Delhi Technological University, Delhi, India
E-mail: ¹anuraag.dsm13@gmail.com, ²raj_yadav1974@yahoo.co.in

Abstract

Purpose—Marketers have adopted Social media in business model, utilizing it for the purpose of understanding consumer's perception. They have moved further ahead by using social media as a channel to communicate with consumers for promotional purposes as well as to create a positive brand image. Over the period of time Social media and social networking sites have evolved into a medium for Consumer Relationship Management (CRM) where marketers are using social media to manage consumer requests, queries, and grievances etc. The purpose of this paper is to understand the integration of social media into CRM and its evolution into Social CRM.

Approach—Review of literature which discusses the use of social media and social networking sites for the purpose of building positive relations with consumers and then to Manage those relations using social media and social networking sites.

Findings—It identifies different factors which affects social CRM. It also suggests strategies for marketers to implement an effective Social CRM.

Implications—This paper would help marketers, researchers and academicians in understanding Social CRM better and would provide a base for further empirical research.

Keywords: Social CRM, Social media, Social networking sites, online social network

1. INTRODUCTION

With introduction of Web 2.0 [13] there was a drastic change in how people and organizations interacted with each other. It maximized communication and addresses the masses using online Communities, Blogs or Wikis. With Internet communication becoming more and more customer centric, the customer is no longer limited to a passive role in his or her relationship with a company [3, 10].

Organizations have their traditional processes and information systems such as CRM which has its own detailed database pertaining to knowledge about markets, customer information's. But on the other hand, customers discuss offerings and provide help to each other in the Social Web. Whether this social web can be used by marketers and organizations to build and manage relationships with the customers is one popular topic that has been discussed both in

academic research and business discussion. A new phenomenon in understanding buyers' needs and reaching new customers is social media. Organizations are capturing data from tools such as LinkedIn, Facebook and blogs, and attempting to integrate this information into their sales process, and focusing on using this internet phenomena to their advantage by using social media for CRM. Using this new Technology for increasing business and sales through relationship development with customers. [24, 23]. This paper is an attempt to understand the social CRM and how it can be used by marketers to their benefit.

2. DEFINING CRM

Within an organization, which deals with customers at a daily basis; CRM is very important when it comes to organizational approach to communicate and extend out to the customers [12]. It can be viewed as a maintaining a network between the organizations and the customers for mutual benefit [16]. If we were to give generalized definition of CRM then it would be that a general definition will be that it is an approach followed by organizations in understanding customers behavior by different meaningful communications, so as to increase customer profitability by increasing and improving customer acquisition, customer retention, customer loyalty. It is concerned with how an organization manages relationships with its customer using its various resources; namely, communications channels, interactive processes and various other contacts [7]. A more concise definition for CRM is:

"CRM refers to an all-embracing management approach, which seamlessly integrates sales, customer service, marketing, field support, and other functions that touch customers" [19].

Today the organization have understood that the customers have become an important resource and it is important to maintain relationship with them, which can be utilized for understanding their preferences and creating offers, products, services as per their needs [11, 14, 4]. CRM is an approach which follows both relationship management and the marketing and management theories and approaches [8]. Effectively managing customer relationships has becoming a task which is being given a higher priority and new

approaches are being used by organizations to improve the customer's satisfaction, sales and customer's loyalty [2, 9].

3. CRM PROCESS FRAMEWORK

A traditional CRM approach comprises of front-end operations that interacts and obtain data about the customer. This data is mostly consolidated from various points of contact with the customer and is fed to a central database warehouse. Apart from this data, the warehouse also collects data from other outside sources and provides a more solid ground for analysis. Data analysis is done by various data mining processes and the output from these process is transferred to a central repository where the firm employees might access it.

With technology being advancing at a fast pace, business organizations have been enabled to automate their business processes. CRM is a consolidated and a broad term which includes processes, strategies and applications working in sync to create a common grounds with customer and they enable organization with a single point of contact when it comes to being connected with customers. To have a healthy relationship with the customers it is imperative to monitor the behaviors and perceptions exhibited by the customer in each transaction and then providing them what they want.

CRM process framework has three functionalities [17]:

1. *Operational*-These are the solutions which involve customer touch points at the front end. Technological applications and systems are integrated into those parts of the business where the customer makes direct contact with the organization or the employee of the firm. This operational has its backend connected to an ERP system which collects the data generated by each interaction. Typical CRM solutions that fit into this category are customer sales and service, sales force automation, marketing automation and field services.
2. *Analytical*-The data collected from the operational is analyzed for improvement in business performance. Using relevant and useful analytical techniques, organizations can forecast regarding customer behavior, identifying relevant customer segments, identifying potential customers etc.
3. *Collaborative*-CRM gives way to facilitation of collaborative channels or services to facilitate interactions between customers and employees. This collaborative effort produces lot of data which is rich in customer information. It analyses the data using data mining and other technologies and in turn feeds the result (i.e. knowledge gained) back to the operational and collaborative CRM technologies.

All customers do not comply positively to the organizations profitability. Some contribute negatively some contribute positively. It is at the organizations behest to nurture the profitable customers. Using CRM to identify and then opening channels of communications using the technology specifically

meant for the purpose is what CRM is being utilized in organizations. It integrates all the front end operations so that the system remembers the customer and all the past interactions. Organizations may enjoy competitive advantage over its competitors by building mutually beneficial relationships with the customers which makes it difficult for the competitors to replicate and for customer to switch over.

4. EMERGING IMPACT OF INTERNET ON CRM

With internet technologies being evolved each year, people have exposure to various applications and internet tools which enhances their experience when it comes to using internet. Somehow this phenomena has infiltrated into their expectations when it comes to marketers engaging and creating relations with their customers. These trends can be as follows [17]:

1. *Increase in globe market space*-Internet has made this world global village where anyone from anywhere; irrespective of the country, region and continent; can communicate with each other. Customers from different regions may indulge in communication pertaining to a similar marketer or a similar market. Thus, involving exchange of information at a global level, which might spread word of mouth about the market or the marketer.
2. *Availability*-Internet is available at all times and thus any service using internet is accessible at any time. Marketers and customers are getting attracted towards various Internet technologies and applications for utilization.
3. *Speed*-Customers expect to be delivered a service at a fast speed. With internet technologies innovating exponentially, Internet speed is increasing and thus using web based application is becoming a need of time as it is better than the conventional methods.
4. *Merging of Time Zones*-Internet Time zone is becoming more and more prevalent as the physical time zones are being merged into each other.

The above trends focus on the efficiency and the better service that can be improvised and improved by using the Internet. CRM has been used as an information system within an organization but using internet its scope can be expanded beyond organization and the customers can be included directly in the CRM system.

5. THE SOCIAL CRM

With new technology emerging as the time advances forward, the dynamics of the on-to-one relationship between the organization and the customers is rapidly evolving. Internet and other technologies has given access to massive amount of information, which gives them deep insights about the any organization, its products, services and pricing etc. This information when amalgamated with the information gathered

by fellow customers and their experiences, thoughts and feeling; shapes their opinions about a product or a service. Web 2.0 and its collaborative technologies such as blogs, wikis, social networking sites etc., play an important part in this exchange of information.

Introduction of Social media has completely changed the scenario of online communication when it comes to meaningful communication between the organizations and their targeted segment in the population. It has also affects the customers and their use of social media to engage themselves and participate in social networks, where they create, share and exchange information with other customers, and build relationships with other customers [8]. By use of social media customers are able to interact with nearly any company and voice their opinion through the social media and social networking channels at their disposal.

It has been suggested by researchers that the CRM Technologies provide a better value to an organization when they are collaborated with other resources and processes within the organization [22; 21, 20]. Merging the present CRM technologies with social media presents a more collaborative approach involving network-focused customer relationship management. Social CRM has emerged as a new term which focuses on this new method of managing customer relationships and developing them [5]. It is defined as a merging and integrating the front end activities where customer is directly engaged, using the social media applications as the new technology to connect with customer in a more collaborative and meaningful conversations leading to better customer relationships [6,18]. Marketers and organizations are now recognizing the immense potential that social media can provide when it comes to connecting and communicating with customers, and have considered investing in CRM technologies which include social media the recent years. Investments on social CRM by organizations has exceeded \$1 billion in 2013 and it is expected to increase higher in the coming years as the social media technologies upgrade themselves [15].

6. SOCIAL CRM FRAMEWORK

Social CRM activities are not based on the problems faced by marketers which are technology driven, and can be solved by technology driven solution by an organization. Instead, all the activities incorporated as the social CRM activities are to taken up and executed as a whole at the organization's cultural levels. To create an environment and to implement Social CRM following capabilities should be developed by an organization [1]:

1. *Monitoring the social web*—Keeping a vigil on the communication going on the social web and collecting data and insights through systematic planning and processes to understand the perceptions, needs, wants and attitude of the customer. This can easily be done by participating in the social web just like any other

customer, and understand the dynamics of the target customers and their communities.

2. *Assessing and analyzing the outcomes of monitoring*—Data collected from the social web is then carefully analyzed to understand the opportunities and threats that prevail in the social web, which can be addressed by using Social CRM
3. *Create strategies and create a framework*—Building a strategy to take up social CRM by selecting various channels which are used by customer on the social web such as blogs, social networking sites, forums, wikis etc. A clear framework or structure is needed to create a guideline with specific purposes.
4. *Testing*—Using a small controllable section of the social web to test the strategy to determine whether the framework and the tools used to implement it are working as desired and calculating the ROI of the social CRM on this controlled testing.
5. *Implementing*—After Testing has been successful it can be implemented after outlining the desired activities on the social web along with defining the necessary systems and tools for this purpose. This is further supported by determining the roles and responsibilities of the employees, their incentives and the business targets.
6. *Review the Activities*—Social web has a dynamic environment which is ever changing. Adapting to this dynamic nature and improvising the social CRM activities, and upgrading them is a must. For this purpose the activities done under social CRM should be regularly assessed.-

This is a step-by-step framework which gives a structure to formulate any social CRM strategy for a successful social CRM implementation, but this framework is not enough as getting each step correct to its details is important. Each step in this framework should acquire capabilities in three major areas which are as follows [1]:

1. *Business Functions*—Building capabilities from generating new ideas and innovation to marketing and then to sales leading to services.
2. *Organizational Structures*—Including skilled people capable of understanding and implementing social CRM and how to adapt dynamically
3. *Incentive Structure*—Designing a structure to promote the use of social CRM and its constant up gradation.

Apart from the above three areas plans for development of the culture within the organization that encourages the use of technology platforms supportive of social CRM which include tools and Social CRM specific systems; and organizational culture which creates an environment for employees and focuses on collaborating with each other and creating a transparent and swift structure within the organization. It is also important to integrate the social CRM activities and processes within the IT architecture of the organization.

7. CHALLENGES FOR MARKETERS

Companies develop a social site to attract sales and they buy monitoring technology to hear what customers are saying, but they fail to use social media as another channel to optimize the customer experience. Following are the challenges marketers might face while implementing Social CRM [1]:

1. *Excess of Information*–Social media generates a lot of data which comprises of both structured and unstructured data. Organizations have a big challenge to process and analyze this heaps and heaps of data generated by social media. They may face a difficult choice of selecting relevant information from the heaps of data and therefore, some important data might get neglected.
2. *Ignoring to Understand the Customers*–Marketers might focus too much on social media sites as a means to direct marketing and generation of new leads; and might completely ignore the important fact that, it is also a channel through which they can listen and understand what the customer perceives about them, their product or their brand. They face a challenge as to creating a web portal or site which engages customers as well as extend support to the customers. Monitoring and responding effectively using the social channels to reach out to the customers is another challenge that the marketers face.
3. *Investment Decision*–Deciding about the level of investment an organization should make on the social technologies comprising of blogs, wikis, forums, social networking sites and other such platforms can be a hard decision which might be difficult to come up to. Apart from this they might also be unsure regarding the monitoring of the social web and selecting the right tools and systems for this purpose

8. CONCLUSION

The emergence of the Social Web established a new information source and interaction channel for individuals. Businesses now start to recognize the Social Web as more than an inexpensive channel for word-of-mouth marketing or targeted advertising through communities. With customers being the center of attention, it is but only logical to couple technologies like social media to existing customer-centric management systems, for better and enhanced performance of the relationship management.

Organizations need to take up social media into account while planning the CRM processes, activities and management systems. Since social media is a source of huge amount of data, organizations need to understand their capabilities of handling, storing and analyzing such big data. By following basic framework of social CRM they can build up their own customized and enhanced social CRM systems.

REFERENCES

- [1] Acker, O., Gröne, F., Akkad, F., Pötscher, F., & Yazbek, R. (2011). Social CRM: How companies can link into the social web of consumers. *Journal of Direct, Data and Digital Marketing Practice*, 13(1), 3-10.
- [2] Armstrong, G., & Kotler, P. (2004). *Marketing: An introduction*. Upper Saddle River: Prentice Hall.
- [3] Berthon, P. R., Pitt, L. F., Plangger, K., & Shapiro, D. (2012). Marketing meets Web 2.0, social media, and creative consumers: Implications for international marketing strategy. *Business Horizons*, 55(3), 261–271.
- [4] Gneiser, M. (2010). Value-based CRM. *Business & Information Systems Engineering*, 2(2), 95-103.
- [5] Greenberg, P. (2010). CRM at the speed of light. *Social CRM strategies, tools, and techniques for engaging your customer*. New York: McGraw-Hill.
- [6] Greenberg, P. (2010). The impact of CRM 2.0 on customer insight. *The Journal of Business and Industrial Marketing*, 25(6), 410–419.
- [7] Grönroos, C. (2000). *Service management and marketing—A customer relationship management approach*. New York: John Wiley & Sons Ltd.
- [8] Gummeson, E. (2002). Relationship marketing in the new economy. *Journal of Relationship Marketing*, 1(1), 37–55.
- [9] Kostojohn, S., Johnson, M., & Paulen, B. (2011). *CRM fundamentals*. New York: Apress.
- [10] Malthouse, E. C., Haenlein, M., Skiera, B., Wege, E., & Zhang, M. (2013). Managing customer relationships in the social media era: introducing the social CRM house. *Journal of Interactive Marketing*, 27(4), 270-280.
- [11] McKenn, R. (1991). *Relationship marketing: Successful strategies for the age of the customer*. Cambridge: MA Perseus Books.
- [12] Minna, R., & Aino, H. (2005). Customer knowledge management competence: Towards a theoretical framework. *Proceedings of the 38th Hawaii International Conference on System Sciences*.
- [13] O'Reilly, T. (2005). *What is Web 2.0-Design Patterns and Business Models for the Next Generation of Software*. <http://www.oreillynet.com>.
- [14] Peppers, D., Rogers, M., & Dorf, B. (1999). Is your company ready for one-to-one marketing. *Harvard Business Review*, 77(1), 151-160.
- [15] Sarner, A., Thompson, E., Davies, J., Drakos, N., Fletcher, C., Mann, J., et al. (July 25). *Magic Quadrant for Social CRM*. Gartner (Retrieved from www.gartner.com).
- [16] Shani, D., & Chalasani, S. (1992). Exploiting niches using relationship marketing. *The Journal of Consumer Marketing*, 9(3), 33-42.
- [17] Srivastava, M. (2012). *Customer Relationship Management (CRM): A Technology Driven Tool*. Editorial Office, 14.
- [18] Trainor, K. J. (2012). Relating social media technologies to performance: A capabilities based perspective. *Journal of Personal Selling and Sales Management*, 32(3), 317–331.
- [19] Xu, Y., Yen, D., Lin, B., & Chou, D. (2002). Adopting customer relationship management technology. *Industrial Management & Data Systems*, 102(8), 442-452.

-
- [20] Chang, W., Park, J. E., & Chaib, S. (2010). How does CRM technology transform into organizational performance? A mediating role of marketing capability. *Journal of Business Research*, 63(8), 849–855.
 - [21] Srinivasan, R., & Moorman, C. (2005). Strategic firm commitments and rewards for customer relationship management in online retailing. *Journal of Marketing*, 69(4), 193–200.
 - [22] Jayachandran, S., Sharma, S., Kaufman, P., & Raman, P. (2005). The role of relational information processes and technology use in customer relationship management. *Journal of Marketing*, 69(4), 177–192.
 - [23] Jelinek, R., Ahearne, M., Mathieu, J. & Schillewaert, N. (2006). A Longitudinal Examination of Individual, Organizational and Contextual Factors on Sales Technology and Adoption and Job Performance. *Journal of Marketing Theory and Practice*, 14(Winter), 7-23.
 - [24] Hunter, G. & Perreault, J. W. D. (2006). Sales Technology Orientation, Information Effectiveness, and Sales Performance. *Journal of Personal Selling and Sales Management*, 26(2), 95-113.

Study of Biodegradation on Packaging Films Derived from Potato Starch and Maleic Anhydride Grafted LDPE and LDPE Polymer

Manjari Sharma

Department of Applied Sciences, Ambedkar Institute of Advanced Communication Technologies and Research,
Geeta Colony, Delhi-110031

Abstract: Maleated low density polyethylene (with 0.5% grafted maleic anhydride) & low density polyethylene have been mixed (1:1) to prepare base material, which has been further mixed with Potato Starch (0-15%) in single step through commercial grade twin screw extruder. Using prepared material packaging films were blown and thus prepared samples were tested for its strength following standard biodegradation testing methods for tensile strength, percentage elongation and for melt flow index. Prepared system should have comparable mechanical strength (tensile and %age elongation which gets severely affected by mixing natural polymer) to that of synthetic polymers like LDPE and should be degradable. Hence, tensile strength, percentage elongation study was conducted and since MFI is indirect indicator biodegradability, MFI study was also conducted to find level of biodegradation among samples. Observations are, after degradation i) 40% tensile strength reduction was found in 15% starch mixed samples during composting study and at the same time 68% percentage reduction in elongation at break was found. MFI study carried out on samples also indicated that MFI has increased in samples of higher starch contents and indirectly indicating the higher possibility of degradation. 20% Weight loss observed indicating the degradability enhanced and probably synthetic polymer backbone got involved in the process for which starch is responsible. It could have been due to chemical reactivity between hydroxyl group of starch and maleic anhydride group of LDPE backbone at molecular level.

Keywords: LDPE: Low Density Polyethylene; LDPE-g-mA: Low Density Polyethylene-grafted-maleic Anhydride; Biodegradable Polymer.

1. Introduction

Large scale commercial use of synthetic polymers and their eco-friendly disposal is a critical phenomenon, which is more than a half century old. The need of biodegradable plastics has significantly increased, not only due to increasing environmental concerns but also due to depletion of petroleum resources likely to be exhausted within 70 years from now, as per recent survey.

Biodegradation is one of the simplest processes, which take place in normal environmental conditions and can be of immense use for degradation of polymeric materials. It is one of the 12 Principles of Green Chemistry which can be implemented through use of natural phenomenon of biodegradation, accordingly study presented here has been planned. The present work aims at preparing a cost effective biodegradable polymer, meeting desired properties requirements, and naturally bio-degradable.

Considering practical approach, natural and synthetic polymers were mixed to create systems. Since, polar and non polar components cannot be mixed directly, starch was chemically treated with glycerol (up to 30%)[1], and low density polyethylene was grafted with 0.5% maleic anhydride. Grafted LDPE and LDPE mixed in a ratio of 1:1 and then mixed with starch (0-30%) (system-I) for preparing the system and its physiochemical characteristics were analysed [2]. Conceptually maleic anhydride present in LDPE shall provide reactive sites for the reaction in between hydroxyl group of starch with anhydride group of LDPE to form ester bond in between polar and non polar components. Thus created system showed improved chemical reactivity

in between synthetic and natural polymer immiscible compounds.

Prepared systems (in different combinations) then have been characterized though, Morphological study, Mass Flow Index, Mechanical testing[2] & weight loss study. Confirmation of chemical reactivity in between maleic anhydride containing low density polyethylene and starch had been done by FTIR:ATR analysis. DSC & XRD analysis indicated that crystallinity decrease linearly with the linear increase in starch contents. XRD confirmed the increase in crystal size of the system which may be attributed to the development of secondary bonds (H-bonds / Vander wall's forces) between the carbonyl group of LDPE & hydroxyl group of starch. Thermal stability of the prepared system did not had any impact of the starch up to 30%. The maleic anhydride group present in the LDPE played a key role in reducing the interfacial energy and thereby promoting the interfacial adhesion between the starch and LDPE-g-mA and the uniformity in the system has been observed through SEM analysis. Study of mechanical properties of prepared system show that the tensile strength and percentage elongation have been decreased with the increase in starch contents. At 5% starch mixing these properties have been decreased marginally while up to 15% the decrease was significant after that these have decreased drastically.

Considering the practical utility as packaging applications and observations as above, in search of finding optimization level of starch in the composition, system has been prepared[3,4]. Accordingly, the starch concentration varied with an interval of 2.5% up to 15% (called as System-II) to

enhance the accuracy of the system where the acceptable level has been obtained.

The system thus prepared from practical application point of view, has been exposed to compost environment under controlled aerobic conditions for biodegradation testing for a

period of one year and then testing of decomposed samples for weight loss, strength & Melt Flow Index has been conducted. The results of this study are presented here. The Sample compositions being referred as System –II are tabulated in Table1.

Table 1: Sample Compositions

S. No. (Films)	LDPE composition	Starch composition	S. No.	LDPE composition	Starch composition
Sample 1	LDPE-g-mA + LDPE	0%	Sample 5	LDPE-g-mA + LDPE	10.0%
Sample 2	LDPE-g-mA + LDPE	2.5%	Sample 6	LDPE-g-mA + LDPE	12.5%
Sample 3	LDPE-g-mA + LDPE	5.0%	Sample 7	LDPE-g-mA + LDPE	15.0%
Sample 4	LDPE-g-mA + LDPE	7.5%			

2. Biodegradation of Polymeric Material

From Chemical Perspective:

Aerobic biodegradation: $C_{POLYMER} + O_2 \rightarrow CO_2 + H_2O + C_{RESIDUE} + C_{BIOMASS}$

3. Biodegradation Methodology

Composting site have been selected at Nursery in Delhi College of Engineering located at latitude 28°45'N and longitude 77°07'E. During sampling, ambient conditions and compost conditions have been monitored. The variation of Average, Minimum, and Maximum Temperatures recorded at the same location in ambient and in compost have been shown in figures 1 to 5.

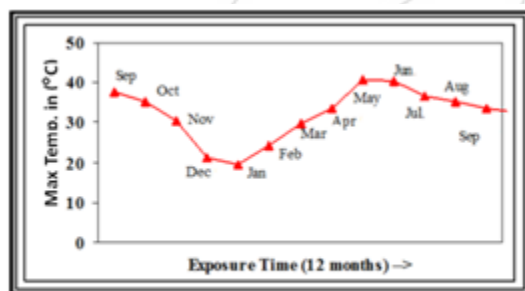


Figure 1: Max ambient temperature changes



Figure 2: Min ambient temperature change

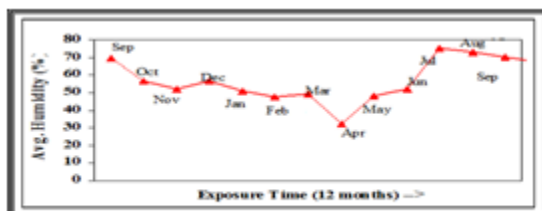


Figure 3 : Avg. ambient humidity (%) change

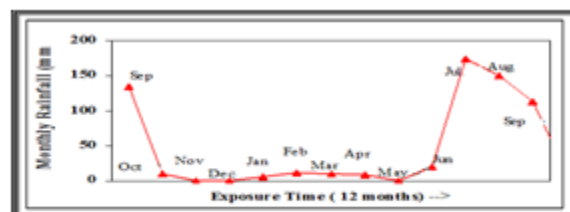


Figure 4: Monthly Rainfall (mm) changes

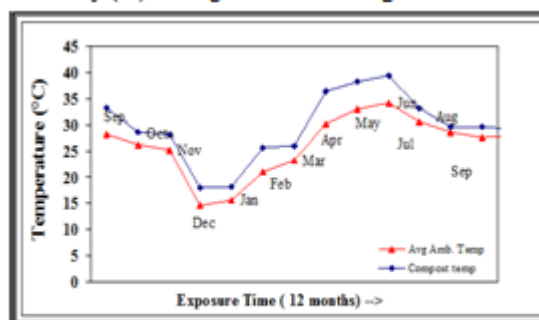


Figure 5: Average Temp variation in ambient and compost

Compost has been prepared as prescribed in the study by Eldsater & Karlsson(1999) [5,6]. The biodegradability test was performed in a laboratory scale composter of 4' x 3' x 6' size. Compost had been prepared more than six months before the sampling. The moisture content was maintained by periodic addition of water in the compost. The composting bin was covered by small fragments of green

grass. For maintaining aerobic conditions in the composting, network of perforated pipes laid down in the bin and have been pumped with normal air compressor.

3.1 Sampling Procedure

- Sample Size: Films of size 5x5 cm in 3 replicates have been used.
- Samples placement: The all samples with three replicates placed in approx. 30cm distance vertically and horizontally in between samples and such kind of 5 layers were made.
- Samples removal: After composting, samples were removed for testing at defined intervals of 1, 3, 6, 9, 12 Months.
- The samples were washed in the distilled water, dried, wrapped in a clean paper and stored at 25°C.

3.2 Constitution of Compost

The biodegradability tests were performed in a laboratory scale composter and the size of films was 5X5 cm. (5 replicates). The constitution [7,8,9] of solid waste mixture (compost) used for biodegradability testing was as follow: (dry 51 weight): 40.8 % shredded leaves, 11.4 % cow manure/ dung, 15.8% newspaper and computer paper, 2% white bread, 7.8 % saw dust, 19.2 % food waste (dry milk, potato, carrot, banana and other vegetables) and 3.0 % urea. Total dry weight was ~5 kg. The moisture content was maintained by periodic addition of water and temperature profile of the compost during testing is shown The composting bin was covered by small fragments of green grass and moisture content was maintained by periodically spraying of water. To avoid anaerobic conditions, the bin was constantly aerated with oxygen through a hollow tube. Composting temperature varied with the temperature of the surrounding atmosphere.

3.3 Evaluation of polymer degradation

The biodegradation levels in the samples were evaluated by measuring the weight loss, tensile properties & Melt Flow Index of the blown film samples at different intervals, so that comparison of properties could be done through the results obtained.

3.4 Biodegradation Assessment:

- a) **Weight Loss:** Weight loss of the films was determined by weighing the samples before and after biodegradation in compost. The percentage weight loss the film samples calculated by following equation (1).

$$\text{Weight Loss (\%)} = \frac{W_i - W_f}{W_i} \times 100 \dots \text{Equation (1)}$$

Where W_i is the initial weight of the sample before degradation (g). And W_f is the final weight of the sample after degradation (g)

- b) **Tensile Properties (ASTM D-882):** Tensile test of rectangular film specimen (10x180) mm have been conducted using Universal Testing Machine at a crosshead speed of 50 mm/ min and a gauge length of 10 cm according to ASTM D882. At least (05) five specimens of each sample were tested.
- c) **Melt Flow Index (MFI) (ASTM D-1238)** The MFI of biodegradable samples calculated using instrument M/s Rosand UK make. The working capacity of the instrument is in the range of 0-325°C with an accuracy of $\pm 0.1^\circ\text{C}$. ASTM D 1238 method has been adopted for the testing.

4. Results and Discussion

4.1 Weight Loss study

The variation of %Weight loss in samples having starch composition up to 15% during composting is shown in figure 6.

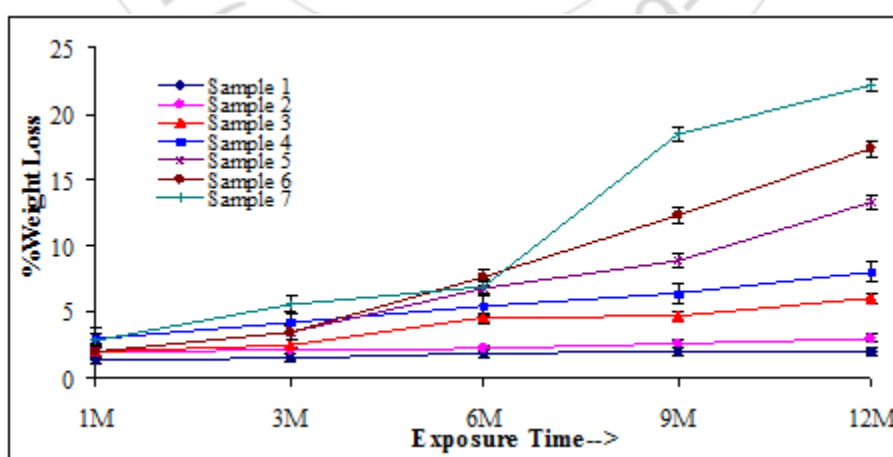


Figure 6: Variation of % Weight loss in Samples of 15% Starch during composting

It may be seen that the percentage weight loss of the biodegradable films increased with increasing potato starch incorporation in agreement to the result obtained by Pranamuda [8]. The percentage weight loss of the samples takes place by the hydrolysis mechanism. Hydrolysis occurs at the ester linkages, which allows the molecular weight of

the samples to be decreased by fungi and bacteria in the compost.

Weight loss increases with the increase of exposure duration. Weight loss within the period of investigation has ranged from 1.3 to 3% in the first month of degradation

which have gone up from 1.96 to 22.1% in 12 months. However, other studies have indicated weight loss of maximum 2% in 12 months for starch- polyethylene composites having 25.0% starch in LLDPE [9]. Observation of weight loss during the study period shows that weight loss was highest during 6-9 months duration (summer season). The weight loss was 11.56% for the sample No.7 having 15% starch. The increased rate of degradation may be attributed to the environmental conditions during this period. Since, Delhi is very close to semi arid zone the maximum ambient temperature shooted up to 38.8°C during winter months and relative humidity have gone up to 75.3 % (%RH) during monsoon season. At this point of time the temperature and humidity inside the compost remains even higher. Ishak et al. [10] have suggested that attack of micro-organisms is high during warm and humid climatic conditions causing degradation of properties and product failure.

Microorganisms attack on samples and liberate enzymes that breakdown potential food into assimilable chemical fragments. Here, in the samples degradation humid and warm environment might have facilitated the enzymatic attack, where micro-organisms have attacked the polymer films samples and liberated more and more enzymes. Because of which highest weight loss in the study duration have been recorded. The micro-organisms attack here on the samples of biodegradable polymer composition (LDPE grafted with maleic anhydride / LDPE (1:1) in various compositions of potato starch contents) have not only break down the potato starch but also attacked on the LDPE backbone which is rich in oxygen containing ester group. Hence, total 22.1% degradation of the samples having maximum starch contents of 15% show that the degradation in the LDPE backbone has also taken place. This is inline to the expectations considered for selection of materials and grafting with maleic anhydride for preparing biodegradable polymer.

4.2 Mechanical Properties Study

The degradation of mechanical properties of samples of 15% starch contents during composting has been studied with respect to tensile strength and percentage elongation.

a) Tensile Strength and Percentage Elongation

Figure 7 and 8 show the loss in tensile strength and percentage elongation of blown film samples (LDPE grafted with maleic anhydride / LDPE (1:1) in various compositions of potato starch 15% contents) plotted against exposure time during composting. As the micro-organisms consumed starch, the plastic matrix loses its structural integrity which is reflected in the decline of tensile properties. After six month's exposure of film samples in compost, tensile strength of the film samples has reduced up to 42% while elongation at break has reduced up to 69% of the corresponding initial values.

The elongation at break is the most affected parameter and it is observed to be more sensitive measure to the extent of degradation than the tensile strength. It is clear from the results that the decline of elongation is greater in film sample having higher starch contents. This is because the

elongation at break of LDPE depends on its density and hence on its degree of crystallinity, [11-13] the denser and hence the more crystalline material, less ductile it becomes.

This decrease in mechanical properties may be attributed to the phenomenon of moisture absorption inside the compost. Water has plasticization effect on starch based plastics. The absorption of water by film, due to hydroxyl group of starch, decreases H-bonding between the polymer chains resulting in plasticization of the sample. This leads to swelling of starch and likely to weaken the interface in the starch polyethylene composition.

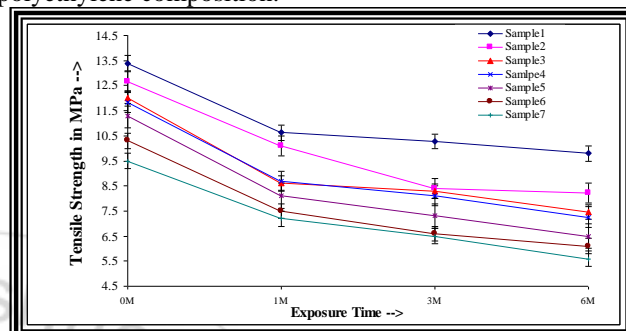


Figure 7: Variation of Tensile Strength

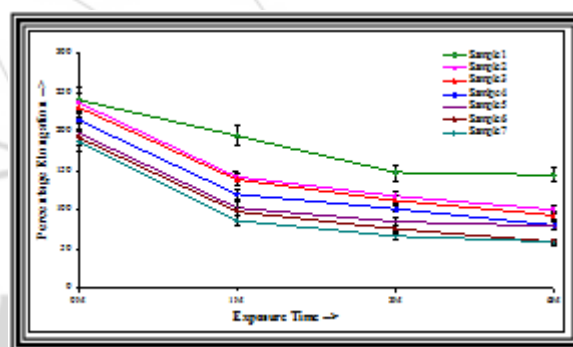


Figure 8: Variation of Percentage Elongation

4.3 MFI : Melt Flow Index (MFI) (ASTM D- 1238)

Melt flow index measures the rate of extrusion of plastic materials passing through specific length and diameter under prescribed conditions of temperature and load. The different grades of same polymers have different MFI value, which is used to characterize them. MFI gives the idea about the uniformity of the flow rate of the plastic. MFI is indirect measurement of degradation. The MFI study is the macroscopic study of the plastic material, which is directly related to the molecular weight of the test specimen of that polymeric material. MFI of all samples have increased with the exposure time of the compost. Initially it was having no significant impact, however after three months this has increased significantly and after six up to 12 months it has increased more than two folds. Which indicate the continuous degradation of samples.

5. Percentage Reduction

Percentage reduction in properties of LDPE/LDPE grafted maleic anhydride/starch biodegradable polymer films with time of composting have been given in figure 9 which have been observed during composting of prepared samples of biodegradable polymer blown films.

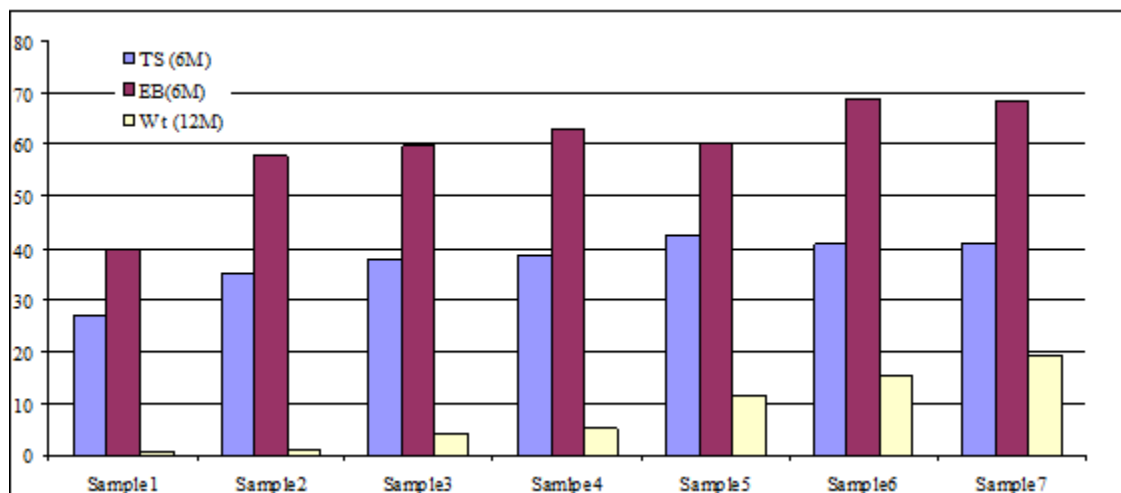


Figure 9: Percentage reduction in properties of LDPE/LDPE grafted maleic anhydride/starch biodegradable polymer films with time of composting

TS – Tensile Strength EB – Elongation at Break, Wt – Weight Loss

6. Conclusion

These 15%starch content based blown film samples were exposed in compost environment for the biodegradation study. The degraded samples over the span of 12 months were analyzed through Weight loss analysis, Mechanical properties analysis and MFI.

The biodegradation study indicated that the overall percentage reduction in tensile strength was nearly 40%, percentage reduction & in Elongation at break was nearly 68% and percentage reduction & in weight loss of the degraded film samples was near 20%. The weight loss of nearly 20% indicates that the introduction of maleic anhydride group in the LDPE, which formed the ester bond with hydroxyl group of starch, has helped in the degradation of film samples.

References

- [1] Gupta A. P., Sharma Manjari, and Kumar Vijai, J. Poly. Plast. Tech. Eng., 47, 953-959(2008).
- [2] A. P. Gupta, Vijai Kumar, Manjari Sharma, and S. K. Shukla, Taylor and Francis Group, UK, 48,6, 587-594(2009).
- [3] A. P. Gupta • Vijai Kumar • Manjari Sharma, Journal of Polymers and the Environment, Springer, 18, 484–491(2010)
- [4] A. P. Gupta • Manjari Sharma* , Journal of Polymers and the Environment, Springer, 18, 492–499 (2010).
- [5] C.Eldsater, S.Karlsson, and A.C. Albertsson, Polym Degrad Stab, 64 (1999), p.177.
- [6] Carina Eldsaeter, Sigbritt Karlsson, Ann-Christine Albertsson, Polym Degrad Stab, 64; 177-183: 1999.
- [7] Jitendra K. Pandey, K. Raghunatha Reddy, A. Pratheep Kumar and R.P. Singh. Polym. Degrad. Stab., 88(2); 234-250:2005.
- [8] Pranamuda H., J Envir Polym Degrad, 4;1-7:1996.
- [9] Goheen S. M. and Wool R. P., J Appl Polym Sci, 42;2691-2701: 1991.

- [10] Ishak Mohd., Taib R, Ishaku US, Chapter 4, Handbook of Engineering Biopolymer, Stoyko Fakirov Devis Bhattachryya, Hanser Publication, Munich, 126,137,144-147:2007.

- [11] Chandra, R. and Rustogi R., Polym. Degrad Stab, 56;185-202:1997.

- [12] Dalev P. G., Patil R.D.,Mark J. E., Vassileva E. And Fakirov S., J Polym Sci, 78;1341-1347: 2000.

- [13] Valles-Lluch A, Contat-Rodrigo L and Ribes-Greus A, J Appl Polym Sci, 90; 3359-3373:2003.

ASTM Methods

- 1) ASTM D-882: Standard Test Method for Tensile Properties of Thin Plastic Sheeting
- 2) ASTM D-1238: Standard Test Method for Melt Flow Rates of Thermoplastics by Extrusion Plastometer.

Sustainable bis-benzoxazines from cardanol and PET derived terephthalamides

Pratibha Sharma, Bimlesh Lochab, Devendra Kumar, and Prasun Kumar Roy

ACS Sustainable Chem. Eng., **Just Accepted Manuscript** • DOI: 10.1021/
acssuschemeng.5b01153 • Publication Date (Web): 14 Dec 2015

Downloaded from <http://pubs.acs.org> on December 20, 2015

Just Accepted

"Just Accepted" manuscripts have been peer-reviewed and accepted for publication. They are posted online prior to technical editing, formatting for publication and author proofing. The American Chemical Society provides "Just Accepted" as a free service to the research community to expedite the dissemination of scientific material as soon as possible after acceptance. "Just Accepted" manuscripts appear in full in PDF format accompanied by an HTML abstract. "Just Accepted" manuscripts have been fully peer reviewed, but should not be considered the official version of record. They are accessible to all readers and citable by the Digital Object Identifier (DOI®). "Just Accepted" is an optional service offered to authors. Therefore, the "Just Accepted" Web site may not include all articles that will be published in the journal. After a manuscript is technically edited and formatted, it will be removed from the "Just Accepted" Web site and published as an ASAP article. Note that technical editing may introduce minor changes to the manuscript text and/or graphics which could affect content, and all legal disclaimers and ethical guidelines that apply to the journal pertain. ACS cannot be held responsible for errors or consequences arising from the use of information contained in these "Just Accepted" manuscripts.



Sustainable bis-benzoxazines from cardanol and PET derived terephthalamides

Pratibha Sharma^{a,b}, Bimlesh Lochab^{c**}, Devendra Kumar^b, Prasun Kumar Roy^{a*}

- a. Centre for Fire, Explosive and Environment Safety, DRDO, Timarpur, Delhi 110054, India.
- b. Department of Applied Chemistry and Polymer Technology, Delhi Technological University, Delhi 110042, India.
- c. Department of Chemistry, School of Natural Sciences, Shiv Nadar University, UP 203207, India.

Corresponding author. Tel.: +911123907191; Fax: +911123819547.

Co-corresponding author. Tel.: 0120-2663801

* E-mail addresses: pk_roy2000@yahoo.com (Prasun Kumar Roy)

** bimlesh.lochab@snu.edu.in (Bimlesh Lochab)

Abstract

This paper deals with the preparation of sustainable benzoxazines which exhibit enormous potential to compete with the existing petro-based advance performance thermosets. The phenolic component used for the synthesis of benzoxazine is derived from naturally occurring cardanol, which is obtained from cashew nut tree, *Anacardium occidentale*. Polyethylene terephthalate (PET) was chosen as a sustainable feedstock for the amine fraction used to prepare benzoxazine monomer containing amide linkages. Microwave assisted aminolysis of PET was performed to obtain bis-(amino-ethyl) terephthalamide (BAET) and α,ω -aminoligo(ethylene terephthalamide) (AOET), which were employed as the difunctional amine for the preparation of bis-benzoxazines. In comparison to traditional method, microwave assisted aminolysis of PET was found to be significantly faster and the reaction completion time could be brought down appreciably. Mannich like condensation of cardanol with PET derived terephthalamides and paraformaldehyde led to the formation of bis-benzoxazines with amide linkages, the structure of which was confirmed through FT-IR and $^1\text{H-NMR}$ spectroscopy. The curing behavior of the bis-benzoxazines was studied using non-isothermal Differential Scanning Calorimetry. The presence of amide linkages in addition to the polar group formed during the ring opening of benzoxazines led to the improvement in adhesive strength which was quantified in terms of lap shear strength.

Keywords: Sustainable, Benzoxazine, recycling, cardanol, adhesive

Introduction

Exploring alternative renewable feedstock's to meet the ever increasing demands of the chemical industry is an essential step towards sustainable development. The generic aim of the present research is to explore the possibility of deriving economically viable and sustainable polymeric resins from renewable sources for application as advanced performance thermosets. Polybenzoxazines belong to a sub-class of phenolic thermosetting resins, which exhibit extremely exciting properties, notably negligible volume shrinkage during curing¹, low water absorption² and thermal stability without compromising on the excellent mechanical performance³⁻⁴. In fact, benzoxazines are bridging the gap between the mechanically strong polyepoxies and thermally stable maleimides. In addition, the flexibility in molecular designing made possible through the astute choice of the amine and phenolic components bestow an extremely interesting feature to these materials in terms of tunability, which open up new vistas of application⁵⁻⁸.

In the quest to derive sustainable benzoxazines, cardanol nut shell liquid (CNSL) was chosen as the source of phenolic component for the present study. CNSL being a non edible oil, its use as a chemical raw material does not impose any significant pressure on the food-chain. Replacement of petro-based raw material with CNSL for the chemical industry appears to be an extremely attractive proposition, in view of its low cost, relative abundance, and chemically reactivity, amongst other attributes⁹. CNSL is primarily composed of anacardic acid (74-77%), the rest being cardanol, cardol, and 2-methyl cardol. However, commercial-grade CNSL is obtained through roasting which results in the decarboxylation of anacardic acid into cardanol¹⁰. Furthermore, the components of CNSL are themselves mixtures of another four constituents which differ in the degree of unsaturation in the alkyl side chain, namely saturated (5–8%), monoene (48–49%), diene (16–17%) and triene (29–30%)¹¹. The use of cardanol based benzoxazines as the matrix material for fiber-reinforced composites is

well reported ^{8, 12}. The long alkyl chain present in cardanol acts as an intramolecular plasticizer ^{9, 13}, which reduces the viscosity of the resin and renders it suitable as a reactive diluent for commercial benzoxazine resin¹⁴⁻¹⁵. The alkyl chain also increases the flexibility of molecular segments which reflects in their lower glass transition temperature (T_g)¹⁶, however the same leads to higher curing temperatures¹⁴.

Benzoxazines offer extremely interesting possibilities in terms of molecular design flexibility. Introduction of functional groups in addition to the oxazine ring can alter the properties of the resin appreciably¹⁷. In this context, the amide groups bestow flame retardance, chemical resistance and excellent mechanical properties, due to which polyamides find extensive application in fiber and film technology. It is therefore of interest to design benzoxazine monomers containing amide groups in the chain ¹⁸⁻¹⁹. Terephthalamides obtained by aminolysis of polyethylene terephthalate (PET) offer interesting candidacy to prepare diamines with amide groups for possible application as a precursor for synthesizing such bis-benzoxazines.

Bis-benzoxazine preparation usually relies on the reaction of bisphenols with amines²⁰⁻²¹, however the potential of diamines has also been explored^{3, 22-24}. Tertiary recycling of PET using diamines leads to terephthalamides terminated with amine functionalities ²⁵⁻²⁶. The kinetics of PET aminolytic depolymerisation is a rather slow process ²⁷⁻²⁸ due to the heterogeneous nature of the reaction medium ²⁹. Literature, however supports microwave assisted aminolysis as a propitious route towards tertiary recycling of PET wastes ³⁰.

We considered it of interest to reduce the energy requirements for preparation of terephthalamides based amines, by using microwave energy source instead of the conventional heating process. This article presents an environmentally benign process to chemically recycle PET waste into benzoxazines, a value added, industrially significant high

performance material. The monomers were polymerized via thermal ring-opening polymerization to obtain polybenzoxazines with adhesive characteristics.

Experimental

Materials

Post-consumer plastic bottles were used as the source of PET. Disposed off bottles were collected, washed, dried and used after removing the caps and labels. Bottles were cut into small pieces (6 mm x 6 mm), before microwave assisted aminolysis in the presence of ethylene diamine (ED). Cardanol ($\rho = 0.9272\text{--}0.9350\text{ g cm}^{-3}$; iodine value 250; Acid Value Max 5; Hydroxyl Value 180-190) was obtained from Satya Cashew Chemicals Pvt. Ltd. (India). Cardanol possess double bonds in the alkylene chain at the m-position, as monoene (25%), diene (40%) and triene (34%), and unidentified product (rest). The HPLC trace of cardanol is presented in the supplementary section (Figure S1)²⁴. Paraformaldehyde, ethylene diamine; sodium sulphate and chloroform from CDH were used as received. Double distilled water was used throughout the course of this work.

Characterization

Fourier Transform Infrared (FT-IR) spectra of samples were recorded using a Thermo scientific FT-IR (NICOLET 8700) analyzer with an attenuated total reflectance (ATR) crystal accessory. The angle of incidence of the germanium ATR crystal used was characteristically 45° and the spectra was recorded in the wavelength range 4000-500 cm^{-1} , with a resolution of 4 cm^{-1} . Bruker AC 500 MHz Fourier Transform Nuclear Magnetic Resonance (FT-NMR) spectrometer was used to record the ^1H -NMR of the samples. The spectrum was recorded in deuterated chloroform (CDCl_3) and dimethylsulphoxide (DMSO) using tetramethylsilane (TMS) as the internal standard. Thermal behavior was investigated using Perkin Elmer Diamond STG-DTA under N_2 atmosphere (flow rate = 50 ml min^{-1}) in the temperature range

50-700 °C. A heating rate of 10 °C/min and sample mass of 5.0 ± 0.5 mg was used for each experiment. Calorimetric studies were performed on a differential scanning calorimeter (DSC) (TA instruments Q 20). A heating rate of $10^\circ\text{C min}^{-1}$ and sample mass of 5.0 ± 0.5 mg was used for each experiment. For dynamic DSC scans, samples (10 ± 2 mg) were sealed in aluminum pans, and heated from 0 to 300 °C at $10^\circ\text{C min}^{-1}$ under Nitrogen atmosphere to minimize oxidative degradation of the sample during curing. Prior to the experiments, the instrument was calibrated for temperature and enthalpy using standard Indium and Zinc. Thermal equilibrium was regained within 1 min of sample insertion, and the exothermic reaction was considered to be complete when the recorder signal leveled off to the baseline. The total area under the exothermic curve was determined to quantify the heat of curing and % crystallinity. The enthalpy of fusion associated with the melting of pristine PET ($\Delta H_{f,100\% \text{ crystalline}}$) has been reported to be 135.8 Jg^{-1} ³¹.

The surface morphology of samples was studied using a Scanning Electron Microscope (Zeiss EVO MA15) under an acceleration voltage of 1 kV. Samples were mounted on aluminium stubs and sputter-coated with gold and palladium (10 nm) using a sputter coater (Quorum-SC7620) operating at 10-12 mA for 120 s.

High performance liquid chromatography analysis of the PET aminolysates was performed using an Agilent Technologies 6540 series HPLC instrument equipped with a C18 column (Grace Alltima, 150mm long x 4.6 mm), Mobile phase: Methanol; Flow rate: 1.5 mL/min; UV detection at 280 nm. The Mass spectra was recorded using a High resolution mass spectrometer equipped with electrospray ionization interface (ESI). Positive ion mode was used for all the analyses and cationizing agents were not employed.

Lap shear strength (LSS) of bonded steel plates (Roughness, R_a 0.42–0.51 μm) was measured in accordance with ASTM standard D1002 using Universal Testing System (International equipments) at a crosshead speed of 1.3 mm min^{-1} .

Microwave assisted aminolysis of PET

PET depolymerisation was performed in a microwave reactor (Anton Paar Monowave 300) equipped with a digital temperature control and pressure monitoring system using 30 mL teflon coated silicone sealed borosilicate glass reaction tube. PET flakes (1g) together with requisite amounts of ethylene diamine were sealed under nitrogen atmosphere and allowed to react under isothermal conditions at different temperatures (100-250 °C) in a microwave synthesiser. The PET:ED molar ratio was varied from 1:2 to 1:16 to investigate the effect of the same on the PET conversion. The reaction vessel was cooled to room temperature and the mixture was filtered through a copper wire mesh (0.5 x 0.5 mm pore size). The remaining PET flakes were weighed and the extent of PET conversion was determined gravimetrically as follows^{29, 32}:

$$\text{PET conversion(\%)} = \left(\frac{M_{\text{PET, Initial}} - M_{\text{PET, residual}}}{M_{\text{PET, Initial}}} \right) \times 100$$

where, $M_{\text{PET, Initial}}$ and $M_{\text{PET, residual}}$ refer to the initial mass of PET and the mass of PET flakes remaining unreacted in the reaction medium respectively.

The white product formed as a result of PET aminolysis is a mixture of terephthalamides, which can be separated on the basis of their solubility difference in ethanol²⁶. For separation purposes, the aminolysed product was refluxed in ethanol for 2 h, followed by filtration after cooling to room temperature. The ethanol insoluble residue (Part A) was washed with acetone and dried at 50 °C for 24 h. The filtrate was concentrated and placed in an ice bath to yield crystalline powder (Part B) which was filtered, washed with acetone to remove unreacted ethylene diamine and ethylene glycol, prior to drying at 40-45 °C for 6 h. Mass spectrometry, as discussed later, suggest that the ethanol soluble fraction (part B) is bis-(amino ethyl) terephthalamide (BAET,

$\text{NH}_2\text{CH}_2\text{CH}_2(\text{NHCOC}_6\text{H}_4\text{CONHCH}_2\text{CH}_2)_n\text{NH}_2$ where $n = 1$), while the ethanol insoluble fraction (Part A) comprised of α,ω -aminoligo(ethylene terephthalamide) (AOET, $\text{NH}_2\text{CH}_2\text{CH}_2(\text{NHCOC}_6\text{H}_4\text{CONHCH}_2\text{CH}_2)_n\text{NH}_2$ where $n \geq 2$).

Preparation of Bis-benzoxazine containing amide groups

A mixture of cardanol (5g, 16.4 mmol) BAET (2.06 g, 8.2 mmol), and paraformaldehyde (1 g, 32.9 mmol), was slowly heated to 80°C under constant stirring for 1 h, followed by heating at 90 °C for 2 h. The reaction led to the evolution of water and the colour of the reaction medium changed from yellow to red brown. Upon cooling, water (10 mL) was added and organic layer was extracted with chloroform (20 mL). The organic layers were combined and washed with aqueous NaOH solution (0.5 N, 100mL) followed by washing with water (3 x 30 mL), drying over sodium sulphate and filtration. The solvent was removed under reduced pressure to give C-BAET as a red sticky oil. Yield 88 %.

The method for the preparation of C-AOET is similar to that of C-BAET, except the amount of reactants used: cardanol (5 g, 16.4 mmol), paraformaldehyde (1 g, 32.9 mmol), AOET (3.62 g, 8.2 mmol) was slowly heated to 80 °C and maintained under stirring for a period of one hour, followed by heating at 90 °C for 4 h. C-AOET was obtained as red sticky oil. Yield 83%.

Adhesive strength of resin

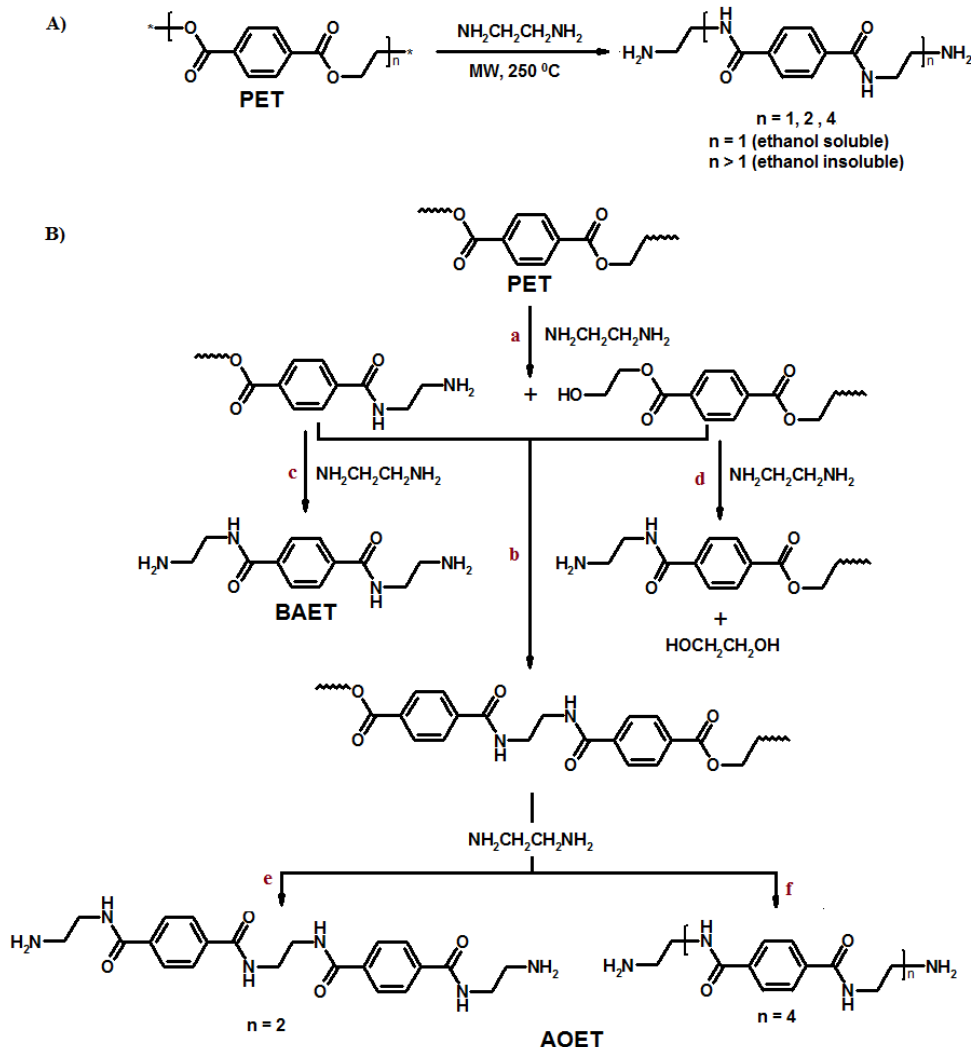
To quantify the adhesive nature of the bis-benzoxazines, ~ 0.05 g of the liquid resin was coated on steel plates ($15 \times 15 \text{ mm}^2$). The assembly was clamped with paper clips and kept at 80 °C for 30 min, and cured in an air oven at 80 -180 °C (30 min) followed by heating at 214 °C (1 h) for the C-BAET and 238 °C (1 h) for C-AOET. The thickness of adhesive layer was maintained at ~ 0.23-0.46 mm. A total of 6 replicates were tested per sample and the average value has been reported.

Results and Discussion

Microwave assisted aminolysis of PET in the presence of ethylene diamine was performed to yield terephthalamides which were used to synthesize sustainable bis-benzoxazine containing amide groups by reacting with cardanol as a renewable source of phenol.

Aminolysis of PET

Detailed characterization of PET is presented in the supplementary section (Figure S2-S3). As is apparent from the DSC and TG traces, PET exhibits a sharp melting endotherm peaking at ~246 °C (crystallinity = 27.2 %) and undergoes a single step pyrolytic degradation commencing at 400 °C. Aminolytic depolymerization of PET was performed under microwave irradiation with an aim to reduce the reaction time and energy as compared to the conventional process. The reaction is expected to result in the formation of terephthalamides of different molecular weights as per the reaction scheme presented in Scheme 1A, the product composition being dependant on the relative quantities of PET and ethylene diamine in the reaction medium. In the presence of excess ethylene diamine, formation of bis(2-amino ethyl) terephthalamide (BAET) is expected, as shown in Scheme 1B(c). However, the condensation of the half-aminolysed moiety with the terminal ester group of PET, followed by its further aminolysis results in the formation of higher oligomers i.e α,ω -aminoligo(ethylene terephthalamide) (AOET) as per the reaction (b)-(f) in Scheme 1B³³⁻³⁵, which was separated from BAET based on solubility differences in ethanol²⁶. Higher molecular weight terephthalamide (AOET) is ethanol insoluble, while BAET, being ethanol soluble was recovered through solvent evaporation. The designated names, structural representation and masses of the products are given in Table 1. The terephthalamides obtained through PET aminolysis were characterized using mass spectrometry.



Scheme 1: A) Aminolysis of PET B) Oligomer formation during PET aminolysis.

The mass spectrum of ethanol soluble terephthalamide fraction (Part B) eluted at 0.389-0.649 min is presented in Figure 1. The associated chromatogram is presented in the inset. The appearance of peak at m/z 251.1510 in the spectrum is attributed to the presence of BAET ionized by H^+ . The other peaks at 273.1210 is due to BAET ionized by Na^+ and fragments for $[BAET-NH_2]^+$ at m/z 234.1263, $[BAET-2NH_2]^+$ at m/z 215.1297 which suggest the molecular formula of BAET to be $NH_2CH_2CH_2NHCOC_6H_4CONHCH_2CH_2NH_2$.

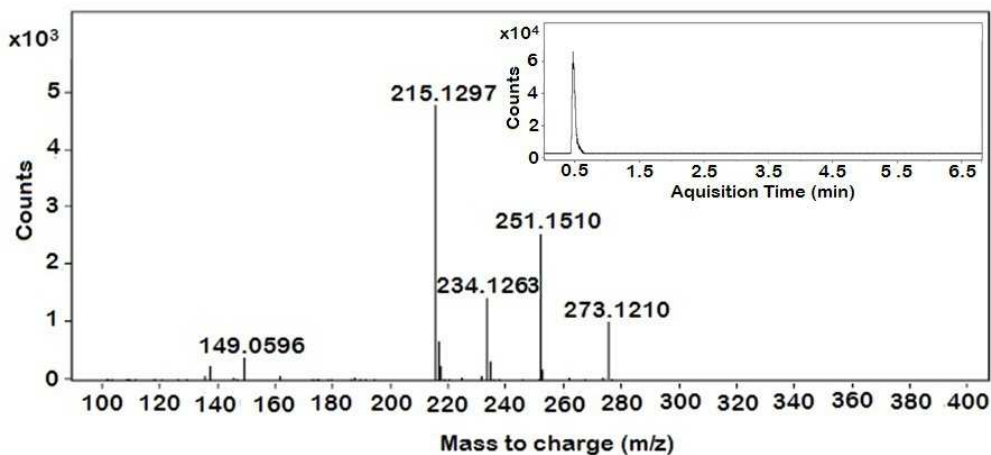


Figure 1: Mass spectra of ethanol soluble terephthalamide fraction eluted at 0.389-0.649 min.

The mass spectrum of ethanol insoluble fraction (Part A) eluted at 0.116 min is presented in Figure 2 and the associated chromatogram is presented in the inset. The peak profile is suggestive of the presence of more than a single component. The principal constituent terephthalamide in part A, $\text{NH}_2\text{CH}_2\text{CH}_2(\text{NHCOC}_6\text{H}_4\text{CONHCH}_2\text{CH}_2)_n\text{NH}_2$, is the dimer ($n=2$) which is confirmed by the appearance of peak at m/z 441.2227. However, the presence of tetramer ($n = 4$) is also confirmed by the appearance of peak at m/z 881.4319 ($n=4$) ionized by H^+ (Table 1).

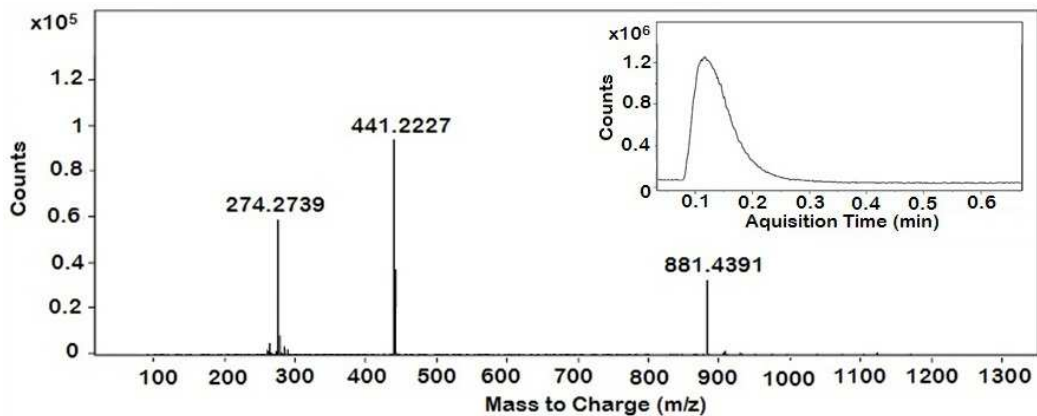


Figure 2: Mass spectra of ethanol insoluble terephthalamide fraction eluted at 0.116 min.

Table 1: The molecular formula and expected molecular masses of the terephthalamides.

Designation	Molecular Formula	Expected Molecular Mass (amu)
BAET (ethanol soluble fraction)	$\text{NH}_2\text{CH}_2\text{CH}_2\text{NHCOC}_6\text{H}_4\text{CONHCH}_2\text{CH}_2\text{NH}_2$	250.1430
AOET (ethanol insoluble fraction)	$\text{NH}_2\text{CH}_2\text{CH}_2(\text{NHCOC}_6\text{H}_4\text{CONHCH}_2\text{CH}_2)_n\text{NH}_2$	440.2172 (n=2) 880.4348 (n=4)

Effect of reaction temperature on PET conversion

The effect of increasing temperature on PET aminolysis was studied by following the extent of PET conversion, the results of which are presented in Figure 3. As expected, an increase in the reaction temperature led to an increase in PET conversion. At lower temperatures ($T \leq 150^\circ\text{C}$), PET conversion is rather negligible ($\leq 2\%$). However, as the temperature is raised to 250°C , complete conversion can be effected within 10 min.

The notable increase in the rate can be attributed to the melting of the solid PET flakes at 246°C , which leads to the formation of a homogenous reaction medium. On the other hand, the solid-liquid reaction remains largely diffusion controlled, which accounts for the slower rates of reaction at lower temperatures²⁶.

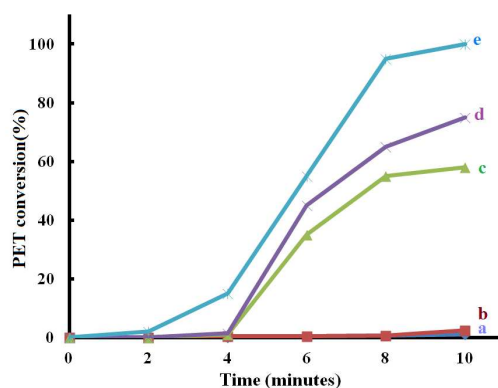


Figure 3: PET conversion as a function of the reaction temperature and time a) 100 b) 150 c) 220 d) 230 e) 250 °C (PET:ED::1:6)

Aminolysis initiates at the solid-liquid interface with the diffusion of the amine into the solid PET, resulting in the swelling of the polymer followed by its depolymerization into terephthalamides of lower molecular weight. Amorphous regions are expected to be more susceptible to degradation^{29, 36} which was confirmed by morphological investigations. The SEM images of the surface of recovered PET are presented in Figure 4. It can be seen, the smooth surface of neat PET develops cracks, with the extent of corrugation increasing with time. The crystallinity of PET flakes was found to increase from 27.2 to 37.2 % due to diffusion of lower terephthalamides from PET as well as solvent induced crystallization of the polymer³⁷.

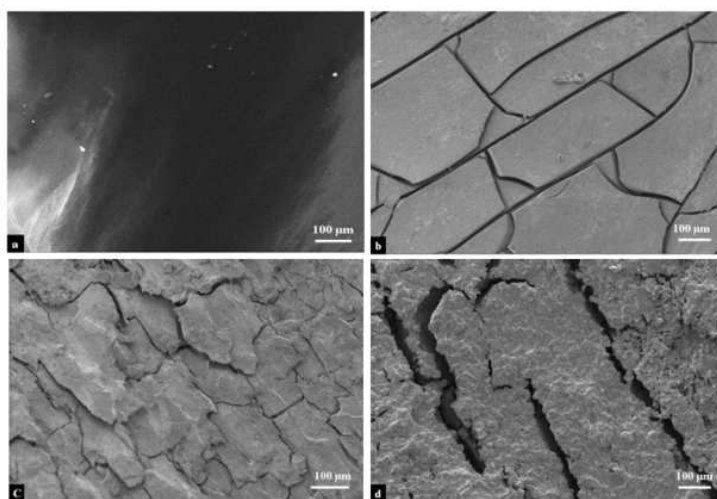


Figure 4: Scanning electron micrographs of PET films (a) Neat PET films and residual PET after reacting with ethylene diamine for duration of (b) 4 (c) 6 (d) 8 mins.(reaction temperature=230 °C, PET:ED :: 1:6)

Representative plots showing the variation of operating parameters during microwave assisted PET aminolysis at two different temperatures (230 and 250 °C) is presented in the supplementary section (Figure S4). It can be seen that the temperature and pressure increase initially and remain practically constant thereafter, while the microwave power drops significantly after the rapid initial increase.

PET aminolysis has been reported to be a slow process requiring extended time periods for completion. A recent study revealed that the uncatalysed aminolytic depolymerisation of PET under electrical heating required more than 17 h, in the presence of excess ED (PET:ED::1:8)²⁶. Our studies are clearly suggestive of the advantages associated with microwave assisted PET aminolysis. The same is attributed to the high loss factor of ED ($\delta = 0.573$), which is indicative of the strong ability of the diamine to convert electromagnetic energy to heat³⁸⁻³⁹.

Effect of reactant ratio on PET conversion and product composition.

The effect of increasing PET:ED on the extent of PET conversion is presented in Figure 5(i). It is to be noted that on the basis of stoichiometry (Scheme 1), PET:ED of 1:2 is sufficient to effect complete depolymerization of PET. However, under these conditions, only 30 % conversion could be effected, which increased with increasing amounts of ED in the reactant medium. Complete PET conversion could only be effected as the PET:ED ratio increased to 1:6, under the experimental conditions employed.

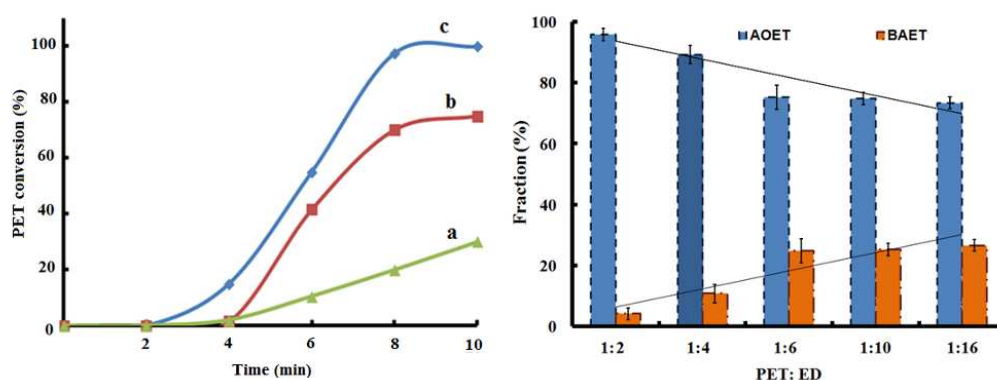


Figure 5: i) PET conversion as a function of reaction time and PET : ED ratio a) 1:2 b) 1:4 and c) 1:6 ii) Relative fraction (%) of AOET & BAET as a function of PET:ED ratio (reaction temperature 250 °C, time= 10 mins)

The effect of varying PET: ED ratio on the relative fraction (%) of AOET and BAET is presented in [Figure 5\(ii\)](#). As per Carothers relation, increasing the stoichiometric imbalance between the reactants in the system precludes the formation of higher molecular weight species⁴⁰. Assuming that all the ester linkages in PET have equal probability of undergoing aminolysis, regardless of their position in the chain and the molecular weight of the polymer, the extent of depolymerisation resulting in the formation of lower molecular weight terephthalamides is expected to increase with higher amounts of ED in the reaction medium. It can be seen that the product mixture obtained at lower PET:ED comprise primarily of higher species (AOET) with lesser amounts of BAET, the amount of which increases with increasing ED. Interestingly, increasing the amount of ED in the medium beyond PET:ED:: 1:6 did not exert any pronounced effect on the product composition. The variation in BAET yield (%) with PET:ED ratio, as quantified in terms of the ratio of amount of BAET experimentally obtained to the theoretical prediction is reported in the supplementary section ([Figure S5](#)), which shows that maximum BAET yield can be obtained under PET:ED ::1:6 at a reaction temperature of 250 °C.

As expected, the FT-IR spectra of AOET and BAET ([Figure S6](#), Supplementary Section) is rather similar, with characteristic $\nu_{\text{C=O,amide}}$ at 1626 cm^{-1} , $\nu_{\text{N-H,1}^\circ}$ at 3342 cm^{-1} and $\nu_{\text{N-H,2}^\circ}$ at 3280 cm^{-1} ⁴¹. The relative intensity of the peaks associated with NH stretching of 1° and 2° amines in BAET was higher as compared to AOET, which was quantified in terms of the ratio of their absorbance. This ratio (0.57, BAET and 0.49 AOET) clearly indicates that the concentration of 1° amine in BAET is greater than in AOET, in line with the structure presented in [Scheme 1](#).

The terephthalamides fractions were also characterized using ^1H -NMR spectroscopy using DMSO (Figure 6). The ^1H -NMR spectrum of BAET (Figure 6a) shows resonances at ~ 8.0 ppm (4H, s, aromatic), 3.2 ppm (4H, t, $\text{CONHCH}_2\text{CH}_2\text{NH}_2$) and 2.7 ppm (4H, t, $\text{CONHCH}_2\text{CH}_2\text{NH}_2$). The ^1H -NMR spectrum of AOET (Figure 6b) shows resonances at ~ 8.0 ppm (8H, s, aromatic), 3.4 ppm (4H, t, CONHCH_2), 2.7 ppm (4H, t, $\text{CONHCH}_2\text{CH}_2\text{NH}_2$), 4.3 ppm (4H, s, $\text{CONHCH}_2\text{CH}_2\text{NHCO}$). The appearance of a singlet centered at 4.3 ppm in the spectra of AOET is due to the symmetrical ethylene group in between two amide groups in addition to the peaks of asymmetrical ethylene group in between an amide and an amine group at 3.4 and 2.7 ppm of part B.

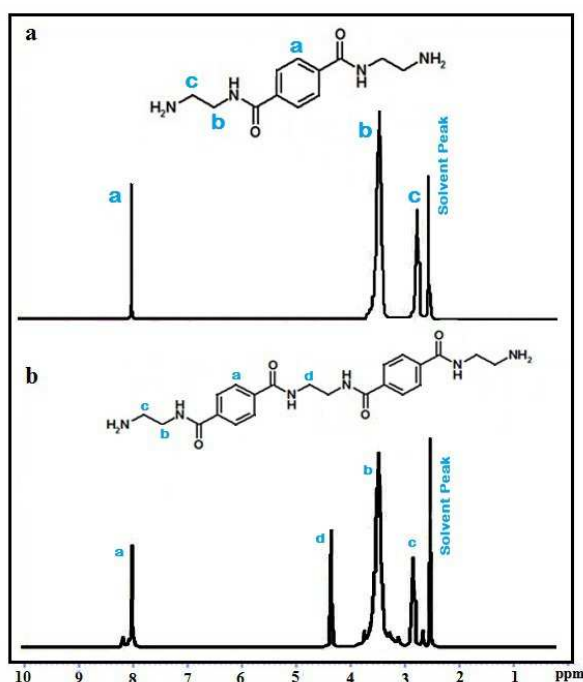


Figure 6: ^1H -NMR spectra a) BAET b) AOET

The DSC traces of BAET and AOET are presented in Figure 7. The sharp endotherm appearing at 181.7 and 298.4 $^{\circ}\text{C}$ are associated with the melting of BAET and AOET respectively. It is to be noted that the melting point of the terephthalates obtained by glycolysis of PET in the presence of ethylene glycol is much lower; 110 and 160 $^{\circ}\text{C}$ for bis-

(hydroxyethyl) terephthalate (BHET) and oligomers respectively³². This difference in the melting points of PET glycolysates and aminolysates can be attributed to the strong intermolecular H –bonding between the amide groups in terephthalamide which is absent in the analogues esters.

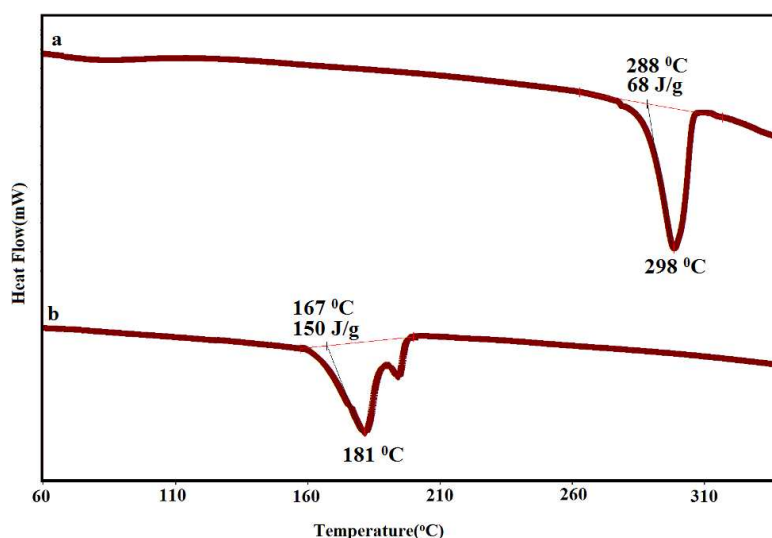
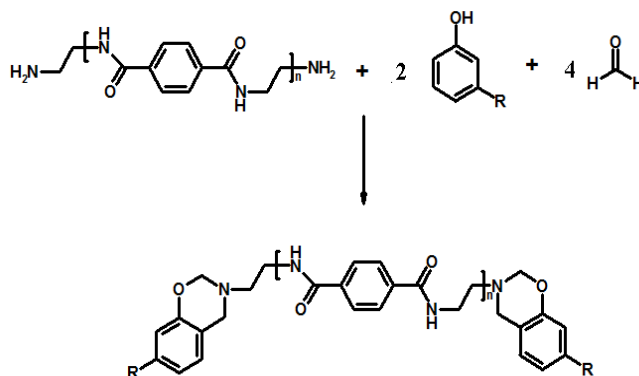


Figure 7: DSC traces a) AOET b) BAET

Synthesis of bis-benzoxazines

Bis-benzoxazines containing amide linkages were prepared using a solventless route by reacting cardanol with the PET derived terephthalamides obtained by PET aminolysis as per the reaction scheme presented in Scheme 2. The oxazine ring formed by Mannich like condensation of cardanol with terephthalamide and paraformaldehyde (2:1:4) is capable of undergoing ring opening polymerization leading to the formation of a crosslinked network. The presence of amide linkage in view of the H-bonding is expected to alter the properties of the resin appreciably. The benzoxazine resins obtained by the reaction of cardanol and formaldehyde with BAET and AOET have been referred to as C-BAET and C-AOET respectively.



Scheme 2: Bis-benzoxazine formation by reaction of terephthalamide with cardanol and formaldehyde

The FT-IR spectra of cardanol, C-BAET & C-AOET is presented in [Figure 8](#). The benzoxazine monomers, showed the absence of O-H and N-H at ~ 3335 , >3161 cm^{-1} , suggestive of complete utilization of cardanol and amine towards formation of oxazine ring. In addition to the stretching bands associated with the aromatic and alkene (3008 cm^{-1}), and aliphatic (2926 and 2854 cm^{-1}) C-H vibrations, other characteristic absorption bands observed in the spectra can be attributed to the C=C (~ 1600 cm^{-1}), asymmetric and symmetric stretching vibrations of C-O-C (~ 1245 cm^{-1} and ~ 1030 cm^{-1}), CH_2 wagging (1370 cm^{-1}), and asymmetric stretching vibrations of C-N-C (1116 cm^{-1}) respectively supporting the presence of double bonds and oxazine ring in Bz monomers. In cardanol, the peak at 990 cm^{-1} can be attributed to the C=C-H vinylenic C-H out-of-plane bend associated with the alkylene chain. Benzoxazine monomers showed a bimodal peak centered at 990 and 960 cm^{-1} associated with the out-of-plane bending vibrations of C-H bond due to alkylene double bond and oxazine ring respectively ⁴².

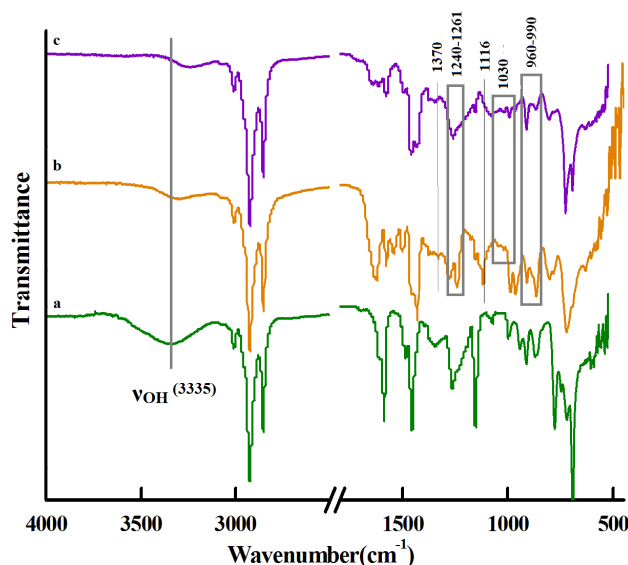


Figure 8: FT-IR spectra: a) cardanol b) C-BAET c) C-AOET

The ^1H -NMR of both the bis-benzoxazine resins was recorded using CDCl_3 as solvent and presented in Figure 9. C-BAET exhibit characteristic resonances at ~ 5.3 ppm (4H, m, ArOCH_2N) and ~ 4.7 ppm (4H, s, ArCH_2N) suggesting the conversion of hydroxyl to oxazine functionality (Figure 9a). Similarly, C-AOET formation was confirmed by the appearance of resonance at ~ 5.4 ppm (4H, m, ArOCH_2N) and ~ 4.6 ppm (4H, s, ArCH_2N) (Figure 9b). The intensity ratio of the signals associated with the oxazine moiety at 4.6 (singlet) and 5.4 ppm (multiplet) is expected to be 1:1. However, the same was found to be higher in the present study, which can be attributed to the resonance of alkylene protons present in cardanol (m, CH= , $\text{CH}_2=\text{CH-}$) at the same position as ArOCH_2N (~ 5.4 ppm). In cardanol based benzoxazines this ratio has been reported to be 1:3²⁴. This deviation from 1:1 can also be ascribed to the oligomerisation of the benzoxazine resin. The protons associated with the $>\text{CH}_2$ in the mannich base formed as a result of ring opening appear in the region 3.5-4 ppm which overlap with the peaks associated with the amine protons (BAET and AOET) in the same region as can be seen in the NMR spectra.

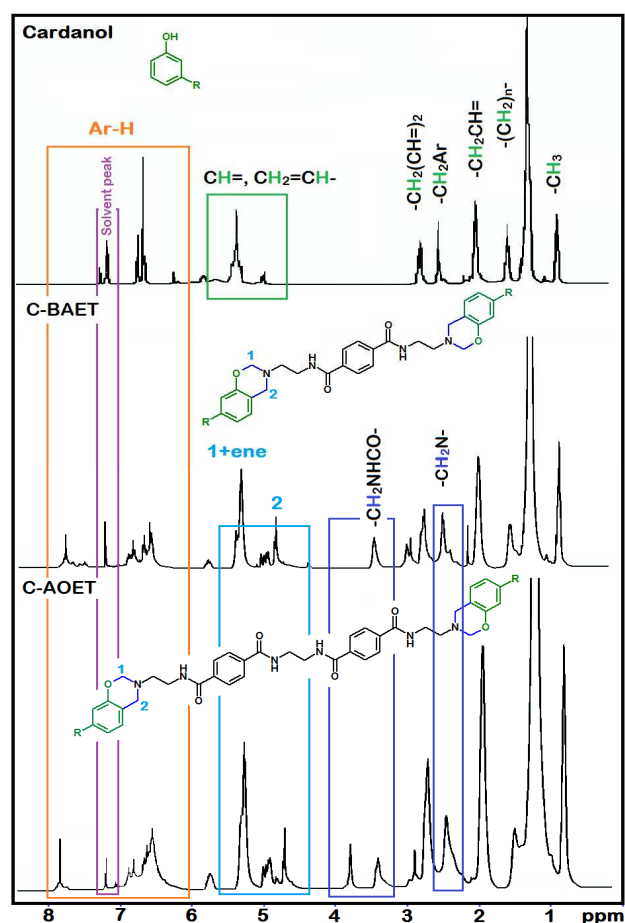


Figure 9: ^1H -NMR spectra a) Cardanol b) C-BAET c) C-AOET

To investigate the curing behavior of the benzoxazine resins, non-isothermal calorimetric studies were performed and the curing profiles are presented in Figure 10. It can be seen that the temperature associated with the curing of C-BAET ($T_{\text{peak}} = 214\text{ }^{\circ}\text{C}$) is relatively lower than C-AOET ($T_{\text{peak}} = 238\text{ }^{\circ}\text{C}$). This is in accordance with previous studies, where increasing the chain length between benzoxazine moieties leads to a increase in curing temperature²². In our previous studies, we have reported the curing behavior of cardanol based mono-benzoxazine, which was found to cure at relatively higher temperature ($T \sim 242\text{ }^{\circ}\text{C}$)²⁰. Our studies clearly suggest that increasing the functionality can lead to substantial lowering of the curing temperature^{24, 43}. Further, the molar enthalpy associated with the

polymerization for C-AOET is lower than C-BAET, which can again be credited to the larger number of oxazine rings per unit mass in the latter.

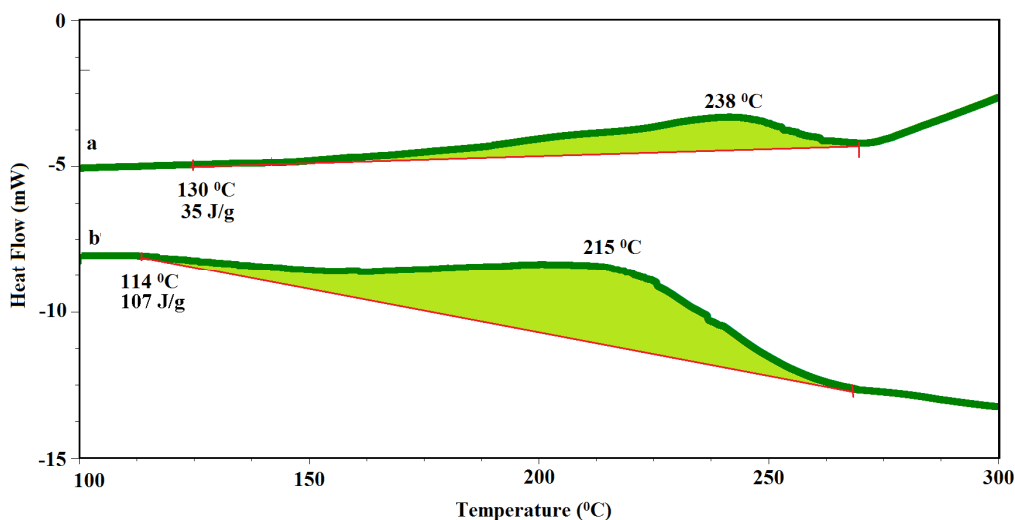


Figure 10: DSC Traces: a) C-AOET b) C-BAET

The TG-DTG traces of the cured benzoxazines (C-AOET and C-BAET) are presented in the supplementary section (Figure S7). The benzoxazine resins prepared in the present work were found to exhibit excellent thermal stability with the temperature associated with 5 % wt. loss being 298 and 380 °C for C-BAET and C-AOET respectively, suggesting their application in demanding areas requiring high thermal stability.

Adhesive property

The adhesive nature of the bis-benzoxazine resin was quantified as per the standard procedure and the result in terms of lap shear strength (LSS) are presented in Table 2 and the representative load-displacement curve is presented in supplementary section (Figure S8). It is to be noted that the LSS is dependent on several factors, particularly the ability of the resin to wet the substrate, its inherent adhesive nature, temperature, thickness of the resin and type of failure. The presence of larger number of polymerizable molecules in benzoxazines which

undergo thermally activated ring opening polymerisation in the absence of catalyst form cross linked networks on metal surfaces⁴⁴. The ring opening of oxazine moieties generates specific groups which are capable of undergoing H-bonding, such as –OH and >N- as shown in supplementary section (Figure S9) and FTIR of cured resin (Figure S10), in addition to the amide linkages which are already available in the main chain. Due to the presence of larger number of polymerizable benzoxazine in C-BAET as compared to C-AOET, the lap shear strength of the former was found to be relatively higher than which advocate the use of these resins as healants for self healing applications⁴⁵⁻⁴⁷.

Table 2: Lap Shear Strength of benzoxazine resins

<i>Benzoxazine Resin</i>	<i>Lap Shear Strength (kgcm⁻²)</i>
C-BAET	38.2 ± 3.9
C-AOET	28.3 ± 3.1

Conclusion

Microwave assisted aminolytic depolymerization of PET in the presence of ethylene diamine (ED) was performed to yield terephthalamides which were used to prepare benzoxazine containing amide linkages. The effect of temperature and the molar ratio of PET: ED on the extent of PET conversion and relative percentage fraction of AOET and BAET was studied. Complete conversion of PET could be affected by performing the reaction at temperature close to the melting point of PET, at PET:ED:: 1:6. Increasing the concentration of ED further did not affect the product composition appreciably. The amine terminated terephthalamides were used to synthesize benzoxazine resins containing amide linkages in the presence of cardanol as the phenolic component using Mannich type condensation. The resins were characterized using FT-IR and ¹H-NMR and the curing behaviour was investigated by non-isothermal DSC. The cured resins exhibited high thermal stability ($T_{5\%} > 300$ °C) and excellent lap shear strength (C-AOET = 28 kg cm⁻², C-BAET =

38 kg cm⁻²). Our studies indicate that microwave irradiation can accelerate the kinetics of PET aminolysis resulting in shorter reaction times, and the products hence obtained can be transformed to a sustainable high performance resin.

Acknowledgments

The authors gratefully acknowledge Director, CFEES for providing logistic support to perform this work. B.L. gratefully acknowledges DRDO for funding this researchwork vide Grant number CFEES/TCP/EnSG/CARS/18/2014. Thanks are also due to Dr P. Mukhopadhyay (AIRF, JNU) for providing assistance in characterisation facility.

Supplementary Information

HPLC chromatogram of cardanol (Figure S1), Characterisation of PET (Figures S2-S3), Microwave Profile of PET Aminolysis (Figure S4), BAET yield (Figure S5), FTIR Spectra of terephthalamides (Figure S6), TGA traces of cured C-AOET and C-BAET (Figure S7), Representative load displacement curve (Figure S8), Functional groups in polybenzoxazine involved in H-bonding with the contact surface (Figure S9), FTIR Spectra of cured polymer (Figure S10)

References

1. Ishida, H.; Low, H. Y. A Study on the Volumetric Expansion of Benzoxazine-Based Phenolic Resin. *Macromolecules* **1997**, *30* (4), 1099-1106.
2. Ishida, H.; Allen, D. J. Physical and mechanical characterization of near-zero shrinkage polybenzoxazines. *J. Polym. Sci., Part B: Polym. Phys.* **1996**, *34* (6), 1019-1030.
3. Shen, S. B.; Ishida, H. Development and characterization of high-performance polybenzoxazine composites. *Polym. Compos.* **1996**, *17* (5), 710-719.
4. Ghosh, N. N.; Kiskan, B.; Yagci, Y. Polybenzoxazines—New high performance thermosetting resins: Synthesis and properties. *Prog. Polym. Sci.* **2007**, *32* (11), 1344-1391.
5. Yagci, Y.; Kiskan, B.; Ghosh, N. N. Recent advancement on polybenzoxazine—a newly developed high performance thermoset. *J. Polym. Sci., Part A: Polym. Chem.* **2009**, *47* (21), 5565-5576.
6. Thirukumaran, P.; Shakila Parveen, A.; Sarojadevi, M. Synthesis and Copolymerization of Fully Biobased Benzoxazines from Renewable Resources. *ACS Sustainable Chemistry & Engineering* **2014**, *2* (12), 2790-2801.
7. Taskin, O. S.; Kiskan, B.; Aksu, A.; Balkis, N.; Weber, J.; Yagci, Y. Polybenzoxazine: A Powerful Tool for Removal of Mercury Salts from Water. *Chemistry-A European Journal* **2014**, *20* (35), 10953-10958.
8. Calo, E.; Maffezzoli, A.; Mele, G.; Martina, F.; Mazzetto, S. E.; Tarzia, A.; Stifani, C. Synthesis of a novel cardanol-based benzoxazine monomer and environmentally sustainable production of polymers and bio-composites. *Green Chemistry* **2007**, *9* (7), 754-759.
9. Voirin, C.; Caillol, S.; Sadavarte, N. V.; Tawade, B. V.; Boutevin, B.; Wadgaonkar, P. P. Functionalization of cardanol: towards biobased polymers and additives. *Polym. Chem.* **2014**, *5* (9), 3142-3162.
10. Tyman, J. H. P.; Wilczynski, D.; Kashani, M. A. Compositional studies on technical cashew nutshell liquid (cnsL) by chromatography and mass spectroscopy. *J Am Oil Chem Soc* **1978**, *55* (9), 663-668.
11. Trevisan, M. T. S.; Pfundstein, B.; Haubner, R.; Würtele, G.; Spiegelhalder, B.; Bartsch, H.; Owen, R. W. Characterization of alkyl phenols in cashew (*Anacardium occidentale*) products and assay of their antioxidant capacity. *Food Chem. Toxicol.* **2006**, *44* (2), 188-197.
12. Rao, B. S.; Palanisamy, A. Monofunctional benzoxazine from cardanol for bio-composite applications. *React. Funct. Polym.* **2011**, *71* (2), 148-154.
13. Mohapatra, S.; Nando, G. B. Cardanol: a green substitute for aromatic oil as a plasticizer in natural rubber. *RSC Adv.* **2014**, *4* (30), 15406-15418.
14. Campaner, P.; D'Amico, D.; Longo, L.; Stifani, C.; Tarzia, A.; Tiburzio, S. Chapter 19 - Study of a Cardanol-Based Benzoxazine as Reactive Diluent and Toughening Agent of Conventional Benzoxazines. In *Handbook of Benzoxazine Resins*, Agag, H. I., Ed. Elsevier: Amsterdam, 2011; pp 365-375.
15. A. Attanasi, O.; S. Behalo, M.; Favi, G.; Lomonaco, D.; E. Mazzetto, S.; Mele, G.; Pio, I.; Vasapollo, G. Solvent Free Synthesis of Novel Mono- and Bis-Benzoxazines from Cashew Nut Shell Liquid Components. *Curr. Org. Chem.* **2012**, *16* (21), 2613-2621.
16. Greco, A.; Brunetti, D.; Renna, G.; Mele, G.; Maffezzoli, A. Plasticizer for poly (vinyl chloride) from cardanol as a renewable resource material. *Polym. Degrad. Stab.* **2010**, *95* (11), 2169-2174.

17. Kawaguchi, A. W.; Sudo, A.; Endo, T. Synthesis of highly polymerizable 1,3-benzoxazine assisted by phenyl thio ether and hydroxyl moieties. *J. Polym. Sci., Part A: Polym. Chem.* **2012**, *50* (8), 1457-1461.
18. Agag, T.; Arza, C. R.; Maurer, F. H.; Ishida, H. Primary amine-functional benzoxazine monomers and their use for amide-containing monomeric benzoxazines. *Macromolecules* **2010**, *43* (6), 2748-2758.
19. Agag, T.; Arza, C. R.; Maurer, F. H.; Ishida, H. Crosslinked polyamide based on main-chain type polybenzoxazines derived from a primary amine-functionalized benzoxazine monomer. *J. Polym. Sci., Part A: Polym. Chem.* **2011**, *49* (20), 4335-4342.
20. Lochab, B.; Varma, I.; Bijwe, J. Thermal behaviour of cardanol-based benzoxazines. *J. Therm. Anal. Calorim.* **2010**, *102* (2), 769-774.
21. Baranek, A. D.; Kendrick, L. L.; Narayanan, J.; Tyson, G. E.; Wand, S.; Patton, D. L. Flexible aliphatic-bridged bisphenol-based polybenzoxazines. *Polym. Chem.* **2012**, *3* (10), 2892-2900.
22. Allen, D. J.; Ishida, H. Physical and mechanical properties of flexible polybenzoxazine resins: Effect of aliphatic diamine chain length. *J. Appl. Polym. Sci.* **2006**, *101* (5), 2798-2809.
23. Allen, D. J.; Ishida, H. Polymerization of linear aliphatic diamine-based benzoxazine resins under inert and oxidative environments. *Polymer* **2007**, *48* (23), 6763-6772.
24. Shukla, S.; Mahata, A.; Pathak, B.; Lochab, B. Cardanol Benzoxazines - Interplay of Oxazine Functionality (Mono to Tetra) and Properties. *RSC Adv.* **2015**, DOI:10.1039/c5ra14214h.
25. Fukushima, K.; Lecuyer, J. M.; Wei, D. S.; Horn, H. W.; Jones, G. O.; Al-Megren, H. A.; Alabdulrahman, A. M.; Alsewailem, F. D.; McNeil, M. A.; Rice, J. E.; Hedrick, J. L. Advanced chemical recycling of poly(ethylene terephthalate) through organocatalytic aminolysis. *Polym. Chem.* **2013**, *4* (5), 1610-1616.
26. Hoang, C. N.; Dang, Y. H. Aminolysis of poly(ethylene terephthalate) waste with ethylenediamine and characterization of α,ω -diamine products. *Polym. Degrad. Stab.* **2013**, *98* (3), 697-708.
27. Soni, R.; Singh, S. Synthesis and characterization of terephthalamides from poly(ethylene terephthalate) waste. *J. Appl. Polym. Sci.* **2005**, *96* (5), 1515-1528.
28. Soni, R.; Teotia, M.; Dutt, K. Studies on synthesis and characterization of a novel acrylic aromatic amide oligomer of aminolysed endproducts generated from pet waste with hydrazine monohydrate and its photocuring with acrylate monomers. *J. Appl. Polym. Sci.* **2010**, *118* (2), 638-645.
29. Chaudhary, S.; Surekha, P.; Kumar, D.; Rajagopal, C.; Roy, P. K. Microwave assisted glycolysis of poly(ethylene terephthalate) for preparation of polyester polyols. *J. Appl. Polym. Sci.* **2013**, *129* (5), 2779-2788.
30. Achilias, D. S.; Tsintzou, G. P.; Nikolaidis, A. K.; Bikiaris, D. N.; Karayannidis, G. P. Aminolytic depolymerization of poly(ethylene terephthalate) waste in a microwave reactor. *Polym. Int.* **2011**, *60* (3), 500-506.
31. Jog, J. Crystallization of polyethyleneterephthalate. *Journal of Macromolecular Science, Part C: Polymer Reviews* **1995**, *35* (3), 531-553.
32. Roy, P. K.; Mathur, R.; Kumar, D.; Rajagopal, C. Tertiary recycling of poly(ethylene terephthalate) wastes for production of polyurethane-polyisocyanurate foams. *J. Env. Chem. Eng.* **2013**, *1* (4), 1062-1069.
33. Aspinall, S. R. Ethylenediamine. IV.1 Monoalkyl Derivatives. *J. Am. Chem. Soc.* **1941**, *63* (3), 852-854.

34. Bergeron, R. J.; Garlich, J. R.; Stolowich, N. J. Reagents for the stepwise functionalization of spermidine, homospermidine, and bis(3-aminopropyl)amine. *J. Org. Chem.* **1984**, *49* (16), 2997-3001.
35. Jacobson, A. R.; Makris, A. N.; Sayre, L. M. Monoacylation of symmetrical diamines. *J. Org. Chem.* **1987**, *52* (12), 2592-2594.
36. Manju; Kumar Roy, P.; Ramanan, A.; Rajagopal, C. Post consumer PET waste as potential feedstock for metal organic frameworks. *Mater. Lett.* **2013**, *106* (0), 390-392.
37. Agarwal, U. S.; de Wit, G.; Lemstra, P. J. A new solid-state process for chemical modification of PET for crystallization rate enhancement. *Polymer* **2002**, *43* (21), 5709-5712.
38. Kim, Y. J.; Varma, R. S. Microwave-assisted preparation of cyclic ureas from diamines in the presence of ZnO. *Tetrahedron Lett.* **2004**, *45* (39), 7205-7208.
39. Narwade, B. S.; Gawali, P. G.; Pande, R.; Kalamse, G. M. Dielectric studies of binary mixtures of n-propyl alcohol and ethylenediamine. *J. Chem. Sci.* **2005**, *117* (6), 673-676.
40. Carothers, W. H. Polymers and polyfunctionality. *Transactions of the Faraday Society* **1936**, *32* (0), 39-49.
41. Chapter 8 - Aliphatic Amines. In *Interpreting Infrared, Raman, and Nuclear Magnetic Resonance Spectra*, Nyquist, R. A., Ed. Academic Press: San Diego, 2001; pp 143-148.
42. Lochab, B.; Shukla, S.; Varma, I. K. Naturally occurring phenolic sources: monomers and polymers. *RSC Adv.* **2014**, *4* (42), 21712-21752.
43. Lochab, B.; Varma, I.; Bijwe, J. Blends of benzoxazine monomers. *J. Therm. Anal. Calorim.* **2013**, *111* (2), 1357-1364.
44. Aydogan, C.; Kiskan, B.; Hacioglu, S. O.; Toppare, L.; Yagci, Y. Electrochemical manipulation of adhesion strength of polybenzoxazines on metal surfaces: from strong adhesion to dismantling. *RSC Adv.* **2014**, *4* (52), 27545-27551.
45. Sharma, P.; Lochab, B.; Kumar, D.; Roy, P. K. Interfacial encapsulation of bio-based benzoxazines in epoxy shells for temperature triggered healing. *J. Appl. Polym. Sci.* **2015**, DOI:10.1002/app.42832.
46. Sharma, P.; Shukla, S.; Lochab, B.; Kumar, D.; Kumar Roy, P. Microencapsulated cardanol derived benzoxazines for self-healing applications. *Mater. Lett.* **2014**, *133*, 266-268.
47. Kiskan, B.; Yagci, Y. Self-healing of poly(propylene oxide)-polybenzoxazine thermosets by photoinduced coumarine dimerization. *J. Polym. Sci., Part A: Polym. Chem.* **2014**, *52* (20), 2911-2918.

Sustainable bis-benzoxazines from cardanol and PET derived terephthalamides

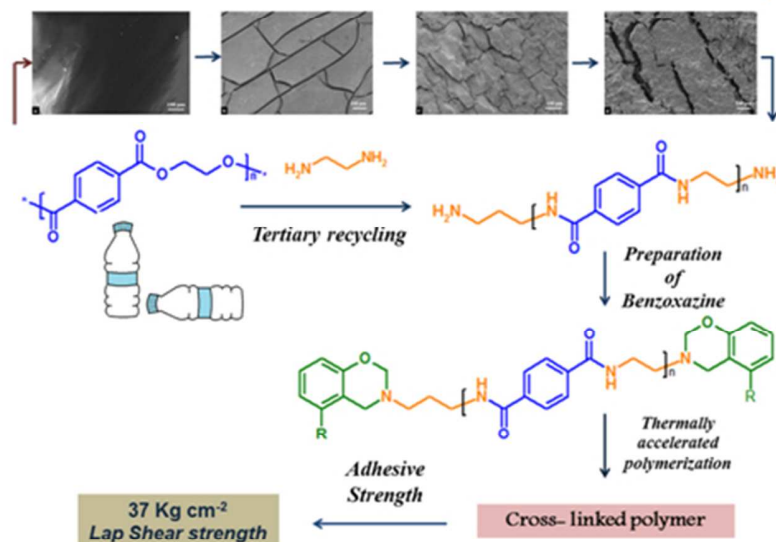
Pratibha Sharma, Bimlesh Lochab, Devendra Kumar, Prasun Kumar Roy



Preparation of sustainable benzoxazine resins containing amide linkages based on naturally occurring cardanol and aminolysed polyethylene terephthalate (PET).

Sustainable bis-benzoxazines from cardanol and PET derived terephthalamides

Pratibha Sharma, Bimlesh Lochab, Devendra Kumar, Prasun Kumar Roy



Preparation of sustainable benzoxazine resins containing amide linkages based on naturally occurring cardanol and aminolysed polyethylene terephthalate (PET).

Graphical Abstract
151x113mm (96 x 96 DPI)

Theoretical modeling of the plasma-assisted catalytic growth and field emission properties of graphene sheet

Suresh C. Sharma and Neha Gupta

Citation: [Physics of Plasmas](#) **22**, 123517 (2015); doi: 10.1063/1.4938506

View online: <http://dx.doi.org/10.1063/1.4938506>

View Table of Contents: <http://scitation.aip.org/content/aip/journal/pop/22/12?ver=pdfcov>

Published by the [AIP Publishing](#)

Articles you may be interested in

[Conversion of CH₄/CO₂ to syngas over Ni-Co/Al₂O₃-ZrO₂ nanocatalyst synthesized via plasma assisted co-impregnation method: Surface properties and catalytic performance](#)

[J. Appl. Phys.](#) **114**, 094301 (2013); 10.1063/1.4816462

[Role of ion density in growth, transport, and morphology of nanoparticles generated in plasmas](#)

[Appl. Phys. Lett.](#) **101**, 083103 (2012); 10.1063/1.4746396

[Plasma stabilisation of metallic nanoparticles on silicon for the growth of carbon nanotubes](#)

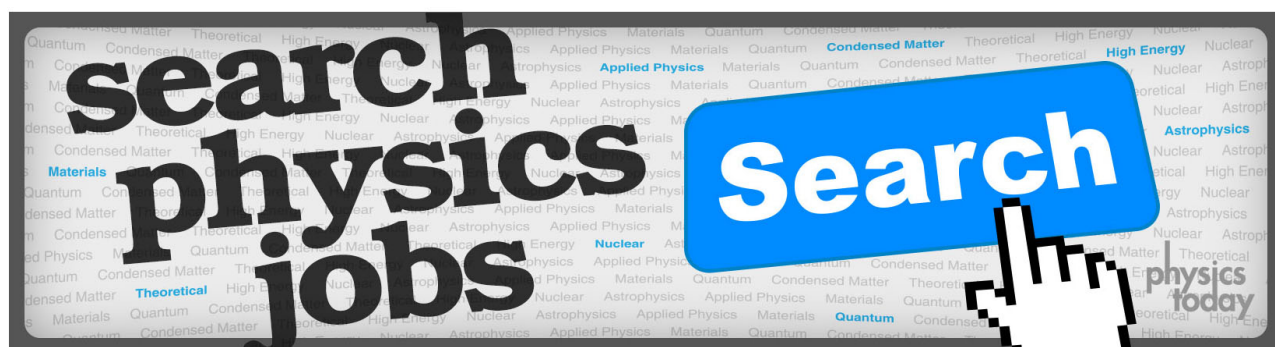
[J. Appl. Phys.](#) **112**, 034303 (2012); 10.1063/1.4740468

[Plasma-assisted growth and nitrogen doping of graphene films](#)

[Appl. Phys. Lett.](#) **100**, 253107 (2012); 10.1063/1.4729823

[Single-step, catalyst-free plasma-assisted synthesis and growth mechanism of single-crystalline aluminum nitride nanorods](#)

[Appl. Phys. Lett.](#) **97**, 213103 (2010); 10.1063/1.3517507



Theoretical modeling of the plasma-assisted catalytic growth and field emission properties of graphene sheet

Suresh C. Sharma and Neha Gupta

Department of Applied Physics, Delhi Technological University (DTU), Shahbad Daultpur, Bawana Road, Delhi-110042, India

(Received 9 September 2015; accepted 9 December 2015; published online 24 December 2015)

A theoretical modeling for the catalyst-assisted growth of graphene sheet in the presence of plasma has been investigated. It is observed that the plasma parameters can strongly affect the growth and field emission properties of graphene sheet. The model developed accounts for the charging rate of the graphene sheet; number density of electrons, ions, and neutral atoms; various elementary processes on the surface of the catalyst nanoparticle; surface diffusion and accretion of ions; and formation of carbon-clusters and large graphene islands. In our investigation, it is found that the thickness of the graphene sheet decreases with the plasma parameters, number density of hydrogen ions and RF power, and consequently, the field emission of electrons from the graphene sheet surface increases. The time evolution of the height of graphene sheet with ion density and sticking coefficient of carbon species has also been examined. Some of our theoretical results are in compliance with the experimental observations. © 2015 AIP Publishing LLC.

[<http://dx.doi.org/10.1063/1.4938506>]

I. INTRODUCTION

Prior works on the growth of carbon nanotubes led to the invention of vertical graphene.¹ In the current years, there has been a deluge interest in the area of research of carbon nanostructures of various dimensionalities such as fullerenes (0-D), carbon nanotubes (1-D), graphene (2-D), and diamond films (3-D). Among them, graphene, the basic structural element of other allotropes of carbon, has inspired academicians and industrial researchers due to its miraculous properties² in many sides. The economical mass production of graphene has been the major concern for electronic applications. Some of the major approaches for the synthesis of graphene include mechanical exfoliation, chemical exfoliation, chemical vapor deposition, and several others.³ Among these techniques, CVD in the presence of plasma is the most viable one to meet the standards of the graphene.

Compared with other CVD methods, plasma enhanced chemical vapor deposition technique (PECVD) offers plentiful rewards, for instance, low temperature growth; better control over nanostructure position, size, and shape; high versatility; and growth of nanostructures with selected properties.^{4,5} Plasma plays a significant role in the nanostructure synthesis.⁶ Recently, Wang *et al.*⁷ reported that plasma accelerates the motion of the hydrocarbon radicals, enhances the deposition of hydrocarbon ions onto the substrate surface, and promotes the separation of carbon nanoflakes (CNFs) from the substrate. The growth of nanostructures is strongly affected by the ion and electron fluxes from the plasma and may be well effectively controlled by the proper selection of the plasma parameters. Extensive studies have been done to study the influence of RF power, feedstock gas ratio, electron-temperature, hydrogen gas, and growth time on the structure, growth rate, and dimensions of the graphene sheet.^{8–13}

Nang and Kim⁸ have observed that with the increase in plasma power and growth time, the structural quality of the graphene films is improved and the thickness of graphene is gradually decreased, finally saturating to a single layer graphene (cf. Figs. 2 and 3 of Nang and Kim⁸).

Liu *et al.*⁹ have observed that upon increasing the RF power from 500 to 700 W, the deposited carbon material changes from 1-D to 2-D structure and when the RF power increases to above 800 W the growth ratio decreases. The decreasing growth ratio has been attributed to the etching effect of hydrogen radical that overtake the benefit of providing more energetic ions at 800 W RF power.

Jiang *et al.*¹⁰ have studied the effect of gas flow rate on the growth of graphene sheet. They observed that under a certain methane flow rate and ratio of CH₄ to H₂, the size of the graphene flake increases with growth time and then get saturated. They have shown that the synthesized films possess excellent field emission (FE) properties with the field enhancement factor of 1.1×10^4 .

Levchenko *et al.*¹¹ have fabricated the graphene flake on Y-Ni catalyst using magnetic-field enhanced plasma and have analytically studied the variation of graphene flake size with surface temperature, plasma density, and the electron temperature as parameters. They observed that graphene flake size decreases with the plasma density and electron temperature.

Kim *et al.*¹² have synthesized graphene film on Ni foil by microwave PECVD (MPECVD) method and found that the number of layers of graphene increases by decreasing the mixing ratio of hydrogen and methane.

Chan *et al.*¹³ have shown that high quality graphene films on Cu films are synthesized by increasing the hydrogen concentration by plasma-assisted thermal CVD. Their results indicate that as the H₂ flow rate increases, intensity ratio of 2D peak to G peak, i.e., I_{2D}/I_G increases from 0.98 to 2.29.

Till date, several experimental evidences incorporating the effects of catalyst and electric field due to plasma on the vertical growth mechanism of graphene sheet have been given.^{14–16} In the catalytic growth, hydrocarbon gas is dissociated on the catalyst surface, whereas in the absence of catalyst, the free radicals, ions, and reactive species are formed by the collision of feedstock gas (hydrocarbons) and electrons in the plasma.¹⁷ Many theoretical models^{18–20} have also been claimed to study the growth kinetics of the graphene sheet.

Zhu *et al.*¹⁴ reported that initially graphene layers grow parallel to the substrate and then the top carbon layers curl upward due to sufficient level of force at the grain boundaries. They also revealed that the growth direction of the carbon nanosheets is determined by the induced polarization of the graphitic layers associated with the electric field in the plasma sheath.

Terasawa and Saiki¹⁵ have studied and explained the growth mechanism of graphene on Cu by PECVD method. In their findings, they have mentioned that the growth of the first layer is due to the catalytic nature of Cu, while the growth of the second and subsequent layers is mainly caused by the radicals generated in plasma.

Ghosh *et al.*¹⁶ have demonstrated the effect of substrate on the growth of graphene nanosheets. They have explained the growth mechanism of vertical graphene nanosheets assisted by electron cyclotron resonance chemical vapor deposition (ECR-CVD) by eliciting the formation of nucleation centers for nanographitic (NG) island formation during surface-plasma interaction, coalescence of islands, and generation of stress at NG grain boundaries.

Zangwill and Vvedensky¹⁸ have presented a rate theory of graphene growth on metals. They have revealed that the two-dimensional graphene islands grow by the attachment of five-atom clusters and the smallest stable precursor to the graphene growth is formed when six of the mobile five-atom clusters collide.

Mehdipour and Ostrikov¹⁹ have studied the metal-catalyzed nucleation and growth of graphene using CVD. In this case, they involved the complete cycle of neutral gas-surface interactions and surface processes. They have also explained the dual role of hydrogen in the Cu-catalyzed growth of graphene.

Kim *et al.*²⁰ have modeled the nucleation and growth of graphene by CVD on Cu surface in the framework of Langmuir adsorption theory and 2-D crystallization. Their model provides the identification of the range of growth parameters (temperature and gas pressures) that leads to the final surface coverage of graphene.

Moreover, many works on graphene synthesis have reported that the plasma treated graphene sheets have better FE properties.^{10,21–24} It has been observed that the field enhancement factor of graphene sheet is inversely proportional to the thickness of graphene^{25,26} and hence lesser thickness corresponds to higher field emission current densities.

Malesevic *et al.*²¹ have found that the few-layer graphene (FLG) synthesized by the MPECVD technique are the good field emitter with low turn-on field of 1 V/ μm and field

amplification factor was observed up to 7500. They have also revealed that the FLG grown with high H_2/CH_2 gas ratio are better field emitters as compared to low H_2/CH_2 gas ratio.

Shih *et al.*²² have investigated the effect of plasma treatment on the growth, structure, and field emission properties of the two-dimensional CNFs and revealed that the field emission properties get enhanced on increasing the RF power. They have also illustrated the effect of substrate temperature on the morphology of CNFs.

Wang *et al.*²³ have developed a back gated triode emission device based on field emission characteristic of carbon nanosheets, which were synthesized by the RF-PECVD method. The field emission current was stable for >200 h at 1.3 mA emission current level. They imputed this result to the high purity and uniform height distribution of the carbon nanosheets.

Srivastava *et al.*²⁴ have shown that the increase in microwave power strongly affect the structure and morphology of the quasi two-dimensional carbon films. The normal alignment of the films to the substrate, increased density, and reduced size are the main contributing factors to the characteristics of field emission from the carbon nanofilms.

The existing growth models^{18–20} describe the growth of graphene sheet in the absence of plasma and do not explain the effect of plasma parameters on the growth and field emission properties of the graphene sheet. In the present paper, we try to present a kinetic model to explain the plasma-assisted catalytic growth process of the graphene sheet accounting the plasma sheath effects and various surface processes. In this work, we solve the first order differential kinetic equations to study the dependence of thickness and height of graphene on the plasma parameters and henceforth account their effects on the field enhancement factor.

The remainder of the manuscript is structured as follows: In Sec. II, we present a theoretical model, including the charging rate of the graphene sheet, kinetic equations of the electrons, ions and neutrals, and the growth rate equation of the graphene sheet due to diffusion of carbon clusters on catalyst surface to study the effects of plasma parameters on the growth of the graphene sheet. Results of the present work are discussed in Sec. III, and finally, conclusion is given in Sec. IV.

II. MODEL

This paper enlightens the catalyst-assisted growth of graphene sheet in $\text{Ar} + \text{H}_2 + \text{C}_2\text{H}_2$ plasma, C_2H_2 acts as a carbon source gas. The plasma consisting of electrons, ions of acetylene (C_2H_2^+), hydrogen (H^+) denoted as ions of types 1 and 2, respectively, and neutrals of type 1 (acetylene, C_2H_2) and type 2 (hydrogen, H_2) is considered. Copper (Cu) catalyst over the silicon (Si) substrate is considered. The complete d-electron shell of copper resulting in low chemical affinity, minimal solubility of carbon, and less precipitation of carbon from copper bulk make copper an effective catalyst for the graphene.²⁷

The present model considers the following elementary processes for the nucleation and growth of graphene sheet on catalyst-substrate surface in plasma.

- (1) First, the applied plasma power fragments the catalyst film to catalyst nanoparticles, subsequently leading to the formation of localized nucleation centers.⁶
- (2) The hydrocarbon ions formed due to ionization of gas within the chamber, pass through the plasma sheath, and then via thermal dissociation, hydrogen induced decomposition (dehydrogenation), and several other processes, they adsorb, diffuse, and eventually attach each other to form C-atom clusters.¹⁹
- (3) These carbon-clusters diffuse and collide to form graphene islands, and thereafter, coalescence of these graphene islands leads to the formation of large graphene islands. This leads to the parallel growth of graphene.¹⁹
- (4) However, the coalescence of the graphene islands cause stress at the grain boundaries, whose release favors the vertical growth of graphene.¹⁶ The electric field generated by plasma ensures the motion of hydrocarbon ions towards the grain/island boundaries, leading to the formation of vertical graphene sheet.

Following Tewari and Sharma,²⁸ we consider the sheath kinetics to investigate the structure of sheath formed near the substrate. We assume that the electric field within the sheath is along the z -axis. The sheath equations are

$$\left(\hat{i} \frac{\partial}{\partial x} + \hat{j} \frac{\partial}{\partial y} + \hat{k} \frac{\partial}{\partial z} \right) \cdot (n_p \vec{v}_p) = f_{iz} n_e, \quad (1)$$

$$M_p n_p v_p \frac{dv_p}{dz} = e n_p E - M_p n_p f_{pn} v_p, \quad (2)$$

$$\frac{d^2 \phi(x)}{dz^2} = -4\pi \sum q_p \xi_p n_p, \quad (3)$$

where Eqs. (1), (2), and (3) represents the continuity equation, ion-momentum balance equation, and Poisson equation, respectively, p refers to either electron(e), $C_2H_2^+$ or H^+ , n_p is their number density, M_p is their mass in plasma, v_p is their fluid velocity, f_{iz} is the ionization frequency, E is the electric field, f_{pn} is the collision frequency, ξ_p is the p th ion to electron number density ratio, q_p is the change of the species, ϕ is the electrostatic potential, $\sum_p \xi_p = 1$, and $0 < \xi_p < 1$.

A. Charging of the graphene

The charge developed on the graphene surface is determined by the accretion of electrons and positively charged ions on the surface of the graphene sheet

$$Q'[\tau] = I_{i1gn} + I_{i2gn} - \gamma_e I_{egn}, \quad (4)$$

where Q is the charge over the graphene sheet, γ_e is the sticking coefficient of electrons, $I_{ijgn} = n_{ij}(x)(lt + ht + lh)\left(\frac{k_B T_{ij}}{2\pi^2 m_{ij}}\right)^{\frac{1}{2}} \left\{ \frac{2}{\sqrt{\pi}} \left(\frac{eV_s}{k_B T_i}\right)^{\frac{1}{2}} + \exp\left[\frac{eV_s}{k_B T_{ij}}\right] \operatorname{erfc}\left[\left(\frac{eV_s}{k_B T_{ij}}\right)^{\frac{1}{2}}\right] \right\} \times \exp\left[-\frac{eU_s}{k_B T_s}\right]$, $I_{egn} = \left(\frac{k_B T_e}{2\pi^2 m_e}\right)^{\frac{1}{2}} n_e(x)(lt + ht + lh) \exp\left[\frac{eV_s}{k_B T_e} + \frac{eU_s}{k_B T_s}\right]$ are the ion and electron

collection current on the graphene surface, respectively. T_{ij} is the ion temperature, m_{ij} is the ion mass (j refers to either 1 or 2 type of positively charged ion as explained earlier), l, t , and h are the length, thickness, and height of the graphene sheet, respectively, T_s is the substrate or catalyst temperature (assuming catalyst and substrate to be at the same temperature), V_s is the surface potential of the graphene sheet (refer Eq. (A2) of the Appendix), T_e is the electron temperature, m_e is the mass of electron, U_s is the substrate bias, $n_{ij}(x) = n_{ij0} \left(1 - \frac{2e\phi(x)}{m_{ij} v_{i0}^2}\right)$ is the ion density in the plasma sheath; v_{i0} is the ion velocity at any point within the plasma, $n_e(x) = n_{e0} \exp\left[\frac{e\phi(x)}{k_B T_e}\right]$ is the electron density in plasma sheath; $\phi(x)$ is the electrostatic potential, n_{e0} is the electron density in plasma sheath, $\phi(x) = \phi_0 \exp\left(-\frac{|x|}{\lambda_d}\right)$, ϕ_0 is the negative potential at the surface, and k_B is the Boltzmann constant. The negative substrate bias is to attract and accelerate the positive species in plasma to stick into and form the nanostructures.²⁹

The first and second term on the right hand side of Eq. (4) describe the charge developed on the graphene surface due to accretion of positively charged ions of type 1 and 2, i.e., ions of acetylene and hydrogen, respectively. The third term represents the decrease in charge due to accretion of electrons at the surface of the graphene sheet.

B. Kinetic equation of electron density

$$n'_e(\tau) = (\beta_1 n_1 + \beta_2 n_2) - (\alpha_1 n_e n_{i1} + \alpha_2 n_e n_{i2}) - \gamma_e n_{gn} I_{egn}, \quad (5)$$

where β_1 and β_2 are the coefficient of ionization of the constituent neutral atoms due to external field, n_e is the electron number density, n_{i1} and n_{i2} are the ion number density of ion types 1 and 2, respectively, and n_1 and n_2 are the number density of neutral types 1 and 2, respectively.

$\alpha_j(T_e) = \alpha_{j0} \left(\frac{300}{T_e}\right)^k \text{cm}^3/\text{s}$ is the coefficient of recombination of electrons and positively charged ions,³⁰ $k = -1.2$ is a constant, and j refers to either 1 or 2 type of ions.

Equation (5) indicates the growth of electron density in the plasma system due to ionization of neutral atoms, recombination of electrons and ions, and electron collection current at the surface of the graphene. The first term on the right hand side of Eq. (5) is the gain in electron density per unit time because of ionization of neutral atoms. The second and third terms display the decaying rate of the electron density due to the electron-ion recombination and the electron collection current at the surface of the graphene, respectively.

C. Kinetic equation of positively charged ion density

$$n'_{i1}(\tau) = \beta_1 n_1 - \alpha_1 n_e n_{i1} - n_{gn} I_{i1gn} - J_{ai1} + J_{desorp1}, \quad (6)$$

$$n'_{i2}(\tau) = \beta_2 n_2 - \alpha_2 n_e n_{i2} - n_{gn} I_{i2gn} - J_{ai2} + J_{desorp2} + J_{th}, \quad (7)$$

where $J_{aij} = \frac{P_i}{(2\pi m_{ij} k_B T_{ij})^{3/2}} \times \frac{n_{ij}}{J_{ij}}$ is the adsorption flux onto the catalyst substrate surface, P_i is the partial pressure of adsorbing species, $J_{desorpj} = j_{ij} \nu \exp(-\frac{\epsilon_{ai}}{k_B T_{ij}})$ is the desorption flux from the catalyst–substrate surface, j refers to either 1 or 2 type of ions, ν is the thermal vibration frequency, ϵ_{ai} is the adsorption energy, j_{ij} is the ion flux on the catalyst substrate surface, $J_{th} = j_H \nu \exp(-\frac{\delta \epsilon_{th}}{k_B T_s})$ is the flux of type 2 ion (namely, hydrogen) on account of thermal dehydrogenation, $\delta \epsilon_{th}$ is the activation energy of thermal dehydrogenation, and j_H is the hydrogen ion flux at catalyst–substrate surface.²⁸

Eqs. (6) and (7) refer to the growth rate of positively charged ions in plasma system. The first term on the right hand side describes the gain in ion density per unit time on account of ionization of neutral atoms. The next two terms represent the rate of decrease in positively charged ion density due to electron-ion recombination and ion collection current at the surface of the graphene, respectively. The fourth and fifth term denotes adsorption and desorption of ions to/from the catalyst-substrate surface, respectively. The last term in Eq. (7) represents the increase in hydrogen ion number density in plasma because of thermal dehydrogenation.

D. Kinetic equation of neutral atoms

$$n'_1(\tau) = \alpha_1 n_e n_{i1} - \beta_1 n_1 + n_{gn}(1 - \gamma_{i1}) I_{i1gn} - n_{gn} \gamma_1 I_{1gn}, \quad (8)$$

$$n'_2(\tau) = \alpha_2 n_e n_{i2} - \beta_2 n_2 + n_{gn}(1 - \gamma_{i2}) I_{i2gn} - n_{gn} \gamma_2 I_{2gn}, \quad (9)$$

where $I_{jgn} = n_j (lt + ht + lh) (\frac{k_B T_n}{2\pi m_j})^{1/2}$ is the neutral collection current at the surface of graphene, j refers to either 1 or 2 type of neutral atom, T_n is the neutral temperature, m_j is the mass of neutral atom, n_j is the neutral atom density, γ_j is the sticking coefficient of neutral atom, and γ_{ij} is the ion sticking coefficient.

Eqs. (8) and (9) describe the growth rate of number density of neutral atoms of types 1 and 2; the first term of the right side denotes the gain in neutral atom density per unit time due to electron–ion recombination. The remaining terms represent the decaying rate of neutral atom density due to ionization, gain in neutral density due to neutralization of ions collected at the surface of the graphene, and accretion of neutral atoms of species 1 and 2 on the surface of the graphene, respectively.

E. Kinetic equation for the growth of graphene nuclei

In the preliminary stage, catalyst (Cu) film fragments into nanoislands of Cu.⁶ The diameter of islands is known to be function of the thickness of the catalyst film. The island size increases with the thickness of the catalyst film.³¹ Since the catalyst activities depend on the size of the catalyst particle, therefore, the morphology, growth rate, and type of carbon nanostructure formed changes with the catalyst-island size. Small catalyst particles favor the growth of carbon nanotubes while the large catalyst particles promote the

growth of graphene.³² The present model considers the size of the catalyst nanoparticle to be 40 nm.¹⁵

Following Tewari and Sharma,²⁸ Mehdipour and Ostrikov¹⁹

$$\begin{aligned} \frac{d}{d\tau}(\pi r_g^2) = & \left[\left\{ 2n_{CH} \nu \exp\left(\frac{-\delta E_i}{k_B T_s}\right) + 2\theta_{CH} J_{i1} y_d + 2J_{i1} \right. \right. \\ & + \frac{J_{i1} \sigma_{ads} J_{i2}}{\nu} + J_c \} m_c + \left\{ J_{i1} (1 - \theta_i) + \frac{J_{i1} \sigma_{ads} J_H}{\nu} \right. \\ & \left. \left. + J_{i1} \exp\left(\frac{-\delta E_i}{k_B T_s}\right) \right\} m_{i1} \right] \\ & \times \frac{2\pi r_{cat}}{\pi r_{cat}^2 \rho_{cat}} \left(D_1 \exp\left(\frac{-E_{sdC}}{k_B T_s}\right) \right. \\ & \left. + D_2 \exp\left(\frac{-E_{sdCl}}{k_B T_s}\right) \right) \times \left(\frac{1}{I_{i1g}} \right) + \gamma_{C_2H_2} \pi r_{cat}^2 I_{C_2H_2g}, \end{aligned} \quad (10)$$

where r_g is the radius of the graphene nuclei, r_{cat} is the radius of the catalyst nanoparticle, and ρ_{cat} is the mass density of the catalyst particle. $I_{ijg} = (\pi r_g^2 (\frac{8k_B T_i}{\pi m_{ij}})^{1/2} n_{ij}(x) [1 - Q\gamma_{ji}] \exp[-\frac{eU_i}{k_B T_s}])$ is the ion collection current at the surface of the graphene nuclei, (where, j refers to either 1 or 2 type of ion); $\gamma_{ji} = \frac{e^2}{r_g k_B T_s}$,

$I_{jg} = (\pi r_g^2 (\frac{8k_B T_n}{\pi m_j})^{1/2} n_j)$ is the neutral collection current at the surface of the graphene nuclei, j refers to either 1 or 2 type of neutral atom, $\gamma_{C_2H_2}$ is the neutral atom sticking coefficient, and $n_{CH} = (\theta_{CH} \nu_0)$ (Denysenko and Ostrikov³³) is the surface concentration of CH; θ_{CH} is the surface coverage by C_2H_2 radicals³³ and $\nu_0 (\approx 1.3 \times 10^{15}) \text{ cm}^{-2}$ is the number of adsorption sites per unit area,³³ $m_c (= 12 \text{ a.m.u})$ is the mass of the carbon atom and $m_{i1} (= 26 \text{ a.m.u.})$ is the mass of type 1 (i.e., $C_2H_2^+$) ions, δE_i is the thermal energy barrier ($\approx 1.87 \text{ eV}$),¹⁹ $J_{ij} = (n_{ij} (\frac{k_B T_e}{m_{ij}})^{1/2})$ is the flux of type j ion²⁸ (where j refers to 1 or 2 type of ion), $y_d (\approx 2.49 \times 10^{-2} + 3.29 \times 10^{-2} \times E_i)$; where E_i is the ion energy in eV is the stitching probability,³⁴ $\sigma_{ads} (\approx 6.8 \times 10^{-16} \text{ cm}^2)$ is the cross-section for the reactions of atomic hydrogen,³³ $J_\alpha = (\frac{n_\alpha v_{th\alpha}}{4})$ is the flux of impinging species α (where $\alpha = C, H$); C and H stands for carbon and hydrogen species, respectively, n_α and $v_{th\alpha}$ are the number density and thermal velocity of α species, respectively,³³ $D_1 \exp(-\frac{E_{sdC}}{k_B T_s})$ and $D_2 \exp(-\frac{E_{sdCl}}{k_B T_s})$ are the surface diffusion coefficients of carbon monomers and C-atom clusters, respectively, with the corresponding activation energies, $E_{sdC} = 0.1 \text{ eV}$ and $E_{sdCl} = 0.82 \text{ eV}$, respectively.¹⁹

Eq. (10) traces the development of graphene island on the catalyst nanoparticle. The adsorption, surface diffusion, and accretion of carbon atoms on the surface of the catalyst via thermal dissociation, ion induced dissociation, decomposition of positively charged ions, interaction of adsorbed acetylene ions with atomic hydrogen from plasma, thermal dissociation of carbon source gas of acetylene ions, and other processes leads to the formation of C-atom clusters.¹⁹ The surface diffusion (with energy barrier E_{sdCl}) and agglomeration of these clusters lead to the formation of graphene island (with radius r_g).¹⁹

In Eq. (10), the first term in the first bracket on the right side (see Ref. 33) accounts for the carbon yield on the catalyst surface due to thermal dissociation of acetylene ions (with activation energy of thermal dissociation, δE_i); the second term (see Ref. 33) denotes the carbon yield due to ion induced dissociation of C_2H_2 /ion-induced incorporation of neutrals (see Ref. 34); the third term refers the decomposition of acetylene ions, i.e., $C_2H_2^+$; the fourth term (see Ref. 33) describes the interaction of ions with atomic hydrogen from the plasma; and the fifth term (see Ref. 33) is the rate of the incoming flux of carbon atoms onto the catalyst particle. The terms in the second bracket refers to the adsorption flux of type 1 ions to the catalyst surface, interaction of adsorbed type 1 ions with atomic hydrogen from plasma, and thermal dissociation of hydrocarbon source gas C_2H_2 , respectively. The term $D_1 \exp(-\frac{E_{sdC}}{k_B T_s})$ and $D_2 \exp(-\frac{E_{sdCl}}{k_B T_s})$ accounts for the surface diffusion of carbon monomers (with energy barrier E_{sdC}) and carbon clusters (with energy barrier E_{sdCl}), respectively, onto the catalyst surface per unit area mass density. The factor I_{i1g} accounts for the ion collection current on the growing graphene island. The last term denotes the sticking of neutral atoms of type 1, i.e., acetylene to the graphene island.

F. Growth rate equation for the graphene sheet

In the initial stage, formation of graphene islands result in the planar growth of graphene. We believe that the length of the graphene advance during the course of the planar growth and we presume its value to be $1.6 \mu\text{m}$.¹⁰ However, the parallel growth of graphene eventually switches to the vertical growth due to the stress developed at the graphene island boundaries. Ion bombardment, temperature gradients, and lattice mismatch between catalyst-substrate surface and graphitic material are the main causes of this stress.³⁵ Under the influence of the electric field due to plasma, carbon atoms diffuse at the graphene island boundaries raising the height and thickness of the graphene sheet in the upward direction. Finally, the etching of carbon due to hydrogen results in the decrease in the thickness of the graphene

$$l \frac{d(h \times t)}{d\tau} = \left(\frac{n_1}{\nu} \times D_1 \exp\left(-\frac{E_d + E_{inc}}{k_B T_s}\right) \right) \frac{\pi r_g^2}{2\pi r_g} \times (I_{i1gn}) + (\gamma_{C_2H_2} I_{C_2H_2gn}) \times \frac{M_{gn}}{\rho_{gn}}, \quad (11)$$

$$[h(\tau) + l] \frac{d(t)}{d\tau} = \left\{ J_{i2} \exp\left(\frac{-\delta E_{sdh}}{k_B T_s}\right) + J_{i2}(1 - \theta_t) + J_{i2} + \theta_{CH} \left(J_{i2} y_d + \nu_0 \nu \exp\left(\frac{-\delta E_i}{k_B T_s}\right) \right) \right\} \times \frac{h(\tau)}{n_{i2}} + \gamma_{C_2H_2} \pi r_g^2 I_{C_2H_2gn}, \quad (12)$$

where ρ_{gn} is the graphene sheet density and M_{gn} is the mass of the growing graphene sheet ($M_{gn} \approx 12 \text{ g}$).

Eq. (11) describes the increase in area of the graphene sheet due to diffusion of carbon atoms at the graphene island boundaries, and ion and neutral collection current at the

growing graphene sheet. The first term on the right side of the Eq. (11) describes the diffusion (with energy barrier, $E_d \approx 0.13 \text{ eV}$)¹⁴ and attachment of carbon atoms (with energy barrier, $E_{inc} \approx 0.4 \text{ eV}$)³⁶ to the border of the growing graphene sheet. The factor I_{i1gn} corresponds to the ion collection on the growing graphene sheet, and the last term accounts the sticking of neutral atoms of acetylene on the graphene sheet.

Eq. (12) describes the decrease in thickness of graphene sheet due to etching of carbon by hydrogen atoms. In Eq. (12), the first term on the right hand side refers the incoming flux of type 2 ion, i.e., hydrogen due to thermal dehydrogenation of type 1 ions (see Ref. 33); the second term accounts the adsorption of type 2 ions to the surface. The third term (see Ref. 33) is the decomposition of positively charged ions of type 2; the fourth term (see Ref. 33) describes ion induced dissociation of acetylene; and the fifth term (see Ref. 33) is due to the incorporation of hydrogen ions due to thermal dissociation of acetylene ions. The last term denotes the sticking of neutrals of acetylene on the surface of the graphene sheet.

G. Energy balance equation for the graphene sheet

$$\begin{aligned} RF \text{ power} &= \frac{d}{d\tau} (M_{gn} C_p T_s) \\ &= I_{egn} \left[\gamma_e \varepsilon_{egn}^s + (1 - \gamma_e) \delta_{egn} \left[\varepsilon_{egn}^s - \left(\frac{3}{2} k_B \right) T_s \right] \right] \\ &\quad - \left(\frac{3}{2} k_B \right) [I_{1gn} [\gamma_1 T_n + \delta_{1gn} (1 - \gamma_1) (T_n - T_s)] \\ &\quad + I_{2gn} \delta_{2gn} (T_n - T_s)] + [I_{i1gn} (\varepsilon_{i1gn}^s + I_{z1}) \\ &\quad + I_{i2gn} (\varepsilon_{i2gn}^s + I_{z2})] - \left(\frac{3}{2} k_B \right) \\ &\quad \times [(1 - \gamma_{1i}) I_{i1gn} + I_{i2gn}] T_s - A \left[\varepsilon \sigma (T_s^4 - T_a^4) \right. \\ &\quad \left. + \left[n_1 \left(\frac{8k_B T_n}{\pi m_1} \right)^{\frac{1}{2}} + n_2 \left(\frac{8k_B T_n}{\pi m_2} \right)^{\frac{1}{2}} \right] k_B (T_s - T_n) \right], \end{aligned} \quad (13)$$

where $M_{gn} (= (l \times h \times t) \rho_{gn})$ is the mass of the graphene sheet, $A (= lt + lh + th)$ is the surface area of the graphene sheet, C_p is the specific heat capacity of graphene sheet ($C_p \approx 2.1 \text{ J g}^{-1} \text{ K}^{-1}$), $\varepsilon_{egn}^s (= 2k_B T_e)$ is the mean energy of electrons collected by graphene,³⁰ $\delta_{egn} (= 2 \frac{m_e}{M_{gn}})$ is the fraction of excess energy of electron lost in a collision with graphene sheet,³⁰ $\delta_{ign} [= \frac{2m_i}{(m_j + M_{gn})}]$ is the fraction of excess energy of an atom lost in a collision with the graphene sheet,³⁰ T_a is the ambient temperature, T_n is the temperature of the neutral atomic species, I_{z1} and I_{z2} are the ionization energies of neutral atoms 1 and 2, respectively ($I_{z1} = 11.26 \text{ eV}$ and $I_{z2} = 13.5 \text{ eV}$), $\varepsilon_{ijgn}^s (Z) = \left(\left(\frac{(2 \frac{eV_s}{k_B T_i})}{(1 - \frac{eV_s}{k_B T_i})} \right) - \frac{eV_s}{k_B T_i} \right) k_B T_i$ (see Ref. 30) is the mean energy collected by ions at the surface of

graphene sheet, ϵ is the emissivity of the material of the graphene sheet, and σ is the Stefan–Boltzmann constant.

Eq. (13) illustrates the effect of RF power on the mass of the graphene sheet. The first two terms in Eq. (13) represents the rate of energy transferred to the graphene sheet due to sticking accretion and elastic collision by constituent species of complex plasma. The third term accounts the ionization of neutral species 1 and 2 resulting in the collection of ions on the surface of graphene sheet, and the fourth term is due to sticking accretion of ions 1 and 2 on the graphene surface. The last term is the rate of energy dissipation of the graphene through radiation and conduction to the host gas.

H. Field enhancement factor

Following Watcharotone *et al.*²⁵ and Miller *et al.*,²⁶ the expression for the field enhancement factor of graphene can be written as

$$\beta \approx \frac{h}{t}, \quad (14)$$

where h is the height of the graphene sheet and t is the thickness of the graphene sheet.

III. RESULTS AND DISCUSSION

The present work serves an analytical model for studying the plasma-sheath-related effects on the graphene growth. In particular, we study the role of different plasma parameters on the growth and field emission properties of graphene sheet with catalyst effects. In the plasma process, substrate-catalyst surface is separated from the plasma by a sheath. The electric field directed from the plasma bulk toward the surface plays a vital role in the growth process of graphene sheet. Due to the variations of the plasma parameters, the sheath thickness changes, which in turn affects the electric field strength, thereby, affecting the electron and ion collection current to the graphene surface.

We assume that the applied plasma power ionizes the neutral gas atoms, thereby creating active species, which fragments the catalyst film into catalyst nanoparticles. Various processes such as thermal and ion-induced dissociation of hydrocarbon gas, decomposition and adsorption of positively charged ions of acetylene, interaction of ions with hydrogen, surface diffusion of species, and several others have been taken into account to the catalyst surface. In the present example, we have accounted the parallel as well as vertical growth of graphene sheet. At the first stage, the diffusion and attachment of carbon atoms at the catalyst surface results in the formation of C-clusters. These clusters diffuse and stitch together to form graphene islands, leading to the parallel growth of graphene. During the second stage, the parallel growth of graphene sheet switches to the vertical growth due to the development of stress at the graphene island boundaries. The nucleation and growth behavior of vertical graphene sheet is strongly affected by the in-built electric field associated with plasma, which is responsible for delivery of carbon atoms to the graphene island boundaries and surfaces of the growing vertical graphene sheet. At

this stage, graphene sheet grows in height via ion and neutral collection current at the graphene island boundaries and thickens due to diffusion and attachment of carbon atoms at the peripherals of the growing carbon platelets. Further increase in height and thickness occurs due to ion and neutral collection current at the lateral surfaces as well as at the top surface of the growing vertical graphene sheet. This is in accordance with the growth possibilities proposed by Zhao *et al.*¹⁷ for two-dimensional nanostructures. In this case, they proposed that the growth may occur at the contact line between the graphene and substrate, at the active steps/edges on two sides of the graphene sheet, and at the free edges of the graphene sheet [cf. Fig. 2(f) of Zhao *et al.*¹⁷]. The growing edges are then terminated by the etching effect of hydrogen.

Numerical calculations have been carried out to study the dependence of the dimensions (i.e., thickness and height) of the graphene sheet on the plasma parameters (i.e., electron density and temperature, ion density of both types 1 and 2, and temperature), which subsequently influence its field emission properties.

We have solved Eqs. (1)–(13) simultaneously at the appropriate boundary conditions, viz., at $\tau = 0$, electron number density $n_{e0}(=10^{11} \text{ cm}^{-3})$, ion number density $n_{i10}(=0.7n_{e0})$, $n_{i20}(=0.5n_{e0})$, neutral atom density $n_{10} = n_{20}(=10^{12} \text{ cm}^{-3})$, electron temperature $T_{e0}(=1.7 \text{ eV})$, ion temperature $T_{i0}(=2200 \text{ K})$, neutral temperature $T_{n0}(=2000 \text{ K})$, mass of ion 1 $m_{i1}(=26 \text{ a.m.u for acetylene } (\text{C}_2\text{H}_2^+))$, mass of ion 2 $m_{i2}(=1 \text{ amu for } (\text{H}^+))$, density of catalyst Cu $\rho_{ct}(=8.96 \text{ g/cm}^3)$, coefficient of recombination of electrons and ions $\alpha_{10} \approx \alpha_{20}(=1.12 \times 10^{-7} \text{ cm}^3/\text{s})$, $\kappa = -1.2$, and substrate temperature $T_s(=600^\circ \text{C})$.

Other parameters used in the calculations are thermal energy barrier on the catalyst surface $\delta E_i(=1.87 \text{ eV})$, energy barrier for diffusion of carbon monomers $E_{sdC}(=0.1 \text{ eV})$ and for carbon clusters $E_{sdCl}(=0.82 \text{ eV})$, energy due to dehydrogenation of C_2H_2 $\delta E_{sdh}(=1.7 \text{ eV})$, sticking coefficient of electron $\gamma_e(=1)$, and sticking coefficient of ion $\gamma_{ij}(=1)$. With the aid of MATHEMATICA software and using all the above values, we solve all the differential Eqs. (1)–(13) simultaneously to study the dependence of height and thickness of graphene sheet on plasma parameters.

Fig. 1 shows the schematic representation of the growth stages of graphene sheet on the catalyst-substrate surface in the presence of plasma. The sketch represents the fragmentation of catalyst film into catalyst nanoparticles, diffusion of carbon monomers to the catalyst particles, diffusion of carbon clusters leading to the formation of graphene island, and finally the vertical growth of graphene sheet due to stress developed at the island boundaries.

Fig. 2 shows the variation of potential of the rectangular graphene sheet along the vertical growth axis, i.e., z -axis. From Fig. 2, it can be seen that the potential of the rectangular graphene sheet decreases linearly as the distance from the surface is increased.

Fig. 3 shows the time-variation of the thickness of the graphene sheet for different electron number densities and electron temperatures (i.e., $n_{e0} = 10^{10} \text{ cm}^{-3}$ and $T_{e0} = 1.5 \text{ eV}$, $n_{e0} = 10^{11} \text{ cm}^{-3}$ and $T_{e0} = 1.7 \text{ eV}$, $n_{e0} = 10^{12} \text{ cm}^{-3}$ and $T_{e0} = 1.9 \text{ eV}$). From Fig. 3, it can be seen that the thickness of

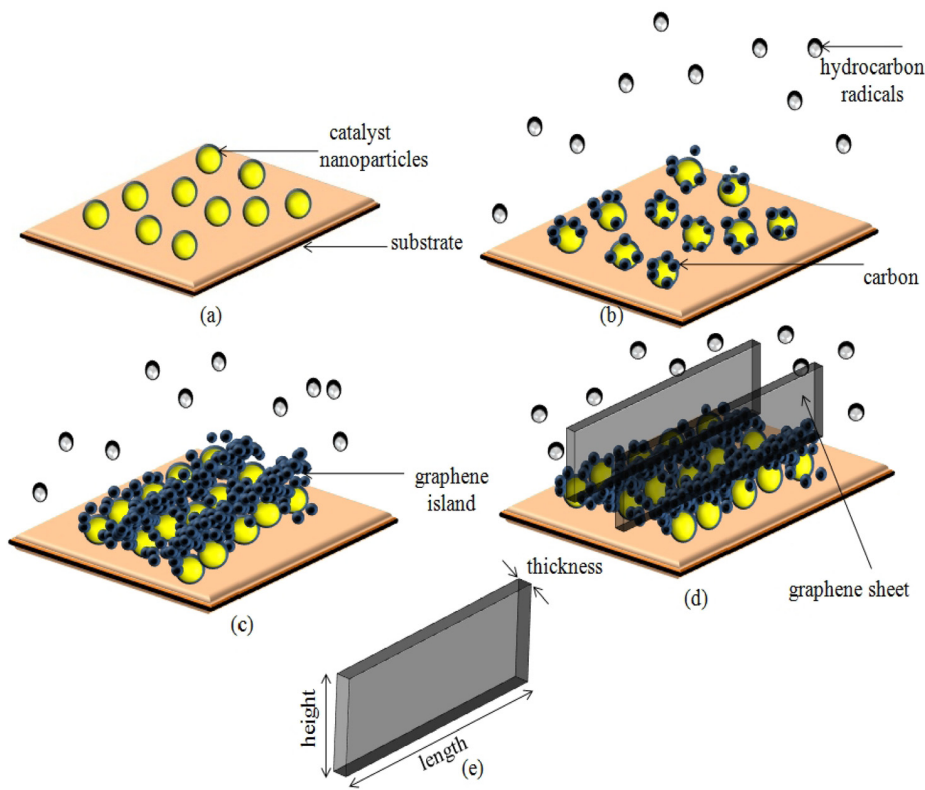


FIG. 1. Schematic representation of the formation of graphene sheet under plasma: (a) formation of catalyst nanoparticles on the substrate surface, (b) cluster formation due to the diffusion of carbon atoms on the catalyst nanoparticles, (c) diffusion of clusters leading to the formation of graphene islands, (d) growth of graphene sheet at the boundaries of graphene islands, and (e) scheme of the graphene sheet considered.

the graphene sheet increases with time and then attains a saturation value. The figure also shows the decrease in graphene sheet thickness with electron density and temperature. This happens because for larger values of electron density and temperature, the rate of ionization of neutral atoms increases due to which the number density of positively charged ions and electron increases; therefore, the number of neutral atoms of type 1 available for accretion decreases. Hence, the thickness of the graphene sheet saturates at a lower value.

Fig. 4 illustrates the variation of thickness of graphene sheet with time for different number density and temperature of ions of type 2 (i.e., $n_{i20} = 10^{10} \text{ cm}^{-3}$ and $T_{i0} = 2100 \text{ K}$, $n_{i20} = 10^{11} \text{ cm}^{-3}$ and $T_{i0} = 2150 \text{ K}$, $n_{i20} = 10^{12} \text{ cm}^{-3}$ and $T_{i0} = 2200 \text{ K}$). From Fig. 4, it can be seen that the thickness of the graphene sheet decreases with the increasing number density of type 2 ions, i.e., of hydrogen ions. This is answerable to the fact that with the increasing density of hydrogen

ions, the etching of graphene sheet at the edges increases. We assume that two processes occur in our growth mechanism, viz., carbon deposition on the surface and etching of the graphene sheet. On increasing the number density of hydrogen ions, the etching effect becomes more prominent resulting in the decrease in the thickness of the graphene sheet. The theoretical findings of Fig. 4 are in compliance with the experimental observations of Kim *et al.*¹² and Chan *et al.*¹³

Fig. 5 displays the time evolution of thickness of graphene with RF power, i.e., RF power (= 50 W, 100 W, and 200 W). From Fig. 5, it can be seen that as the RF power is

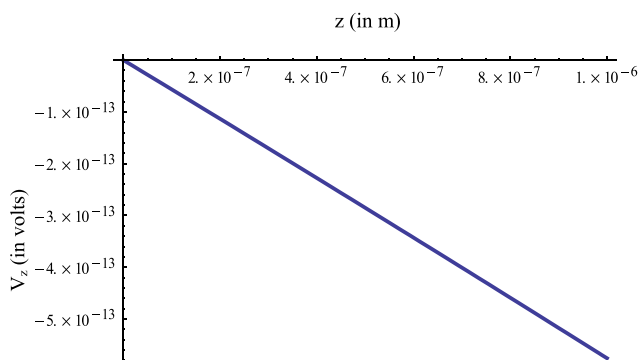


FIG. 2. The variation of potential due to the rectangular graphene sheet along the vertical growth axis (z-axis).

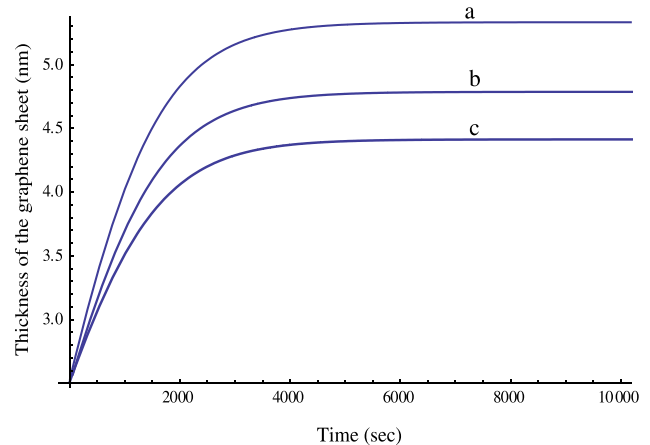


FIG. 3. This figure illustrates the time variation of the thickness of the graphene sheet for different electron densities and temperatures (where a, b, and c correspond to $n_{e0} = 10^{10} \text{ cm}^{-3}$ and $T_{e0} = 1.5 \text{ eV}$, $n_{e0} = 10^{11} \text{ cm}^{-3}$ and $T_{e0} = 1.7 \text{ eV}$, $n_{e0} = 10^{12} \text{ cm}^{-3}$ and $T_{e0} = 1.9 \text{ eV}$, respectively). The other parameters are given in the text.

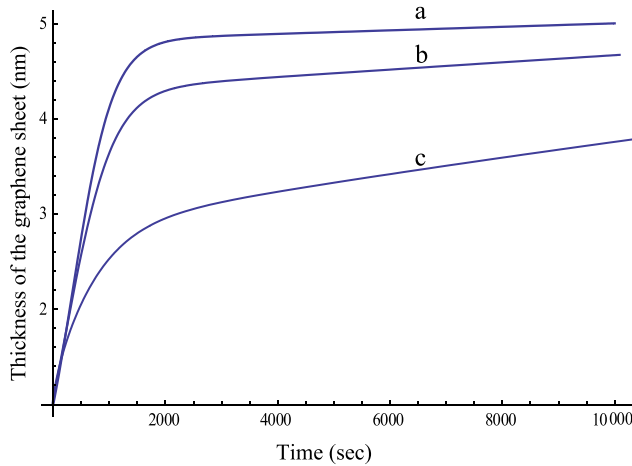


FIG. 4. This figure illustrates the time variation of the thickness of the graphene sheet for different ion densities and temperatures of type 2 ion (where a, b, and c correspond to $n_{i20} = 10^{10} \text{ cm}^{-3}$ and $T_{i0} = 2100 \text{ K}$, $n_{i20} = 10^{11} \text{ cm}^{-3}$ and $T_{i0} = 2150 \text{ K}$, $n_{i20} = 10^{12} \text{ cm}^{-3}$ and $T_{i0} = 2200 \text{ K}$, respectively). The other parameters are given in the text.

increased, the graphene sheet of lesser thickness is observed. This is attributable to the fact that with the increasing RF power the electric field in the plasma sheath increases, thereby increasing the ion bombardment to the vicinity of the graphene sheet, which consequently etches up the graphene sheet. The results of Fig. 5 comply with the experimental observations of Nang and Kim⁸ and Liu *et al.*⁹

Fig. 6 shows the time-variation of the height of the graphene sheet for different ion density and temperature of type 1 ion (i.e., $n_{i10} = 10^{11} \text{ cm}^{-3}$ and $T_{i0} = 2150 \text{ K}$, $n_{i10} = 10^{12} \text{ cm}^{-3}$ and $T_{i0} = 2200 \text{ K}$, $n_{i10} = 10^{13} \text{ cm}^{-3}$ and $T_{i0} = 2250 \text{ K}$). Fig. 6 indicates that upon increasing the number density and temperature of type 1 ion, the height of the graphene sheet increases. As the ion density and temperature of type 1 ion increases, the thickness of the plasma sheath increases and faster generation of carbon monomers occurs; consequently, more diffusion of the carbon ions take place, thereby increasing the height of

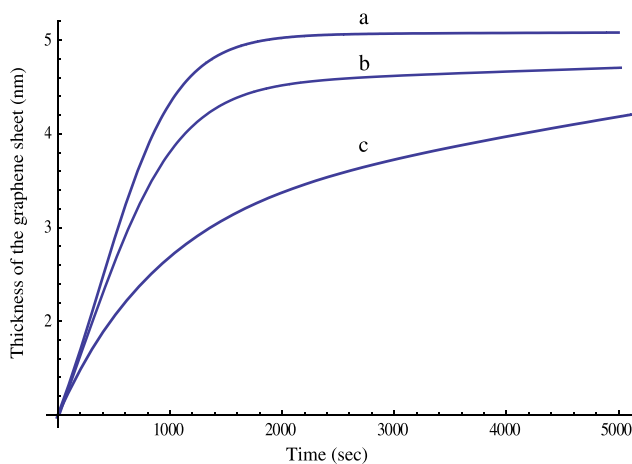


FIG. 5. The time variation of the thickness of the graphene sheet for different RF power (where a, b, and c correspond to RF power = 50 W, 100 W, and 200 W, respectively). The other parameters are given in the text.

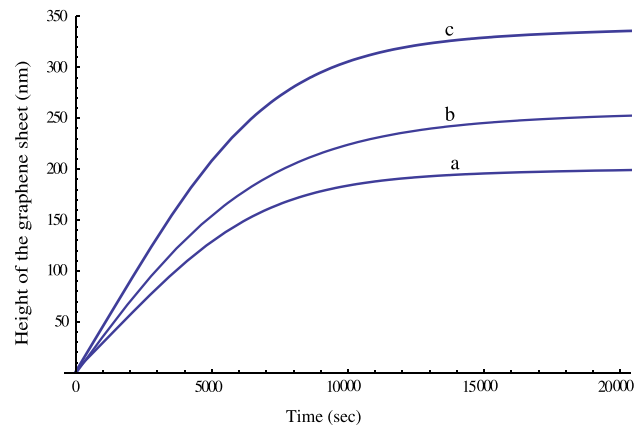


FIG. 6. The time variation of the height of the graphene sheet for different ion density and temperature of type 1 ion (where a, b, and c correspond to $n_{i10} = 10^{11} \text{ cm}^{-3}$ and $T_{i0} = 2150 \text{ K}$, $n_{i10} = 10^{12} \text{ cm}^{-3}$ and $T_{i0} = 2200 \text{ K}$, $n_{i10} = 10^{13} \text{ cm}^{-3}$ and $T_{i0} = 2250 \text{ K}$, respectively). The other parameters are given in the text.

the graphene sheet. The results of Fig. 6 are in compliance with the experimental findings of Jiang *et al.*¹⁰ (cf. Fig. 4 of Jiang *et al.*¹⁰).

Fig. 7 shows the time-evolution of the height of the graphene sheet for different values of the sticking coefficients of the atomic species of the type 1 (i.e., $\gamma_1 = 0.3, 0.6$, and 1.0). The sticking coefficient gives the probability of incorporation of the atomic species into the growing nanostructure.³⁴ From Fig. 7, it can be seen that the steady state can be achieved faster as sticking coefficient approaches to unity.

We have hitherto studied the time-evolution of height and thickness of the graphene sheet for a particular set of parameters and further in order to understand the effect of plasma parameters on the field emission factor $\beta (\approx \frac{h}{t})$, where h is the height and t is the thickness of graphene sheet), we estimated the variation of field enhancement factor with the graphene sheet thickness for different electron densities and temperatures and RF powers. It is found that the field enhancement factor increases with the increase in the plasma parameters (electron densities and

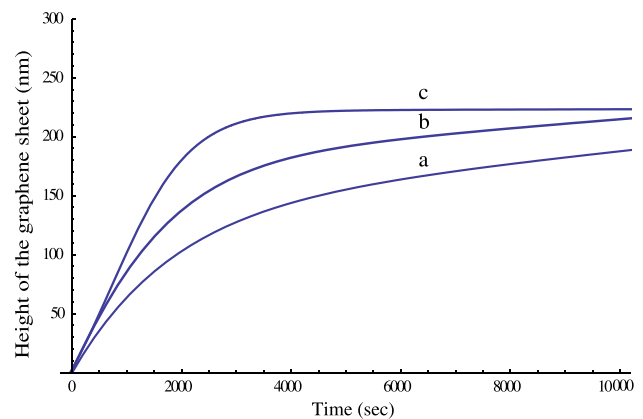


FIG. 7. The time variation of the height of the graphene sheet for different sticking coefficients of atomic species (where a, b, and c correspond to $\gamma_1 = 0.3, 0.6, 1.0$, respectively). The other parameters are given in the text.

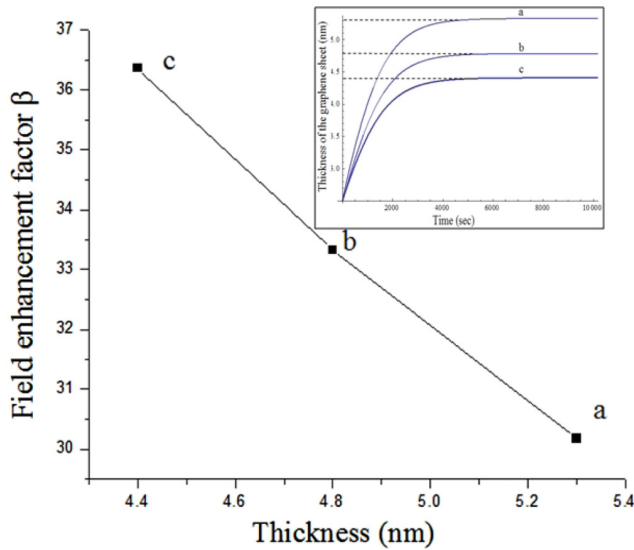


FIG. 8. The variation of field enhancement factor β with the thickness of graphene sheet corresponding to different electron densities and temperatures (where a, b, and c corresponds to different values of β at the saturated value of thickness corresponding to different electron densities and temperatures, i.e., a ($=n_{e0} = 10^{10} \text{ cm}^{-3}$ and $T_{e0} = 1.5 \text{ eV}$), b ($=n_{e0} = 10^{11} \text{ cm}^{-3}$ and $T_{e0} = 1.7 \text{ eV}$), and c ($=n_{e0} = 10^{12} \text{ cm}^{-3}$ and $T_{e0} = 1.9 \text{ eV}$). The inset corresponds to the saturated value of thickness at different electron densities and temperatures.

temperatures) and RF powers (cf. Figs. 8 and 9, respectively). Figs. 8 and 9 illustrate the variation of field enhancement factor with respect to the saturated value of thickness corresponding to different electron densities and temperatures, and RF powers, respectively. In this case, β has been calculated for a fixed value of height (i.e., $h = 160 \text{ nm}$) of the graphene sheet as height has little influence on the field enhancement factor of individual carbon nanostructures.³⁷ The above result is attributed to

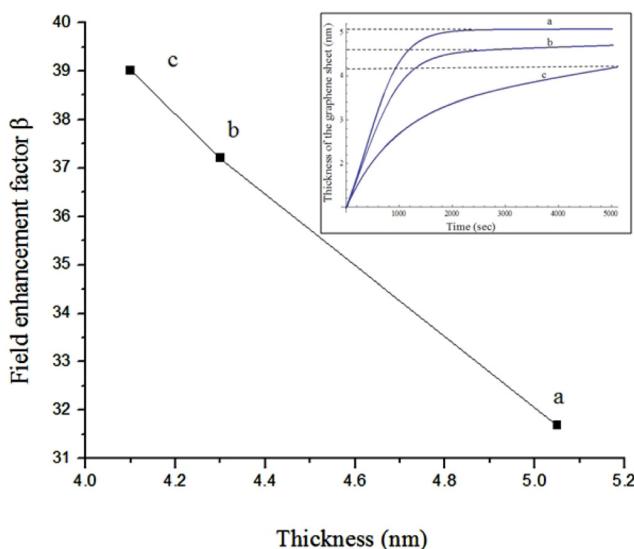


FIG. 9. The variation of field enhancement factor β with the thickness of graphene sheet corresponding to different RF powers (where a, b and c corresponds to different values of β at the saturated value of thickness corresponding to different RF powers, i.e., a ($= 50 \text{ W}$), b ($= 100 \text{ W}$), and c ($= 200 \text{ W}$). The inset corresponds to the saturated value of thickness at different RF powers.

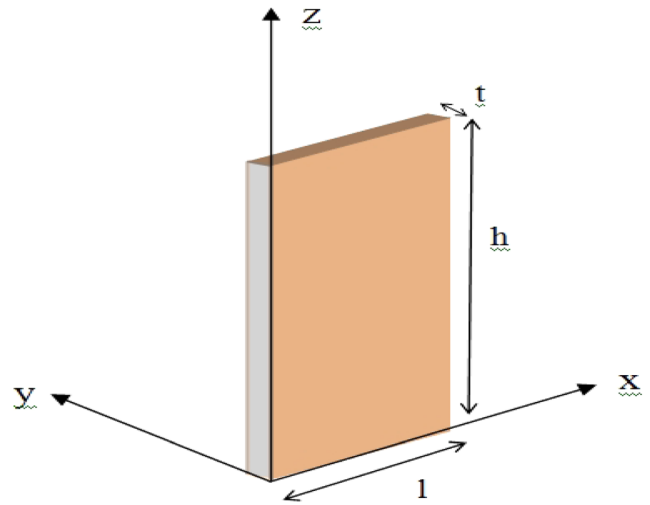


FIG. 10. The 3-D view of rectangular graphene sheet.

the fact that with increase in the plasma parameters (electron densities and temperatures), and RF powers, the thickness of the graphene sheet decreases (cf. Figs. 3 and 5, respectively), which consequently enhances the field enhancement factor ($\beta \propto \frac{1}{t}$ for a fixed value of h) of the graphene sheet.

Using the results obtained, it can be concluded that by suitably varying the plasma parameters, the graphene sheet of large height and lesser thickness can be obtained. The large field enhancement factor ($\beta \approx \frac{h}{t}$) can be estimated by manipulating the plasma parameters, and RF power. This result is similar to the experimental observations of Shih *et al.*²² and Srivastava *et al.*²⁴ Therefore, the present work would pave the way for highly efficient graphene-based field emitters.

An individual vertical graphene nanosheet typically has a tapered shape,³⁸ i.e., its thickness reduces from a few layer graphene at the base to being atomically thin at the top. In the present paper, the authors have shown that thickness decreases with the plasma parameters and RF power but a more practical and realistic study of tapered graphene sheet will be presented in a future article.

IV. CONCLUSION

An analytical model to investigate the growth kinetics of the catalyst-assisted graphene sheet has been developed, and its field emission properties have been estimated. Under the inclusion of plasma sheath effects, kinetics of charge neutrality; number density of electrons, ions, and neutrals; and diffusion of carbon monomers and carbon clusters on the catalyst surface, the effect of various plasma parameters on height and thickness of the graphene sheet have been examined. It is observed from our study that upon the increase in the plasma power and plasma parameters, the thickness of the graphene sheet gets reduced, and consequently, the field emission of electrons from graphene surface increases. This work is envisioned practically to manufacture the highly desirable field emitter devices based on graphene sheet.

ACKNOWLEDGMENTS

The authors are thankful to Professor M. S. Sodha for valuable discussions and one of the authors (Ms. Neha Gupta) is thankful to Ms. Aarti Tewari and Mr. Ravi Gupta for their kind support and encouragement during preparation of this manuscript. This work has been partially supported by the Department of Science and Technology (DST), Government of India.

APPENDIX: POTENTIAL DUE TO RECTANGULAR GRAPHENE SHEET

Following Ref. 39, we consider a charged rectangular graphene sheet in 3-D space. The geometry of the problem is given in Fig. 10. l, h , and t are the length, height, and thickness of the graphene sheet, respectively.

Potential due to the sheet in 3-D space is given by

$$V = \frac{1}{2} \times \frac{1}{4\pi\epsilon_0} \times \frac{e}{l \times t} \left[-2z \left(\tan^{-1} \left(\frac{J}{2t\sqrt{N}} \right) + \tan^{-1} \left(\frac{K}{2t\sqrt{P}} \right) + \tan^{-1} \left(\frac{L}{2t\sqrt{Q}} \right) + \tan^{-1} \left(\frac{M}{2t\sqrt{R}} \right) \right) \right. \\ \left. + (t-2y) \log(l-2x+\sqrt{N}) + (l-2x) \log(t-2y+\sqrt{N}) - (t-2y) \log(-l-2x+\sqrt{P}) \right. \\ \left. + (l+2x) \log(t-2y+\sqrt{P}) - (l-2x) \log(-t-2y+\sqrt{Q}) + (t+2y) \left(\log(l-2x+\sqrt{Q}) \right. \right. \\ \left. \left. - \log(-l-2x+\sqrt{R}) \right) - (l+2x) \log(-t-2y+\sqrt{R}) \right], \quad (\text{A1})$$

where

$$J = (l-2x)(t-2y), \quad K = (l+2x)(t-2y), \quad L = (l-2x)(t+2y), \quad M = (l+2x)(t+2y), \\ N = \sqrt{(l-2x)^2 + (t-2y)^2 + 4z^2}, \quad P = \sqrt{(l+2x)^2 + (t-2y)^2 + 4z^2}, \\ Q = \sqrt{(l-2x)^2 + (t+2y)^2 + 4z^2}, \quad R = \sqrt{(l+2x)^2 + (t+2y)^2 + 4z^2}.$$

Now, the potential due to sheet along z-axis

$$V_z = \frac{1}{(l \times t)} \times 7.2 \times 10^{-10} \left(-8z \tan^{-1} \left(\frac{l \times t}{2z\sqrt{S}} \right) - 2l \log(-t + \sqrt{S}) + 2l \log(t + \sqrt{S}) - 2t \log(-l + \sqrt{S}) + 2t \log(l + \sqrt{S}) \right), \quad (\text{A2})$$

where $S = l^2 + t^2 + 4z^2$.

¹Y. Wu, P. Qiao, T. Chong, and Z. Shen, *Adv. Mater.* **14**, 64 (2002).

²C. N. R. Rao, A. K. Sood, K. S. Subrahmanyam, and A. Govindaraj, *Angew. Chem. Int. Ed.* **48**, 7752 (2009).

³Y. H. Wu, T. Yu, and Z. X. Shen, *J. Appl. Phys.* **108**, 071301 (2010).

⁴S. Vizireanu, S. D. Stoica, C. Luculescu, L. C. Nistor, B. Mituand, and G. Dinescu, *Plasma Sources Sci. Technol.* **19**, 034016 (2010).

⁵I. Levchenko, M. Keidar, S. Xu, H. Kersten, and K. Ostrikov, *J. Vac. Sci. Technol. B* **31**, 050801 (2013).

⁶K. Ostrikov, *Plasma Nanoscience* (John Wiley and Sons, 2008).

⁷B. B. Wang, K. Zheng, Q. J. Cheng, and K. Ostrikov, *Appl. Surf. Sci.* **325**, 251 (2015).

⁸L. V. Nang and E.-T. Kim, *J. Electrochem. Soc.* **159**, K93 (2012).

⁹W. Liu, T. Dang, Z. Xiao, X. Li, C. Zhu, and X. Wang, *Carbon* **49**, 884 (2011).

¹⁰L. Jiang, T. Yang, F. Liu, J. Dong, Z. Yao, C. Shen, S. Deng, N. Xu, Y. Liu, and H.-J. Gao, *Adv. Mater.* **25**, 250 (2013).

¹¹I. Levchenko, O. Volotskova, A. Shashurin, Y. Raites, K. Ostrikov, and M. Keidar, *Carbon* **48**, 4570 (2010).

¹²Y. Kim, W. Song, S. Y. Lee, C. Jeon, W. Jung, M. Kim, and C.-Y. Park, *Appl. Phys. Lett.* **98**, 263106 (2011).

¹³S. H. Chan, S. H. Chen, W. T. Lin, M. C. Li, Y. C. Lin, and C.-C. Kuo, *Nanoscale Res. Lett.* **8**, 285 (2013).

¹⁴M. Zhu, J. Wang, B. C. Holloway, R. A. Outlaw, X. Zhao, K. Hou, V. Shutthanandan, and D. M. Manos, *Carbon* **45**, 2229 (2007).

¹⁵T.-O. Terasawa and K. Saiki, *Carbon* **50**, 869 (2012).

¹⁶S. Ghosh, K. Ganesan, S. R. Polaki, T. Mathews, S. Dhara, M. Kamruddin, and A. K. Tyagi, *Appl. Surf. Sci.* **349**, 576 (2015).

¹⁷J. Zhao, M. Shaygan, J. Eckert, M. Meyyappan, and M. H. Rummeli, *Nano Lett.* **14**, 3064 (2014).

¹⁸A. Zangwill and D. D. Vvedensky, *Nano Lett.* **11**, 2092 (2011).

¹⁹H. Mehdipour and K. Ostrikov, *ACS Nano* **6**, 10276 (2012).

²⁰H. Kim, E. Saiz, M. Chhowalla, and C. Mattevi, *New J. Phys.* **15**, 053012 (2013).

²¹A. Malesev, R. Kemps, A. Vanhulsel, M. P. Chowdhury, A. Volodin, and C. V. Haesendonck, *J. Appl. Phys.* **104**, 084301 (2008).

²²W.-C. Shih, J.-M. Jeng, C.-W. Tsou, J.-T. Lo, H.-C. Chen, and I.-N. Lin, *Jpn. J. Appl. Phys., Part 1* **49**, 08JF11 (2010).

²³S. Wang, J. Wang, P. Miraldo, M. Zhu, R. Outlaw, K. Hou, X. Zhao, B. C. Holloway, D. Manos, T. Tyler, O. Shenderova, M. Ray, J. Dalton, and G. Mc Guire, *Appl. Phys. Lett.* **89**, 183103 (2006).

²⁴S. K. Srivastava, A. K. Shukla, V. D. Vankar, and V. Kumar, *Thin Solid Films* **492**, 124 (2005).

²⁵S. Watcharotone, R. S. Ruoff, and F. H. Read, *Phys. Proc.* **1**, 71 (2008).

²⁶R. Miller, Y. Y. Lau, and J. H. Booske, *Appl. Phys. Lett.* **91**, 074105 (2007).

²⁷S. Riikonen, A. V. Krashennnikov, L. Halonen, and R. M. Nieminen, *J. Phys. Chem. C* **116**, 5802 (2012).

²⁸A. Tewari and S. C. Sharma, *Phys. Plasmas* **21**, 063512 (2014).

²⁹C. H. Lin, H. L. Chang, M. H. Tsai, and C. T. Kuo, *Diamond Relat. Mater.* **11**, 922 (2002).

³⁰M. S. Sodha, S. Misra, S. K. Misra, and S. Srivastava, *J. Appl. Phys.* **107**, 103307 (2010).

³¹M. Chhowalla, K. B. K. Teo, C. Ducati, N. L. Rupasinghe, G. A. J. Amaratunga, A. C. Ferrari, D. Roy, J. Robertson, and W. I. Milne, *J. Appl. Phys.* **90**, 5308 (2001).

³²J. L. Qi, F. Zhang, X. Wang, L. X. Zhang, J. Cao, and J. C. Feng, *RSC Adv.* **4**, 44434 (2014).

- ³³I. Denysenko and K. Ostrikov, *J. Phys. D: Appl. Phys.* **42**, 015208 (2009).
- ³⁴N. V. Mantzaris, E. Gogolides, A. G. Boudouvis, A. Rhallabi, and G. Turban, *J. Appl. Phys.* **79**, 3718 (1996).
- ³⁵J. Chen, Z. Bo, and G. Lu, *Vertically-Oriented Graphene: PECVD Synthesis and Applications* (Springer International Publishing, Switzerland, 2015).
- ³⁶I. Denysenko and N. A. Azarenkov, *J. Phys. D: Appl. Phys.* **44**, 174031 (2011).
- ³⁷Z. Xu, X. D. Bai, and E. G. Wang, *Appl. Phys. Lett.* **88**, 133107 (2006).
- ³⁸K. Davami, M. Shaygan, N. Kheirabi, J. Zhao, D. A. Kovalenko, M. H. Rummeli, J. Opitz, G. Cuniberti, J.-S. Lee, and M. Meyyappan, *Carbon* **72**, 372 (2014).
- ³⁹See <http://blog.wolfram.com/2012/09/27/3d-charges-and-configurations-with-sharp-edges/> for potential due to the rectangular graphene sheet in 3-D space.

Accepted Manuscript

Title: Ultrasensitive THz - plasmonics gaseous sensor using doped graphene

Author: Amrita Purkayastha Triranjita Srivastava Rajan Jha



PII: S0925-4005(15)30783-8
DOI: <http://dx.doi.org/doi:10.1016/j.snb.2015.12.055>
Reference: SNB 19456

To appear in: *Sensors and Actuators B*

Received date: 18-8-2015
Revised date: 14-12-2015
Accepted date: 16-12-2015

Please cite this article as: A. Purkayastha, T. Srivastava, R. Jha, Ultrasensitive THz - plasmonics gaseous sensor using doped graphene, *Sensors and Actuators B: Chemical* (2015), <http://dx.doi.org/10.1016/j.snb.2015.12.055>

This is a PDF file of an unedited manuscript that has been accepted for publication. As a service to our customers we are providing this early version of the manuscript. The manuscript will undergo copyediting, typesetting, and review of the resulting proof before it is published in its final form. Please note that during the production process errors may be discovered which could affect the content, and all legal disclaimers that apply to the journal pertain.

Ultrasensitive THz - plasmonics gaseous sensor using doped graphene

Amrita Purkayastha¹, Triranjita Srivastava² and Rajan Jha^{1*}

¹Nano Photonics and Plasmonics Laboratory, School of Basic Sciences, IIT Bhubaneswar, Odisha

²Department of Physics, Kalindi College, University of Delhi, New Delhi 110008, India
Email: rjha@iitbbs.ac.in, rajaniitd@gmail.in

Abstract

We propose a Surface Plasmon Resonance (SPR) based gas sensor in terahertz frequency with Otto configuration based on attenuated total reflection (ATR) technique using free standing doped graphene monolayer. Angular interrogation method has been used to study the performance of the sensor in terms of sensitivity and detection accuracy. Different chemical potential of graphene monolayer has been investigated to study its effect on these performance parameters. The results show that the optimisation of the gap distance between the prism base and the graphene monolayer has significant effect on the reflectivity of SPR sensing. This SPR based gas sensor shows ultrahigh sensitivity of 34.11 deg/RIU along with an ultrahigh Figure of Merit (FOM) of more than 1150 RIU⁻¹.

1. Introduction

The collective oscillations of free charge carriers at a metal-dielectric interface gives rise to Surface Plasmon Polariton (SPP) provided the dielectric constant of the two media is of opposite sign [1]. Such SPPs are known to be non-radiative in nature and exhibit strong field enhancement at the interface and are found to be extremely sensitive to any changes in the environmental conditions [2] due to which they form the platform of plasmonics; highly miniaturized and ultrafast technology. The resonant excitation of SPPs at the metal- dielectric interface gives rise to the phenomenon of Surface Plasmon Resonance (SPR), which constitute the core of many SPR based devices and sensors in particular[3]. In the past few decades, the study of SPR sensors has been focussed mostly in the visible and near infrared regimes with the use of conventional noble metals like gold and silver [2-3].However, the terahertz regime (0.1 to 10 THz) is still unexplored to a large extent although it holds great promise in biological and security sensing applications. This is because, THz radiation is nonionizing in nature and many complex molecules exhibit signature spectra in THz frequency due to their inherent rotational and vibrational modes in the THz frequency band [4]. In principle, terahertz plasmonics combines the high sensitivity of SPR and broadband spectra of biological molecules in terahertz frequencies, which has huge potential in terahertz sensing [5]. However, SPR sensing in terahertz regime suffers from major drawbacks with the refractive indices of the conventional SPR active metals being extremely high in the terahertz regime as their intrinsic plasma frequency lies in the ultraviolet frequency region. Consequently, SPPs in the terahertz regime are found to be extremely unconfined and corresponds to Zenneck waves [6] with low electric field intensity at the metal-dielectric

interface. These weakly bound fields exhibit weak interaction between the incident radiation and analyte, which limits the sensitivity of the terahertz SPR sensors. To overcome the limitations of poor confinement, tunable SP-like modes supported on metal surfaces corrugated with nanoholes or nanorods have been proposed [7]. Also, artificially engineered structures, or metamaterials, such as periodically perforated metallic plates [8], hollow square-ended brass tubes [9], Sievenpiper mushrooms, and periodic patches [10-11] have been designed to produce the optical SPP behaviour in the low-frequency i.e. terahertz region. But, these structures are bulky size and have complex design, which requires high-end new technology and as such cannot be actively tuned. Also the field confinement is not as strong as desired.

Recently, theoretical works have argued that SP excitation at terahertz frequencies with highly doped monolayer graphene is feasible [12]. Graphene, a 2D form of carbon having atoms arranged in honeycomb lattice [13] has been used for SP generation in terahertz frequencies, thereby, providing a suitable alternative to noble-metal plasmons. They exhibit much larger confinement and have relatively long propagation distances, with the advantage of being highly tunable via electrical and chemical doping [14-15]. In this paper, we present a comprehensive study on the performance of a terahertz gaseous sensor based on Otto configuration using doped graphene monolayer. Angular interrogation technique has been used to analyse the optimal gap distance between the prism base and graphene monolayer for effective excitation of SPP. Further, we analyse the dependence of sensitivity on the chemical potential and the refractive index of the gaseous medium. The figure of merit (FOM) has also been calculated by taking into account the full width at half maxima (FWHM) of the SPR curve.

2. Design consideration and theory

Figure 1 illustrates the schematic of the proposed gaseous sensor in Otto configuration. THz radiation is incident on a high index prism of refractive index n_p and doped graphene monolayer is sandwiched between two homogenous media of dielectric constant ϵ_d and ϵ_A . Here, we have considered $\epsilon_A=1$ which gives us the free standing configuration of graphene. The gaseous analyte is considered in the gap of thickness ' d_a ' between prism base and monolayer graphene (MLG).

A p-polarized collimated terahertz beam is incident on one facet of Germanium prism and refracted to the bottom face with an internal incident angle θ_o [16]. After interacting with the gaseous analyte present inside the gap, the modulated radiation reflects off the prism base and exits from the other facet of prism into the THz spectrometer as shown in Fig. 1. The obtained reflectivity variation exhibits a sharp minimum at resonance angle for which the following condition (Eq. 1) is to be satisfied for the resonance excitation of SPP

$$k_{spp} = k_{||} = \frac{2\pi}{\lambda_o} n_p \sin \theta_o \quad (1)$$

where k_{spp} is the propagation constant of the SPP.

It is to be noted that for our calculations, we have considered graphene conductivity derived within random phase approximation at zero temperature to be [17]

$$\sigma(\omega) = \frac{ie^2}{\pi \hbar} \left[\frac{\mu}{\hbar(\omega + i\tau^{-1})} - \frac{1}{4} \ln \frac{2\mu + \hbar(\omega + i\tau^{-1})}{2\mu - \hbar(\omega + i\tau^{-1})} \right] \quad (2)$$

where τ is the phenomenological relaxation time, e is the charge of an electron and μ is the chemical potential of the monolayer graphene. The first term in the equation corresponds to the intraband contribution whereas the second term is the interband contribution. In the terahertz regime, with high chemical potential of the graphene monolayer ($\hbar\omega \ll \mu$), the intraband contribution dominates and graphene acts as metal with a drude like conductivity given by [14]

$$\sigma = l \frac{e^2 \mu}{\pi \hbar^2 (\omega + l\tau^{-1})} \quad (3)$$

where the chemical potential μ is determined by the carrier concentration $n_0 = (\mu/\hbar v_F)^2/\pi$ with v_F = Fermi velocity and $\omega = k_0 c$ is the angular frequency and the local limit $\omega \gg \tau^{-1}$. Further, the effective thickness of graphene monolayer has been taken to be $t_g = 0.34$ nm with an equivalent dielectric constant as given below [12]

$$\epsilon_g = 1 + \frac{l\sigma}{\omega \epsilon_0 t_g} \quad (4)$$

By matching the boundary conditions for the n_1 -Graphene monolayer- n_a system (Fig. 1), the SP dispersion can be derived as [15]

$$\frac{n_1^2}{k_{z1}^2} + \frac{n_a^2}{k_{za}^2} + \frac{\sigma}{\omega \epsilon_0} = 0 \quad (5)$$

where $k_{zi} (i=1,a) = \sqrt{k_{sp}^2 - n_i^2 k_0^2}$ is the transverse wavenumber of the SP.

Also, different methods like hetero atom doping, including arc discharge, chemical vapor deposition, electro thermal reaction and ion-irradiation approaches can be used for graphene doping. Moreover, the chemical modification and the method of electrostatic field tuning is alternative route for doping graphene along with dopants like nitrogen and boron [18, 19]. However, for our analysis of proposed sensor, we employed standard Transfer Matrix Method (TMM) [20]. Sensitivity and Figure of Merit (FOM) are the two parameters we have used to analyse the performance of the proposed sensor, which are defined as:

(i) Sensitivity of the SPR sensor using angular interrogation method is defined as the ratio of the change in resonance angle (θ_{SPR}) with the change in the refractive index (n_a) of the sensing layer:

$$S_n = \frac{\partial \theta_{SPR}}{\partial n_a},$$

(ii) Figure of Merit (FOM) estimates the performance of the sensor and is defined as the ratio

of sensitivity to FWHM: $FOM = \frac{S_n}{FWHM}$

3. Results and Discussions

It is to be mentioned that the frequency dependent dielectric constant of the graphene largely affects not only the resonance condition but the nature of the SPR curve. The real part of the dielectric constant defines the shift in the resonance angle and the significance of imaginary part lies in the determination of the FWHM of the SPR curve, which is responsible for the detection accuracy of the sensor. In order to understand these effects, in fig 2(a) and fig 2(b), we plot the variation of real and imaginary part of dielectric constant of graphene monolayer with terahertz frequency for three different chemical potential values $\mu = 0.8$ eV, 1.2 eV and 1.6 eV respectively. One can see that the value of real part of permittivity is extremely high in comparison to the imaginary part of the permittivity i.e., for high chemical potential MLG, we see that $|\Re \epsilon_g| \gg |\Im \epsilon_g|$ in the local limit ($\omega \gg \tau^{-1}$), which shows that graphene monolayer would support highly confined SPP modes at terahertz frequencies.

It is to be noted that the proposed sensor would exhibit high performance only if, the structural parameters i.e. chemical potential of graphene and the gap thickness ' d_a ' is optimized for the resonance excitation of the SPP. In the proposed structure, both these parameters are found to be interrelated. Figure 3, illustrates the variation of optimized gap thickness for resonant excitation of SPP with respect to the chemical potential of graphene. It is observed that with increase in chemical potential of the graphene monolayer, the optimised gap distance (the gap thickness for which, the obtained reflectivity is minimum) also increases. The reason is attributed to the fact that with increasing chemical potential, the real

as well as imaginary part of the dielectric constant of the graphene monolayer increases, due to which the modal field confinement decreases, and the air gap thickness for the resonant excitation increases. Thus, the proposed sensor has two degrees of freedom; the gap thickness and the chemical potential of graphene, which can be tailored for the high performance.

On the basis of optimized air gap for a given potential, Fig 4(a) illustrates the 3D plot of minimum reflectivity with respect to the resonance incident angle for different values of d_a (gap distance). This shows that the minimum reflectance first decreases with increasing gap distance, zero at 18 μm and then increases, indicating that there exists an optimal value of the gap distance for which the complete power gets transferred from incident wave to the SPP at a given chemical potential. It is also observed that there exists a minimum and maximum gap thickness of 13 μm and 25 μm for which there is significant coupling between the evanescent wave of the incident radiation and SPPs, while beyond this range of gap thickness the SPR vanishes. This is because at gap thickness less than 13 μm , a considerable part of the energy reradiates back into the prism [21] which prohibits the SPP excitation, whereas at thickness greater than 25 μm the gap distance is too large for the evanescent wave to excite the SPP. Further, Fig 4 (b), illustrates the reflection spectra for the sensor comprising of graphene monolayer of chemical potential 0.8 eV, for three different gap thicknesses $d=13 \mu\text{m}$, 18 μm and 22 μm . It is observed that the reflectivity is zero only for the gap thickness of 18 μm , thereby indicating the resonant excitation of SPP mode i.e. at this value complete energy gets coupled to the SPP. Further, the SPR curve broadens with the increase in the gap distance. Simultaneously, it is also observed that the resonance angle decreases with increasing gap distance, because the propagation constant of the SPP decreases, which results into weakly confined SPP.

To study the sensitivity of the sensor with above optimized gap distance, fig. 5 shows the variation of sensitivity with respect to the chemical potential of graphene for two different

gaseous analyte (refractive index = 1.000 and 1.020). It is observed that the sensitivity is higher at larger refractive index of the analyte for the considered range of chemical potential. Also, the sensitivity decreases with increase in the chemical potential of the graphene monolayer. This is because, at higher chemical potential, doping levels is higher, which decreases the SPP mode confinement as graphene becomes more like a perfect conductor with increased conductivity and supports SPP modes whose modal fields extend more into the dielectric media. Therefore, we found that for high sensitivity the sensor should operate at a lower chemical potential ($\mu=0.8$ eV for air gap of $18\text{ }\mu\text{m}$).

Now in order to study the performance of the sensor Fig.6 illustrates the variation of sensitivity as well as FWHM with the refractive index of the gaseous analyte of the proposed sensor having gap thickness $18\text{ }\mu\text{m}$ and graphene monolayer with chemical potential 0.8 eV . We see that the sensitivity increases from 29.92 deg/RIU for $n_d=1.000$ to 34.96 deg/RIU for refractive index $n_d=1.100$ as the resonance conditions for different gaseous analytes is satisfied at different resonance angle. We also found that FWHM decreases indicating enhanced detection accuracy (inverse of FWHM). The increase in detection accuracy may be attributed to the low absorption at terahertz frequency, i.e. at THz frequencies different loss mechanism becomes inactive as the conductivity is only from the intraband part and the interband loss becomes negligible, thereby decreasing absorption loss and hence FWHM decreases [22]. To quantify the overall performance of the sensor, we calculated the FOM. The FOM increases with increasing n_a as can be seen in fig.7 as FWHM decreases with increasing n_a and as a result, the FOM increases. The FOM values for $n_a=1.000$, 1.050 and 1.100 is found to be 962.0579 , 1058.824 and 1169.231 RIU^{-1} respectively which is higher than reported in the literature [23-25].

4. Conclusions

In conclusion a SPR based gas sensor using free standing doped graphene monolayer in terahertz has been proposed. Doped graphene monolayer acts as a plasmonic active material in terahertz which has been used for the excitation of SPP in an Otto-prism setup. The coupling efficiency of the evanescent wave and the SPP is found to be dependent on the gap distance between the prism base and the doping of monolayer graphene thereby influencing the sensitivity and the detection accuracy of the sensor. It is also found that with increasing chemical potential of the graphene monolayer, there is an increase in an optimal gap distance at which the strongest coupling occurs. We found that the sensitivity of the sensor increases from 29.92deg/RIU for $n_a = 1.000$ to 34.96deg/RIU for $n_a = 1.100$ along with the detection accuracy which increases from 32.15 deg^{-1} for $n_a = 1.000$ to 33.44 deg^{-1} for $n_a = 1.100$ thereby providing an ultrahigh FOM ($\sim 1150 \text{ RIU}^{-1}$) for the proposed sensor. We believe that such type of study will open a new window for high performance plasmonic sensor: a well-developed research area in and around visible, for terahertz sensing.

Acknowledgement

The present work is partially supported by MHRD funded project “CENEMA”.

References

- [1] S. A. Maier, *Plasmonics: Fundamentals and Applications: Fundamentals and Applications* (Springer, 2007).
- [2] W. L. Barnes, A. Dereux, and T. W. Ebbesen, Surface plasmon subwavelength Optics, *Nature*, 424, 824, (2003).
- [3] J. Homola, S. S. Yee and G. Gauglitz, “Surface plasmon resonance sensors: review *Sens. Actuators B-Chemical*54 (1999)3–15.
- [4] T. R. Globus, D. L. Woolard, T. Khromova, T. W. Crowe, M. Bykhovskaia, B. L. Gelmont, J. Hesler, and A. C.Samuels, THz-Spectroscopy of Biological Molecules, *J. Biol., Phys.* 29(2–3), 89 (2003).
- [5] A. Hassani and M. Skorobogatiy, Surface Plasmon Resonance-like integrated sensor at terahertz frequencies for gaseous analytes, *Opt. Exp.* 16, 20207(2008).
- [6] H. Barlow and A. Cullen, Surface waves, *Proc. IEE Part III: Radio Commun. Eng.* 100(68), 329 (1953).
- [7] J. B. Pendry, L. Mart’ín-Moreno L, and F. J. Garcia-Vidal, Mimicking surface plasmons with structured surfaces, *Science* 305, 847 (2004).
- [8] R. Ulrich and M. Tacke, Submillimeter waveguiding on periodic metal structure, *Appl. Phys. Lett.* 22, 251 (1973).

- [9] A. P. Hibbins, B. R. Evans, and J. R. Sambles, Experimental verification of designer surface plasmons, *Science* 308, 670–672 (2005).
- [10] M. J. Lockyear, A. P. Hibbins, and J. R. Sambles, Microwave surface-plasmon-like modes on thin metamaterials. *Phys. Rev. Lett.* 102(7), 073901 (2009).
- [11] Haizi Yao and Shuncong Zhong, High-mode spoof SPP of periodic metal grooves for ultrasensitive terahertz sensing, *Opt Express*, 22(21), 25150(2014).
- [12] Choon How Gan, Analysis of surface plasmon excitation at terahertz frequencies with highly doped graphene sheets via attenuated total reflection, *Appl. Phys. Lett.* 101, (2012).
- [13] Novoselov et.al. *Science*, Electric Field Effect in Atomically Thin Carbon Films 306(5696), 666, (2004).
- [14] Frank H. L. Koppens, Darrick E. Chang, and F. Javier Garcia de Abajo, Graphene plasmonics: A platform for strong light-matter Interaction, *Nano Lett.*, vol 11(8), (2011).
- [15] C. H. Gan, H. S. Chu, and E. P. Li, *Phys. Rev. B*, Synthesis of highly confined surface plasmon modes with doped graphene sheets in the mid infrared and terahertz frequencies, vol 85, 125431 (2012).
- [16] E. V. Loewenstein, D. R. Smith, and R. L. Morgan, Optical constants of metal oxides in the far infrared region, *Appl. Opt.* 12, 398(1973). 10
- [17] B. Wunsch, T. Tauber, F. Sols, and F. Guinea, Dynamical polarization of graphene at finite doping, *New J. Phys.* 8, 318 (2006).
- [18] B. Guo, L. Fang, B. Zhang, and J.R. Gong, Graphene doping: a review, *Insciences Journal*, 1(2), 80-89 (2011).

- [19] Z. Lin, G. H. Waller, Y. L. M. Liu, C. P. Wong, Simple preparation of nanoporous few-layer nitrogen-doped graphene for use as an efficient electro catalyst for oxygen reduction and oxygen evolution reactions, *Carbon* 53, 130-136 (2013).
- [20] P.K. Maharana, S. Bharadwaj and R. Jha, Electric field enhancement in surface plasmon resonance bimetallic configuration based on chalcogenide prism, *J. of Appl. Phys.* 114, 014304 (2013).
- [21] A. Otto, Excitation of nonradiative surface plasma waves in silver by the method of frustrated total reflection, *Z. Angew. Phys.* 21(4), 398(1968).
- [22] M. Jablan, H. Buljan, and M. Soljacic, Plasmonics in graphene at infra-red frequencies, *Phys. Review B*, 80, 245435 (2009).
- [23] R. Singh, W. Cao, I. A. Naib, L. Cong, W. Withayachumnanku and W. Zhang, Ultrasensitive terahertz sensing with high-Q Fano resonances in metasurfaces, *Appl. Phys. Lett.*, 105, 171101 (2014).
- [24] L. Cong, S. Tan, R. Yahlaou, F. Yan, W. Zhang, and R. Singh, Experimental demonstration of ultrasensitive sensing with terahertz metamaterial absorbers: A comparison with the metasurfaces, *Appl. Phys. Lett.*, 106, 031107 (2015).
- [25] Y. Zhang, T. Li, B. Zeng, H. Zhang, H. Lv, X. Huang, W. Zhang and A.K. Azad, A graphene based tunable terahertz sensor with double Fano resonances, *Nanocall*, 7, 2682 (2015).

Figure Captions

Fig1: Schematic diagram showing the sensing mechanism via attenuated total reflection using a high-refractive-index prism and graphene monolayer at Terahertz frequency.

Fig 2(a): Real part of ϵ_g as a function of frequency for different chemical potential (b): Imaginary part of ϵ_g as a function of frequency for different chemical potential.

Fig 3: Variation of air gap with chemical potential for monolayer graphene.

Fig 4: (a) 3D plot of the variation of minimum reflectance with resonance angle and gap distance, (b) Variation of reflectance with incident angle for different value of gap distances.

Fig 5: Variation of sensitivity of the gas sensor with respect to the chemical potential of monolayer graphene for two different refractive indices of the gaseous analyte.

Fig 6: Variation of sensitivity and FWHM with refractive index of the gaseous analyte. Inset: The SPR reflectance curve for two different refractive index of gaseous analyte.

Fig 7: Variation of FOM with refractive index of gaseous analyte.

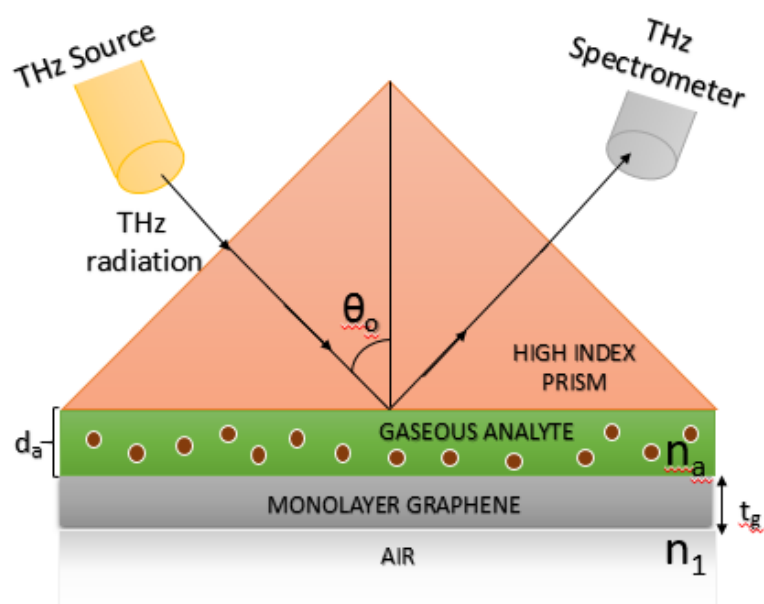


Figure 1

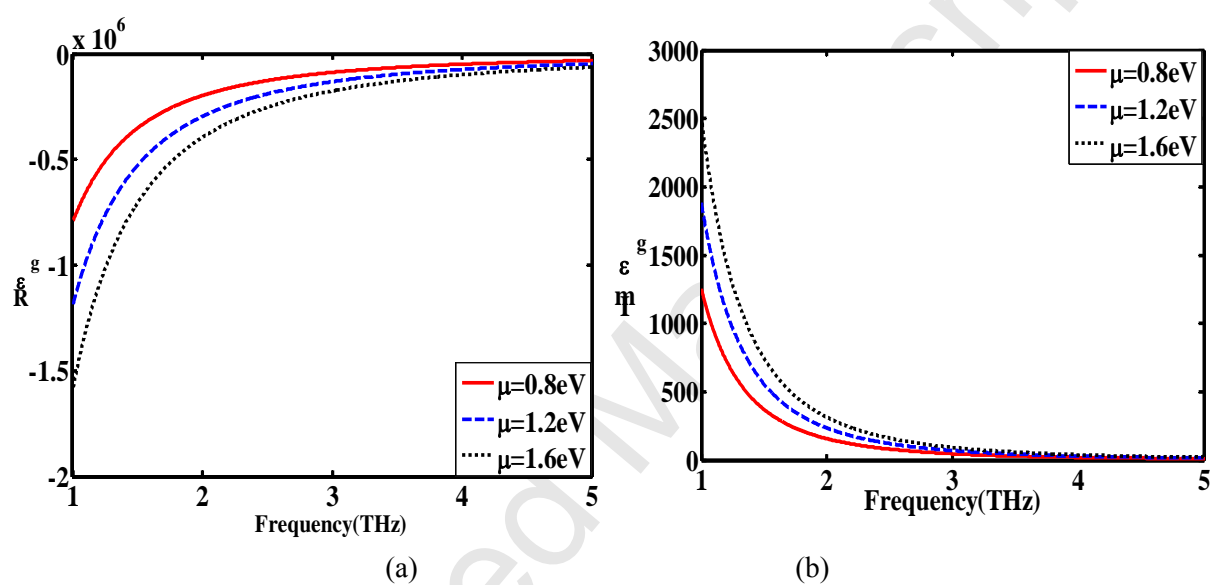


Figure 2

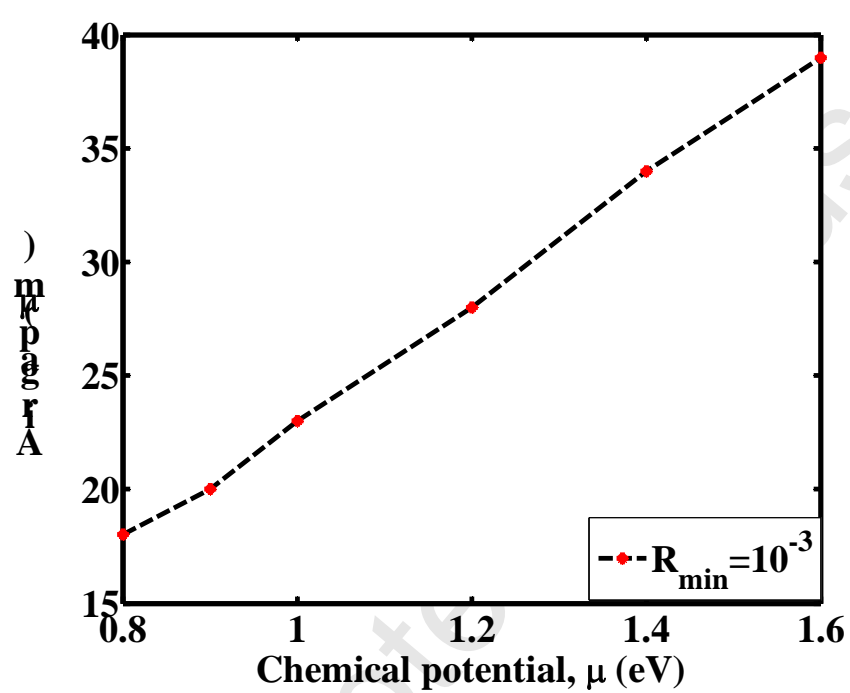


Figure 3

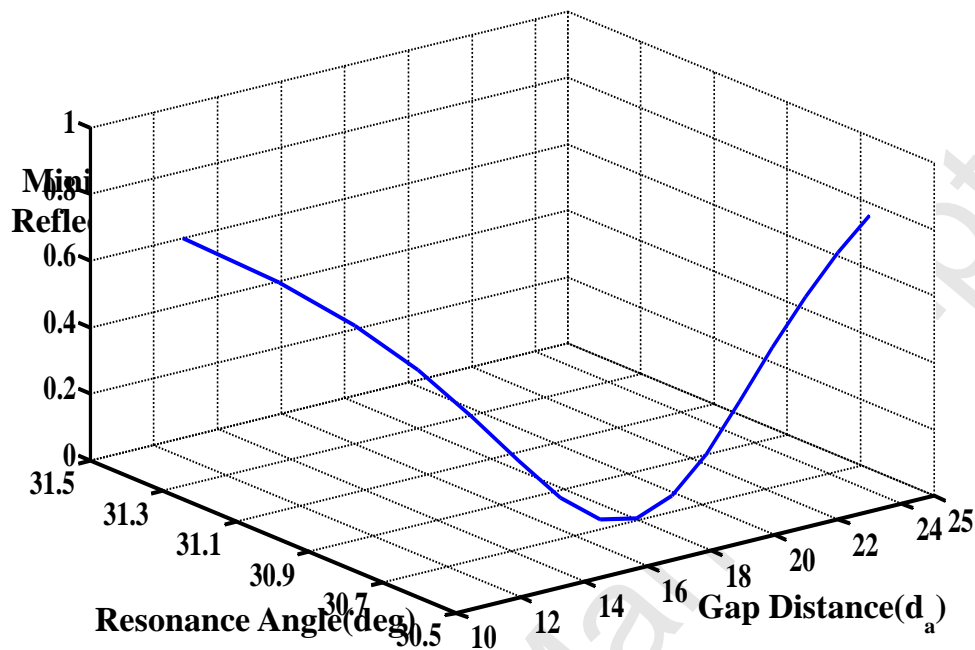


Figure 4(a)

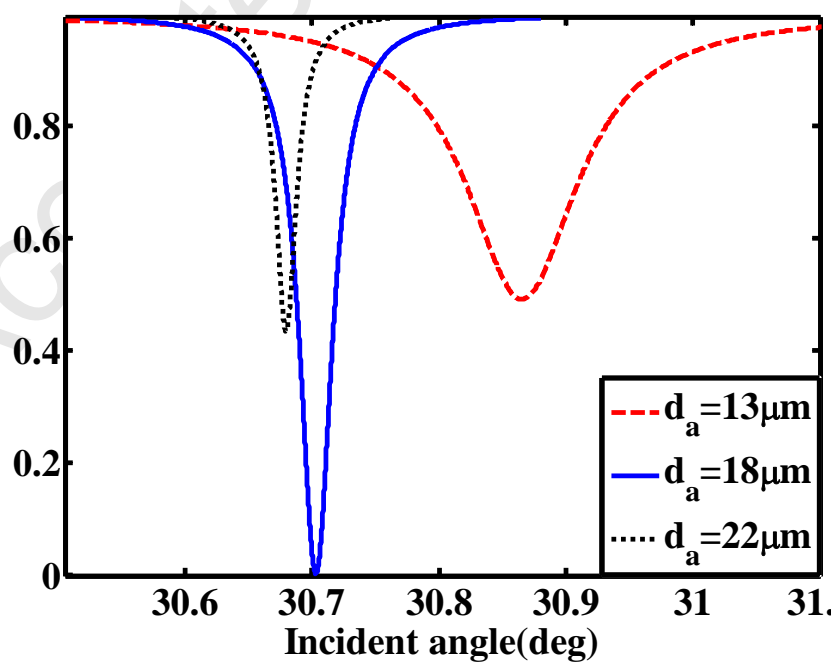


Figure 4(b)

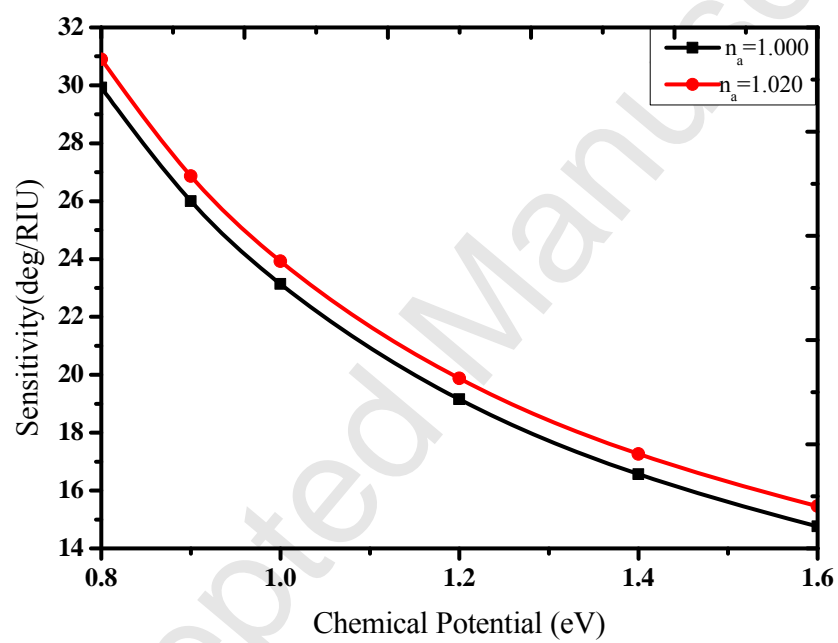


Figure 5

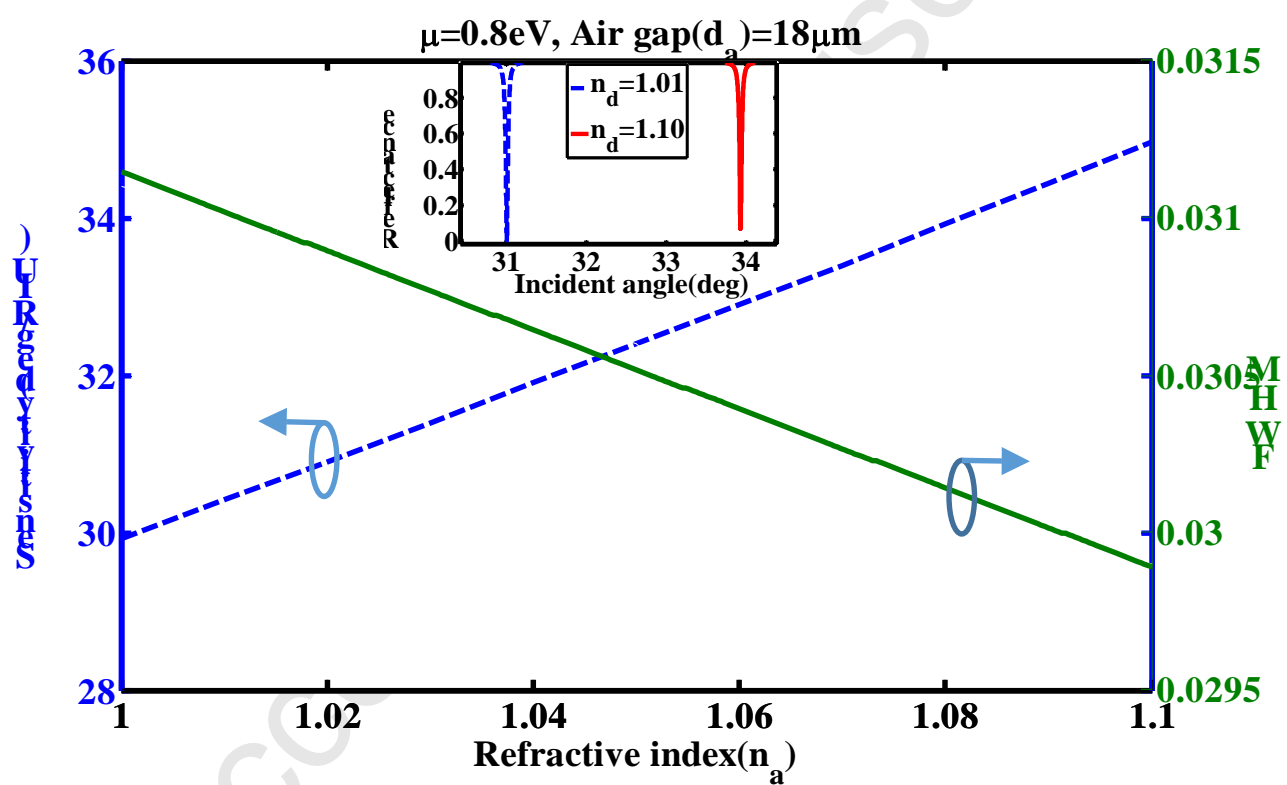


Figure 6

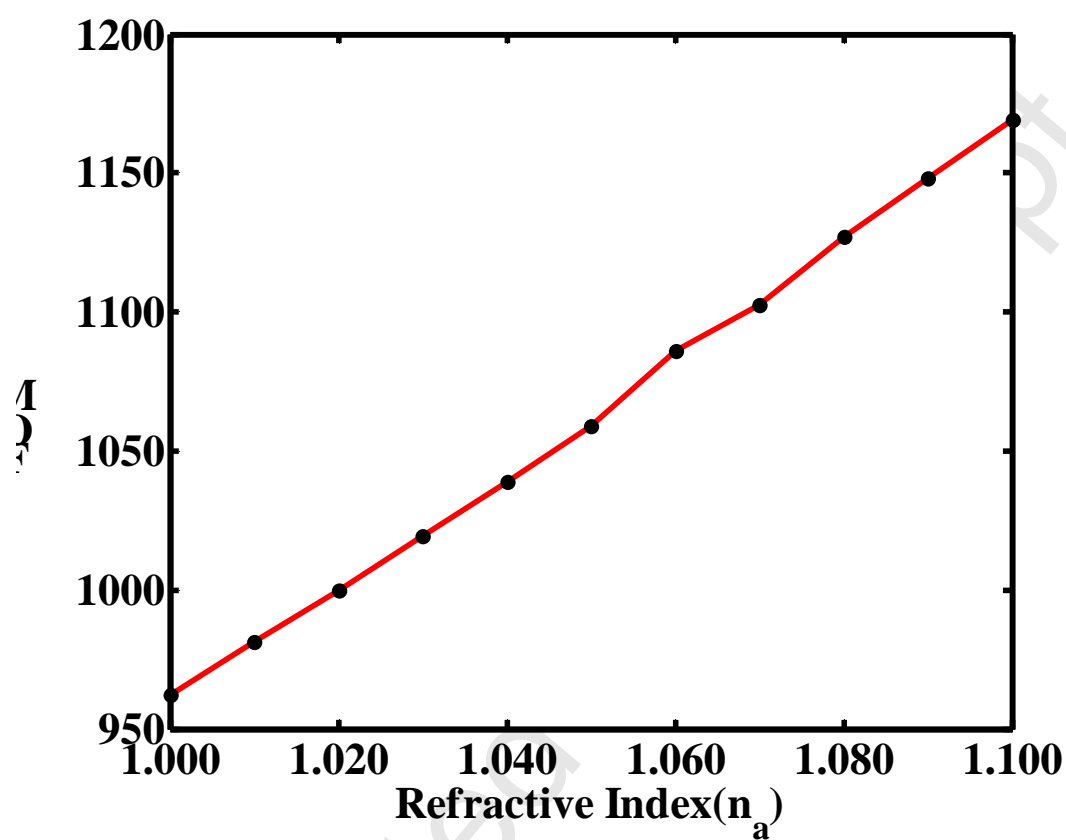


Figure 7

Biographies

Amrita Purkayastha received her B.Sc degree from Delhi University and joined IIT Bhubaneswar for her MSc. Since December 2013 she was working at Nanophotonics and Plasmonics Laboratory at IIT Bhubaneswar for her master thesis.

Triranjita Srivastava received her M.Sc. degree from DDU Gorakhpur University, Gorakhpur, U.P., India in 2005 and Ph.D degree from Indian Institute of Technology Delhi, India in 2010. From April 2011 to May 2012, she was an Assistant professor in department of Applied Physics at Delhi Technological University, Delhi, India. Currently, she is working as Assistant Professor in department of Physics, Kalindi College (University of Delhi), New Delhi, India. Her areas of research are plasmonics, integrated optics and optical sensors. She has published more than 20 research papers in different international journals of repute.

Rajan Jha received his MSc and PhD degree from Indian Institute of Technology Delhi, India in 2001 and 2007 respectively. From early 2008 to July 2009, he was a post-doctoral researcher at ICFO–The Institute of Photonics Sciences, Barcelona, Spain. He is a recipient of 2015 ICO-ICTP Gallieno Denardo award, received DAAD Fellowship in 2013 and was awarded JSPS fellowship in 2009. He is an Associate of Indian Academy of Sciences, Bangalore and Regular Associate of International Centre for theoretical Physics-ICTP. He is currently working as Assistant Professor of Physics in School of Basic Sciences at Indian Institute of Technology Bhubaneswar, India. He is a regular member of Optical Society of America (OSA) and is a life member of Optical Society of India (OSI). His areas of research are Sensors, Waveguides & interferometer. He has published more than 50 research articles including a review article in international journals of repute.